Studying mechanosensing at the molecular level by combining cell stretching and super-resolution microscopy : the case of integrin adhesions and the cytoskeleton

José Filipe Nunes Vicente

université de BORDEAUX

THÈSE PRÉSENTÉE
POUR OBTENIR LE GRADE DE

DOCTEUR DE

L'UNIVERSITÉ DE BORDEAUX

ÉCOLE DOCTORALE DES SCIENCES DE LA VIE ET DE LA SANTÉ
SPÉCIALITÉ : BIOLOGIE CELLULAIRE, NEUROSCIENCES

Par José Filipe NUNES VICENTE

Studying mechanosensing at the molecular level by combining cell stretching and super-resolution microscopy: the case of integrin adhesions and the cytoskeleton

Sous la direction de : Grégory GIANNONE

Soutenue le 27 Novembre 2020

Membres du jury :

Mme. MONTCOUQUIOL, Mireille	Directeur de recherche (INSERM), NCM	Présidente
M. GRASHOFF, Carsten	Professeur, IMCB, University of Münster	Rapporteur
M. THÉRY, Manuel	Directeur de recherche (CEA), IHU	Rapporteur
Mme. LÉVÊQUE-FORT, Sandrine	Directeur de recherche (CNRS), ISMO	Examinatrice
M. LETERRIER, Christophe	Chargé de recherche (CNRS), INP	Examinateur
M. NASSOY, Pierre	Directeur de recherche (CNRS), LP2N	Invité
M. GIANNONE, Grégory	Directeur de recherche (CNRS), IINS	Directeur de thèse

‘Those who have crossed

With direct eyes, to death's other kingdom

Remember us - if at all - not as lost

Violent souls, but only

As the hollow men

The stuffed men.’

T.S. Elliot

Para o João Pedro Amado Coelho Nunes Vicente,

O teu mano doutorou-se. Gostava que estivesses aqui.

‘In the beginning the Universe was created. This has made a lot of people very angry and been widely regarded as a bad move.’

Douglas M. Adams

Acknowledgements

Throughout the course of this PhD, I heard people describing it in many curious ways. A ‘marathon’, a ‘rollercoaster’, ‘driving a car’, ‘you actually look healthy’ and other ambiguous expressions. I believe any expression can be correct, depending on your state of mind. A PhD is a particular experience, one where we are often pushed to the limit, and when things often do not go as we intended. Still, I can gladly say I finish this PhD as a more complete researcher and human, but also aware that I still have a lot to improve. And while we emphasize a lot the importance of the self in achieving a PhD (or anything in the current society), nothing would be possible without the help, guidance, sacrifice and friendship of many along the way.

I would start by thanking to all the people who, amidst a global pandemic, gladly accepted to evaluate my PhD work and be a part of my jury. My sincere gratitude to Carsten Grashoff and Manuel Théry for accepting to be the referees of this thesis. A gratitude which extends to the remaining members of the jury committee, Sandrine Levêque-Fort, Christophe Leterrier and Mireille Montcouquiol. A special mention to the invited member Pierre Nassoy, not only for his presence but for all the fruitful collaborations our teams have engaged in throughout the years.

My next thought goes to my mentor and supervisor Grégory Giannone. I often say to people that Greg, before all the rest, has a valuable trait: he is a scientist but also a human being. He cares, he encourages and he thinks about his students and the lab. He has made me feel valued and appreciated from day one, being an immense source of help, wisdom and motivation. Greg is still the guy with more than 20 years of research experience who reacts like a child when he sees a beautiful super-resolution image or a Drosophila larvae moving around. His sheer enthusiasm and passion for science are a great inspiration, one that sometimes comes out as stress or agitation, which I understand; he wants to try everything and answer all the questions. Shouldn’t we all be like that? Also, he is are one heck of a scientist. I became a little less of a tool in science because of him.

Then, but not less important, comes the rest of our lab. Olivier Rossier, which is the closest thing to a reincarnation of a rock star in science and can alternate successive jokes with very insightful hints and advices. My office colleagues who are no longer in the lab, Amine Mehidi and Thomas Orré, did a great job in introducing me to all the wonderful aspects of French culture (depends on our perspective of course). But they also passed me the obsession for figure making, macro development and a succulé scientific integrity. I owe them a lot, for better and for worse. Ani Jose, my Malayali boomer friend and optics genius, I truly believe some of our conversations in the office grant us a special place in hell or in heaven. Thank you for being such a great (or terrible) counterpart and knowing every dank corner of the internet. Our lab manager, Mélanie Fabre, whom I deeply thank every day for being so cool and relaxed, which makes everything

seem so easy and smooth in the lab. Zeynep for being always in such a cheerful mood and for her many years as a true workhorse of a technician; and Tianchi for setting up alone a great Drosophila project which will be very helpful in my future work. Florelle, which in paper was from the Choquet team, but in her heart was a Giannone; you were a great adoptive lab (and desk) mate and I will miss your absurd jokes and rants about the Béarn. And, of course, all my other lab colleagues for their presence and help: Adrien, Maureen, Armand, RK, Sophie and Lucas. I also have to thank one of the best collaborators of my project, Cécile Leduc, for her kindness, support and enthusiasm. We make every experiment count!

For all the microfabrication work performed on this thesis, I have to thank the elite group of cell organizers at IINS. Nathalie and Aurélien, for their excellent support and technical advice, as well as their positive (and slightly sarcastic) mood. And of course Pierre-Olivier, who in 10 minutes can tell you all about the corporate world of cell solutions, give you plenty of great advice, make fun of you and later go for a beer. A pity that he supports PSG.

I am fully aware of how lucky I am for having done my PhD in such a renowned institute such as the IINS, in a great campus such as the Neurocampus Bordeaux. Especially coming from a scientific background of a country where funding is not always available. I am grateful for the 4th year of PhD extension grant given by LABEX Bordeuax. At IINS, I could count with an extremely dedicated culture team (neurons and cell lines!), one that spoils us way too much, as well as amazing technical personnel in molecular biology and biochemistry. I would like to thank Rémi Sterling in particular for all the tutorials on technical drawing and 3D-milling, as well as the book recommendations and insightful conversations. And Sébastien de la Comédie Française for nice football discussions and for being a top level person. I would also like to thank all my lab mates and buddies in IINS: Matthieu Lagardère, Matthieu Meunier, Léa, Camille, Sandra, Benjamin, Margherita, Giorgia, Ingrid, Andrea, Marine, Agatha, Zoé, Dario, Ruth and Aron for all the nice happy hour discussions, parties and moments. Also for my buddies at other institutes: Camille Quilgars, Paula, Chistopher, Vangelis, Louisa, Suzanne, Tifenn and Thomas Kerloch.

Throughout these years in Bordeaux, I was lucky enough to have met fantastic people and formed a group of unique friends, one which I will forever cherish. Moving away will also be tough because I'm not sure if I will ever have the wholesome group I had here. I have to start of course with the holy Triad of the Apocalypse. Dr. José de la Cruz, who is simply a fantastic human being and a Sir of many crafts: non-official tourist guide of Bordeaux, a man of class, science and ganso, a craftsman of francesinha and Sá Pessoa, purveyor of CRF, traveler of San Sebastian and Angôuleme, the list goes on. If you don't win a Nobel or at least a MacArthur grant, it's because the world is in shambles. Soon-to-be Dr. and musician Tomás JordSi, melancholic and enthusiast, proud and vulnerable, and a source of great ideas: 'let's go there, buy one chicken, one bread and a bottle of wine: simple, tasty and cheap'. In the words of the immortal Pau Donés, 'Bonita la amistad, bonita la risa, bonita la gente cuando hay calidad'. And finally, Dr. Thiago Campello:

the terrible pun that always lands, the router to my internet, Italia Marriage Cup 2017, o sarrabulho da minha cabidela, the wood for my sheep, and the Air that I breathe after drinking from the always-full glass. You are the adoptive brother I wish I had.

For Κωνσταντίνα, my (next door) lab mate, former (and missed) flat mate and current (hopefully forever) friend, it's hard to find words because probably we used them all. Luckily, we never run out of things to say. May we always enjoy each other's company as if we had just met. Vernon and Alex for being the sweetest, craziest, most open-minded party hosts I met here in Bordeaux. Marlene, who is a force of nature, a great dinner host, and an extremely original character; but keep in mind that this is not a sad dedication, so I won't go any further. Mario, whom I have travelled with a lot within a few square meters, similar to me in so many things, different in so many others. Probably because of all the places where we go on our heads. A special mention for Camille, Vladmir Cauchemar, Eva, Alessandro, Mattia Pau and Julio, for being more than just friendly lab mates, but also great homies, partygoers and travel companions.

Não podia, como é óbvio, esquecer a nossa comunidade lusófona de investigação, que tanto cresceu e mudou nos úlitmos anos. Os nossos jantares míticos de Natal, as almoçaradas de domingo que acabam em borracheira, os concertos, as saídas à última da hora, as aulas de francês e claro o golo do ÉDER. À Eva, mulher de grande carácter e que abandonou Bordeaux demasiado cedo, espero que encontremos sempre um cantinho para beber um sem rótulo e bater um Jimi Hendrix ao som de Pink Floyd ou de OMIRI. Muitas foram as festas aí em que o pessoal deu mais que tudo, e só por sorte a casa não foi, literalmente, abaixo. Ânia, sempre pronta para uma conversa de uma hora a meio do dia de trabalho, um almoço que descamba em caos e não te preocupes, és mais jovem que muitos. À Alexandra e à Nanci, que chegaram aqui comigo e por quem tenho um carinho especial. Teremos sempre Paris e, sobretudo, uns aos outros. Mas está na hora de seguir caminhos diferentes, por favor não façam post-doc no mesmo sítio que eu, ficava mais contente se me viessem visitar.

Je dois aussi remercier au groupe du Muay Thäi, en particulier à Kevin et à Shaft, mais aussi à tous les nakmuays du dojo. Pendant 4 ans, vous avez soulagé tous mes stresses et pressions du travail en utilisant une méthode très efficace : celle de se faire casser la gueule avec de l'amour. J'ai aussi réussi ce doctorat grâce au Muay Thäi, parce qu'on apprend toujours à aller au-delà de nous-mêmes, à bien maîtriser les bases, à respecter son adversaire et à jamais lâcher.

My friends here in Bordeaux are amazing; but the ones in Portugal do not lag behind. I wish they could all co-exist elsewhere other than my head. Manuel Maria Osório, companheiro da MÁ BIDA, você é um uísque em qualquer lugar ao som de GRUPO NOVO ROCK. Aventuremo-nos pela MÁ BIDA em LISBONERA ou NUMANCIA buscando a derradeira festa. Tudo será narrado n'O Seu livro, o prolongamento Natural desta Tese. João Pedro, fonte aleatória de ideias e caos, ordem desorganizada dos elementos da matéria. Turbilhão que roda acima de muitos e que me percebe como poucos. Sempre que regresso a Portugal fazemos/falamos/não falamos/não

existimos/explodimos/implodimos e isso faz-me muita falta na vida. Vouzela, o resto da malta que por lá passa, e que me fazem apreciar e muito as minhas férias. Marcel, PhD e imigrante, monsieur de classe e atleta, e amigo de longa data, a ver se finalmente fazemos uma viagem. Ao grande mestrado de BCM, tão inteligentes como avariados, e que mostram que a ciência é esforço e talento mas também convívio, jantares e borga, porque sem isso nada vale a pena.

La Família de Coimbra, um rochedo, e uma fonte constante de grandes viagens internacionais durante esta tese. Bélgica foi antes, mas não se esquece. Aprendi aí a andar de bicicleta e o resto é história, agora são 100 km por dia se for necessário. Londres para inglês ver, Berlinde atrás do maluco, Craconacóvia, comida 10/10 (em todos os restaurantes e não só), Buda&Peste entre uma sauna e o bar das ruínas. E tantos foram os jantares de Ano Novo que tão bem me fizeram, regressava a Bordeaux cheio (em todos os sentidos). Débora e Alexandre, é agora que eu penso no campismo da Figueira e os anos saltaram, eu juro que saltaram. Débora, nem sei quantas vidas já vivemos em 10 anos, e quantas conversas tivemos. Não prometo que volto já, mas ainda há muito a dizer (e a viver). Haja vinho, bordel e lágrimas, e está tudo bem. Alexandre, piadas secas, garrafeira 10/10 e um amigo para a vida (com seguro e tudo); João, porque já alcançou muito, lutou muito, foi sempre leal e nunca fez disso um drama; toda a gente podia aprender contigo. À Ticha, que sofreu para me ensinar a andar de bicicleta em Antuérpia e acabou com um sapato estragado, o que simboliza bem a paciência que sempre teve para mim.

A minha família preparou-me para isto sem eu nunca me aperceber. São uns autênticos escroques. Foi a liberdade, de pensamento e de escolha. Foi a abertura de espírito, a união, o humor em momentos impossíveis. E aqueles discos do Gainsbourg no carro? A roadtrip França 2007? Não digam que não estava ali marosca. Ao papá, (psicólogo?), por me ensinar que nunca se deve esperar nada do dia de amanhã, a não ser uma vitória do Benfica. Agora já percebo Sócrates: a escola nunca acaba e os professores nunca morrem. Deixei assim às galinhas, a luta pela capoeira. À mamã, que não existe, porque ninguém pode ser assim tão boa pessoa. Eu tento gostar genuinamente dos outros, mas tu abusas. O papá, provavelmente ainda a pensar na sorte que teve, diz que não sabemos quão especiais somos por te termos a ti. Eu sei, só que pronto, é mais fácil brincar. Para a TOTÓRIA, que vai dizer que não percebe nada desta tese quando sabe muita coisa. De ti só espero uma coisa: que sejamos amigos para sempre, mas sem merdas. Ao João, se eu pudesse voltar atrás, não te deixava cair. Nunca mais.

I would like to finish this with someone who I only met in my last year of PhD. However, I have the impression it has been a long time since you first wanted me to shut up and stop bothering everyone at the party. You saw through my skin and decided to pick me up and protect me. You broke all my boundaries and took me to a world which I had never seen before. You are a plant who blossoms every day in a different way and makes me smile in the most unexpected occasions. Your soul is strangely akin to mine, to a point that freaks me out sometimes. In our weirdness and in our enthusiasm, loving you is so natural that it became part of me.

Abstract

Detection and conversion of mechanical forces into biochemical signals is known as mechanotransduction. From cells to tissues, mechanotransduction events regulate migration, proliferation and differentiation in physiological and pathological processes such as immune response, development and metastasis. Integrin adhesion sites (IAS) are mechanosensitive complexes structures essential for many of these processes, regulating cell adhesion, intracellular signaling and force transmission. Mechanosensing is based on protein deformations and reorganizations in response to force. However, the molecular mechanisms of mechanosensing in live cells remain poorly understood. Using a cell stretching device compatible with super-resolution microscopy (SRM) and single protein tracking (SPT), we explored the nanoscale deformations and reorganizations of individual proteins inside mechano-sensitive structures. We achieved SRM after live stretching on intermediate filaments, microtubules and integrin adhesion sites. Simultaneous SPT and stretching showed that while integrins follow the elastic deformation of the substrate, actin filaments and talin also displayed lagged and transient inelastic responses associated with active actomyosin remodeling and talin deformations. Capturing acute reorganizations of single-molecule during stretching showed that force-dependent vinculin recruitment is delayed and depends on the maturation state of integrin adhesions. Thus, cells respond to external forces by amplifying transiently and locally cytoskeleton displacements enabling protein deformation and recruitment in mechano-sensitive structures. We then adapted our strategy to decipher the molecular mechanisms of mechanosensing in neurons. In the nervous system, mechanotransduction regulates pain sensation, axonal guidance, proprioception, and brain trauma. The membrane periodic skeleton (MPS), a subcortical periodic actin-spectrin lattice, could have potential mechanosensitive roles in axons and dendrites. We modified our cell stretching device to enable long-term neuronal culture and stretching of neurons combined with SRM/SPT imaging of MPS proteins.

Keywords: Mechanosensing, integrin adhesion sites (IAS), cytoskeleton, cell stretching, super resolution microscopy, single particle tracking.

Résumé

La détection et la conversion des forces mécaniques en signaux biochimiques sont connues sous le nom de mécanotransduction. Des cellules aux tissus, les événements de mécanotransduction régulent la migration, la prolifération et la différenciation lors de processus physiologiques et pathologiques, tels que la réponse immunitaire, le développement et la formation de métastases. Les sites d'adhésion intégrine-dépendant (IAS) sont des structures complexes mécanosensibles essentielles qui régulent l'adhésion cellulaire, la signalisation intracellulaire et la transmission de force au cours de ces mêmes processus. La mécanosensibilité cellulaire est basée sur la déformation et la réorganisation des protéines en réponse à des forces. Cependant, les mécanismes moléculaires de la mécanosensibilité dans les cellules vivantes restent mal compris. En utilisant un dispositif d'étirement cellulaire compatible avec la microscopie de super-résolution (SRM) et le suivi de protéines individuelles (SPT), nous avons exploré les déformations et les réorganisations à l'échelle nanométrique des protéines au sein de structures mécano-sensibles. Nous avons réalisé des acquisitions de SRM sur des filaments intermédiaires, des microtubules et des sites d'adhésion intégrine-dépendant après étirement de cellules vivantes. Des experiences d'etirement cellulaire combinées au suivi de proteines individuelles ont montré que les intégrines suivent le déplacement élastique du substrat. Par contre, les filaments d'actine et la talin présentent également des réponses inélastiques différées et transitoires associées à un remodelage actif du cytosquelette actomyosine et à des déformations de la talin. La détection de la réorganisation des proteines à l'echelle moleculaire pendant l'étirement a montré que le recrutement de la vinculine force-dépendant est différé et dépend de l'état de maturation des sites d'adhésion intégrine-dépendant. Les résultats obtenus démontrent que la réponse mécanique des protéines n’est pas obligatoirement déclenchée par une transmission directe des forces externes. Au contraire, une contrainte mécanique externe déclenche une réponse active et déphasée de la cellule. Ce mécanisme amplifie les stimuli mécaniques faibles pour déformer ou recruter des protéines lors de la mécanosensibilité cellulaire. Nous avons ensuite adapté notre stratégie experimentale pour décrypter les mécanismes moléculaires de la mécanosensibilité dans les neurones. Dans le système nerveux, la mécanotransduction régule la sensation de douleur, le guidage axonal, la proprioception et les traumatismes cérébraux. Le squelette périodique membranaire (MPS), un réseau périodique sous-cortical d'actine et de spectrine, pourrait jouer un rôle mécanosensible dans les axones et les dendrites. Nous avons modifié notre dispositif d'étirement cellulaire pour le rendre compatible avec des cultures neuronales de plusieurs jours, afin d'étudier les réponses mécaniques des protéines composant le MPS par imagerie SRM/SPT.

Mots-clés: mécanosensibilité, sites d'adhésion intégrine-dépendant (IAS), cytosquelette, étirement cellulaire, microscopie de super-résolution, suivi de proteínes individuelles.

Table of Contents

List of Figures

Abbreviations

ABP – Actin binding protein
ABS – Actin binding site
ADP – Adenosine diphosphate
AFM – Atomic force microscopy
AIS – Axon Initial Segment
AnkG – Ankyrin G
Arp 2/3 – Actin-related-protein 2/3
ATP – Adenosine triphosphate
CAM – Cell adhesion molecule
Cas – CRK-associated substrate
CNS – Central nervous system
DNA – Deoxyribonucleic acid
DNA-PAINT – DNA Point Accumulation for Imaging in Nanoscale Topography
DONALD – Direct Optical Nanoscopy with Axially Localized Detection
ECM – Extracellular matrix
FAK – Focal adhesion kinase
FAs – Focal adhesions
FRAP – Fluorescence recovery after photobleaching
FRET – Fluorescence resonance energy transfer
FXs – Focal complexes
GFP – Green fluorescent protein
GTP – Guanosine triphosphate
IAS – Integrin Adhesion Sites
IFs – Intermediate Filaments
KO – Knock-out
L_p – Persistence length
mDia – mouse Diaphanous 1
MEF – Mouse embryonic fibroblast
MPS – Membrane periodic skeleton
MSD – Mean square displacement
NAs – Nascent adhesions
nN – Nanonewton
OT – Optical trap
PAINT - Point Accumulation for Imaging in Nanoscale Topography
PALM – Photoactivated Localization Microscopy

PIP_2 – Phosphatidylinositol 4,5-bisphosphate
pN – Piconewton
PNN – Perineuronal network
PSD-95 – Postsynaptic density protein 95
PSF – Point spread function
PSGL-1 – P-selectin glycoprotein ligand-1
Rac1 – Ras-related C3 botulinum toxin substrate 1
RESOLFT – Reversible Saturable Optical Linear Fluorescence Transitions
RhoA – Ras homologous member A
RNA – Ribonucleic acid
ROCK – Rho-associated, coiled-coil containing protein kinase or Rho kinase
SAF – Supercritical angle fluorescence
SFs – Stress fibers
SFK – Src family kinase
SIM – Structured Illumination Microscopy
SMFS – Single molecule force spectroscopy
SMLM – Single Molecule Localization Microscopy
SPT – Single particle tracking
sptPALM – Single particle tracking Photoactivated Localization Microscopy
SRM – Super resolution microscopy
STED – Stimulated Emission Depletion microscopy
STORM – Stochastical Optical Reconstruction Microscopy
SynCAM – Synaptic cell adhesion molecule
TIRF – Total Internal Reflection Fluorescence
ULF – Unit length filament
VASP – Vasodilator-stimulated phosphoprotein
VBS – Vinculin binding site

Preface

UFC: Ultimate Force Championship

Over the course of the last 15 years of my life, I have been an amateur athlete and keen enthusiast of martial arts and combat sports. My first steps were guided by discipline of karate, followed by the intensity of kickboxing and the current all-out madness of muay thäi. In all these various sports, one cannot avoid but marveling at the mechanics of the human body. How, after 6 months of clashing tibias with devastating low-kicks, our bones seem thicker and sturdier, as if they adapt to the impact. German anatomist and surgeon Julius Wolff had first described this in the 19th century, stating that the bone in a healthy person or animal will adapt to the loads under which it is placed. How, after excruciating routines of stretching, one is finally able to deliver a perfect high kick on the opponent's head through a newly acquired flexibility. And, of course, how our core progressively stiffens to countless punches and front kicks. Indeed, through martial arts, our bodies change from the outside but even more from the inside, where muscles, ligaments, bones and tendons become progressively adapted to the strenuous demands of martial arts. But, if we stop or ignore a proper training routine, we can quickly fall back to where we started. This is particularly gruesome flexibility-wise, where a constant stretching routine is required to avoid feeling rusty and clumsy when lifting the legs. All these mechanical responses and adaptations are truly fascinating to witness and, in my case, helped fostering my interests in the field of mechanobiology.

Mechanical forces are a continuous part of our lives and we are continuously sensing them, both consciously and unconsciously. The most immediate are touch and mechanical pain; the comfort of a chair, the sand in our feet, a roundhouse kick in the face, they all rely on touch or pain, on sensing the forces exerted by our surroundings. It is also the most omnipresent one; we can close our eyes and pretend to be blind, but touch will never go away. But, beyond touch or pain, many of our organs change their volume periodically, which is detected by specialized mechanoreceptors in a process known as 'stretch sensation' (Umans and Liberles, 2018). For instance, as the stomach fills over the course of a meal, sensory neurons detect the changes in volume and signal to the brain in order to inhibit feeding and promote digestion. We have thus to thank force sensing to prevent us from eating to death. Similar processes can be found in the heart (blood pressure), the lungs (breathing) or in the bladder (urination), each one with a specific goal (Umans and Liberles, 2018).

Even before birth, mechanical forces have already shaped and fine-tuned the embryo at the cellular and tissue level. They determine the orientation of the spindle during division, crucial for tissue growth and differentiation; they also regulate cell migration, differentiation and subcellular distribution of proteins, all to ensure a correct embryonic development (Nicoletta I.

Petridou et al., 2017). Many of these processes are equally important in adult organisms; cells continuously push and pull on their surroundings, and in turn are subjected to the compression from their neighbors and the substrate. It is therefore is not a surprise that, when this tightly run force-sensing ship has a leak, things go awry; cancer cells cannot properly integrate mechanical forces, which promotes their proliferation, tumor invasion and metastasis (Mohammadi and Sahai, 2018).

Across these various examples, there are two emergent concepts that will be central to this PhD thesis. First, there is mechanosensing, which is the set of mechanisms through which cells detect mechanical forces and stimuli. Second, there is mechanotransduction, which is the overall process by which cells detect mechanical forces and convert them into biochemical stimuli, eliciting specific responses. In many of these processes, cell adhesions play a central role in sensing and transmitting forces, as well as in mediating different signaling pathways.

Although we have amassed a considerable knowledge on the effect of mechanical forces in biological systems, the molecular mechanisms of mechanosensing are still unclear. How do cells detect organ stretch? Or changes of stiffness? And how do proteins inside cells respond to mechanical stress? The main goal of this PhD thesis was precisely to unveil the molecular mechanisms of mechanosensing governing force sensing in live cells. Over the course of the Introduction, I will reflect on how forces can be generated, detected and converted into biochemical signals through the interplay between different mechanosensitive structures. I will highlight how a molecular understanding of mechanosensing has emerged from *in vitro* force manipulations of proteins. The methods used in these studies will also be detailed, as single molecule force manipulation constitutes a strong basis of this work. I will follow this by a comprehensive review on integrin adhesion sites (IAS), which are the main mechanosensitive structures studied in this thesis. I will shift from a macro-scale perspective to a nano-scale description, approaching how IAS are nano-partitioned specialized complexes where protein dynamics is tightly coupled to force sensing and transmission. I will also highlight some of the important partners involved in IAS mechanosensing (talin, vinculin) and how they can act synergistically to detect mechanical forces. The main goal of this thesis was thus to explore the molecular mechanisms of mechanosensing in IAS.

Afterwards, I will discuss on how the cytoskeleton has a dual in mechanosensing and mechanotransduction by responding to forces. Finally, I will finish the introduction by addressing mechanosensing and mechanotransduction in neurons. I will also focus on an emergent cytoskeletal periodic lattice known as the membrane periodic skeleton (MPS). We do not know yet if the MPS is mechanosensitive; I intend to explore this possible connection, which constitutes the second goal of this PhD thesis.

However, this PhD thesis veers both into biological and methodological territory; if the main goal was to indeed explore the molecular mechanosensing in the IAS and later in the MPS,

it is of equal importance to develop methods to do so. In the Methods section, I will review the two major approaches I have used throughout this PhD work: cell stretching and super-resolution microscopy. In my work, I have combined them by developing a cell stretching device compatible with super-resolution microscopy and single particle tracking. I will finish this Methods section by providing a detailed preprint protocol describing the conception and application of the device for various experiments.

Using this approach, we studied the nanoscale deformations and reorganizations of individual proteins or protein assemblies inside mechanosensitive structures. This work has recently been published in Nature Cell Biology (Massou, Nunes Vicente, Wetzel et al. 2020), under the title 'Cell stretching is amplified by active actin remodelling to deform and recruit proteins in mechanosensitive structures'. In first section of the Results, I will present this publication, which constitutes the main part of the results in this PhD thesis. Again, this work is placed on that same intersection between methodology and mechano-biology. Thus, it first describes the development of a micromechanical device to combine cell stretching with super resolution microscopy and single particle tracking in various structures, from IAS to cytoskeletal filaments. Then, in a more mechano-biological perspective, we captured the acute mechanical response of proteins inside IAS in response to mechanical stretch. Finally, we studied individual protein reorganizations and recruitments inside IAS. We revealed that cells respond to external forces by amplifying transiently and locally cytoskeleton displacements enabling protein deformation and recruitment in mechano-sensitive structures.

In the second section of the Results, I will present how we adapted the stretching device to study MPS mechanosensing in neurons. Here, the majority of the results concern the development of new methods to stretch neurons and capture the mechanical response of the MPS using SRM and SPT. I will show how we enabled long-term culture of neurons on the device, imaged the mechanical response of MPS components with various SRM/SPT techniques and micropatterned the device to control cell geometry and orientation. With this, we have enabled a similar approach to what was performed in IAS: to capture the acute mechanical response of MPS proteins but also the nanoscale reorganization of the MPS in response to stretching.

Over the course of my PhD, I also developed other parallel projects. In the last section of the Results, I will present a third project in which we aimed to characterize the nanoscale dynamics and organization of β3-integrin in dendritic spines. For this, we studied the regulation of β3-integrin dynamics with SRM and SPT in wild type and integrin mutants.

Finally, in the Discussion and Perspectives, I will discern about the results I obtained throughout this thesis, with special relevance for our recent publication available on Chapter 3 (Results). I will expand on the discussion already present on the paper, while also approaching different perspectives and future experiments that could stem from our observations.

INTRODUCTION

1. Mechanobiology and mechanosensing: structures and mechanisms

Mechanobiology is an emergent field in the interface of physics, biology and engineering, which aims to understand how physical or mechanical forces shape cells and organisms. In this chapter, I will describe how cells can sense mechanical stimuli and convert them into biochemical signals, a process known as mechanotransduction. I will also present the main subcellular structures involved in such interactions. At the molecular level, mechanical force can deform and reorganize proteins, as well as reinforce or destabilize their interactions: I will approach several of these mechanisms. This molecular basis of mechanotransduction has emerged in great part due to *in vitro* force manipulations of individual proteins, molecular force sensors and other innovations. I will focus on single molecule force spectroscopy methods (optical and magnetic tweezers, atomic force microscopy), as well as molecular force sensors

1. On Growth and Form

'Among the forces which determine the forms of cells, whether they be solitary or arranged in contact with one another, this force of surface-tension is certainly of great, and is probably of paramount importance. But while we shall try to separate out the phenomena which are directly due to it, we must not forget that, in each particular case, the actual conformation which we study may be, and usually is, the more or less complex resultant of surface tension acting together with gravity, mechanical pressure, osmosis, or other physical forces'.

D'Arcy Wentworth Thompson, **1917, *On Growth and Form***

In 1917, the mathematician and biologist D'Arcy Wentworth Thompson published his book *On Growth and Form,* a seminal work on how the shape of animals and plants is influenced by scale and force (Thompson and Bonner, 2014). From the influence of tension in the form of an algae disc to the curvature of the shells found in nature, the work D'Arcy Wentworth Thompson is now considered a cornerstone of modern mechanobiology. Works elaborated prior

to Thompson's book had already suggest that tissues and organs could sense mechanical forces. Julius Wolff proposed in the 19th century that changes in the architecture and form of bones occurred as a consequence of mechanical stress, according to mathematical rules – known as 'Wolff's law' (Ruff et al., 2006). In 1868, Ewald Hering and Josef Breuer revealed a mechanosensory mechanism in the respiratory system known as the Hering–Breuer (HB) inspiratory reflex. The HB reflex is triggered by increased gas pressure in the airways and lungs to prevent over-inflation of the lung (Widdicombe, 2006).

As nicely described by the aforementioned works, a vast variety of mechanical forces shape and control all the biological systems. Mechanobiology – the science that studies this same relationship - has been largely revolutionized over the last thirty years due to impressive advances in imaging, molecular biology and methods to apply and measure forces. We now have a much deeper understanding of how mechanical forces control multiple cellular processes, from differentiation to morphogenesis. Compared to Wolff's or Thompson's works, we have also understood that this is not governed by mathematical laws, but rather by a complex interplay between mechanical forces, subcellular structures and biochemical pathways. In order understand this relationship, we first need to explore some of the main players involved in such mechanisms:

1. The extracellular matrix (ECM), which supports cells and influences cellular functions through its mechanical properties. Forces applied on the ECM will also impact cell behavior;
2. The subcellular structures that transmit and generate forces, probe the microenvironment, establish cell-ECM/cell-cell interactions and mediate both the detection and response to mechanical forces.

2. Extracellular matrix

The extracellular matrix (ECM) is both a component of the cell microenvironment and a product of cellular activity itself. Cells establish the ECM during development by secreting different proteins and are continuously remodeling it. Conversely, ECM physical and chemical properties influence cell behavior and physiology, controlling migration, growth, differentiation and survival (Cui et al., 2015; Dupont et al., 2011; Koser et al., 2016; Lo et al., 2000; Segel et al., 2019). This dynamic crosstalk is particularly relevant at the mechanochemical level; cells sense and regulate ECM mechanical properties to promote mechanical homeostasis (Hall et al., 2016; Van Helvert et al., 2018; Humphrey et al., 2014; Kim et al., 2017). Cells are also extremely sensitive to mechanical loads imposed on the ECM or on the adhesive substrate. Strains and stresses can modulate traction forces, cytoskeletal networks and activate signaling cascades (Chen et al., 2013; Hoffman et al., 2012; Hu et al., 2019; Rosowski et al., 2018).

Mechanical properties of the ECM comprise three main physical modules: stiffness, topology and confinement. Stiffness – the stress required to deform the tissue when it is strained – is probably the most well studied parameter, especially because it considerably varies across different organs and tissues, as well as throughout development (Barnes et al., 2017; Iwashita et al., 2014; Moore et al., 2010; Wells, 2013). Variations can go up to several orders of magnitude, from the extremely soft and deformable brain (<1kPa) to the highly stiff and resistant bone (15 GPa for cortical bone) (Barnes et al., 2017; Wells, 2013). ECM and tissue stiffness is a key aspect in regulating cell proliferation, differentiation, motility and survival (Dupont, S. Nature 2011, Meredith, J Mol. Biol. 1993). Emerging cell mechanics modules include porosity and nanotopology. The latter can be linked to the nano-organization of adhesive structures (Changede Nat Materials 2018, Van Helvert NCB 2018).

The mechanical properties of the ECM are largely dependent on a group of ECM core components: elastic fibers (composed by elastin and associated proteins), collagen, glycosaminoglycans (GAGs) and the related proteoglycans (Humphrey Nat Rev 2014). Elastic fibers confer both extensibility and resilience to tissues, while collagen contributes both to the stiffness and strength of tissues (Fig. 1). Among the proteoglycans, fibronectin regulates cellular processes, maintains tissue organization and participates directly in tissue repair (Wing Fibro 2011). ECM components are deposited by different cell types, of which fibroblasts are the main effectors; they deposit elastin for elastic fibers and different collagen types, as well as fibronectin (Humphrey Nat Rev 2014). Due to the sheer variability of components and properties, the ECM can greatly vary in composition and architecture; pathological conditions such as cancer can also alter ECM morphology (Fig. 1) (Despotović et al., 2020).

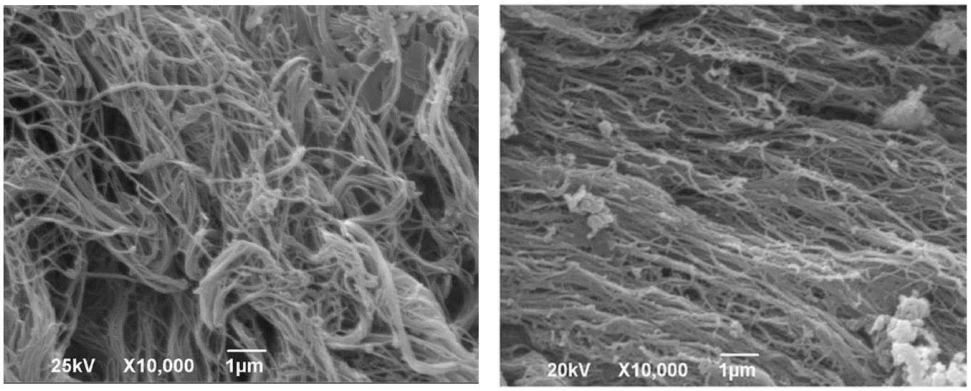

Figure 1: Different Morphologies of collagen fibers in the ECM

a, Representative scanning electron microscopy (SEM) images of collagen fibers in the lamina propria of colon mucosa in healthy human patients (left) and in cancer patients, 10 cm away from the malignant tumor (right). In healthy patients, collagen fibers form a relatively dense network with different microarchitectures, containing both fiber bundles but also many looser fibrils. Conversely, in the vicinity of the tumor, fibers are thicker and more aligned. Scale bars: 1 µm. Figure adapted from Despotović et al. 2020.

3. Structures involved in sensing, transmitting and generating mechanical forces

3.1. Cytoskeleton

The musculoskeletal system provides shape and support to the body through the combined action of bones, muscles, tendons, cartilages, ligaments and many other elements. A similar structure is recreated at the cellular scale: the cytoskeleton, a network of specialized proteins, regulates cell shape, movement and physiology. Three major elements comprise the cytoskeleton of mammalian cells: actin filaments, microtubules and intermediate filaments, along with associated proteins (Fig. 2). Similar to our musculoskeletal system, which also allows us to sense and exert forces, the cytoskeleton is also crucial in sensing, transmitting and generating mechanical forces. In parallel, the cytoskeleton is also a very dynamic entity, undergoing constant remodeling, which in turn is crucial for functions as diverse as cell morphogenesis, intracellular trafficking, cell migration, mitosis, synaptic plasticity or axonal outgrowth (Bard et al., 2008; Chazeau et al., 2014; Duarte et al., 2019; Dumont et al., 2012a; Katsuno et al., 2015; Latorre et al., 2018; Patel-Hett et al., 2011).

3.1.1. Actin filaments

In their essential configuration, actin filaments are linear, double-stranded polymers with a diameter of 5-9 nm (Holmes et al., 1990), composed by monomers of G-actin. Actin filaments are polarized, displaying two dynamically distant ends, called barbed (+) end and pointed (-) end. The barbed end elongates 10 times faster than the pointed end, at a rate of 11.6 $\mu M.s^{-1}$ (Pollard, 1986). Through *in vitro* measurements, actin filaments were shown to have a persistence length (L_p) in between 10-17 µm, according to different measurements (Gittes et al., 1993; Harasim et al., 2013). This parameter can be defined as the distance over which a filament changes orientation along its length, meaning that bending of one end does not affect the other (Blanchoin et al., 2014). If the filament is shorter than L_p, it behaves like a rigid rod. However, the *in vitro* values are not always verified in live cells, since mechanical constraints and protein activity (actin-binding or motor) bend actin filaments below their persistent length (Kovar et al., 2006; Murrell and Gardel, 2012).

A remarkable feature of actin filaments is the sheer variety of structures they can form throughout the cell: lamellipodium, stress fibers, filopodia, blebs or dendritic spines, each one with a specific organization and function (Blanchoin et al., 2014). Such variety results from the intrinsic properties of actin but also from the vast array of proteins – more than 100 - that can interact with actin filaments, known as actin binding proteins (ABPs). These include actin

nucleators and elongators (formin, Arp2/3) (Machesky et al., 1999; Romero et al., 2004), severing proteins (cofilin) (Galkin et al., 2011), regulators of polymerization (profilin) (Carlsson et al., 1977) and capping proteins (adducin) (Kuhlman et al., 1996). These proteins, together with their respective partners, are spatiotemporally coordinated across the cell to regulate the architecture and dynamics of actin structures (Chazeau et al., 2014; Mehidi et al., 2019). Another critical element that associates to actin filaments is myosin, a family of proteins involved in contractility. Of particular interest to this work are the myosin II class of motor proteins, which are mostly expressed in non-muscle cells, and are hence commonly known as non-muscle myosin II (NM II) motor proteins. There are three isoforms of NM II – A, B, C – which play key roles in cell adhesion and migration (Vicente-Manzanares et al., 2009). Over the course of this PhD thesis, I will refer to them as myosin II proteins.

Through these various subcellular structures and interactions, the actin cytoskeleton regulates a variety of cellular functions, including cell motility and migration, axonal growth, muscle contraction, cytokinesis, phagocytosis or synaptic transmission (Pollard Science 2009, Blanchoin Phys Rev 2014, Chazeau Cell Mol Life Sci 2016). This also requires a tight coordination between actin turnover and remodeling. It is therefore not surprising that dysfunctions in the actin cytoskeleton are so tightly linked to different pathologies. Altered motility is a hallmark of metastasis, which in turn can stem from mutations in ABPs and aberrant actin dynamics (Fife et al., 2014). Deregulation of actin dynamics can also lead to impaired immune responses(Pfajfer et al., 2018) and neurodegenerative disorders (Kommaddi et al., 2018)

3.1.2. Microtubules

Microtubules are long polymers composed of α and β-tubulin heterodimers that associate laterally to form hollow cylinders. They are characterized by two main features. First, an intrinsic polarity with a minus end and a plus end and second, they are highly dynamic structures, undergoing either growth or shrinkage (Brouhard and Rice, 2018). Growth occurs by adding guanosine triphosphate (GTP)-Tubulin dimers to the microtubule plus end, where a stabilizing cap is formed; if this cap is lost, then shrinkage occurs. Microtubules switch frequently between these two states, a process known as dynamic instability. This is controlled by microtubule-associated proteins (MAPs), such as polymerases or molecular motors, who coordinate to determine whether microtubules grow or shrink (Brouhard and Rice, 2018). Dynamic microtubules are able to exert pushing and pulling forces which are essential for cell division, driving chromosome segregation and centrosome separation - but also in organelle positioning (Vleugel et al., 2016). Microtubules are also essential in trafficking of vesicle cargoes and organelles (by acting as tracks), as well as in the intracellular organization of organelles.

Another key functional aspect of microtubules is that they are the most rigid of all cytoskeletal polymers. Their flexural rigidity, or rigidity to bending, is ~100 times higher than actin filaments *in vitro* (Gittes et al., 1993). As a consequence, their persistence length is also several orders of magnitude higher than other cytoskeletal biopolymers (Hawkins et al., 2010). Several reports place it between 1-10 mm; as a comparison, the persistence length of actin filaments is thought to be ~10-20 µm (Blanchoin et al., 2014; Gittes et al., 1993; Hawkins et al., 2010). Such features are essential for the role of microtubutles in intracellular trafficking, directional migration or connecting and pulling chromosomes during cell division (Brangwynne et al., 2007).

3.1.3. Intermediate Filaments

Intermediate filaments consist of a superfamily of cytoplasmic and nuclear proteins (~65 genes) providing structural support to cells, organelles and tissues. Unlike actin and tubulin, intermediate filament proteins are fibrous and lack enzymatic activity. Therefore, the process of self-assembly into filaments is passive (Sanghvi-Shah and Weber, 2017). The formation of intermediate filaments follows a hierarchical scheme, derived after years of experiments based on *in vitro* assays pioneered by H. Herrmann and U. Aebi (Herrmann and Aebi, 2016) and is composed of 3 steps: (i) IF proteins form stable tetramers composed of two coiled-coil dimers lined up in a half-staggered anti-parallel manner. Because of this anti-parallel symmetry, the assembled tetramers are not polar. Lateral aggregation of about 8 tetramers forms a unit-length-filament (ULF) of approximately 60 nm in length. (ii) Longitudinal annealing of ULFs lead to the formation of immature filaments of about 16 nm diameter and a few microns in length. (iii) Filaments undergo a third step of radial compaction which gives rise to mature 10 nm diameter filaments (Herrmann and Aebi, 2016). Such organization might be one of the reasons for the unique structural and mechanical properties of intermediate filaments, which are highly stretchable (Block et al., 2018; Hu et al., 2019). Intermediate filament genes can be portioned into six major classes (I-VI) based on gene structure, sequence homology and assembly properties. The expression pattern of these different types of proteins depends on the type of tissues, the differentiation state and external cues. Among these families, type I-III proteins are particularly important since they contain keratin and vimentin. Both these filaments are crucial for a vast variety of cellular functions such as cell migration (Helfand et al., 2011; Liu et al., 2015a), signal transduction (Havel et al., 2014; Ivaska et al., 2005) and cell division (Duarte et al., 2019; Serres et al., 2020). Moreover, other two types of intermediate filaments are important in the context of this work: nuclear lamins (type V), which provide a mechanical and structural scaffold for the nucleus, and the neurofilaments (type IV), for their important roles in neuronal architecture.

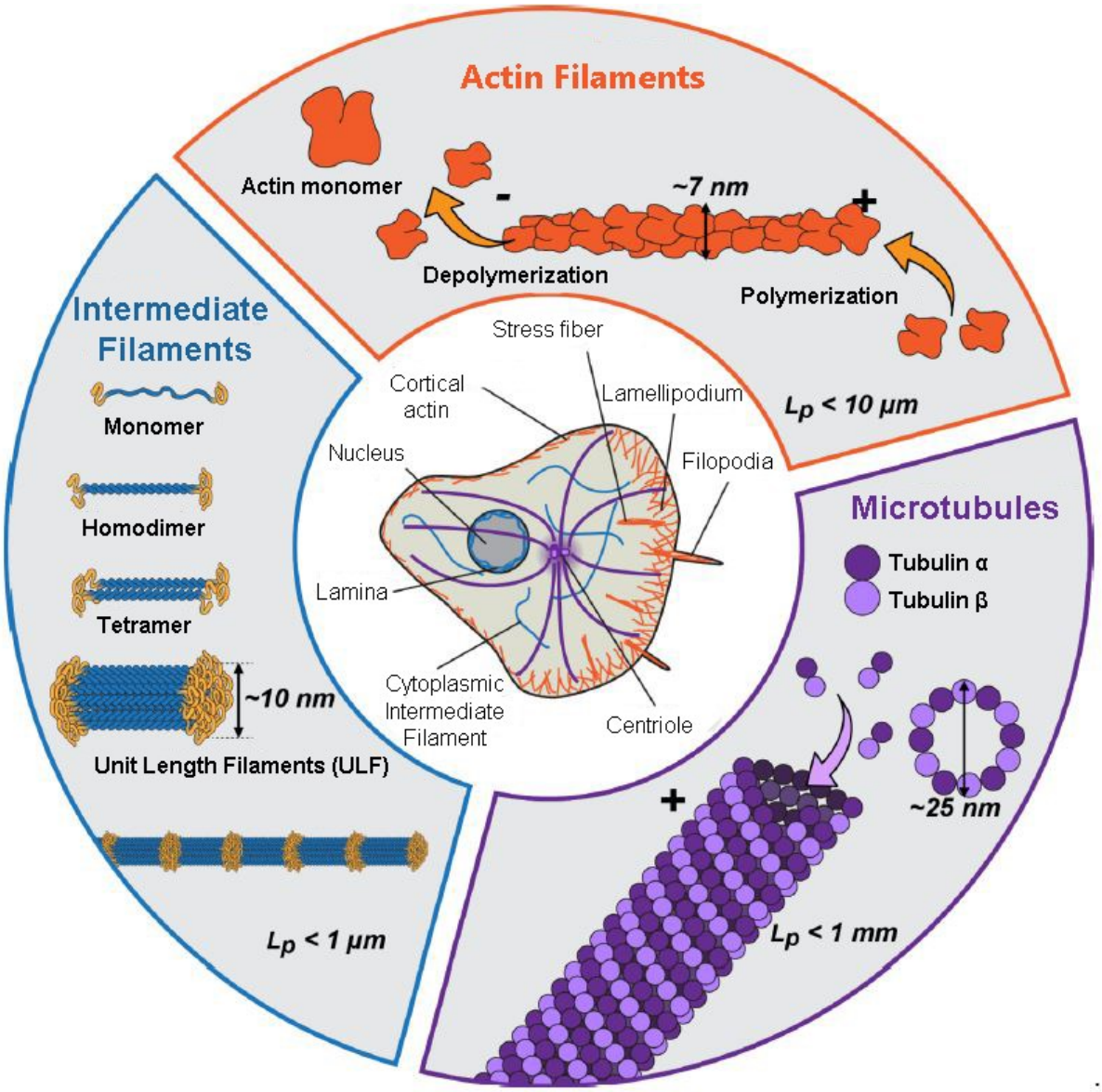

Figure 2: Cytoskeleton of eukaryotic cells

Schematic of the three main cytoskeleton elements of eukaryotic cells: actin filaments, intermediate filaments and microtubules (L_p : persistence length).

3.2. The lamellipodium

Besides cellular adhesion complexes, cytoskeleton-based protrusions and processes are crucial to explore the cellular microenvironment and drive cell migration. The lamellipodium consists of a thin, broad membrane projection (Fig. 3a) enclosing F-actin branched networks (Fig. 3b), propelled by actin polymerization (Ponti et al., 2004; Svitkina and Borisy, 1999; Symons and Mitchison, 1991). The lamellipodium is a highly versatile structure involved in different processes.

First and foremost, it is responsible for initiating cell migration (Giannone et al., 2004, 2007; Ponti et al., 2004); in addition, it also serves as a site for the formation of cell-ECM adhesions (Choi et al., 2008) and is important in the generation of intracellular forces (Giannone et al., 2004, 2007). Lamellipodium formation is highly coordinated at the spatiotemporal scale and reflects the power of F-actin and ABPs coupled to other signaling molecules. Rho guanosine triphosphatases (GTPases), and in particular Rac1, are crucial to drive lamellipodium formation (Ridley and Hall, 1992; Wu et al., 2009), whereas the Arp2/3 complex drives the branched assembly of the F-actin network (Chen et al., 2010). Lamellipodium protrusion is thus associated with continuous F-actin polymerization against the plasma membrane edge. This is crucial to promote membrane protrusion and drive cell motility, but also generates a 'retrograde' actin flow opposite to the direction of cell movement (Ponti et al., 2004). The retrograde flow is harnessed by cell-ECM adhesions to generate traction forces (Giannone et al., 2007), thus conferring the lamellipodium a dual role in cell function and behavior.

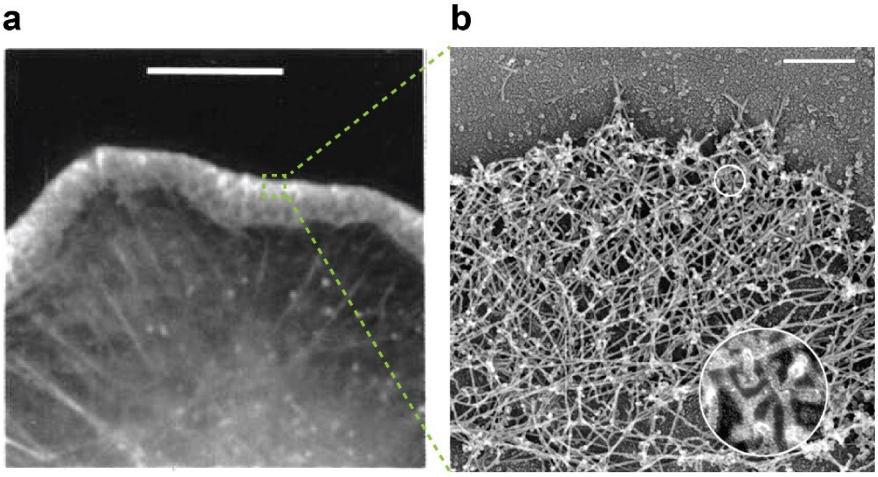

Figure 3: Lamellipodium: a branched actin network leading membrane protrusion

a, Fluorescence image of a lamellipodium in a fibroblast stained with rhodamine-actin. Adapted from Symons and Mitchison 1991. **b,** Structural organization of the lamellipodium in S2R+ cells obtained with electron microscopy. Actin filaments form a dense, highly branched dendritic network. Note the circular magnified inset revealing actin filament branching. Adapted from Biyasheva et al. 2004.

3.3. Cell-ECM adhesions: Integrin adhesion sites (IAS)

Forces generated by the cytoskeleton are exerted across the cell microenvironment; conversely, mechanical forces arising from the ECM and neighboring cells are sensed by the cytoskeleton and converted into biochemical signals (Han and de Rooij, 2016) (Han, Trends Cell Biol 2016). Such mechanical connections are made possible by cell-cell and cell-ECM adhesion sites. Sensing of the ECM mechanical and physical properties occurs mostly through integrin adhesion sites (IASs) (Fig. 4a), which also mediate force transmission between the cells and the

substrate (Orré et al., 2019). Integrins are a class of heterodimeric transmembrane receptors which bind various ECM components, such as fibronectin or collagen (Kechagia et al., 2019). In parallel, they indirectly engage the actomyosin machinery through a series of interacting partners (talin, vinculin) (Orré et al., 2019).

IAS can assume different morphologies across time, space and cell type, which will be later detailed. Briefly, IAS initiate as nascent adhesions (NAs), which are small, dot-like structures in the lamellipodium (Choi et al., 2008). Through the action of myosin II and intracellular forces, NAs can further mature to focal adhesions (FAs), which are probably the most well characterized class of IASs. Focal adhesions (FAs) are elongated, micrometer-sized integrin clusters associated with a functional plaque of regulatory and signaling partners connecting them to actomyosin filaments and bundles (Orré et al., 2019). FAs are highly stratified into functional nano-layers (Case et al., 2015; Kanchanawong et al., 2010; Stubb et al., 2019) and act as large signaling hubs (Chen et al., 2013; Pasapera et al., 2010; Wang et al., 2001). IAS maturation, architecture, mechanosensing and dynamics will be later addressed in detail.

3.3.1. Podosomes: a protrusive and adhesive structure

A different class of cell-ECM adhesions are podosomes (Fig. 4b), which can be described as dynamic adhesive structures found in cell types such as macrophages, osteoclasts, invasive tumor cells or dendritic cells (Bouissou et al., 2017; van den Dries et al., 2019a; Van Den Dries et al., 2013). Besides adhesion, podosomes also drive cell protrusion and ECM degradation, as well as mechanosensing (van den Dries et al., 2019b; Labernadie et al., 2014). Podosomes are characterized by a submembranous dense actin core formed by Arp2/3 polymerization (Murphy and Courtneidge, 2011). The core embodies two different actin modules: a central protrusion module of branched actin filaments surrounded by a peripheral protrusion module with linear filaments (van den Dries et al., 2019b). The actin core is surrounded by a ring of adhesive and regulatory proteins. Integrins within the ring mediate ECM adhesion, while talin, vinculin and paxillin are required for the podosome to protrude into the substrate (Bouissou et al., 2017; Rafiq et al., 2019). The ring is connected to a cap structure above the actin core which contains contractile actomyosin filaments (van den Dries et al., 2019b). Dorsal connecting actin filaments, which appear to contain myosinII, link individual podosomes into higher order arrays (van den Dries et al., 2019a).

At the core of podosomes, F-actin produces protrusion forces which are balanced by traction forces at the ring (Bouissou et al., 2017). Protrusion forces are mechanosensitive and become stronger in stiffer substrates (Labernadie et al., 2014). Interestingly, previous studies have reported that actomyosin tension could either be required (Van Den Dries et al., 2013) or dispensable for podosome integrity (Yu et al., 2013), which could be cell type-dependent. A more

recent work suggests that microtubule-dependent myosin inhibition is necessary for maintaining podosome integrity (Rafiq et al., 2019). Thus, podosome function and activity will be dependent on the correct regulation and coordination of actomyosin contractility, either through its activation on inhibition.

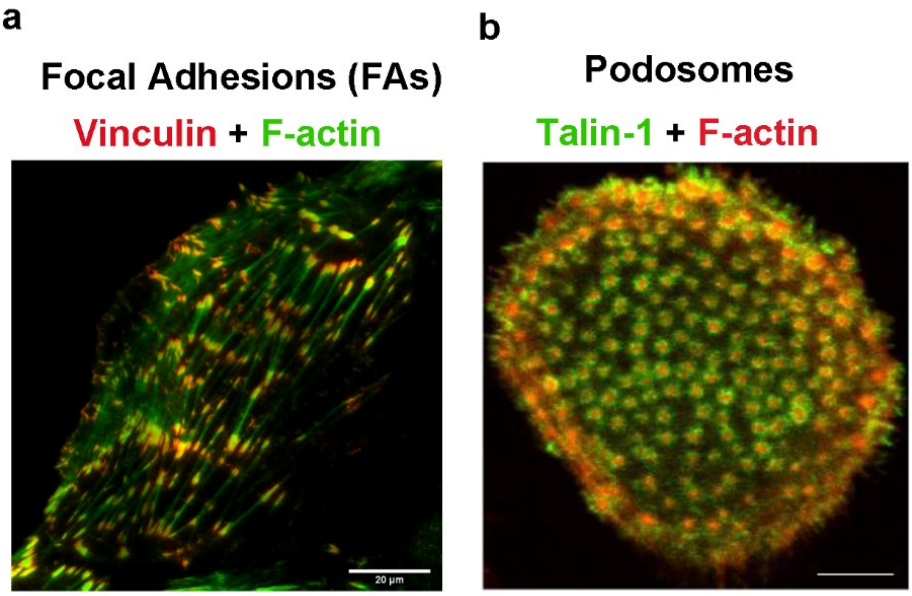

Figure 4: Morphology of two classes of cell-ECM adhesions: focal adhesions (FAs) and podosomes

a, Focal adhesions (FAs) observed in a LLC-PK1 epithelial cell imaged with total internal reflection (TIRF) microscopy. Lifeact-GFP (green) binds and labels F-actin. Focal adhesions are marked by vinculin mCherry (red). Scale bar: 20 µm. FAs are visible as elongated, dense clusters in contact with the substrate. Adapted from University of Connecticut Microscopy Center (United States) (https://confocal.uconn.edu/image-and-movie-gallery/). **b,** Podosomes observed in a confocal image of a primary human macrophage stained for F-actin (red) using Alexa-Fluor-568–phalloidin and for talin-1 (green) using a specific primary antibody. Scale bar: 5 µm. Podosomes are visible throughout the entire macrophage, with a ring-like talin structure surrounding an actin core. Adapted from van den Dries et al., 2019b.

3.4. Adherens junctions

Collective cell behavior, either during morphogenesis or cell migration, depends considerably on cell-cell interactions. Intracellular mechanical coupling is mediated by specialized complexes known as adherens junctions (Ladoux and Mège, 2017). Similar to cell-ECM adhesions, adherens junctions are also composed by adhesion molecules, of which there are two main families: cadherins and nectins, with cadherins being the most studied family (Ladoux and Mège, 2017). They mediate adhesion through *cis* or *trans* interactions between their ectodomains, followed by oligomerization or dimerization. In the case of cadherins, their intracellular regions

interact with actomyosin through specialized cytoplasmic proteins known as catenins. Cadherin-catenin coupling is essential for cell-cell adhesion and force transmission. Vinculin, an important FA protein, also mediates this dynamic coupling by interacting with catenins, thus contributing for the formation of adherens junctions (Buckley et al., 2014).

4. How are forces generated in tissues and cells

Mechanical forces can be generated at different scales, ranging from the movement and contraction of limbs and organs to cellular forces exerted during migration or spreading. As D'Arcy Wentworth Thompson suggested in *On Growth and Form*, forces can take multiple variations, as well as the mechanics of the environment. Taking as example the circulatory system, the blood flow exerts both shear stress and cyclic stretch on the blood vessel wall. Both these forces will have an impact on endothelial and smooth muscle cells; in cases of high pressure, hypertension leads to changes in the physiology and shape of vessel wall (Anwar et al., 2012; Hoffman et al., 2011)

Box 1 – The case of stretching

Stretching is one of the most common mechanical forces in the body and arises from a series of physiological but also pathophysiological processes. From the beating of the heart to muscle contractions, soft tissues and visceral organs are continuously subjected to cycles of stretch and compression. Lungs expand and relax during breathing (Widdicombe, 2006), the bladder stores urine (Araki et al., 2008) and the gut stretches in response to food intake (Widdicombe, 2006). Movement is another source of mechanical stretch at various forms, such as the muscle contraction and deformation of nerves during limb motion (Loh et al., 2018; Phillips et al., 2004). Moreover, multiple instances of sustained stretching occur in the body, both during injury (brain trauma)(Vieira et al., 2016) but also physiological activities (bladder expansion, muscle contraction) (Araki et al., 2008).

4.1. Forces at the cellular level

Force generation at the cellular level is as important as force at a tissue or organ level. Cells are continuously exerting forces on their microenvironment, especially on the extracellular matrix (ECM) and on other cells. Through adhesive complexes and cytoskeletal protrusions, cells continuously pull and push on the ECM and on other cells during cell migration, proliferation or

tissue invasion. During cell division, microtubule-dependent forces pull the chromatids apart during mitosis, while actin contractility mediates cytokinesis. Actin polymerization against the membrane during migration also generates multiple forces within the cell, contributing for protrusion and adhesion. Indeed, the cytoskeleton is the main machinery involved in the generation of cellular forces. In parallel, it is also one of the main force sensors, an aspect that will later be detailed.

A particularly interesting aspect of cell-dependent forces is that cell motility and proliferation are not a condition sine qua non for exerting forces, since cells considered as 'immobile' can generate multiple forces. Cells are continuously probing the mechanical and chemical properties of their substrates, even when immobile. In response to variations of stiffness or ligand spacing, cells adjust their contractility, exerting traction forces on the ECM (Oria et al., 2017; Wolfenson et al., 2016). Local contractions can also occur at the level of cell-cell junctions, allowing to sense the rigidity of other cells (Yang et al., 2018). Actomyosin contractility is also an inner source of tension, due to the presence of actomyosin contractile bundles known as stress fibers. Moreover, mature neurons – considered as immobile and post-mitotic cells – rely on actin polymerization and flow to control the shape and size of dendritic spines (Chazeau et al., 2014; Mikhaylova et al., 2018). Synapses also establish adhesive complexes, which in turn can be mechanically coupled to the actin flow to drive synapse remodeling (Chazeau et al., 2015).

As D'Arcy Wentworth Thompson had proposed *On Growth and Form*, membrane tension – the modern equivalent of surface tension - is also a permanent force in cells. Defined as the surface free energy per unit area, membrane tension provides a powerful counteracting force to actin polymerization or hydrostatic pressure (Derényi et al., 2002). This in turn can regulate actin networks and cell motility. Moreover, changes in membrane tension is also important in the regulation of mechano-sensitive ion channels (e.g. Piezo) (Brohawn et al., 2014; Zhao et al., 2018). The plasma membrane also possesses specialized cup-shaped pits, known as caveolins. In response to stretch, caveolae flatten and disassemble, a mechanism which is thought to buffer membrane tension during mechanical stress (Sinha et al., 2011)

5. Mechanotransduction and mechanosensing

Through their various specialized subcellular structures and protein assemblies, cells can detect mechanical stimuli and convert them into biochemical signals, eliciting specific intracellular responses. This process, known as mechanotransduction, is the basis for the regulation of cellular functions by mechanical forces. Accordingly, sensing of mechanical forces is called mechanosensing. As an example, when sensory periphery neurons in the lung are stretched during organ expansion, their mechanoreceptors (e.g. Piezo2) are activated

(Nonomura et al., 2017). This stimulus is then converted into neuronal impulses and transmitted to the brain, which in turn will regulate breathing and lung inflation (Umans and Liberles, 2018; Widdicombe, 2006). Stretch sensing is an example of mechanosensing; the full conversion of force to a neuronal impulse and subsequent responses is an example of mechanotransduction. Overall, mechanotransduction comprises a huge variety of effects and mechanisms, and is far better understood if decomposed into a series of processes (Box2).

Box 2 – Mechanotransduction: a useful guide

- **Mechanotransduction:** Overall process by which cells detect a mechanical stimulus and transduce it into a biochemical signal, eliciting an intracellular response.
- **Mechanosensing:** The act of sensing a mechanical stimulus by the cell.
- **Mechanosensitive:** A subcellular structure or protein complex which is sensitive to mechanical stimuli by undergoing force-dependent conformational changes such as deformation or reorganization.This can trigger also the recruitment of binding partners (Del Rio et al., 2009).
- **Mechanosignaling:** An intracellular signaling event which is triggered by a mechanical force such as shear stress or cyclic strain. This can involve phosphorylation of a target protein (Sawada et al., 2006), influx of a secondary messenger (e.g. Ca^{2+})(Zhao et al., 2018) or translocation of a transcription factor (Dupont et al., 2011).
- **Mechanoresponse:** The final response of a cell after detection of a mechanical stimuli and activation of specific mechanosignaling pathways. It can consist of changes in cell morphology, expression of target proteins or changes in cell proliferation and migration.
- **Mechanotransmission:** How forces are transmitted across the cell and different subcellular structures; it can occur from the cytoskeleton to the ECM and vice-versa, but also internally, for instance from the cytoskeleton to the nucleus.

One of the earliest known reports of mechanotransduction was previously mentioned in the preface: Wolff's law, which later was found to reflect the mechanoadaptation of bones (Ruff et al., 2006). Another classic example of mechanotransduction is the differential response of cells to substrates of different stiffness, which was first described in the 1950s (Sanford et al., 1954). Stiffness, in general, is an essential stimuli regulating mechanotransduction pathways involved in cell proliferation, migration and differentiation (Levental et al., 2009; Lo et al., 2000; Segel et al., 2019). In the brain, one of the softest tissues in the body, axons and neurons can migrate along

stiffness gradients (Kozer Nat Neurosci 2016), and mechanochemical properties of the ECM can regulate synaptic transmission (Frischknecht et al., 2009), neuronal activity (Lantoine et al., 2016) and neurogenesis (Segel et al., 2019).

In physiology and disease, shear stress and cyclic strain arising from blood flow can alter protein expression and the inflammatory response of endothelial blood vessel cells (Anwar et al., 2012; Hoffman et al., 2011). Mechanotransduction is also a key element in stretch sensing of organ expansion, which occurs especially in the heart, lungs, bladder and stomatch. In addition to the previously described example in the lung, sensory gut neurons and neuroendocrine cells respond to mechanical forces to regulate intestinal peristalsis, secretion and digestion (Alcaino et al., 2018; Mazzuoli and Schemann, 2012).

One common principle of mechanotransduction is that many structures that generate and/or convey force within the cells are also mechanosensitive; this is case of the cytoskeleton, which both generates and senses forces, but also of IAS, which are mechanosensitive entities and transmit actomyosin-generated forces to the ECM. Nonetheless, it is increasingly clear that many other macromolecular assemblies involved in key cellular processes are mechanosensitive. This includes the nucleus (Nava et al., 2020), adherens junctions (Yonemura et al., 2010), kinetochores (Dumont et al., 2012a), and the caveolae (Sinha et al., 2011).

Mechanotransduction does not influence only the cell behavior; it can also modify the substrate itself. Cells can also respond to ECM properties by continuous remodeling of the ECM itself, either in a reversible or non-reversible manner. This process is often described as mechanoreciprocity (Paszek and Weaver, 2004). Effects of this crosstalk include stiffening of the matrix and re-alignment of the fibers (Hall et al., 2016) , but also proteolytic degradation (Wolf et al., 2007) and alterations in nanotopology (Kim et al., 2017). In addition, forces exerted by the cell can also unfold and stretch ECM proteins, giving rise to force transduction pathways (Klotzsch et al., 2009). ECM-cell mechanoreciprocity is also crucial in disease, especially in fibrosis and cancer (Goetz et al., 2011; Lan et al., 2013).

5.1. Molecular mechanisms of mechanosensing in living cells – the next border?

Over the last decades, several pathways of mechanotransduction and have been characterized. However, the molecular mechanisms behind mechanosignaling and mechanosensing in living cells remain elusive. It remains to be clarified which molecules enable mechanosensing in different subcellular structures or how they are engaged in response to different forces (shear stress vs cyclic stretch, for instance). The same can be said for mechanosignaling: which are the main players and how do they interact with mechanosensitive molecules? Nonetheless, we are not in the dark, since several mechanisms have already been

characterized through elegant studies. In this regard, recent innovations in micromanipulation methods and force sensors have largely contributed to this field.

The current consensus is that mechanosensing is mediated by force-dependent conformational changes of mechanosensitive proteins. At the molecular level, mechanical force can deform and reorganize proteins, as well as reinforce or destabilize their interactions (Fig. 5) (Buckley et al., 2014; Jiang et al., 2003; Del Rio et al., 2009; Sawada et al., 2006). A common outcome is the unfolding of protein domains in response to force, with different consequences. First, protein unfolding can activate ligand binding sites (Fig. 5a); the IAS protein talin unfolds when mechanically stretched with magnetic tweezers *in vitro*; triggering vinculin (Del Rio et al., 2009; Yao et al., 2016). Alternatively, protein unfolding can also expose cleavage sites (Fig. 5b); the notch receptor 2 unfolds in response to force exerted through atomic force microscopy (AFM), triggering the proteolytic cleavage by the metalloprotease TACE (TNF-alpha-converting enzyme) (Stephenson and Avis, 2012). Finally, protein unfolding can also expose non-polar hydrophobic residues (such as cysteine, glycine and alanine), which will interact with other biomolecules, changing the function of the protein (Johnson et al., 2007).

Force-dependent protein extension can also expose or obstruct binding sites for kinases, triggering (or not) the phosphorylation of mechanosensitive proteins (Fig. 5c). This is the case of the Crk-associated substrate (Cas) family of proteins, which undergo force-dependent extension, exposing kinase binding sites. This triggers phosphorylation and consequent downstream signaling (Sawada et al., 2006). Other proteins such as lamin undergo the opposite effect, with mechanical force hindering the access to phosphorylation sites (Buxboim et al., 2014).

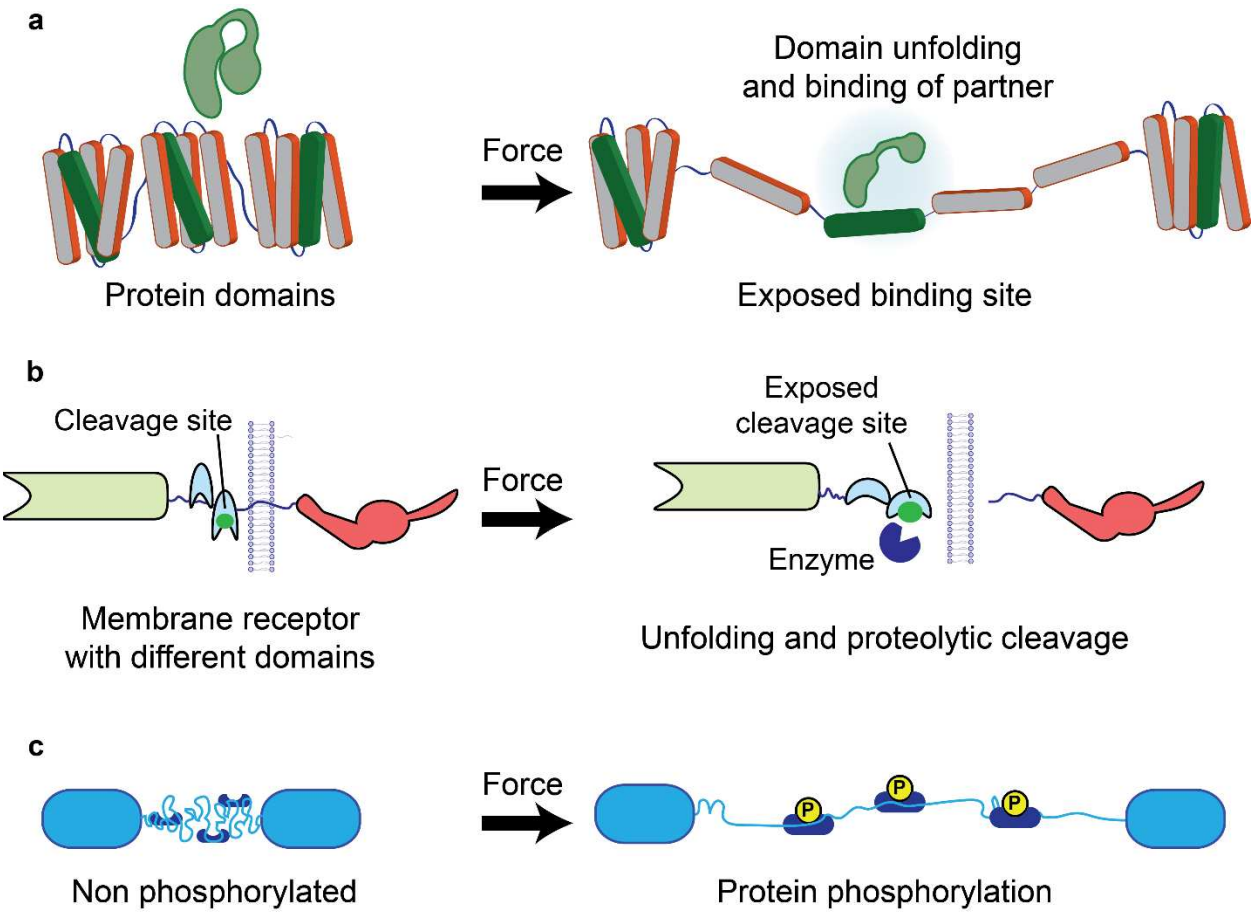

Figure 5: Different mechanosensing mechanisms based on protein deformation and reorganization

a, Unfolding of globular protein domains in response to force can expose binding sites for different interacting partners, triggering their recruitment. Alternatively, unfolding of domains can also lead to the dissociation of binding partners. **c,** In response to force, extension of domains exposes cleavage sites for proteolytic enzymes, resulting in the cleavage of intracellular receptor domains, as seen for Notch receptor. **b,** Protein force-dependent extension can expose phosphorylation residues such as tyrosines, leading to protein phosphorylation and mechanosignaling.

Finally, mechanical forces can also alter the lifetime of protein-protein non covalent bonds, either stabilizing or destabilizing them (Fig. 6). Protein-protein bonds usually have finite lifetimes, ranging from milliseconds to days. When the force applied shortens the lifetime of a bond, this is referred to as a slip bond (Fig. 6b). Slip bonds are the most commonly observed interaction in biology. Talin, for instance, forms a 2 pN slip bond between integrin-fibronectin complexes and the actin cytoskeleton (Jiang et al., 2003). By opposition to slip bonds, some molecules form 'catch bonds', whose lifetime will increase with the applied tensile force (Fig. 6c) (Evans and Calderwood, 2007). Despite being less common than slip bonds, catch bonds are

common in cytoskeletal and adhesive structures, providing a way for molecules to grip tightly and stabilize their linkage in response to mechanical stress (Buckley et al., 2014; Evans and Calderwood, 2007; Evans et al., 2004; Huang et al., 2017b; Marshall et al., 2003). Importantly, catch bonds do not maintain their behavior indefinitely, rather displaying it over a force range; they usually revert back to slip bonds as the force increases beyond that range (Fig. 6c) (Huang et al., 2017b; Marshall et al., 2003). The first experimental observations of catch bonds were reported for the leukocyte adhesion bond between P-selectin/L-selectin and the glycoprotein ligand 1 (PSGL-1) (Fritz et al., 1998; Marshall et al., 2003). These could provide a mechanism for tethering and rolling of flowing leukocytes on vascular surfaces (Marshall et al., 2003). Further catch bonds were reported between $\alpha_5\beta_1$ integrin and fibronectin (Friedland et al., 2009; Kong et al., 2009), as well as between actin filaments and the cadherin-catenin complex (Buckley et al., 2014) or vinculin (Huang et al., 2017b). We will discuss about the implications of catch and slip bonds in IAS mechanosensing later in the introduction, as well as their dependence on loading rate.

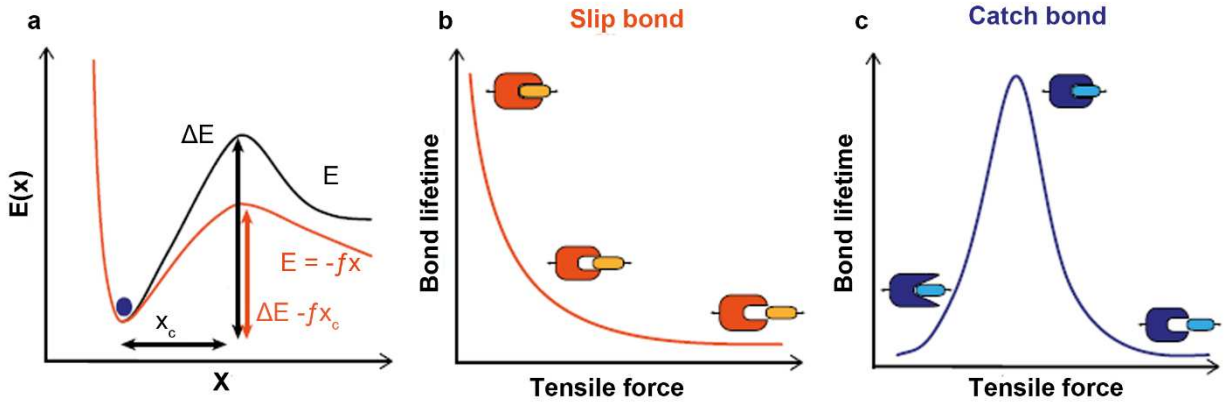

Figure 6: Slip and catch bonds

a, Energy landscape of a non-covalent receptor-ligand bond. The potential minimum of such a bond corresponds to the bound state and dissociation occurs by crossing the transition state barrier, whose height is represented by ΔE (black). The dissociation rate increases when ΔE decreases. X_c represents the distance between the potential minimum and the transition point. Application of an external force, f, decreases the height of that barrier to ΔE - fX_C (orange), which in turn increases the dissociation rate. **b,** As a result of the phenomenon described in **a,** the lifetime of a slip bond decreases upon application of an external tensile force. Due to the exponential relationship between these factors, a small increase in force can greatly increase the dissociation rate. **c,** Conversely, in a catch bond, the lifetime of the bond increases over a given force range upon application of external tensile force; eventually, at higher forces, bond lifetime decreases again, displaying slip bond behavior. **a-c,** Figure adapted from Helms et al. 2016.

Over the previous mechanisms shown in this section, I admit that the boundary between mechanosensing and mechanosignaling is not always clear, and might depend on the mechanism

itself. On one hand, the unfolding of talin rod domains and consequent recruitment of vinculin is an example of structural mechanosensing. The same for the vinculin-actin or $\alpha_5\beta_1$ integrin-fibronectin catch bonds (Huang et al., 2017b; Kong et al., 2009). On the other hand, the unfolding and phosphorylation of Cas protein, while initially being a mechanosensitive response based on force-dependent extension, will likely activate downstream signaling. Therefore, it consistutes both a mechanosensing and mechanosignaling mechanism, dependent on the step. One could establish the boundary between mechanosensing and mechanosignaling as a scenario of structural modifications vs activation of signaling pathways, respectively. The same reasoning can be applied for transcription factors that are translocated to the nucleus in response to stiffness variations (Dupont et al., 2011). Initially, such factors are mechanosensitive because they respond to changes in mechanical properties, but their translocation constitutes a signaling pathway that will eventually regulate gene expression.

One common aspect of several of these studies is that they were performed *in vitro* with purified proteins and different force spectroscopy methods (AFM, optical tweezers, and magnetic tweezers). Therefore, it is unclear whether the same principles can be extrapolated to living cells and respective subcellular structures. Here, the mechanosensitive response of proteins lies in a complex interplay of factors. First of all, cells are continuously exerting and sensing forces, which not only vary across space and time (Kumar et al., 2018; Plotnikov et al., 2012) but also in magnitude and orientation (Plotnikov et al., 2012; Swaminathan et al., 2017). By opposition to an *in vitro* force spectroscopy experiments, where the applied forces are carefully controlled and quantified, the force patterns within the cell will likely change the response of individual molecules. Moreover, proteins interact with multiple binding partners in mechanosensitive structures, which in turn can modulate recruitment or signaling pathways. While the talin-vinculin mechanosensitive switch can be fine-tuned *in vitro* using purified proteins, talin in living cells is associated to IAS, interacting with several partners (Goult et al., 2018); hence, force-dependent recruitment of vinculin will probably be more complex. Same could be applied for phosphorylation of target proteins or cleavage of membrane receptors. In this regard, the presence of the plasma membrane is another key factor to have into account: it constitutes an inner source of tension, mediates protein dynamics and recruitment, and contains signaling lipids such as phosphatidylinositol 4,5-bisphosphate (PIP_2) (Chinthalapudi et al., 2014) However, I want to stress out that this is not a pointless aim against *in vitro* force spectroscopy studies: these were of essential importance in grasping the molecular basis of mechanosensing and protein interactions in response to force. Without these studies, we would not have the slightest idea of how proteins unfold or how adhesions strengthen under force. Drawing principles from these studies is a key element in transferring molecular mechanosensing to subcellular structures in live cells.

5.2. Stretching and mechanotransduction.

Mechanical stretch is more than a passive stimulus; as a matter of fact, it is an essential physical cue that influences many physiological and pathological processes. In various sports, as well as in the medical field, muscle and tendon stretching are commonly used to improve flexibility and strength, extend the range of motion and reduce injuries (Behm et al., 2015; Perrier et al., 2011). This suggests that stretching can enhance the resistance and elasticity of muscles and tendons. Stretching modality itself can be of extreme matter; in static stretch, a singular motion is held in place for at least ten seconds, while in dynamic stretch the motions are executed repeatedly, with joints and muscles going through a full range of motion. Dynamic stretch has been shown to improve sportive performance (force, power, sprint and jump) compared to static stretching (Opplert and Babault, 2018). Although at a higher scale, such differences already suggest that, at the cellular level, stretching parameters (speed, loading rate, and magnitude) will also have a different impact. As already mentioned, expansion of organs such as the heart, lung or stomach will trigger stretch sensing pathways controlling blood pressure, breathing and digestion, respectively (Umans and Liberles, 2018).

Mechanical stretching activates several cellular mechanotransduction pathways involved in neuronal transmission, morphology, proliferation or differentiation. Mechanosensitive ion channels in specialized sensory neurons open/close in response to membrane deformation, changing neuronal activity (Das ECR 2019); these are important in transmitting mechanical pain (Beaulieu-Laroche et al., 2020), regulating lung inflation (Nonomura et al., 2017), and mediating proprioception (Woo et al., 2015).

Sensation and transmission of stretching forces are also mediated by integrin and IAS-dependent pathways, coupled to the cytoskeleton (Chen et al., 2013; Hsu et al., 2010; Sigaut et al., 2018). Cyclic uniaxial stretch reorients the cell's long axis perpendicular to the applied stretch, which is thought to minimize resistance to stretch. Different cell types exhibit this behavior, such as osteoblasts (Nagayama et al., 2012), endothelial cells (Hsu et al., 2010), osteosarcoma cells (Hsu et al., 2010), epithelial stem cells (Nava et al., 2020), and fibroblasts (Faust et al., 2011). As essential hubs in the transmission of substrate mechanical forces to the cytoskeleton, IASs are the perfect candidate to mediate stretch-induced reorientation. Indeed, mature FAs also undergo reorganization, remodeling and orthogonal reorientation to the applied stretch (Chen et al., 2013; Sigaut et al., 2018). In parallel, several IAS-associated molecules such as integrin, paxillin or zyxin mediate the cytoskeletal reorganization in response to stretch (Hoffman et al., 2012; Rosowski et al., 2018; Sawada and Sheetz, 2002a; Sigaut et al., 2018). However, it is still unclear how individual proteins within IAS respond to mechanical stretch. Moreover, cell-cell adhesions also play an important role in stretch-responses, especially regarding the conformational changes in cell layers (Nava et al., 2020). Different adhesions could act synergistically to mediate response to stretching; further research is also required in this topic.

5.3. Mechanotransduction in cancer

Aberrant mechanotransduction is one hallmark of certain diseases, especially in regards cancer. Tumours are stiffer than normal tissues, a property which is commonly used in medical diagnosis (Sinkus et al., 2000). These altered mechanics are thought to arise due to a combination of factors. First of all, tumour microenvironment can be characterized by high ECM deposition and crosslinking, which increases tumour stiffness (Levental et al., 2009; Plodinec et al., 2012). This is further enhanced by high cell proliferation combined with blood vessel leakage and defective lymphatic drainage, which increase internal pressure. The global increase of stiffness promotes tumor invasion and metastasis, which is primarily mediated by IAS-dependent mechanotransduction pathways. Collagen crosslinking-induced stiffness promotes growth of mature FAs and integrin clustering, driving tumor invasion (Levental et al., 2009). Clustering of integrins is has been shown to result from the high expression of bulky glycocalyx proteins such as mucin, which funnel integrins into mature FAs (Paszek et al., 2014). This promotes IAS-dependent signaling and adhesion, which in turn could enhance metastasis. Other pathways include translocation of transcription factors to the nucleus, promoting expression of pro-proliferation and pro-migratory genes (Dupont et al., 2011; Lamar et al., 2012). Moreover, increased tumour stiffness can promote epithelial-to-mesenchymal (EMT) transition, which is also required for metastasis (Wei et al., 2015).

Although the increased stiffness of tumours is a key factor in proliferation and migration of cancer cells, it is also possible that cancer cells might eventually be unable to sense rigidity. In the 1950s, pioneer studies revealed how cancer cells could grow in soft agar in an anchorage-independent manner, by opposition to non-cancerous cells (Sanford et al., 1954). Recent evidence in this field indicates that transformed cancer cells lose their rigidity sensing complexes, leading to a hyperactivation of traction forces and mechanotransduction pathways (Yang et al., 2020). The bulky glycocalyx could also contribute to this by promoting integrin clustering and consequent mechanical loading of integrin, independently of actomyosin contractility (Paszek et al., 2014). However, such mechanisms require further clarification; it would be of special interest to see how the loss of rigidity sensing is coordinated with increased tumor stiffness to promote further cancer cell proliferation and migration.

6. The mechanobiologist's toolbox

The study of mechanotransduction and mechanobiology in general requires specific tools to study how biological systems generate and respond to mechanical forces. These methods can be broadly divided into three categories. First, techniques that apply forces to biological systems (cells and proteins) and measure their response. This includes optical and magnetic tweezers,

atomic force microscopy (AFM), soft membrane stretching, and other assays (Neuman and Nagy, 2008). Second, methods to measure cell mechanics; although these are also based on application of force, they extract properties such as cell stiffness, rheology or fracture stress (Wu et al., 2018). Here, we find techniques such as parallel-plate rheometry, magnetic twisting cytometry and again AFM, among other methods (Wu Nat Methods 2018). Finally, the third class consists of methods to quantify forces actively generated by the cell (Roca-Cusachs NCB 2017). This encompasses traction force microscopy (TFM), micropillars, optical tweezers, and molecular force sensors, as well as other methods.

In the context of this PhD thesis, we will especially focus on the techniques used to apply forces to biological systems. This will cover two aspects: 1) single molecule force spectroscopy, which is the set of techniques that probe the structural changes in biomolecules in response to mechanical force (optical tweezers, magnetic tweezers, AFM); and 2) cell stretching with elastomeric substrates. In addition, we will briefly discuss methods to measure cellular forces, with emphasis on molecular force sensors.

6.1. Single molecule force spectroscopy

From the invention of the atomic force microscope and optical tweezers in the decade of 1980, single molecule force spectroscopy (SMFS) has become a powerful tool to study the forces and motions behind protein function and activity. Such a broad description could fit almost anything; concrete examples include the mechanical unfolding of proteins (Rief et al., 1997; Yao et al., 2016), motion of molecular motors (Svoboda and Block, 1994), RNA polymerase transcriptional activity (Abbondanzieri et al., 2005) or the role of forces in integrin-cytoskeleton linkages (Choquet et al., 1997; Jiang et al., 2003). Therefore, it is without surprise that SMFS is, among its various applications, an essential item in the mechanobiologist's toolbox.

Among the various SMFS techniques, three end up by taking the 'podium' (without a clear winner): optical tweezers, magnetic tweezers and atomic force microscopy (AFM). These methods have different principles but all of them allow to apply and in return measure forces in single molecules (Neuman and Nagy, 2008). They can also be distinguished by their spatial and temporal resolution, displacement and force range and applications. Many seminal SMFS studies were performed with purified proteins in *in vitro* systems (Buckley et al., 2014; Oberhauser et al., 1998; Rief et al., 1997; Del Rio et al., 2009). However, these methods can also be applied in live cells, with equally relevant insights (Choquet et al., 1997; Chronopoulos et al., 2020; Jiang et al., 2003; Kong et al., 2009). Among other emerging techniques, flow-induced stretching with microfluidic setups has been used to study the mechanical response of actin filaments (Jégou et al., 2013) and microtubules (Aumeier et al., 2016; Schaedel et al., 2015).

6.1.1. Optical tweezers

Optical tweezers were demonstrated for the first time in 1986 as a method to achieve 'optical trapping of dielectric particles by a single-beam gradient force trap' (Ashkin et al., 1986). Since then, optical tweezers emerged as a fundamental technique in a variety of fields, including medicine, plant physiology, nanoengineering and mechanobiology. For us to understand their importance, two of the authors of this seminal paper were lauded with the Nobel Prize in Physics: Steven Chu in 1997, for trapping and cooling of atoms, and Arthur Ashkin in 2018, for being the original 'father' of optical tweezers.

Optical tweezers use optical traps, created by focusing a laser beam to a diffraction-limited spot in the specimen plane. Optical traps, in turn, generate a three-dimensional force on dielectric particles, which can be resolved into two components. First, a gradient force F_{grad} , transversal to the direction of the beam, and created by the interaction between the polarized dielectric particles and the gradient near the laser focus, (Ashkin, 1997). Second, a scattering force F_{scat} which is pointed along the direction of the incident light. To form a stable trap with optical tweezers, F_{grad} needs to overcome F_{scat} , which is usually achieved with a steep gradient formed by high numerical aperture (NA) objectives (Ashkin, 1997; Neuman and Nagy, 2008). Particles ranging from tens of nanometers to tens of micrometers can be stably trapped, including atoms (Beugnon et al., 2007), single cells (Neuman et al., 1999), organelles (Gao et al., 2016), and polyesterene or silica beads (Choquet et al., 1997; Huang et al., 2017b). The latter are commonly used as a handle to manipulate a variety of biomolecules, such as DNA (Wang et al., 1997) or proteins (Huang et al., 2017b). Together, optical tweezers deliver sub-angstrom spatial resolution and <10 µs temporal resolution, with a force-range of 0.1-100 pN (Arbore et al., 2019; Neuman and Nagy, 2008). This force range is adapted to study nucleic acid folding, catch/slip protein bonds or receptor/ligand interactions in the adhesive context. Conversely, AFM or magnetic tweezers are usually the method of choice for studying protein unfolding. This has been attributed to the higher force range of such techniques (up to nanonewtons), which is adapted to the larger forces usually required for protein unfolding, which were shown to surpass the 100 pN (Oberhauser et al., 1998; Rief et al., 1997). However, previous studies with magnetic tweezers have also shown that forces in the scale of 5-25 pN are enough to unfold protein domains (Yao et al., 2014, 2016). Thus, it can also be a matter of spatial resolution; magnetic tweezers can offer more precision in measuring the displacements of beads, and are thus more suitable for studying protein unfolding in comparison to optical tweezers.

Here, we will focus on two groups of experiments performed with optical tweezers and protein-coated beads: 1) single protein force spectroscopy in *in vitro* systems and 2) applying and measuring forces on and molecular bonds in live cells. For this, it is important to understand how forces and bead displacements are related (Box 3).

Box 3 – Forces and bead displacements in optical traps

When studying protein-protein interactions, beads are functionalized with one of the proteins of interest. When this protein binds its respective partner either *in vitro* or in living cells, the mechanical/physical connection arising from this bond is transmitted to the beads, causing their displacement from the trap. This creates a restoring force that is applied to the molecular bond. Since an optical trap is equivalent to a simple spring, the magnitude of this force can be calculated by Hooke's law ($F = -kx$), where k is the stiffness of the trap and x is displacement of the trapped beads caused by this force (Buckley et al., 2014).

6.1.1.1. Optical tweezers in single molecule force spectroscopy

The first biological application of optical tweezers in SMFS consisted in determining the stepwise motions and forces of the molecular motor kinesin along microtubules (Block et al., 1990; Svoboda and Block, 1994; Svoboda et al., 1993). Here, optically trapped beads coated with kinesin were placed along fixed microtubules. Beads were displaced by kinesin movements, with breaking points corresponding to kinesin detachment from microtubutles. Subsequently, optical tweezers have been used to study folding kinetics and the mechanistic properties of various proteins such as titin (Kellermayer et al., 1997), ribonucleases (Fazal et al., 2015) or calmodulin (Stigler et al., 2011). More recently, optical tweezers were detrimental to unveil the actin-cadherin-catenin catch bond behavior as well as the directional catch bond between vinculin and actin (Fig. 7a,b) (Buckley et al., 2014; Huang et al., 2017b). Both studies employed a similar assay, consisting of an actin filament held taut by two optical traps while a platform bead coated with the binding partner (cadherin/catenin complex or vinculin) moves back and forth (Fig. 7a). This assay allows to assess the influence of force in bond lifetime by arresting the motorized stage when the trap-exerted force exerts a certain threshold (Fig. 7b) (Huang et al., 2017b).

6.1.1.2. Optical tweezers in live cells

In the context of live cells, optical tweezers provided valuable insights on the role of local forces in integrin-cytoskeleton linkage and IAS maturation (Choquet et al., 1997; Galbraith et al., 2002; Giannone et al., 2003; Jiang et al., 2003). Pioneering experiments on integrin sensing of local ECM rigidity were performed using beads coated with a fibronectin fragment and placed on the lamellipodium of cells with optical traps (Choquet et al., 1997). Restriction of bead movement mimicked the attachment to a rigid ECM site, which induced the strengthening of integrin-cytoskeleton bonds. Similar approaches revealed how this phenomenon was dependent on talin

(Giannone et al., 2003) as well as the role of force in IAS maturation through vinculin recruitment (Galbraith et al., 2002). In the latter work, changing the surface area of the ligand bound to the bead was detrimental for maturation of focal complexes. However, none of these studies actually measured forces between individual molecules in live cells, something that was achieved in 2003 by Jiang and colleagues (Jiang et al., 2003). In this study, the role of talin in mediating a slip bond between integrin and the actin cytoskeleton linkage was demonstrated using optical traps to measure the forces between individual integrin-cytoskeleton bonds (Fig. 7 c,d). Similar to the other studies, fibronectin-coated beads were trapped on a motile lamellipodium; and moved rearward with similar speed as the actin flow, suggesting mechanical connections between integrins and actin cytoskeleton. Displacement creates restoring forces which are exerted on the bead-cytoskeleton linkage, which increase as the bead moves away from the trap center. This tension increases until the the force required to break the weakest connection is reached, triggering an abrupt recoil towards the trap center (Fig. 7c). Force required for these 'breaking events' can be measured from the bead displacement from the center of trap at the time of breaking (Box 3 and Fig. 7d); in this work, use of optical traps revealed a slip bond of 2 pN for integrin-actin cytoskeleton bonds (Fig. 7d), which was dependent on talin. Thus, optical tweezers can also deliver measures of individual bonds in live cells, proving themselves as versatile methods in a mechanobiologist's toolbox.

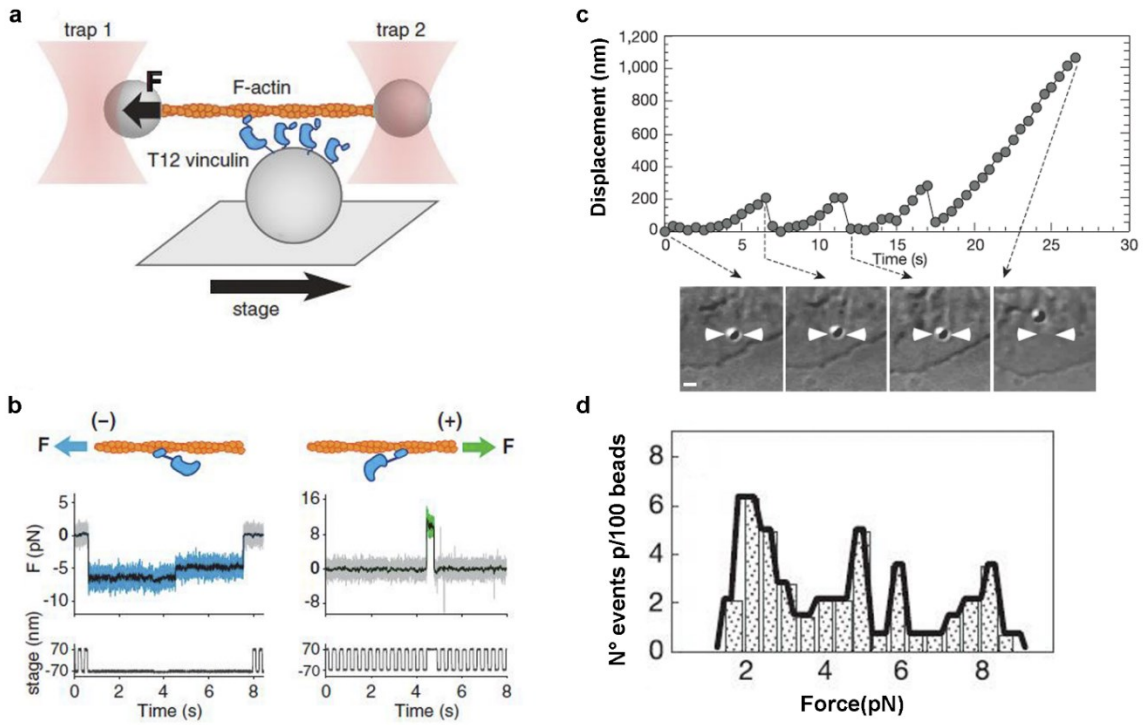

Figure 7: Optical tweezer-based assays in SMFS

a, To study the bond lifetime between vinculin and actin, an actin filament attached to two microspheres is held taut by two optical traps. A platform bead is coated with vinculin and moved back and forth by a motorized stage. Vinculin binding results on the displacement of one of the trapped microspheres, causing a restoring force that is applied to the molecular bond (Box 3). **b,** Both optical traps exert force on the actin filament. The plots represents the total force transmitted from both traps to the vinculin molecules versus time, for the two movements of the platform: towards the (-) pointed end or towards the (+) barbed end of the actin filament. If force surpasses a defined threshold, stage motion halts until the detachment of vinculin bound molecules, which allows to determine the lifetime of actin-vinculin bonds. When force is directed towards the (-) pointed end, the bond lifetime is visibly longer compared to when force is directed towards the (+) barbed end. **a-b**, Adapted from Huang et al. 2017b. **c,** Fibronectin-trimer coated beads are trapped in a motile lamellipodium, causing them to move rearward at ~60 nm/s. Plot represents the displacement of a cell-bound fibronectin-trimer-coated bead from the trap center against time. As the beads move out of the trap, restoring forces exert force on the bead-cytoskeleton linkage; when the breaking force is reached, beads return to the center (breaking events) (top). Sequential DIC images of the bead, showing bead movement and the breaking events (bottom). The arrows in the lower panels indicate the position of the laser trap. Scale bar, 500 nm. **d,** Distribution of the number of breaking events per 100 beads for different force values, showing that most breaking events occur around 2 pN. This represents a specific, molecular slip bond that is broken repeatedly by a force of 2 pN. Force is calculated as explained on Box 3. **c-d,** Adapted from Jiang et al. 2003.

Applications of optical tweezers in applying/measuring forces at the cell surface extend beyond IAS mechanosensing and force transmission. Further examples include studies on endocytosis (Shergill et al., 2012) and receptor-ligand interactions in immunity (Feng et al., 2017). In the latter, functionalized beads can apply mechanical loads on T cells; this assay revealed that T-cell activation is sensitive to mechanical load, which also modulates the number of ligands required for activation (Feng et al., 2017). Moreover, it is also possible to manipulate structures inside the cell, although these applications are still being developed. This could be achieved either by internalizing the beads or by directly controlling organelles such as vesicles, lipid droplets or mitochondria (Arbore et al., 2019; Gao et al., 2016; Sparkes, 2016).

Overall, SMFS and live cell assays reveal the power of optical tweezers in understanding the molecular mechanisms of mechanosensing, both *in vitro* and in live cells. The latter was particularly relevant for grasping the interplay between force and IAS mechanosensing. Nonetheless, some disadvantages exist, such as photodamage induced by the laser trap or the non-specific trapping of particles (Neuman and Nagy, 2008). Importantly, and even if intracellular manipulations are possible, optical traps cannot probe proteins within crowded macromolecular structures in the interface between the cell and the surface. This prevents a detailed understanding of force transmission and mechanosensing across IASs, for instance.

6.1.2. Magnetic tweezers

The first magnetic tweezers were assembled in 1996, to study the elasticity of individual DNA supercoiled molecules (Strick et al., 1996). Conceptually, magnetic tweezers are similar to optical tweezers: a magnetic particle/bead is 'trapped' in an external magnetic field by a force proportional to the gradient of the square of the magnetic field. This bead can be coated with a specific handle for DNA or a protein of interest. Creation of the magnetic field can be achieved through different methods: the most straightforward consists of a pair of permanent magnets, which pull the bead towards the gap between them (Strick et al., 2000). Electromagnetic tips can also be used to create magnetic fields towards the source of the field and to the tip of the electromagnetic core/needle (Chronopoulos et al., 2020). In many of these variations, computer programs and algorithms allow to track the 3D bead position in real time.

Compared to optical tweezers, magnetic tweezers allow to apply higher forces, up to 1 nN for electromagnetic tweezers. The rotational capacity of the method was essential in studying the elasticity of supercoiled DNA (Strick et al., 1996). Moreover, many implementations allow to both manipulate and rotate the magnetic particles at the same time, thus allowing to change the orientation of forces (Gosse and Croquette, 2002). They also provide the advantage of multiplexing, enabling to manipulate multiple biomolecules at the same time (Sarkar and Rybenkov, 2016) . However, magnetic tweezers are less versatile compared to AFM or optical tweezers.

In the field of SMFS, one of the most known applications of magnetic tweezers were the *in vitro* studies on the unfolding of talin rod domains and vinculin recruitment, using purified proteins (Del Rio et al., 2009; Yao et al., 2016). However, implementations such as electromagnetic tweezers and nano/micro-tweezers can also be used to manipulate proteins in live cells with high precision at the nano-Newton (nN) scale (Aermes et al., 2020; Chronopoulos et al., 2020) . A recent work with uselectromagnetic tweezers in live cells has unveiled how the proteoglycan adhesion receptor syndecan-4 can modulate cell mechanics through an integrin-kindlin-Ras homologous member A(RhoA) based pathway (Chronopoulos et al., 2020). Nonetheless, and despite their various applications for mechanosensing in live cells, magnetic tweezers, cannot probe proteins within crowded macromolecular structures in the interface between the cell and the surface.

6.1.3. Atomic force microscopy

Atomic force microscopy (AFM) differs from the two previous methods since it is both an imaging and force spectroscopy technique. An atomic force microscope is a scanning probe microscope with two main components: a cantilever with a sharp tip, which acts as flexible sensor, and a piezoelectric positioner, which controls the sample position with nanometric

precision. A focused laser beam is reflected off the surface of the cantilever onto a position-sensitive detector (PSD). The cantilever applies a preset force or deformation on the sample, which exerts a resisting force, deflecting the the cantilever. These deflections can be monitored by the displacement of the reflected laser spot on the PSD. Finally, the AFM transduces the forces exerted by the sample on the cantilever by measuring the angular deviations of the laser beam (Hughes and Dougan, 2016; Neuman and Nagy, 2008). AFM allows to measure and apply forces from the piconweton to the micronewton range with high spatial (from sub-nanometer to micrometer scale) and temporal (sub-millisecond) precision (Hughes and Dougan, 2016; Krieg et al., 2019; Neuman and Nagy, 2008). The applications and implementations of AFM are very diverse and are in continuous evolution: covering all of them would be out of the scope of this introduction (Dufrêne et al., 2017; Krieg et al., 2019). In the context of our work, AFM is particularly relevant due to its applications in single molecule force spectroscopy (SMFS) and on cell mechanics.

6.1.3.1. AFM and cell mechanics

Through surface indentations, AFM can both generate topographical maps of the cell surface but also measure various parameters of cell mechanics. Here, the cantilever applies a preset force to an adherent cell or tissue, and the corresponding resistance force from the cell deformation is recorded (Wu et al., 2018). From here, force can be plotted against distance or time; the latter is particularly useful when mechanical properties change over time or in measuring rheological parameters (Moeendarbary et al., 2013; Stewart et al., 2011). Different mechanical parameters can be characterized, such as the elastic (Young's) modulus, which reflects the stiffness of the structure. In this regard, it is important to highlight that elastic moduli can change considerably with indentation speeds and force profiles, but also across cells in the same sample (Wu et al., 2018). Other mechanical parameters include pressure, tension, viscosity and energy dissipation. In the context of mechanobiology, AFM has been crucial to understand the contribute of the glycocalyx, cytoskeleton, cytoplasm and the intracellular pressure in cell elasticity, as well as the protrusive forces of migrating cells (Krieg et al., 2019).

6.1.3.2. AFM and single molecule force spectroscopy

In single molecule force spectroscopy, AFM is used to measure intra and intermolecular forces with piconewton resolution (AFM-SFMS). Initial instalments of AFM-SFMS aimed to stretch single proteins and assess their force response. The higher force ranges achieved by AFM, compared to optical tweezers – which are limited to ~100 pN – were crucial for these assays. Pioneer studies in AFM-SMFS were conducted at the labs of Julio Fernandez and Herman Gaub on the force-dependent unfolding of the sarcomeric protein titin and the ECM protein tenascin

(Oberhauser et al., 1998; Rief et al., 1997). Here, the cantilever was modified to act as a 'molecular force probe', moving only in the axial direction, while proteins were adsorbed on the surface (Fig. 8a). Proteins interacting with the cantilever tip were then pulled/stretched at constant speed, generating force-extension curves (Fig. 8b). When proteins are mechanically stretched, they generate a restoring force, which is measured by the deflection of the cantilever; extension, on the other hand, is the distance between the surface and the cantilever tip. For titin and tenascin, force-extension curves display a characteristic sawtooth pattern with multiple force peaks: 150-300 pN for titin and 100-200 pN for tenascin (Fig. 8b). This pattern is consistent with stepwise increases in the contour length of a polymer, with each peak corresponding to unfolding of one domain (Oberhauser et al., 1998; Rief et al., 1997). Seminal studies on titin and tenascin were instrumental to characterize force-dependent protein unfolding, which would later be considered as one of the keys to mechanosensing. The same principle was applied to spectrin - a cytoskeletal protein which we will later discuss– and revealed that the force required to unfold spectrin alpha-helical domains was five to ten times lower (25-35 pN) compared to titin or tenascin (Rief et al., 1999). This suggests that forces stabilizing spectrin domains are weaker than hydrogen bonds found on the domains of titin or tenascin. Importantly, it reveals how AFM not only allows to characterize protein unfolding but also the underlying forces ruling protein structure, with possible functional implications. Several other studies on protein unfolding have been performed ever since, revealing multiple unfolding pathways (Dietz et al., 2006) or the importance of pulling direction (Carrion-Vazquez et al., 2003).

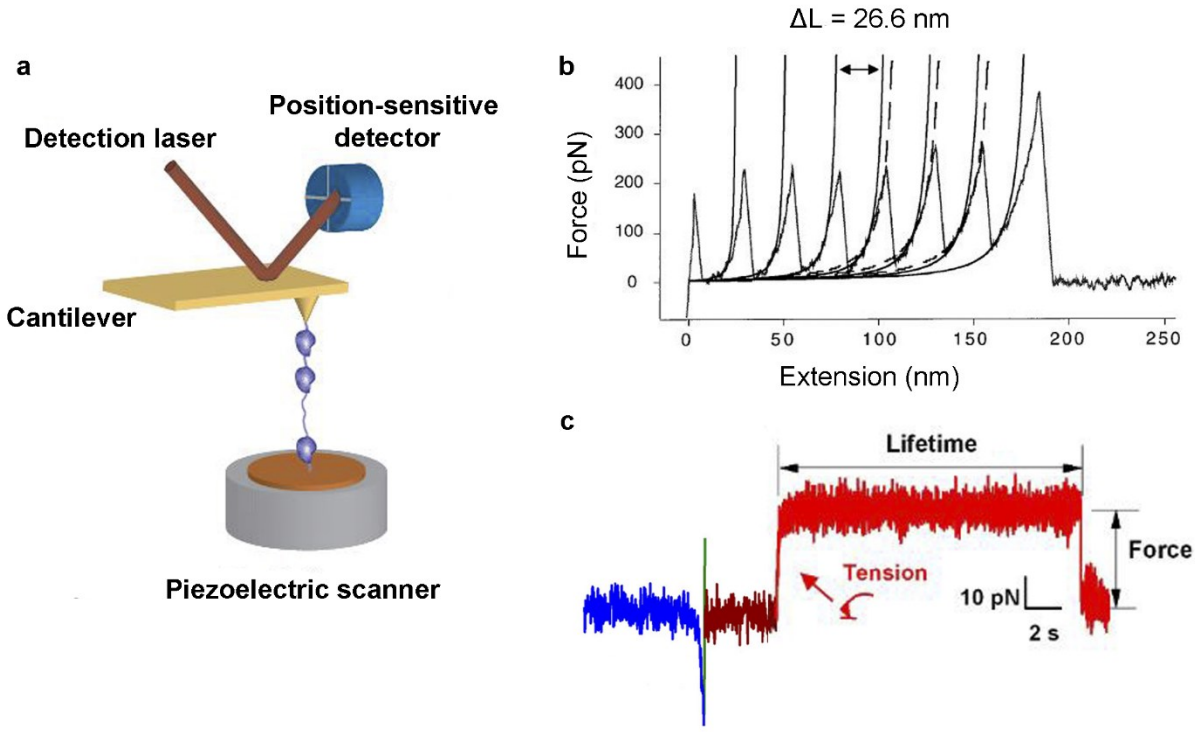

Figure 8: AFM-SMFS to study protein unfolding and catch bonds

a, Cartoon of the atomic force microscope, which consists of a cantilever with a sharp tip (yellow) held above a piezoelectric scanning stage (gray). A laser beam, reflected off the cantilever tip into a position-sensitive detector (PSD), is used to monitor the deflections of the cantilever. Proteins are adsorbed onto a substrate (such as gold) which is placed on top of the piezoelectric scanning stage. In a typical AFM pulling experiment, single proteins or polyproteins (purple) – an tandem array of protein repeats connected by a polypeptide linker - are attached to the sample surface (such as copper or gold) and the AFM cantilever tip. The piezoelectric stage is retracted along the axial direction, increasing the separation between the cantilever and the sample surface. The force on the molecule is provided by the cantilever deflection, and the extension of the molecule is equal to the separation between the AFM tip and the sample surface. Adapted from Neuman and Nagy 2008. **b,** A characteristic force-extension AFM curve obtained for a recombinant construct comprising eight immunoglobulin domains of the muscle protein titin. Each unfolding event increases the contour length of the unfolded polypeptide by ~26.6 nm (corresponding to 89 residues per domain), which originates a characteristic sawtooth pattern with regular force peaks. Unfolding can be described by a worm-like chain (WLC) model, which here uses two persistence lengths: 0.8 nm, which fits best the response at lower forces (continuous lines), and 0.4 nm, more adequate for higher forces, (dashed lines). Adapted from Rief et al. 1997, 1999. **c,** A force-scan AFM trace for integrin adhesion to fibronectin. Initially, the surface is moved to contact with the cantilever (blue trace), retracted to avoid non-specific adhesion formation (green trace) and then kept around 0.5 s (brown trace) to allow for bond formation. An increase of tension can be seen after that period (red trace), indicating that retraction resulted in a tensile force indicating adhesion. Once the pulling force reaches a preset value, the cantilever deflection is kept at that point to apply a constant force. The lifetime of the bond at that force is measured until bond failure, when the cantilever springs back to zero mean force (final red trace). Adapted from Kong et al. 2009.

Over the last two decades, AFM-SFMS has also emerged as a powerful tool to study receptor-ligand interactions, including bacterial-host adhesions (Milles et al., 2018), antibody-antigen bonds (Sulchek et al., 2005) and cell-ECM adhesions (Kong et al., 2009). Concering the latter point, AFM-SFMS allowed to demonstrate a catch bond between integrin $\alpha_5\beta_1$ and fibronectin, with implications for IAS mechanosensing (Kong et al., 2009). Here, the cantilever was functionalized with a fibronectin fragment and placed in contact with purified integrins, applying a constant force (Fig. 8c). Lifetime of this force increased in the range of 10-30 pN, indicating the presence of a catch bond (Kong et al., 2009). Several of these studies, as well as new implementations of AFM for studying other molecular bonds, rely on various pulling protocols, which allow for better force control. In the seminal works of Rief and Oberhauser (Oberhauser et al., 1998; Rief et al., 1997), pulling was performed at constant speed. This is prone to drift and could lead to underestimation of the unfolding forces for early-unfolding domains (Zheng et al., 2011b). To minimize this, subsequent studies used modes of 'force clamp' or 'force ramp', where force is either hold at a given value or increased linearly with time, respectively. These two methods can directly observe force-dependent kinetics of protein unfolding (Oberhauser et al., 2001) and receptor-ligand complex rupture (Kong et al., 2009), such as shown for integrin $\alpha_5\beta_1$ and fibronectin. This highlights how the force profile can largely influence single molecule response to force, which will likely be even more complex *in vivo*.

6.2. Studying cellular forces

Currently, there is a variety of ever-growing methods to measure forces actively applied by cells. These can be divided into different categories, and previous publications have used different criteria (Polacheck and Chen, 2016; Roca-Cusachs et al., 2017). For instance, methods can also be divided according to whether they are based or not in materials of known mechanical properties. The first category, where mechanical properties are known, includes traction force microscopy (TFM), cantilevers and micropillars, and molecular force sensors. The second category, where mechanical properties are not known, includes laser ablation or monolayer stress microscopy (Roca-Cusachs et al., 2017). The complexity of the sample is one of the main aspects to take into account: there are methods to measure forces applied by tissues, cell groups, a single cell or individual proteins. The latter are of extreme interest to study molecular mechanosensing and force transmission (Austen et al., 2015; Brockman et al., 2018; Grashoff et al., 2010; Stabley et al., 2012). Individual proteins within mechanosensitive structures are under tension and undergo force-dependent conformational changes (Grashoff et al., 2010). Such forces are often in the scale of piconewtons (pN) and can control multiple biological processes. Moreover, individual cytoskeleton-ECM linkages within adhesions are crucial for force loading and ligand spatial sensing. Thus, it is critical to measure force sensing at the molecular scale. With this in mind, a vast variety of molecular force sensors has been developed over the last decade,

with special emphasis on two categories: fluorescence resonance energy transfer (FRET)-based tension sensors and DNA tension sensors (Fig. 9).

6.2.1. FRET-based tension sensors

FRET-based tension sensors are genetically encoded and ideally posed to measure intracellular forces. They are usually composed of two GFP-like fluorophores connected by a mechanical peptide linker (Austen et al., 2015; Grashoff et al., 2010; Ringer et al., 2017). Upon force application to the molecule, the mechanical linker is stretched, reducing FRET between the two fluorophores. The sensitivity and range of the sensor are determined by the mechanical properties of the linker and the FRET range of the fluorophores (Austen et al., 2015; Grashoff et al., 2010; Ringer et al., 2017). For instance, the F40 tension sensor module (F40-TSM) is composed by a 40-amino-acid-long elastic peptide which gradually elongates when forces between 1-6 pN are applied (Fig. 9a). F40-TSM has been extensively used to characterize mechanotransduction events in various cells and organisms; examples include the force-bearing by vinculin in mature FAs (Grashoff Nature 2010), the pre-stressing of β-Spectrin in touch receptor neurons (Krieg NCB 2014) or the constitutive tension on E-cahderin at cell-cell contacts (Borghi PNAS 2012). Nonetheless, some molecular forces are higher, such as the ones experienced by integrins, thus requiring FRET-based tension sensors with higher force ranges. In this regard, biosensors with the 35-aa-long villin headpiece peptide (HP) display a force range between 7-10 pN and have been used to study the mechanical response of talin (Austen NCB 2015). Another possible limitation is the sensitivity of force sensors with a gradual response; F40-TSM, for instance, is limited at forces below 6 pN. A recent new sensor based on a ferredoxin-like (FL) linker peptide provided a more digital-like force response; the sensor undergoes a huge drop in FRET efficiency when force is increased from 3 to 5 pN, exhibiting a higher sensitivity in lower force ranges (Fig. 9b) (Ringer Nat Methods 2017). Moreover, the FL-sensor can be applied with multiplexing by dual-color fluorescence lifetime imaging (FLIM). This versatile tension sensor was used to study tension gradients across different domains of talin, but also to calculate the fraction of mechanically engaged talin molecules.

6.2.2. DNA-hairpin sensors

Integrin-ECM linkages transmit bidirectional forces at the piconewton scale. In general, cell surface receptors exert forces on their ligand, either on the substrate but also on other cells, such as the case of T cell receptors and respective antigens. In this regard, DNA mechanotechnology is emerging as powerful way to measure forces on the cell surface at the piconewton scale (Brockman et al., 2018; Stabley et al., 2012; Zhang et al., 2014). DNA tension sensors include two main components: a spring that extends in response to force, and a

fluorophore-quencher pair. In existing tensors, the spring/linker consists of a stem-loop DNA hairpin (Fig. 9c) (Brockman et al., 2018; Stabley et al., 2012; Zhang et al., 2014). Applied force beyond a certain threshold unfolds the hairpin and results in fluorophore dequenching. Each sensor is anchored to the surface on one end and to a cell receptor on the other end. Compared to TFM, DNA hairpin tension sensors are more versatile in terms of substrate (can be used in glass and other polymers), while still providing live-cell measurements of cellular forces with pN resolution. Moreover, hairpin tension sensors are highly tunable and display a digital-like force response. DNA Hairpin tension sensors have enabled to study integrin forces during early cell adhesion (Fig. 9c) (Zhang et al., 2014) as well as the magnitude and 3D orientation of integrin traction forces in mouse fibroblasts and human platelets (Brockman et al., 2018) DNA-origami tension sensors with multiple tunable hairpins have also been developed, enabling to study the role of multiple interacting receptors in mechanotransduction (Dutta et al., 2018).

6.2.3. Current limitations of molecular sensors

Both FRET and DNA force/tension sensors have expanded force measurement to the realm of single molecules. Nonetheless, some drawbacks still remain, including the discrepancies in force measures between different techniques (Roca-Cusachs et al., 2017) and the influence of force loading profiles in molecular extension. When compared to DNA-based sensors, FRET-based sensors might be less sensitive, but the recent digital-like FL sensor constitutes a significant improvement. Conversely, current DNA-based sensors are susceptible to nuclease degradation and are thus inadequate for measuring forces inside living cells, by opposition to FRET-based sensors (Blanchard and Salaita, 2019). Moreover, both techniques rely on ensemble measures of molecular forces, averaging possible variations in individual linkages, which could be relevant for local force-sensing events. In this regard, a recent technique has integrated DNA hairpin tension probes with DNA point accumulation for imaging in nanoscale topography (PAINT) ((Liu et al., 2016). Known as tPAINT, this elegant method allows to map piconewton mechanical events with ~25-nm resolution, providing a more single-molecule approach for force measurements in cells (Brockman et al., 2020).

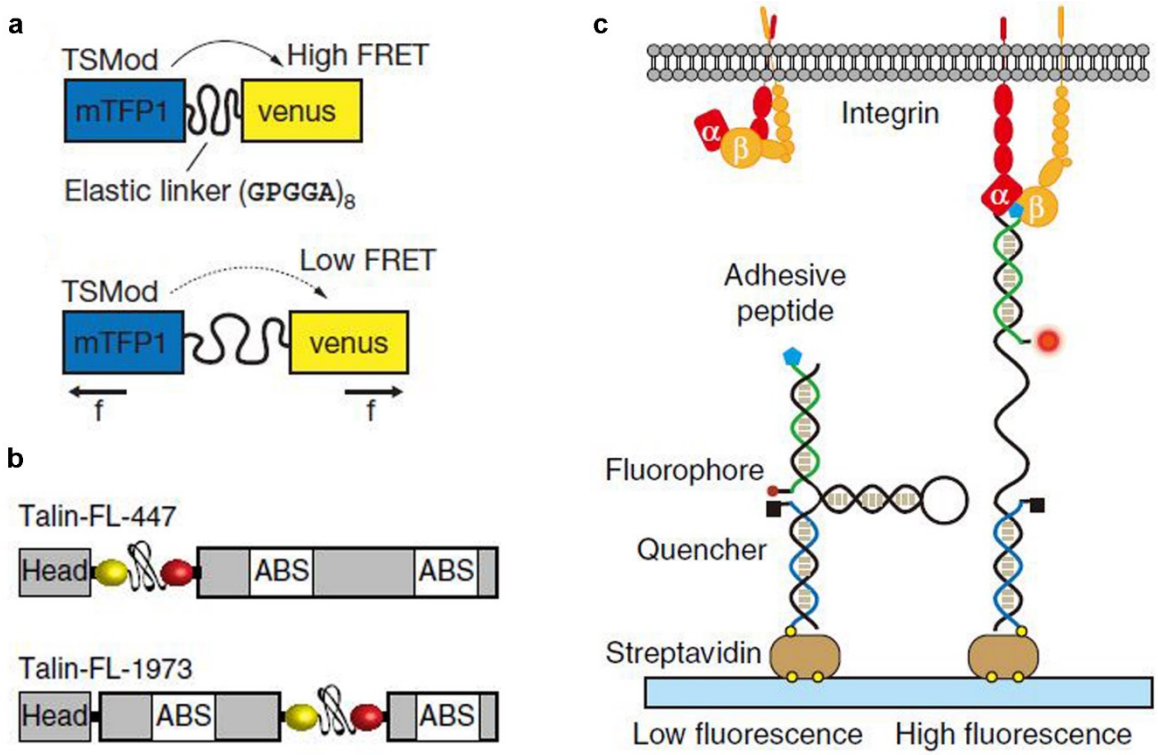

Figure 9: Molecular FRET and DNA hairpin force sensors

a, Vinculin FRET tension sensor module (VinTSMod) consisting of an elastic 40-amino acid long flagelliform linker sequence (GPGGA) inserted between two fluorophores (mTFP1 and venus (A206K)), which undergo FRET. The linker sequence gradually elongates when forces of 1-6 pN are applied, resulting in a decreased FRET efficiency between mTFP1 and venus (A206K). Adapted from Grashoff et al. 2010. **b,** A talin FRET tension sensor composed by a different linker sequence – a ferredoxin-like (FL) linker peptide – inserted between two fluorophores: yPet (yellow) and mCherry (red). When the sequence elongates, the Talin-FL sensor displays a unique digital-like force response with a substantial FRET efficiency drop between 3 and 5 pN, different from the gradual response of VinTSMod. Moreover, the FRET pair can be inserted into two different sites of the talin rod domain: near the N-ter (top) or near the C-ter (bottom), allowing to measure tension in different regions of the protein. Adapted from Ringer et al. 2017. **c,** DNA hairpin tension sensor to measure integrin forces, composed of three oligonucleotides assembled through hybridization of 21-mer handles: 1) an anchor strand tagged with a quencher and immobilized onto the streptavidin-coated surface (blue), 2) a stem-loop DNA hairpin that unfolds under tension (blacks), and 3) a peptide displaying ligand strand conjugated to a fluorophore (green). Both the fluorophore and the quencher are coupled to report the force-induced unfolding of the hairpin. Adapted from Zhang et al. 2014.

2. Cytoskeleton-generated forces

Intracellular-generated forces play a key role in various processes, from migration to cell division. The main generator of intracellular forces, the cytoskeleton, engages various mechanisms to exert force, which depend on the dynamics of its components as well as associated proteins. In this chapter, I describe first how actin filaments can generate force either through their own polymerization or in combination with myosin, an essential partner in contractility. I will approach how these forces can be harnessed to drive cell migration and protrusion via the molecular clutch model. I will also present how actomyosin filaments organize into different stress fibers, as well as their functions within the cell. Finally, I will approach microtubule-dependent pushing and pulling forces, which are a key element in mitosis.

1. Force generated by actin filaments

1.1. Actin filament polymerization

Actin filaments mediate a considerable amount of mechanical responses in eukaryotic cells. Between the variety of actin structures within the cells and the dynamics of actin networks, the actin filaments can generate and transmit forces controlling several cellular processes. A striking example are the forces generated by actin polymerization in the lamellipodium, which drive protrusion of leading edge membranes in migrating cells (Bisi et al., 2013). In the lamellipodium, Arp2/3 complex assembles a dense network of branched actin filaments. The elongation of each filament generates piconewton forces, which propel the front end of cells to move. (Pollard and Cooper, 2009). By observing *in vitro* the buckling of individual actin filaments capped by formin with evanescent wave microscopy, Kovar and Pollard obtained a polymerization force of around ~1 pN for polymerizing actin filaments (Kovar and Pollard, 2004). This force reached a maximum of ~1.3 pN, close to the theoretical value of 2 pN. However, this study represents the behavior of a single actin filament while buckling; polymerization-dependent force can be influenced by many factors, such as the incident angle, filament length, actin networks and filament bundling. Another optical trap-based study was used to study force generated by filament bundles against a load; surprisingly, force was also around ~1 pN (Footer et al., 2007). The most likely explanation is that only the longest filament is in contact with the barrier at any given moment; filament length within the bundle can also fluctuate to exchange

the load (Footer et al., 2007). This result could be counterintuitive with the dynamic of filopodia, thin actin-rich cytoplasmic protrusions that extend beyond the lamellipodia to probe the microenvironment (Kress et al., 2007). Forces on filopodia have been found to be between 1-10 pN (Kress et al., 2007); small parallel bundles such as the ones in filopodia could likely exhibit the same behavior as filament bundles *in vitro*. Such limitations could be surpassed by ABPs. However, it is not clear if the load can be distributed differently in other bundle or membrane configurations. On the other hand, in lamellipodia, actin filaments form a branched network rather than a bundle. Assuming that each filament can produce the same amount of force parallel to its axis, the contact angle θ with the membrane can result in higher membrane pushing (Dmitrieff and Nédélec, 2016). Parallel forces F_a correspond to perpendicular forces $F_a/\sin\theta$; if $\sin\theta > 1$, perpendicular forces will be amplified (Dmitrieff and Nédélec, 2016). The contact angle is both determined by the branching angle imposed by Arp2/3 and by orientations of the branched network with respect to the leading edge (Weichsel and Schwarz, 2010).

Force-dependent polymerization is not the only accepted model for generation of forces at the lamellipodium; indeed, an alternative model suggests that the lamellipodium behaves similar to a gel rather than a branched network (Sykes and Plastino, 2010). In this model, forces would be generated by new actin networks over the precedent ones. It is important to mention, though, that branched actin networks generate pushing forces involved in many other processes besides leading edge protrusion; these include the motility of intracellular pathogens (Welch and Way, 2013), endocytosis (Mooren et al., 2012), formation of tight cell adhesions (Efimova and Svitkina, 2018)and dendritic spine morphology and plasticity (Chazeau et al., 2014; Kim et al., 2013).

Polymerization of F-actin against the leading edge membrane also results in a counterforce that drives the F-actin network rearward, resulting in retrograde F-actin flow in the lamellipodium. The lamellipodial actin network undergoes fast retrograde flow (5-20 nm/sec) (Fig. 10a) and exhibits actin 'treadmilling': while F-actin polymerizes at the front, the entire network flows back and depolymerizes (Fig. 10b) (Ponti et al., 2004; Vallotton et al., 2003). The lamellipodium overlaps with a less dynamic actin network characterized by slower flow and a punctate pattern of filament turnover, known as the lamella (Fig. 10a,b). Lamellpodium and lamellum have distinct molecular signatures, with ABPs such as Arp2/3 and cofilin in the lamellipodium and myosinII and tropomyosin in the lamellum (Ponti et al., 2004). Here, myosin-II contraction reorganizes actin and slows down the retrograde flow from 5-20 nm/sec to 2-5 um/min. Perturbing actin polymerization or depolymerization selectively affects filament turnover and retrograde flow in the lamellipodium, whereas myosin II inhibition selectively blocks lamella retrograde flow (Ponti et al., 2004). Thus, F-actin polymerization appears to drive fast retrograde flow in the lamellipodium, while myosin-II contraction drives a slower flow in the lamellum. However, it important to note that these differences are highly dependent on the

correct segregation of lamellipodium and lamellum. For instance, when the FA protein vinculin is depleted, the steep drop of flow velocity between both regions is abolished (Thievessen et al., 2013). This reveals how the molecular and kinetic profile of each network is crucial to drive differences on flow speed but also on subsequent formation and maturation of integrin-ECM adhesions (Choi et al., 2008; Giannone et al., 2007). Moreover, when both regions are 'mixed', both myosin-II contractility and F-actin polymerization will contribute for the overall retrograde flow. (Jurado et al., 2005). In this regard, the lamellipodium displays periodic contractions.

In addition, cell edge protrusion driven by actin polymerization is not continuous; instead, it was previously demonstrated to be a cyclic process composed of periodic protrusions and retractions (Giannone et al., 2004; Ponti et al., 2004). This periodicity results from the spatial, temporal and mechanical coordination of lamellipodial actin, myosin motors and adhesion site formation. These elements combine to generate periodic contractions of lamellipodial F-actin, which drive the formation of transient integrin-paxillin clusters and generate actin rearward waves bound to α-actinin and myosin light chain kinase (MLCK) (Giannone et al., 2004). Such contractions could enable the mechanical probing of the substrate and enable IAS formation, an aspect which will later be discussed in detail.

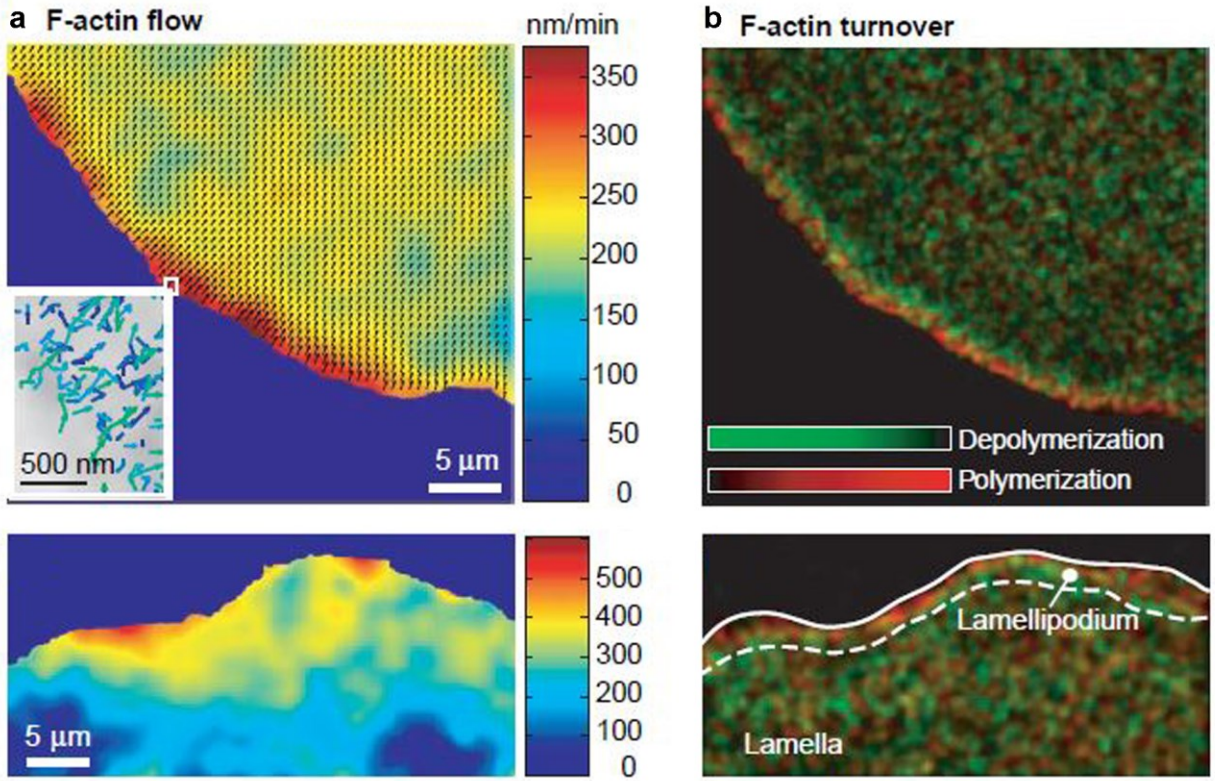

Figure 10: F-actin flow and turnover define lamellipodium and lamella in migrating cells

a, F-actin flow measured by quantitative fluorescence speckle microscopy (qFSM) in newt lung epithelial cells (top) and potoroo kidney (PtK1) epithelial cells (bottom). Colors encode flow speed, and vectors, flow direction. Inset: Individual speckle trajectories over 200 s; time evolution, dark blue to light green. A thin band of flow is visible (1 to 3 µm) along the leading edge where speckles undergo fast flow (300/500 nm/min) towards the cell center, corresponding to the lamellipodium. A larger and slower flow area is visible after the band (100 to 250 nm/min), corresponding to the lamella. **b,** F-actin turnover measured by qFSM in newt lung epithelial cells (top) and potoroo kidney (PtK1) epithelial cells (bottom). Time-averaged F-actin turnover (60 frames). Red channel, assembly rate; green, disassembly rate. The lamellipodium can be identified as a similar 1-3 µm band of strong polymerization seen along the leading edge, which transitions into a narrow band of depolymerization, corresponding to the lamella. **a-b,** Figure adapted from Ponti et al. 2004.

1.1.1. The molecular clutch model

Retrograde F-actin flow is converted into different forces throughout the cell, an event which has been proposed to occur through the molecular clutch hypothesis (Fig. 11). In the most studied and conventional scenario, retrograde F-actin flow is coupled to IASs in adherent cells to generate traction forces on the substrate and membrane protrusion (Case and Waterman, 2015; Giannone et al., 2009). The clutch is considered 'engaged' when the actin cytoskeleton is indirectly connected to ECM-bound integrins through a series of viscous protein linkages involving IAS proteins such as talin. When actin polymerization and myosin contraction are constant, IAS-mediated engagement reduces flow velocity and converts it into reward traction forces on the substrate (Case and Waterman, 2015; Giannone et al., 2009). This is coupled with the continuous polymerization at the leading edge, driving membrane protrusion and cell migration. Such a model has been extensively studied and validated in live cells, although the molecular clutch model will not be exclusive for cell-ECM adhesions (Case and Waterman, 2015). Cell-cell adherens junctions, for instance, can be excellent sites for force transmission through a molecular cutch. α-catenins bind to the filamentous (F)-actin and can also recruit vinculin, establishing the mechanical connection between cell-cell adhesion proteins and the contractile actomyosin cytoskeleton (Ladoux and Mège, 2017). Retrograde actin flow can be converted by this 'alternative' molecular clutch, transmitting forces between neighboring cells. Moreover, integrin-based complexes can also mediate cell-cell adhesions, such as the complex between integrin lymphocyte function-associated antigen 1 (LFA-1) and the intercellular adhesion molecule 1 (ICAM-1), which mediates leukocyte-endothelial cell adhesion (Walling and Kim, 2018). While LFA-1 integrin can connect to the leukocyte actin cytoskeleton via talin (Walling and Kim, 2018), ICAM-1 can indirectly bind the actin cytoskeleton through α-actinin (Celli et al., 2006). Thus, a molecular clutch-based interaction between two cell types could transmit F-actin retrograde flow force to drive leukocyte extravasation of T cells into the lymph node and tissue.

Not all cells migrate in an adhesion-dependent fashion within a 2D environment, which is the case of amoeboid cells such as leukocytes. A recent study has shown that leukocytes can transmit forces by coupling retrograde flow of actin to the topography of the substrate, creating retrograde shear forces that drive the cell body forwards (Reversat et al., 2020). This reveals how the retrograde F-actin flow is a powerful and versatile force-generating entity within both the migrating and adhesive cell.

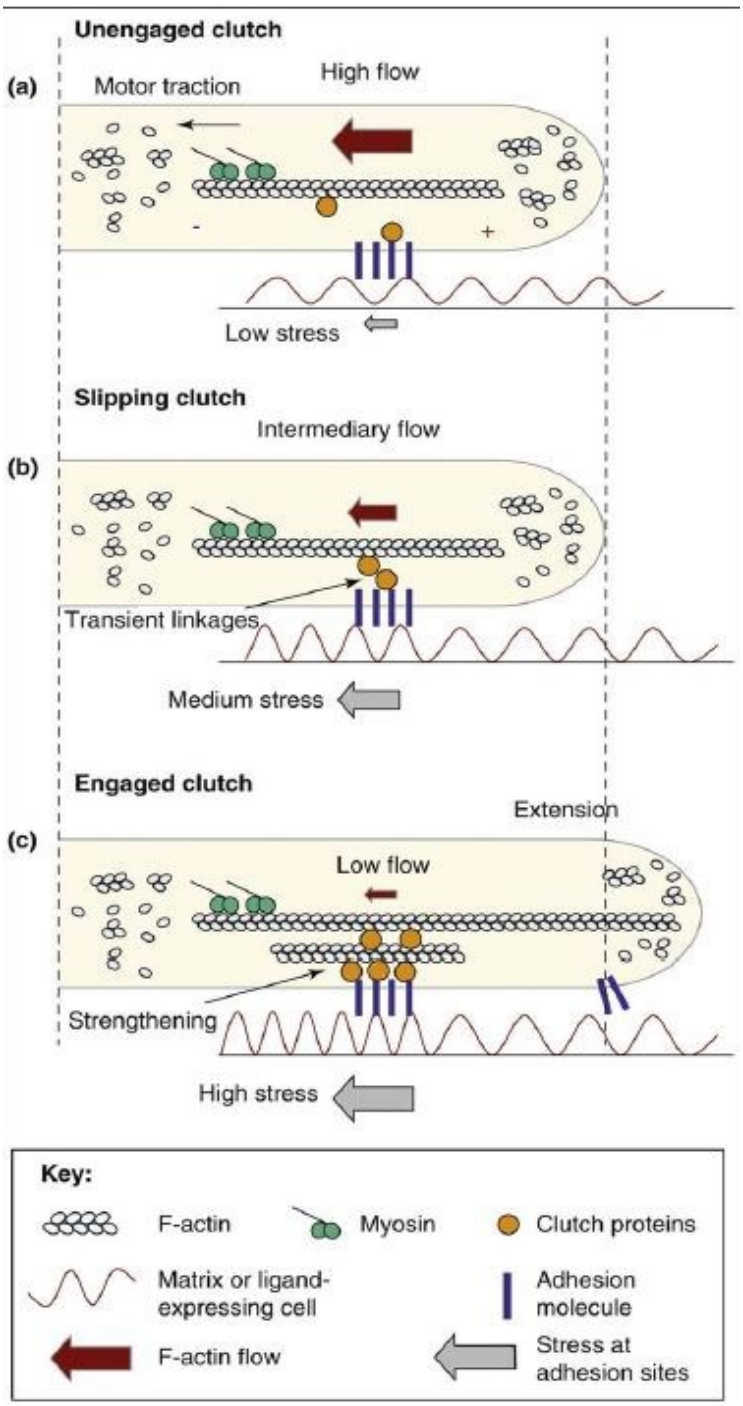

Figure 11: The molecular clutch hypothesis

Three potential states of a molecular clutch. Side view of a lamellipodium moving on a substrate. Adhesive proteins (blue) are bound to extracellular ligands in the ECM (red). At the leading edge of the lamellipodium, actin polymerization against the membrane generates a retrograde actin flow, which is further modulated by myosin II contractility in the lamella. The dynamic engagement of actin retrograde flow with ECM-bound integrin is mediated by clutch molecules, specific for different adhesion types (IASs in this schematic, but also adherens junctions or leukocyte-mediated adhesions). **a,** When the clutch is not engaged to connect actin to the ECM, only rapid retrograde flow is verified, without leading edge protrusion and no traction force on the ECM. **b,** Slipping clutch, where transient weak connections are formed between the Factin flow and ligand/receptor complexes through clutch proteins. **c,** When the molecular clutch is 'engaged', forces generated by polymerization of actin filaments are physically transmitted to the ECM, resulting in slowing of retrograde flow, traction force on the ECM and a net edge protrusion. Figure adapted from Giannone et al. 2009.

1.2. Actomyosin contractility and stress fibers

The actomyosin cytoskeleton produces contractile forces which are essential for cell morphology, division, migration and differentiation (Tojkander et al., 2012). These are mostly generated by either actomyosin bundles or stress fibers in adherent cells. Stress fibers consist of linear bundles of actin filaments associated with myosin-II and α-actinin, among other cytoskeletal proteins (Burridge and Guilluy, 2016). Activity and assembly of stress fibers is dependent on RhoA-activation to promote myosin-dependent contractility (Oakes et al., 2017; Smith et al., 2010). Frequently, stress fibers are anchored at either one or both ends to mature FAs, transmitting myosin-generated forces across FAs and onto the substrate. Accordingly, tension-dependent IAS maturation is often accompanied by stress fiber assembly. However, these might be more than concomitant events, since stress fiber assembly has shown to be required for adhesion maturation by serving as a structural template over a wide range of tensions.

Over the last two decades, it has become clear that stress fibers do not assume a single type of structure inside the cell. They can change in morphology, organization and association with IASs (Fig. 12) (Hotulainen and Lappalainen, 2006; Schulze et al., 2014; Tojkander et al., 2012). An initial distinction can be made between dorsal and ventral stress fibers (Fig. 12a,b). Dorsal stress fibers are actin filaments anchored to IASs only at the distal end and they do not contain myosin-II, extending back toward the nucleus and upwards toward the dorsal cell surface (Fig. 12a,b) (Tojkander et al., 2012). Although they lack the ability to contract, dorsal stress fibers can act more as stabilizers and a platform for assembling other stress fibers (Hotulainen and Lappalainen, 2006; Schulze et al., 2014; Tojkander et al., 2012). In this regard, stress fibers are often referred to as actomyosin bundles, but dorsal stress fibers fall out of this category. This reflects the complexity of stress fiber organization and their roles within the cells. Ventral stress fibers, on the other hand, are attached to IASs at both ends and are often located at the posterior part of the cell (Fig. 12a,b) They constitute the main contractile machinery in many cell types (Hotulainen and Lappalainen, 2006; Tojkander et al., 2012). Their formation reveals how different types of stress fibers can combine to create new structures, as ventral stress fibers have been shown to arise from the combination of dorsal stress fibers and transversal arcs (Hotulainen and Lappalainen, 2006; Schulze et al., 2014). The latter, which are often included as a specific class of stress fibers, do not attach to IASs and are pulled by the retrograde F-actin flow from the leading edge towards the cell center (Fig. 12a,d) (Burnette et al., 2011; Shemesh et al., 2012). A fourth class of stress fibers is the perinuclear actin cap, consisting of stress fibers positioned around the nucleus (Fig. 12e) (Khatau et al., 2009). The perinuclear actin cap confers shape to the nucleus and mediates mechanotransduction of external forces transmitted to the nucleus (Khatau et al., 2009; Nava et al., 2020).

Combination of different stress fibers and actomyosin bundles allows to create a contractile actomyosin network spanning over the entire cell. This network can transmit forces over long cellular distances, surpassing the scale of a single filament. An example of such 'global' contractility is the isotropic distribution of tension across mature FAs upon an anisotropic external stress (Kumar et al., 2019). Conversely, local photoablations of stress fibers can affect the global traction field, thus showing how local force transmission is also important for the network stability. Nonetheless, it is important to understand how force is transmitted across this network, especially in regard to stress fibers. If they behave as independent entities only contacting other stress fibers, how can they contribute to force transmission across the cell? A recent study involving micropatterning, force measurements and modelling has shed new light on the mechanics of subcellular actin networks (Vignaud et al., 2020). Stress fibers were shown to be connected to a cortical actin meshwork, rather than discrete entities linked to the extracellular environment via IASs (Fig. 12e). Both the cortical meshwork and the stress fibers are elastic and contractile, forming an integrated network of actomyosin elements. Throughout this network, the architecture of actomyosin changes, with dynamic interactions between different components. Such unique emergent properties will be central for force transmission across the cell, as well as modulation of traction forces.

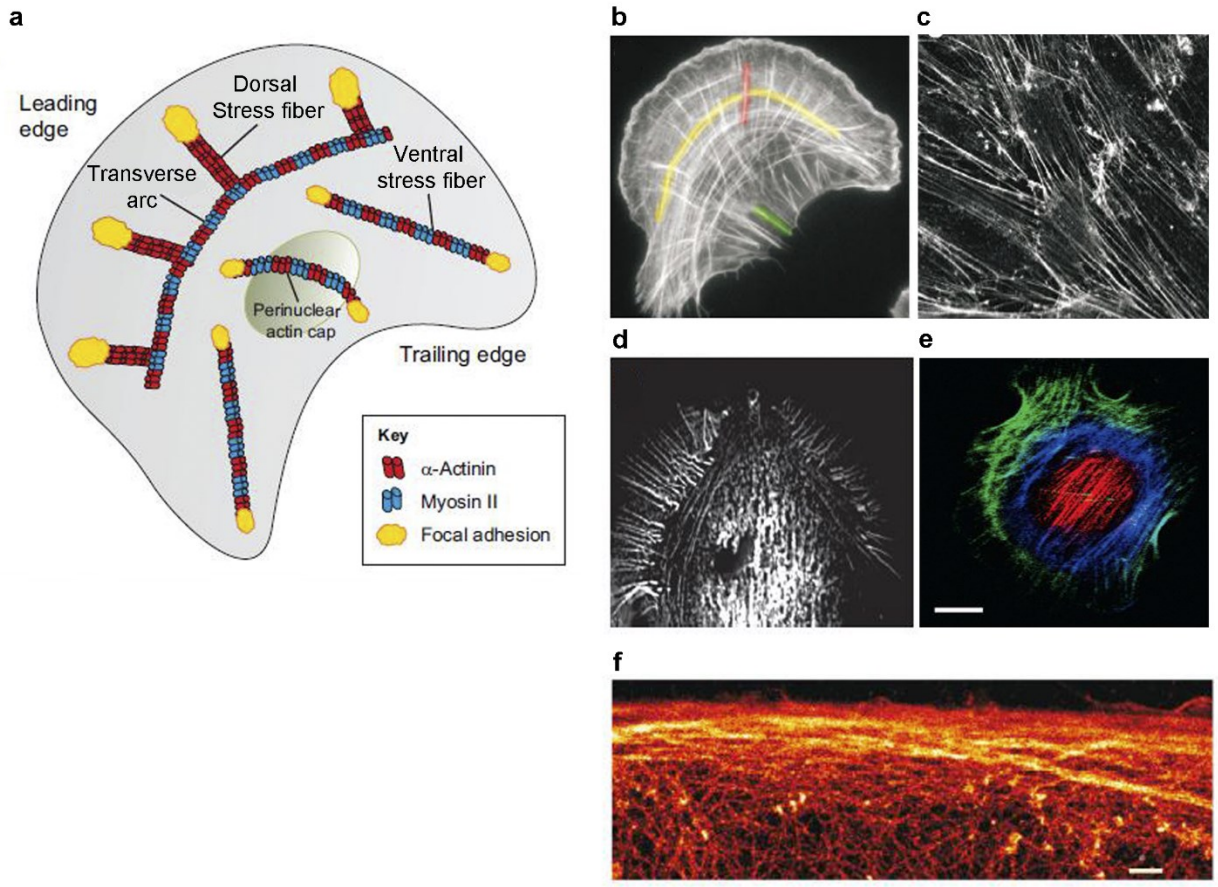

Figure 12: Different stress fiber morphologies:

Different types of stress fibers in cultured animal cells. **a,** Schematic presentation of the stress fiber network of motile mesenchymal cells. These cells can contain at least four discrete categories of stress fibers; (i) dorsal stress fibers, (ii) transverse arcs, (iii) ventral stress fibers, and (iv) perinuclear actin cap bundles. **b,** The stress fiber network of a motile U2OS cell. Shown here are examples of dorsal stress fibers, arcs and ventral stress fibers, indicated with red (dorsal), yellow (arcs) and green (ventral) lines, respectively. **c,** Stress fibers in human umbilical vein endothelial cells (HUVECs). In these cells, stress fibers from neighboring cells are physically connected through discontinuous adherens junctions. **d,** Visualization of actin arcs in a living neuron isolated from Aplysia.**a-d** Adapted from Tojkander et al. 2012. **e,** Perinuclear actin cap of a mouse embryonic fibroblast (MEF). The image is a reconstruction of confocal sections from the apical (red), mid-height (blue) and basal (green) surface. Scale bar = 10 µm. Adapted from Khatau et al. 2009. **f,** Peripheral stress fibers are interconnected with the surrounding actin cortex in retinal-pigmented epithelial cells (RPE1), here visualized with a Stochastic Optical Reconstructed Microscopy (STORM) image of the actin network. Scale bar = 1 µm. Adapted from Vignaud et al. BioXriv 2020. The actin filaments in all the panels shown are visualized by phalloidin staining.

2. Generation of forces by microtubules

Microtubules are highly dynamic entities which undergo a continuous switch between phases of growth and shrinkage, known as dynamic instability. This behavior is influenced by parameters as the rate of growth vs shrinkage as well as the frequency of switching from one state to another. Microtubule-associated proteins (MAPs), including plus end tracking proteins (+TIPs), microtubule polymerases/depolymerases and regulatory kinesins, are the major coordinators of microtubule dynamics and organization (Brouhard Nat Rev 2018). The class of +TIPs is particularly important because they can establish interactions with intracellular structures while MTs polymerize (Akhmanova Nat Rev 2015). Through such mechanisms, +TIP proteins can crosslink microtubules to actin, interact with FA scaffolding or modulate axonal guidance (Shimamoto Dev Cell 2015). Overall, dynamic instability is a key process to regulate microtubule network in response to different cues. Equally important, it can be harnessed by cells to exert pushing and pulling forces, controlling processes such as chromosome segregation during mitosis or organelle positioning. Thus, similar to actin dynamics, microtubule polymerization and depolymerization together with associated proteins an important mechanism for cellular force generation.

2.1. Microtubules and pushing forces

Microtubules are organized from the microtubule organizing center (MTOC), where the minus end is often embedded and nucleation is promoted. Growing microtubules can continue to polymerize after contacting an obstacle – cell cortex, organelles or protein complexes –which is thought to be dependent on thermal fluctuations (Howard and Garzon-Coral, 2017; Vleugel et al., 2016). This will slow down the microtubule growth and generate pushing forces, which are hence dependent on microtubule polymerization. These forces have been shown to reach a maximum of 5-10 pN *in* vitro, similar to the forces generated by motor proteins such as dynein or kinesin (Howard and Garzon-Coral, 2017). Their outcome can often depend on the nature of the obstacle; microtubules will often deform or displace flexible obstacles, while rigid obstacles will cause the microtubule to push itself. Compressive loads will cause bending, buckling and looping of microtubules, which are also in the base of many biological events (Lazarus et al., 2015).

Pushing forces have long been known to be crucial for mitotic spindle formation and positioning (Howard and Garzon-Coral, 2017). In some cells and organisms, the centrosome is associated to the nucleus during cell cycle. Microtubules growing against the cell cortex on opposite tips of the cell will generate pushing forces, displacing the nucleus. The balance between opposite pushing forces will center the mitotic spindle and consequently the nucleus (Vleugel et

al., 2016). Importantly, in larger eukaryotic cells, microtubule buckling hinders the transmission of forces. Hence cells will rely mostly on pulling forces for this same effect.

Microtubules can interact with a vast amount of organelles and protein complexes through the +TIP proteins. Thus, pushing forces can also contribute to organelle architecture and positioning. Microtubule plus ends have been shown to push endoplasmic reticulum (ER) and mitochondrial tubes, the latter influencing motility and mitochondrial distribution (Li et al., 2015b; Waterman-Storer and Salmon, 1997). Nonetheless, this is still a relatively unclear subject.

2.2. Microtubules and pulling forces

Conversely to pushing forces, pulling forces are produced by microtubule depolymerization. Shrinking microtubules will generate pulling forces, transmitted to objects 'coupled' to the microtubule ends (Brouhard and Rice, 2018). This 'coupling' requires objects to maintain load-bearing attachments throughout the microtubule shrinking. The most extensively studied example also comes from mitosis, where pushing and pulling forces are continuously integrated. First, when microtubules are anchored to the cell cortex during shrinkage, they can generate a tensile force that will pull the centrosome towards the cortex. Positioning of the centrosome depends considerably on dynein, a minus-end directed motor, which is particularly crucial during interphase and mitosis. Although pulling forces are usually anti-centering, the contrary can also occur, depending on the geometry of the cell or the anchoring of the microtubules to the centrosome or the cortex.

During mitosis, sister chromatids attach to microtubules from opposing centrosomes in a bipolar fashion, in order to correctly segregate the chromosomes over the daughter cells. This coupling is ensured by the kinetochore, a large protein complex which attaches chromosomes to the growing and shrinking ends of a microtubule (Brouhard and Rice, 2018; Vleugel et al., 2016). At metaphase, pulling forces from depolymerizing microtubules are transmitted via the kinetochore to the attached chromatids, promoting their physical separation. Kinetochores are composed by over 80 different proteins and form load-bearing attachments between chromatin and spindle microtubules, essential for coupling of pulling forces (Foley and Kapoor, 2013). Interestingly, kinetochores exhibit two spatially separated passive and active interfaces with microtubules (Dumont et al., 2012a). This can reflect different molecules or interactions and might confer advantages to kinetochores. An active interface generates force to drive kinetochore movement, while a passive frictional interface allows for persistent binding regardless of microtubule dynamics. Moreover, kinetochores are compressed during their movement, which might also confer them emergent mechanosensitive properties.

3. Integrin Adhesion Sites

Integrin adhesion sites are macromolecular protein complexes that mediate cell-ECM adhesion, mechanosensing and force transmission, acting also as signaling hubs. In this chapter, I start by briefly describing their composition and the different morphologies that IAS can assume across time and space. However, to better understand how IAS mediate adhesion, mechanosensing and force transmission, it is essential to go into the deep end of the pool: this means looking at IAS as nano-partitioned structures where single protein dynamics, organization and even orientation take a new relevance. I will highlight several of these aspects, from the 3D nano-organization to the dynamics, recruitment and force transmission at different IAS components. Then, I will focus on three IAS components: talin, vinculin and zyxin. I will approach how the talin-vinculin mechanosensitive axis is crucial for IAS function, reinforcement and maturation, integrating *in vitro* studies with insights from live cells and force sensors. I will also describe how these proteins are recruited to IAS and how vinculin can be regulated by force. For zyxin, I will highlight its force-sensitive nature that confers it a sort of 'shuttling ability'. I will finish by approaching some higher-level effects of IAS activity and signaling in cell growth, migration and differentiation.

1. IAS: a general perspective

Cells sense the biochemical and mechanical properties of the ECM through integrin-based adhesion sites (IASs). Integrins, the cornerstone of IASs, transmit forces and signals between the ECM and actomyosin filaments, a bidirectional process which is highly dependent on their structure (Kechagia et al., 2019; Orré et al., 2019). Integrins are heterodimeric membrane receptors composed by non-covalently interacting α-subunits (18 types) and β-subunits (8 types) which combine for at least 24 unique heterodimers (Park and Goda, 2016). Different heterodimer combinations will specify the binding to a vast variety of ECM ligands (fibronectin, laminin, RGD) but also to membrane receptors on other cells (Kechagia et al., 2019; Orré et al., 2019). Both α- and β-subunits are transmembrane proteins composed of a large extracellular domain, a transmembrane helix and a short cytoplasmic tail (Fig. 13) (Kechagia et al., 2019; Orré et al., 2019). Integrins can either exist in a 'closed', inactive conformation, or in an 'open', active conformation (Fig. 13) (Bouvard et al., 2013). Integrin activation can either occur through biochemical or mechanical pathways, which often coexist in live cells. This often involves two possible mechanisms: 'outside-in' activation via an ECM ligand such as fibronectin(Schiller et al.,

2013a) , or 'inside-out' activation through integrin activators talin and kindlin (Fig. 13) (Calderwood et al., 2013; Sun et al., 2019).

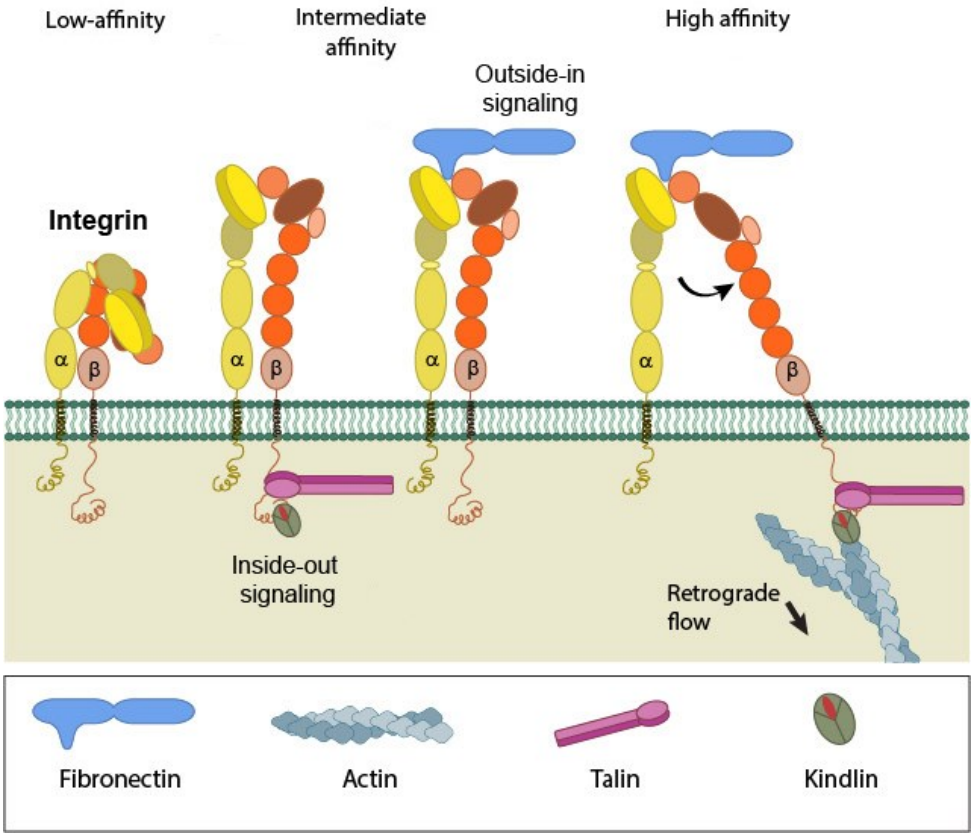

Figure 13: Integrin activation

Low-affinity integrin (heterodimer with α subunit in yellow and β subunit in orange) has an inactive, bent conformation. Large extracellular domains, transmembrane helices and cytoplasmic tails are represented. Binding of interacellular partners talin and kindlin (inside-out signaling) or extracellular partners such as fibronectin (outside-in signaling) activates integrin, promoting the transition to an intermediate affinity state, characterized by a more open conformation and extension of the large extracellular domains. High affinity, fully active integrin engages with both ECM and the actin retrograde flow, transmitting traction forces. The hallmark of a high affinity, fully active integrin, is the separation of the cytoplasmic tail domains. Figure adapted from MBI Info (Singapore) (https://www.mechanobio.info/what-is-mechanosignaling/what-is-the-extracellular-matrix-and-the-basal-lamina/what-is-integrin/how-is-integrin-activated/.)

Integrins directly engage the ECM through their extracellular domain, while the intreacellular tail connects to actin filaments through a plaque of numerous adaptor, signaling and scaffolding proteins (Martino et al., 2018; Orré et al., 2019). Of these, talin and vinculin can be considered two key elements; together, they constitute the main mechanosensitive axis

involved in IAS maturation, reinforcement and force transmission, but also act as a scaffold for many other signaling proteins (Atherton et al., 2015; Carisey et al., 2013; Elosegui-Artola et al., 2016; Goult et al., 2018; Yang et al., 2014b). Signaling proteins recruited to IASs include paxillin, zyxin, focal adhesion kinase (FAK) or the p130 Crk-associated substrate (p130Cas), which activate or mediate different biochemical and mechanosignaling pathways (Chen et al., 2013; Hoffman et al., 2012; Myers and Gomez, 2011; Pasapera et al., 2010; Wang et al., 2001). Of note is also the presence of actin cross-linkers such as α-actinin, crucial for organizing actomyosin bundles at IASs (Choi et al., 2008), and kindlin, which co-activates integrins together with talin (Calderwood et al., 2013; Theodosiou et al., 2016)

Among the IASs, focal adhesions (FAs) are key structures in cellular adhesion and mechanotransduction(Geiger and Yamada, 2011; Sun et al., 2016a). FAs are large macromolecular complexes composed of integrin clusters that indirectly bind actin filaments through a plaque of regulator and signaling proteins. In *in vitro* cell models on 2D substrates, FAs assume an elongated morphology with micrometer-sized dimensions; conversely, *in vivo* FAs are more punctate, probably as a consequence of a 3D cellular microenvironment (Cukierman et al., 2001). IASs are highly dynamic structures that undergo continuous assembly and disassembly throughout cell migration, spreading and other processes. This entire process will be discussed in detail in the next section. IASs usually are initiated at the lamellipodium, near the leading edge, forming dot-like structures known as nascent adhesions (NAs) (Fig. 14a) (Choi et al., 2008). Intracellular forces and recruitment of multiple proteins will lead to the maturation of NAs into elongated focal adhesions (FAs), which being to mature at the lamellipodium-lamella interface (Fig. 14b,d,e). In the initial steps of this process, NAs can first mature into larger focal complexes (FXs) at the lamellipodium-lamella interface, which are induced by constitutively activated Rac (Choi et al., 2008; Nobes and Hall, 1995; Zaidel-Bar et al., 2007a) (Nobes Cell 1995, Choi NCB 2008, Zaidel-Bar JCS 2007). FAs can further mature into fibrillar adhesions, long streaks or arrays of dots with thin actin cables crosslinked by the actin binding protein tensin, which is characteristic of fibrillar adhesions (Zaidel-Bar et al., 2003) (Fig. 14c). Throughout this entire section, we will refer to integrin adhesions in a general context as IASs, and in specific events and functions as FAs (e.g. 3D nano-scale organization of FAs) or NAs (e.g. assembly of NAs).

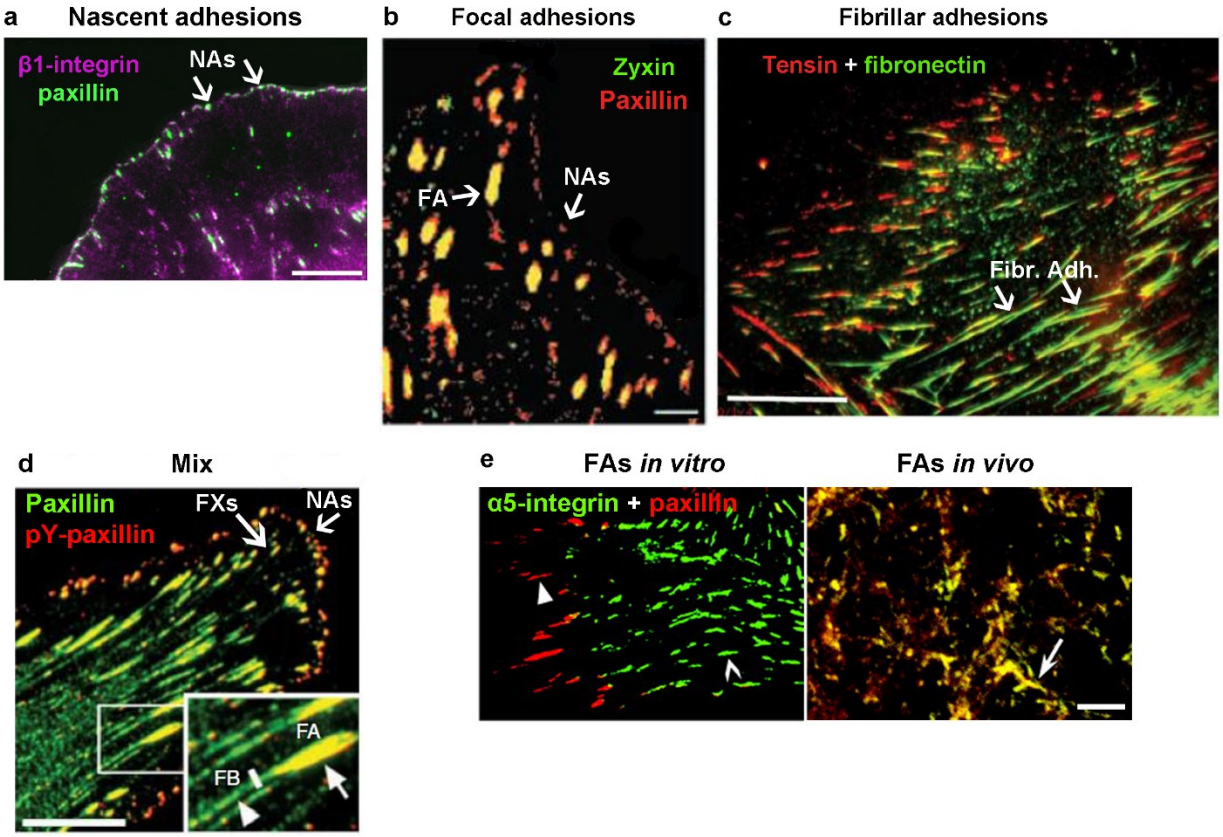

Figure 14: Different morphologies of IASs according to their maturation and cellular context

a, Nascent adhesions (NAs) imaged in CHO cells expressing human β1 integrin (green) and endogenous paxillin (magenta). Both proteins localize in small, dot-like nascent adhesions that form a thin outline near the leading edge, as indicated by the white arrows. Scale bar: 10 µm. Adapted from Choi NCB 2008. **b,** Focal adhesions (FAs) and nascent adhesions (NAs) observed in endothelial cells co-transfected with YFP-paxillin and CFP-zyxin. NAs and FAs are visibly different, in composition, morphology and position. FAs contain both zyxin and paxillin, display an elongated morphology and are located behind the lamella; NAs, on the other hand, are smaller, contain only paxillin and are located in the advancing lamellipodium. Adapted from Zaidel-Bar et al. 2003. **c,** Fibrillar adhesions (arrows) formed by a WI38 human lung fibroblast, stained for tensin (red) and fibronectin (green). Fibronectin fibrils are primarily associated with tensin-rich fibrillar adhesions, which are located towards the center of the cell. Adapted from Geiger and Yamada 2011. **d,** Four major forms of IAS (NAs, FXs, FAs and fibrillar adhesions) simultaneously present in porcine aortic endothelial cells labeled for paxillin (green) and tyrosine-phosphorylated paxillin (red): dot-like NAs at the lamellipodium near the leading edge, focal complexes (FX) at the lamellipodium-lamella interface, “classical” focal adhesions (FA), and fibrillar adhesions (FB) located near FAs but more toward the cell center, in which FN fibrils are prominent. Paxillin is tyrosine-phosphorylated in NAs, FXs and FAs, but not in fibrillar adhesions. Adapted from Zaidel-Bar, Itzkovitz, et al. 2007. **e,** Difference of IASs between *in vitro* and *in vivo* systems. Confocal images of NIH-3T3 mouse fibroblasts seeded on fibronectin-coated coverslips (left) and transverse cryostat tcraniofacial mesenchyme sections of an E13.5 mouse embryo (right), stained for α5-integrin (green) and paxillin (red). FAs *in* vivo display a different morphology as well as a different composition: α5-integrin colocalizes with paxillin in FAs *in vivo* but not in a 2D substrate *in vitro*. Adapted from Cukierman et al. 2001.

1.1. From nascent to mature focal adhesions

1.1.1. Initiation of adhesions: the role of integrin-actin connections and mechanical forces

The formation and maturation of IASs is tightly linked to cell migration and results from the interplay between actin polymerization, mechanical forces and integrin signaling. IASs initially form at the leading edge of migrating cells, in the lamellipodium (Choi et al., 2008; Giannone et al., 2007). These nascent adhesions (NAs) are small (< 1µm), dot-like transient structures with relatively short lifetimes (up to 1 min). Their formation is tightly coordinated with leading edge retraction and protrusion rate (Choi et al., 2008; Giannone et al., 2004, 2007). NAs contain integrins, talin, vinculin, and signaling molecules like FAK (Alexandrova et al., 2008; Choi et al., 2008; Zaidel-Bar et al., 2003).

Initiation of IASs is thought to involve interactions between actin and integrin at the lamellipodium as well as actin polymerization (Giannone et al., 2007, 2009). First of all, coupling of integrins to ECM and actin is higher near the leading edge (<0.5 mm from the edge), where integrins undergo specific force-dependent reinforcement in response to matrix rigidity (Jiang et al., 2006; Nishizaka et al., 2000). Second, the rate of actin polymerization is correlated with the rate of adhesion site formation (Choi et al., 2008), and inhibiting actin polymerization leads to the disassembly of NAs (Alexandrova et al., 2008; Choi et al., 2008). Moreover, the faster the cells move, the shorter the lifetime of NAs will be (Choi et al., 2008). The role of actin polymerization, ABPs or actomyosin contractility in formation of NAs it is still unclear, but there are various possible links. First, the Arp 2/3 complex, which mediates actin nucleation, can form signaling complexes with FAK and vinculin, coupling actin polymerization and NA formation (DeMali et al., 2002; Serrels et al., 2007). Second, vasodilator-stimulated phosphoprotein (VASP), which binds to the barbed end of actin and associates with vinculin and zyxin, can also be released from the leading edge to initiate adhesion sites (Giannone et al., 2007). Finally, a more recent study proposed a model for NA assembly based on fluorescence fluctuation methods (Bachir et al., 2014); α-actinin, an actin-crosslinking protein, transiently associates with integrin into complexes that help nucleate NAs within the lamellipodium. These integrin complexes contained kindlin but not talin, which was only recruited when NAs where already formed. However, α-actinin only helps in the initial nucleation, but only enters the adhesions later throughout maturation.

Initiation and assembly of IASs could also be driven by mechanical forces, although this is still an unclear subject. Initial observations from Galbraith and colleagues (Galbraith et al., 2002) showed that application of mechanical force – either internal, through beads, or external, through laser traps – triggered the formation of NAs. In addition, by using the molecular clocking of lamellipodium periodic contractions (Giannone et al., 2004), it was possible to decipher how

the architecture and dynamics of actin networks are coupled to force-generation and IAS initiation (Fig. 15) (Giannone et al., 2007). Here, myosin II was shown to pull the rear of the lamellipodial actin network, causing upward bending, edge retraction and initiation of new IAS. The network then separates from the edge and condenses over the myosin, with IAS assembling at the separation zone. Protrusion resumes as lamellipodial actin regenerates from the front and polymerizes against the leading edge, growing rearward until it reaches the newly assembled myosin, initiating the next cycle. Therefore, periodic contractions are controlled by the lamellipodial actin itself, which periodically regenerates and separates in phase with protrusion and retraction (Fig. 15). Moreover, these studies reveal how force can be used by macromolecular complexes as a signal driving different biological functions, which otherwise could not be performed via biochemical mechanisms.

These observations suggest that mechanical force and myosinII-dependent contractility can promote initiation of IASs. However, depletion of myosin II A and B by knockdown does not prevent the formation and turnover of NAs in the lamellipodium (Choi et al., 2008), suggesting that initiation of IASs is independent of myosin II. One possible hypothesis is that IASs could be initiated by myosinII-independent forces that result from the polymerization-driven retrograde F-actin flow. This is in line with the fact that NAs are only stable within the lamellipodium but disassemble when the depolymerizing actin in the lamellipodium rear passes over them (Choi et al., 2008). However, the generation of MII-dependent periodic contractions could also coordinate a discrete formation formation of NAs, enabling to stabilize the protruding lamellipodium and mechanical probing (i.e. stiffness) of the ECM (Giannone et al., 2004). Mechanisms could thus variate according to the substrate properties and act synergistically within the same cell. Moreover, the cell type can also introduce variability in the observations due to the presence of NAs with different stabilities. CHO cells, used in myosinII-depletion studies, have NAs with longer lifespans in the lamellipodium (Choi et al., 2008). In contrast, the NAs in MEF cells, also used in studies on mechanical force and myosin II contractility, have a shorter lifespan within the lamellipodium and tend to stabilize and mature at the lamellipodium-lamellum interface (Choi et al., 2008).

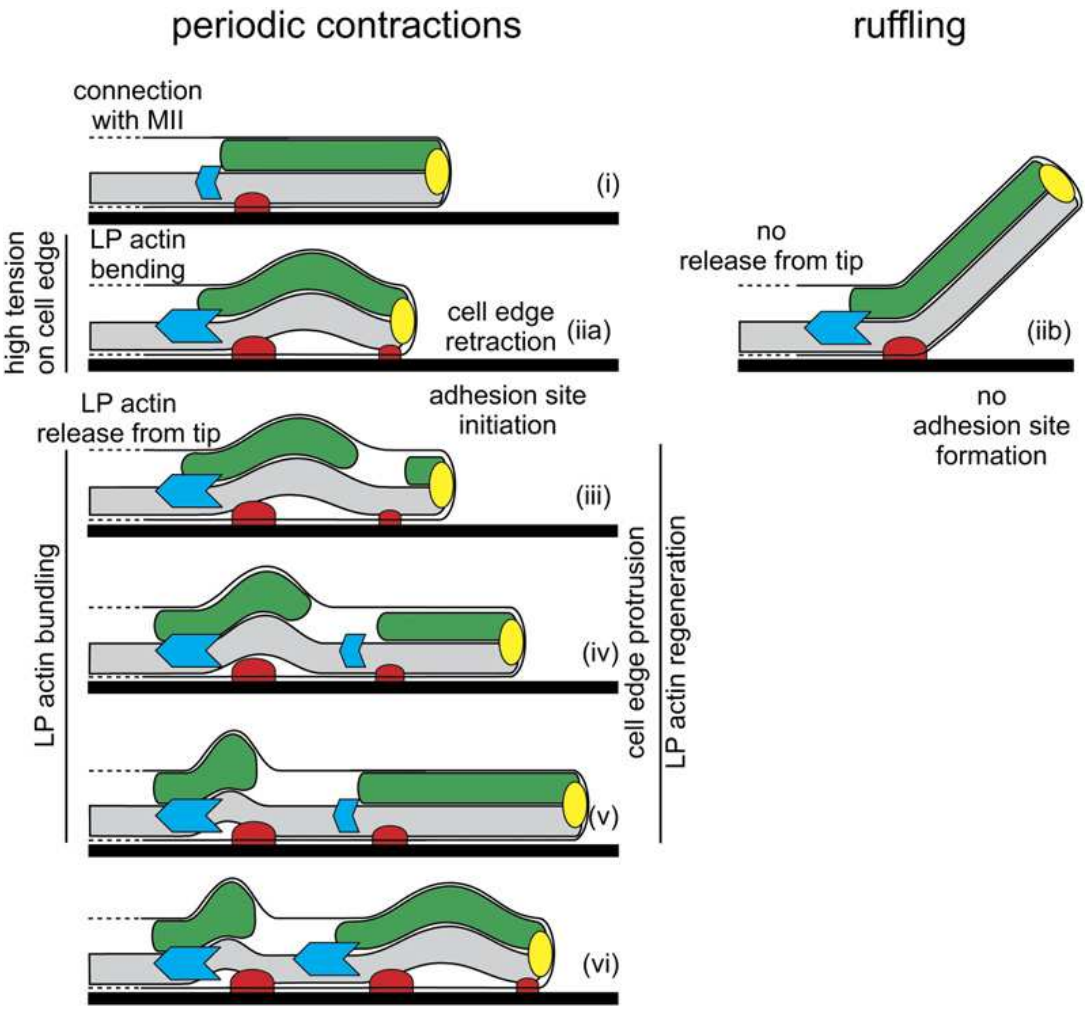

Figure 15: Shematic representation of lamellipodial-actin periodic regeneration

The lamellipodium (LP actin) (green) is above the lamellum (LM) (gray). Actin polymerization at the protrusion tip causes the back of the LP actin network to grow toward the back until it reaches an adhesion site (i) where a MII cluster (blue) forms. MII pulls the LP actin, generating high tension on the cell front, causing LP bending, edge retraction, and initiation of new adhesion sites (red) on the ECM (black rectangle) (iia). The LP actin continues to be pulled until it is released from the tip (iii) and edge protrusion restarts. A new LP actin network immediately resumes growth, suggesting that the actin polymerization machinery (yellow) is still present at the cell tip (iv). The released LP actin, still pulled by MII, further condenses into a bundle at the back of the previous adhesion site (v), while the newly growing LP actin reaches the next adhesion site and the cycle begins anew (vi). LP ruffling (iib) occurred in the case when the total bond energy connecting LP actin to the edge is greater than the bond energy of nascent adhesion sites to the ECM. Figure adapted from Giannone et al. 2007.

1.1.2. Maturation of NAs into FAs: mechanical force and myosin II take over

NAs have a very short lifetime of ~1min; after that, and as the lamellipodium moves forward, they can either disassemble or mature into FAs, which can be identified as elongated, centripetal adhesions in the cell periphery (Fig. 14b, d, Fig.16) (Zaidel-Bar et al., 2007b). This transition process is dependent on mechanical forces (Galbraith et al., 2002; Giannone et al., 2003) as well as myosin II activity (Choi et al., 2008; Pasapera et al., 2010; Vicente-Manzanares et al., 2007). Initial maturation of NAs can give rise to focal complexes (FXs) at the lamellipodium-lamellum interface (Fig. 14d) (Choi et al., 2008; Galbraith et al., 2002; Zaidel-Bar et al., 2003). In general, FXs are transient entities which serve as anchors for slowing down retrograde actin flow and exert traction forces. Focal complexes differ from NAs in their location and size, but the molecular composition is mostly similar (Choi et al., 2008; Nobes and Hall, 1995). Transition from NAs to focal complexes is dependent on mechanical forces, since it is triggered by myosin light chain kinase activity (Totsukawa et al., 2004). Moreover, formation of focal complexes also occurs at beads containing fibronectin fragments (unable to promote formation of complete FAs) upon application of mechanical forces through optical traps (Choquet et al., 1997; Galbraith et al., 2002). This process involves recruitment of vinculin (Galbraith et al., 2002) and talin (Giannone JCB 2003). In talin knockout cells, formation of focal complexes is impaired after mechanical stretch, suggesting that talin is essential for force-dependent initiation and stabilization of adhesions (Giannone et al., 2003). In these studies, the concept of NAs was not yet well established, hence it is likely that some observations of FXs were actually identifying NAs (Zaidel-Bar et al., 2003). Nonetheless, FXs are an intermediate structure between NAs and FAs, whose formation corresponds to the initial steps of IAS maturation. They can be considered a sort of 'maturing adhesions', with distinct morphology of NAs but with a similar molecular signature.

Further maturation of FXs FAs is accompanied by protein recruitment, especially α-actinin, which in turn is also essential for adhesion maturation (Fig. 16). IAS maturation is thought to be oriented by a template of actin filaments which in turn depends on the actin cross-linking activities of α-actinin and myosin II (Choi et al., 2008). Moreover, myosinII activity is also crucial for adhesion elongation and maturation (Choi et al., 2008; Pasapera et al., 2010; Vicente-Manzanares et al., 2007). Thus, myosin II is a key regulator of cell migration and adhesion, one that integrates both crosslinking and contractile activity at different adhesion maturation stages (Fig. 16). The role of myosin II-mediated contractility in IAS maturation is consistent with previous studies showing how external mechanical forces are essential for adhesion maturation (Riveline et al., 2001) and stabilization (Balaban et al., 2001). Overall, actomyosin-mediated mechanical force is a key element driving FA maturation (Fig. 16). This is thought to occur mostly through the talin-vinculin mechanosensitive axis (Ciobanasu et al., 2014), which will be discussed later. Briefly, actomyosin-mediated tension can lead to the formation of a talin-vinculin complex, which

reinforces actin binding to IASs, triggering their maturation (Atherton et al., 2015; Thievessen et al., 2013).

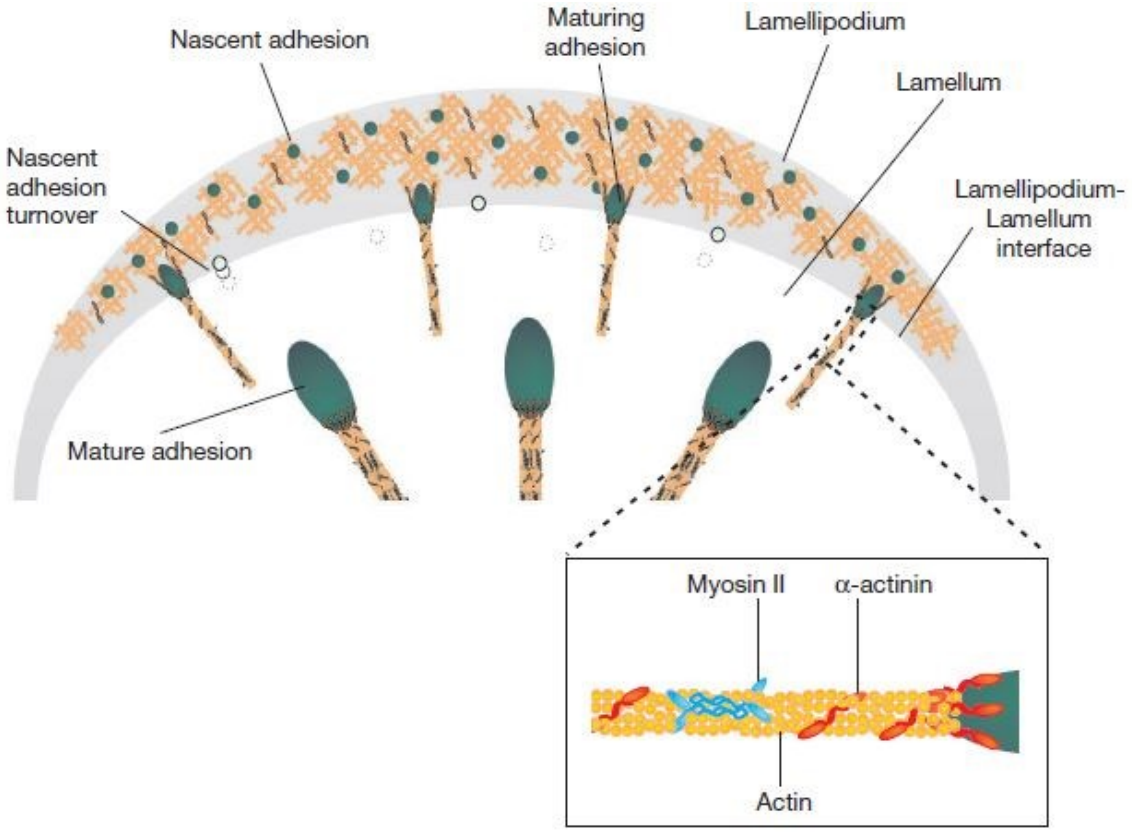

Figure 16: IAS maturation: from early NAs to mature FAs.

During membrane protrusion, NAs initially assemble as puncta in the lamellipodium (grey band), a process dependent on actin polymerization and interactions between integrin and actin or integrin and α-actinin. NAs remain small and stable within the lamellipodium; they turnover as the depolymerizing rear of the lamellipodium moves over them. Alternatively, myosin II contractility can drive IAS elongation and maturation along an actin template. Crosslinking actions of α-actinin and myosin II are also critical for IAS elongation and maturation. Adapted from Choi et al. 2008.

1.2. Molecular Composition of IAS

IASs are highly heterogeneous entities composed of a vast variety of proteins. Several proteomic studies have revealed that IASs are actually enriched in thousands of proteins (Byron et al., 2012; Humphries et al., 2009; Schiller et al., 2013b). Such complexity is further increased by the presence of phosphorylation states and the possible combinations of integrin heterodimers, which in turn will recruit specific partners. Nonetheless, a more recent study has identified a subset of 60 proteins consistently found in IASs, known as the “consensus adhesome” (Horton et al., 2015). This includes subnetworks of protein interactions forming 4 modules: (1) α-

actinin-zyxin-VASP, (2) FAK-paxillin, (3) kindlin-ILK-PINCH, and (4) talin-vinculin. These IAS components can attain different phosphorylation states: some proteins are phosphorylated specifically in response to integrin-ECM linkage, while others are constitutively phosphorylated prior to recruitment (Horton et al., 2015) and some are specifically recruited by given integrin subtypes. Moreover, the composition of IASs is not stationary across their lifetime, with maturation and mechanical tension strongly affecting IAS composition, as it will be described in the following sections. Despite the insight on IASs composition, interaction maps and proteomic approaches do not probe for instance whether the reduction of a protein is dependent on force-sensitive interactions or through another force-dependent partner. Indeed, the aforementioned approaches do not provide enough knowledge on the sub-cellular location, duration, strength, order of recruitment, and nature (competitive or cooperative) of protein-protein interactions at IASs.

2. IAS: towards a nanoscale and molecular understanding

Throughout the next sections, we will integrate how novel techniques such as super-resolution microscopy or single particle tracking have unveiled the molecular architecture and dynamics of IASs. In a certain way, we are witnessing an evolution of IASs towards structures that depend on their nanoscale organization and behavior of single molecules; we intend to highlight that transition throughout the next sections. Equally important, mechanosensing at IASs is dependent on how forces will change protein conformation, interactions and binding or enzymatic activities. We will discuss about several of these mechanisms in the next sections, while integrating them with protein dynamics and their nanoscale organization.

Several groundbreaking *in vitro* studies have revealed how IAS proteins undergo force-dependent conformational changes or change their interactions in response to force (Ciobanasu et al., 2014; Huang et al., 2017b; Del Rio et al., 2009; Yao et al., 2016). However, it is important to assess whether how these mechanosensitive events occur in subcellular structures in live cells. Recent force-measuring techniques in live cells provide insights into the nanoscale regulation of proteins and how they 'bear' intracellular tension, which is extremely helpful in this context. Moreover, force micromanipulation methods such as optical tweezers also provided key insights on the mechanical response of different IAS proteins, although they can only access the dorsal surface of cells. Thus, we still need to access IASs in crowded macromolecular environments while capturing their mechanosensitive response to external and internal mechanical forces.

2.1. IAS are 3D entities with heterogeneous protein distribution in the plane of plasma membrane and axial direction.

For several decades, there was a gap between the knowledge on composition of FAs and their ultrastructure, which remained largely unknown. Several studies showed that ligand spacing could indeed modulate cell adhesion and motility, suggesting that IASs could exhibit a precise nanoscale architecture. A study performed shortly after the advent of super-resolution microscopy and single particle tracking further contributed to this hypothesis. Here, the authors showed that FA proteins were organized into functional nanoclusters throughout adhesion complexes (Shroff et al., 2007). In 2010, the emergent nanoscale architecture and structural organization of mature FAs was finally revealed by Kanchanawong and colleagues (Kanchanawong et al., 2010). Using 3D iPALM super-resolution microscopy, this study demonstrated that mature FAs exhibit a precise 3D nanoscale architecture, vertically stratified along the axis perpendicular to the plasma membrane (Fig. 17) (Kanchanawong et al., 2010). Integrins are separated from actin by a ~40nm core domain containing intertwined layers formed by specific adhesion proteins. Integrin cytoplasmic tails are tightly confined around the inner plasma membrane, together with FAK and paxillin, forming the integrin signaling layer (ISL), within ~30nm around the plasma membrane (Fig. 17). Above the ISL, vinculin and the talin rod co-localize in the force transduction layer (FTL) (Fig. 17). This compartment regulates force transmission and provides a structural basis for the molecular clutch. Finally, in the upper region of FAs, actin, α-actinin, zyxin and VASP will constitute the actin regulatory layer (ARL) (Fig. 17). Proteins in this layer contribute for IAS maturation (Choi et al., 2008) and regulate stress fiber formation and homeostasis (Smith et al., 2010), among other roles. It is important to note, though, these functional compartments are not isolated from each other. Actin exhibits a broader distribution across FAs, with a low density region covering the FTL.

Stratification of IASs will likely go beyond the structural aspect and have a functional role. Separation of proteins can impose constraints on protein-protein interactions; proteins in similar layers will likely interact more and for longer periods. Protein segregation itself can evolve with IAS maturation, as observed for vinculin. First of all, mutants which increase activation of vinculin promote an upwards shift in distribution from the ISL to the FTL and ARL (Case et al., 2015). The same effect is verified after the washout of cells treated with blebbistatin, which inhibits myosin II activity and consequent IAS maturation. During the first five minutes after blebbistatin washout, IASs undergo coordinated growth and maturation. Vinculin is first recruited to the ISL of maturing IASs 1 min after washout. After five minutes, when IASs display an elongated, mature morphology, vinculin undergoes an upwards shift to the FTL and ARL (Case et al., 2015). Thus, as IASs undergo myosinII-dependent maturation, vinculin nanoscale localization changes from the ISL to the upper layers. Shift in distribution is likely linked to talin-mediated vinculin activation

(Case NCB 2015). Overall, this reveals how forces are correlated with separation of proteins into functional layers over time.

The 3D molecular architecture of IASs also reveals some of the forces exerted across IASs, which can dictate the orientation of IAS components. These exhibit highly polarized orientations across 3D functional layers, with functional implications for IASs. Integrins, for instance, are co-aligned and oriented along the long axis of FAs, which depends both on ligand binding and talin linkage to F-actin (Swaminathan et al., 2017). Integrin-mediated forces appear to be radially aligned in the (x,y) plane and oriented in the z-axis with an angle of 40°.Talin, on the other hand, is diagonally extended across mature FAs, with the tail displaced at least 30nm above the head domain, with an angle of 15° to 25° relative to the plane of the membrane (Kanchanawong et al., 2010; Liu et al., 2015b). Since this angle is fitting the force orientation, it is likely that talin is oriented by forces applied across IASs .The diagonal orientation of talin, in turn, could stem from actomyosin pulling on the talin rod, unfolding different domains and recruiting vinculin to expose VBSs. This could lead to talin acting as a molecular ruler across the IASs, determining the vertical stratification. Indeed, another study involving iPALM showed that talin length modulates the gap between integrin and actin in a linear manner, thereby implicating the integrin–talin–actin complex as the primary mechanical linkage in IASs. (Liu et al., 2015b). Vinculin also displays anisotropy, with the head located above or below the tail according to the IAS morphology and cell type (Case et al., 2015; Stubb et al., 2019).

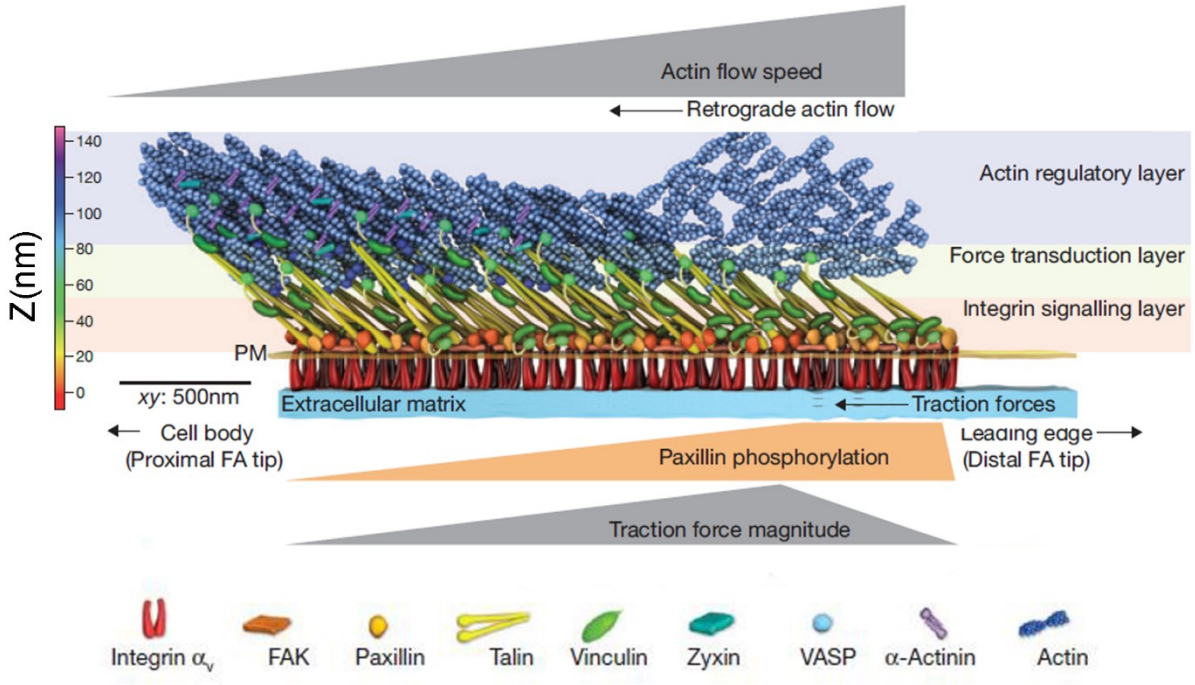

Figure 17: 3D nano-structure of mature FAs.

Z axis represents the height relative to the plane of the plasma membrane, in nanometers. Figure adapted from Kanchanawong et al. 2010 and Case and Waterman 2015.

The nanoscale organization of IASs appears to be conserved between different cell types, but a recent study on cornerstone FAs in human pluripotent stem cells (hPSCs) has challenged this vision (Stubb et al., 2019). Cornerstone FAs are found in the edges of hPSC colonies and possess a highly stratified 3D nanoscale architecture with key differences in regards to previous studies. First, both talin and vinculin are higher at cornerstone FAs, and vinculin exhibits an unusual orientation with the head domain located above the tail. This could reveal a role of vinculin in maintenance of pluripotent cells or be the consequence of interactions with specific integrin heterodimers. Secondly, actin was shown to form two coexisting vertical layers separated by a ~50 nm gap in the top of cornerstone FAs, each one of them with a correspondent α-actinin layer. Presence of two separated layers suggests that the low actin density ~50 nm gap might itself be another functional compartment. Finally, a striking aspect of cornerstone FAs is the presence of both KANK1 and 2, positioned vertically around FAs. This could enable proximity between KANKs and the FTL, which is especially relevant giving the interactions between KANK and Talin (Sun et al., 2016b). Moreover, KANK is crucial for microtubule-dependent control of FA size via the interactions with talin (Rafiq et al., 2019; Sun et al., 2016b). Spatial stratification of scaffold proteins such as KANK could be integrated into the 3D architecture of FAs, controlling the segregation of proteins into nano-domains or IAS maintenance. Changes in IAS nanoscale organization can also occur across different tissues: talin, in *Drosophila*, has three different orientations in the IAS of muscle, wing and germband retraction, which in turn are modulated by actomyosin and vinculin (Klapholz et al., 2015). This variety reflects a differential force sensing and reveals how molecular architecture can change in function of the developmental context.

Protein distribution within IASs can also change across the (x,y) plane parallel to the plasma membrane, which might have a functional impact. Importantly, (x,y) distribution is more relevant to look at when considering IASs as 3D stratified structures, since it can further diversify the functions of different nano-layers. Mature FAs present both a distal tip, closer to the leading edge of the cells, and a proximal tip, which is closer to cell body. Vinculin, for instance, is progressively higher from the distal to the proximal tip (Case et al., 2015), which reflects a possible activation gradient. Similarly, talin-C is also higher at the proximal tip, suggesting again a gradient of vertical extension along FA length, which in turn will be correlated with higher vinculin activation. Phosphorylated paxillin also accumulates along the distal tip, once again reflecting a possible gradient of vinculin activation (Zaidel-Bar et al., 2007a), since phosphorylated paxillin is thought to regulate vinculin recruitment (Case et al., 2015). Protein segregation in the (x,y) plane can also occur from the edges to the center of the adhesions, as seen in cornerstone FAs from hPSCs. For instance, β5 and β1 integrin are spatially segregated in the ISL, with β5-integrin assuming a ring-like distribution around the edges and β1 integrin more concentrated in the center (Stubb et al., 2019). Distinct nanoscale organization of integrin

isoforms has also been observed in other studies: Rossier and colleagues showed that β1-integrin was twofold less enriched than β3-integrin in FAs (Rossier et al., 2012) In cornerstone FAs, Talin also displays higher clustering around the edges, where vinculin is located at a higher position compared to the center (Stubb et al., 2019). This unique architecture of FA cornerstone edges could be linked to interactions with specific scaffold partners such as KANK, but it could also have specific roles in maintaining the pluripotence of the cells. Interestingly, IASs can also organize other cell-surface receptors involved in different signaling pathways, such as the Transforming growth factor β receptors (TβRs) (Rys et al., 2015). TβRI is enriched in FAs, while TβRII is mostly excluded from FAs, appearing only at the edges of FAs. 'Sequestering' of TβRI by FAs is dependent on tension and can contribute for modulating distinct kinase signaling pathways involved in cell proliferation or apoptosis (Rys et al., 2015).

2.1.1. Heterogeneous force distribution in IASs in the (x,y) plane

Besides protein stratification and segregation, mechanical forces can also be heterogeneously distributed within IASs. This can influence IAS mechanosensing and, as we discussed before, it can be correlated with the molecular architecture of IASs and protein orientation. Along the (x,y) plane, the highest tension is usually found at the center of mature FAs (Liu et al., 2014; Morimatsu et al., 2015). This is correlated with paxillin recruitment, but less with talin or vinculin (Morimatsu et al., 2015). This suggests that forces are not transmitted perpendicularly to the membrane, since talin, paxillin and vinculin are shifted towards the cell center relative to ECM tension. Diagonal orientation of both talin and integrin-exerted forces further strengthens this hypothesis. Therefore, these results, together with 3D polarization experiments, support a model where forces are exerted on the integrin-talin-actin linkage and oriented towards the cell center.

Force distribution can also oscillate within IASs over time or with adhesion dynamics, which in turn can contribute to adhesion assembly and mechanosensing (Kumar et al., 2018; Plotnikov et al., 2012). In 2012, Plotnikov et al. demonstrated that traction forces are often skewed towards the distal tip of mature FAs, which could contradict the idea of the highest tension being found at FA center (Plotnikov et al., 2012). However, the same study also found that FAs can actually exhibit two populations: a 'weak' state where traction force is stable and centered on the FAs, and a 'strong', dynamic state where peak traction fluctuates between the distal tip and the center of FAs. This 'tugging' FA fraction actually displays higher traction forces when the peak is moving towards the center, which is in agreement with the maximum of tension found in the center. Tugging FA dynamics appear dependent on paxillin phosphorylation and vinculin binding, again highlighting the role of this module in IAS organization. Perturbation of paxillin phosphorylation and vinculin binding narrows down the range of stiffness for durotaxis

and slows down cell migration speed, revealing how FA tugging is important in ECM mechanosensing (Plotnikov et al., 2012). A more recent study with FRET sensors showed that talin exhibits higher tension at growing FAs at the leading edge and 'sliding' FAs at the trailing edge, with high tension corresponding to the region of assembly (Kumar et al., 2018). By contrast, stable FAs had relatively constant talin tension along their length. Interestingly, one consistent aspect was that areas with high talin tension contained well-aligned actin filaments (Kumar et al., 2018). It is thus possible that regions of talin tension and well-aligned actin filaments are the principal sites of assembly or IAS growth.

2.2. Dynamics of IASs analyzed with super-resolution microscopy and single particle tracking

IASs are not composed by densely packed molecules which remain stable throughout IAS lifetime; instead, they are highly dynamic structures, composed by nanoclusters of different dimensions with variable dynamic properties. The molecular architecture of IASs is generated from precise sequences of molecular events which guide proteins to specific nano-layers, fostering specific interactions. Understanding the molecular path of IAS proteins is a key step to unveil their functions and how they are regulated.

IASs are surrounded by a variety of subcellular organelles and structures, including the plasma membrane, the cytosol, the actin cytoskeleton or microtubules. Thus, proteins can enter or leave specific layers within the IASs using a path involving any of these components. Yet, the complexity is increased by interactions with other proteins, either binding partners or regulator proteins. For instance, the building blocks for IASs might be composed by single molecules but also by pre-assembled complexes (Fig. 18a) (Hoffmann et al., 2014). Moreover, the molecular paths of IAS proteins are both dependent on activator inhibitor proteins (integrin) or on the proteins themselves (talin and kindlin) (Orre et al., 2020; Rossier et al., 2012). However, the majority of the knowledge on protein-protein interactions during integrin activation is derived from studies where the complexity of adhesive structures was reduced or even absent. These approaches often involve flow cytometry with suspended cells (Tadokoro et al., 2003) or *in vitro* biochemistry (Woodside et al., 2002), where the transient interactions are ignored, as well as the *in vivo* cellular environment. In addition, both the duration and subcellular locations of molecular events are unknown, as well as their nanoscale organization.

The recent development of super-resolution microscopy (SRM) and single particle tracking (SPT) techniques has allowed to study protein motion within subcellular compartments in live cells. SRM and SPT techniques have unveiled the correlation between protein dynamics and protein activation and/or binding states in different structures, including IASs (Rossier et al., 2012), dendritic spines (Chazeau et al., 2014) or the lamellipodium (Mehidi et al., 2019).

Moreover, they also contribute to characterize fast cycles of inactivation/activation (Mehidi et al., 2019) and study protein segregation into 3D nano-domains, as explained above for the nanoscale architecture of IASs Overall, several of these applications were essential to better understand the dynamic nature of IASs and the underlying protein interactions, activation and binding states. One of the most striking examples concerns integrin immobilization, which is higher inside than outside FAs, suggesting binding to ECM ligands or intracellular partners. In parallel, integrin immobilization also correlates with its activation, since this effect is mimicked by Mn2+, an integrin activator. Thus, integrin activation is correlated with its immobilization. In parallel, integrin full long-lived immobilization requires a tripartite interaction with fibronectin and ABPs such as talin (Rossier et al., 2012). This reveals how the dynamics of a particular protein in IASs is not only dependent on the protein itself, but also on the interactions with ligands and binding partners.

Once integrin is immobilized within IASs, it does not remain in this state forever. Indeed, integrins inside FAs cycle from slow free-diffusion to immobilization states which can last for seconds to tens of seconds (Leduc et al., 2013; Rossier et al., 2012; Tsunoyama et al., 2018). Immobilization reflects the activation of integrin and is thought to be responsible for the mechanical linkage of the actin cytoskeleton. Moreover, when cells are treated with Rho-associated protein kinase (ROCK) inhibitor Y-27632, which reduces myosin II-generated tension, both the fraction and lifetime of integrin immobilizations are largely (Tsunoyama et al., 2018). This shows how integrin immobilizations are dependent on traction forces, thus implying that integrin diffusion/immobilization cycles are important to regulate IAS stability and architecture (Tsunoyama et al., 2018). Importantly, such data has to be extracted with SPT techniques allowing for measurement of longer trajectories, such as labelling with organic fluorophores (Rossier et al., 2012; Tsunoyama et al., 2018) or gold nano-particles (Leduc et al., 2013).

Recruitment of proteins to IASs, as previously mentioned, can follow different paths. These can involve direct recruitment from the cytosol, lateral diffusion within the plasma membrane, or transport by the cytoskeleton. Talin, which also regulates integrin dynamics, is thought to be recruited to IASs directly from a cytosolic pool, a process mediated by actin or vinculin (Fig. 18b) (Rossier et al., 2012). Direct cytosolic recruitment of talin implies that talin is not stably bound to free-diffusing integrins outside IASs. This also might suggest that integrin inhibitors such as ICAP-1 or SHARPIN could be bound to integrins outside IASs, and displaced by integrin activators enriched in IASs.

IAS proteins interact extensively between themselves and are associated in specific functional nanolayers. Thus, it is likely that they are recruited as protein complexes, forming ‘building blocks’ to assemble IASs. Using fluorescence cross-correlation spectroscopy (FCCS) and fluorescence recovery after photobleaching (FRAP), researchers have found that IASs are extensively pre-assembled in the cytosol, through the formation of multi-protein building blocks

(Fig. 18a) (Hoffmann et al., 2014). In stationary IASs, there is a symmetrical release and recruitment of the same types of protein complexes, which simultaneously ensures the maintenance of IAS architecture and the constant renewal of the cytosolic pool of building blocks. Although this particular study does not focus on the nanoscale dynamics of individual IAS proteins, it provides a clear picture of IASs as dynamic entities which are built from precise 'rules'. Indeed, the pre-assembled 'building blocks' mostly correspond to the different functional layers, revealing how this dynamic assembly is tightly correlated with the nanoscale architecture of IASs. Building blocks can also undergo internal reorganization throughout time, as seen for vinculin upwards shift that occurs with IAS maturation.

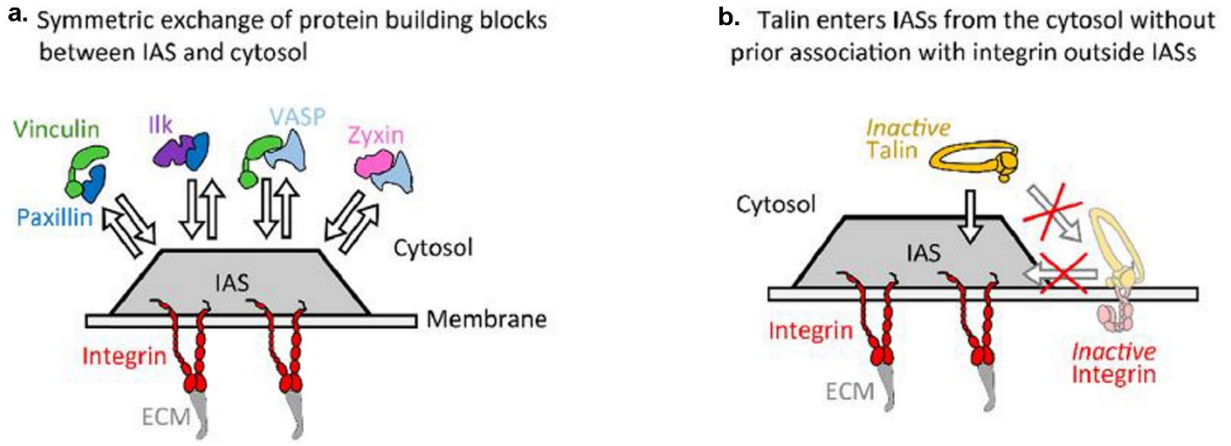

Figure 18: Dynamics of protein recruitment into IAS

a, Different IAS components can be pre-assembled as protein complexes in the cytosol and subsequently recruited to IAS. Such 'building blocks' could be functionally related to IAS nano-layers. **b,** As shown by single particle tracking experiments coupled to super-resolution microscopy, talin enters and immobilizes within IASs directly from the cytosol without prior diffusion with inactive integrins at the membrane. Figure adapted from Orré et al. 2019.

2.3. Mechanical regulation of protein activation and interactions at the basis of mechanotransduction

It is now widely accepted that IASs are extremely heterogeneous and dynamic structures, rather than passive entities connecting the actin cytoskeleton to the ECM. Thus, mechanotransduction at IASs is adapted to their structural complexity and is intrinsically dependent on protein dynamics and organization at the nanoscale. Mechanosensing in IASs is based on deformation and reorganization of proteins in response to force. This in turn can expose cryptic sites for ligand binding (Del Rio et al., 2009; Yao et al., 2014, 2016), or sites for proteolytic

cleavage (Stephenson and Avis, 2012). For instance, unfolding of talin by external mechanical forces or actomyosin tension triggers vinculin recruitment *in vitro* (Ciobanasu et al., 2014; Del Rio et al., 2009), which could lead to IAS maturation and increase of traction forces. Conformational changes can also expose or obstruct binding sites for kinases, triggering (or not) the phosphorylation of mechanosensitive proteins. This is the case of the cellular apoptosis susceptibility (Cas) family of proteins, which undergo force-dependent extension, exposing kinase binding sites (Sawada et al., 2006). This can trigger phosphorylation and consequent downstream signaling. Interestingly, p130Cas is required for cellular reorientation upon cyclic stretch in a mechanotransduction, probably through force-dependent phosphorylation (Niediek et al., 2012). Other proteins such as lamin undergo the opposite effect, with mechanical force hindering the access to phosphorylation sites (Buxboim et al., 2014). Despite not being directly part of IASs, lamin is connected to the cytoskeleton and can mediate nuclear mechanosensing, which in turn could involve force-dependent reduction of phosphorylation.

Moreover, both catch and slip bonds are highly relevant in the context of cell-ECM adhesions. For instance, the lifetime of $\alpha_5\beta_1$ or $\alpha_V\beta_3$ integrin–fibronectin binds is prolonged when of force is applied (Chen et al., 2017; Kong et al., 2009), showing how applied forces can actually enhance adhesion strength (Elosegui-Artola et al., 2016; Friedland et al., 2009). Such mechanisms could be further modified by stretching of fibronectin through mechanical forces, which exposes cryptic binding sites. Vinculin, a key IAS regulator and force bearer, exhibits a directional catch bond behavior with actin, which can be crucial for reinforcing adhesions and even determining tissue patterning (Huang et al., 2017b). Talin, on the other hand, maintained a 2 pN-slip bond in minimal matrix complexes, consisting of actin, integrin and a trimer of fibronectin molecules (Jiang et al., 2003). This slip bond could apply a low level of force to a minimal actin-integrin-ECM linkage until formation of more bonds or a force response (Jiang Nature 2003).

Bond lifetime is usually defined as the strength divided by the loading rate, defined as the speed at which the force is applied. Thus, loading rate will also influence catch and slip bond behavior (Evans and Calderwood, 2007; Evans et al., 2004; Sarangapani et al., 2011). Certain catch bonds involved in cell adhesion require fast loading rate for increase of bond strength, such as the interaction between integrin $\alpha_4\beta_1$ and the ligand VCAM (Evans and Kinoshita, 2007). Changes of loading rate can also lead to catch-slip transitions (Evans et al., 2004). The leukocyte adhesion bond P-selectin glycoprotein ligand 1 (PSGL-1)–P-selectin displays a catch bond behavior at loading rates higher than 300 pN/sec, but below that value it behaves as a slip bond (Evans et al., 2004). Catch-slip transitions were also reported for the same bond exerted to different forces: increasing the force on the P-selectin interaction with PSGL-1 first prolonged (catch) and then reduced (slip bond) the bond lifetime (Marshall et al., 2003; Yago et al., 2004). Although this was observed for leukocyte adhesions, a similar process could occur in IAS as forces fluctuate with tugging (Plotnikov et al., 2012) or maturation (Kumar et al., 2018). Another aspect

to consider in catch and slip bonds is that proteins are continuously subjected to mechanical forces in IASs, which could confer a sort of 'force history' to particular bonds. Indeed, application of cyclic forces to fibronectin–integrin α5β1 bonds switch the bond from a short-lived state with 1-s lifetime to a long-lived state with 100-s lifetime (Kong et al., 2013). This behavior has been termed 'cyclic mechanical reinforcement' (CMR) and could modify the response of talin after stretch-relaxation cycles in IASs (Margadant et al., 2011) or the vinculin-actin catch bond (Huang et al., 2017b).

2.4. Mechanosensing at single molecule level and coupling of proteins to actin flow

At the level of the molecular clutch, retrograde actin flow will engage with multiple proteins through a series of catch/slip bonds, which in turn will influence the dynamic and mechanical behavior of IAS proteins. This results in two widely observed events: the slowing down of the retrograde flow at mature FAs (Alexandrova et al., 2008; Gardel et al., 2008; Hu et al., 2007; Rossier et al., 2012; Thievessen et al., 2013) and, consequently, higher traction forces (Balaban et al., 2001; Gardel et al., 2008). It is also likely that the retrograde flow is transmitted to the different IAS proteins, including integrin, actin, talin or vinculin, since they also exhibit retrograde flow at lower or comparable speeds equal to or slower than the local actin retrograde flow (Alexandrova et al., 2008; Gardel et al., 2008; Hu et al., 2007; Rossier et al., 2012; Thievessen et al., 2013). This will lead to different behaviors: stationary (integrins, FAK, zyxin and paxillin), moving with the F-actin flow (α-actinin) or binding alternatively to flowing F-actin and immobile integrins (talin, vinculin) (Hu et al., 2007). However, the nanoscale dynamics and organization of IASs will strongly modulate force transmission and sensing across IASs. First of all, the 3D molecular architecture of IASs obliges forces to be transmitted across different nano-layers and multiple protein-protein bonds. One of the consequences is the polarization of different proteins, such as talin (15-25° angle), which is thought to be defined by the actin flow. Transmission across 3D nano-layers will likely cause dissipation of forces as they propagate throughout the different layers until reaching the ISL. In some cases, the flow speed of proteins becomes progressively lower as a consequence. Hu and colleagues, three years before the first work on IAS 3D nano-partitioning, had shown that α-actinin, co-localized with actin more than 60 nm above the plasma membrane displayed a retrograde flow ~25-fold higher than paxillin and $\alpha_V\beta_3$ integrin (Hu et al., 2007). Talin and vinculin, as expected, displayed values between integrin and α-actinin. Although this work precedes the findings of Kanchanawong and colleagues on IAS nano-partitioning (Kanchanawong et al., 2010), the different flow speeds are in mostly agreement with the different layers. However, this is not always a linear variation; a previous study has also shown that β1-integrin flows at the same speed as talin and actin (Rossier et al., 2012). Only the fraction

of flowing integrin is decreased, which could be more related to the nano-organization of the protein or to slip bond behavior. Moreover, as the nano-architecture of IASs changes with their maturation, this will also affect force transmission. For instance, the upward shift of vinculin during IAS maturation will likely change its engagement with actin and thus affect protein flow, as well as traction force. Another aspect to consider is the change itself of the speed of the flow between NAs, which form in the lamellipodium, and FAs, which start to mature at the lamella and experience a progressively lower flow as the leading edge advances (Gardel et al., 2008).

The organization of IASs will also affect the scale at which force is transmitted or sensed. As previously described in this section, mechanical forces are heterogeneously distributed across IASs. Together with the highly nanoscale partitioning of IASs, this supports a hypothesis where force transmission and generation at IASs is mediated by units structured at sub-micron scale, probably at the scale of protein complexes and single molecular linkages. Supporting this view, SRM and SPT experiments have shown that different classes of integrins are nano-partitioned in FAs, giving rise to different ECM-cytoskeleton coupling (Rossier et al., 2012). β3-integrins are highly enriched in FAs and are mostly stationary, while β1-integrins are more sparsely accumulated and display substantially more rearward movements (~3-fold higher compared to β3-integrins) (Fig. 19) (Rossier et al., 2012). This difference of motion is apparently dependent on their extracellular domain. This implies that specific classes of integrins are differently coupled to actin filaments, acting as 'nanoscale adhesion units' which will modulate transmission of actomyosin forces to the substrate. SPT has also revealed how the fraction of talin moving rearward in FAs is low compared to F-actin. Absence of rearward movements of talin does not necessarily indicate that the protein is not connected to the actin flow. Instead, it can stem from simultaneous binding to stationary integrins and flowing F-actin, a process which could be mediated by multiple slipping bonds (Jiang et al., 2003). Indeed, talin displays multiple stretching-relaxation cycles within mature FAs (Margadant et al., 2011). Moreover, as previously discussed, high talin tension is correlated with alignment of actin filaments, supporting a connection between talin and the actin flow (Kumar et al., 2018).

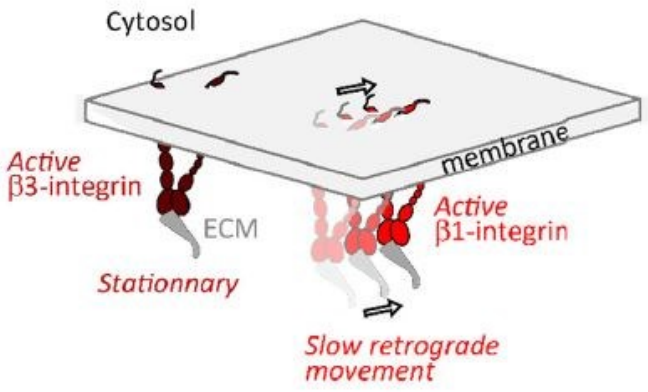

Figure 19: Different flow of integrins in IAS

Despite being active, ligand-bound β3-integrins (crimson) are mostly stationary within IAS, while ligand-bound β1-integrins display a more prominent slow retrograde movement. This can reflect different engagements with the actin retrograde flow but also other IAS components. Figure adapted from Orré et al. 2019.

In line with the hypothesis of force sensing and generating units within IASs, a recent study has demonstrated how force loading and distribution at the individual molecular clutch is a key aspect for IAS-mediated rigidity sensing (Oria et al., 2017). When the spacing between integrin ligands was increased, FA growth was promoted for softer substrates, but as the rigidity increased, FAs were rendered unstable and collapsed. This collapse was reverted by inhibiting myosin II with blebbistatin. A modified molecular clutch model was proposed to explain this behavior, where an increased ligand spacing leads to a higher force loading per clutch, increasing integrin recruitment. As rigidity increases, clutches with higher spacing will reach a force threshold faster, thus promoting FA collapse. This elegant study highlights how sub-micron adhesive units within IASs might be crucial for controlling force sensing and transmission.

3. Talin – a mechanosensitive and mechanosignaling hub

3.1. Structure of talin

Talin is a cytosolic multi-domain protein which plays a key role in both cell adhesion and mechanosensing (Atherton et al., 2015; Austen et al., 2015; Elosegui-Artola et al., 2016; Giannone et al., 2003). First, it promotes integrin activation; then, couples integrins to the actomyosin cytoskeleton, ensuring force transmission. Thus, talin is essential for adhesion growth, dynamics and stability in developing organisms (Klapholz CB 2015, Conti Development 2009). Vertebrates possess two talin isoforms: talin-1 and talin-2, which share 76% of their protein sequence (Gough and Goult, 2018). Most of the focus has been directed towards talin-1, whose knockout is embryonic lethal in mice, causing developmental defects such as arrested gastrulation (Monkley et al., 2000). Depletion of talin-1 also leads to impaired cell spreading and adhesion (Zhang et al., 2008), as well as impaired platelet aggregation (Nieswandt et al., 2007). Talin-2 is less studied and, despite the similarities with talin-1, there are some key differences. First, while talin-1 is ubiquitiously expressed, talin-2 expression is more restricted, with high levels of expression mostly in the brain, kidney and heart muscle (Gough and Goult, 2018). Moreover, and although both talins localize to mature FAs, only talin-2 localizes to fibrillar adhesions for the most part (Praekelt et al., 2012). Further differences in fine-tuning of mechanical engagement have been found (Austen et al., 2015); still, further differences between both talin isoforms remain to be characterized.

The multifunctional nature of talin is intrinsically linked to its structure and organization, which allows talin to bind both integrin and F-actin, among many other partners (Calderwood et al., 2013; Goult et al., 2018). The structure of talin consists of an N-terminal head region, composed of an atypical FERM domain with 4 globular segments (F0 to F3), and followed by an

unstructured linker connected to the C-terminal 'rod' (Fig. 20a). The talin rod is formed by 13 helical bundle domains, each one composed by 4 and 5-helix bundles. The talin head region binds cytoplasmic integrins through the FERM domain while the talin rod binds actin though two actin-binding sites (ABS2 and 3) (Fig. 20a) (Calderwood et al., 2013; Goult et al., 2018) . This is a rather simplistic view, since both the head and rod regions will bind several other partners in the context of cell adhesions. One of the most important is vinculin, an intracellular protein essential for force transmission, adhesion stabilization and regulation of other IAS-associated proteins (Atherton et al., 2015; Carisey et al., 2013; Grashoff et al., 2010). The talin rod contains 11 cryptic vinculin binding sites (VBSs), buried inside the 13 helical bundle domains (Fig. 20a) (Del Rio et al., 2009; Yao et al., 2016). When purified talin is stretched with magnetic tweezers, unfolding of talin rod exposes one or more of these VBSs, triggering recruitment of vinculin (Del Rio et al., 2009; Yao et al., 2016). Using an *in* vitro reconstituted network, Ciobanasu and colleagues also revealed that actomyosin tension is enough to stretch talin, allowing the binding of vinculin, thus providing a possible mechanism for talin-vinculin binding in live cells (Ciobanasu et al., 2014).

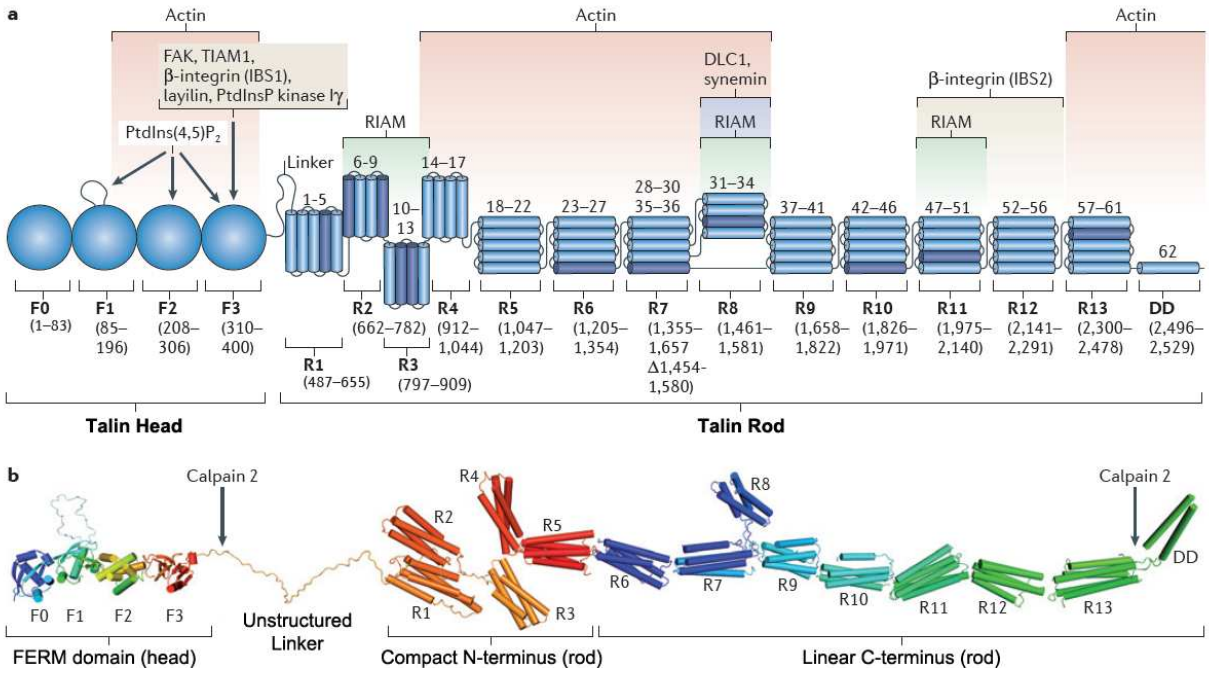

Figure 20: Domain organization and structure of talin

a, The domain organization of talin-1. The amino-terminal talin head comprises an atypical talin FERM domain containing F0, F1, F2 and F3 domains, which include the actin binding site (ABS) 1. The head domain is connected to the flexible talin rod through an unstructured linker of ~80 residues. The rod is composed of thirteen 4- or 5-helix bundle domains (R1–R13) and a single helical dimerization domain (DD) at the carboxyl terminus. Domain boundaries and the interaction sites for talin-binding proteins are indicated. 9 of the 13 talin rod helix bundle domains contain VBSs, of which there are 11 in total (dark blue). 3 binding sites (R2-R3, R8 and R11) for RIAM are also visible, as well as two other ABSs: R4-R8 ABS2,

flanked by R3-R9, and the ABS3, located in the C-terminus. Talin 2 is predicted to have the same domain structure. **b,** Structural model of talin showing the distinct organization of talin rod domains positions of the calpain 2 cleavage sites. Because the N termini and C termini of the three 4-helix bundles (R2–R3–R4) are positioned at the same end of the bundle, this region (Compact N-terminus) will be more compact than the long succession of 5-helix bundles linked via their N termini and C termini (Linear C-terminus). DLC1, deleted in liver cancer 1; FAK, focal adhesion kinase; IBS; integrin-binding site; PtdIns(4,5)P_2, phosphatidylinsotitol-4,5-bisphosphate; PtdInsP kinase Iγ, phosphatidylinositol 4-phosphate 5-kinase type Iγ; TIAM1, T lymphoma invasion and metastasis-inducing 1. **a-b,** Figure adapted from Calderwood et al. 2013.

3.2. Talin recruitment to IASs and integrin activation

A key function of talin is to activate integrins and initiate IAS formation. Binding of talin to integrin can actually be the triggering event for integrin immobilization, which requires talin to be activated. Cytoplasmic talin is autoinhibited through head-rod interactions, which must be released to activate the protein (Goult et al., 2009; Song et al., 2012). A recent cryo-electron microscopy has shed new light on this autoinhibited conformation: first, the rod domains entangle the protein into a 15 nm-compact globular structure. This structure is interlocked by interactions between the F2 and F3 FERM subdomains and the R12 and R9 rod domains (Dedden et al., 2019). This simultaneously shields the acess to both integrin, actin and membrane binding. Release of talin autoinhibition will enhance integrin binding and activation, but will also promote actin binding (Klapholz and Brown, 2017). The activation and recruitment of talin itself are thought to involve several possible mechanisms and differ between cell types. For instance, the Rap1-GTP-interacting adaptor molecule (RIAM) pathway supports a mechanism where talin is first recruited to the membrane for activating integrins (Lee et al., 2009; Yang et al., 2014b). RIAM is a Rap1 effector containing a pleckstrin homology (PH) domain, allowing RIAM to anchor to the membrane (Vigouroux et al., 2020). RIAM localizes talin to the plasma membrane, releasing the autoinhibition and promoting integrin binding and inside-out activation (Lee et al., 2009). Quantitative mapping analysis revealed that binding of RIAM to talin F3 head domain occludes the inhibitory interactions with the talin rod, allowing talin to bind integrin (Yang et al., 2014b).

Talin can also be directly recruited by ligand-bound integrins in the membrane without diffusing on it, which fits the behavior of single talin molecules. Indeed, sptPALM experiments revealed that talin does not exhibit barely any membrane diffusion inside or outside mature FAs. Since experimental conditions made impossible to detect any cytosolic diffusion, it is likely that talin is mostly cytosolic and it is not co-diffusing with integrins before integrin activation and immobilization (Rossier et al., 2012). SPT experiments from the same study also revealed that the C-terminal talin THATCH mutant, comprising an actin and vinculin-binding site, did not display membrane free-diffusion. Conversely, talin head alone exhibited prominent membrane diffusion outside and inside FAs, but no immobilization inside FAs (Rossier et al., 2012). These differences

reflect the auto-inhibition of talin in the cytosol, which will likely be relieved inside IASs. Talin is likely recruited to IASs directly from a cytosolic pool, probably through F-actin binding (Rossier et al., 2012). Recruitment of talin can occur through various integrin-binding sites in the head and rod, as well as ABS3 (Klapholz and Brown, 2017). However, it is also possible that talin establishes transient RIAM-mediated interactions with the membrane, sufficient to activate talin and promote integrin binding (Yang et al., 2014b). In line with this, talin interactions with the cell membrane are essential to activate talin through PIP_2, which severs the head-tail autoinhibitory interaction (Saltel et al., 2009). Disruption of talin-PIP_2 interaction affects talin localization to the cell membrane, integrin activation and focal adhesion formation (Chinthalapudi PNAS 2018). A combination of the two hypothesis suggests that talin is recruited directly from the cytosol either to the membrane via RIAM, PIP_2 or to adhesion sites via F-actin binding, undergoing subsequent activation and binding to integrins. Different pathways can be temporally coordinated throughout IAS formation and maturation. Finally, proteins such as FAK can also contribute to talin recruitment to NAs in mammalian cells (Lawson et al., 2012).

3.3. Mechanosensing at the talin rod

Talin mechanosensing relies on the conformational change of the 13 talin rod domains (R1-R13) under force. The mechanical behavior of these domains has been revealed through different *in vitro* experiments where purified talin was stretched with high-precision magnetic tweezers (Del Rio et al., 2009; Yao et al., 2014, 2016) Of these, only one characterized the response of all the 13 rod domains, which undergo reversible switch-like behaviors when subjected to force/relaxation cycles (Yao et al., 2016) (Fig. 21a). The rod domains unfold at characteristic forces, which range between 5 and 25 pN, and the domains rapidly refold when force is reduced to < 3pN. Interestingly, four distinct groups of domains can be defined based on their response to different force values. The unfolding of rod domains allows to considerably extend the talin rod: each unfolding event yields a step size of ~30-40 nm, for a possible maximum of ~500 nm. As a consequence, talin extension can vary between different lengths. Indeed, inside adhesions, the retrograde flow of actin will stretch and release talin in multiple stochastic cycles, leading to fluctuations of talin extension in the range of 50-350 nm (Margadant et al., 2011). Kinetic simulations show that this stochastic unfolding of talin domains maintains the average force in the talin-mediated linkage below 10 pN (~5-6 pN), even when talin is extended beyond the physiological range. Thus, force-dependent stochastic unfolding/refolding of the talin rod allow talin to act as a molecular shock absorber. Talin mediated force buffering will likely affect adhesion integrity and the loading/unloading rate on the whole ECM-integrin-talin-cytoskeleton pathway.

Characterization of mechanical behavior of rod domains also allowed to better understand the force-dependent exposition of VBSs. Among all the rod domains, R3 is considered the weakest, since it unfolds under the lowest force (~5 pN). R3 also contains two VBSs, meaning it will likely be the initial mechanosensor in talin and engage vinculin to reinforce adhesions (Del Rio et al., 2009). However, all the talin rod domains containing a VBS (9 domains for a total of 11 VBSs) bind vinculin over physiological ranges. Hence, all 11 VBSs in talin can be exposed by stretching and consequently recruit vinculin. However, in the presence of vinculin, talin unfolding for all VBS containing domains is irreversible, whereas in the absence of vinculin, unfolding is reversible (Fig. 21b) (Yao et al., 2014, 2016). Therefore, binding of vinculin locks talin rod domains in the unfolded conformation, stabilizing the talin-vinculin complex and preventing domain refolding when force is released (Fig. 20c) (Yao et al., 2014, 2016). This is line with results obtained in *in vitro* reconstituted networks, where talin refolding is kinetically limited by vinculin (Ciobanasu et al., 2014). However, the talin rod is still stretched and relaxed even in the presence of vinculin (Fig. 21b,c) ; thus, even if vinculin locks the rod domains in an unfolded conformation, talin can still behave as a spring. This could occur through the unfolding of other domains and also via helix-to-coil transitions. Moreover, the association of vinculin to talin rod domains is reversible at larger forces, since vinculin dissociates from the talin rod at forces higher than 25 pN (Yao et al., 2014). This is probably caused by helix-to-coil transitions that occur when α-helices are rendered unstable by high forces (Gao et al., 2019), which could lead to dissociation of vinculin from IAS. Interestingly, a recent study with magnetic tweezers has shown that the binding of vinculin head to the unfolded R3 domain actually induces a coil-to-helix contraction, which is likely required to properly bind vinculin to the VBS. (Tapia-Rojo et al., 2020). Thus, force is required for vinculin binding to unfolded rod domains but also hampers this interaction, since vinculin binding has to work mechanically against the pulling force by contracting talin. The double effect of force establishes an optimal binding force range for vinculin to talin, one which is likely surpassed at higher pulling forces, rendering vinculin binding unfavorable.

It is of note to mention that rod domains interact with other proteins besides vinculin. Among them, the R8 domain is known to have a VBS but also to serve as a binding hotspot for several 'LD-motif' containing proteins, such as RIAM, paxillin, α-synemin and KANK (Goult et al., 2018). The R8 domain exhibits an unusual behavior cooperative unfolding with the R7 domain, which keeps R8 folded at forces it would be unable to withstand on its own (Yao et al., 2016). This might be a protective mechanism to maintain the signaling activity of R8, which could be silenced after VBS exposure and vinculin binding. Based on their response to force, talin rod domains act as a series of mechanochemical switches who can combine for different mechanical states and recruitment of other mechanosensitive proteins. Unfolding of the talin rod domain is a key element for the role of talin in sensing the mechanical properties of the matrix or externally applied forces. The tension and release cycles resulting from engagement of retrograde flow,

combined with the magnitude of forces, determine the folding/refolding of domains and binding/unbinding of ligands.

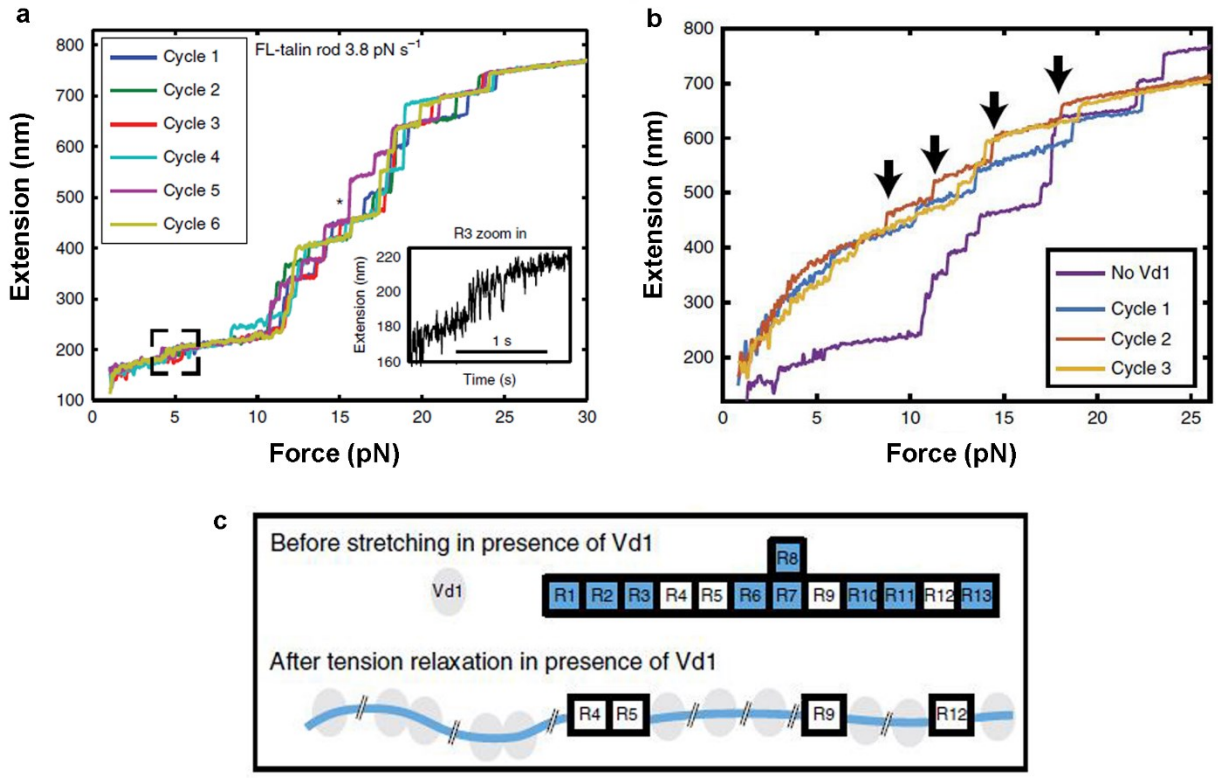

Figure 21: Talin mechanical response and vinculin recruitment

a, Unfolding force-extension of talin rod in response to force applied with magnetic tweezers at a loading rate of 3.8 pN s^{-1}. 12 extension steps (~30-40 nm) can be observed, corresponding to the unfolding of talin rod domains of ~120-170 amino acids (50-70 nm contour length). The inset shows the unfolding step of the R3 domain at ~5 pN, the first domain to undergo force-dependent unfolding. Different curves represent repeated force cycles from a single protein tether. Thus, the unfolded domains rapidly refold since these force-extension cycles are nearly identical. **b,** Unfolding force-extension curves in the absence of vinculin domain 1 (Vd1) (purple curve, no Vd1) and in the presence of 100 nM Vd1 (cycles 1-3). In the absence of Vd1, the curve displays the same 12 unfolding steps as in **a,** but in the presence of 100 nM Vd1, only four unfolding steps are observed (marked by arrows). This shows how vinculin binding to unfolded talin rod domains prevents talin refolding after force is released. **c,** Schematic displaying the conformational changes in the talin rod in the presence of vinculin. Figure adapted from Yao et al. 2016.

3.4. Talin mechanosensing in adhesion assembly and force transmission

Several studies suggest that talin contributes directly to adhesion assembly, maturation and force transduction through a series of mechanosensitive events involving the rod domain, as

well as actin and vinculin binding (Atherton et al., 2015; Elosegui-Artola et al., 2016; Thievessen et al., 2013). These studies, performed in live cells, draw several aspects from *in vitro* experiments on talin force response. Nonetheless, early works from the Sheetz lab, prior many of these *in vitro* studies, had already identified talin as an important element for initiation and reinforcement of actin-integrin-ECM linkages in live cells (Giannone et al., 2003; Jiang et al., 2003). Based on previous observations, talin-mediated mechanosensing in adhesion assembly and maturation can be broadly divided into two steps. Initially, activated talin binds integrin via FERM domains and engages actin through the ABS3, which is a fundamental step in adhesion initiation (Atherton et al., 2015). One of the mentioned studies from Sheetz's lab revealed that talin maintained a 2 pN-slip bond in minimal matrix complexes, consisting of actin, integrin and a trimer of fibronectin molecules (Jiang Nature 2003). This slip bond could apply a low level of force to a minimal actin-integrin-ECM linkage until formation of more bonds or a force response (Jiang Nature 2003).

Following initial talin engagement, actomyosin-mediated tension leads to unfolding of the talin rod (Ciobasanu Nat Comm 2014), likely via the R3 domain, which is considered the initial talin mechanosensor (Del Rio Science 2009, Atherton Nat Comm 2015). This is thought to occur via the ABS3 site in talin, which engages F-actin, allowing for transmission of actomyosin tension and talin stretching (Fig. 22). Unfolding of the talin R3 domain exposes the two cryptic high-affinity VBSs, (Del Rio et al., 2009; Yao et al., 2016), triggering vinculin recruitment. Interestingly, vinculin could promote talin-actin interactions independently of ABS3 by directly binding to talin in an active state. This could explain why constitutively active vinculin bypasses the requirement of ABS3 to triggering IAS formation and maturation (Atherton et al., 2015; Carisey et al., 2013).

Force-dependent (or not) vinculin binding reinforces the mechanical linkage of talin to actin filaments and contributes for IAS stabilization and maturation (Austen et al., 2015; Ciobanasu et al., 2014; Elosegui-Artola et al., 2016; Thievessen et al., 2013). Supporting this idea, talin unfolding and vinculin binding were shown to trigger adhesion growth in response to increased substrate rigidity (Elosegui-Artola et al., 2016). Moreover, another study using a FRET-based force sensor revealed that talin mediates constitutive mechanical linkages: a main subset experiencing forces above 7 pN, and a secondary subset experiencing forces above 10 pN (Austen et al., 2015). However, in vinculin-deficient cells, these values drop to 1-6 pN, revealing the importance of vinculin in reinforcing the actin-talin mechanical linkage.

The mechanical engagement can also vary across the talin rod domain. Using a digital-like multiplexing force sensor, Ringer and colleagues revealed that talin displays an intramolecular tension gradient. In the talin rod region closer to the N-terminal, tension reaches ~7 pN , while at the C-terminal, tension is lower (~3 pN). This gradient is dependent on extracellular rigidity and, more importantly, vinculin binding; in vinculin-negative cells, tension at is markedly reduced, but only for N-terminal. Thus, vinculin binding to talin and mechanical reinforcement

will likely occur at the N-terminal regions of the talin rod domain. Importantly, vinculin binding appears to require prior mechanical engagement of talin to actin filaments (Austen et al., 2015), hence supporting an initial talin-actin interaction via ABS3 before vinculin is recruited (Atherton et al., 2015). Interestingly, the mechanical engagement of talin was shown to be isoform-specific. First, talin-2 are more exposed to tension compared to talin-1. Second, in the absence of all C-terminal ABSs, talin-2 retains its tension and talin-2 FAs are still vinculin positive, which is not the case for talin-1. Thus, vinculin recruitment to talin-2 is independent of F-actin binding to the C-terminal. Such effects are dependent on the R1-R3 rod domains (Austen et al., 2015). This also has an impact on IAS-mediated rigidity sensing, since talin-2 cells spread more efficienty on soft substrates, which actomyosin contractility is less pronounced.

Force-dependent unfolding of the R3 domain can also reinforce adhesions by relieving the inhibition of the ABS2, allowing it to bind F-actin (Fig. 22b) (Atherton et al., 2015). Indeed, the R3 domain flanks ABS2 in the R4-R8 region, and ABS2 is inhibited by R3 and R9 domains (Atherton et al., 2015). Thus, combination of vinculin binding to talin and ABS2/ABS3 binding to actin can further stabilize talin in IASs (Fig. 22d). An essential aspect throughout all these processes is that vinculin blocks talin rod domains in an unfolded configuration *in vitro* (Fig. 21b,c), (Yao et al., 2014, 2016), thus generating a positive feedback that could reinforce mechanical linkages at IASs. In parallel, the mechanics of talin-vinculin interactions *in vitro*, where vinculin also works against the pulling force to bind talin rod domains, suggest a possible negative feedback that maintains the mechanical homeostasis of IAS. At higher forces, α-helices are rendered unstable and vinculin cannot overcome the pulling force to contract talin, hence triggering its dissociation (Tapia-Rojo et al., 2020; Yao et al., 2014).

One interesting aspect about talin mechanosensing is that vinculin is not the only partner of talin; indeed, many other proteins can bind the rod domains, such as KANK or RIAM. In this regard, RIAM has recently been implied in a new mechanosensitive mechanism involving the talin rod (Vigouroux et al., 2020). In *in vitro* reconstituted networks, actomyosin-generated tension promoted the dissociation of RIAM from R1-R3 or R11 talin constructs, which is kinetically followed by vinculin association (Vigouroux et al., 2020). Thus, talin-RIAM interaction is mechanosensitive and it can work as a conformational switch, one where RIAM and vinculin exchange in response to mechanical force, promoting IAS maturation. In addition, talin-KANK interactions are important to target microtubules to IASs, contributing to maintain FA size and protect podosomes (Rafiq Nat Materials 2019). This highlights yet another role of talin in regulating IASs through its multiple signaling partners.

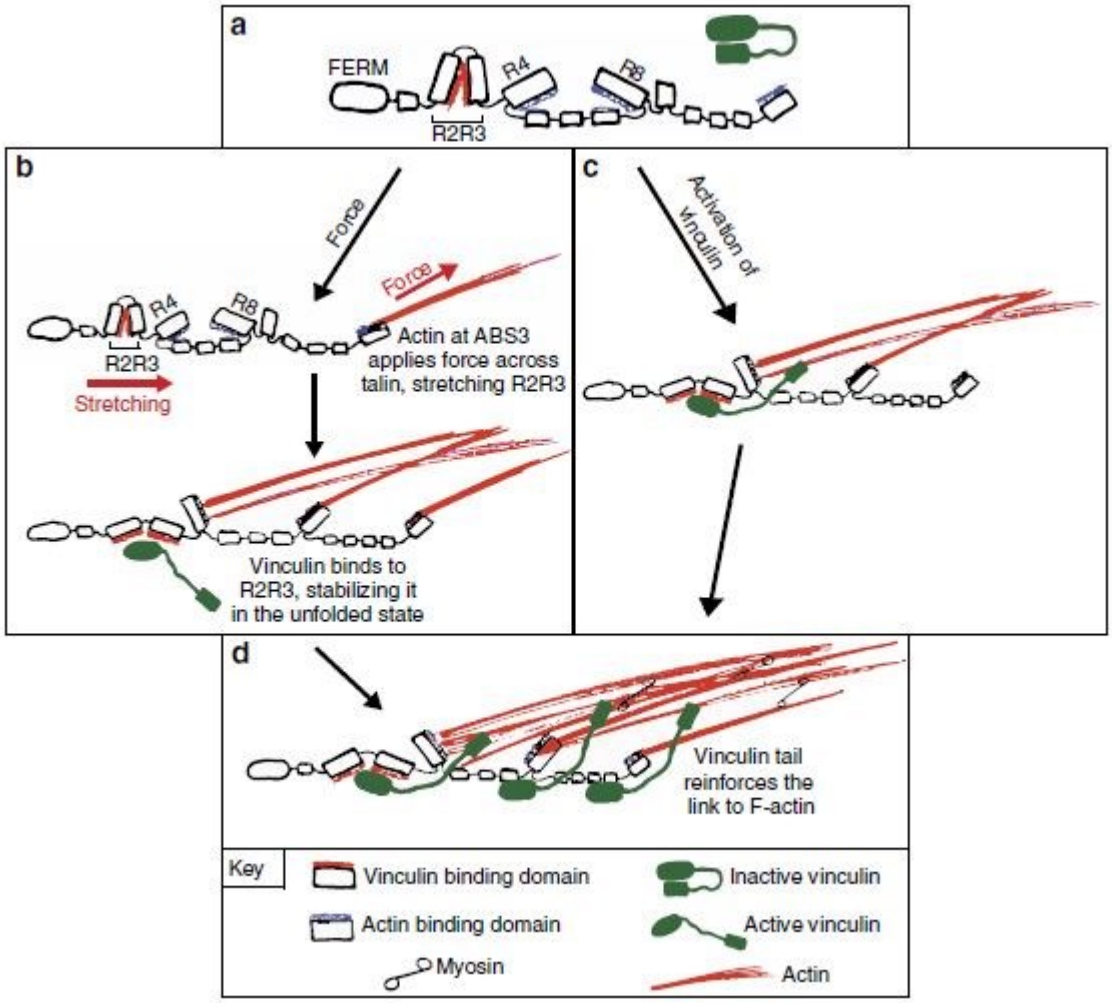

Figure 22: Talin mechanosensing and vinculin-dependent IAS reinforcement

a,Talin in the unfolded state, with the cryptic vinculin binding sites at R2-R3 and ABS2 at R4-R8. inactive vinculin represented in green. **b,** Talin binds actin at ABS3, which is thought to support the force for the initial events leading to IAS maturation. In response to actomyosin-dependent tension exerted at ABS3, talin rod is stretched, unfolding R2-R3 domain, the initial mechanosensitive switch, triggering vinculin binding. This, in combination with force, relieves the inhibitory effect of R3 on ABS2, allowing further actin binding. **c,** Talin can also bind actomyosin through a vinculin-driven pathway, where active vinculin unlocks ABS2. **d,** Full engagement of talin with actin occurs via ABS2 and ABS3, with vinculin stabilizing the unfolded talin conformation and talin-actin linkage. **a-d,** Figure adapted from Atherton et al. 2016.

4. Vinculin – A multiscale force bearer

One cannot spell talin without vinculin, especially concerning mechanosensing at IASs. Indeed, by describing talin mechanosensing and function we accidentally ended up by also introducing some of the roles of vinculin in IAS stabilization and force transmission. Vinculin is an

intracellular IAS protein composed of a head domain (Vh) and a tail region (Vt) separated by a flexible proline-rich neck linker (Fig. 23a,b) (Atherton et al., 2016; Bays and DeMali, 2017). In cells, vinculin can either adopt an extended, active form (Fig. 23c), or an inactive, auto-inhibited state in which a head-tail interaction mask binding sites (Fig. 23c) (Atherton et al., 2016; Bays and DeMali, 2017). Inactive, folded state exists within the cytoplasm, while the activated form of vinculin localizes mostly to IASs. Here, several binding sites to its many partners are exposed, including talin (head domain), VASP, vinexins and ponsin (neck domain) or F-actin (tail domain). Therefore, vinculin is essential for the complete engagement of IASs with the actomyosin contractile machinery, regulating force transmission, IAS stabilization and maturation, cytoskeleton dynamics, and cell migration (Carisey et al., 2013; Case et al., 2015; Grashoff et al., 2010; Rothenberg et al., 2018; Thievessen et al., 2013). Genetic knockout of vinculin *in vivo* is lethal in mice embryos, leading to severe defects in the development of the heart and the nervous system (Xu et al., 1998). Vinculin-deficient cells also display impaired cell spreading and migration, as well as lower traction forces and stiffness (Alenghat et al., 2000; Mierke et al., 2008; Xu et al., 1998). Defects in embryonic development and morphogenesis are likely a result of impaired/altered cell migration due to vinculin depletion, although vinculin might also have tissue-specific roles, especially in the heart (Shiraishi et al., 1997; Xu et al., 1998). Conversely, expressing constitutively active vinculin compromises Rac1-mediated polarized cell migration (Carisey et al., 2013). Therefore, vinculin activity needs to be tightly controlled to ensure coordinated cell migration.

4.1. Vinculin recruitment and activation: integrating contractility and molecular partners

As previously explained in the section on 3D nanoscale organization of IASs, vinculin is recruited to the ISL in NAs in its inactive state. As IASs undergo coordinated myosin II-dependent maturation, talin binding activates vinculin, promoting an upward shift in the nanoscale localization of vinculin from the ISL to the FTL and ARL (Case et al., 2015). Previous studies have showed that vinculin is recuited to disassembling/assembling NAs (Giannone et al., 2004, 2007) and that vinculin enters NAs simultaneously with paxillin and FAK (Choi et al., 2008). Thus, these components will be recruited to NAs either individually or in clusters in response to common events (Choi et al., 2008). In addition, vinculin enters NAs after actin and α-actinin, with a slight delay in regards to talin (Choi et al., 2008). Vinculin is likely recruited to NAs after these three proteins to then undergo subsequent activation, a process which is likely dependent on myosin II contractility. This is supported by the fact that myosin II activity is required to ensure localization of vinculin at mature FAs (Case et al., 2015; Pasapera et al., 2010). Recruitment of vinculin is crucial for the formation and maturation of IAS triggered by external forces (Galbraith

et al., 2002; Giannone et al., 2003). Therefore, force and intracellular contractility are key players in both recruitment and activation of vinculin; however, it is equally important to assess the various molecular mechanisms by which this can take place.

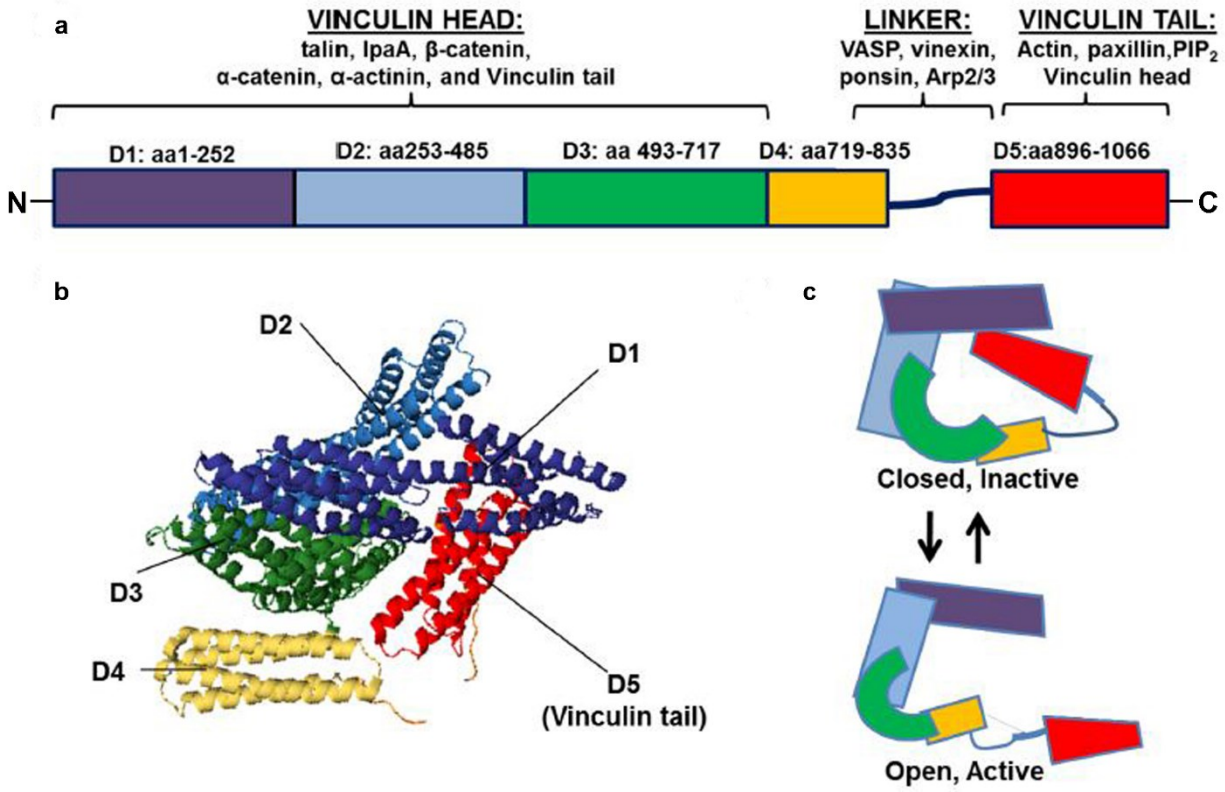

Figure 23: Vinculin structure and binding partners

a, Vinculin is composed of anti-parallel α-helical bundles organized into five distinct domains. Each helix is shown in a different color. Domains 1-3 constitute the vinculin head (Vh) (purple, blue, green) while domain 5 comprises the tail (Vt) (red). Binding sites for many proteins are marked on the respective domains; these allow vinculin to act as a master regulator in recruitment and release of IAS components (Carisey CB 2013) **b,** Ribbon diagram derived from human full-length vinculin crystal structure shows the inactive, auto-inhibited closed conformation of vinculin, held by intramolecular interactions between the head and tail domains. Vinculin tail domain can be seen as 5-helix pack (red) **c,** Vinculin cycles between an inactive, closed conformation (top) and an open, active conformation. Conformational changes in C-terminal tail domain could drive vinculin activation and transition to an active state. Different models suggest that either one ligand (such as talin) or the combination of two ligands are required to displace Vh from Vt, promoting a transition to an active, open conformation. **a-c,** Figure adapted from Bays and DeMali 2017.

Vinculin has several binding partners, which increases the number of possible routes for recruitment and activation of the protein. Therefore, recruitment of vinculin to IASs, as well as

the release of the autoinhibitory head-tail bond, might involve several mechanisms. Talin, as the major binding partner of vinculin in IASs, is essential for vinculin recruitment and activation. As explained in the previous section, Talin contains 11 cryptic VBS, which are exposed after force-induced unfolding of the different talin rod domains, recruiting vinculin (Del Rio et al., 2009; Yao et al., 2014, 2016). Using a FRET-based force sensor which decreases FRET efficiency when vinculin is in an active conformation, Case and colleagues found that talin binding is required for vinculin activation at FAs (Case et al., 2015). Briefly, wild-type vinculin displays lower FRET ratios inside compared to outside FAs, indicating that the protein is selectively active inside FAs. Conversely, a mutation that inhibits talin binding to the vinculin *in vitro* (Vinculin-A50I) (Cohen et al., 2005) leads to a similar FRET ratio inside and outside FAs, revealing that talin binding is indeed required for selective vinculin activation at IASs. This mutant is also localized lower in the FAs (in the ISL) compared to wild type vinculin (FTL and ARL), meaning that talin binding is also required for the upwards shift in vinculin localization. However, Vinculin-A50I still localizes to FAs, which indicates that even in the absence of talin binding, vinculin can be recruited to IASs (Case et al., 2015). Moreover, evidence from *in vitro* studies suggests that talin per se might not be sufficient to activate vinculin (Bakolitsa et al., 2004; Cohen et al., 2005). Crystallography studies revealed that vinculin head, tail and proline rich domains are conformationally and thermodynamically linked (Bakolitsa et al., 2004). Thus, it is possible that vinculin recruitment and activation in IASs can only occur through the combined binding of at least two ligands/proteins to distinct regions. It is also interesting to note that several *in vitro* studies with talin stretching and vinculin binding were performed with the purified vinculin head domain, which lacks the auto-inhibitory interactions (Del Rio et al., 2009; Yao et al., 2014, 2016).

The most likely scenario is that recruitment and activation of vinculin in IASs will involve a combination of talin and another protein or ligand (Fig. 24a). F-actin is a likely candidate, given that vinculin possesses F-actin binding sites in the tail domain, and F-actin could act synergistically with talin to activate vinculin (Bakolitsa et al., 2004). This is supported by an *in vitro* study where only the combination of both talin rod and F-actin can bind vinculin and change its conformation to an active state (Chen et al., 2006). However, a study performed in FAs revealed that vinculin mutations that reduce actin binding have no discernible effect in vinculin activation or nanoscale localization (Case et al., 2015). Therefore, it is still unclear whether F-actin binding is required for vinculin activation at IASs.

Paxillin phosphorylation has also been identified as a possible additional mechanism in vinculin recruitment and activation, in combination with myosin II activity (Case et al., 2015; Pasapera et al., 2010). Pasapera and colleagues previously showed that inhibition of myosin II with blebbistatin leads to a reduction of the vinculin content in mature FAs, but also to a decrease in paxillin-vinculin interactions and FAK-mediated paxillin phosphorylation (Pasapera et al., 2010). Interestingly, paxillin phosphorylation increases paxillin-vinculin interactions.

Phosphomimetic mutants of paxillin (tyrosine residues 31 and 118) rescue the effects of blebbistatin in paxillin-vinculin interactions and also the blebbistatin-induced reduction vinculin in small immature IASs (Pasapera et al., 2010). Thus, FAK-mediated phosphorylation of paxillin can mediate myosin II-dependent vinculin recruitment to IASs, thus conferring an important role to paxillin in adhesion mechanosensing. A more recent paper, however, revealed that paxillin knock-down results in no changes in vinculin targeting to the FAs or in vinculin activation at FAs (Case et al., 2015). This could suggest that paxillin is not specifically required for vinculin recruitment or activation and that myosin II-dependent recruitment of vinculin could follow other paths. Still, paxillin knock-down resulted in an upwards shift of vinculin towards the FTL and ARL, which suggests that paxillin is specifically important to target inactive vinculin to the ISL, but not to recruit it (Case et al., 2015). This is also supported by the fact that paxillin can bind vinculin regardless of talin binding, again reinforcing the link between paxillin and inactive vinculin (Case et al., 2015). Interestingly, expressing phosphomimetic paxillin (tyrosine residues 31 and 118) in paxillin-depleted cells rescues the nanoscale localization of vinculin. Moreover, phosphorylation of paxillin in maturing IASs is coordinated with vinculin recruitment to ISL during blebbistatin washout. Thus, targeting of inactive vinculin to the ISL is probably mediated by paxillin phosphorylation (Case et al., 2015). Recent evidence confirms that paxillin interacts with both inactive talin and vinculin, further strengthening this hypothesis (Atherton et al., 2020).

By combining these results, a possible model for vinculin recruitment and activation can be defined in two steps: first, NAs assemble in a myosin II-independent fashion, through integrin activation and recruitment of paxillin and talin. Myosin-II dependent maturation of IASs leads to paxillin phosphorylation via FAK. Phosphorylated paxillin can cycle between IASs and the cytoplasm, forming labile interactions with vinculin, which have been previously reported (Pasapera et al., 2010). Vinculin is then ‘handed over’ to talin, actin or other partners at NAs, further activating vinculin and stabilizing adhesions (Fig. 24b).

In conclusion, recruitment of vinculin to mature IAS will likely happen through a coordinated action of many of these pathways and partners. The most important of them is still force, exerted through myosin II contractility, especially during IAS maturation.

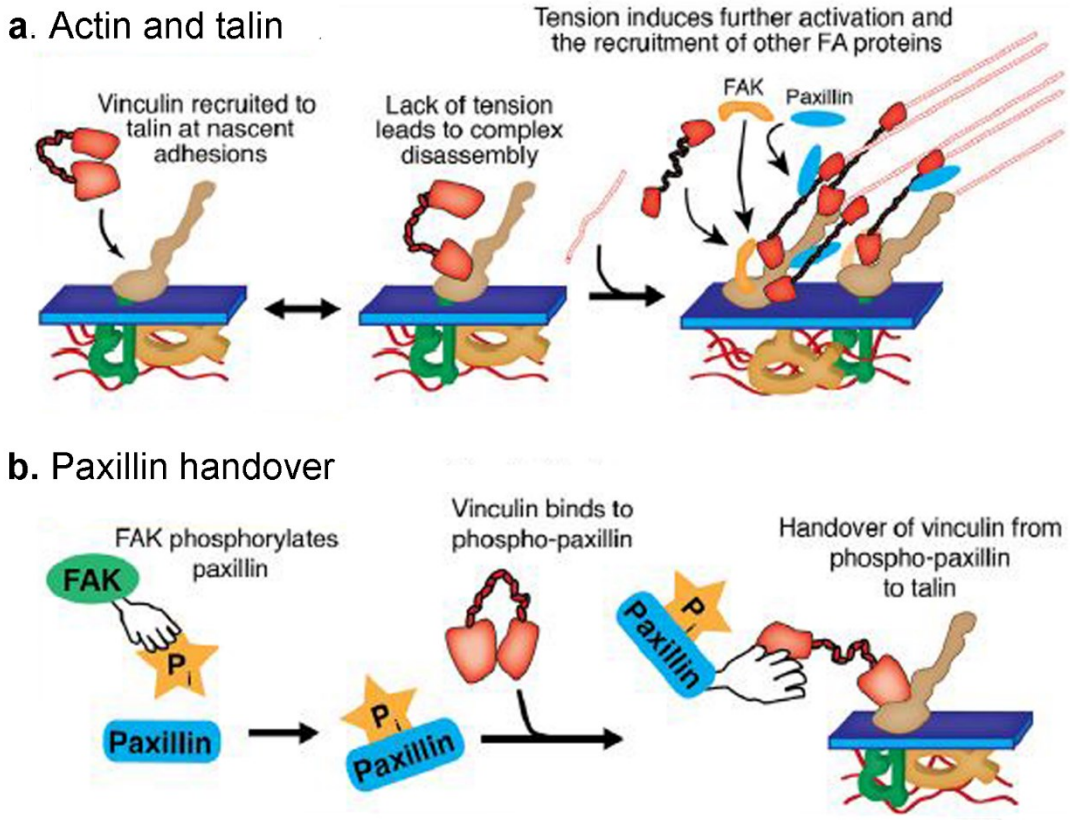

Figure 24: Two possible modes of vinculin recruitment

a, Combination of actin and talin binding to promote a transition from inactive to active vinculin (red). If actomyosin-mediated tension is absent, vinculin is not fully active and dissociates **b,** FAK-mediated paxillin phosphorylation (likely induced by myosin II) targets vinculin to the IAS. As IAS mature, vinculin binds to talin. **a-b,** Figure adapted from Atherton et al. 2016.

4.2. Regulation of vinculin by force

The correlation between IAS maturation and vinculin activation highlights how vinculin is tightly regulated by force. For instance, when myosin II is inhibited by blebbistatin, vinculin is released from FAs, suggesting that myosin II contractility is essential to maintain vinculin in IASs (Pasapera et al., 2010). Release of intracellular tension of or ROCK inhibition with Y-27632 also leads to an almost complete loss of vinculin from adhesions within 30 min, which is not recovered. Therefore, intracellular tension appears to be required to maintain vinculin and recruit vinculin to IASs. However, several studies have also pointed out that vinculin can remain associated to IASs even in the absence of force (Atherton et al., 2015; Carisey et al., 2013). This apparently contradictory behavior can be interpreted at the light of talin binding and vinculin activation. Indeed, these observations were specific for vinculin mutants that are either constitutively active (vinT12) or truncated to expose talin-binding sites (vin258) (Carisey et al.,

2013). In mitochondria, vinculin constructs with exposed talin binding sites are able to activate and bind talin with high affinity in the absence of force (Atherton et al., 2020). Importantly, vinculin localization was artificially targeted to mitochondria; thus, some important interactions happening in IASs are not taking place in this context. In IASs, this behavior is maintained: active vinculin can bind talin and localize with talin in IASs independently of actomyosin tension. This is in agreement with the previous reported force-independent stability of FAs in the presence of constitutively active vinculin mutants (Carisey et al., 2013). However, in cells expressing constitutively active vinculin, decrease of myosin II contractility with Y-27632 will cause bending and buckling of FAs, although without their disassembly (Atherton et al., 2020). When combining full length and vinculin mutants vinT12 or vin258, release of actomyosin tension causes the release of full length vinculin but not the mutants. Moreover, actomyosin-dependent activation of vinculin by talin induces a positive feedback that reinforces the actin-talin-vinculin linkage (Ciobanasu et al., 2014). Therefore, even if actomyosin-mediated tension is not required for vinculin-talin interactions, it is essential to maintain vinculin in an activated IAS-stabilizing state and ensure full maturation of tensile IASs.

4.3. Force bearing and force transmission by vinculin in adhesion reinforcement and stability

Vinculin is not only recruited by force; it also transmits it. As a matter of fact, vinculin has the ability to directly bear force, which in turn is crucial for stabilization of adhesions and force transmission between the actomyosin cytoskeleton and ECM. Grashoff and colleagues, using FRET-based molecular tension sensors, demonstrated that vinculin is required to stabilize FAs under tension (Grashoff et al., 2010). Consequently, failure of vinculin to bear force is linked to disassembly of FAs in migrating cells (Fig. 25a,c). In line with this, Thievessen and colleagues previously showed that vinculin slows down F-actin retrograde flow in both the lamellipodium and the lamellum, while vinculin KO causes a loss of traction forces on the ECM (Thievessen et al., 2013). The latter has been confirmed by a more recent study (Rosowski et al., 2018). All this suggests that vinculin converts actomyosin-generated forces into traction forces on the ECM (Fig. 25d). This highlights the role of the protein as a ‘force bearer’, which is also important to transmit forces in the other sense, i.e. from the ECM to the cell. For instance, vinculin KO cells do not undergo reorientation after uniaxial stretching, showing that vinculin is important in the transmission of stretching forces (Carisey et al., 2013).

Force transmission at the molecular clutch involves a series of dynamic catch and slip bonds between actin flow and multiple FA proteins. Vinculin could reinforce adhesions in response to force precisely through interactions with actin. This hypothesis is supported by a recent *in vitro* study with optical traps, revealing that vinculin forms a directional catch bond with

actin (Fig. 7a,b) (Huang et al., 2017b). When the force experienced by vinculin was directed towards the pointed (-) end, catch bond lifetime was ~10 times longer compared to the barbed (+) end of the actin filament. Interestingly, actin filaments near the leading edge are almost all oriented with their barbed (+) ends facing the membrane. Computational modelling revealed that randomly oriented filaments subjected to the directional catch bond eventually acquire spatial asymmetry with the barbed (+) ends facing the membrane. Therefore, this asymmetric catch bond behavior reveals that vinculin not only increases adhesion resistance to mechanical load, but can also be crucial to organize actin cytoskeleton polarity. This can contribute for 1) the role of vinculin in polarized cell migration (Fig. 25b) (Carisey et al., 2013) or 2) can impact higher levels of organization, influencing tissue patterning or embryonic development (Xu et al., 1998). In addition, although the vinculin tail alone is enough to ensure the catch bond, the directionality is sensitive to the angle of the applied load. Hence the head positioning can change the force experienced by the tail, which is especially relevant given the different orientations found for vinculin in IASs. For instance, in the FAs of U2OS cells, vinculin head is located below the tail (Case et al., 2015), but in the cornerstone FAs of hIPSCs, the orientation is the opposite (Stubb et al., 2019). Thus, it is likely that the directionality of the actin-vinculin catch bond behavior might change *in vivo* across different cell types and IAS morphologies, with consequences for actin cytoskeleton polarity. However, the opposite can also be true, if actin polarity influences the catch bond with vinculin, then changes of polarity could modulate vinculin orientation. The same can happen due actomyosin activity, which can control talin orientation in different *Drosophila* tissues (Klapholz et al., 2015). Interestingly, this directionality of force transduction and reinforcement has also been observed for the interactions between the vinculin head and talin VBSs (Kluger et al., 2020). Vinculin head-VBS complexes are stabilized when force is applied through a shear-like geometry, while zipper-like pulling will promote dissociation of the interaction. Overall, vinculin appears to be highly sensitive to the orientation of forces and actin filament polarity, which confers it a central role in IAS force sensing/transmission and cell migration.

Besides the force-dependent reinforcement or destabilization of vinculin-mediated interactions, vinculin can also contribute to stabilize adhesions through other mechanisms. For instance, active vinculin stabilizes integrin in high-affinity ligand-bound conformations via interactions with talin, which in turn promotes cell adhesion (Humphries et al., 2007). Moreover, active vinculin is an important regulator of recruitment and release of multiple IAS components, such as paxillin, zyxin or α-actinin (Carisey et al., 2013). This has an important effect in polarized cell migration. Thus, it is likely that local mechanical stimuli (stretch, changes in rigidity) will further modulate this ability of vinculin in recruiting and releasing IAS proteins, although this is yet unclear.

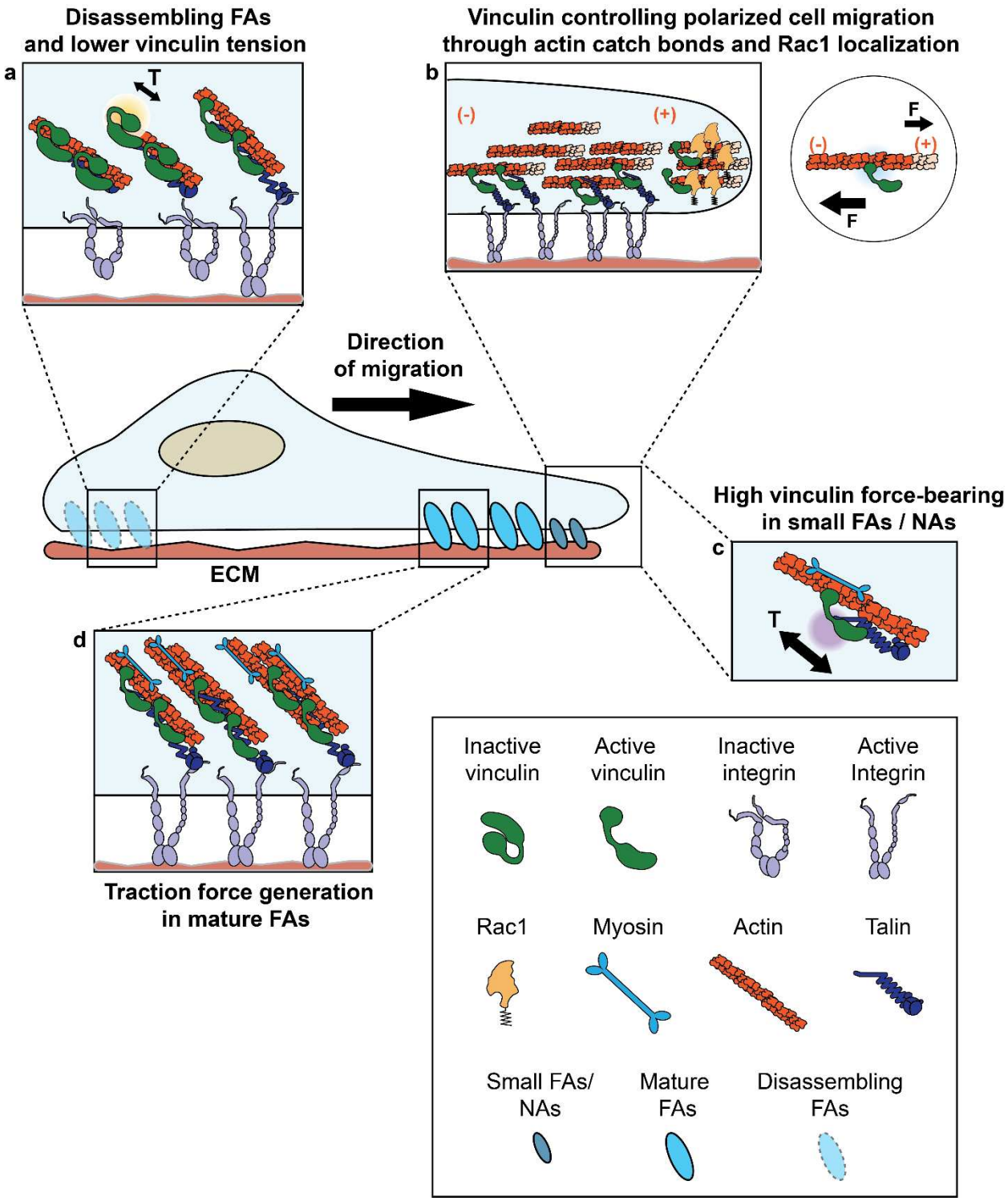
Disassembling FAs
and lower vinculin tension
a
T
Vinculin controlling polarized cell migration
through actin catch bonds and Rac1 localization
b
(-)
(+)
F
(-)
(+)
F
Direction
of migration
ECM
High vinculin force-bearing
in small FAs / NAs
c
T
d
Traction force generation
in mature FAs
Inactive
vinculin
Active
vinculin
Inactive
integrin
Active
Integrin
Rac1
Myosin
Actin
Talin
Small FAs/
NAs
Mature
FAs
Disassembling
FAs

Figure 25: Vinculin force bearing and force-dependent interactions in IAS regulation and polarized cell migration

a, Disassembling FAs in retracting edges are characterized by lower vinculin force-bearing. **b,c** In protruding edges, vinculin promotes polarized cell migration and displays high force-bearing in small FAs/NAs. **b,** Two possible mechanisms for vinculin-dependent polarized cell migration are depicted here. First, vinculin directional-catch bond with actin towards the (-) pointed end (right inset) could orient actin filaments with the barbed end towards the leading edge, promoting polarized cell migration. This has been observed *in vitro* and still needs to be validated in living cells. Moreover, vinculin is required for a polarized localization of Rac1 in order to promote directional cell migration. **c,** Vinculin in small FAs/NAs at protruding edges displays high tension and thus high force-bearing. **d,** Vinculin is essential for reinforcing mature FAs and for traction force generation.

5. Other components of mechanotransduction

Despite the vast importance of the talin-vinculin axis in mechanotransduction, numerous other players will also have a key role in many of these events. LIM-domain containing proteins, such as zyxin, paxillin and Hic-5, have been shown to mediate force response and regulate downstream mechanosensitive pathways in conjunction with the cytoskeleton. Here, we focus mostly on zyxin, which was one of the main targets of the PhD experimental work. Nonetheless, paxillin is also an extremely relevant protein for mechanotransduction. Paxillin is phosphorylated upon integrin engagement with the ECM, activating various signaling cascades involved in cell migration (López-Colomé et al., 2017). Moreover, paxillin accumulates in IAS in response to sustained stretching (Chen et al., 2013; Sawada and Sheetz, 2002b), and local application of force (Von Wichert et al., 2003a). Finally, paxillin interacts with vinculin, which might have an important role in vinculin recruitment and/or positioning at IASs. Indeed, paxillin is phosphorylated in response to myosin II contractility (Pasapera et al., 2010), which in turn can mediate vinculin axial redistribution at IAS (Case et al., 2015). In conclusion, paxillin constitutes a mechanosensitive signaling module in IAS, one which will activate various mechanotransduction pathways in the cell.

5.1. Zyxin – A force-dependent shuttle

The LIM protein zyxin is also localized to IASs, linking actin cytoskeleton to the membrane and regulating actin dynamics. However, zyxin is not only restricted to IASs; it also localizes to stress fibers, actin filaments and can also enter the nucleus. Shuttling of zyxin between different cellular compartments and structures is dependent on mechanical cues, which in turn will activate specific zyxin-mediated pathways. Structure of zyxin is characterized by two main motifs: a N-terminal proline-rich domain and the C-terminal LIM domains (LIN-11, Isl-1 and MEC-3) (Fig.

26) (Smith et al., 2010; Wang et al., 2019b). The N-terminal proline-rich domain harbors binding sites for multiple partners such as α-actinin and the Ena/VASP, which are crucial for actin polymerization and crosslinking (Smith et al., 2013). On the other hand, the C-terminal LIM domains are important for localizing zyxin to FAs and SFs (Hoffman et al., 2012), and are essential for zyxin force-sensing functions (Smith et al., 2013). These LIM domains consist of double-zinc finger motifs which mediate interactions of zyxin with transcription factors (Martynova et al., 2008), p130Cas (Hoffman et al., 2012), cysteine-rich protein (CRP) (Sadler et al., 1992) and many other proteins. LIM domains are present in a variety of proteins including transcription factors, kinases and IAS proteins such as paxillin, which are involved in several biological processes such as cytoskeleton organization or organ development. Outside the N and C-terminal zyxin domains, the 230-280 region mediates interaction between zyxin and nectin, which is required for localization to cell-cell adhesions (Call et al., 2011).

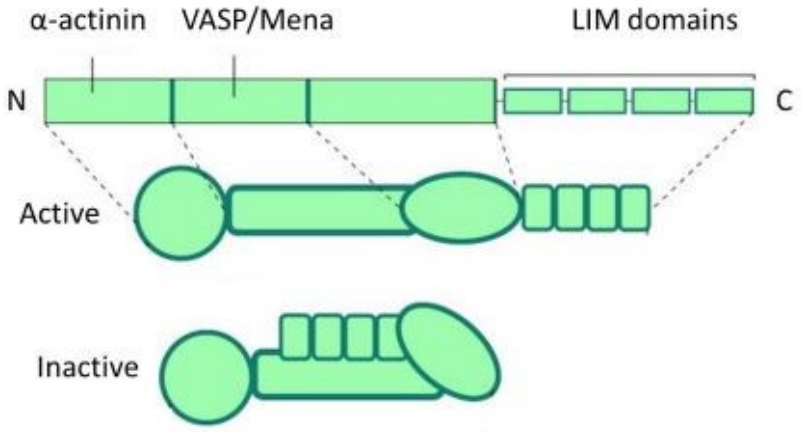

Figure 26: Molecular structure of zyxin and its domains

The N-terminus of zyxin has four proline-rich ActA repeats (amino acids 50-120) for the interaction with actin regulators Ena/VASP and Mena, as well as α-actinin binding sites (amino acids 1-50) (Smith Trends Cell Biol 2014, Wang ERM 2018. On the other hand, C-terminal LIM domains (after amino acids 392) contain cysteine/histidine zinc-coordinating LIN-11, Isl-1 and MEC-3, which are essential for its location to IASs and SFs, force-induced targeting, and protein interactions. The central region comprises two leucine-rich nuclear export sequences and relevant serine phosphorylation sites, as well as nectin binding sites in (amino acids 230-280), mediating zyxin localization at cell-cell adhesions. Figure adapted from MBI info (Singapore) (https://www.mechanobio.info/what-is-mechanosignaling/what-is-the-extracellular-matrix-and-the-basal-lamina/what-are-focal-adhesions/what-is-zyxin/).

Throughout IAS assembly and maturation, zxyin is recruited in later stages compared to vinculin or talin or paxillin. Conversely, in disassembling adhesions, zyxin is among the first proteins to dissociate, including during actomyosin inhibition (Lavelin et al., 2013). In mature FAs, zyxin displays a high turnover rate, which can be up to 4-5 times faster compared to talin and vinculin (Stutchbury et al., 2017). Interestingly, zyxin and paxillin, who both share LIM domains,

display similarly faster turnover rates (Stutchbury et al., 2017). The pool of mobile zyxin within mature FAs is also higher compared to other proteins which display higher stably bound fractions in FAs, such as paxillin and vinculin (Legerstee et al., 2019). Fast cycling of zyxin at IASs might be directly related to its role as in actin polymerization and organization, rather than being an integral part of the integrin-talin-actin linkage (Hirata et al., 2008). Contributing to this idea, zyxin displays a higher dynamically bound fraction within FAs closer to the ventral edge of the cell and pointing towards the edge of the cell (Legerstee et al., 2019). Adhesions with this specific orientation require stronger actin-IAS links in order to generate protrusion/retraction forces. Adjustment of zyxin dynamics could increase the number of available actin binding sites in these adhesions (Legerstee et al., 2019).

The shuttling of zyxin between IASs and stress fibers also reflects the crucial role of zyxin as a mechanosensor and mechanotransducer within the cell. Zyxin does not associate with all adhesions or actin filaments equally; instead, it is recruited to force-bearing adhesion sites and tension zones. For instance, in migrating cells, zyxin accumulates at force-bearing sites at the leading edge, but not at the trailing edge, a process which is dependent on internally applied force (Uemura et al., 2011). Perhaps the most striking example is the mobilization of zyxin to stress fibers in response to externally applied forces, such as uniaxial cyclic stretch (Fig. 27) (Hoffman et al., 2012). This is accompanied by dissociation of zyxin from mature FAs, once again revealing that zyxin is not permanently associated to IASs, especially under mechanical stress. However, zyxin can also exhibit the opposite behavior; Zyxin can accumulate in mature FAs in response to uniaxial sustained cell stretching (Hirata et al., 2008). This shows how the type of mechanical stimulus can influence the response of zyxin; variations in the response could also be a consequence of the fast dynamics of the protein. Interestingly, this is not exclusive of 'global' external stress; local perturbations can induce zyxin localization to SFs (Smith et al., 2010) or to mature FAs (Hirata et al., 2008). The LIM domains mediate both the localization to FA but also the targeting to SFs after cyclic stretch, once again showing how zyxin structure is adapted to a mechanosensitive shuttling. Zyxin recruitment to SFs is also crucial for the reinforcement of SFs observed upon cyclic stretch. This, in turn, is also mediated by the downstream recruitment of other partners interacting with zyxin, more precisely α-actinin and VASP, which are crucial for cytoskeleton stability under stress (Hoffman et al., 2012). VASP also shares with zyxin a fast turnover at FAs and similar dynamically/stably bound fractions, suggesting that this protein could also respond to force and accumulate at force-bearing sites. The force response of VASP, and by extent α-actinin, still needs to be further characterized. This highlights how protein dynamics are intrinsically linked to their mechanosensitive properties.

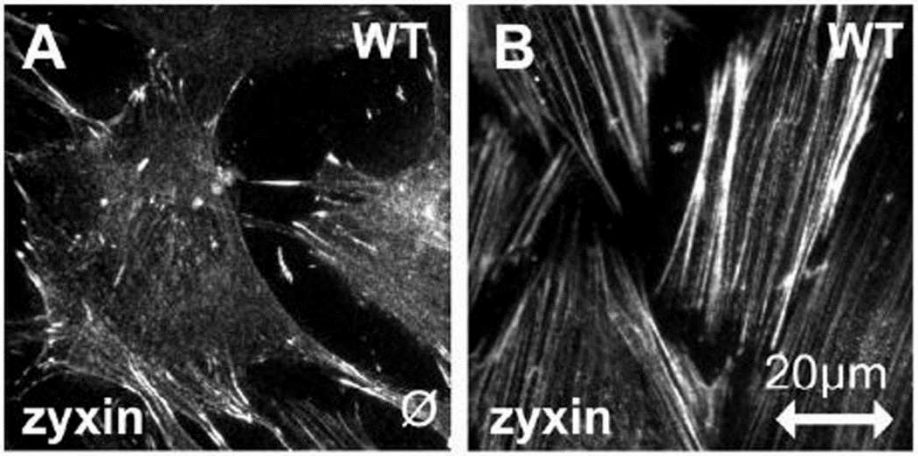

Figure 27: Zyxin is mobilized from mature FAs to SFs after cyclic stretching

Wild-type (WT) fibroblasts on unstretched membranes (ø) (A) or after uniaxial cyclic stretch (2 h, 15%, 0.5 Hz) (B), fixed and immunostained for zyxin. Before stretch, zyxin is located mostly at mature FAs; after uniaxial cyclic stretch, zyxin is enriched at SFs and less prominent at FAs. Figure adapted from Hoffmann et al. 2012.

Recruitment and mobilization of zyxin to the cytoskeleton is not limited to a context of external stress. SFs undergo spontaneous thinning and elongation events, which quickly and robustly trigger zyxin recruitment (Fig. 28) (Smith et al., 2010). This allows SF repair and prevents these same events from evolving to catastrophic breaks. Interestingly, LIM domains are required for zyxin recruitment to SF strain sites (Smith et al., 2013). Similar to what is observed in uniaxial cyclic stretch, zyxin regulates subsequent recruitment of α-actinin and VASP to SF strain sites (Fig. 28). Both proteins are required to stabilize the strain sites, with different functions. On one hand, α-actinin has a primary role in restoring actin and preventing ruptures, probably through crosslinking of actin filaments (Fig. 28). VASP might be more of an enhancer of zyxin action, which again fits into the rapid cycling dynamics shared by both proteins (Fig. 28). Additionally, VASP could promote actin polymerization at barbed filament ends (Hoffman et al., 2012). Paxillin is also recruited to SF strain sites and stabilizes them by altering actin dynamics (Smith et al., 2013). However, by opposition to VASP and α-actinin, paxillin recruitment to SF strain sites is independent of zyxin. Still, LIM domains in paxillin are also required for SF strain targeting (Smith et al., 2013), once again revealing their importance for the functions of LIM-containing proteins.

SF strain events are triggered by changes in actomyosin contractility, which suggests that zyxin might be important to regulate cytoskeleton tension. Indeed, local contractility in SFs and consequent increase of strain lead to zyxin recruitment, both at the region of contraction but also at the interface between SFs and mature FAs (Oakes et al., 2017). Coordinated zyxin recruitment is crucial to maintain the elasticity of SFs over long time scales. In conclusion, zyxin

is an important contributor to cytoskeleton homeostasis by quickly responding to changes in cell contractility or extrinsic forces. Depending on the mechanical forces in play, zyxin can also be recruited to IASs. Further studies on the force influence in zyxin nanoscale dynamics are required to dissect zyxin mechanosensing.

Some important questions still remain concerning force-dependent zyxin mobilization to SFs. The first concerns whether zyxin undergoes conformational or chemical changes in response to external or internal forces, in order to facilitate the protein recruitment. Uniaxial cyclic stretch induces zyxin phosphorylation, which is dependent on MAPK signaling (Hoffman et al., 2012). This could relieve intramolecular inhibitory interactions and enhance both SF targeting and VASP/α-actinin interactions. Further studies are required to understand how phosphorylation modulates these interactions. Moreover, it is unknown whether the same mechanism also happens during monitoring and repair of SF strain events. Secondly, it is still unclear how zyxin is recruited to SF strain sites and how are these acting as binding sites. One possible explanation is based on the high density of free actin barbed ends that has been observed in strain sites (Smith et al., 2010). These could act like binding sites and promote the recruitment of zyxin through its phosphorylation and formation of complexes with actin capping proteins. However, a recent *in vitro* study revealed that purified LIM domains from zyxin have a very low affinity for F-actin barbed ends (Winkelman et al., 2020). In this regard, LIM domains are perhaps a more suitable candidate to mediate force-dependent recruitment of zyxin to FAs or SFs. The same *in vitro* study revealed that purified LIM domains from mammalian zyxin bind to mechanically stressed F-actin networks but do not associate with relaxed actin filaments (Winkelman et al., 2020). Thus, tandem LIM domains in zyxin could recognized F-actin conformations that are common in the presence of mechanical stress and SF strains. Interestingly, the same effect is also observed for LIM domains from a paxillin-like protein, implying that paxillin could also recognize altered conformations of F-actin when is recruited to SF strain sites (Smith et al., 2013). Alternatively, strain can change the conformation of actin or actin-binding proteins, exposing zyxin binding sites. This has been described for Filamin A, which undergoes force-dependent unfolding and exposure of binding sites for RhoGTPases (Ehrlicher et al., 2011), a similar process to talin unfolding and vinculin recruitment.

The dynamics and force-dependent shuttling of zyxin really display how local mechanosensitive events can contribute to the overall activity of the cell. This is highlighted for instance by how zyxin is specifically recruited to force-bearing sites in order to control cell migration, a more general process. Another example of this ‘remote’ action consists in the regulation of transcription by zyxin(Martynova et al., 2008).

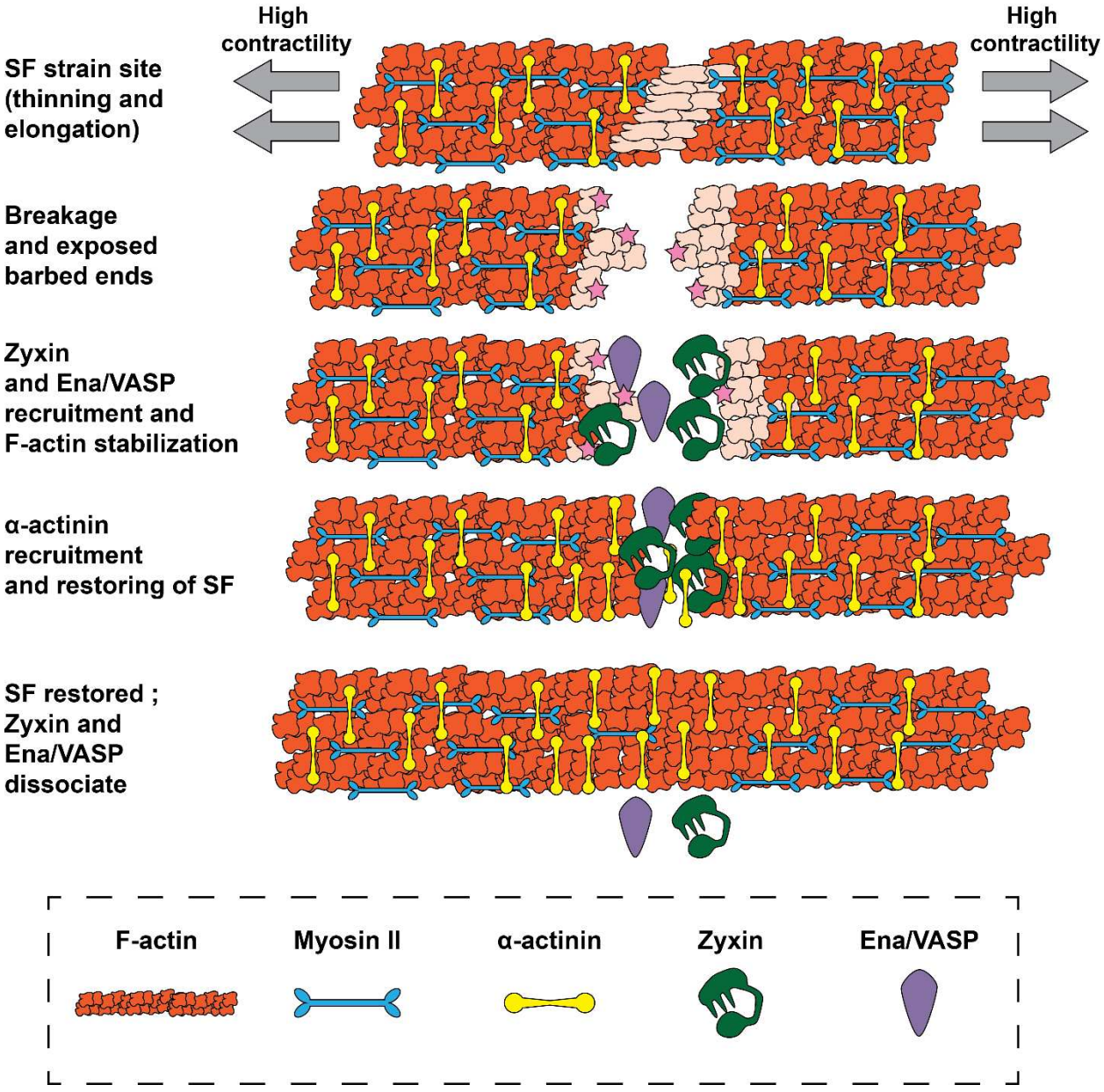

Figure 28: Zyxin, VASP and α-actinin-mediated repair of SF strains

Increased contractility and force or external stresses can lead to SF strain events, characterized by elongation, thinning and exposed barbed (+) ends of actin filaments. From here, SF strain sites can either be repaired (as shown in the schematic) or evolve to catastrophic breaks. Reparation initially requires recruitment of zyxin via its LIM domains, followed by association of Ena/VASP proteins, which can contribute to stabilize actin filaments. This is followed by the recruitment of α-actinin, which has a primary role in restoring F-actin at the SF damage site and preventing catastrophic breaks. As SFs are restored, the repair complex disassembles.

6. IASs as a mechanosensitive unit controlling cellular processes

Force sensing and transmission at IASs must not be seen as isolated and discrete events within a cell, but rather as local forms of mechanosensing and mechanosignaling which will influence many processes at a cellular scale. These include rigidity sensing, cell migration, spreading, growth and even transcription (Dupont et al., 2011; Elosegui-Artola et al., 2016; Paszek et al., 2014; Plotnikov et al., 2012; Wolfenson et al., 2016). In return, several of these processes will depend on the nanoscale dynamics of IAS and force transmission at a single molecule level. As previously mentioned, force loading at the individual molecular clutch is a key mechanism for IAS growth and rigidity sensing (Elosegui-Artola et al., 2016). Indeed, molecular force loading can integrate rigidity, substrate topography and contractility to drastically modulate cellular-scale processes such as ECM sensing, IAS growth and cell spreading (Oria et al., 2017). Besides force loading, the IAS 'tugging' behavior also contributes to similar larger scale processes. Indeed, when tugging dynamics are disrupted by interfering with the paxillin phosphorylation/vinculin pathway, cell migration across a stiffness gradient becomes less persistent and more randomized. Thus, IAS tugging dynamics can promote durotaxis (Plotnikov et al., 2012). This shows how individual IAS force fluctuations can be used to sense local stiffness to direct cell pathfinding during development or pathological processes such as metastasis. Regarding the latter, there is a strong correlation between stiffness of the tumor microenvironment and activation of metastatic pathways (DuChez et al., 2019). Although it is not yet clear whether tumor cells employ durotaxis, IAS tugging dynamics could eventually play a role in cell migration during metastasis. Besides stiffness, cancer cells also exhibit an altered glycocalyx, which conveys cues from the microenvironment to signaling pathways starting at the plasma membrane (Paszek et al., 2014). Expression of bulky glycocalyx proteins (glycoproteins) such as mucin was shown to facilitate integrin clustering and focal adhesion assembly through a kinetic trap mechanism (Paszek et al., 2014). Physical forces between bulk glycoproteins and integrins lead to mechanical loading of integrins, independent of actomyosin contractility. Glycoprotein-dependent tension on matrix-bound integrins also activated integrin-dependent pathways involved in cell growth and survival. This interplay between glycoproteins and IASs reveals how IASs can integrate membrane topography to alter their mechanical state, with consequences on cell behavior.

IAS dynamics can also control cell migration in the absence of any gradients. A recent study has shown how the collective behavior of mature FAs can be integrated to control the directionality of cells without any gradient, a process known as ratchetaxis (Lo Vecchio et al., 2020). Indeed, the gap between adhesive motifs can increase the directionality of migrating fibroblasts over timescales of days. Moreover, an asymmetric distribution of FAs is correlated to

cell direction, with each FA being translated into a force with known components. Thus, the geometry of adhesive regions also governs cell motion, with more uniform geometries decreasing cell directionality (Lo Vecchio et al., 2020). Local dynamics and distribution of IASs can be integrated over long-term cellular motion, acting as continuous sensors of the microenvironment in order to regulate cellular processes.

Integration of IAS signaling at a higher scale can also affect protein expression and cell differentiation. IASs are indirectly connected to the nucleus through the interactions between actin cytoskeleton and nuclear lamins. Moreover, multiple IAS proteins (talin, FAK, zyxin) interact with transcription factors (Dupont et al., 2011; Zhao et al., 2003). This leads to IAS-dependent regulation of gene transcription in response to force sensing or ECM mechanical properties. A well-known example is the effect of substrate stiffness in plasticity of cell differentiation (Dupont et al., 2011; Segel et al., 2019) Among other factors, this is dependent on signalling to the transcriptional coactivators YAP (Yes-associated protein) and TAZ (transcriptional coactivator with PDZ-binding motif). YAP/TAZ shuttle between the cytoplasm and the nucleus in a stiffness-dependent manner, with stiffer substrates promoting YAP/TAZ nuclear translocation and consequent increase of transcription (Dupont et al., 2011). YAP/TAZ nuclear localization is correlated with IAS formation (Elosegui-Artola et al., 2016; Oria et al., 2017) and is controlled by talin mechanosensing, since talin-depleted fibroblasts display impaired YAP/TAZ nuclear shuttling in response to stiffness. Triggering of YAP/TAZ nuclear translocation is apparently regulated by talin unfolding, showing how molecular mechanosensing can control processes at cellular level and longer timescales. Besides YAP/TAZ, IAS-associated proteins can control the activity of other transcription factors such as Kruppel-like factor 8 (KLF8), which is a target of FAK (Zhao et al., 2003). Other transcription factors such as Hypoxia-induced factors (HIF) exhibit force-dependent translocation (Kassianidou et al., 2019). However, the connection between IAS mechanosensing and activation of other pathways besides YAP/TAZ shuttling is still unclear. Furthermore, despite evidence of IAS-nucleus crosstalk, it is less clear which proteins mediate the transmission of the signals between IAS force sensing and the nucleus. Other mechanosensitive structures can contribute to modulate the process, such as cell-cell adhesions or mechanosensitive ion channels. IASs can also integrate the signals from other structures, which confers a whole new level of complexity to the conversion of local IAS mechanosensing and dynamics to higher-scale cellular processes.

4. Mechanotransduction at the cytoskeleton

The cytoskeleton possesses the particular feature of both sensing and applying force. While actin filaments and the actomyosin machinery are often seen as the source of tension behind IAS mechanosensing, they also respond to force, changing their conformation and activity. Actin-binding proteins could be an essential element in this response; interestingly, some mechanisms could be akin to the ones seen in IAS, revealing how molecular mechanosensing shares features across different subcellular structures. Intermediate filaments, in turn, are both important in force buffering and transmission, but they could also be involved in mechanosignaling pathways given the various partners they interact with. Finally, microtubules are by far the most rigid biopolymers on the cytoskeleton; however, they often bend and twist in cells, which indicates that they are sensitive to mechanical forces. Overall, the properties of different cytoskeletal proteins could be intrinsically linked to their role in mechanotransduction. In this chapter, I will explore the specialized mechanisms employed by different cytoskeleton proteins to sense and respond to mechanical stimuli.

1. Mechanotransduction by actin filaments

Actin filaments are involved in mechanotransduction through various mechanisms, such as conformational changes in both actin filaments and actin-binding proteins (Ehrlicher et al., 2011; Hayakawa et al., 2014), or alterations of polymerization kinetics (Jégou et al., 2013). Actin filaments are not structurally static, rather displaying a variety of conformations, which can influence the interactions with actin-binding proteins. Previous studies have shown that mechanical tension can lead to conformational changes in actin filaments. Cofillin, an actin-severing protein, increases the twist and decreases the rigidity of the filaments, which in turn might facilitate the severing mechanism (Harris et al., 2018). Tensile forces up to 30 pN reduce cofillin severing activity, which implies a change of conformation in the actin filaments to a more rigid/less twisted state (Hayakawa et al., 2014).

In parallel, force applied to filaments can enhance the binding of myosin II motor domain, generating a feedback loop that increases tension and locks the filaments in a stable state (Uyeda et al., 2011). Conformational changes can also affect actin branching, since Arp2/3 preferentially

forms branches on the convex face of a curved actin filament *in vitro* (Risca et al., 2012). Authors have proposed a model where transient, local and large fluctuations of curvature lead to a conformational change in the filament, favoring Arp2/3 branch nucleation (Risca et al., 2012). Overall, the effect of mechanical load on actin filaments still requires further clarification and would strongly benefit from new single molecule imaging and force sensing techniques.

One aspect extensively approached throughout this introduction is that protein mechanosensing relies heavily on protein deformation and reorganization. Numerous actin-binding proteins organize and regulate the structure, dynamics and organization of the actin cytoskeleton (Pollard and Goldman, 2018). These, in turn, can undergo conformational changes in response to force, thus contributing to the mechanosensitive properties of the actin cytoskeleton. A possible mechanism involves unfolding of actin-binding proteins, exposing binding sites for other regulatory proteins, similar to the interactions of vinculin with talin (Ciobanasu et al., 2014; Del Rio et al., 2009; Yao et al., 2016). FilaminA, a major actin cross-linker, undergoes conformational changes in the rod2 domain when subjected to mechanical force (Fig. 29). This exposes a cryptic binding site for β-integrin recruitment while also separating two repeats, leading to the dissociation of FilGAP, a GTPase involved in Rac signaling (Ehrlicher et al., 2011). Force-dependent regulation of FilaminA constitutes a clear molecular mechanotransduction mechanism within the actin cytoskeleton, one which can modulate its binding activity upon mechanical strain.

More recently, FilaminA has also been linked to force redistribution after cyclic stretching (Kumar et al., 2019). Previous studies have showed that various adhesive cells reorient their FAs and SFs in a direction nearly perpendicular to applied force when they are subjected to uniaxial cyclic stretching. This mechanism is thought to minimize the stress or strain applied to the cells and has been observed in a vast variety of cell types such as osteoblasts, endothelial cells or fibroblasts (Hsu et al., 2010; Nagayama et al., 2012). This effect has been largely attributed to IAS-mediated mechanotransduction, but the actin cytoskeleton could also play a role. In their work, Kumar and colleagues demonstrated that FilaminA was required for the isotropic increase in talin tension after an anisotropic cyclic stretching (Kumar et al., 2019). These results fit with previous ultrastructural observations of a cortical actin network in fibroblasts composed by a meshwork of filaments, which connects and integrates SFs with different orientations (Eghiaian et al., 2015; Svitkina, 2018). Known as the isotropic actin network, this cortical network can also be contractile, as recently demonstrated (Vignaud et al., 2020). FilaminA preferentially localizes to the contact points between the isotropic actin network and SFs, suggesting it plays a role in the connectivity of this network. Moreover, FilaminA appears to be under tension in cells (Nakamura et al., 2014), suggesting load-bearing properties. Hence, it is likely that cell stretching increases tension in actin SFs and the isotropic cortical network, with FilaminA serving as a tension buffer which will redistribute forces on FAs (Kumar et al., 2019). However, it still remains

to be assessed whether this behavior is also dependent on rod2 domain conformational changes. Interestingly, β-integrin binding appears to be unnecessary for force redistribution, suggesting that other domains besides the rod2 domain might be involved. Nonetheless, the role of FilaminA highlights a possible collaboration between actin network mechanosensing and IASs in response to external stresses, one that we sought to clarify throughout this thesis.

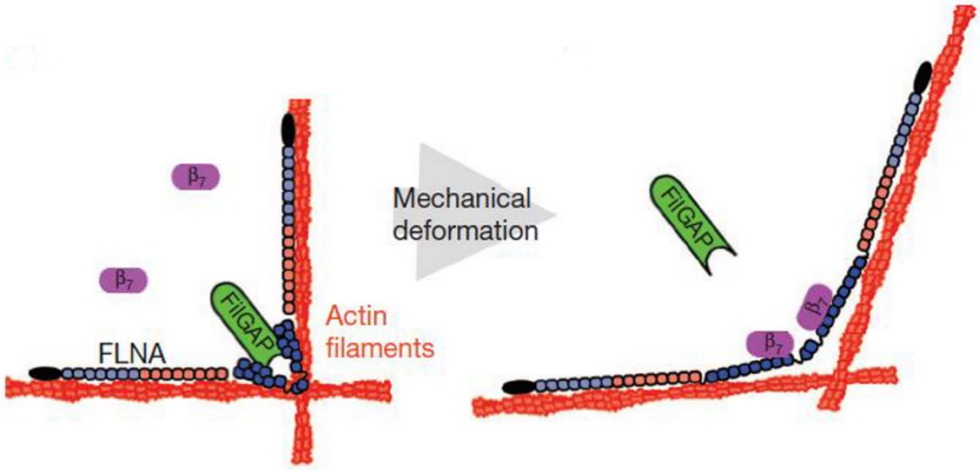

Figure 29: Mechanosensing in Filamin A

Filamin A associates to actin filaments and contains 3 distinct domains: 1) the actin binding domain (black), 2) the rod-1 region (light blue and orange), composed of repeates 1-7 (light blue) and 8-15 (orange), and 3) the compact rod-2 region, consisting of repeats 16-23 (dark blue). When FilGAP (green) binds repeats 23 the cytoplasmic domain of β7-integrin (purple) is unbound. When FilaminA is deformed by mechanical force, the cryptic integrin binding site on repeat 21 is exposed, leading to β7-integrin binding and dissociation of FilGAP due to separation of repeats 23. This shows yet another example of force-dependent conformational changes leading to structural mechanosensing. Figure adapted from Ehrlicher et al. 2011.

Other actin-binding proteins display preferential accumulation in mechanically stressed regions in response to mechanical load, such as myosin-II or α-actinin (Schiffauer CB 2016). This mechano-accumulation can occur in two modes: a fast, diffusion-based accumulation and a slower, myosin II-dependent cortical flow phase. For α-actinin, mechano-accumulation appears to be dependent on a catch-bond formation, once again revealing similar mechanisms to the ones found in adhesive structures (Schiffhauer et al., 2016). Thus, mechano-accumulation of actin-binding proteins can serve as a rapid adaptive response to mechanical stress, but also as a long-term network mechanism controlling cell shape. In this regard, myosin IIB exhibits cell-type and cell-cycle-specific mechanosensitivity (Schiffhauer et al., 2016). Hence, accumulation of actin-binding proteins can be spatiotemporally coordinated, which in turn can be critical for tissue development or pathology. Given the sheer amount of actin binding proteins and

regulators, it is of extreme interest to unveil new force-depending unfolding or catch/slip-bond behaviors.

Actin filaments generate and transmit pushing forces through the conversion of polymerization energy to mechanical work. These forces are required for many cellular processes such as membrane protrusion, endocytosis or motility. However, actin filaments and networks can also respond to mechanical forces, which alter their density and organization through modulation of actin polymerization. Although the molecular impact of force needs further clarification, two possible mechanisms have been suggested. First, mechanical force can affect the polymerizing activity of some formin homology proteins (Courtemanche et al., 2013; Jégou et al., 2013), which are responsible for actin filament elongation. However, studies performed with microfluidic flow *in vitro* have yielded conflicting results. On one hand, when pN-scale pulling forces are applied to filaments elongated by surface-anchored formin mDia1, the elongation rate of filaments increases up to two-fold (Jégou et al., 2013). This reveals that formin mDia1 is mechanosensitive and that polymerization increases with force; moreover, mDia1 also places filaments under mechanical tension. On the other hand, small forces on actin filaments elongated by yeast formin Bni1p markedly reduce formin-mediated polymerization in the absence of profilin, but result in faster polymerization in the presence of profilin (Courtemanche et al., 2013). Presence of profilin might revert conformational changes that decrease polymerization (Courtemanche et al., 2013). Further studies are required to dissect the role of formins, but the presence of other ABPs might have a strong effect.

Second, mechanical load against pushing/polymerizing actin filaments can affect the assembly, architecture and dynamic properties of actin networks. A recent study from Bieling et al has provided a key contribution to this topic (Bieling et al., 2016). This work revealed that mechanical loading of *in vitro* actin networks increases network density and decreases growth velocity. Together, both effects contribute to enhance the power and efficiency of the branched actin network, increasing the fraction of polymerization energy converted into mechanical work. A recent complementary study has highlighted this force-velocity relationship in response to membrane tension and consequent effects in living cells (Mueller et al., 2017). Increased tension also triggers a dense network with various filament angles. Conversely, decreased tension accelerates polymerization and causes a shift to a sparse network. Here, filaments grow perpendicular to the membrane, with steeper-angle filaments eliminated due to loss of membrane contact and action of capping proteins. Thus, adaptive mechanisms involving speed or density of the actin network can fine-tune protrusive forces in response to mechanical loads (Mueller et al., 2017). Moreover, at a macroscopic scale, mechanical loading on growing actin networks has been shown to enhance their stiffness and mechanical resilience (Bieling et al., 2016).

Overall, mechanisms of force adaptation and sensing in actin filaments can act at different space and time scales. Local force/tension variations can regulate filament polymerization through formin/profilin or conformational changes, with immediate effects (Courtemanche et al., 2013; Jégou et al., 2013). Binding of FilaminA to β-integrin (Ehrlicher et al., 2011) or mechanoaccumulation of myosin (Schiffhauer et al., 2016), while representing local effects of forces, can control processes at a broader, cellular scale. For instance, FilaminA, by mediating force buffering and distribution, could mediate the reorientation of entire subcellular structures and cells(Kumar et al., 2019). MyosinII exhibits a slow accumulation in mechanically stressed regions, dependent on cortical flow, hence acting as a mechanism controlling cell shape(Schiffhauer et al., 2016). Mechanical loads against polymerizing filaments can confer a certain 'mechanical memory' to actin networks, hence regulating their adaptation to mechanical loads across time (Bieling et al., 2016; Mueller et al., 2017). In this regard, further studies are necessary to unveil the molecular basis and nanoscale dynamics underlying these adaptive responses. How could FilaminA mechanosensing contribute for the entire reorientation of the cell axis and IASs? Could formin mechanosensing dictate cell protrusion? How can the slow accumulation of myosin dictate cell morphology? Moreover, 'mechanical memory' itself can also change the adaptive responses of actin networks that modulate protrusion forces. It would thus be of extreme interest to assess how the response to mechanical loading will change if the actin network has been mechanically 'pre-conditioned'.

2. Mechanical response of microtubules

The dynamical behavior of microtubules is responsible for various cellular processes, many of which require the microtubule network to sustain mechanical loads. Mechanical stability of microtubules is crucial for intracellular trafficking (Franker and Hoogenraad, 2013), polarized cell migration (Etienne-Manneville, 2013)and chromosome separation during cell division (Brangwynne et al., 2007). Microtubules are perfectly suited to this role, since their flexural rigidity and persistence length are far higher than other cytoskeletal proteins (Gittes et al., 1993; Hawkins et al., 2010). However, in living cells, microtubules are not only subjected to thermal forces; instead, they experience various internal and external forces (Brangwynne et al., 2007), such as the fluid flow in flagella or cilia (Goetz et al., 2014), F-actin flow (Waterman-Storer and Salmon, 1997), myosin-dependent contractility (Yvon et al., 2001) or deformation by other cytoskeletal networks in the cytoplasm (Hu et al., 2019). As a consequence, microtubules move, bend and break, at both long and short length scales (Odde et al., 1999).

Despite all these structural inputs, the mechanical response of microtubules to force is still unclear, as well as whether they play a role in mechanotransduction or not. By combining flow-exerted force on dynamic microtubules seeded on micropatterns, Schaedel and colleagues

revealed that microtubules are able to self-repair in response to mechanical stress *in vitro* (Schaedel et al., 2015). When microtubules were subjected to repeated cycles of flow, they bent more, indicating that they became softer under mechanical stress. Microtubule softening was associated to the presence of structural defects in the microtubule lattice. Similar to cracks and holes in a pillar or in a tube, these appear more often in rapidly polymerizing microtubules (Janson and Dogterom, 2004), which were more susceptible to stress-dependent softening (Schaedel et al., 2015). Interestingly, the increase of the rest period between flow cycles appeared to restore stiffness, suggesting that microtubules can self-repair. After laser-induced photodamage, repair was shown to be highly correlated with the incorporation of tubulin dimers along the lattice. Moreover, local photodamage was also extended to a larger portion of the microtubule. Together, these results suggest that microtubule stress-induced softening arises from pre-existent 'cracks' in the lattice, which upon mechanical forces will tend to propagate and deform adjacent filaments with progressive extension (Fig. 30). Filament rearrangement and 'patchwork' by incorporation of tubulin dimers allows the microtubules to self-repair. Interestingly, the mechanical resistance of microtubules can also be enhanced by tubulin acetylation (Xu et al., 2017), which could cooperate with these repair mechanisms.

Microtubule self-repair in response to mechanical forces could have several roles in living cells, especially in areas where microtubules are subjected to stress. Experiments in live cells found that incorporation of tubulin dimers occurred preferentially in regions of where the microtubule lattice is likely to experience geometrical and mechanical constraints (Aumeier et al., 2016). These include microtubule crossover, bundles and bending sites; strikingly, the frequency of repair events in these regions was similar to the frequency of rescue events, which consist in the arrest of depolymerization followed by regrowth (Aumeier et al., 2016). When performing laser-induced photodamage in live cells or in *in vitro* microtubules, rescue also occurred at the exact same spot as repairs. Thus, microtubule self-repair appears to promote microtubule rescue by arresting polymerization and inducing regrowth (Aumeier et al., 2016). Microtubule rescue is dependent on free tubulin incorporation, which is consistent with the previous work of Schaedel on self-repair (Schaedel et al., 2015). One powerful feature of this repair-rescue axis is that it can be potentiated by damage itself: in situations of repeated damage *in vitro*, depolymerization was prevented for a longer period of time (20 min), compared with a single damage (5 min); as a consequence, microtubules became longer. Similarly, in live cells, repeated photodamage protected microtubules from depolymerization and resulted in their elongation, with microtubules aligning parallel to the cell edge. Therefore, it is likely that microtubule repair will elicit a mechanosensitive feedback loop that 1) protects microtubules and 2) promotes their extension in regions of high mechanical strain and bundling, thereby controlling microtubule growth inside the cell (Aumeier et al., 2016). It would be of extreme interest to assess the response of this mechanosensitive loop to other mechanical forces (stretching), as well as its interplay with IASs.

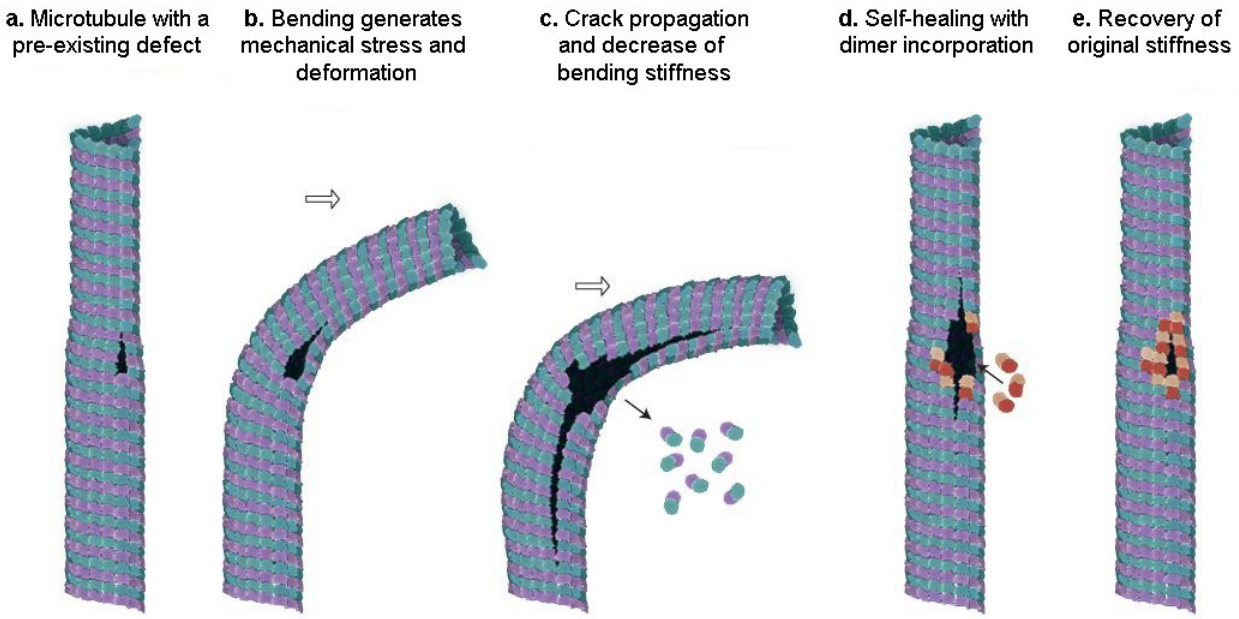

Figure 30: Microtubule mechanical response

Figure adapted from Schaedel et al. 2015.

Although IASs are often associated with the actomyosin machinery, their central role in cell adhesion and mechanosensing will place them in contact with microtubules. Indeed, alterations of microtubule dynamics are linked with changes in IAS morphology; microtubule depolymerization leads to an increase in mature FA size (Bershadsky et al., 1996), while microtubule outgrowth has the opposite effect (Ezratty et al., 2005). In podosomes, microtubule depolymerization has the opposite effect, leading to their disassembly. One possible mediator of this IAS-microtubule connection is the protein KANK, which can establish physical connections between IASs and microtubules (Bouchet et al., 2016; Rafiq et al., 2019; Sun et al., 2016b). Both KANK1 and KANK2 interact with talin at IASs and with the microtubule docking complex, as well as with EBPs and motor proteins (Bouchet eLife 2016, Sun NCB 2016, Rafiq Nat Materials 2019). Microtubules were also shown to regulate both podosome and mature FA morphology through KANK proteins and reorganization of myosinII via Rho/ROCK pathway (Rafiq et al., 2019). Coupling of microtubules to IASs via KANK suppresses the Rho-GTP/ROCK pathway and reduces the formation of myosinII filaments, which work as the effectors in this interaction. Uncoupling this interaction suppresses podosome formation and stimulates formation and growth of stress fiber-associated FAs (Rafiq et al., 2019). Therefore, IAS are remodeled as a result of this mechanism: microtubules protect podosomes via KANK/Rho/ROCK/myosin II pathway and suppress FA growth through the same pathway.

This mechanism reveals how microtubules can directly crosstalk with mechanosensitive adhesive structures such as IASs to regulate their morphology and function. In line with this, repair/rescue events leading to microtubule elongation could remodel IAS through KANK-mediated connections. This could have an impact in different IAS-mediated pathways controlling cell migration, adhesion, spreading or differentiation. In this regard, cell movement can be directed towards the area of microtubule elongation after repetitive damage (Aumeier et al., 2016), which could involve cross-talk with actin filaments but also the IAS.

3. Mechanotransduction of intermediate filaments

Cytoplasmic intermediate filaments transmit and conduct force between and within cells, but they can also modulate signal transduction pathways. Vimentin and keratin intermediate filaments regulate integrin activation (Ivaska et al., 2005) and can drive the formation and maturation of IASs via Rac1/FAK, among other pathways (Havel et al., 2014; Tsuruta and Jones, 2003). Intermediate filaments can also serve as signaling platforms or scaffolds for signaling proteins, involving often the extracellular signal-regulated kinase pathway (Sanghvi-Shah and Weber, 2017; Sivaramakrishnan et al., 2009). Therefore, the response of intermediate filaments to mechanical stimuli can be divided into two main components: one, a mechanosensing role based on force transmission and redistribution; and two, a mechanosignaling role involving different signal transduction pathways.

Cytoplasmic intermediate filaments have been shown to bear tension in stretched cells and maintain cell shape and stiffness during deformations (Latorre et al., 2018). Plus, intermediate filaments display an extreme stretchability (Block et al., 2018). Thus, force-induced extension and conformational changes in intermediate filaments could redistribute forces and dissipate strain energy in cells subjected to deformation. Shear stress has been shown to induce reorganization of both vimentin and keratin filaments, which is thought to involve increased phosphorylation via protein kinase C (PKC) (Sivaramakrishnan et al., 2009). A more recent study has evidenced the important role of vimentin intermediate filaments in ensuring cell integrity during stretches up to 300% (Hu et al., 2019). Maintenance of structural and mechanical integrity by vimentin was possible via two mechanisms: the hyperelastic behavior of vimentin intermediate filaments and the dissipation of mechanical strain energy. The latter occurred mostly through the deformation of surrounding cytoplasm elements such as actin filaments and microtubules (Hu et al., 2019). Such behavior reflects the interconnectivity of the different cytoskeletal elements to collectively respond to mechanical deformations in order to ensure cell integrity. Different elements act together rather than isolated; indeed, vimentin-actin network interactions were previously described to regulate nuclear mechanics (Keeling et al., 2017).

Moreover, intermediate filaments can be pre-modulated by other cytoskeletal networks, with actin influencing keratin rigidity (Nolting and Köster, 2013).

Mechanoprotection by a hyperelastic and strain-dissipating vimentin network will likely allow the cell to withstand large deformations during tissue invasion, wound healing and even metastasis. However, the molecular basis of these behaviors still needs further clarification, since the properties of individual filaments are also unclear. In this regard, a combination of modelling and force clamp experiments revealed that nonequilibrium folding/unfolding of helices in vimentin monomers is linked to tensile memory and to dissipation of energy (Block et al., 2018). Further studies in live cells will be key to understand how these conformational changes can modulate energy dissipation and mechanoprotection and by intermediate filaments.

The conformational changes occurring in intermediate filaments can also affect the different signaling pathways mediated by them, which in turn can have consequences in cytoskeleton organization. Vimentin can regulate RhoA signaling and respective GEF proteins to modulate actin stress fiber assembly and contractility, (Jiu et al., 2017), which could explain why high vimentin expression is correlated with enhanced migration and invasion of cancer cells. Thus, tensile forces can promote vimentin-dependent modulation of the Rho-ROCK pathway and reinforce stress fibers, as previously described (Fujiwara et al., 2016). Moreover, similar to IAS-associated and actin-binding proteins, vimentin could also undergo conformational changes to reveal cryptic binding sites or promote dissociation of binding partners. Force application to epithelial cells leads to rapid accumulation of tensin 4 in keratin intermediate filaments. This reveals how the keratin network could mediate mechanotransduction via force-dependentprotein recruitment (Cheah et al., 2019). Moreover, the vimentin Cys327 site gets blocked under tension (Johnson et al., 2007). In a general manner, the mechanosignaling aspects of intermediate filaments are less well characterized than mechanoprotective and force dissipating responses. Nonetheless, given the extraordinary molecular architecture and stretchability of intermediate filaments, other signaling pathways could be modulated by this intriguing cytoskeleton element.

5. Neuronal mechanotransduction and the membrane periodic skeleton

Neurons are subjected to numerous mechanical forces, shaping their development and function. In the brain, the ECM possesses unique chemical and mechanical properties; in this chapter, I will address how these can greatly influence neurodevelopment and synaptic transmission, Moreover, neurons are stretched and relaxed during physiological activities such as locomotion or muscle contraction, but also in pathological events (e.g. concussions and traumatic brain injuries). I will describe how these forces can modulate neuronal activity, drive pain sensation and promote synaptogenesis. Neuronal tension is another key aspect in their mechanical response, one which is largely dependent on spectrin, a specialized cytoskeletal protein. In mature neurons, spectrin and actin form a robust, submembranar periodic lattice known as the membrane periodic skeleton (MPS), spanning across the entire length of the axon, as well as some regions in dendrites. I will describe how the MPS is composed as well as its emergent structural and signaling roles; given the context of this PhD work, I will focus on the possibility of the MPS being a mechanosensitive structure, something we tried (and are currently trying) to explore.

1. Neuron mechanosensing

For the last decades of research, neuronal cell development and functioning has been mostly associated to biochemical pathways and factors. However, a surmounting amount of new evidence suggests that the mechanical properties of the ECM are also highly important in neuronal migration (Koser et al., 2016), axonal guidance (Moore et al., 2009), neurogenesis (Segel et al., 2019), synaptic plasticity (Frischknecht et al., 2009) and neural network formation (Lam et al., 2019). Indeed, the ECM configuration in the central nervous system (CNS) is adapted to many of these functions. First, ECM in the CNS is softer than many other tissues in the body, which in turn will regulate neuronal migration and neurite outgrowth. For instance, soft substrates will promote faster migration of cortical neurons (Lantoine Biomaterials 2016). Axonal guidance can also be integrated into stiffness gradients; retinal ganglion cell axons grow towards softer tissues, a process which is dependent on mechanotransduction and mechanosensitive channels (Fig. 31) (Koser et al., 2016). Moreover, the stiffness of brain ECM will change with ageing and neurodegenerative diseases, such as multiple sclerosis or Alzheimer's disease (Barnes et al.,

2017). This will likely lead to changes in mechanotransduction across the brain. Second, the ECM in the CNS has a unique composition that includes a high abundance of hyaluronic acid, proteoglycans and glycoproteins (e.g. laminin) (Long and Huttner, 2019). This gives rise to structures such as the perineuronal network (PNN), a specialized ECM scaffold composed by chondroitin sulfate proteoglycan (CSPG) which surrounds the soma and dendrites of several mammalian neuronal cell types (Fawcett Nat Reviews 2019). The PNN is critical for the regulation of synaptic plasticity, stabilization of synapses, and neuroprotection (Bukalo et al., 2007; Carstens et al., 2016; Frischknecht et al., 2009; Romberg et al., 2013).

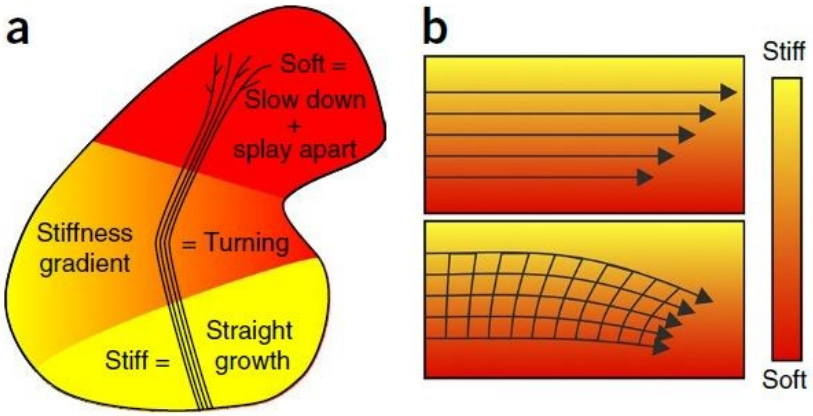

Figure 31: Integrating neuronal migration, stiffness gradients and mechanosensing in *Xenopus* brain development

The schematic shows the mechanical control of axon growth in the optic pathway of *Xenopus* central nervous system. In this well-understood model of axon pathfinding, retinal ganglion cell (RGC) axons leave the retina via the optic nerve, cross the midline at the optic chiasm, grow along the contralateral brain surface in the optic tract (OT) and terminate in the optic tectum. **a,** In the diencephalon/ telencephalon (yellow), stiffness of the substrate promotes a straight growth; on their way, axons encounter a stiffness gradient (orange), which turns the optical tract towards the softer side axon. Growth slows down and eventually stops as they reach the tectum (red), which is softer and promotes unbinding and branching. **b,** How a stiffness gradient can 'turn' axons towards the softer substrate. When axonal bundles migrate in a stiffness gradient, velocity is faster on stiffer substrates. However, as axons fasciculate in the optical tract, they are mechanically coupled; thus, faster axons on the stiffer side may be pulled towards the slower axons on the softer side, leading to reorientation of the axonal bundle towards the softer side (tectum). **a-b**, Figure adapted from Kozer et al. 2016.

To interpret and respond to different mechanical cues, neurons employ a series of mechanosensitive proteins, integrin-based adhesions and motile structures, such as the growth cone. This sensory-motor process explores the neuronal microenvironment, integrating biochemical and mechanical cues into axonal guidance and pathfinding during development

(Kerstein et al., 2015). To ensure this, axon growth cones engage the retrograde actin flow through molecular clutches located at integrin adhesion complexes, known as point contacts (Bard et al., 2008; Myers and Gomez, 2011). Thus, growth cone-driven motility presents clear similarities with the lamellipodium-based migration in mesenchymal cells. Dynamics of point contacts and cytoskeleton engagement are governed by different signaling molecules such as RhoGTPases or FAK (Myers and Gomez, 2011; Woo and Gomez, 2006). Integrin-ECM interactions in neuronal development are also important for synaptogenesis; for instance, deletion of β1-containing integrins compromises sustained neurotransmitter release in mature synapses (Huang et al., 2006).

In later stages of neuronal maturation, mechanotransduction and mechanosensing are equally crucial to modulate synaptic plasticity, neuronal activity and communication. Degradation of the ECM in primary neurons affects the synaptic mobility of AMPA receptors (AMPARs) and short-term synaptic plasticity, revealing the importance of cell-ECM interactions in the dynamic of transmembrane receptors (Frischknecht et al., 2009). Integrins are expressed in mature neurons and are associated with all the components of a tetrapartite synapse (Park and Goda, 2016). For instance, synaptic β1 and β3-integrins appear to regulate long-term potentiation and shape neural circuit properties by regulating actin polymerization and modulating the trafficking and mobility of synaptic receptors (Charrier et al., 2010; Cingolani et al., 2008; Pozo et al., 2012). β3-integrins, in particular, control the number and composition of synaptic AMPA receptors (AMPARs), which in turn will affect homeostatic synaptic scaling (Cingolani et al., 2008). This, in turn, might be dependent on interactions between β3-integrins and the GluA2 subunit, which can regulate AMPAR endocytosis (Pozo et al., 2012).

Besides cell-ECM adhesions, neurons also establish trans-synaptic cell-cell adhesions mediated by synaptic cell adhesion molecules (CAMs), such as neurexins, neuroligins and cahderins (Chamma and Thoumine, 2018). These are essential for synaptic plasticity and stabilization of postsynaptic receptors, among other roles (Chamma and Thoumine, 2018). Synaptic CAMs also engage cytoskeletal elements and scaffolding proteins, controlling morphological plasticity in dendritic spines. This is particularly relevant for the actin cytoskeleton, since actin dynamics and branched actin networks control spine morphogenesis, motility and plasticity (Chazeau et al., 2014; Hotulainen and Hoogenraad, 2010; Korobova and Svitkina, 2010) Dendritic spines also display actin flow, which slows down as filopodia stabilize and mature to spines (Chazeau et al., 2014). This maturation process was shown to be mediated by the mechanical coupling between trans-synaptic N-cahderin adhesions and the actin flow (Chazeau et al., 2015).

1.1. Neuron stretching

Similar to other cell types, stretching and strain are two of the major mechanical forces involved in neuron mechanosensing (Das et al., 2019). Neurons can either be directly deformed by the action of stretching or innervate organs that undergo continuous contraction and relaxation cycles, such as the heart or the muscles. Locomotion is a major source of neuronal strain, through limb movements and muscle contractions. The mammalian median nerve in the forearm can deform up to ~23% for different finger postures (Loh et al., 2018), while mammalian sciatic nerves can experience localized strains up to 30% during regular limb movements (Phillips et al., 2004). Proprioception, the sense of self-movement, depends on sensory neurons that innervate specialized mechanoreceptors in the muscles and tendons, such as the muscle spindles. These sensory neurons become deformed or stretched when muscles and tendons contract or extend, and then adjust the contractions via feedback loops with the central nervous system (Proske and Gandevia, 2012). These neurons are sensitive to different strain aspects such as rate and duration, and express combinations of mechanosensitive channels often involving Piezo2 (Woo et al., 2015). Specialized stretch-sensitive neurons are found for other actions and stimulus, such as touch and pressure(Umans and Liberles, 2018).

Neuron stretching is not limited to the peripheral nervous system though; the brain itself undergoes significant deformations. Even at mild activities such as jumping or heading a football, brain regions can experience strains that go up to 5% (Bayly et al., 2005; Feng et al., 2010). During traumatic events, faster brain deformation, compression or stretching lead to traumatic brain injury (TBI). This in turn, will cause diffusive axonal injury (DAI), characterized by white matter denaturation, focal hemorrhage and axonal breakage (Vieira et al., 2016). The cellular and molecular mechanisms of mechanotransduction in response to neuronal stretching are not fully understood, although there are several known aspects. One of the most established is that mechanosensory neurons sense organ and muscle stretch mostly through mechanosensitive ion channels, including Piezo1/2 (Coste et al., 2010), transient receptor potential (TRP) channels (Li et al., 2006) or TACAN (Beaulieu-Laroche et al., 2020). Forces applied to the mechanosensitive channels will regulate their gating and thus the ion flow, changing neuronal activity. Two possible mechanisms might regulate this: mechanical forces stemming from the plasma membrane (force from lipid) (Anishkin et al., 2014) or physical interactions with the ECM or cytoskeleton (force from filament) (Martinac, 2014). First, changes in plasma membrane mechanics such as tension, bending or stretching will promote a conformational change in the ion channel towards an open state, generating action potentials and hyperexcitability (Tyler, 2012). Alternatively, if the force from the membrane is not enough to cause this transition (Liang and Howard, 2018), ion channels can interact with ‘tethers’ at the cytoskeleton or the ECM, facilitating force transfer to the channel (Martinac, 2014).

Given that stretching controls mechanosensitive channel opening, it is likely that it will also modulate electrophysiological properties in neurons. Neurons stretched at 60% display lower rates of action potential firing and bursting (Magou et al., 2015). Other studies reveal similar effects in the impairment of calcium activity and post-synaptic currents (Bianchi et al., 2019; Goforth et al., 2011). However, several of these studies often apply considerably high strains (30-75%) to study the impact of stretch injury in electrophysiological activities, often mimicking TBI contexts (Slemmer et al., 2002). Despite being extremely important to understand the mechanisms behind trauma or dysfunction, such studies might overlook pathways activated during physiological stretching at lower strain percentages and strain rates. Another important aspect to consider is the strain rate, which is thought to contribute for post-injury pathology and injury in neurons (Bar-Kochba et al., 2016).

Besides the regulation of mechanosensitive channels, neuron stretching can also trigger mechanisms favoring synapse formation. For instance, in the embryonic nervous system of *Drosophila*, axons at the neuromuscular junction (NMJ) are under continuous mechanical tension, which contributes to vesicle clustering at the presynaptic terminal (Siechen et al., 2009). Mechanically stretching these axons by pulling the postsynaptic muscle will increase the vesicle clustering, hence showing how mechanical stretch can also activate particular sets of neurons via synaptic connections (Siechen et al., 2009). Axonal tension is hallmark of *Drosophila* embryonic motor neurons, which maintain a rest tension and behave like viscoelastic solids (Jagannathan Rajagopalan et al., 2010). This is thought to be dependent on actomyosin contractility (Tofangchi et al., 2016). Mechanical stretching can also influence other aspects of neurodevelopment; the simple pulling of neuronal processes in early developmental stages can give rise to new axon-like extensions adding to the pre-existent axon (Lamoureux et al., 2002).

1.2. Spectrin: a mechanosensitive protein in neuronal function

Overall, studies on *Drosophila* have provided valuable inputs for the interplay between axonal tension and neuronal stretching (Jagannathan Rajagopalan et al., 2010; Siechen et al., 2009; Tofangchi et al., 2016). Indeed, generation of tension in axons might be essential for stretching responses, changing the mechanical properties of neurons and protecting them from shock or degeneration (Krieg et al., 2014, 2017a). However, the structures responsible for maintaining tension in neurons and regulating mechanoprotection remain to be characterized. In addition, these same structures could also have a mechanosensitive role linked to their tension-generating functions. The cytoskeletal protein spectrin could be a key element for many these processes. Spectrin is a scaffold protein ubiquitously expressed in all cell types, which provides structural support to the plasma membrane and contributes for the organization of membrane proteins (Bennett and Lorenzo, 2013). Humans and other mammals express a number

of spectrin isoforms (Brown et al., 2015); for instance, mouse neurons express βII, βIII and βIV spectrin in different subcellular compartments (Han et al., 2017; Xu et al., 2013). All isoforms exhibit similar crystal structures (Fig.32), consisting of multiple, anti-parallel repeats of 3-helix bundle domains (Fig. 32b) (Brown et al., 2015) .

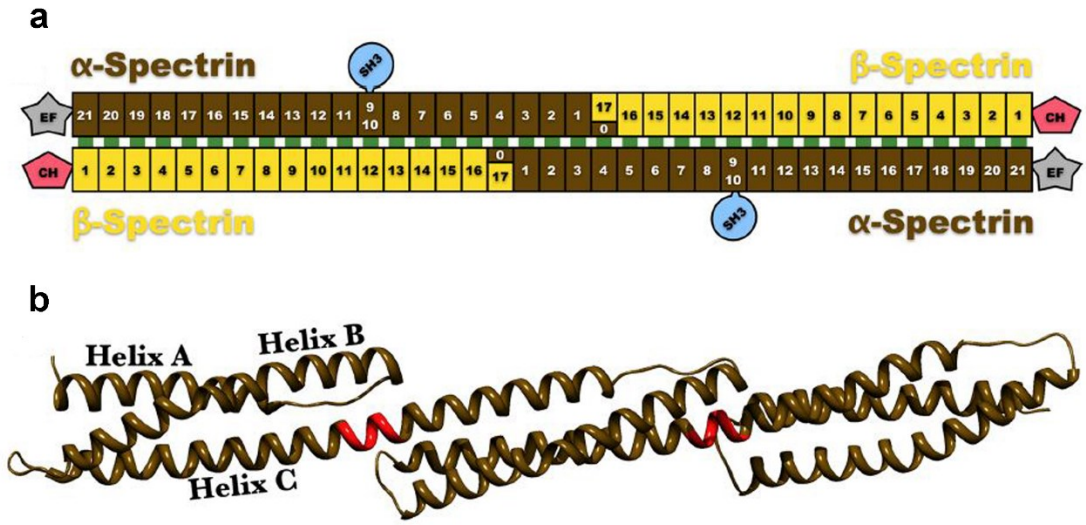

Figure 32: Structure of spectrin

a, Domain organization of erythroid spectrin tetramers, which are composed by multiple three-helix bundle repeats (α-spectrin—brown spectrin repeats; β-spectrin—yellow spectrin repeats). α-spectrin contains 20 repeats while β-spectrin contains at least 16 repeats. Spectrin tetramers usually have a length of 200 nm, but it can vary according to the cell. The pink pentagons labeled CH are the actin binding domains. Other known spectrin domains are labeled EF, SH3 and PH. **c**, Ribbon diagram representation of three consecutive spectrin repeats (brown), which form a three-helix bundle, linked by 5-residue regions (red). **a-b,** Figure adapted from Brown et al. 2015.

Spectrin associates to actin and ankyrin to form a specialized membrane skeleton, responsible for establishing plasma membrane domains and anchoring membrane proteins such as cell adhesion molecules (CAMs) (e.g. L1CAM, neurofascin, α-catenin) or ion channels (e.g. cardiac and neuronal sodium channels) (Bennett and Lorenzo, 2013; Machnicka et al., 2014). The actin-spectrin membrane skeleton is very well characterized in erythrocytes, where it assumes a 1D quasi-hexagonal organization and is crucial for withstanding high shear stress and shape changes (Pan et al., 2018). In the nervous system, spectrin is also required for organization of plasma membrane domains such as the axon initial segment or the Ranvier nodes (Dzhashiashvili et al., 2007; Galiano et al., 2012) , ensuring the correct functioning of neurons. Deletions or mutations of α and β-spectrin (αII, βII,βII βIV) impair axonal connectivity and axon initial segment (AIS) formation, cause mislocalization of neurotransmitter receptors and lead to overall neurodegeneration (Huang et al., 2017a; Lorenzo et al., 2019). In this regard, mutations of human

βIII-Spectrin are associated to spinocerebellar ataxia type 5 (SCA5), a human neurodegenerative disease that causes limb ataxia and slurred speech, among others (Avery et al., 2017).

2. The membrane periodic skeleton

More recently, an impressive series of studies involving super resolution microscopy have unveiled and characterized an actin-spectrin periodic lattice in axons, known as the membrane periodic skeleton (MPS). The MPS consists of a series of actin 'rings' interconnected by spectrin tetramers with a period of ~180-200 nm (Leterrier et al., 2015; Vassilopoulos et al., 2019; Xu et al., 2013). The MPS was the first structure to ever be 'discovered' through super-resolution microscopy, using stochastic optical reconstruction microscopy (STORM) (Fig.33) (Xu et al., 2013). Several proteins associate to the MPS, such as ankyrin, myosin or adducin, each one contributing to MPS organization and functions(Costa et al., 2020; Leite et al., 2016; Leterrier et al., 2015; Xu et al., 2013). Ankyrin acts as a submembrane organizer in axon initial segment (AIS) (Leterrier et al., 2015), while adducin is thought to cap actin filaments within the rings, regulating their diameter (Leite et al., 2016). Myosin II, on the other hand, can play contractile or scaffolding roles depending on the subcellular location in regards to the actin rings (Costa et al., 2020). Myosin II light chains colocalize with the actin rings, while the heavy chains are disposed along the longitudinal axis of the axon, crosslinking actin rings (Costa et al., 2020).

Moreover, the MPS can also organize transmembrane proteins such as ion channels and cell adhesion molecules (Leterrier et al., 2015). After the first study unveiling the existence of the MPS, it was assumed that actin rings were composed by short F-actin filaments capped by adducin (Xu et al., 2013). A recent study has challenged that model, by showing through correlative super-resolution/platinum replica electron microscopy that actin rings are actually composed by two long, intertwined actin filaments, connected by a mesh of spectrin molecules. (Vassilopoulos et al., 2019).

In dendrites and the soma, MPS is present to a lesser extent, alternating patches of periodic 1D structures with a more 2D-polygonal organization, similar to what is found on erythrocytes (Fig. 34) (Pan et al., 2018). However periodic F-actin structures are quite abundant in dendritic spine necks, suggesting that the MPS might specifically associated with thinner neuronal processes (Fig. 34) (Bär et al., 2016). Nonetheless, the reduced prevalence of MPS in dendrites might be a consequence of lower βII-Spectrin levels, since overexpression of βII-Spectrin triggers a much more widespread distribution of the MPS in dendrites (Zhong et al., 2014). In this regard, it would be of interest to understand how the MPS interacts with the branched actin networks in dendritic spines (Chazeau et al., 2014; Korobova and Svitkina, 2010).

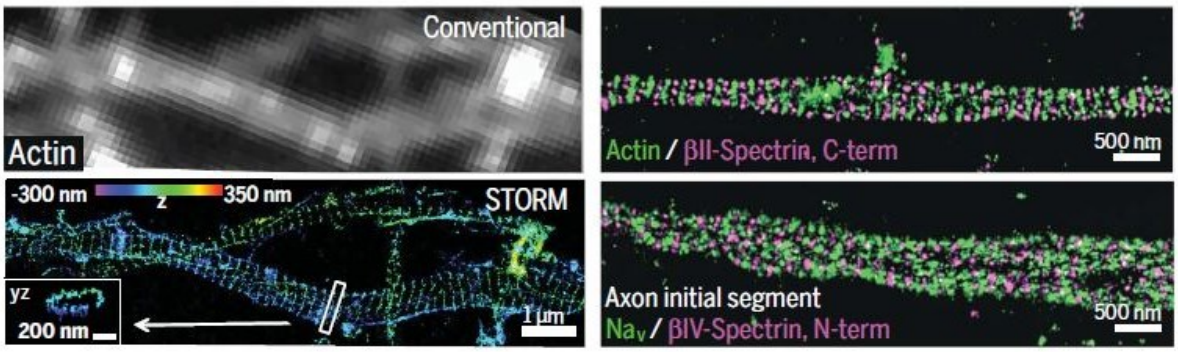

Figure 33: The first observation of MPS using STORM super-resolution microscopy

Quasi-1D periodic MPS observed in axons by using STORM. Left: Comparison of diffraction-limited (top) and 3D-STORM (bottom) images of actin in axons, stained with Phalloidin-Alexa647. STORM image shows the periodic distribution of actin rings along the axon that is obscured by diffraction-limited imaging. Right: Two-color STORM images showing the periodic distributions and nanoscale organization of actin, spectrins (βII- and βIV-spectrin), and voltage-gated sodium channels (Nav). Notice how the axon initial segment (AIS) is specifically enriched in periodic βIV spectrin and how Nav channels assume a periodic distribution. Figure adapted from Xu et al. 2013 and Sigal, Zhou, and Zhuang 2018.

Even within the axon, the organization and composition of the MPS will change in specialized domains, often influencing the anchoring of proteins involved in neuronal functions (Fig. 34). The most striking case is the AIS, where the MPS exhibits a specific organization, with β4/α2-spectrin tetramers spacing periodic actin rings (Leterrier et al., 2015; Xu et al., 2013). The submembranous scaffold protein ankyrin G (ankG) acts as a master organizer of AIS, by controlling both ion channel clustering and maintenance of neuronal polarity. AnkG is placed at the center of the spectrin tetramer and binds β4-spectrin, microtubules, Nav channels and cell adhesion molecules NF-186 and NrCAM (Leterrier et al., 2011, 2015; Xu et al., 2013). Phosphorylated myosin light chain (pMLC), an activator of contractile myosin II, is also selectively enriched in the AIS, where it associates with actin rings (Berger et al., 2018). These interactions can modulate structural plasticity in the AIS via myosin II contractility (Fig. 34)

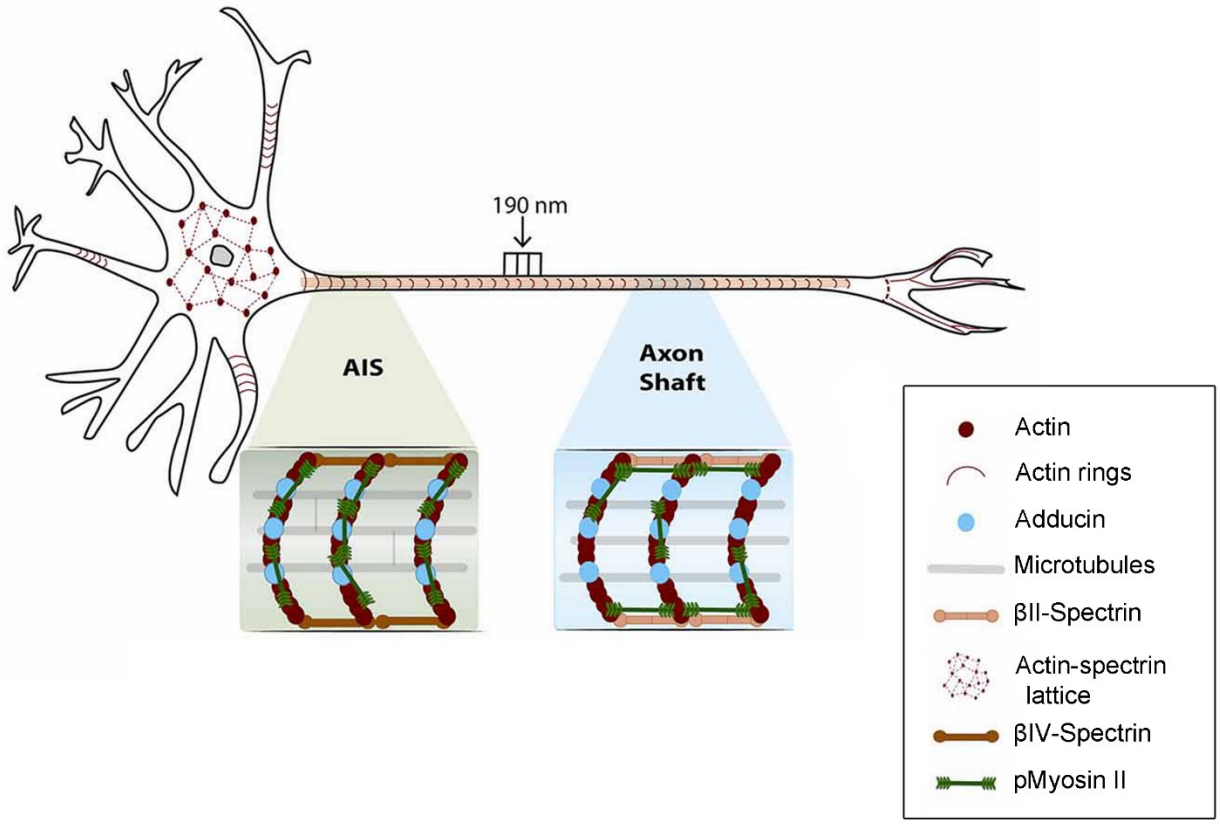

Figure 34: Overview of MPS structure in neurons

Different organizations of the actin-spectrin cytoskeleton can be seen for different neuronal compartments. Actin rings span along the entire length of the axon, consisting of actin filaments (dark red) capped with adducin (blue) and interconnected by spectrin tetramers (beige or brown). The AIS exhibits a specific organization, with βIV-spectrin connecting the actin rings. The somatodendritic compartment is characterized by a combination of MPS patches in spines (and particularly spine necks) and a quasi-2D actin-spectrin polygonal lattice, reminiscent of erythrocytes, more common in the soma. This schematic, in light of recent findings, is no longer fully representative, as the rings are thought to be composed by two long, intertwined actin filaments. Figure adapted from Costa et al. 2018.

The formation of MPS occurs in parallel to neuronal development and depends both on the components and the compartments of neurons. In hippocampal neurons, βII-Spectrin assumes a periodic distribution in hippocampal cultured neurons as early as day-in-vitro (DIV) 2, but limited to the proximal axon. This is then propagated along the entire axon as neurons develop, covering the totality of the axon by DIV6/7 (Zhong et al., 2014). Actin seems to be delayed 2-3 days in regards to βII-Spectrin, which might reflect a lower stability of F-actin filaments in early neurons. Interestingly, the final MPS organization in the AIS is only visualized completely at DIV12, suggesting that β4-spectrin and AnkG are incorporated later in the neuron development (Zhong et al., 2014).

The MPS is ubiquitously present in the mature axons of different neuronal types across assessed so far, including (but not only) multiple subtypes of excitatory and inhibitory neurons but also motor and sensory neurons (Fig. 35a) (D'Este et al., 2015, 2016, 2017; He et al., 2016) . Moreover, the MPS is also observed across different species such as chicken, *C.elegans* and *Drosophila* (Fig. 35b) (He et al., 2016). This suggests that the MPS might be part of an evolutionarily conserved mechanism in neuronal development.

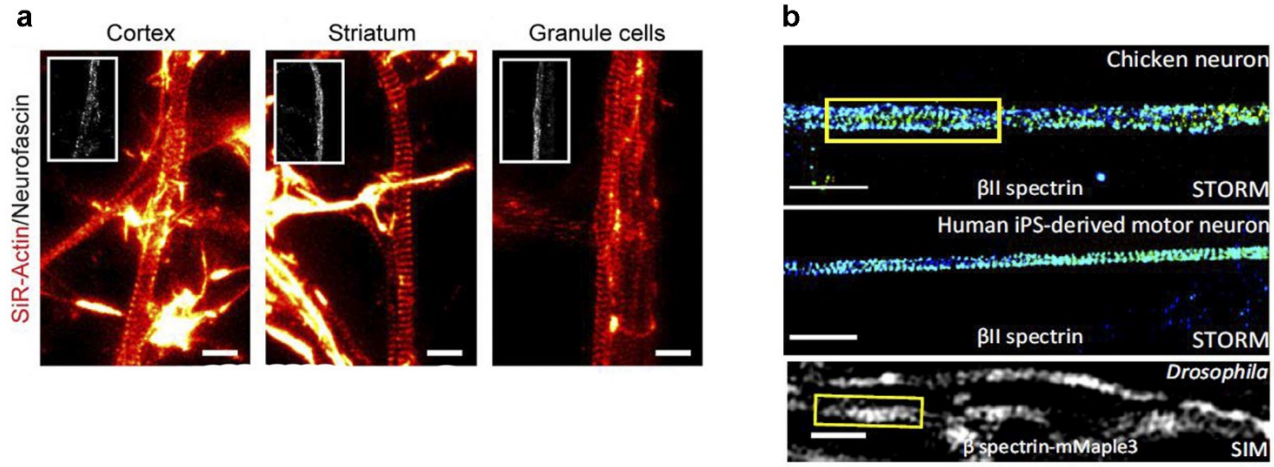

Figure 35: Distribution and ubiquity of MPS

a, MPS is present across different types of neurons in the central nervous system. Representative live STED images of SiR-Actin in the axons of cortical neurons (left), striatal neurons (middle) and cerebellar granule cells (right). Insets represent neurofascin, an axonal marker. Adapted from D'Este et al. 2016. **b,** Presence of the MPS across a range of species. Representative STORM images of immunolabeled βII spectrin in the axons of cultured chicken neurons (top) and human iPS-derived motor neurons (middle). Representative live structured illumination microscopy (SIM) image of β spectrin-mMaple3 in Drosophila neurons imaged in Drosophila brain tissues (bottom). Adapted from He et al. 2016.

2.1. The functions of the MPS: emergent roles in signaling and mechanosensing

Despite the considerable knowledge on MPS structure and organization, less is known about its functions in neurons. Based on the roles of spectrin/actin lattices in other cells, initial hypothesis pointed to the MPS as a structural sub-membrane scaffold for the axon, responsible for maintaining axonal integrity and structure. In conditions that favor axonal degeneration, such as trophic factor withdrawal (TFW), MPS is rapidly disassembled (Unsain et al., 2018; Wang et al., 2019a), remaining low in until axonal fragmentation or growth cone collapse. Nonetheless, these results do not exclude the possibility that MPS disassembly could be just a secondary

consequence of axonal degeneration. However, MPS disassembly occurs before caspase activation and even when apoptotic pathways are blocked (Wang et al., 2019a). Moreover, pharmacological stabilization of F-actin stabilizes the MPS and prevents pro-degenerative retrograde signals as well as axonal degeneration(Unsain et al., 2018; Wang et al., 2019a). Therefore, MPS disassembly and destruction after TFW is an essential event triggering pro-degenerative retrograde signaling and axonal fragmentation.

Besides axonal stabilization, studies suggest a link between MPS and microtubule dynamics, although it is not yet clear how they cooperate. Depolymerization of actin and consequent MPS depletion in *Drosophila* neurons leads to defects in microtubule polymerization and gaps in microtubule bundles, which are enhanced by the absence of the microtubule stabilizing protein Shot (Qu et al., 2017). Thus, MPS appears to be important to regulate microtubule organization and polymerization in axons. Since the transport of organelles along the axons is heavily dependent on microtubules, MPS could also regulate axonal transport by modulating microtubule organization. Indeed, in the AIS, ankG – a main MPS component - connects to microtubules via end binding proteins (EBPs) EBP1 and EBP3 (Leterrier et al., 2011). Recent super-resolution experiments revealed that in the AIS, the C-terminus of ankG extends away from the plasma membrame ~35 mm into the cytoplasm, where it could recruit and organize microtubules (Leterrier et al., 2015). Thus, the MPS could contribute for axonal trafficking and vesicle sorting in the AIS by coordinating a microtubule network through ankG and EBP-mediated interactions.

Other components of the MPS have been associated with axonal transport. Depletion of capping protein adducin enlarges the diameter of the MPS and leads to an impairment in mitochondrial and organelle transport across the axon (Leite et al., 2016). However, this effect could arise from other adducin-mediated pathways and be independent of MPS organization. In line with a possible MPS role in axonal transport, another study has shown that knocking-out βII-spectrin also affects organelle bidirectional transport in axons, reducing both the fraction of motile vesicles and their transport speed (Lorenzo et al., 2019). This is likely mediated by βII-Spectrin interactions with motor proteins such as kinesin. However, this appears to be independent of MPS formation, since organelle transport is not affected in distal axons of young neurons (DIV2), where MPS is not present yet (Lorenzo et al., 2019). Thus, although the MPS is required to maintain microtubule polymerization, it is yet unclear whether this will also have an impact in axonal transport of vesicles and organelles.

Transmembrane proteins such as ion channels and CAMs are organized by the MPS in axons, suggesting that this structure may mediate membrane-dependent signaling. In line with this, a recent study has demonstrated that the MPS also acts as structural platform for G-protein coupled receptor (GPCR) and CAM-mediated receptor tyrosine kinase (RTK) transactivation (Zhou et al., 2019). The MPS dynamically regulates different signaling molecules, bringing GPCRs, CAMS,

RTKs and Src family kinases into proximity, leading to RTK transactivation and ERK signaling (Fig. 36a) (Zhou et al., 2019). Interestingly, MPS itself can exert negative feedback on this action, since ERK signaling leads to caspase-mediated MPS degradation and thus the disassembly of this signaling platform (Zhou et al., 2019).

Spectrin, which is central to MPS function, has been shown to regulate mechanical properties and display mechanosensitive behaviors in different cell types (Duan et al., 2018; Wu et al., 2017). A typical αII/βII spectrin tetramer contains at least 72 repeats (Fig. 32) (Brown et al., 2015), which can unfolded by force, conferring spectrin a considerable extensibility. Moreover, unfolding/refolding of spectrin repeats could also serve as a mechanism of force buffering, similar to what is seen on the talin rod domain. Together, these properties can contribute to different cellular processes, such as the significant deformations that erythrocytes undergo when traversing small capillaries. In *C.Elegans,* β-spectrin is required for maintaining tension in touch receptor neurons, which in turn is essential for touch sensation (Krieg et al., 2014). Furthermore, β-spectrin and microtubules collaborate to protect axons and dendrites from mechanical stress, by maintaining neuronal elasticity and tension (Krieg et al., 2017a). In addition, spectrin exhibits a mechanosensitive accumulation in response to shear deformation at the fusogenic synapse between muscle cells in *Drosophila* (Duan et al., 2018). Therefore, given the different roles of spectrin in regulating mechanical properties, the MPS could also act as a mechanosensitive structure. However, it is also possible that the MPS, through spectrin-dependent functions, could be more of a mechanoprotective structure responsible for maintaining axonal tension and buffering forces.

In this regard, a recent study combining neuronal stretching, cytoskeleton perturbation and modelling has for the first time exposed MPS-dependent mechanoprotection, which is dependent on spectrin (Fig. 36b,c) (Dubey et al., 2019). First, by using an optical based force apparatus, axons were shown to exhibit a strain softening behavior due to their ability to buffer tension. Presence of the MPS throughout the axon was crucial for tension homeostasis, acting as a 'shock buffer' to protect axons against stretch-induced deformations. Using modelling and simulations, this behavior was shown to be achieved through unfolding and refolding of spectrin repeats (Fig. 36b,c) (Dubey et al., 2020). This study highlighted for the first time a mechanoprotective role of the MPS which depends largely on unfolding/refolding of spectrin to buffer tension across axons. Although this reveals a more mechanoprotective role for the MPS, it also opens up the possibility of the MPS acting as a mechanosensitive structure through force-dependent changes in spectrin conformation. Spectrin has several binding domains for several proteins such as GPCRs or CAMs (Bennett and Lorenzo, 2013). Unfolding of spectrin in response to force could expose binding domains and induce recruitment of specific transmembrane proteins, similar to what is seen for talin (Ciobanasu et al., 2014; Del Rio et al., 2009; Yao et al., 2016). Alternatively, at the level of AIS, mechanical force could also destabilize the interactions

between the MPS and sodium channels, leading to an increase in their diffusion and changes in electrical activity. Ankyrin is also a suitable candidate for MPS mechanosensing, since it also possesses multiple binding sites for signaling molecules. Moreover, the MPS can also act as a signaling platform for Src family kinases (Zhou et al., 2019), which in turn are involved in integrin-mediated mechanosignaling, inclusively in response to cyclic stretching (Chen et al., 2013; Niediek et al., 2012). Therefore, the MPS could also mediate mechanosignaling pathways through Src phosphorylation in response to mechanical stretching. All of these aspects will have to be taken into account when exploring axonal mechanosensing and force-dependent responses at the level of the MPS.

Finally, and supporting the idea of the MPS as a mechanosensitive assembly, recent works have demonstrated how the MPS constitutes an actomyosin network where myosin II interacts with actin rings (Costa et al., 2020) and accumulates in the AIS (Berger et al., 2018). Through this association, myosin II activity regulates the expansion and contraction of the axonal diameter, which in turn modulates the axonal transmission of electrical impulses (Costa et al., 2020). Moreover, myosin II light chain phosphorylation and myosin II activity at the AIS can regulate its structural plasticity (Berger et al., 2018). Thus, MPS mechanosensing via the actomyosin network can impact both the structural and electrophysiological properties of axons.

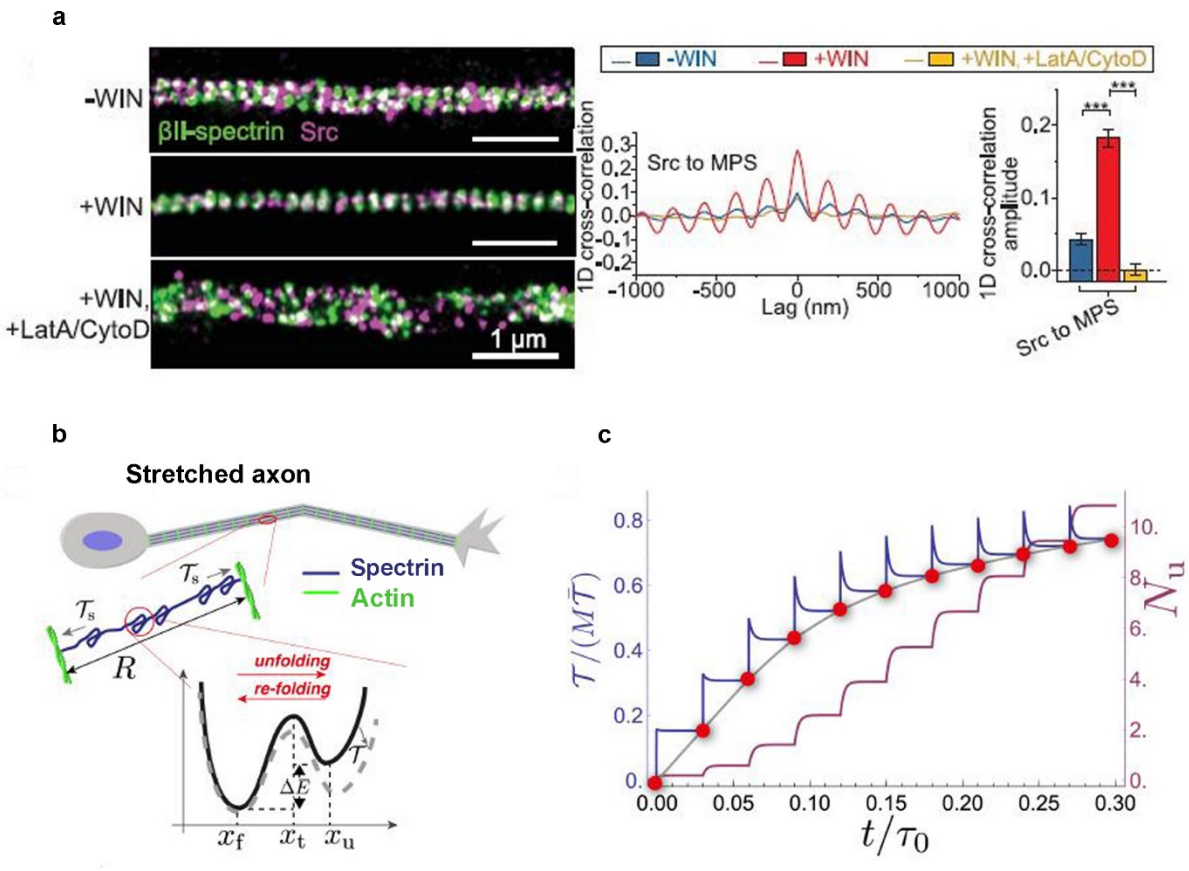

Figure 36: Possible signaling and mechanosensitive roles of the MPS

a, The MPS as a signaling platform. Left: Two-color STORM images of βII-spectrin (green) and Src kinase (magenta) in axons of rat primary hippocampal untreated neurons (top), when treated with a cannabinoid receptor type 1 (CB1) agonist WIN (middle and bottom). Right panels represent the average 1D cross-correlation functions and 1D cross-correlation amplitudes between the distributions of βII-spectrin and Src. When neurons are treated with WIN, Src kinase becomes more colocalized with the MPS and acquires a periodic distribution. Disrupting MPS abolishes this effect. This suggests that the MPS acts a signaling platform by bringing membrane receptors and intracellular messengers into proximity. Adapted from Zhou et al. 2019. **b-c,** The MPS as a possible shock tension buffer, adapted from Dubey eLife 2020. **b,** Schematic of a stretched axon showing unfolding/re-folding of spectrin repeats as a mechanism for tension relaxation. When an axon is suddenly stretched at constant strain, the tension is not constant, but instead relaxes over time; this arises from unfolding and re-folding of spectrin repeats along a spectrin tetramer, dissipating elastic energy. The inset shows the variations of energy landscape for the unfolding/re-folding of a spectrin repeat, with X_f representing the folded state and X_u the unfolded state. State transitions depend on the tension per spectrin tetramer (T_s), which is equivalent to the overall tension *T* divided by the number of tetramers *M* in an axon. **c,** Model calculation for a single spectrin tetramer for multiple step-strain protocol. Following a jump in strain, tension versus time (dark purple) quickly rises, followed by relaxation to a steady-state value (red points, passed through by the equilibrium force versus extension curve (gray)), as spectrin repeats (N_u, burgundy) progressively unfold. Long after the strain step, tension relaxation tends to a steady-state T_{ss} whose values follow the red dots in the equilibrium force versus extension curve. This reflects the tension buffering behavior seen in neurons after strain (not shown).

6. Objectives of the thesis

The main goal of this PhD work was to unveil the molecular mechanisms of mechanosensing in different subcellular structures, from IAS to the MPS. Specific goals included:

1. Develop a method to capture the nanoscale reorganizations and deformations of individual proteins inside mechano-sensitive structures in response to external forces. For this, we aimed to:
    a. Develop a cell stretching device compatible with SRM and SPT.
    b. Validate this method for different subcellular structures such as IAS and cytoskeletal filaments.
    c. Adapt this method to various SRM and SPT modalities, more precisely sptPALM, DNA-PAINT and STED.

2. Apply this method to study the molecular mechanosensing of IAS, with two particular axis:
    a. Capture the acute mechanical response of IAS proteins (talin, integrin, actin) upon live cell stretching.
    b. Characterize the reorganization and recruitment of IAS proteins (vinculin, talin, zyxin) in response to live cell stretching.

3. Determine whether the MPS in neurons is mechanosensitive. For this particular end we aimed to:
    a. Adapt the stretching device to neuronal culture and imaging.
    b. Capture the acute mechanical response of MPS components in response to live cell stretching.
    c. Assess the changes in the nanoscale organization of the MPS in response to live cell stretching.
    d. Achieve the control of orientation and geometry of cells on the stretching device

METHODS AND APPROACHES

In this chapter, I will present the main methods and approaches used throughout this thesis to address our biological and experimental questions. In our work, we have designed a micromechanical cell stretching device compatible with super-resolution microscopy and single particle tracking. Therefore, in this chapter, I will first discuss about cell stretching methods, with special emphasis on the use of elastomeric substrates and stretching parameters that can influence the cellular response. Then I will introduce the concept of super-resolution microscopy and its vast array of techniques, highlighting the ones used throughout this thesis.

The step by step protocol to generate and assemble the micromechanical device, and the procedure to perform cell stretching combined with super-resolution microscopy (SRM) and single protein tracking (SPT) is available at Nature Protocol Exchange. This protocol has been included in the end of this chapter.

Our approach allowed to capture the acute mechanical response and reorganizations of proteins inside mechanosensitive structures. A detailed methodological description of the different experiments we performed and their respective analysis can be found on our recent publication (Massou, Nunes Vicente, Wetzel et al. 2020). This publication has been included in the Results chapter. Finally, we have also submitted a publication on using single-protein tracking to study protein interactions during integrin-based migration, at Methods in Molecular Biology. This publication has been added as an Annex in the end of this thesis.

1. Cell stretching

Cells and tissues are continuously stretched on the body, activating different mechanotransduction pathways. Therefore, it is critical to develop experimental approaches to mimic stretching in a controlled environment. Previously in this introduction, I discussed about single molecule force spectroscopy methods such as optical tweezers, which also allow to stretch proteins and even subcellular structures. In this chapter, I will focus on various cell stretching devices which do not deliver a readout *per* se such as SMFS methods; instead, they allow to study the impact of stretching in various cellular processes. I will especially highlight elastomeric deformable substrates, which we used in our work to study the mechanical response of proteins in mechanosensitive structures. I will also discuss on the importance of picking the correct stretching protocol and the various parameters which can influence the cellular response.

1. Systems for stretching cells

Choosing a particular stretching method and protocol will depend on many factors, such as the cell type, the mechanical response in question or the context we pretend to recreate. If the goal is to study the mechanical response of blood vessels, then it will be more adequate to mimic the shear stress induced by blood flow. However, if the aim is to deform adhesive cells such as fibroblasts, then stretchable substrates will probably be better to mimic the deformation of the underlying matrix in vivo. Stretching can also be local, by pulling or poking specific regions of the cell with micropipettes. Below we present different systems used for stretching.

1.1. Elastomeric substrates

Stretching devices composed of elastomeric substrates have been widely used to apply controlled deformations to adherent cells (Fig. 37a,b,c). Elastomeric substrates mostly consist of silicon or biocompatible polydimethylsiloxane (PDMS). The latter is particularly suitable since its stiffness, thickness and viscoelasticity can be tightly controlled (Schürmann et al., 2016). In many uniaxial/biaxial stretching devices, cells are spread on coated elastomeric substrates and then stretched using piezo-electric motors, rods, clips or micro-screws, among other systems (Chen et al., 2013; Cui et al., 2015; Hoffman et al., 2012; Panzetta et al., 2019).

PDMS and silicon-based devices have been extensively used to study the effects of uniaxial stretching in subcellular and cellular processes. Subcellular events assessed by stretching include IAS dynamics, orientation and assembly (Chen et al., 2013), cytoskeleton reorganization and nuclear softening (Nava et al., 2020). Concerning cellular responses, stretching has been used to study and regulate cell proliferation, differentiation, stiffness or alignment, among many other processes (Panzetta et al., 2019). In this regard, elastomer-based stretching devices can be specifically tuned according to the aim of the study. Substrate thickness, stiffness or the mode of stretching itself are adapted to the cell type and stimulus in question.

Despite their vast applications, elastomer-based stretching devices carry some important limitations. For instance, many devices are built for uniaxial stretching in rectangular elastomer membranes, lacking the isotropic or biaxial components of physiological stretching *in vivo*. Thus, important mechanosensitive pathways in live cells could be overlooked in the absence of isotropic or bixial stretching. To achieve this, a common approach consists in introducing loading posts underneath the elastomeric membrane, which is pulled down by applying suction, creating equibiaxial stretching (Fig. 37c) (Schürmann et al., 2016; Tijore et al., 2018). This approach has been commercialized under the *FlexCell* system (Banes, 2013). Alternatively, a recently designed system consists of circular PDMS membranes connected to a translation ring through multiple hooks. Continuous rotation of the ring is transmitted to the PDMS membrane, generating isotropic stretching (Schürmann et al., 2016).

The combination of stretching and live cell imaging is essential to study the mechanical response of cells. Various stretching devices based on elastomeric substrates are capable of live cell imaging, which is often performed at specific time points of the stretching protocol (Chen et al., 2013; Cui et al., 2015; Jungbauer et al., 2008; Panzetta et al., 2019). This includes commercial systems such as the *FlexCell* or the *Cytostretcher* (Curi-Bio). Usually, live imaging is performed in combination with low numerical aperture objectives (often 10-20X) and upright or inverted microscopes. However, many of these systems have limitations, such as uneven stretch ratios or defocusing (Jungbauer et al., 2008). First, this poses issues for acquisitions after large deformations, leading to loss of the in-plane image. But, more importantly, such limitations are especially incompatible with real-time imaging during stretching, which is critical for capturing the dynamics of mechanosensitive processes. Some devices could potentially enable this (Chen et al., 2013; Sinha et al., 2011) or have actually achieved it (Shao et al., 2013), but they are either limited to low-magnification imaging or they are incompatible with automatic focusing during stretching (Shao et al., 2013). Alternatively, the commercial *Cytostretcher-LV* system enables real-time imaging and automatic focusing during stretching. However, it is equally important in science to seek less expensive, customizable and open-access systems. Moreover, various features of the previous systems (elastomer thickness, deformations, and mechanical drift) prevent them from assessing mechanosensitive responses at the nanoscale.

1.2. Other stretching systems

Although elastomeric substrate-based devices are widely used and even commercialized for cell stretching, many other methods are available. In certain occasions, these methods might even be more adequate for the study in question. For instance, if the aim is to apply local stretching in certain regions of the membrane or segments of the cell, a more 'individual' micromanipulator is required. Glass micropipettes and needles have been extensively used in that regard, especially in neurobiology, with successful results (Lamoureux et al., 2002; Siechen et al., 2009). Stretching individual *Drosophila* axons with glass micropipettes allowed to study the role of neuronal tension in presynaptic vesicle clustering (Siechen et al., 2009). Other micropipette studies were performed in neurite outgrowth.

More recently, emergent stretching systems have expanded the variety of stimuli that can be applied to cells. Using alginate-PEG biocompatible hydrogels, researchers were able to apply extreme deformations of 300% to fibroblasts, something that would not be possible with conventional elastomeric substrates (Fig. 37d) (Hu et al., 2019). In the field of neuron mechanosensing, a recent work has implemented an optical fiber-based apparatus to stretch live axons and measure their elastic modulus (Dubey et al., 2020). Finally, an elegant approach by Srivastava and colleagues (Srivastava et al., 2017, 2020) consists in 'squashing' the cells instead of stretching their substrate. Despite being quite different from conventional stretching experiments, 'cell squashers' can mimic load application and cell compression *in vivo*.

2. How and when to stretch

Choosing the adequate stretching protocol is as essential as picking the right stretching method or system, since it will also reflect how the stimulus can occur *in vivo.* This will involve multiple parameters, including stretching magnitude, strain rate, duration and frequency. Muscle and lung cells, for instance, are subjected to continuous cycles of stretching and relaxation in the body(Das et al., 2019; Umans and Liberles, 2018). To obtain more physiologically relevant measures for these tissues, cyclic stretching is far more adequate than single/sustained stretching. Conversely, sustained/prolonged stretch also occurs *in vivo*, either during traumatic injuries or during physiological contexts such as long-term muscle contraction and urine retention by the bladder(Chen et al., 2013; Umans and Liberles, 2018; Vieira et al., 2016). Here, cyclic stretch is less adequate to study the response of these tissues. However, even for the same cells or tissues, both cyclic and sustained stretch can occur, with specific responses. Epithelial cells, for instance, undergo a well-characterized reorientation of stress fibers in response to cyclic stretching (Hsu et al., 2010). Conversely, when subjected to uniaxial sustained stretching, these cells will exhibit a slow, orientation-specific disassembly of mature FAs and loss of cell polarity

(Chen et al., 2013). The duration of both sustained and cyclic stretches can further modulate their impact and activate different mechanisms. In the case of FA disassembly, this is preceded by a rapid FA growth in the early phase of sustained stretch. Moreover, an increase in the duration of cyclic stretching enhances its effects on cell spreading, polarization and stress fiber formation (Cui et al., 2015). Conversely, cytoskeleton stiffness has been reported to increase immediately after stretching, remaining mostly unaltered after 2 hours of sustained stretching (Panzetta et al., 2019). Finally, in a context of cyclic stretching, strain rate also takes a special relevance, since it limits the relaxation time. This has consequences in cytoskeletal tension and stress fiber turnover; stress fiber alignment increases at higher strain rates, as well as the phosphorylation of key proteins (e.g. ERK or MAPK) in stretching-mediated responses (Hsu et al., 2010).

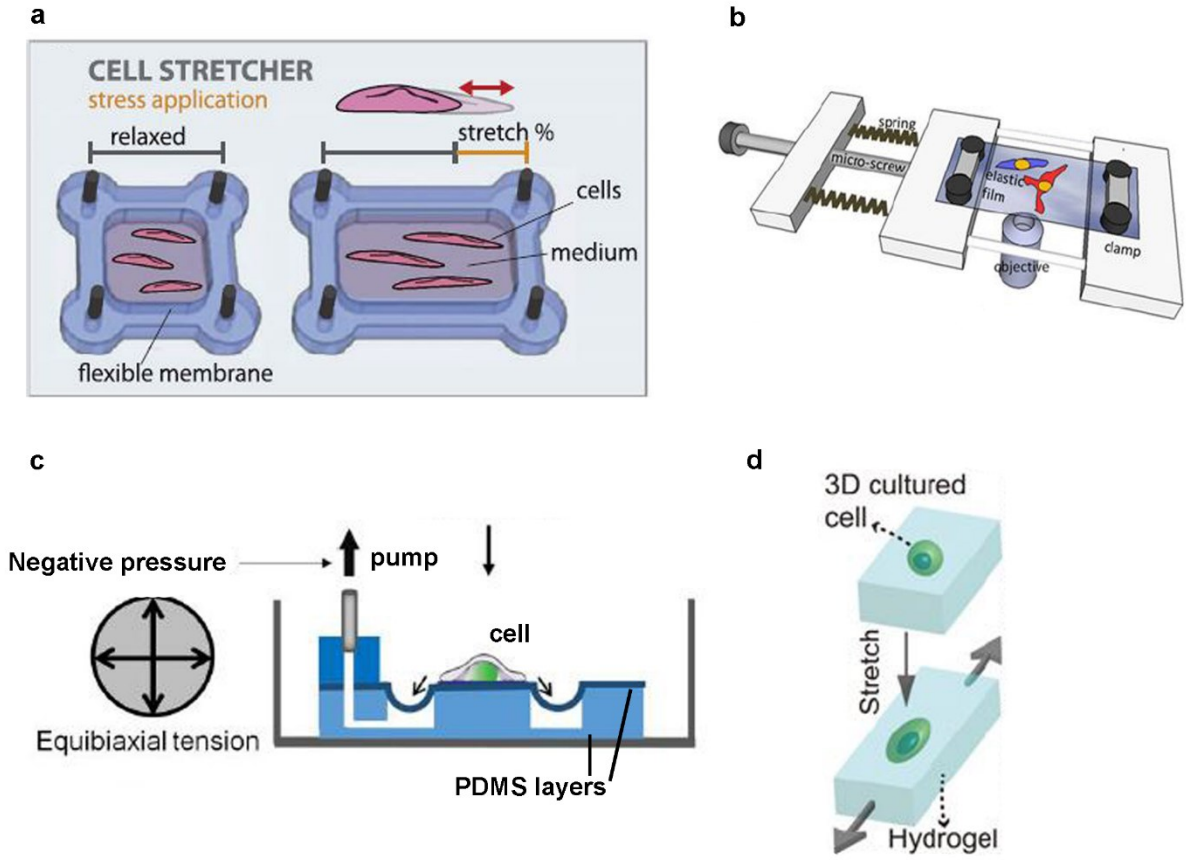

Figure 37: Elastomer and gel-based cell stretching devices

a, Cell stretcher consisting of an elastomeric PDMS membrane and coated with fibronectin, which is stretched by a linear motor (Bonakdar et al., 2012). **b,** stretching device composed by a fibronectin-coated elastic silicon film fixed by two parallel clamps and a microscrew; adjusting the microscrew allows to apply uniaxial stretching to cells. Thickness (100 µm) and transparency of the silicon film allow to perform live cell FA dynamics before and after stretching (Chen et al., 2013). **c,** Equibiaxial cell stretching achieved by placing a thin PDMS membrane on PDMS pillars and applying negative pressure with a pump (Tijore et al., 2018). **d,** PEG-alginate 3D hydrogels allow to stretch cultured cells up to 300% (Hu et al., 2019).

During the course of a normal day, cells and tissues of the human body can experience a vast range of stretching percentages. Thus, the magnitude of stretching is an extremely important aspect to take into account. The nervous system is a representative example; while the brain undergoes 2-5% small-scale stretching during mild activities (e.g. jumping), some nerves can experience local strains of 25-30% during regular limb movements or torsions (Loh et al., 2018; Phillips et al., 2004). Muscles are also deformed at variable amplitudes, with ligaments usually experiencing stretches below 6% (Page, 2012). Stretching magnitudes can be tightly controlled in experimental settings, especially in cell lines, enabling to study several subcellular and cellular responses. For the same cell type, increasing/decreasing magnitude can have different outcomes; higher magnitudes can potentiate the effects, but also lead to opposite behaviors. For instance, cell spreading and polarization are increased at small-scale 3-5% stretching, but decrease when stretching is increased to 15% (Cui et al., 2015). This behavior can reflect specific pathways activated in the cell for more extreme deformations, which are more likely to trigger adverse effects. In neurons, increasing stretches from 25 to 70% lead to progressive impairment of Ca2+ activity (Bianchi et al., 2019). However, the concept of 'extreme deformations' is not to be taken as a synonym of cellular dysfunction. Certain cells undergo extreme deformations as part of their physiological role, such as fibroblasts during wound healing. Here, stretching systems can be tuned for extremely high percentages, such as the 300% stretch used to characterize the hyperelasticity of vimentin filaments (Hu et al., 2019). Differential responses to increasing magnitudes can also be due to the existence of mechanisms with different sensitivity. A previously discussed example consists of the response of epithelial cell monolayers and their nucleus to different stretching percentages. While a 5% stretch triggers chromatin fluidization and nuclear softening, 40% stretch leads to a reorientation of the cell layer in the perpendicular direction to stretch. Although the larger percentage can also modulate chromatin organization, this effect is less pronounced; conversely, small scale 5% stretch fails to emulate the cell reorientation. Conversely, certain mechanisms are not sensitive to stretch magnitudes: the rapid FA growth and slow FA disassembly observed during sustained stretch show no differences between 5 and 10% stretch (Chen et al., 2013).

Choosing a particular magnitude of stretching should also reflect the deformations of the tissue *in vivo*. However, there is a lack of measurements of stretching percentages in live tissues, organs or cells, both in physiological and pathological conditions. A better understanding of this topic would not only provide us with more realistic percentages but also with how they evolve over time. New stretching protocols could be tuned to reflect changes of stretching magnitude experienced by a specific tissue, rather than employing linear increases of stretching.

A deeper molecular understanding of cellular mechanosensing, together with the development of new methods, has given rise to emergent factors controlling the stretching response. Among them, substrate pre-strain has been shown to modulate the response to stretch

(Panzetta et al., 2019). Fibroblasts and osteoblasts cultured in pre-stretched substrates (6 and 9%) displayed higher stiffness than control cells, suggesting that cells can detect the mechanical history of the substrate. Moreover, the increase of stiffness is similar to the one verified in cells cultured in non-stretched substrates and subsequently stretched (Panzetta et al., 2019). Thus, stiffness can change regardless of how deformation occurs. Such studies could be expanded to different cellular types and subcellular structures, as well as to other stretching modalities. Indeed, it is yet unclear whether cyclic stretch or strain rate could modify the sensing of 'substrate history' by cells. The pre-stress of the cell itself can also influence the response; valvular interstitial cells with high pre-stress decrease their traction forces in response to cyclic stretch, whereas cells with low pre-stress display the opposite behavior (Cirka et al., 2016). Again, further research is required for this specific topic; it would be of interest to assess whether geometrical/adhesive constraints (via micropatterning, for instance) could influence these responses.

2. Super-resolution microscopy

Throughout the previous chapters, we have often mentioned how super-resolution microscopy (SRM) techniques have revolutionized our understanding of molecular and cellular biology. They have delivered new insights on the nanoscale organization of IASs and on the correlation of dynamics and protein function. Moreover, they allowed to unveil new macromolecular assemblies such as the MPS. Here, in this chapter, I discuss how super-resolution microscopy managed to cleverly 'trick' a centuries-long barrier in order to image a vast array of subcellular structures and complexes at the nanoscale. I will also approach some of the main SRM techniques used nowadays, with particular incidence for the ones employed in this PhD thesis.

1. Super-resolution microscopy: origin and principles

Fluorescence microscopy has revolutionized biology by allowing us to 'see' the molecular organization, interactions and processes of biological systems. Due to its low invasiveness and sample preservation, fluorescence microscopy allows to study living systems and can image large volumes. Moreover, easy implementation of multichannel imaging allows to visualize interactions and co-localization between different proteins (Sigal et al., 2018). However, for several decades, the spatial resolution of fluorescence microscopy was limited due to the diffraction of light (Abbe, 1873).

1.1. Abbe's diffraction limit and optical imaging resolution

In an optical imaging system, resolution is defined as the smallest distance between two points for which both these points can still be distinguished (Vangindertael et al., 2018). Resolution can be improved through improvements in optics and sample preparation, as well as shorter wavelengths, although biological systems are limited to mid-longer wavelengths in the

visible and near-infrared spectrum. However, a physical limit will always be reached based on the laws of light diffraction, as proposed by the physicist Ernst Abbe in 1873 (Abbe, 1873). Abbe described how an optical microscope will image a radiating point source not into a point, but a spatial distribution of intensity. For any given aperture shape, that distribution is known as the point spread function (PSF), which is the blurred image of a point-like object in 3D. When projected to the image plan, the PSF can be seen as a bright circle (Airy disk) surrounded by alternating dark and bright concentric rings (Airy Pattern), first identified by Airy in 1835 (Airy, 1835). Resolution can thus be defined as the distance between two partially overlapping Airy patterns such that they can still be distinguished as separate entities. Based on these concepts, Abbe proposed the following equation for determining the resolution of an optical imaging system:

$$d = \frac{\lambda}{2NA}$$

Here, d represents the minimum distance between 2 points that can still be resolved, λ the wavelength of the observed light and NA is the numerical aperture of the objective. Assuming a visible light spectrum between 400-750 nm and that the typical NA of an oil immersion objective is usually below 1.5, the lateral resolution will thus be limited to ~200 nm. This limit, also known as Abbe's diffraction limit, still remains unchallenged nowadays, and is even higher in the axial direction (z) (≥500 nm, and often more), since the PSF has an oblong shape. These limitations prevent a detailed observation of subcellular structures (dendritic spines), protein assemblies (nuclear pore complexes), organelles (mitochondria, endosomes) and cytoskeletal assemblies (microtubules, actin filaments), all with dimensions below 200 nm and often separated by only a few tens of nanometers (Jimenez et al., 2020).

1.2. 'Tricking' the Abbe's limit: towards super-resolution microscopy

In 1994, Stefan Hell and Jan Wichmann proposed that stimulated depleted emission microscopy (STED) could overcome the diffraction limit (Hell and Wichmann, 1994). The first practical application would be reported six years later at Stefan Hell's lab, with STED delivering lateral and axial resolutions below the diffraction limit (Klar et al., 2000). In parallel, William Moerner demonstrated in 1997 that GFP mutants demonstrated on/off blinking behavior in their individual fluorescence emission (Dickson et al., 1997). Finally, Eric Betzig, together with Jennifer Lippincott-Schwartz, used this on/off switching of fluorescent proteins to demonstrate photo activation localization microscopy (PALM) for super resolved imaging in biological samples (Betzig et al., 2006). Their combined works gave rise to a whole new field of far field super-resolution microscopy (SRM), also termed nanoscopy, one where the diffraction limit could be bypassed

(but not broken) through a combination of elegant approaches. Delivering resolutions as lower as 10 nm, super-resolution microscopy techniques have unveiled with unprecedented detail the nanoscale organization of cells and proteins. In 2014, Betzig, Hell and Moerner were awarded with the Nobel Prize in Chemistry for the creation of super-resolution microscopy. Importantly, near field SRM – known as scanning near-field optical microscopy (SNOM) - has existed for several decades before the demonstration of SRM in biological systems (Ash and Nicholls, 1972). However, SNOM has mostly been used in materials science and nanotechnology (Wang and Xu, 2015).

Over the last decade and a half, we have witnessed a truly impressive emergence of super-resolution microscopy techniques. This has been well accompanied by new optical systems, innovative computation methods and application to multiple sample types. Underlying the variety of SRM methods, there is a common principle: the ability to distinguish molecules that are closer than the diffraction limit. Depending on the approach, SRM techniques can be broadly divided into two major classes: 1) coordinate-stochastic SRM, or single molecule localization microscopy (SMLM) (Fig. 38a), and 2) coordinate targeted techniques (Fig. 38b) (Sahl et al., 2017). In addition, there are other methods that constitute a class per se, such as structured illumination microscopy (SIM) (Maglione and Sigrist, 2013) and MINFLUX (Balzarotti et al., 2017).

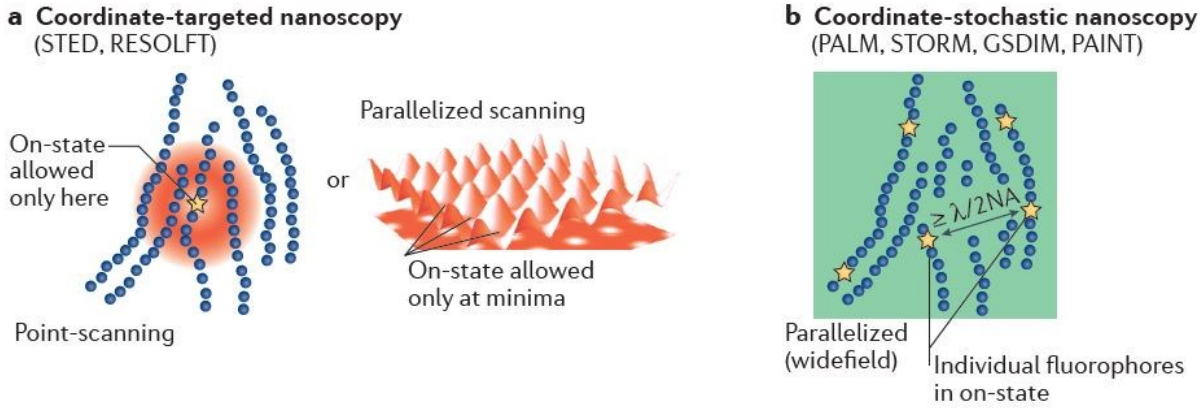

Figure 38: The two major SRM modalities

a, In coordinate-targeted nanoscopy, the sample is scanned with a specific light pattern (doughnut, red) , which is used to switch the fluorophores off while only fluorophores at the intensity minima remain 'on'. Fluorescence is thus confined to a targeted spot of sub-wavelength size. This approach can also be parallelized for higher temporal resolution. **b,** In coordinate-stochastic nanoscopy, which includes photo-activated localization microscopy (PALM), stochastic optical reconstruction microscopy (STORM), ground state depletion with individual molecule return (GSDIM) and points accumulation for imaging in nanoscale topography (PAINT), fluorophores are stochastically converted to the on state, such that only a single fluorophore resides within a diffraction limited volume at a given time. **a-b,** Figure adapted from Sahl, Hell, and Jakobs 2017.

2. Single Molecule Localization Microscopy techniques

The first category consists of coordinate stochastic approaches based on Single Molecule Localization Microscopy (SMLM), which include Stochastic Optical Reconstruction Microscopy (STORM)(Rust et al., 2006), Photoactivated Localization Microscopy (PALM) (Betzig et al., 2006), and Point Accumulation for Imaging in Nanoscale Topography (PAINT) (Sharonov and Hochstrasser, 2006). These techniques stochastically trigger the emission of a subset of fluorescent molecules for every image frame so that only a single fluorophore within the diffraction-limited volume is able to emit. If well isolated, each fluorophore can be localized with high precision. This localization process is repeated for thousands of frames – by stochastically switching on and off new subsets of fluorophores – allowing to reconstruct a final super-resolved image, containing millions of localizations obtained over time (Jimenez et al., 2020). SMLM-based techniques rely on stochastic blinking of specific fluorescent probes: 1) for STORM, organic dyes commonly used for immunolabeling (Rust et al., 2006); 2) for PALM, photactivatable fluorescent proteins (Betzig et al., 2006); 3) for PAINT, dyes or dye-labelled ligands freely diffusing in the imaging medium (Giannone et al., 2010).

2.1. Single particle tracking PALM (sptPALM)

PALM can be combined with Single Particle Tracking (SPT) methods to perform sptPALM SRM acquisitions. The principles of this technique, together with its analysis and different implementations (such as fast sptPALM) are fully explained in a book chapter soon to be published at Methods in Molecular Biology (Springer), intitled 'Single-Protein Tracking to Study Protein Interactions during integrin-based migration'. This book chapter, of which I am a co-author, can be consulted in the Appendix section of this PhD thesis.

2.2. DNA-PAINT

In PAINT, objects are imaged by dyes or dye-conjugated ligands which freely diffuse in the medium and transiently bind the target (Giannone et al., 2010; Sharonov and Hochstrasser, 2006). PAINT is accessible to implement and does not require special photoactivatable dyes such as PALM/STORM, relying only on the diffusive properties of probes to reach the target. The original implementation of PAINT was used to image lipid membranes and artificial vesicles with dyes. However, dynamic information of molecules could not be obtained, and the targeting was based in electrostatic coupling or hydrophobic interactions, limiting the range of biomolecules that could be imaged (Giannone et al., 2010; Sharonov and Hochstrasser, 2006). A second implementation of PAINT allowed to continuously and stochastically label membrane

biomolecules in living cells with fluorescent ligands (such as antibodies), while imaging the samples with oblique illumination (Giannone et al., 2010). Known as universal PAINT (uPAINT), this method delivers super-resolved images and long single-molecule trajectories (up to tens of seconds), enabling to study the dynamics of surface proteins such as AMPARs (Giannone et al., 2010). Despite several improvements to original PAINT, uPAINT still lacks the programmable kinetics of ligand-target interactions (Jungmann et al., 2014).

In 2010, a new PAINT SRM-technique was developed, termed DNA-PAINT (Jungmann et al., 2010). This new approach uses DNA molecules as labelling and imaging probes, known as the docking and imager strands, respectively. The DNA docking strand is fixed to the target via antibodies or chemical tags (e.g Halo or SNAP), while the imager strand is conjugated to an organic dye and diffuses freely in the imaging buffer (Fig. 39a) (Jungmann et al., 2010, 2014; Schnitzbauer et al., 2017). Using organic dyes allows to bypass some of the limitations of photoactivatable dyes/proteins, and gives access to a vast range of fluorophores which are not suitable for other SMLM methods such as STORM or PALM.

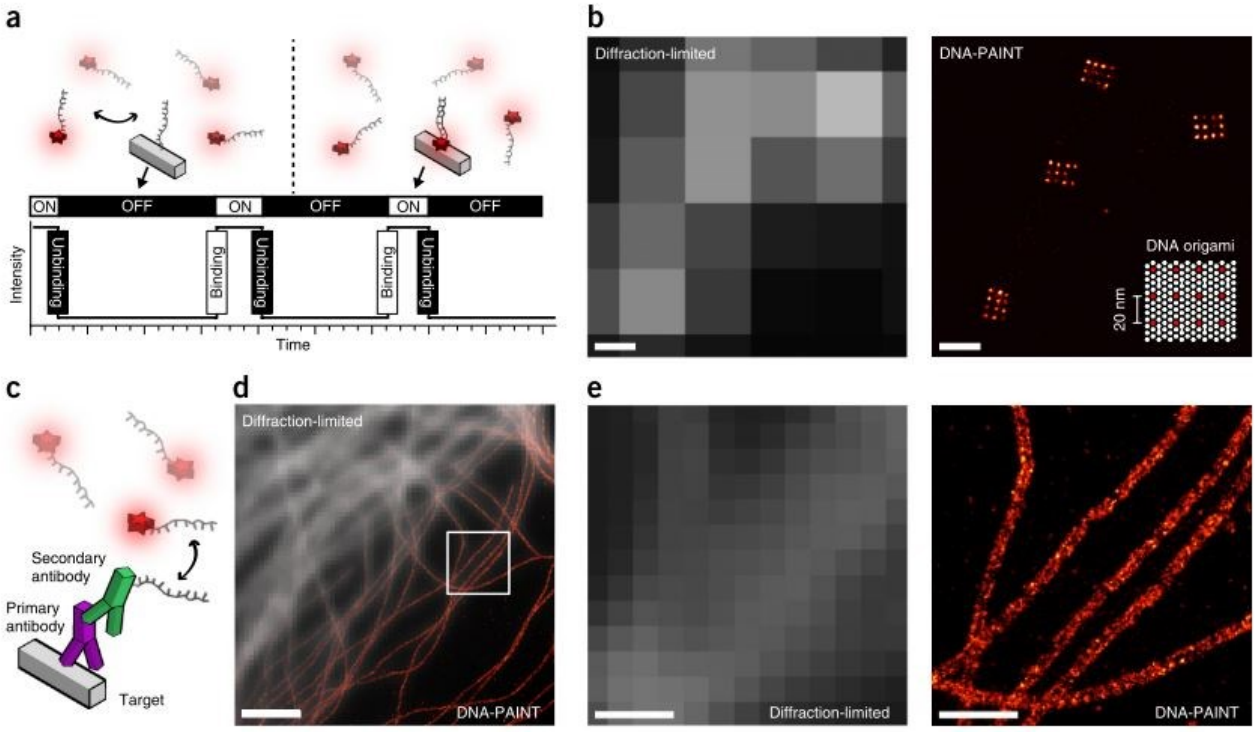

Figure 39: DNA-PAINT SRM imaging

a, Similar to other PAINT techniques, DNA-PAINT relies on the transient binding of probes, here known as 'imager strands'. When they bind the complementary docking strand, this results in a 'blinking' event, as seen by the intensity vs time curve. ON represents the dwell time of the bound state, and OFF the dark time. b, Imaging of 12-docking strand DNA origamis with DNA-PAINT, with diffraction limited image (left)

and DNA-PAINT image (right). **c,** An *in situ* strategy for labelling and imaging target proteins with DNA-PAINT, where the a primary antibody is labelled with a secondary antibody conjugated to a docking strand. **d,** overlay of a diffraction-limited (top left) and DNA-PAINT image (bottom right). **e,** Diffraction-limited (left) and DNA-PAINT image(right) of the region highlighted in **d. a-d,** Figure adapted from Schnitzbauer et al. 2017.

In DNA-PAINT, the imager strand transiently binds to the complementary docking strand, which generates a 'blinking' event (Fig. 39a). Dwell time of the bound state depends only the stability of the DNA conjugate, which can be modulated by changing the G-C content of the strands, temperature or buffer salinity (Schnitzbauer et al., 2017). On the other hand, the frequency of binding events, which depends on the dwell time of the unbound state (or dark time), can be tuned by changing the concentration of imager strand or the hybridization kinetics. Overall, DNA-PAINT allows to control the binding kinetics independently of dye photophysics (Schnitzbauer et al., 2017). This confers it a significant advantage over other SMLM techniques. First of all, precise control of binding kinetics by modulating DNA structure and influx rate enables a high localization precision (Schnitzbauer et al., 2017). First of all, by programming the binding duration, the number of photons detected for a single blinking event is extremely high (Schnitzbauer et al., 2017). Second, the continuous influx of imaging strand, coupled with specific imaging buffers, considerably minimizes the risk of photobleaching, ensuring high photon detection (Jungmann et al., 2014). This allows to achieve considerable improvements in resolution up to ~5 nm, thus approaching the molecular scale (Fig. 39b,d,e) (Jungmann et al., 2014; Schnitzbauer et al., 2017). However, the nonfluorogenic nature of the imager strands – they are fluorescent even when unbound – imposes some limitations on the technique. First of all, it limits DNA-PAINT to optical sectioning methods such as Total Internal Reflection Fluorescence (TIRF), light-sheet or spinning disk confocal microscopy, due to the fluorescent background of non-bound imager strands(Jungmann et al., 2014; Schueder et al., 2017). Second, increasing the imager concentration for faster acquisition speeds directly results in an increase in background fluorescence. Thus, there is an upper threshold for the imager strand concentration required for an optimal signal-to-noise-ratio. This, in turn, limits the acquisition speed of DNA-PAINT imaging, lasting up to 3-4 hours for the highest spatial resolution. To tackle this issue, a recent study has increased 10-fold the speed of DNA-PAINT acquisitions without losing spatial resolution (Schueder et al., 2019). Optimization of the DNA sequences and buffer salinity allowed to minimize the dark time of the imager, thus enhancing acquisition speed without sacrificing spatial resolution (Schueder et al., 2019). Sequence design avoided hairpin formation and was aimed at reducing dark time as much as possible. With new DNA sequences and higher buffer salinity, it was possible to achieve better resolutions at lower imager concentrations for the same target (Schueder et al., 2019).

In addition, DNA-PAINT possesses other important advantages; since the technique does not rely on antibodies or fluorescent proteins to label the samples, it allows for multiplexing through Exchange-PAINT techniques. DNA strands can simply be washed out and replaced with new orthogonal sequences, which can be combined with the same fluorophore (Jungmann et al., 2014). Multiplexing has been extended to 3D by combination with spinning-disk confocal microscopy (Schueder et al., 2017). Finally, the tuning of binding kinetics allows to analyze blinking events without dwelling into dye photophysics; this, together with minimal photobleaching, enables to perform quantitative imaging with DNA-PAINT, known as qPAINT (Jungmann et al., 2016).

Due to all its innovations, DNA-PAINT has been used to image multiple proteins and organelles with nanometer-scale resolution, such as actin filaments, nuclear lamins or mitochondria (Jungmann et al., 2014; Schueder et al., 2019; Strauss et al., 2018). Nonetheless, DNA-PAINT it is mostly limited to fixed samples; introducing DNA strands in live cells could lead to their denaturation and affect the cells (Schnitzbauer et al., 2017). A recent study has found a possible way to counteract this, by using aptamers - RNA oligonucleotides that bind proteins – to perform live labelling of membrane proteins in cells (Strauss et al., 2018). However, further developments are required in this field to fully achieve live cell DNA-PAINT imaging.

3. Coordinate Targeted techniques

The second category consists of targeted light-structuring techniques that switch fluorophores between on and off emission states of at precise spatial coordinates (Sahl et al., 2017; Sigal et al., 2018). The pioneering method in this field was Stimulated Depletion Emission Microscopy (STED) (Hell and Wichmann, 1994). STED was followed by Reversible Saturable Optical Linear Fluorescence Transitions (RESOLFT) (Grotjohann et al., 2011). Both techniques bypass the diffraction limit by coupling a focused excitation beam to a spatially patterned ‘depletion’ beam, typically in a shape of a doughnut, with intense laser in the outer region. Conversely, the intensity is near zero in the center of the doughnut, hence only the fluorophores in this region will emit light, giving rise to super-resolved images. STED relies on an almost instantaneous depletion of emission through stimulated depletion of fluorophores and fluorescent proteins (Klar et al., 2000) (Fig. 40). RESOLFT, on the other hand, uses transitions of photoswitchable proteins and their respective molecular states with longer lifetimes (ms to s) as on and off states (Grotjohann et al., 2011).

3.1. STED: the pioneer SRM

Out of the three main coordinate targeted SRM techniques, STED is the most popular one. STED can be both performed in live and fixed samples and it can be easily implemented in a lab, with commercial configurations that deliver resolutions below 50 nm. However, the high STED laser intensities may lead to cell photo-toxicity or fast photo-bleaching of fluorophores, complicating the acquisition of time-lapses to retrieve dynamical live-cell information (Danzl et al., 2016). There are however cases where STED could be used in live experiments with fluorescent proteins (e.g. GFP, YFP), concerning mostly volume labelling (YFP in neuronal dendritic spines, (Tønnesen et al., 2014)) or proteins that possess fast turnover (paxillin-GFP (Inavalli et al., 2019)). Live STED can also be performed with organic fluorophores that can cross the plasma membrane, such as silicon rhodamine (SiR), which was used to label the actin cytoskeleton or microtubules (D'Este et al., 2015; Lukinavičius et al., 2014). Specific proteins could also be labeled with SiR using for instance SNAP-tagged proteins as used for example for mitochondria live STED imaging (Stephan et al., 2019). Photo-toxicitiy can also be minimized by employing fast resonant scanners and predominant use of far-red depletion and excitation wavelengths (Kilian et al., 2018). Implementations such as RESCue-STED (Staudt et al., 2011) which avoids unnecessary excitation and de-excitation cycles, protected STED (Danzl et al., 2016) using multiple off states, have significantly reduced photobleaching and overall light dosage in STED nanoscopy.

Another emergent advantage of STED is the possibility of performing multiplexing acquisitions. Recent studies have shown how STED can deliver up to four-color nanoscopy in live and fixed samples using a combination of organic dyes (Winter et al., 2017). Moreover, STED with exchange fluorophores has recently been introduced, substantially increasing signal duration with a constant label density. (Spahn et al., 2019). In addition to aforementioned improvements, STED nanoscopy has seen multiple developments in image resolution, contrast, speed, deep tissue imaging etc. (Bergermann et al., 2015; Sarmento et al., 2018; Urban et al., 2011).

STED nanoscopy techniques (and by extension RESOLFT) are often based on single point scanning, which constitutes a drawback for widefield imaging due to long acquisition times. To tackle this, optical lattices have been developed to achieve parallelization of STED nanoscopy (Bergermann et al., 2015; Yang et al., 2014a). Optical lattices consist of artificial crystals of light, created through interference. Similar to atomic lattices, optical lattices contain spatially periodic patterns of electromagnetic fields. In a simplistic representation, optical lattices allow to create multi-arrays of depletion doughnuts, separated by the period of the interference lattice. When applied to STED nanoscopy, optical lattices have enabled faster acquisition, approaching it from video-rate nanoscopy (Bergermann et al., 2015). The same principle has been successfully applied to RESOLFT nanoscopy (Chmyrov et al., 2013).

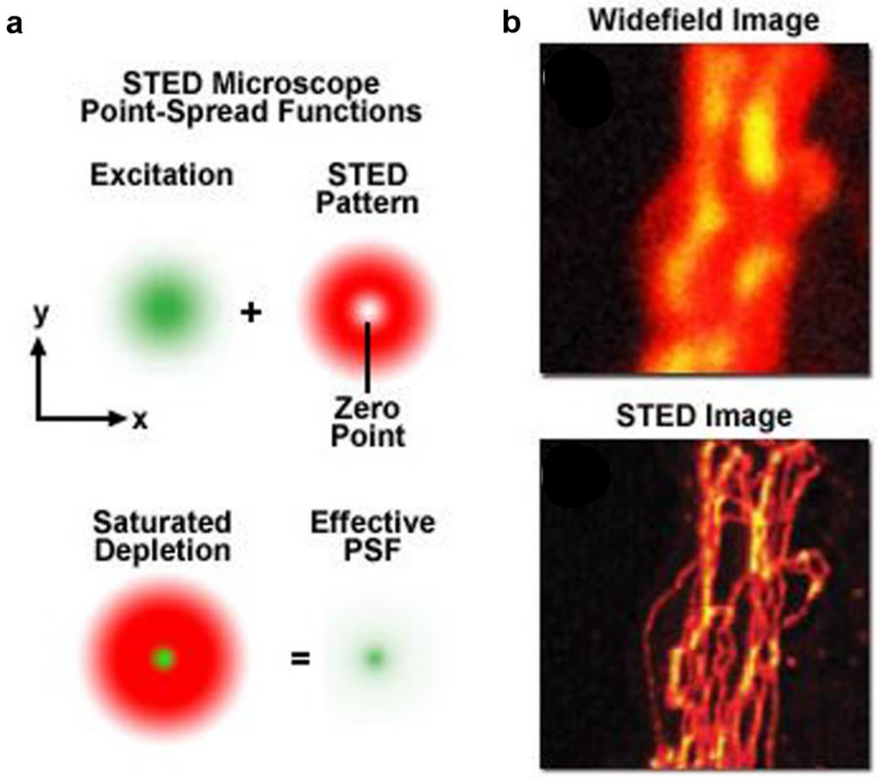

Figure 40: Principle of STED nanoscopy

a, STED uses two synchronized beams for sample illumination: an excitation pulse, which is a Gaussian beam with a diffraction-limited spot size (green), which excites the fluorescent molecules. This is followed by a doughnut-shaped beam as the depletion laser (red), where only at the exact center of focus the intensity is equal to zero. All the excited molecules that are exposed to the doughnut-shaped depletion beam will be switched-off by transferring them back to the ground S0 state. The green laser excitation spot is superimposed on the red STED depletion laser profile, dramatically reducing the size of the effective PSF. **b,** Comparison of widefield (top) and STED (bottom) images of microtubules stained with Alexa Fluor 594 demonstrate the increased spatial resolution afforded by STED. **a-b,** Figure adapted from Zeiss online (zeiss-campus.magnet.fsu.edu/tutorials/superresolution/stedconcept/indexflash.html).

4. Other classes of SRM

4.1. SIM

The third class of SRM methods is structured illumination microscopy (SIM). SIM uses similar illumination patterns compared to lattice-STED and lattice-RESOLFT, consisting of a series of sinusoidal striped patterns of high spatial frequency applied in different orientations. The interaction between the illumination patterns and the sample produces interference patterns named Moiré fringes (Maglione and Sigrist, 2013; Sigal et al., 2018). Unlike STED and RESOLFT, that produce raw images, the information contained in the SIM patterns is processed by

algorithms in order to obtain a final image. SIM delivers higher temporal resolution with lower light magnitudes, but is typically limited with a lateral resolution of ~100-130 nm. However, through saturated structured illumination with specialized photoswitching proteins, a recent SIM implementation has achieved resolutions down to ~50 nm (Li et al., 2015a).

4.2. MINFLUX – a special combination

SMLM and coordinate targeted SRM techniques possess impressive capabilities, which leads to the question: would it be possible to combine both of their strengths? Recently, the concept of MINFLUX nanoscopy was introduced and applied to cell imaging, delivering resolutions of a size of a molecule(Balzarotti et al., 2017; Gwosch et al., 2020). In MINFLUX imaging, the stochastic on-off switching of individual fluorophores is combined with a targeted excitation beam containing an intensity minimum, such as a doughnut, in order to localize the emitter. The position of individual molecules can be inferred with ultra-high precision by triangulating the position from multiple probing (Balzarotti et al., 2017). MINFLUX constitutes a tremendous development in the field of SRM and has achieved resolutions of ~1nm in DNA origamis (Balzarotti et al., 2017). More recently, MINFLUX has been used to image structures in live and fixed cells with resolutions of ~1-3 nm, allowing inclusively both dual-color and 3D imaging (Gwosch et al., 2020).

5. 3D imaging with SRM

The first and simplest implementations of SRM breached the spatial resolution limit imposed by diffraction of light, but only for the lateral resolution. In those same cases, axial resolution was still limited by diffraction, which hinders the observation of cells in their complete 3D nature and organization. For stochastic SMLM techniques, this can be for instance be improved by engineering the point spread function (PSF) to precisely localize in the z axis. This was initially achieved through astigmatism imaging with a single cylindrical lens, and afterwards with a double cylindrical lens; both strategies were applied to STORM (Huang et al., 2008; Xu et al., 2012). Other methods include bifocal plane imaging, self-bending PSF, double-helix PSF and interferometry (Shtengel et al., 2009); the later has been particularly successful for studying 3D organization of mature FAs (Kanchanawong et al., 2010). However, all these 3D SMLM techniques only measured the relative axial position of fluorophores. To tackle this, recent works have combined SMLM with supercritical angle fluorescence (SAF) microscopy (Bourg et al., 2015; Cabriel et al., 2019). Usually, transmitted light is refracted at the sample/glass coverslip interface due to index mismatch. Refracted light is emitted within the critical angle and known as Undercritical Angle Fluoresence (UAF). However, SAF emission also occurs, more precisely when

the distance between the fluorophore and the interface is smaller than the fluorophore wavelength. This emission becomes propagative for fluorophores in the vicinity of the coverslip. By comparing SAF and UAF emission, it is possible to extract the absolute axial position of the fluorophore. The first SAF-SMLM implementation was known as Direct Optical Nanoscopy with Axially Localized Detection (DONALD) and achieved a localization precision of ~15nm in a range of 500nm above the coverslip (Bourg et al., 2015). DONALD was for instance instrumental to unveil the 3D architecture of podosomes (Bouissou et al., 2017). A recent improvement of DONALD, known as Dual-view Astigmatic Imaging with SAF Yield (DAISY), combines SAF-SMLM with astigmatism-based PSF shaping in order to expand the range of imaging to ~1 µm while keeping a localization precision of ~15 nm (Cabriel et al., 2019).

Concerning STED and RESOLFT, 3D super-resolution imaging has been achieved with depletion illumination patterns around the focal point in 3D, using bottle beams (Klar et al., 2000) or 4-Pi microscopy (Schmidt et al., 2008). More recently, a STED commercial configuration has implemented a programmable spatial light modulator (SLM) to create phase patterns, allowing for 3D STED up to 80 um in tissues (Aberrior).

3. A micromechanical cell stretching device compatible with super-resolution microscopy and single protein tracking

Filipe Nunes Vicente, Sophie Massou, Franziska Wetzel, Amine Mehidi, Dan Strehle, Cecile Leduc, Raphaël Voituriez, Olivier Rossier, Pierre, Nassoy and Gregory Giannone

Published at Protocol Exchange , 27 July 2020

A micromechanical cell stretching device compatible with super-resolution microscopy and single protein tracking

Filipe Nunes Vicente
University of Bordeaux, Interdisciplinary Institute for Neuroscience, UMR 5297; CNRS, Interdisciplinary Institute for Neuroscience, UMR 5297

Sophie Massou
University of Bordeaux, Interdisciplinary Institute for Neuroscience, UMR 5297; CNRS, Interdisciplinary Institute for Neuroscience, UMR 5297

Franziska Wetzel
University of Bordeaux, Laboratoire Photonique Numérique et Nanosciences, UMR 5298; Institut d'Optique & CNRS, Laboratoire Photonique Numérique et Nanosciences, UMR 5298

Amine Mehidi
University of Bordeaux, Interdisciplinary Institute for Neuroscience, UMR 5297; CNRS, Interdisciplinary Institute for Neuroscience, UMR 5297

Dan Strehle
University of Bordeaux, Laboratoire Photonique Numérique et Nanosciences, UMR 5298; Institut d'Optique & CNRS, Laboratoire Photonique Numérique et Nanosciences, UMR 5298

Cecile Leduc
Institut Pasteur Paris CNRS UMR 3691

Raphaël Voituriez
University Pierre et Marie Curie, Laboratoire de Physique Théorique de la Matière Condensée, UMR 7600; CNRS, Laboratoire de Physique Théorique de la Matière Condensée, UMR 7600; University Pierre et Marie Curie, Laboratoire Jean Perrin, UMR 8237; CNRS, Laboratoire Jean Perrin, UMR 8237

Olivier Rossier
University of Bordeaux, Interdisciplinary Institute for Neuroscience, UMR 5297; CNRS, Interdisciplinary Institute for Neuroscience, UMR 5297

Pierre, Nassoy
University of Bordeaux, Laboratoire Photonique Numérique et Nanosciences, UMR 5298; Institut d'Optique & CNRS, Laboratoire Photonique Numérique et Nanosciences, UMR 5298

Grégory Giannone (gregory.giannone@u-bordeaux.fr)
University of Bordeaux, Interdisciplinary Institute for Neuroscience, UMR 5297; CNRS, Interdisciplinary Institute for Neuroscience, UMR 5297

Method Article

Keywords: mechanobiology, mechanosensing, focal adhesions, cytoskeleton,cell stretching,super-resolution microscopy, single particle tracking

DOI: https://doi.org/10.21203/rs.3.pex-961/v1

Abstract

Cell mechano-sensing is based on biomolecule deformations and reorganizations, yet the molecular mechanisms are still unclear. Super-resolution microscopy (SRM) and single protein tracking (SPT) techniques reveal the dynamic organization of proteins at the nanoscale. In parallel, stretchable substrates are used to investigate cellular responses to mechanical forces. However, simultaneous combination of SRM/SPT and cell stretching has never been achieved. Here, we present a cell stretching device compatible with SRM and SPT, composed of an ultra-thin Polydimethylsiloxane (PDMS) layer. The PDMS sheet is gliding on a glycerol-lubricated glass cover-slip to ensure flatness during uniaxial stretching, generated with a 3D-printed micromechanical device by a mobile arm connected to a piezoelectric translator. This method enables to obtain super-resolved images of protein reorganization after live stretching, and to monitor single protein deformation and recruitment inside mechanosensitive structures upon stretching. This protocol is related to the publication 'Cell stretching is amplified by active actin remodeling to deform and recruit proteins in mechanosensitive structures', in Nature Cell Biology.

Introduction

Growing evidence demonstrates that macromolecular assemblies driving critical cellular functions are regulated by mechanical forces. However, the exact molecular mechanisms of force-sensing within most macromolecular assemblies in cells are still unknown. Several innovative techniques allow to measure and generate forces on proteins *in vitro* or within cells [1–4], but they cannot probe protein mechanical responses within crowded macromolecular structures inside the cell or confined at the interface with the extracellular environment.

Super-resolution microscopy (SRM) and single protein tracking (SPT) techniques are ideal to study the dynamic organization of proteins at the nanoscale. There are two major classes of SRM: coordinate stochastic based on Single Molecule Localization Microscopy (SMLM: PALM, STORM, PAINT) [5–7]; or coordinate targeted (STED, RESOLFT)[5–7]. SRM and SPT confirmed, together with fluorescent tension-sensors, that proteins could be stretched under mechanical tension[2,8–10] in mechanosensitive structures. In parallel, stretchable substrates of Polydimethylsiloxane (PDMS) have been coupled with optical imaging to investigate cell responses to external forces[1,11,12]. However, the simultaneous combination of SRM or SPT with cell stretching is extremely challenging, since it requires to combine glass-like optical properties with mechanical stability of the imaged plane during substrate deformation.

SMLM/SPT require the optimal signal to noise ratio of single molecules emission to attain the best spatial resolution (typically 10-50 nm)[5–7]. SMLM/SPT techniques are thus ideally performed in the total internal reflection fluorescence (TIRF) or oblique illumination modes using high numerical aperture (NA) short working distance oil immersion objectives matching the index of refraction of glass slides[5–7,13,14]. In addition, SMLM/SPT techniques rely on object reconstruction or tracking from thousands of imaging

planes, which implies perfect mechanical stability of the sample while imaging. This is incompatible with large deformations and displacements of the substrate in the axis (Z) and plane (XY) of observation during stretching.

Similarly, coordinate targeted STED/RESOLFT nanoscopy techniques perform better using high numerical aperture (NA) short working distance oil immersion or glycerol immersion objectives. Compared to SMLM/SPT techniques, STED like techniques will be less sensitive to drift, as they have low pixel dwell times[15,16]. However, mechanical drift stemming from multiple factors (e.g., motorized and piezoelectric stages) can greatly compromise the performance of the STED system, degrading signal-to-noise ratio and spatial resolution[15,16]. Thus, perfect mechanical stability of the sample has to be ensured throughout acquisitions. Once again, this could be incompatible with large XYZ deformations during stretching.

In most commercial configurations, cell stretching is performed using macroscopic devices and images are acquired after fixation, or thick elastomeric substrates are stretched in combination with low NA objectives and upright microscopes[17,18]. These low magnification configurations are quite permissive to slight defocusing [19]. Various custom-made devices could potentially enable simultaneous stretching and live cell imaging [1,11,19–22]. However, they are either limited to low-magnification imaging or are incompatible with continuous automatic focusing during stretching

Here, we present a cell stretching device compatible with SRM and SPT which enables to study the nanoscale reorganizations and deformations of protein assembly or individual proteins inside mechanosensitive structures[23] (Fig. 1a). This device is composed of an ultra-thin Polydimethylsiloxane (PDMS) layer (10 µm) providing glass-like optical properties compatible with SRM and SPT (Fig. 1b,c). To simultaneously enable substrate stretching and ensure flatness upon deformation, this ultra-thin PDMS layer is deposited on a glycerol-lubricated glass cover-slip (Fig. 1b,c). Glycerol allows the deformable substrate to float freely while avoiding PDMS adhesion and refractive index mismatch. A drop of glycerol is sandwiched between the plasma cleaned PDMS sheet and glass coverslip forming a glycerol layer of ~ 0.7 µm in thickness (Fig. 1c) To manipulate the thin PDMS substrate and avoid any distortions along the optical path, the size of the observation chamber is kept as small as possible (~9 mm2 (Fig. 1b)), and its mechanical stability is reinforced by adding a thicker (40 µm) Gel-Pak frame on top of the thin PDMS sheet (Fig. 1c). To generate uniaxial stretches on the glass-PDMS assembly, we design a 3D-printed micro-device (Fig. 1a,b). The micromechanical device consists of a fixed (holding) arm and a mobile (stretching) arm, connected to a piezo motor, positioned on opposite sides of the observation chamber on the PDMS frame (Fig. 1a,b). A clamp fixes the glass-PDMS slide to the base of the device and to the holding arm (Fig. 1a). The observation chamber or the whole microchip can be filled with culture or observation medium.

Our micromechanical stretching device is compatible with the two major classes of SRM: coordinate stochastic (e.g. PALM, STORM, PAINT) and coordinate targeted (e.g. STED)[5–7,24] (Fig.2). Experiments can

be divided into two main approaches: 1) live stretching and SRM/SPT imaging in live cells (Fig. 2a-c) and 2) live stretching followed by rapid fixation, labelling and SRM imaging (Fig.2d,e).

Concerning the first approach, we can perform SPT acquisitions in cells before and after large (10-50%) or small (2-5%) stretches to study the effect of external stress on protein dynamics and diffusive properties (Fig. 2a). In addition, we can also perform simultaneous live cell stretching (2-5%) and SPT to study acute mechanical response of individual proteins: 1) force-dependent protein unfolding or deformations (Fig. 2b); or 2) force-dependent protein recruitments and reorganizations. Finally, the device can also be used to acquire STED SRM images of live cells that experience stretching (Fig. 2c). Regarding the second approach, the device can be used to perform SRM (e.g. DNA-PAINT, STED, STORM) in fixed cells after live stretching (2-50 %) followed by rapid fixation and labelling for SRM (Fig. 2d,e).

Reagents

Reagents for assembling the micromechanical device

- PDMS (Sylgard 184, Samaro, Cat. No. DE9330)
- PF film XO 1.5 mil (Gel-Pak®)
- Glycerol for fluorescence microscopy (Merck, Cat. No. 1040950250)
- Resin for Stereolitography (SLA) 3D printing. We recommend Grey Pro resin (Formlabs)
- Dow Corning™ High-Vacuum Grease (Fisher Scientific, Cat. No. 14-635-5D)

Reagents for cell culture, sample preparation and imaging

- DMEM High Glucose with Sodium Pyruvate (Biowest, Cat. No.L01606)
- Fetal bovine serum (FBS, Eurobio, Cat. No. CVFSVF00-01)
- GlutaMAX (GIBCO, Cat. No. 35050038)
- Penicillin–Streptomycin (GIBCO, Cat. No. 15140-122)
- HEPES (GIBCO, Cat. No. 15630-056).
- Trypsin (GIBCO, Cat. No. 25300-054)
- Soybean trypsin inhibitor (Sigma, Cat. No. T9003-1G)

· NaCl (Sigma-Aldrich, Cat. No. S5886-5KG)

· KCl (Sigma-Aldrich, Cat. No. P5405-1KG)

· $MgCl_2$ (Sigma-Aldrich, Cat. No. M4880-100G)

· Glucose (Sigma-Aldrich, Cat. No. G7021-1KG)

· Fibronectin (Sigma-Aldrich, Cat. No. 10838039001)

· Phosphate-buffered saline (PBS), pH 7.4

· Nucleofector™ transfection kit for MEF-1 (Lonza, Cat. No. VPD-1004)

· 0.1 µm fluorescent beads (TetraSpeck™ Microspheres, 0.1 µm, ThermoFisher, Cat. No. T7279)

· 90 nm Stabilized Gold Nanoparticles (Cytodiagnostics, CG-90-500)

· Paraformaldehyde, 16% aquous solution (Sigma, Cat. No. P6148)

· Glutaraldehyde, 10% aquous solution (Fisher Scientific, Cat. No. 50-262-01)

Solutions for cell culture, sample preparation and imaging

· Cell culture medium: DMEM High Glucose with Sodium Pyruvate, supplemented with 10% FBS , 2 mM GlutaMAX, 100 U/ml penicillin–streptomycin and 15 mM HEPES.

· Trypsin inactivation medium: DMEM High Glucose with Sodium Pyruvate, 1 mg/ml soybean trypsin inhibitor, 2 mM GlutaMAX, 100 U/ml penicillin–streptomycin, 15 mM HEPES Trypsin inhibitor.

· Ringer solution: 150 mM NaCl, 5 mM KCl, 2 mM CaCl2, 2 mM MgCl2, 10 mM HEPES ,11 mM glucose at pH 7.4.

· Buffer C: 1× PBS at pH 7.2 supplemented with additional 500 mM NaCl, and it can be stored at RT for up to 6 months[24].

Equipment

· Silicon wafers CZ , 4" thickness 525 µm type/dopant , n-P, resistance 10-20 ohm.cm, 1 polished side, Ra < 0.5 nm (Neyco, Cat. No. WAS4P1020)

· Spin Coater SPIN150i-PTFE (SPS Europe, Cat. No. 42024)

· Graphtec cutting plotter (Graphtec Craft ROBO pro, CE5000-40-CRP)

· Heating and drying lab oven

· Glass coverslips no. 1.5H 24x40 mm (Marienfeld, Cat. No. 0107242)

· Expanded plasma cleaner PDC-002 (Harrick Plasma, Cat. No. PDC-002-(230V)) with PlasmaFlo gas mixer (Harrick Plasma, Cat. No. PDC-FMG-2 (230V))

· 3D printer: We recommend the Form series (Form 2 or 3, Formlabs), for SLA 3D printing

· Piezoelectric motor (M-663 Linear Positioning Stage, 19 mm, Linear Encoder, 0.1 µm resolution, PI)

· CharlyRobot 3D milling machine (Mécanumériс)

· Poly(methyl methacrylate) (PMMA) plates (Evonik)

· M3 screws, 20 cm (RS, Cat. No. 849-423)

· Inverted confocal microscope (Leica SP8 WLL2) equipped with a HC PL APO CS2 motCORR 93X Glycerol, NA 1.3 objective. The confocal microscope is equipped of a white light laser 2 (WLL2) with freely tunable excitation from 470 to 670 nm (1 nm steps) and is also equipped with a STED module tunable to STED microscopy. STED module is equipped with 3 depletion lasers: 592 nm, 660 nm and 775 nm.

· Inverted motorized microscope (Nikon Ti) equipped with a CFI Apo TIRF 100x oil, NA 1.49 objective and a perfect focus system PFS-2. Microscope is equipped with 4 continuous wave (cw) lasers (405 nm, 488 nm, 561 nm, 643 nm).

· Nucleofector™ 2b device (Lonza, Cat. No. AAB-1001)

· 37 °C incubator with humidified air containing 5% CO2

· Softwares:

o Computer-Assisted Design (CAD) software, such as Inventor (Autodesk) or open source versions (FreeCAD)

o PreForm (Formlabs)

o Metamorph (Molecular Devices)

o Leica Application Suite X (Leica Microsystems)

o PI Mikro Motor (Physik Instrumente)

Procedure

Fabricating a 10 µm PDMS elastic substrate

1. Using the Graphtec Cutting Plotter, pre-cut an elastomer Gel-Pak frame (40 µm) to the size of the glass coverslip with a squared (3x3 mm) observation chamber.

a. Note: Layout for cutting can be drawn on the software provided by the company or using a plug-in for Adobe Illustrator® and CorelDraw®.

2. Mix PDMS and curing agent in a 10:1 ratio.

3. Centrifuge for 5 min at 2500 rpm to remove air bubbles

4. Spin the PDMS on a silicon wafer to a final thickness of 10 µm.

5. Pre-cure the PDMS for 25 min at 70°C

6. Place the pre-cut Gel-Pak frame in contact with the 10 µm PDMS

7. Curate the whole assembly overnight at 70°C

8. Cut around the Gel-Pak frame with a blunt pair of and gently detach the PDMS substrate from the wafer.

Assembling the micromechanical device

Glass-PDMS assembly

1. Plasma clean 24x40 mm glass coverslips.

2. Spin coat each slide with glycerol to form a uniform glycerol layer of ~0.7 µm thickness.

3. Plasma clean the PDMS substrate for 1 minute, on the side that will glide on the glycerol layer.

4. Immediately after, lay the PDMS substrate onto the glycerol-coated coverslip.

Printing the 3D micro-device

1. Design the fixed (holding) arm, the mobile (stretching) arm and the clamp composing the device on a CAD software.

a. **Note:** For experiments that require sustained stretching after fixation, the design of the holding arm is modified to include a threaded hole, while the stretching arm is enlarged to include two grooves. Two screws allow to clamp the stretching arm onto the holding arm and sustain the stretching.

2. Export the files (.obj or any 3D printing compatible format) and upload them onto PreForm software. Layer thickness should be intermediate or small to avoid imperfections in the final structure. As for the resin, we recommend using Grey Pro resin because it offers high precision, moderate elongation, and low creep (https://formlabs.com/eu/materials/engineering/#grey-pro-resinGrey Pro Resin). This material is ideal for concept modeling and functional prototyping, especially for parts that will be handled repeatedly.

a. **Note:** Ensure that the support material is correctly placed to avoid collapsing of the piece during the printing process.

3. After finishing the printing, wash and cure the pieces according to the requirements of the resin. 3D-printed micro devices can be re-used several times, especially if they are composed of a resin conceived for engineering.

a. **Note:** Although we use SLA 3D printing for our micro-devices, we have also tested 3D micro-devices printed with fused deposition modelling (FDM). It requires polylactic acid (PLA) filaments and it can be easily implemented in a lab, besides having shorter printing times. However, we found that the devices are less resistant and less durable than the ones printed with SLA.

Attaching glass-PDMS assembly to 3D-printed micro-device

1. Cut glass coverslips in small parts with high precision knife.

2. Using superglue or Dow Corning™ High-Vacuum Grease, attach small glass parts to holding and stretching arm.

3. Stick double sided tape to the glass parts on the holding and stretching arm.

4. Place the glass-PDMS assembly inside the clamp and attach them to the holding arm

5. Attach the stretching arm to the glass-PDMS assembly using double-sided tape.

-

Cell preparation

Cell electroporation (24 to 48h before imaging)

Actively dividing immortalized MEFs are cultured in DMEM supplemented medium (see solutions for cell culture) in 75 cm2 flasks.

1. Detach cells with trypsin/EDTA solution (1.5 mL). Inactivate trypsin immediately after detachment by adding serum-containing DMEM (5 ml). Count cells and adjust cell suspension volume to keep 1–2 million cells per tube per experimental condition.

2. Centrifuge cells at 300 × g for 5 min

3. Resuspend the cell pellet in transfection reagent and mix with the DNA plasmids.

a. **Note:** For sptPALM experiments, cells are usually co-transfected with DNAs encoding for the protein of interest, (3–5 µg per condition, e.g., Talin-C-tdEos), and for a GFP-coupled reporter of the structure of interest (1–2 µg per condition, e.g., GFP-paxillin for adhesive structures).

b. **Note:** For STED experiments, if necessary, cells are transfected with a GFP-coupled reporter of the structure of interest (1–2 µg per condition, e.g., tubulin-GFP for microtubules). Presence of a GFP-coupled reporter is only required for low-resolution images of the cells before and after stretching, especially when performing large stretches (e.g. , 30%)

c. **Note:** For DNA-PAINT microscopy, vimentin-Halo can be visualized with Cy3B-labelled DNA imager strands, added to the stretching chamber at variable concentrations (2-5 nM), as previously described [24].

4. For all cases, electroporate the cells with the Nucleofector™ 2b Device using the MEF T-020 program (Lonza Nucleofactor protocol)

5. After electroporation, replate the cells in a 6-well plate (about 0.3 million cells/well) in preheated culture medium and place them in a 37 °C incubator with humidified air containing 5% CO2

Coating the micromechanical stretching device (same day of the experiment)

1. Cover the micromechanical device with 10 µg/ml fibronectin solution (500-750 µl per device) and incubate at 37 °C for 1 to 1.5 hours.

2. Discard the fibronectin solution and wash 4-5 times with PBS.

Sample preparation

1. Wash cells twice with PBS after removing the culture medium

2. Incubate with trypsin–EDTA solution (0.3 ml per well) for 1–3 min at 37 °C for detaching cells.

3. Inactivate trypsin with trypsin inactivation medium (1 ml per well) and count the cells (use any conventional cell counting method).

4. Centrifuge at 300 ×g for 5 min and resuspend cells in warm Ringer medium (1–2 ml). Allow cells to recover for 20-30 min inside the incubator at 37 °C with 5% CO2

5. Spread the cells on the device under a density of 70000-80000 cells per device.

-

Mounting the stretching device for live stretching or large stretches followed by rapid fixation

The following steps are common for mounting and preparing the micromechanical device for stretching experiments in live cells or fixed cells combined with super resolution microscopy and single protein tracking.

1. Prepare a 1:500 solution of TetraSpeck™ 0.1 µm fluorescent beads in warm Ringer solution and add 200-300 µL to each device to adsorb fluorescent beads on the substrate.

2. Mount the piezoelectric motor on a custom holder adapted to the microscope stage. Then, mount the holder on the microscope.

a. **Note:** Custom-made holders should be designed according to specific stage dimensions and can be either 3D-printed or 3D-milled. In this case, we have 3D-milled a PMMA holder for mounting our device on the motorized stage, since 3D-milled parts are often more resistant.

3. Connect the piezoelectric motor controller and launch the PI Mikro Motor software.

4. Mount the micromechanical device on the stage-adapted holder.

5. Attach the stretching arm to the linear stage with a screw

6. Adjust focus to the 3x3 mm observation 10 µm PDMS chamber.

7. Before acquiring any cells, test whether the device is working properly and define parameters for specific stretching percentages. For that, select a region with a good density of fluorescent beads and acquire a snapshot. Measure the distance between two beads in the same horizontal axis (D_{before}). Apply a test stretching by displacing the linear stage of the piezoelectric motor while keeping the same region in focus, either manually or with a custom-written Metamorph routine. Take another snapshot after the stretching and measure again the distance between the same two beads (D_{after}). If D_{after} is larger than D_{before}, then the device is working properly. After that, cell stretching can be performed.

a. **Note:** Stretching percentage is calculated by

, a formula which can be applied for all stretching experiments in order to determine stretching percentage.

b. **Note:** By knowing the displacement and the percentage for the test stretching, it is possible to determine with reasonable precision the necessary displacement to obtain a desired stretching percentage when performing actual cell stretching.

c. **Note:** Step size and speed of motor displacement should be kept consistent throughout all acquisitions.

Live cell stretching combined with super-resolution microscopy and single protein tracking

Stretching and live sptPALM

Cells are imaged at 37°C in the micromechanical device. Here, an inverted motorized microscope (Nikon Ti) was used, equipped with a CFI Apo TIRF 100x oil, NA 1.49 objective and a perfect focus system PFS-2), allowing long acquisition in TIRF illumination mode. For photoactivation localization microscopy, cells expressing mEos2/tdEos tagged constructs were photoactivated using a 405 nm laser (Omicron) and the resulting photoconverted single molecule fluorescence was excited with a 561 nm laser (Cobolt Jive). Both lasers illuminated the sample simultaneously. Their respective power was adjusted to keep the number of the stochastically activated molecules constant and well separated during the acquisition. Fluorescence was collected by the combination of a dichroic and emission filters (dichroic: Di01-R561, emission: FF01-617/73, Semrock) and a sensitive EMCCD (electron-multiplying charge-coupled device, Evolve, Photometric). The acquisition was steered by Metamorph software (Molecular Devices) in streaming mode at 50 Hz. GFP-paxillin was imaged using a conventional GFP filter cube (excitation: FF01-472/30, dichroic: FF-495Di02, emission: FF02-520/28, Semrock).

1. For simultaneous stretching and sptPALM with trapeze like patterns: select a cell and launch a PALM acquisition at high frequency (50 Hz) for the entire field of observation. The duration of the acquisition should comprise the entire trapeze pattern (at least 2500 frames).

2. Several hundred frames after, stretch by displacing the linear stage of the piezoelectric motor. Maintain the cell in the field of observation by compensating for XY displacements using manual repositioning (Nikon stage steered by a joystick) or automated stage repositioning (custom plugin developed in Metamorph). After the stretching has stopped, allow the plateau phase to last for 8-12 seconds before relaxation.

a. **Note:** When looking at focal adhesions (FAs), select cells with most of their FAs aligned almost parallel to the stretching axis in the field of observation.

b. **Note:** Imaging cells closer to the holding arm requires smaller XY repositioning while allowing to reach 6 % stretching.

1. For sequential large stretching and sptPALM (Before vs After): select a cell and, after acquiring an image of the GFP reporter, launch a PALM acquisition at high frequency (50 Hz) for the entire field of observation throughout 4000 frames.

2. Perform large stretching (10-50%) while following the cell displacement with the combination of a dichroic and emission filters (dichroic: Di01-R561, emission: FF01-617/73, Semrock). After stretching is finished, acquire an image of the GFP reporter (to have a perspective of the morphological changes) and launch another sptPALM acquisition.

Stretching and live STED

Cells are imaged at 37°C in the micromechanical device. Here, an inverted confocal microscope (Leica SP8 WLL2) was used, equipped with a HC PL APO CS2 motCORR 93X Glycerol, NA 1.3 objective. The confocal microscope was equipped of a white light laser 2 (WLL2) with freely tuneable excitation from 470 to 670 nm (1 nm steps). Scanning was done using a conventional scanner (10Hz to 1800 Hz). The confocal microscope was equipped with the STED module tunable to STED microscopy. A two-dimensional (2D) STED donut was generated using a vortex phase plate. This STED microscope was equipped with 3 depletion lasers: 592 nm, 660 nm and 775 nm For STED microscopy, cells were imaged with a combination of a WLL2 laser and a 775 nm depletion laser. Fluorescence was collected with an internal hybrid detector. The acquisition was steered by LASX Software (Leica).

1. Perform live labelling of the target protein on the micromechanical device. For actin or tubulin labelling, use SiR-Actin or SiR-Tubulin compounds, according to previous studies and manufacturer's instructions [25].

2. After the labelling, wash the staining solution and incubate the device in warm Ringer solution until the experiment.

3. After bead incubation and mounting of the sample as previously described, select a cell and acquire a confocal image followed by a STED image on a sub region of the cell (pixel size has to be inferior to 20 µm).

4. Stretch the cell according to the desired percentage (e.g. 4 or 30%) and maintain the cell on the field of observation by observation by compensating for XY displacements using manual repositioning (Leica stage steered by a joystick)

5. After stretching, acquire a new confocal image followed by a STED image for the same sub region.

-

Super-resolution microscopy in fixed cells with large stretches

The following steps are required to perform large and sustained stretching followed by rapid cell fixation.

1. Warm 4% PFA with 0.25% Glutaraldehyde at 37°C.

2. After mounting the micromechanical device on the microscope, acquire several low resolution images of GFP markers for different cells.

3. Remove the entire module (device and motor in the stage-adapted holder) and stretch the cells outside the microscope. Immediately after stretching, remove the Ringer solution and fix the cells in warm 4% PFA with 0.25% Glutaraldehyde.

4. After fixation, rinse 3-4X with PBS.

5. Clamp the stretching arm to the holding arm using the thread and groove system and two M3 screws. Afterwards, remove the screw that connects the stretching arm to the motor. With this, stretching is sustained throughout all the subsequent labelling steps and super-resolution imaging.

6. Label target proteins according to the imaging technique.

7. After labelling, and before performing super-resolution imaging, acquire again several low resolution images of GFP markers for the same cells.

DNA- PAINT on fixed cells with large stretches

Cells are imaged at 25°C in Buffer C in the same microscope used for live sptPALM. Cy3B-labelled strands were visualized with a 561 nm laser (Cobolt Jive). Fluorescence was collected by the combination of a dichroic and emission filters (dichroic: Di01-R561, emission: FF01-617/73, Semrock) and a sensitive sCMOS (scientific CMOS, ORCA-Flash4.0, Hammatasu). The acquisition was steered by Metamorph software (Molecular Devices) in streaming mode at 6.7 Hz. Vimentin-GFP was imaged using a conventional GFP filter cube (excitation: FF01-472/30, dichroic: FF-495Di02, emission: FF02-520/28, Semrock). Super-resolution DNA-PAINT reconstruction and drift correction were carried out as described before, using the software package Picasso [24].

1. Dilute the desired imager strand in Buffer C. For instance, Vimentin-Halo was visualized with Cy3B-labelled DNA imager strands.

2. Incubate the micromechanical device with 200-300 µL of 90 nm gold nanoparticles, diluted in PBS with a 1:5 ratio, for 15 min at RT. Gold nanoparticles serve as fiducial markers

3. Wash 3X with PBS and 1X with Buffer C.

4. Add imager strands to the stretching chamber until reaching the ideal density of blinking events. Vimentin-Halo was visualized with Cy3B-labelled DNA imager strands, added to the stretching chamber at variable concentrations (2-5 nM), as previously described [24].

STED on fixed cells with large stretches

Cells are imaged at 25°C in PBS 1X in the same microscope used for live STED, with the same combination of a WLL2 laser and a 775 nm depletion laser.

Troubleshooting

Autofluorescence of the medium inside the micromechanical device

This is likely caused by the 3D-printed micro-device itself. Since resins used for SLA are photoactivable at UV light, they can also be excited by the 405 nm laser used for sptPALM. Detachment of particles from the 3D-printed micro-device will therefore be visible and might interfere with the mEos /tdEos signal. There is no clear information about fluorescence of different SLA resins so, if autofluorescence persists, two possibilities exist. First, the entire holding arm can be covered with Dow Corning™ High-Vacuum Grease, which prevents release of autofluorescent particles. Alternatively, other resins can be tested, such as Black (Formlabs).

PDMS is not stretched

Case 1: During PDMS elastic substrate production, air bubbles formed when Gel-Pak frame was brought in contact with 10 µm PDMS layer on the silicon wafer. Usually this will generate irregularities in the substrate which, if close to the 3x3 mm observation chamber, will affect the stretching.

Case 2: Glycerol coating was incomplete and thus PDMS adhered to the glass.

Case 3: Plasma cleaning of PDMS elastic substrate was not effective (either too long or too short) and thus PDMS is not gliding on glycerol.

Case 4: Stretching arm was not properly attached to the glass-PDMS assembly

Sustained stretching causes the micromechanical device to rupture or leak

The groove and thread system is still rather preliminary and requires further optimization, since it causes pressure on the micro-device, leading to leakage of liquid from inside of the device. Different designing strategies can be developed to sustain stretching, such as two 3D-printed clamps from the side and an adjustable screw in the middle, or simply a 3D-printed rod that blocks the recoil of the arm.

Time Taken

Before experiment:

· Printing one 3D micro-device (holding and stretching arm) : 4 hours

o **Note:** Since 3D micro-devices can be re-used several times, it is more efficient to dedicate a full week to 3D printing in order to have a substantial amount of devices for all experiments.

For experiments:

Day 1

· Preparing the PDMS elastic substrate: 2 hours for 20 substrates

Day 2 and 3

· Cell preparation: 1 or 2 days

Day 3

· Assembling the glass-PDMS ‘sandwich’: 3 hours for 20 substrates

· Assembling the complete micromechanical device: 1 day

Day 4

· Coating the micromechanical device and cell seeding: 3 hours

Anticipated Results

1. Fabricating a 10 µm PDMS elastic substrate

Make sure GelPak frame is placed without air bubbles and that PDMS should be detached carefully after curing overnight. If the elastic substrate is properly made, no air bubbles or irregularities should be visible, especially around the observation chamber.

2. Assembling the micromechanical device

Successful PDMS gliding on glycerol layer can be observed later in the microscope during stretching, by calculating the actual displacement after a test stretching. The device will be properly fully assembled if no medium is leaking from the chamber and the arm remains well attached throughout all subsequent steps.

3. Cell preparation

If the device is well coated and cells are viable after electroporation, detachment and seeding, they should start to spread briefly after seeding. 1h later, spread cells should be visible in the observation chamber of 3x3 µm.

4. Preparing the stretching device for live stretching or large stretches followed by rapid fixation

Bead incubation can be quickly confirmed using GFP filter cube. Successful stretching and viability of the device can be confirmed by performing a test stretch and assessing that the same two beads are more distant between each other after stretching. If the device is assembled correctly, stretches closer to the holding arm will produce smaller displacements.

5. Live cell stretching combined with super-resolution microscopy and single protein tracking

Successful combination of live sptPALM or STED with stretching is achieved if 1) focus is maintained throughout stretching, 2) Live XYZ repositioning is possible throughout stretching and 3) quality of either the single-molecule signal or the STED effect is assured throughout the entire acquisition.

6. Super-resolution microscopy in fixed cells with large stretches

Sustaining the stretching after fixation can be verified immediately after fixation by assessing morphology of the 3x3 chamber on a bench top microscope. If the chamber remains deformed, stretching is maintained. This can also be confirmed when imaging the sample after labelling, by re-measuring the distance between the same two beads used to test the stretching before fixation. For DNA-PAINT acquisitions to be successful, drift correction is a key aspect and has to be ensured.

References

1. Goldyn, A. M., Rioja, B. A., Spatz, J. P., Ballestrem, C. & Kemkemer, R. Force-induced cell polarisation is linked to RhoA-driven microtubule-independent focal-adhesion sliding. *J Cell Sci* **122**, 3644–3651 (2009).

2. Grashoff, C. *et al.* Measuring mechanical tension across vinculin reveals regulation of focal adhesion dynamics. *Nature* **466**, 263–266 (2010).

3. Polacheck, W. J. & Chen, C. S. Measuring cell-generated forces: A guide to the available tools. *Nat. Methods* **13**, 415–423 (2016).

4. Iskratsch, T., Wolfenson, H. & Sheetz, M. P. Appreciating force and shape — the rise of mechanotransduction in cell biology. *Nat. Rev. Mol. Cell Biol.* **15**, 825–833 (2014).

5. Liu, Z., Lavis, L. D. & Betzig, E. Imaging Live-Cell Dynamics and Structure at the Single-Molecule Level. *Mol. Cell* **58**, 644–659 (2015).

6. Sahl, S. J., Hell, S. W. & Jakobs, S. Fluorescence nanoscopy in cell biology. *Nat. Rev. Mol. Cell Biol.* **18**, 685–701 (2017).

7. Huang, B., Bates, M. & Zhuang, X. Super-resolution fluorescence microscopy. *Annu Rev Biochem* **78**, 993–1016 (2009).

8. Kanchanawong, P. *et al.* Nanoscale architecture of integrin-based cell adhesions. *Nature* **468**, 580–4 (2010).

9. Morimatsu, M., Mekhdjian, A. H., Adhikari, A. S. & Dunn, A. R. Molecular tension sensors report forces generated by single integrin molecules in living cells. *Nano Lett.* **13**, 3985–9 (2013).

10. Stabley, D. R., Jurchenko, C., Marshall, S. S. & Salaita, K. S. Visualizing mechanical tension across membrane receptors with a fluorescent sensor. *Nat Methods* **9**, 64–67 (2011).

11. Sinha, B. *et al.* Cells respond to mechanical stress by rapid disassembly of caveolae. *Cell* **144**, 402–413 (2011).

12. Chen, Y., Pasapera, A. M., Koretsky, A. P. & Waterman, C. M. Orientation-specific responses to sustained uniaxial stretching in focal adhesion growth and turnover. *Proc. Natl. Acad. Sci. U. S. A.* **110**, E2352-61 (2013).

13. Giannone, G. *et al.* Dynamic superresolution imaging of endogenous proteins on living cells at ultra-high density. *Biophys J* **99**, 1303–1310 (2010).

14. Rossier, O. *et al.* Integrins β1 and β3 exhibit distinct dynamic nanoscale organizations inside focal adhesions. *Nat. Cell Biol.* **14**, 1057–1067 (2012).

15. Vangindertael, J. *et al.* An introduction to optical super-resolution microscopy for the adventurous biologist. *Methods and Applications in Fluorescence* (2018). doi:10.1088/2050-6120/aaae0c

16. Vicidomini, G., Bianchini, P. & Diaspro, A. STED super-resolved microscopy. *Nature Methods* (2018). doi:10.1038/nmeth.4593

17. Sawada, Y. & Sheetz, M. P. Force transduction by Triton cytoskeletons. *J Cell Biol* **156**, 609–615 (2002).

18. Giannone, G., Jiang, G., Sutton, D. H., Critchley, D. R. & Sheetz, M. P. Talin1 is critical for force-dependent reinforcement of initial integrin-cytoskeleton bonds but not tyrosine kinase activation. *J. Cell Biol.* **163**, 409–419 (2003).

19. Jungbauer, S., Gao, H., Spatz, J. P. & Kemkemer, R. Two characteristic regimes in frequency-dependent dynamic reorientation of fibroblasts on cyclically stretched substrates. *Biophys J* **95**, 3470–3478 (2008).

20. Kosmalska, A. J. *et al.* Physical principles of membrane remodelling during cell mechanoadaptation. *Nat. Commun.* **6**, 7292 (2015).

21. Wang, D. *et al.* Tissue-specific mechanical and geometrical control of cell viability and actin cytoskeleton alignment. *Sci. Rep.* **4**, 6160 (2014).

22. Camelliti, P., Gallagher, J. O., Kohl, P. & McCulloch, A. D. Micropatterned cell cultures on elastic membranes as an in vitro model of myocardium. *Nat. Protoc.* **1**, 1379–1391 (2006).

23. Massou, S. *et al.* Cell stretching is amplified by active actin remodeling to deform and recruit proteins in mechanosensitive structures. *Nat. Cell Biol.* (2020).

24. Schnitzbauer, J., Strauss, M. T., Schlichthaerle, T., Schueder, F. & Jungmann, R. Super-resolution microscopy with DNA-PAINT. *Nat. Protoc.* **12**, 1198–1228 (2017).

25. Lukinavičius, G. *et al.* Fluorogenic probes for live-cell imaging of the cytoskeleton. *Nat. Methods* **11**, 731–733 (2014).

Acknowledgements

We thank Z. Karatas, M. Fabre, R. Sterling, J. Carrere for technical assistance; T. Orré for helpful discussions. C. Poujol, S. Marais (Bordeaux Imaging Center, BIC) for technical help; F. Cordelières. (BIC) for support in kymograph analysis (Kymo Tool Box). We thank J. B. Sibarita (IINS, Bordeaux, France) for his support in sptPALM analysis; V. Studer (IINS, Bordeaux, France) and P.O. Strale (alvéole) for important discussions on microfabrication; M. Cabilic (IINS, Bordeaux, France) for the repositioning plugin developed in Metamorph; T. Schlichthärle, L. Fischer, R. Jungmann (MPI Biochemistry, Munich, Germany) and C. Grashoff (Institute for Molecular Cell Biology, Münster, Germany) for providing materials, support and important discussions on DNA-PAINT; P. Kanchanawong (MBI, NUS, Singapore) for providing the talin1-22–tdEOS (Talin-C), tdEOS-18–Talin1 (Talin-N), mEos2-7–TalinABS (THATCH) constructs. We acknowledge financial support from the French Ministry of Research and CNRS, ANR grant Integractome (GG), ANR grant FastNano (GG), ANR grant IntegrinNanoPlan (GG), ANR Decav-Recav (PN, ANR MecanoCav (PN), Fondation pour la Recherche Médicale (GG), and the Institut National du Cancer (PN).

Figures

Figure 1

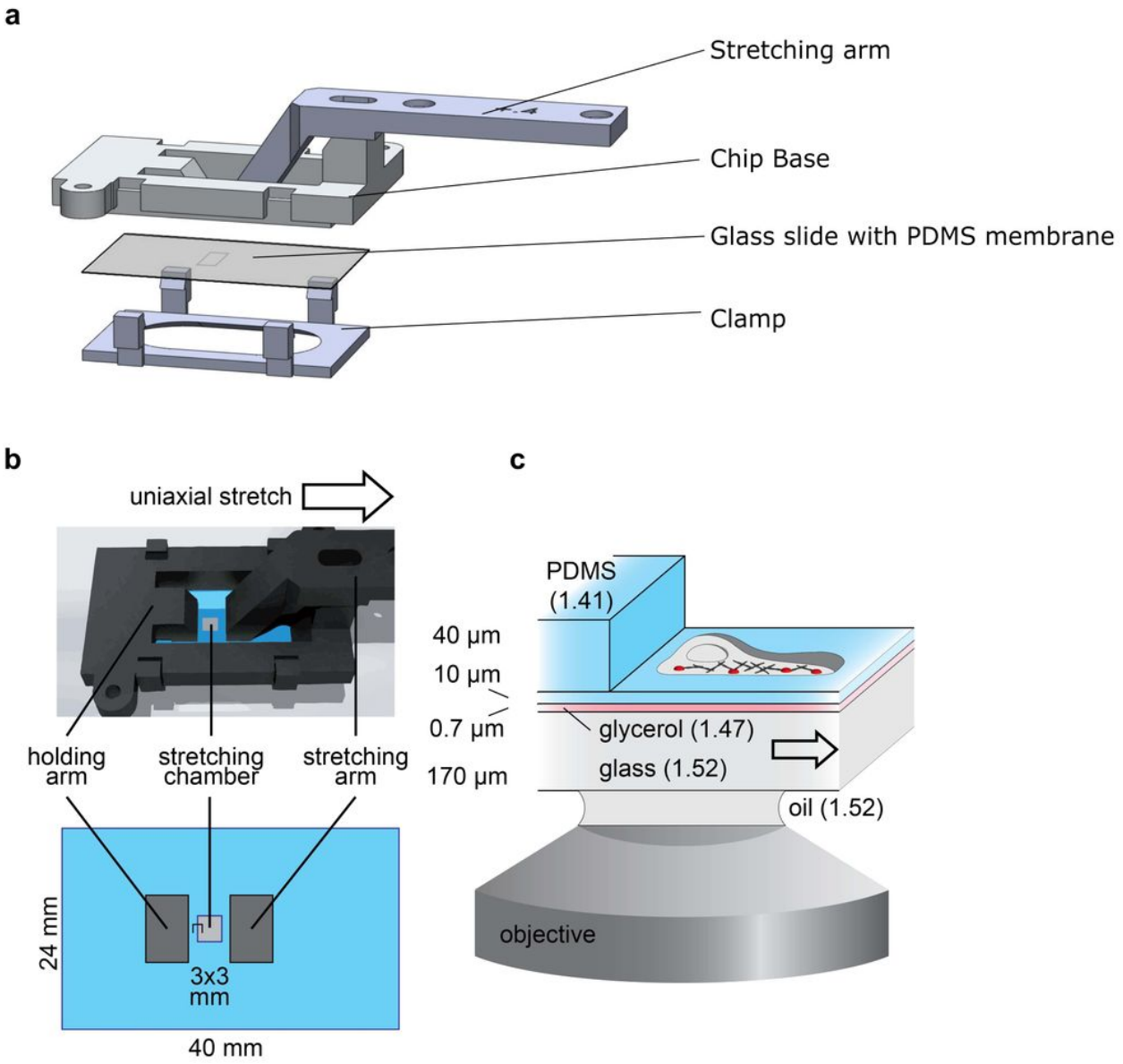

Figure 1

Developing and assembling a micromechanical cell stretching device compatible with super-resolution microscopy. a), Schematic view of the complete 3D-printed device and PDMS elastic substrate, displaying the 3D-printed holding and stretching arms, the PDMS membrane with the stretching chamber gliding on the glycerol-coated glass slide and the 3D-printed clamp holding the system together. b), Schematic view of the 3D-printed micromechanical stretching device composed of a holding arm and a stretching arm connected to a piezo motor (up). Schematic top view of the stretching device showing the positions and dimensions of the stretching chamber (bottom). c), Schematic side view of the glass-glycerol-PDMS assembly formed by the supporting glass (170 µm), the glycerol gliding layer (0.7 µm), the suspended

thin (10 µm) PDMS framed by the thick (40 µm) elastomer (arbitrary scales). All uniaxial stretches are displayed towards the right (white arrows).

Figure 2

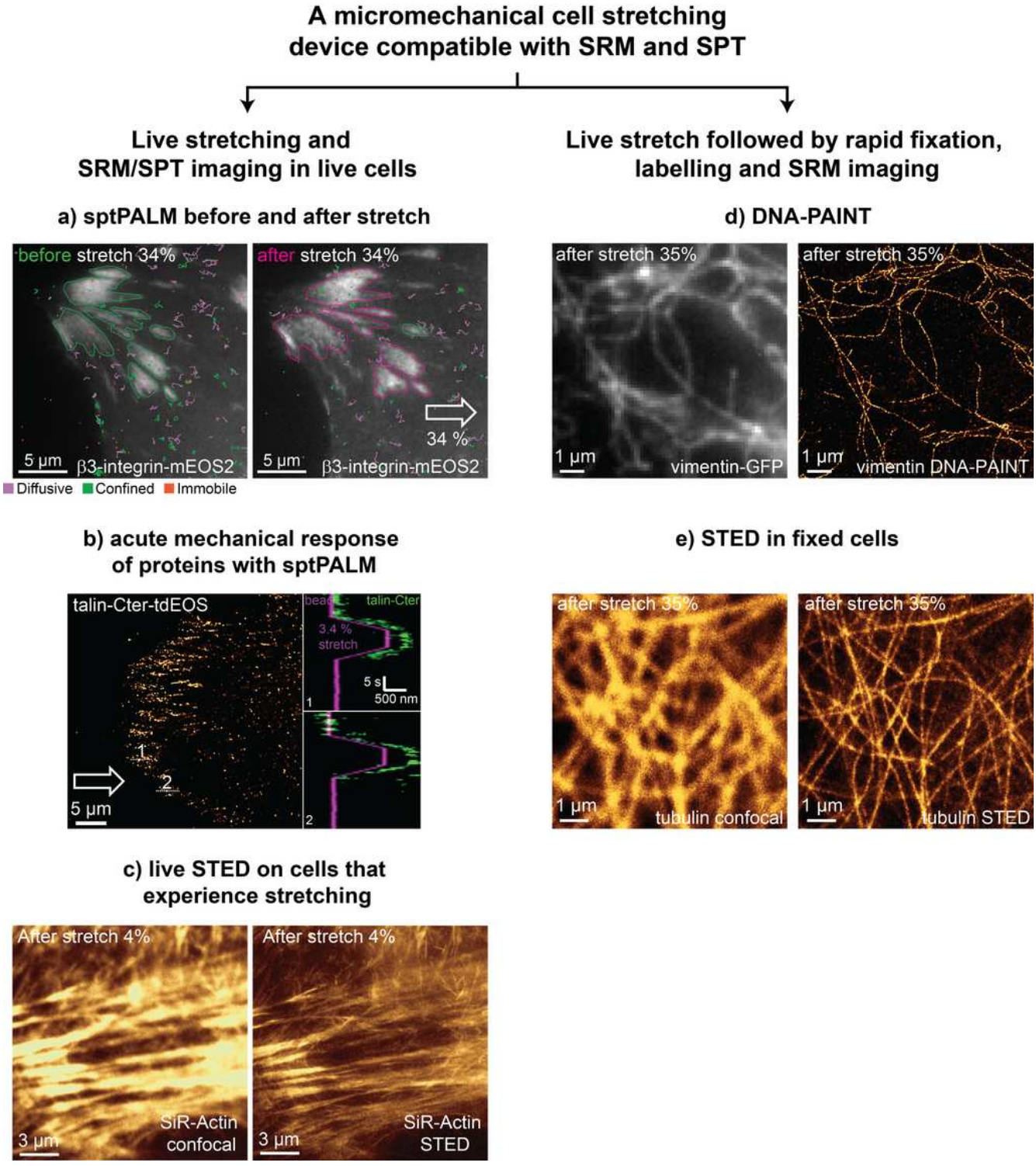

Figure 2

Combination of live stretching with SRM and SPT to study mechanical properties of proteins and macromolecular protein assemblies . (a-c) Combination of live stretching and SRM/SPT in live cells. a) Super-resolution intensity images of β3-integrin-mEos2 in MEFs before (left) and after (right) a 34%

stretch (image acquisition rate 50 Hz, duration > 240 s). Outlines correspond to FAs, labelled by GFP-paxillin (greyscale), before (green) and after (magenta) stretching. Scale bar, 5 μm. b) Projection of all talin-C-tdEos super-resolution intensity images of a trapeze-like pattern time-lapse (stretching 3.4 %, 2 Hz, 40 s) (left). Scale bar, 5 μm. Right, talin-C-tdEos kymographs generated from the trapeze-like pattern time-lapse (as shown in the left panels, dashed lines). Horizontal axis, space (500 nm); vertical axis, time (5 s). The magenta kymograph corresponds to the reference bead, and the green kymographs correspond to talin-C-tdEos. c) Low resolution live confocal image (left) and live STED image (right) of SiR-Actin in a MEF on the PDMS stretching device after 4% stretching. (d-e) Live stretch followed by fixation, labelling and SRM imaging. d) Low resolution fluorescence image of vimentin-GFP (left) and DNA-PAINT super-resolution image of vimentin (right) in a vimentin Knock Out MEF on the PDMS stretching device, after a 35% large stretching followed by rapid cell fixation and labelling. Scale bar, 1 μm. e) Low resolution confocal image (left) and STED super-resolution image (right) of tubulin labelled with ATTO-647N in a MEF (left) on the PDMS stretching device, after 35% large stretching followed by rapid cell fixation and labelling. Scale bar, 1 μm. All uniaxial stretches are displayed towards the right (white arrows).

RESULTS

1. Cell stretching is amplified by active actin remodelling to deform and recruit proteins in mechanosensitive structures

Sophie Massou*, Filipe Nunes Vicente*, Franziska Wetzel*, Amine Mehidi, Dan Strehle, Cecile Leduc, Raphaël Voituriez, Olivier Rossier, Pierre Nassoy and Gregory Giannone

Published at Nature Cell Biology, 27 July 2020
* These authors contributed equally to this work

Here, I will present the main results of my PhD project, which have been recently published in Nature Cell Biology. We developed a micromechanical device compatible with SRM and SPT. We then used it to capture protein deformations and reorganizations inside mechanosensitive structures. This project began to be developed in our lab prior to my arrival. More precisely, an initial version of the micromechanical device had already been developed and used to capture the acute mechanical response of proteins inside IAS. After taking over the project, I adapted the stretching device to perform DNA-PAINT and STED SRM imaging on cytoskeletal proteins, either in fixed or live cells. In parallel, I also developed a method to enable sustained large stretching followed by cell fixation and labelling for SRM. I also scaled up the production of the device with 3D-milling methods, increasing the number of samples for different experimental conditions in the same day. In addition, I performed all the experiments on protein (zyxin, vinculin, talin) recruitment and reorganization inside mature FAs and NAs upon mechanical stretching. For this, I became a co-first author in the publication.

1. Scientific context

Mechanical cues arising from the ECM, the cytoskeleton and the plasma membrane control assembly and function of macromolecular complexes driving fundamental cellular functions (Dupont et al., 2011; Nava et al., 2020; Woo et al., 2015; Zhang et al., 2011). Among these complexes, integrin adhesion sites (IAS) are key mechanosensitive units mediating cell-ECM adhesion, cell migration, mechanotransduction, and force transmission (Elosegui-Artola et al., 2016; Jansen et al., 2017; Oria et al., 2017). Mechanosensing is based on the unfolding and reorganization of individual proteins in response to force, as well as in the reinforcement/destabilization of protein-protein bonds (Chronopoulos et al., 2020; Huang et al., 2017b; Jiang et al., 2003; Del Rio et al., 2009). This molecular understanding of mechanosensing was possible due to *in vitro* mechanical manipulations of purified proteins with techniques such as optical tweezers(Huang et al., 2017b), magnetic tweezers (Del Rio Science 2009, Yao Nat Comm 2016) and AFM (Kong et al., 2009). Stretching of talin with magnetic tweezers leads to vinculin recruitment (Del Rio Science 2009, Yao Nat Comm 2016); force applied to the vinculin-actin bond with optical tweezers unveiled a directional catch bond between these two proteins (Huang Science 2017). However, it is unclear whether these mechanosensitive responses would be replicated in live cells, due to the presence of force patterns, binding partners, membrane tension, among other aspects. Certain of the aforementioned techniques allow to manipulate proteins in living cells, but they can only probe proteins on the dorsal surface of cells(Chronopoulos et al., 2020; Jiang et al., 2003). Therefore, they cannot access crowded macromolecular structures in contact with the substrate, which is the case of IAS. Our goal was to first develop a strategy to apply external forces to cells while simultaneously capturing the mechanical response of individual proteins. Then, we sought to apply this strategy to understand the molecular mechanisms of mechanosensing at IAS in live cells.

2. Results

2.1. Developing a stretching device compatible with SRM and SPT

In this work, we first developed a micromechanical stretching device compatible with super-resolution microscopy (SRM) and single particle tracking (SPT). We then demonstrated that our stretching device is compatible with the two major classes of SRM: coordinate stochastic (SMLM) and coordinate targeted (e.g. STED/RESOLFT). We first performed large, sustained stretching in live cells followed by fixation and labelling for SRM. We then acquired DNA-PAINT images of vimentin or STED images of microtubules. We also acquired STED images of microtubules in live

cells experiencing stretching. Following this, we performed single protein tracking PALM (sptPALM) acquisitions of β3-integrin-mEos2 in MEFs before and after 30% large stretching, with resolutions comparable to glass. In conclusion, our system enables to study the nanoscale reorganizations and deformations of protein assemblies or individual proteins inside mechanosensitive structures. This approach is compatible with crowded macromolecular structures at the interface with the substrate (IAS) but also cytoskeletal structures inside the cell.

2.2. Capturing the acute mechanical response of proteins

In this section, we implemented simultaneous live cell stretching (2-5%) and SPT to study the acute mechanical response of individual proteins within IAS. While β3-integrin followed the elastic displacement of the substrate, actin filaments and talin also displayed lagged and transient inelastic responses. The inelastic responses lead to transient (~ 5 s) and local displacements (~ 250 nm) associated with talin unfolding. Inelastic responses were decreased by cell fixation and myosin II inhibition, indicating a mechanism driven by active remodeling of the actin cytoskeleton. Thus, cells actively react to external forces, amplifying transiently and locally actin cytoskeleton displacements to trigger protein deformation in IAS.

2.3. Studying protein reorganization and recruitment

Finally, in this section, we performed live cell stretching 4% and SPT to study the reorganization and recruitment of proteins within IAS in response to mechanical stretch. We found that zyxin is recruited to mature FAs by small scale 4% stretching, but only in half of the stretched cells. Vinculin, on the other hand, was not recruited to mature FAs at either 4% or 10% stretching. However, vinculin was recruited by 4% stretching to NAs, a process which is not dependent on talin recruitment and which occurred transiently or progressively during the stretching plateau. Thus, molecular vinculin recruitment induced by stretching is delayed and depends on the maturation state of the integrin-talin-cytoskeleton connections.

nature cell biology

TECHNICAL REPORT

https://doi.org/10.1038/s41556-020-0548-2

Cell stretching is amplified by active actin remodelling to deform and recruit proteins in mechanosensitive structures

Sophie Massou[1,2,7], Filipe Nunes Vicente[1,2,7], Franziska Wetzel[3,4,7], Amine Mehidi[1,2], Dan Strehle[3,4], Cecile Leduc[5], Raphaël Voituriez[6], Olivier Rossier[1,2], Pierre Nassoy[3,4] and Grégory Giannone[1,2] ✉

Detection and conversion of mechanical forces into biochemical signals controls cell functions during physiological and pathological processes. Mechanosensing is based on protein deformations and reorganizations, yet the molecular mechanisms are still unclear. Using a cell-stretching device compatible with super-resolution microscopy and single-protein tracking, we explored the nanoscale deformations and reorganizations of individual proteins inside mechanosensitive structures. We achieved super-resolution microscopy after live stretching on intermediate filaments, microtubules and integrin adhesions. Simultaneous single-protein tracking and stretching showed that while integrins followed the elastic deformation of the substrate, actin filaments and talin also displayed lagged and transient inelastic responses associated with active acto-myosin remodelling and talin deformations. Capturing acute reorganizations of single molecules during stretching showed that force-dependent vinculin recruitment is delayed and depends on the maturation of integrin adhesions. Thus, cells respond to external forces by amplifying transiently and locally cytoskeleton displacements, enabling protein deformation and recruitment in mechanosensitive structures.

Growing evidence shows that macromolecular assemblies driving critical cellular functions are regulated by mechanical forces. Mechanical tensions in cells are generated by their extracellular environment[1], the plasma membrane[2] and the cytoskeleton, including microtubules[3] and intermediate[4] and actin[5,6] filaments. Among mechanosensitive structures including cadherin cell–cell adhesions[5], kinetochores[3], caveolae[2] or the nucleus[7], integrin-based adhesions provide an intensively studied model[6,8].

Several innovative techniques have been designed to measure and generate forces on proteins in vitro or within cells[6,9–11], especially for adhesive and cytoskeletal proteins. Forces applied by magnetic tweezers to purified talin, which connects integrins to the actin cytoskeleton, trigger unfolding that reveals hidden binding sites for vinculin[12,13]. Techniques such as atomic force microscopy or optical tweezers have shown that forces exerted directly on proteins stabilize or destabilize interactions[14,15]. However, whether these principles can be applied to proteins in cells is still unclear. These techniques are also used to study biomechanical processes directly in living cells with molecular resolution[6,16]. However, they can only probe proteins on cell dorsal surfaces, and not in crowded macromolecular structures inside cells or confined at the cell interface with the extracellular environment.

Super-resolution microscopy (SRM) and single-protein tracking (SPT) techniques revolutionized cell imaging. By delivering images with spatial resolutions below the diffraction limit of light, these techniques created possibilities to study the architecture and dynamics of biological structures at the protein level in cells[17–20]. There are two major classes of SRM: (1) stochastic approaches based on single-molecule localization microscopy (SMLM; that is, photo-activated localization microscopy (PALM), stochastic optical reconstruction microscopy (STORM) and point accumulation for imaging in nanoscale topography (PAINT)) that use time and space decorrelation of single-molecule emission[17–19]; and (2) targeted light-structuring techniques that control the emission states at precisely defined positions in the sample (that is, stimulated emission depletion microscopy (STED) and reversible saturable optical fluorescence transitions (RESOLFT))[17–19]. Scrutinizing sub-cellular structures using SRM unravelled new protein organizations and showed that proteins are spatially segregated into distinct functional nano-domains. SPT techniques unveiled the correlation between protein dynamics and protein activation and/or binding states. The recent application of SRM and SPT led to a drastic rethinking of macromolecular assemblies including cadherin-based adhesions[21], axons[22], dendritic spines[23,24], actin-based lamellipodia[25] and integrin-based focal adhesions (FAs)[26,27].

Within FAs, SPT enables the study of fast diffusive behaviours of proteins or their slow motions driven by intracellular force transmission[1,27]. SRM and SPT, together with fluorescent tension sensors, confirmed that proteins are stretched under mechanical tension[10,26,28,29]. For example, talin within mature FAs adopts an extended and polarized conformation (50–350 nm) with the integrin-binding site directed outwards and the actin-binding sites oriented inwards[26], possibly by the actin flow. Cellular force fluctuations within mature FAs were proposed to mediate substrate

[1]Interdisciplinary Institute for Neuroscience, UMR 5297, Université de Bordeaux, Bordeaux, France. [2]Interdisciplinary Institute for Neuroscience, UMR 5297, CNRS, Bordeaux, France. [3]Laboratoire Photonique Numérique et Nanosciences, UMR 5298, Université de Bordeaux, Talence, France. [4]Laboratoire Photonique Numérique et Nanosciences, UMR 5298, Institut d'Optique and CNRS, Talence, France. [5]Cell Polarity, Migration and Cancer Unit, UMR 3691, Institut Pasteur Paris and CNRS, Paris, France. [6]Laboratoire Jean Perrin and Laboratoire de Physique Théorique de la Matière Condensée, CNRS - Sorbonne Université, Paris, France. [7]These authors contributed equally: Sophie Massou, Filipe Nunes Vicente, Franziska Wetzel. ✉e-mail: gregory.giannone@u-bordeaux.fr

rigidity sensing[30], which in turn could be correlated with talin stretch–relaxation cycles[31] and vinculin recruitment[12,13,32]. However, the molecular rules underlying mechanosensing in integrin-based adhesions or other mechanosensitive structures are hidden by complex spatiotemporal force patterns generated by the cell. One way to decipher those rules is to actively apply external stretch to cells while monitoring with SRM and SPT the nanoscale reorganizations and deformations of protein assembly or individual proteins inside mechanosensitive structures.

Results

Combining cell stretching with SRM or SPT. Stretchable substrates of polydimethylsiloxane (PDMS) have been coupled with optical imaging to investigate cell responses to external forces[2,9,33]. However, the simultaneous combination of SRM/SPT and cell stretching has never been achieved due to technical limitations (see Supplementary Note 1). Here, we designed a micromechanical device composed of an ultra-thin PDMS layer (10 µm) providing glass-like optical properties compatible with SRM/SPT (Figs. 1 and 2). To simultaneously perform substrate stretching and ensure flatness upon deformation, the PDMS sheet was gliding on a glycerol-lubricated glass cover slip (Fig. 1a,b). To generate uniaxial stretch, we designed a three-dimensional (3D)-printed micromechanical device comprising a fixed holding arm and a mobile arm connected to a piezoelectric translator (Fig. 1a and Supplementary Video 1). Controlled and homogeneous strain was achieved over the entire observation chamber for deformations up to 90%, as demonstrated both numerically and experimentally (Extended Data Fig. 1 and Supplementary Video 2).

Next, we demonstrated that our stretching device is compatible with the two major classes of SRM: coordinate stochastic (SMLM) and coordinate targeted (for example, STED). We used cytoskeleton structures that control cell shape and reorganize during external cell stretching, while serving as gold standards for SRM in cell biology. We acquired low-resolution epifluorescence images before live large stretching (30–50%), followed by rapid cell fixation (Fig. 1c). Cells were labelled for SRM and imaged after stretching, first at low resolution and then with SRM. Our strategy allowed long-lasting acquisitions required for DNA-based PAINT (DNA-PAINT)[34] super-resolution images. We obtained DNA-PAINT images of vimentin intermediate filaments after live stretching of mouse embryonic fibroblasts (MEFs) spread on fibronectin-coated PDMS (Fig. 1d,e and Extended Data Fig. 2a,b). We could also perform STED[18] SRM of microtubules after live stretching, fixation and labelling (Fig. 1f,g and Extended Data Fig. 2c,d). We also demonstrated that our stretching device could be used to acquire STED images of live cells that experience stretching, using live labelling with SiR-tubulin and SiR-actin[35] (Extended Data Fig. 2e–h). Therefore, our stretching device is compatible with the two main SRM modalities, enabling the capture of state-of-the-art super-resolved images of protein reorganization after stretching.

Next, we tested whether our stretching device allows localization of photoactivatable fluorescent proteins (for example, mEos2 and photoactivatable GFP), which possess lower photon budgets reducing localization precision[36], compared with synthetic dyes used for PAINT and STORM (for example, ATTO dyes, Cy dyes and Alexa dyes). This design enabled the localization of individual purified mEos2 and the performance of live PALM and SPT PALM (spt-PALM) acquisitions in cells with resolutions comparable to glass[27,37] (Extended Data Fig. 3). We performed live PALM (Fig. 2a,b) and SPT acquisitions (Fig. 2a,c) before and after stretching of MEFs expressing β3-integrin–mEos2 and paxillin–GFP. Large stretching (~30%) induced FA expansion, as shown in the paxillin–GFP images (Fig. 2d). Importantly, the area of β3-integrin–mEos2 immobilization grew according to FA expansion (Fig. 2b). Mechanical activation of integrins should lead to increased immobilization inside and outside FAs[1,15,27,38]. However, the fraction of immobile β3-integrin was similar before and after stretching (Fig. 2c,e,f), suggesting that force-induced integrin activation dissipates rapidly after stretching. In conclusion, the stretchable elastic substrate we designed is compatible with SRM and SPT and enables nanoscale investigation of the overall changes induced by mechanical forces.

The acute mechanical response of β3-integrins to external forces is elastic. We then assessed the acute mechanical response of cells to force, which required maintaining the cell strictly in focus and in the field of observation during stretching. To compensate for the *XYZ* displacements, we used an autofocus system (*Z*) and manual or automated stage repositioning (*XY*). To test the strain homogeneity at nanometre scales, we tracked fluorescent beads adsorbed on PDMS during trapeze-like patterns composed of stretch–plateau–relax phases (Fig. 3a). All images were registered on an arbitrarily chosen origin bead, seen as immobile in super-resolved time lapses[27]. Bead displacements, measured from kymographs, increased proportionally with the distance from the origin bead (Fig. 3b), attesting the purely elastic and homogeneous response of our device. Accordingly, these displacements could be superimposed after normalization on the position of any given reference bead (Fig. 3c). Likewise, we could extrapolate PDMS displacements at any given positions in the observation field (Fig. 3c). Live *XYZ* repositioning was possible up to 6% stretching. Altogether, these performances allowed us to conduct an in-depth investigation of the mechanical response of individual proteins during adhesion mechanosensing, which has been reported to occur between 2 and 10% stretching[33,39].

Using SPT, we previously measured integrins, actin and talin displacements driven by intracellular force transmission in mature FAs[27]. We demonstrated that β3-integrins are stationary within FAs, while most actin filaments are moving rearward (2–10 nm s^{-1}). Here, we applied trapeze-like patterns to MEFs co-transfected with β3-integrin–mEos2 and paxillin–GFP (Fig. 3d–f and Supplementary Video 3). We then generated super-resolved time lapses at 2 Hz to analyse the acute mechanical response of individual β3-integrins in and out FAs. The displacement pattern of integrins mirrored the shape of the trapeze-like substrate deformation (Fig. 3d and Supplementary Videos 4 and 5). In addition, after normalization on a reference bead (Fig. 3e), the mean response was superimposed on the displacement of the stretchable substrate. Reciprocally, because the PDMS substrate was purely elastic and the deformation was homogeneous (Fig. 3c and Extended Data Fig. 1), we could extrapolate the theoretical displacements of the substrate at the position of each integrin. In this reference frame, the mean local displacement of β3-integrin–mEos2 was similar to that of PDMS (Fig. 3f). Thus, integrin displacements closely followed the elastic displacements of the substrate (Fig. 3g). This indicates that most stationary integrins inside and outside of FAs remained connected to fibronectin when challenged mechanically by stretching (2–5%). Furthermore, this allowed us to test whether proteins mediating a dynamic mechanical coupling of integrins to F-actin[40] follow or deviate from the elastic behaviour of integrins.

The inelastic mechanical response of talin to external forces corresponds to talin unfolding. Among proteins composing this mechanical coupling, talin is critical since it activates integrins, directly connects them to F-actin and supports integrin force sensing[12,13,41–43]. Using SPT, we previously showed that a large fraction of F-actin (74%) is moving rearward compared with talin (25%) and β3-integrins (8%)[27]. This suggests that stationary talins are bound to stationary β-integrins in FAs, probably via their amino-terminal FERM domain[43]. However, whether these talins are simultaneously connected to F-actin via carboxy-terminal actin-binding sites—either fully extended or prompted to extend

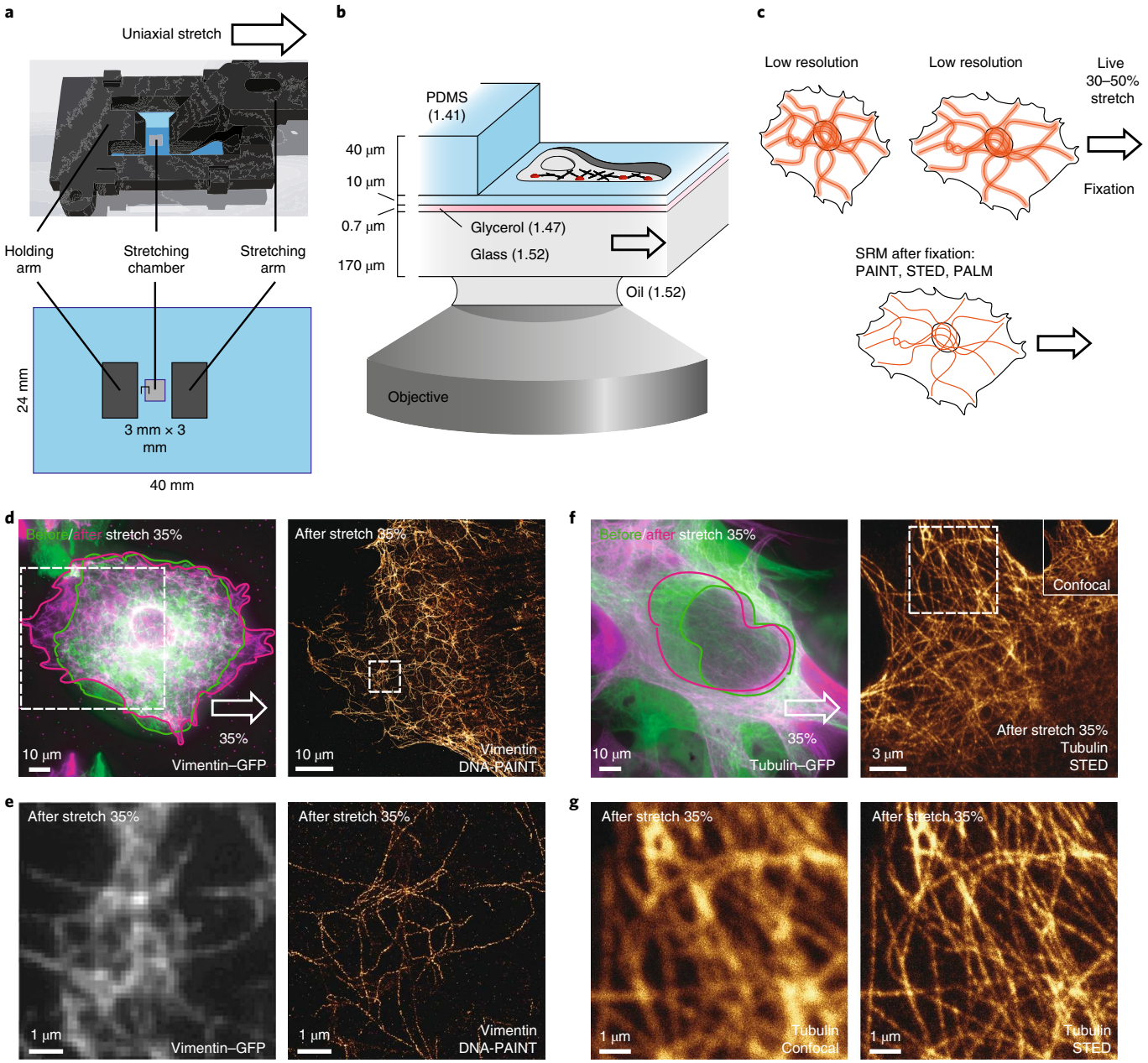

Fig. 1 | Combining cell stretching with SRM. a, Top: schematic of the 3D-printed micromechanical stretching device composed of a holding arm and a stretching arm connected to a piezo motor. Bottom: schematic of the top view of the stretching device, showing the positions and dimensions of the stretching chamber. **b**, Schematic of the side view of the glass–glycerol–PDMS assembly formed by the supporting glass (170 µm), gliding layer (0.7 µm) and suspended thin PDMS (10 µm) framed by the thick (40 µm) elastomer (arbitrary scales). All uniaxial stretches are displayed towards the right (white arrows). **c**, Schematic of the experimental workflow. Low-resolution epifluorescence images were acquired live before large stretching (30–50%) followed by rapid cell fixation. Cells were labelled for SRM and imaged after stretching at low resolution with SRM. **d**, Left: low-resolution fluorescence image of vimentin–GFP in a vimentin knockout MEF on the PDMS stretching device before (green) and after (magenta) a 35% large stretching, followed by rapid cell fixation. The outlines correspond to the cell contour. Right: DNA-PAINT super-resolution image of vimentin after 35% stretching, corresponding to the dashed box in the left panel. **e**, Low-resolution fluorescence image (left) and DNA-PAINT super-resolution image (right) of vimentin of the dashed box in the right panel of **d**, displayed at higher magnification. **f**, Left: low-resolution fluorescence image of tubulin–GFP in a MEF on the PDMS stretching device before (green) and after (magenta) 35% large stretching followed by rapid cell fixation. Outlines define the nucleus. Right: STED super-resolution image of tubulin labelled with ATTO 647N after 35% stretching. The region is out of the field of view displayed in the left panel. Inset: corresponding confocal image of tubulin labelled with ATTO 647N. **g**, Low-resolution confocal image (left) and STED super-resolution image (right) of tubulin for the outlined area in the right panel of **f**, displayed at higher magnification. In **d**–**g**, data are representative of three independent experiments.

by external forces—is unknown. To test the mechanical status of individual talins, we applied trapeze-like patterns to MEFs transfected with talin tagged with tdEos at the carboxy (talin-C) or amino (talin-N) terminus (Fig. 4). A fraction of individual talin-Cs (35%) mirrored the deformation of the substrate (Fig. 4a,b,d). The average talin-C response was superimposed on sub-

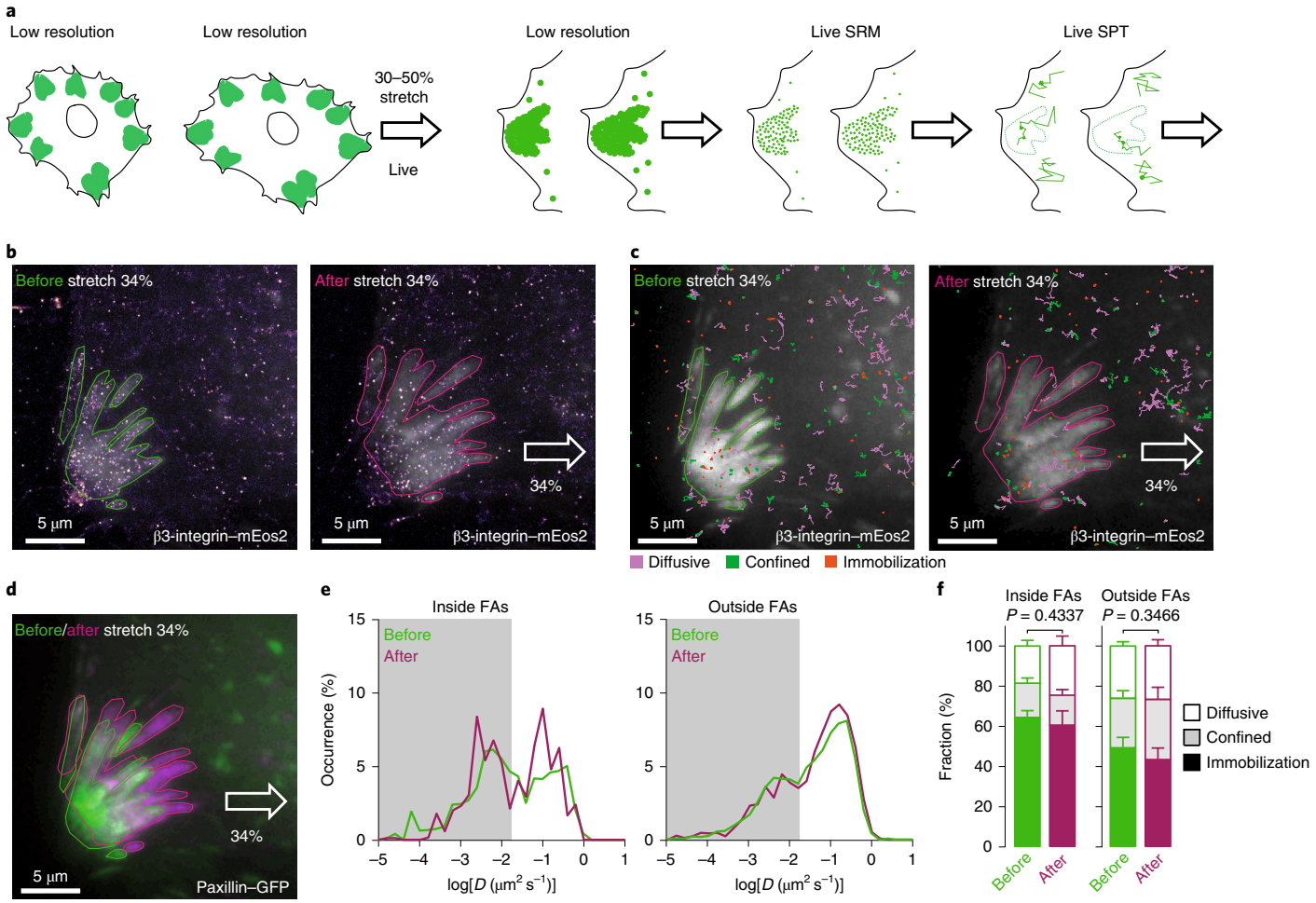

Fig. 2 | Combining cell stretching with live SRM or SPT. a, Schematic of the experimental workflow. Cells were co-transfected with proteins of FAs fused with photoactivatable/photoconvertible fluorescent proteins (for example, mEos2 and mEos3.2) and a reporter of FAs (for example, paxillin–GFP). Low-resolution epifluorescence images were acquired live before and after large stretching (30–50%). Sequences of live SRM or SPT could be acquired before and after stretching. **b**, Super-resolution intensity images of β3-integrin–mEos2 in MEFs before (left) and after (right) a 34% stretch (image acquisition rate: 50 Hz; duration > 240 s). Outlines correspond to FAs, labelled by paxillin–GFP (greyscale), before (green) and after stretching (magenta). Fluorescent beads adsorbed on the stretching chamber were used to measure PDMS deformation. **c**, Corresponding colour-coded trajectories before (left) and after (right) the 34% stretch, overlaid on FAs labelled by paxillin–GFP (greyscale), showing the diffusion modes: free diffusion (magenta); confined diffusion (green); and immobilization (red). **d**, Corresponding low-resolution image of paxillin–GFP before (green) and after (magenta) the 34% stretch. **e**, Distributions of the diffusion coefficient D computed from β3-integrin–mEos2 trajectories inside (left) and outside FAs (right) before (green) and after ~30% stretches (magenta). D values inferior to 0.017 µm² s^{-1} correspond to immobilized proteins. Values represent the average of the distributions obtained from five different cells. **f**, Fraction of proteins undergoing free diffusion, confined diffusion or immobilization inside (left) and outside FAs (right) before (green) and after ~30% stretching (magenta). Values represent the average of the fractions obtained from five different cells (means ± s.e.m. for cells). In **b**–**d**, data are representative of five independent experiments. In **e** and **f**, all of the results for each condition correspond to pooled data from five independent experiments: before stretch (n = 5 cells and 4,643 trajectories; pooled from five independent experiments); and after stretch (n = 5 cells and 3,071 trajectories; pooled from five independent experiments). Statistical significance was determined using two-tailed paired Student's t-tests.

strate displacement after bead normalization (Fig. 4b) and the mean local displacement was close to PDMS displacement (Fig. 4e). Thus, like integrins, a subset of talin-Cs displayed an elastic behaviour. Importantly, a larger fraction of talin-Cs (65%) exhibited a complex displacement incompatible with an elastic response (Fig. 4a,c,d and Supplementary Videos 6 and 7). Immediately after stretching interruption, during the plateau phase, talin-C movements persisted towards the cell centre, as shown by the measured arch-shaped kymographs. After reaching their maximum amplitude and before relaxation, talin-C recoiled back towards the cell periphery (Fig. 4a,c). These inelastic, lagged and transient displacements were not due to atypical strains of the stretchable substrate, since elastic and inelastic responses could occur within very short distances (Fig. 4a and Supplementary Video 6). Bead normalization showed that the inelastic displacements overshot the expected elastic displacements (Fig. 4c). These deviations from the elastic regimen caused additional local displacements (330 ± 30 nm), measured by subtracting the theoretical displacement of the elastic substrate at positions of detected talin-Cs (Fig. 4e). Talin stretching should translate into distinct responses of talin-C versus talin-N, because they respectively bind F-actin and integrins (Fig. 4f). Like talin-C, talin-N displayed elastic and inelastic responses to trapeze-like patterns (Extended Data Fig. 4). However, in contrast with talin-C, the fraction of elastic responses (72%) was higher compared with inelastic responses (28%; Fig. 4d), reflecting binding to integrins.

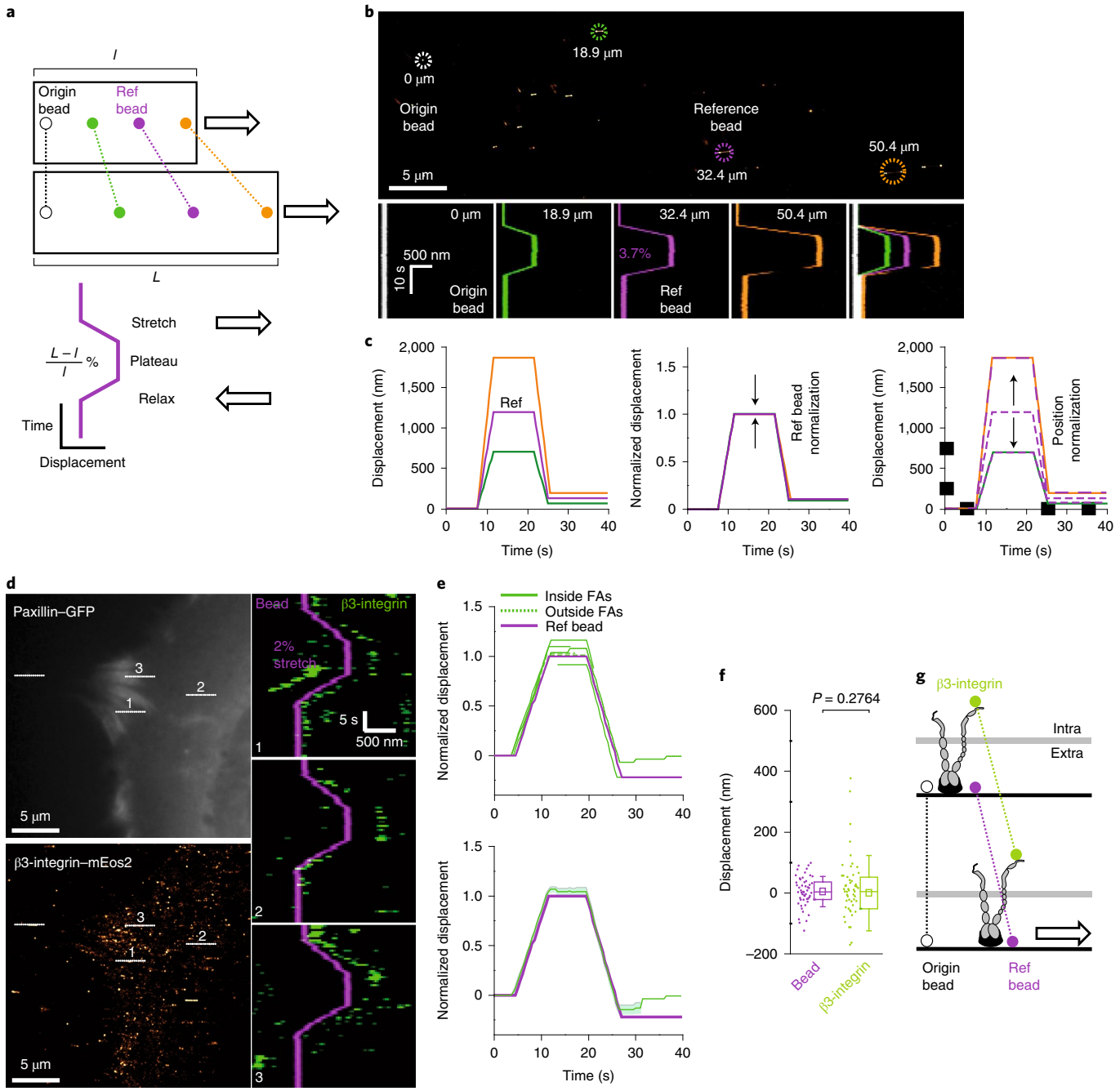

Fig. 3 | The acute mechanical response of β3-integrins to external forces is elastic. a, Schematic of the PDMS mechanical response to trapeze-like patterns (right direction). The origin bead (white) is used for registration and the reference (ref) bead (magenta) is used for displacement and position normalizations. **b**, Mechanical response of a 10-µm PDMS assembly during a trapeze-like pattern measured with adsorbed fluorescent beads. Top: projection of all super-resolved time-lapse images (stretching 3.7%; 2 Hz; 40 s). Bottom: positions of the origin bead (white), reference bead (magenta) and two other beads (green and orange). Bead displacements were measured using kymographs (bottom) generated from the super-resolved time lapse. The *x* axis shows space (500 nm) and the *y* axis shows time (10 s). **c**, Displacement versus time plots for: beads corresponding to **b** (left); orange and green beads after normalization to the initial position of the reference bead (middle); and the magenta bead after normalization to the initial positions of the orange and green beads (right). **d**, Top left: fluorescence image of paxillin–GFP in a MEF on the PDMS stretching device before stretching. Bottom left: projection of β3-integrin–mEos2 super-resolution intensity images of a trapeze-like pattern time lapse (stretching: 2%; 2 Hz; 40 s). Right: β3-integrin–mEos2 kymographs generated from the trapeze-like pattern time lapse (dashed lines; left). The *x* axis shows space (500 nm) and the *y* axis shows time (5 s). The magenta kymograph corresponds to the reference bead and the green kymographs correspond to β3-integrin–mEos2. The signal intermittencies result from the on–off blinking characteristic of single mEos2 molecules. **e**, Top: displacement versus time plot for β3-integrin–mEos2 (green) after normalization to the initial position of the reference bead (magenta). Bottom: mean displacement ± s.e.m. **f**, Boxplots displaying the medians (central lines), means (squares), 25–75% percentiles (box edges) and s.d. (whiskers) of local displacements for β3-integrin–mEos2 versus beads after subtracting the extrapolated PDMS displacements, using the magenta bead after normalization to the initial positions of each β3-integrin–mEos2. In **e** and **f**, $n = 51$ kymographs pooled from three independent experiments. for β3-integrin–mEos2 and $n = 52$ kymographs pooled from three independent experiments for beads. **g**, Schematic of the acute mechanical response of β3-integrin. Statistical significance was determined using two-tailed unpaired Student's *t*-tests.

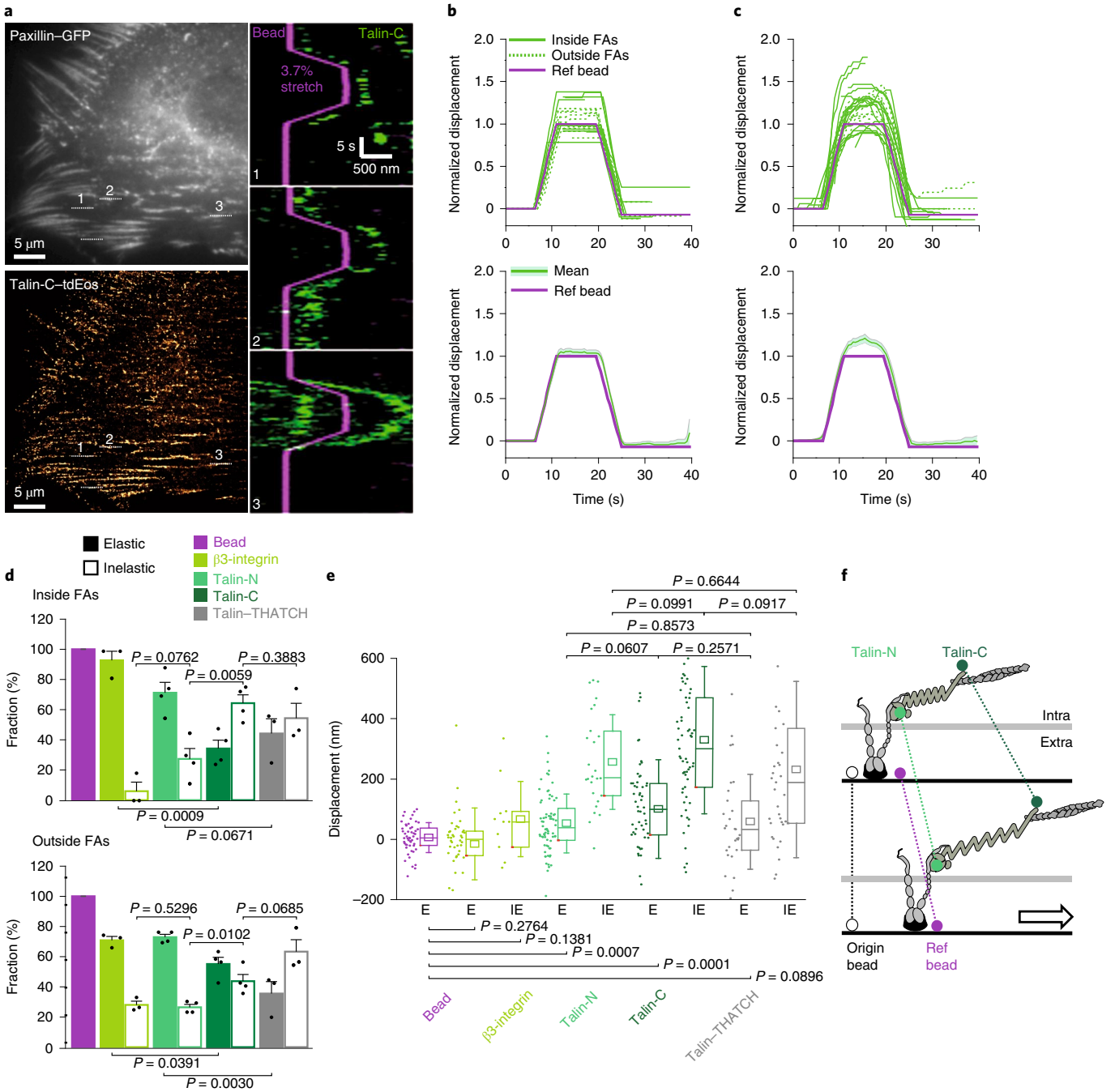

Fig. 4 | Inelastic mechanical response of talin to external forces correspond to talin unfolding. a, Top left: fluorescence image of paxillin–GFP in a MEF on the PDMS stretching device before stretching (right direction). Bottom left: projection of all talin-C–tdEos super-resolution intensity images of a trapeze-like pattern time lapse (stretching: 3.7%; 2 Hz; 40 s). Right: talin-C–tdEos kymographs generated from the trapeze-like pattern time lapse (as shown in the left panels; dashed lines). The *x* axis shows space (500 nm) and the *y* axis shows time (5 s). The magenta kymograph corresponds to the reference bead and the green kymographs correspond to talin-C–tdEos. **b**, Top: displacement versus time plot for elastic responses of talin-C–tdEos (green lines) after normalization to the initial position of the reference bead (magenta line). Bottom: corresponding mean displacement ± s.e.m. **c**, Same as **b** for inelastic responses of talin-C–tdEos. **d**, Fractions of elastic and inelastic responses inside and outside FAs for β3-integrin–mEos2, talin-N–tdEos, talin-C–tdEos and mEos2–talin–THATCH. Values represent the average of fractions obtained from three or four independent experiments (means ± s.e.m.). **e**, Boxplots displaying the median (lines), mean (squares), 25–75% percentile values (box edges) and s.d. (whiskers) of local displacement for β3-integrin–mEos2, talin-N–tdEos, talin-C–tdEos and mEos2–talin–THATCH for elastic (E) and inelastic (IE) responses after subtraction of the extrapolated PDMS displacements. In **b**–**e**, data were pooled from independent experiments as follows: beads (in **e**, $n = 52$ kymographs pooled from three independent experiments); β3-integrin–mEos2 (in **d**, $n = 4$ stretches; in **e**, $n = 51$ kymographs; both pooled from three independent experiments); talin-N–tdEos (in **d**, $n = 4$ stretches; in **e**, $n = 98$ kymographs; both pooled from four independent experiments); talin-C–tdEos (in **d**, $n = 4$ stretches; in **e**, $n = 117$ kymographs; both pooled from three independent experiments); mEos2–talin–THATCH (in **d**, $n = 3$ stretches; in **e**, $n = 66$ kymographs; both pooled from three independent experiments). **f**, Schematic of the acute mechanical response of talin-N and talin-C compared with β3-integrin.

Like talin-C, the carboxy-terminal domain of talin (mEos2–talin–THATCH), which binds and flows with actin in the same upper layer in FAs[26,27], displayed a larger fraction of inelastic responses (Fig. 4d). This suggests that inelastic responses of talin depend on displacements of the actin cytoskeleton. To test this hypothesis, we applied the same trapeze-like patterns to MEFs transfected with actin–mEos2 (Fig. 5). Actin–mEos2 mechanical responses were also partitioned between elastic and inelastic displacements (Fig. 5a–d and Supplementary Video 8). Like talin-C, inelastic displacements (62%) were predominant (Fig. 5d). The average elastic response of actin–mEos2 was superimposed on substrate displacement after bead normalization (Fig. 5b,e). In addition, amplitudes of the local extra displacements measured for the inelastic responses were in the same range as talin displacements (260 ± 20 nm) (Fig. 5c,e). The characteristic rise times of inelastic responses for actin–mEos2 (1.6 ± 0.1 s) and talin-C (1.7 ± 0.1 s) were similar, and corresponded to maximum instantaneous displacement rates (~100 nm s^{-1}) faster than the flow of talin or actin in adhesive structures or the lamella (~5–10 nm s^{-1})[27,40], suggesting that the actin flow is not driving inelastic responses. To compare the rise and recoil times, we applied single stretch–plateau patterns to examine the recoil phase independent of the relaxation (Extended Data Fig. 5 and Supplementary Note 2). The characteristic recoil time of actin–mEos2 was longer (4.6 ± 0.6 s) than the rise time, suggesting that they were triggered by distinct mechanisms. Overall, talin-N displayed mechanical responses similar to integrins, while talin-C behaved like the actin cytoskeleton. These results indicate that a substantial fraction of inelastic displacements for talin-C correspond to talin stretching. Importantly, amplitudes of local extra displacements (~200–300 nm) are in agreement with talin extension lengths measured in vitro[13]. Thus, our results suggest that molecular displacements induced by small (2–5%) cell stretching are transiently (~5 s) and locally amplified by the inelastic response of F-actin, hence triggering talin unfolding.

Transient and active remodelling of the acto-myosin network drives the inelastic response of actin. Deviations from purely elastic responses—especially arch-shaped displacements during the plateau phase (Fig. 5g)—could either reflect the passive viscoelastic properties of the cell, which can induce lagged responses in both rising and recoil phases, or an active cell response[44–47]. On general grounds, a cell can be modelled as a mechanical transducer composed of several elements, which is locally pinned to the elastic PDMS via integrins. If the cell is homogenously elastic (Fig. 5g), 3% stretch would result in minute local extra displacements (Δx) of talin, inconsistent with domain unfolding[12,13] (for example, talin initial length 50 nm; $\Delta x = 1.5$ nm). Assuming that the cell is heterogeneously elastic (Fig. 5g) and composed of softer elements (for example, talin) in series with stiffer elements (for example, integrin and actin), it is found that under an imposed strain the softer elements will undergo larger displacements than their corresponding reference point in the underlying homogeneous substrate. Deformation of talin from 50 nm to the measured ~300 nm corresponds to an effective strain of ~600%, which implies a cell composed of 99.5% rigid versus soft elements (see Supplementary Note 2). Thus, extra displacements of ~200–300 nm (Figs. 4e and 5e) could be attributed to a passive mechanism only if the cell is essentially unable to deform. However, micro-rheology studies have shown that cells could be rapidly deformed[44,48,49]. This suggests that large effective protein deformations cannot be attributed solely to passive effects, but involve an active contraction of actin structures in response to imposed strains (Fig. 5g).

To test whether an active process generated by the cell drives actin inelastic displacements, we performed the same experiments in fixed and permeabilized cells (Fig. 5 and Extended Data Fig. 6a–c). This treatment transforms the actin cytoskeleton into a non-dynamic cross-linked network, preventing reorganization of actin cross-linkers, active actin polymerization or active contraction by myosin motors. Fixation/permeabilization decreased the fraction and mean amplitude of actin–mEos2 inelastic responses (Fig. 5d,e and Extended Data Fig. 6b,c), supporting that they are driven by a dynamic or active response of the cell. Inhibition of myosin II, using *para*-nitroblebbistatin[50], also decreased the fraction and mean amplitude of actin–mEos2 inelastic responses (Fig. 5d,e and Extended Data Fig. 6e,f), suggesting that forces generated by myosin II on actin filaments actively drive these displacements (Fig. 5g).

Molecular vinculin recruitment is delayed and depends on the maturation state of integrin-based adhesions. Until this point, we had applied cell stretching combined with SRM/SPT to study force-dependent protein unfolding or deformations. Next, we tested whether our approach could be used to study protein reorganizations within mechanosensitive structures during external stress (Figs. 6 and 7). We used as a model the force-dependent recruitment of proteins inside integrin-based adhesions. Within FAs, the interaction of proteins containing the zinc-finger-type LIM domain is particularly sensitive to mechanical tension[51,52]. The recruitment of LIM proteins zyxin and paxillin to FAs is induced by cell stretching[33,53,54]. We applied ~4% trapeze-like patterns to MEFs co-transfected with zyxin–mEos3.2 and paxillin–GFP (Fig. 6a,b and Supplementary Video 9). To measure the acute zyxin–mEos3.2 molecular recruitment in mature FAs, we quantified the density of trajectories (trc.μm^{-2}) before, during and after the stretching plateau (Fig. 6c). Cell stretching triggered an increase in zyxin–mEos3.2 trajectories in mature FAs for 50% (4/8) of the cells,

Fig. 5 | Transient and active remodelling of the acto-myosin network drives the inelastic response of actin. a, Top left: fluorescence image of paxillin-GFP in a MEF on the PDMS stretching device before stretching (right direction). Bottom left: projection of all actin-mEos2 super-resolution intensity images of a trapeze-like pattern time lapse (stretching: 2.9%; 2 Hz; 40 s). Right: actin-mEos2 kymographs generated from the trapeze-like pattern time lapse (as shown in the left panels; dashed lines). The *x* axis shows space (500 nm) and the *y* axis shows time (5 s). The magenta kymograph corresponds to the reference bead and the green kymographs correspond to actin-mEos2. **b**, Top: displacement versus time plot for elastic responses of actin-mEos2 (green lines) after normalization to the initial position of the reference bead (magenta line). Bottom: corresponding mean displacement ± s.e.m. **c**, Same as **b** for inelastic responses of actin-mEos2. **d**, Fractions of elastic and inelastic responses inside and outside FAs for actin-mEos2 in control, fixed/permeabilized cells and cells treated with blebbistatin. Values represent the average of fractions obtained from two or three independent experiments (means ± s.e.m.) **e**, Boxplots displaying median (lines), mean (squares), 25–75% percentile values (box edges) and s.d. (whiskers) of local displacements for actin-mEos2 in control, fixed/permeabilized cells and cells treated with blebbistatin for elastic and inelastic responses after subtraction of the extrapolated PDMS displacements. In **b**–**e**, data were pooled from independent experiments as follows: beads (in **e**, $n = 52$ kymographs pooled from three independent experiments); actin-mEos2 (in **d**, $n = 3$ stretches; in **e**, $n = 65$ kymographs; both pooled from three independent experiments); actin-mEos2 fixed/permeabilized (in **d**, $n = 3$ stretches; in **e**, $n = 85$ kymographs; both pooled from three independent experiments); actin-mEos2 blebbistatin (in **d**, $n = 4$ stretches; in **e**, $n = 83$ kymographs; both pooled from two independent experiments) **f**, Schematic of the acute mechanical response of actin. **g**, Model of displacements amplification by transient active remodelling of the actin cytoskeleton. Statistical significance was determined using two-tailed unpaired Student's *t*-tests.

while the remaining cells displayed no detectable variations. This recruitment was reversible since cell relaxation decreased trajectory densities to levels found before stretching (Fig. 6c). Zyxin molecular recruitment, as analysed from kymographs or colour coding of super-resolved time lapses (2 Hz), did not show obvious zyxin association in selective FA regions (that is, the tip, centre or rear) (Fig. 6d,e). Force-induced talin unfolding exposes vinculin-binding sites, as demonstrated at the single-molecule and ensemble level in vitro using purified proteins[12,13,32]. Furthermore, vinculin turnover within integrin-based adhesions is tuned by mechanical forces[55,56]. Hence, we tested whether acute vinculin recruitment in mature FAs is triggered by external forces. We applied ~4% trapeze-like patterns to

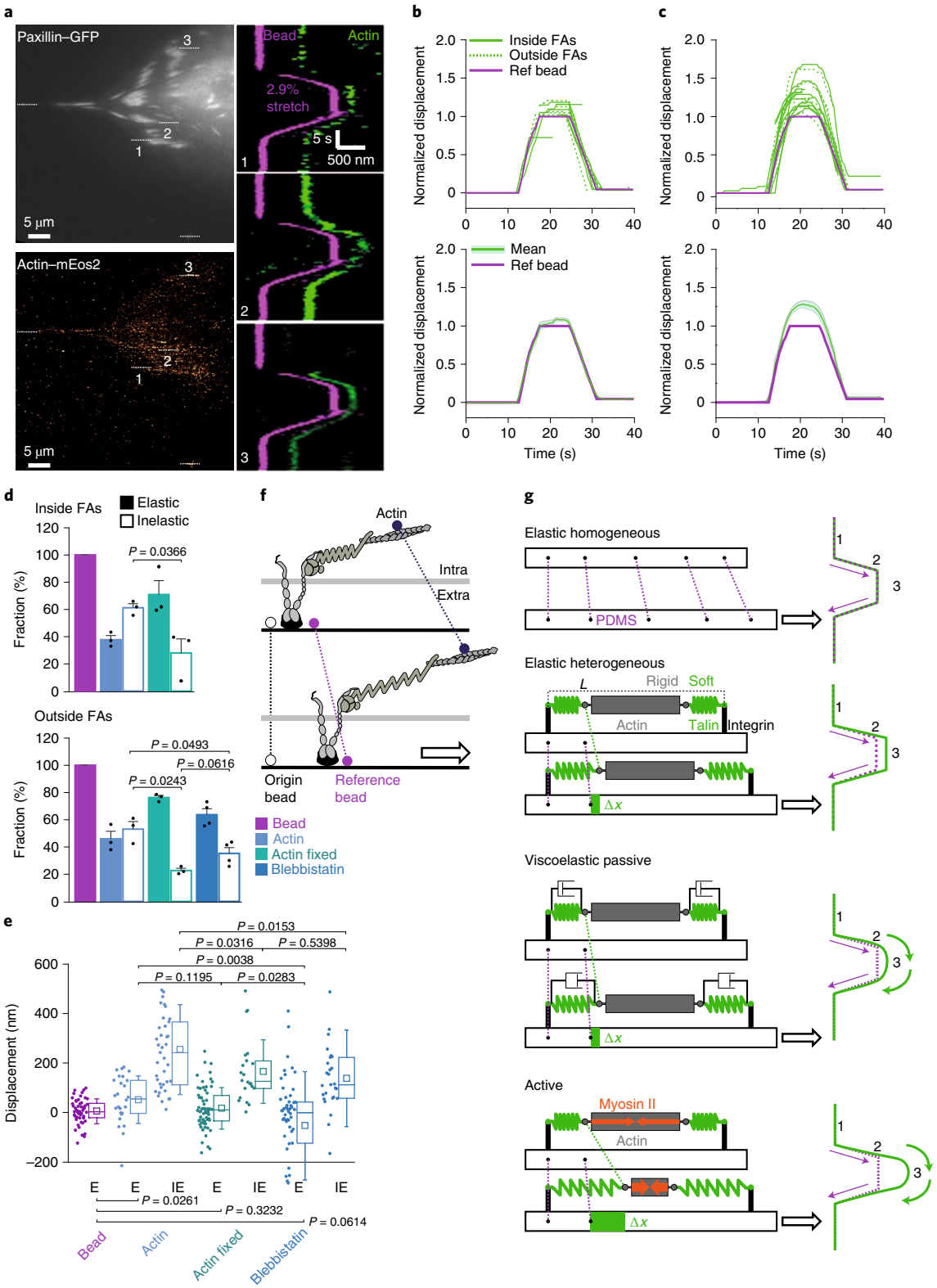

MEFs co-transfected with vinculin–mEos3.2 and paxillin–GFP (Fig. 6f,g). In contrast with zyxin, the density of vinculin trajectories during the stretching plateau did not increase in mature FAs for any of the analyzed (0/7) cells (Fig. 6h and Supplementary Video 10). The same result was found after larger stretches (~10%) (0/5 cells) (Extended Data Fig. 7c). One possible interpretation for this surprising result is that force-dependent recruitment occurs simultaneously with force-dependent dissociation, as demonstrated in vitro[13,57]. Alternatively, force-induced vinculin recruitment could depend on the maturation state of integrin-based adhesions.

Consistent with the hypothesis that vinculin recruitment depends on the maturation state of integrin adhesions, initiation and maturation of nascent adhesions depends on forces generated on early integrin–talin–actin connections[42,58] triggering vinculin recruitment[42,59] and connection to F-actin flows[10,60]. Thus, we performed experiments on nascent adhesions that form in protrusive structures of spreading and migrating cells[61,62]. We applied ~4% trapeze-like patterns to spreading MEFs co-transfected with vinculin–mEos2 and paxillin–GFP (Fig. 7a,b and Supplementary Video 11). In contrast with mature FAs, the density of vinculin–mEos2 trajectories in nascent adhesions increased in ~70% (7/10) of the cells (Fig. 7c). Cell relaxation induced a reduction of trajectories but still above the levels measured before stretching (Fig. 7c). The density of talin-C trajectories in nascent adhesions did not exhibit a large increase upon stretching (responding cells: 28%; 2/7) (Fig. 7j), suggesting that vinculin recruitment occurs mainly on talin residing in nascent adhesions, and not by recruitment of additional talin. Furthermore, the fraction of talin-C displaying inelastic responses was similar for nascent adhesions and mature FAs (Extended Data Fig. 8). Importantly, molecular vinculin–mEos2 recruitment did not reach its maximum immediately after stretching, but progressively or transiently increased during the plateau phase (Fig. 7f). Delayed vinculin recruitment in response to stretch is consistent with the lagged talin-C inelastic response occurring during the plateau (Fig. 4 and Extended Data Fig. 8) and associated with talin unfolding (Fig. 4). Kymograph analysis and colour coding of super-resolved time lapses revealed no region-selective recruitment of vinculin–mEos2 in nascent adhesions (Fig. 7d,e and Extended Data Fig. 9).

Discussion

A molecular understanding of mechanosensing has emerged from in vitro mechanical manipulations of proteins[12–14]. Studies performed by applying force on purified proteins showed that mechanosensing relies on protein unfolding and reorganization. The general consensus is that external stresses applied to cells are directly and instantaneously transmitted to proteins to trigger their deformation and reorganization. However, no experimental strategies enabled the application of external forces to cells while simultaneously capturing the mechanical response of individual proteins. Here, by combining cell stretching with SRM and SPT, we could reveal at the nanoscale the mechanical response of mechanosensitive structures. This enables the study of how polarized macromolecular complexes composed of distinct functional nano-domains[22,24,26] reorganize upon external stretch.

We found that protein deformations inside integrin-based adhesions are not triggered by direct transmission of the external stretch. Upon small (2–5%) stretching, actin filaments and talin displayed both elastic and inelastic responses. Inelastic responses led to lagged and transient (~5 s) local displacements (~250 nm) associated with talin deformations, as suggested by the larger fraction of inelastic responses for talin-C compared with talin-N. These distinct responses could also be interpreted as talin cleavage by calpain—a process triggering FA disassembly[63] or nascent adhesion growth[64]. Importantly, inelastic responses were decreased by cell fixation and myosin II inhibition, indicating a mechanism driven by active remodelling of the actin cytoskeleton. Thus, cells actively react to external forces, amplifying transiently and locally actin cytoskeleton displacements to trigger protein deformation in mechanosensitive structures.

The inelastic responses of actin and talin could also involve local ruptures of the actin cytoskeleton, in particular actin stress fibres. Stress fibres are repaired by recruitment of actin-binding proteins, including zyxin, α-actinin and vasodilator-stimulated phosphoprotein (VASP)[65,66]. Likewise, stimulation of myosin II contractility, using RhoA optogenetic activation, leads to local recruitment of zyxin to stress fibres[67]. Thus, zyxin-mediated stress fibre repair or mechanical homeostasis might be involved in inelastic responses. However, we showed that ~4% stretching did not cause major stress fibre ruptures or recruitment of zyxin and α-actinin to stress fibres (Extended Data Fig. 10a,c,e,f). In contrast, larger (~30%) stretching induced prominent stress fibre ruptures (Extended Data Fig. 10b) and recruitment of zyxin and α-actinin to stress fibres (Extended Data Fig. 10d,g). These results corroborate that rupture/repair events are rare events during ~4% trapeze-like patterns. Moreover, during ~4% trapeze-like patterns, we observed almost no plastic deformations that could correspond to local actin ruptures, since most individual actin, talin-N and talin-C came back to their initial positions (Figs. 4 and 5 and Extended Data Fig. 4). Rare plastic deformations were observed during single stretch–plateau patterns (~4%) where the stretch was sustained (Extended Data Fig. 5d). Nonetheless, these actin cytoskeletal ruptures were unidirectional and faster (~500 nm s^{-1}) than inelastic responses, which

Fig. 6 | Small-scale stretching triggers zyxin reorganization but has no effect on vinculin recruitment in mature FAs. a, Fluorescence image of paxillin–GFP in a MEF on the PDMS stretching device before stretching (right direction). **b**, Projection of zyxin–mEos3.2 super-resolution intensity images for the three phases of a trapeze-like pattern time lapse (stretching: 4.3%; 2 Hz; 8 s per phase): before (left), plateau (middle) and relax (right). The dotted region represents the area used to generate the kymograph in **d**. **c**, Variation of trajectory density (trc μm^{-2}) for zyxin–mEos3.2 ($n = 8$ cells pooled from four independent experiments) throughout trapeze-like patterns, normalized to the density before stretching. The results for individual cells are shown in orange, while the mean trajectory ratio ± s.d. is in bold orange. An increase of >1.1 is represented by a solid line, while an increase of <1.1 is represented by a dotted line. **d**, Zyxin–mEos3.2 kymograph generated from the trapeze-like pattern time lapse. The *x* axis shows space (2 μm) and the *y* axis shows time (10 s). The magenta kymograph represents the reference bead and the green kymographs represent zyxin–mEos3.2. **e**, Colour-coded projection of zyxin–mEos3.2 intensity images during the plateau (red: 0–3 s; green: 4–7 s; blue: 8–11 s; yellow: 11–15 s). **f**, Fluorescence image of paxillin–GFP in a MEF on the PDMS stretching device before stretching (right direction). **g**, Projection of vinculin–mEos2 super-resolution intensity images for the three phases of a trapeze-like pattern time lapse (stretching: 5%; 2 Hz; 8 s per phase): before (left), plateau (middle) and relax (right). The dotted region represents the area used to generate the kymograph in **i**. **h**, Variation of the trajectory density (trc μm^{-2}) for vinculin–mEos2 ($n = 7$ cells pooled from three independent experiments) throughout trapeze-like patterns, normalized to the density before stretching. The results for individual cells are shown in green, while the mean trajectory ratio ± s.d. is in bold green. An increase of >1.1 is represented by a solid line, while an increase of <1.1 is represented by a dotted line. **i**, Vinculin–mEos2 kymographs generated from a trapeze-like pattern time lapse. The *x* axis shows space (2 μm) and the *y* axis shows time (10 s). The magenta kymograph represents the reference bead and the green kymographs represent vinculin–mEos2. **j**, Schematic of zyxin recruitment in mature FAs. In **a**, **b**, **d** and **e**, data are representative of four independent experiments. In **f**, **g** and **j**, data are representative of three independent experiments. Statistical significance was determined using two-tailed Wilcoxon matched-pairs signed-rank tests.

were bidirectional and slower (overshoot phase: ~100 nm s^{-1}; recoil phase: ~20 nm s^{-1}). Thus, although we cannot exclude that inelastic responses might in part be influenced by plastic reorganizations of the actin cytoskeleton, our results support a model were inelastic responses are triggered by active, transient and reversible reorganizations of the actin cytoskeleton. Nevertheless, micrometre-scale stress fibre repair[65,66] or homeostasis[67] and inelastic responses of actin and talin could have common molecular players, although at different spatiotemporal scales.

At the molecular level, mechanical forces reinforce[14,15,38,42] or destabilize[2,41] interactions and expose hidden binding sites fostering protein recruitment, as demonstrated for integrin-based[12,13,32] and cadherin-based[68] adhesions. Combining cell stretching with SRM or SPT yields molecular resolution on protein reorganizations that can be spatially and temporally heterogeneous within mechanosensitive structures. For instance, molecular vinculin recruitment is delayed and depends on the maturation state of the integrin–talin–cytoskeleton connections. This supports the hypothesis that substrate

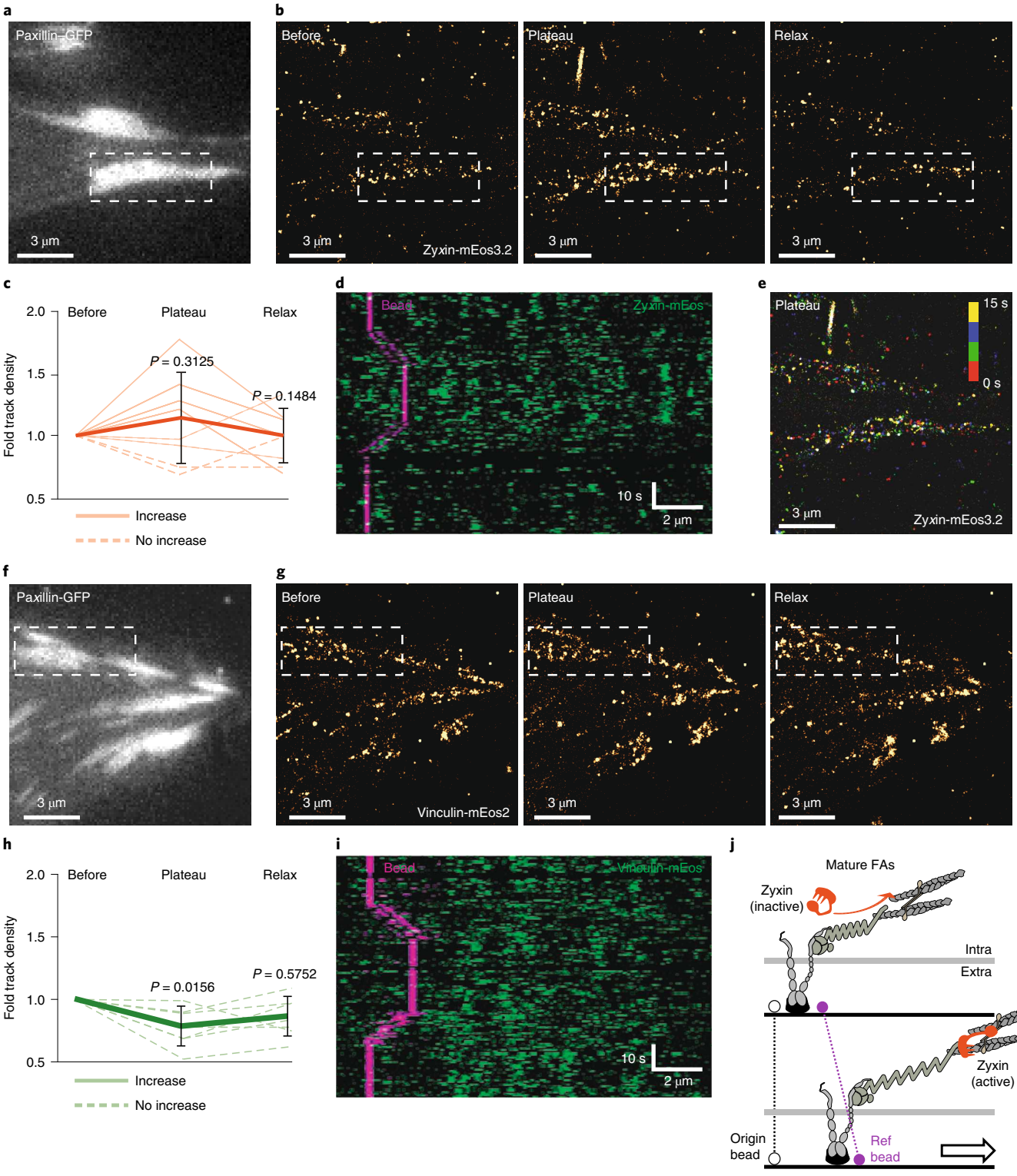

stretching is not directly driving talin unfolding. Instead, our results are consistent with a model where external stresses applied to cells trigger subsequent cellular active responses (for example, active actin reorganization), leading to protein unfolding and recruitment.

The ability of talin to recruit vinculin might depend on its force history and initial tensional state, which might differ in nascent adhesions versus FAs[69]. This is consistent with in vitro experiments using purified talin rod domains and vinculin. Vinculin-unloaded

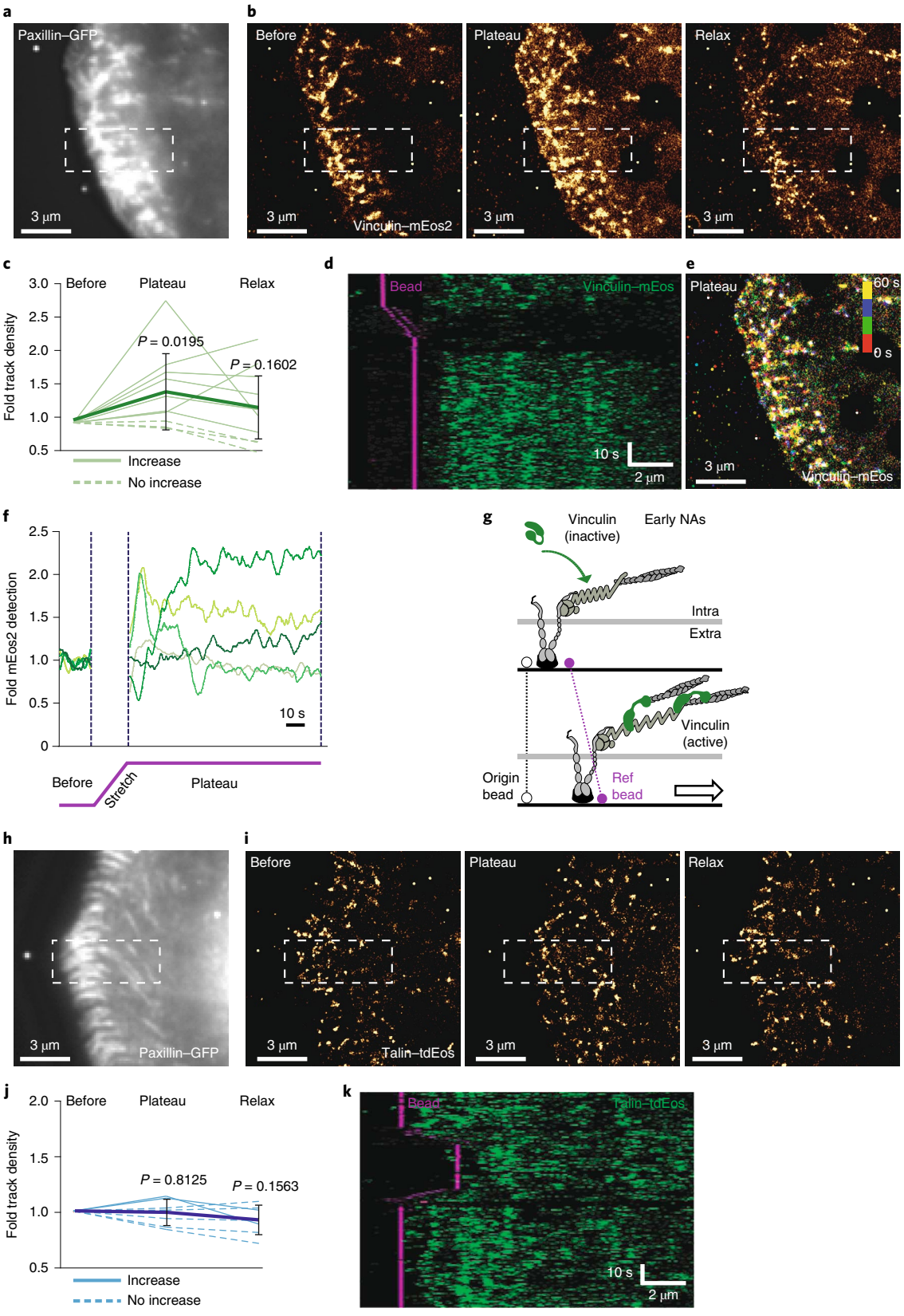

Fig. 7 | Small-scale stretching triggers vinculin recruitment in nascent adhesions without recruitment of additional talin. a, Fluorescence image of paxillin–GFP in a spreading MEF on the stretching device before stretching (right direction). **b**, Projection of vinculin–mEos2 super-resolution intensity images for the three phases of a trapeze-like pattern time lapse (stretching: 4.2%; 2 Hz; 40 s per phase): before (left), plateau (middle) and relax (right). The dotted region represents the area used to generate the kymograph in **d**. **c**, Variation of trajectory density (trc μm^{-2}) for vinculin–mEos2 ($n = 10$ cells pooled from four independent experiments) throughout trapeze-like patterns, normalized to density before stretching. The results for individual cells are shown in green, while the mean trajectory ratio ± s.d. is in bold green. An increase of >1.1 is represented by a solid line, while an increase of <1.1 is represented by a dotted line. **d**, Vinculin–mEos2 kymographs generated from trapeze-like pattern time lapse. The *x* axis shows space (2 µm) and the *y* axis shows time (10 s). The magenta kymograph represents the reference bead and the green kymographs represent vinculin–mEos2. **e**, Colour-coded projection of all vinculin–mEos2 intensity images during the plateau (red: 0–15 s; green: 15–30 s; blue: 30–45 s; yellow: 45–60 s). **f**, Temporal molecular recruitment of vinculin–mEos2 during the plateau, normalized to vinculin–mEos2 detections before stretching. Lines (various green shades) correspond to individual cells. **g**, Schematic of vinculin recruitment in early nascent adhesions. **h**, Paxillin–GFP in a spreading MEF on the stretching device before stretching (right direction). **i**, Projection of talin-C–tdEos super-resolution intensity images for the three phases of a trapeze-like pattern time lapse (stretching: 3.7%; 2 Hz; 8 s per phase): before (left), plateau (middle) and relax (right). The dotted region represents the area used to generate the kymograph in **k**. **j**, Variation of trajectory density (trc μm^{-2}) for talin-C–tdEos ($n = 7$ cells pooled from three independent experiments) throughout trapeze-like patterns, normalized to the density before stretching. The results for individual cells are shown in green, while the mean trajectory ratio ± s.d. is in bold green. An increase of >1.1 is represented by a solid line, while an increase of <1.1 is represented by a dotted line. **k**, Talin-C–tdEos kymographs generated from a trapeze-like pattern time lapse. The *x* axis shows space (2 µm) and the *y* axis shows time (10 s). The magenta kymograph represents the reference bead and the green kymographs represent talin-C-tdEos. Data are representative of four independent experiments (**a**, **b**, **d** and **e**) and three independent experiments (**h**, **i** and **k**). Statistical significance was determined using two-tailed Wilcoxon matched-pairs signed-rank tests.

talin recruits vinculin upon an initial stretch, while vinculin-loaded talin will still be stretched by external forces without recruitment of additional vinculin[13,57]. Stretching of already extended talin might further unfold vinculin-binding domains, leading to vinculin dissociation[13,57]. Thus, the undetectable molecular recruitment of vinculin in mature FAs might be explained by simultaneous recruitment and dissociation upon cell stretching. In contrast, newly recruited talin into nascent adhesions might have lower tensional sates, free from any previous stretching, with all vinculin-binding sites available for recruitment to trigger maturation to FAs. This idea is consistent with the axial redistribution of vinculin observed in nascent adhesions using three-dimensional SRM interferometric PALM in fixed cells[70].

Micro-rheology studies have demonstrated that mechanical stability of actin networks relies on their elastic properties, which are prevalent at short time scales. Conversely, remodelling occurs through inelastic or nonlinear responses leading to stress stiffening or weakening over timescales of seconds to tens of seconds[44–46]. However, conventional micro-rheology methods average over any heterogeneity, inelasticity and time fluctuations occurring at the molecular level. Combining cell stretching and SRM/SPT, our approach paves the way to nano-rheology of the cell. We have captured the excitable nature of the acto-myosin cytoskeleton at the nanoscale, which transiently amplifies displacements induced by extracellular forces, leading to local protein stretching and recruitment. Thus, our findings suggest that mechanosensing must occur within a few seconds, during the local displacement amplification. Substrate mechanosensing could be mediated by fluctuations of intracellular and extracellular forces[9,30,39]; hence, transient amplifications might reset the capability of the cell to respond to successive mechanical stimuli. Spatiotemporal force fluctuation in FAs[30] probably emerges from the heterogeneous tensional/connective states of proteins at the nanoscale[8]. Each stationary protein detected by conventional SRM/SPT conceals its tensional and connectional states, which we unveiled by challenging proteins through a uniform mechanical perturbation. We expect that our approach will be applied to decipher at the molecular level the growing number of mechanosensitive structures or organelles such as caveolae[2], kinetochores[3], hemidesmosomes[4] or the nucleus[7].

Online content

Any methods, additional references, Nature Research reporting summaries, source data, extended data, supplementary information, acknowledgements, peer review information; details of author contributions and competing interests; and statements of data and code availability are available at https://doi.org/10.1038/s41556-020-0548-2.

Received: 5 October 2018; Accepted: 22 June 2020;
Published online: 27 July 2020

References

1. Paszek, M. J. et al. The cancer glycocalyx mechanically primes integrin-mediated growth and survival. *Nature* **511**, 319–325 (2014).
2. Sinha, B. et al. Cells respond to mechanical stress by rapid disassembly of caveolae. *Cell* **144**, 402–413 (2011).
3. Dumont, S., Salmon, E. D. & Mitchison, T. J. Deformations within moving kinetochores reveal different sites of active and passive force generation. *Science.* **337**, 355–358 (2012).
4. Zhang, H. et al. A tension-induced mechanotransduction pathway promotes epithelial morphogenesis. *Nature* **471**, 99–103 (2011).
5. Ladoux, B. & Mège, R. M. Mechanobiology of collective cell behaviours. *Nat. Rev. Mol. Cell Biol.* **18**, 743–757 (2017).
6. Iskratsch, T., Wolfenson, H. & Sheetz, M. P. Appreciating force and shape—the rise of mechanotransduction in cell biology. *Nat. Rev. Mol. Cell Biol.* **15**, 825–833 (2014).
7. Cho, S., Irianto, J. & Discher, D. E. Mechanosensing by the nucleus: from pathways to scaling relationships. *J. Cell Biol.* **216**, 305–315 (2017).
8. Oria, R. et al. Force loading explains spatial sensing of ligands by cells. *Nature* **552**, 219–224 (2017).
9. Goldyn, A. M., Rioja, B. A., Spatz, J. P., Ballestrem, C. & Kemkemer, R. Force-induced cell polarisation is linked to RhoA-driven microtubule-independent focal-adhesion sliding. *J. Cell Sci.* **122**, 3644–3651 (2009).
10. Grashoff, C. et al. Measuring mechanical tension across vinculin reveals regulation of focal adhesion dynamics. *Nature* **466**, 263–266 (2010).
11. Polacheck, W. J. & Chen, C. S. Measuring cell-generated forces: a guide to the available tools. *Nat. Methods* **13**, 415–423 (2016).
12. Del Rio, A. et al. Stretching single talin rod molecules activates vinculin binding. *Science* **323**, 638–641 (2009).
13. Yao, M. et al. The mechanical response of talin. *Nat. Commun.* **7**, 11966 (2016).
14. Huang, D. L., Bax, N. A., Buckley, C. D., Weis, W. I. & Dunn, A. R. Vinculin forms a directionally asymmetric catch bond with F-actin. *Science* **357**, 703–706 (2017).
15. Kong, F. et al. Demonstration of catch bonds between an integrin and its ligand. *J. Cell Biol.* **185**, 1275–1284 (2009).
16. Müller, D. J. & Dufrêne, Y. F. Atomic force microscopy: a nanoscopic window on the cell surface. *Trends Cell Biol.* **21**, 461–469 (2011).
17. Liu, Z., Lavis, L. D. & Betzig, E. Imaging live-cell dynamics and structure at the single-molecule level. *Mol. Cell.* **58**, 644–659 (2015).
18. Sahl, S. J., Hell, S. W. & Jakobs, S. Fluorescence nanoscopy in cell biology. *Nat. Rev. Mol. Cell Biol.* **18**, 685–701 (2017).

19. Huang, B., Bates, M. & Zhuang, X. Super-resolution fluorescence microscopy. *Annu. Rev. Biochem.* **78**, 993–1016 (2009).
20. Rossier, O. & Giannone, G. The journey of integrins and partners in a complex interactions landscape studied by super-resolution microscopy and single protein tracking. *Exp. Cell Res.* **343**, 28–34 (2016).
21. Bertocchi, C. et al. Nanoscale architecture of cadherin-based cell adhesions. *Nat. Cell Biol.* **19**, 28–37 (2017).
22. Xu, K., Zhong, G. & Zhuang, X. Actin, spectrin, and associated proteins form a periodic cytoskeletal structure in axons. *Science* **339**, 452–456 (2013).
23. Nair, D. et al. Super-resolution imaging reveals that AMPA receptors inside synapses are dynamically organized in nanodomains regulated by PSD95. *J. Neurosci.* **33**, 13204–13224 (2013).
24. Chazeau, A. et al. Nanoscale segregation of actin nucleation and elongation factors determines dendritic spine protrusion. *EMBO J.* **33**, 2745–2764 (2014).
25. Mehidi, A. et al. Transient activations of Rac1 at the lamellipodium tip trigger membrane protrusion. *Curr. Biol.* **29**, 2852–2866.e5 (2019).
26. Kanchanawong, P. et al. Nanoscale architecture of integrin-based cell adhesions. *Nature* **468**, 580–584 (2010).
27. Rossier, O. et al. Integrins β1 and β3 exhibit distinct dynamic nanoscale organizations inside focal adhesions. *Nat. Cell Biol.* **14**, 1057–1067 (2012).
28. Morimatsu, M., Mekhdjian, A. H., Adhikari, A. S. & Dunn, A. R. Molecular tension sensors report forces generated by single integrin molecules in living cells. *Nano Lett.* **13**, 3985–3989 (2013).
29. Stabley, D. R., Jurchenko, C., Marshall, S. S. & Salaita, K. S. Visualizing mechanical tension across membrane receptors with a fluorescent sensor. *Nat. Methods* **9**, 64–67 (2011).
30. Plotnikov, S. V., Pasapera, A. M., Sabass, B. & Waterman, C. M. Force fluctuations within focal adhesions mediate ECM-rigidity sensing to guide directed cell migration. *Cell* **151**, 1513–1527 (2012).
31. Margadant, F. et al. Mechanotransduction in vivo by repeated talin stretch–relaxation events depends upon vinculin. *PLoS Biol.* **9**, e1001223 (2011).
32. Ciobanasu, C., Faivre, B. & Le Clainche, C. Actomyosin-dependent formation of the mechanosensitive talin–vinculin complex reinforces actin anchoring. *Nat. Commun.* **5**, 3095 (2014).
33. Chen, Y., Pasapera, A. M., Koretsky, A. P. & Waterman, C. M. Orientation-specific responses to sustained uniaxial stretching in focal adhesion growth and turnover. *Proc. Natl Acad. Sci. USA* **110**, E2352–E2361 (2013).
34. Schnitzbauer, J., Strauss, M. T., Schlichthaerle, T., Schueder, F. & Jungmann, R. Super-resolution microscopy with DNA-PAINT. *Nat. Protoc.* **12**, 1198–1228 (2017).
35. Lukinavičius, G. et al. Fluorogenic probes for live-cell imaging of the cytoskeleton. *Nat. Methods* **11**, 731–733 (2014).
36. Dempsey, G. T., Vaughan, J. C., Chen, K. H., Bates, M. & Zhuang, X. Evaluation of fluorophores for optimal performance in localization-based super-resolution imaging. *Nat. Methods* **8**, 1027–1040 (2011).
37. Betzig, E. et al. Imaging intracellular fluorescent proteins at nanometer resolution. *Science* **313**, 1642–1645 (2006).
38. Friedland, J. C., Lee, M. H. & Boettiger, D. Mechanically activated integrin switch controls $\alpha_5\beta_1$ function. *Science* **323**, 642–644 (2009).
39. Cui, Y. et al. Cyclic stretching of soft substrates induces spreading and growth. *Nat. Commun.* **6**, 6333 (2015).
40. Hu, K., Ji, L., Applegate, K. T., Danuser, G. & Waterman-Storer, C. M. Differential transmission of actin motion within focal adhesions. *Science* **315**, 111–115 (2007).
41. Jiang, G., Giannone, G., Critchley, D. R., Fukumoto, E. & Sheetz, M. P. Two-piconewton slip bond between fibronectin and the cytoskeleton depends on talin. *Nature* **424**, 334–337 (2003).
42. Giannone, G., Jiang, G., Sutton, D. H., Critchley, D. R. & Sheetz, M. P. Talin1 is critical for force-dependent reinforcement of initial integrin–cytoskeleton bonds but not tyrosine kinase activation. *J. Cell Biol.* **163**, 409–419 (2003).
43. Calderwood, D. A., Campbell, I. D. & Critchley, D. R. Talins and kindlins: partners in integrin-mediated adhesion. *Nat. Rev. Mol. Cell Biol.* **14**, 503–517 (2013).
44. Trepat, X. et al. Universal physical responses to stretch in the living cell. *Nature* **447**, 592–595 (2007).
45. Mizuno, D., Tardin, C., Schmidt, C. F. & MacKintosh, F. C. Nonequilibrium mechanics of active cytoskeletal networks. *Science* **315**, 370–373 (2007).
46. Gardel, M. L. et al. Elastic behavior of cross-linked and bundled actin networks. *Science* **304**, 1301–1305 (2004).
47. Bausch, A. R., Ziemann, F., Boulbitch, A. A., Jacobson, K. & Sackmann, E. Local measurements of viscoelastic parameters of adherent cell surfaces by magnetic bead microrheometry. *Biophys. J.* **75**, 2038–2049 (1998).
48. Desprat, N., Richert, A., Simeon, J. & Asnacios, A. Creep function of a single living cell. *Biophys. J.* **88**, 2224–2233 (2005).
49. Wu, P.-H. et al. A comparison of methods to assess cell mechanical properties. *Nat. Methods* **15**, 491–498 (2018).
50. Várkuti, B. H. et al. A highly soluble, non-phototoxic, non-fluorescent blebbistatin derivative. *Sci. Rep.* **6**, 26141 (2016).
51. Schiller, H. B. & Fässler, R. Mechanosensitivity and compositional dynamics of cell-matrix adhesions. *EMBO Rep.* **14**, 509–519 (2013).
52. Horton, E. R. et al. Definition of a consensus integrin adhesome and its dynamics during adhesion complex assembly and disassembly. *Nat. Cell Biol.* **17**, 1577–1587 (2015).
53. Sawada, Y. & Sheetz, M. P. Force transduction by Triton cytoskeletons. *J. Cell Biol.* **156**, 609–615 (2002).
54. Hirata, H., Tatsumi, H. & Sokabe, M. Mechanical forces facilitate actin polymerization at focal adhesions in a zyxin-dependent manner. *J. Cell Sci.* **121**, 2795–2804 (2008).
55. Dumbauld, D. W. et al. How vinculin regulates force transmission. *Proc. Natl Acad. Sci. USA* **110**, 9788–9793 (2013).
56. Rothenberg, K. E., Scott, D. W., Christoforou, N. & Hoffman, B. D. Vinculin force-sensitive dynamics at focal adhesions enable effective directed cell migration. *Biophys. J.* **114**, 1680–1694 (2018).
57. Yao, M. et al. Mechanical activation of vinculin binding to talin locks talin in an unfolded conformation. *Sci. Rep.* **4**, 4610 (2014).
58. Zhang, X. et al. Talin depletion reveals independence of initial cell spreading from integrin activation and traction. *Nat. Cell Biol.* **10**, 1062–1068 (2008).
59. Galbraith, C. G., Yamada, K. M. & Sheetz, M. P. The relationship between force and focal complex development. *J. Cell Biol.* **159**, 695–705 (2002).
60. Thievessen, I. et al. Vinculin–actin interaction couples actin retrograde flow to focal adhesions, but is dispensable for focal adhesion growth. *J. Cell Biol.* **202**, 163–177 (2013).
61. Giannone, G. et al. Lamellipodial actin mechanically links myosin activity with adhesion-site formation. *Cell.* **128**, 561–575 (2007).
62. Choi, C. K. et al. Actin and α-actinin orchestrate the assembly and maturation of nascent adhesions in a myosin II motor-independent manner. *Nat. Cell Biol.* **10**, 1039–1050 (2008).
63. Franco, S. J. et al. Calpain-mediated proteolysis of talin regulates adhesion dynamics. *Nat. Cell Biol.* **6**, 977–983 (2004).
64. Saxena, M., Changede, R., Hone, J., Wolfenson, H. & Sheetz, M. P. Force-induced calpain cleavage of talin is critical for growth, adhesion development, and rigidity sensing. *Nano Lett.* **17**, 7242–7251 (2017).
65. Smith, M. A. et al. A zyxin-mediated mechanism for actin stress fiber maintenance and repair. *Dev. Cell* **19**, 365–376 (2010).
66. Smith, M. A. et al. LIM domains target actin regulators paxillin and zyxin to sites of stress fiber strain. *PLoS ONE* **8**, e69378 (2013).
67. Oakes, P. W. et al. Optogenetic control of RhoA reveals zyxin-mediated elasticity of stress fibres. *Nat. Commun.* **8**, 15817 (2017).
68. Yonemura, S., Wada, Y., Watanabe, T., Nagafuchi, A. & Shibata, M. α-Catenin as a tension transducer that induces adherens junction development. *Nat. Cell Biol.* **12**, 533–542 (2010).
69. Ringer, P. et al. Multiplexing molecular tension sensors reveals piconewton force gradient across talin-1. *Nat. Methods* **14**, 1090–1096 (2017).
70. Case, L. B. et al. Molecular mechanism of vinculin activation and nanoscale spatial organization in focal adhesions. *Nat. Cell Biol.* **17**, 880–892 (2015).

Methods

Cells. MEFs were cultured in DMEM (Gibco) with 10% foetal bovine serum (Gibco), GlutaMAX supplement, 100 U ml^{-1} penicillin-streptomycin, 1 mM sodium pyruvate and 15 mM HEPES. Transient transfections of plasmids were performed 1–3 d before experiments using the Nucleofector transfection kit for MEF-1 and Nucleofector IIb device (Amaxa; Lonza). The cells were detached with 0.05% trypsin and 0.02% EDTA solution (Gibco). The trypsin was inactivated using soybean trypsin inhibitor (1 mg ml^{-1} in DMEM; Sigma–Aldrich) and the cells were washed and suspended in serum-free Ringer medium (150 mM NaCl, 5 mM KCl, 2 mM $CaCl_2$, 2 mM $MgCl_2$ and 10 mM HEPES (pH 7.4)) supplemented with 11 mM glucose. Cells were seeded for 3–5 h on a human fibronectin-coated surface (fibronectin: 10 µg ml^{-1}). The fibronectin was adsorbed for 90 min at 37 °C on the observation chamber of the micromechanical device or on glass coverslips. Vimentin knockout MEFs were kindly provided by H. Herrmann and G. Wiche/C. Leduc, and were previously described[71,72].

DNA constructs. The mouse vimentin–GFP construct was provided by D. Pham-Dinh[73] and vimentin–halo was cloned from vimentin–GFP and tubulin–halo (Addgene; 64691) using a HiFi DNA Assembly Cloning Kit (Biolabs). The tubulin–GFP construct was a gift from M. Sheetz (Mechanobiology Institute (MBI) at the National University of Singapore (NUS), and University of Texas Medical Branch). 6His–β3-integrin–GFP was obtained from human β3-integrin–GFP (provided by N. Kieffer; CNRS/CRP, Luxembourg) by domain swapping using the QuikChange II XL Site-Directed Mutagenesis kit (Stratagene) to introduce the 6His tag and glycine linker in the amino terminus. For the human 6His–β3-integrin–mEos2 (vector: pEGFP-N1), a PCR of mEos2 was done on pRSETa–mEos2 (Addgene) to replace the GFP from human 6His β3-integrin–GFP at the AgeI/BsrGI sites. The actin–mEos2 construct was generated by replacing GFP from pEGFP actin (provided by A. Matus and F. Miescher at the Institute for Biomedical Research, Switzerland) with mEos2 at the AgeI/XhoI sites; the mEos2 fragment was obtained by PCR on pRSETa-mEos2 (Addgene). The paxillin in the paxillin–GFP construct is human. Talin1-22–tdEos (talin-C), tdEOS-18–Talin1 (talin-N) and mEos2-7–talinABS (THATCH) were gifts from P. Kanchanawong (NIH, United States and MBI, NUS, Singapore)[26]. For the vinculin–mEos2 construct, a PCR of vinculin was done on vinculin–GFP and vinculin was inserted on a pmEos2-C1 vector at EcoRI/SacII sites. The zyxin–mEos3.2 construct was purchased commercially (Addgene; 57487), as well as zyxin–mEmerald (Addgene; 54319). The α-actinin–GFP construct was described previously[74]. The fidelity of all constructs was verified by sequencing.

Immunostaining. For immunostainings, cells were fixed in 4% paraformaldehyde, 0.3% glutaraldehyde and 0.3% Triton X-100 in phosphate-buffered saline for 20 min at 37 °C, quenched with glycine (150 mM) for 20 min, permeabilized with 0.3% Triton X-100 for 10 min and blocked in phosphate-buffered saline supplemented with 3% BSA for 90 min. Both primary and secondary antibody incubations were performed in blocking buffer for 1 h at room temperature. The following antibodies were used: mouse monoclonal antibody against mouse α-tubulin (1:750; Thermo Fisher Scientific; 11126) and ATTO 647N-dye-conjugated antibody against mouse immunoglobulin G (1:1,000; Sigma–Aldrich; 50185-1ML-F).

Micromechanical device compatible with SRM. The step-by-step protocol to generate and assemble the micromechanical device, and the procedure to perform cell stretching combined with SRM and SPT can be found in the *Nature* Protocol Exchange repository[75]. To simultaneously enable substrate stretching and ensure flatness upon deformation, we deposited an ultra-thin PDMS sheet (10 µm; Sylgard 184; Samaro DE9330) on a lubricated glass coverslip (#1) (Fig. 1b). To manipulate such a thin PDMS substrate and avoid mechanical distortion, we reinforced its mechanical stability by adding a thicker (40 µm) elastomer frame (PF film X0; 1.5 mil; Gel-Pak) on top of the thin PDMS layer, keeping the size of the observation chamber as small as possible (3 mm × 3 mm; 9 mm^2) (Fig. 1a,b). This 40-µm elastomer frame was pre-cut to the size of the glass coverslip with a squared (3 mm × 3 mm) observation chamber using a Graphtec cutting plotter (Graphtec Craft ROBO pro; CE5000-40-CRP). PDMS was spun on a wafer to a final thickness of 10 µm and pre-cured for 25 min at 70 °C. Then, the pre-cut elastomer frame was brought into contact with the 10-µm-thick PDMS and the whole assembly was cured overnight. Afterwards, the PDMS sheet was detached from the wafer and sandwiched with a lubricant-coated glass coverslip. The lubricant, which served to avoid adhesion and let the deformable substrate float freely, had to be compatible with the physico-chemical properties of PDMS. In particular, PDMS swelling and refractive index mismatch had to be avoided. Based on the comprehensive study of PDMS solvent compatibility from the Whitesides group[76], we selected glycerol (solubility parameter $\delta = 21.1$ cal$^{1/2}$cm$^{-3/2}$; $n_{glycerol} = 1.47$). Low-viscous glycerol (glycerol for fluorescence microscopy; CAS 56-81-5; Merck; 1040950250) was spun on a plasma-cleaned glass coverslip and then sandwiched with the plasma-cleaned PDMS sheet, creating a glycerol layer of ~0.7 µm thickness. This design enabled the localization of individual purified photoactivatable fluorescent proteins (mEos2) adsorbed on the PDMS with a pointing accuracy of ~32 nm for 10 µm PDMS compared with ~23 nm for glass (Fig. 1c and Extended Data Fig. 3b). We could also perform PALM and sptPALM acquisitions in the TIRF mode, with resolutions comparable to glass[27,37] (Fig. 1d and Extended Data Fig. 3). The use of thicker PDMS substrates (50 µm) degraded the resolution and prevented efficient tracking of individual β3-integrin–mEos2 due to the lower density of mEos2 trajectories (Fig. 1c and Extended Data Fig. 3g,h). The spatial resolution of DNA-PAINT acquisitions obtained on the 10-µm PDMS micromechanical device after stretching was ~35 ± 5 nm (full width at half-maximum (FWHM)). The spatial resolution of STED acquisitions under the same conditions was ~145 ± 10 nm, measured with a recently described ImageJ decorrelation plugin[77]. In comparison, the spatial resolution of confocal acquisitions was ~365 ± 12 nm.

To generate uniaxial stretches on the glass–PDMS assembly, we designed a 3D-printed micro-device (Fig. 1a and Extended Data Fig. 1). The micromechanical device consisted of a fixed (holding) arm and a mobile (stretching) arm connected to a piezoelectric motor (M-663 Linear Positioning Stage; 19 mm; Linear Encoder; 0.1 µm resolution; PI) positioned on opposite sides of the observation chamber on the PDMS frame (Fig. 1a). A clamp fixed the glass–PDMS assembly to the base of the device and to the holding arm (Fig. 1a and Extended Data Fig. 1). The observation chamber or the whole microchip could be filled with culture or observation medium.

During SRM/SPT acquisitions, the flatness and the glass-like optical properties of the glass–glycerol–PDMS assembly enabled continuous focusing using an autofocus system (Perfect Focus System; PFS-2; Nikon) that relies on light reflection at sharp transitions between refractive indexes—in this case, between the 10-µm PDMS sheet and water. To register super-resolution intensity images and to measure PDMS deformation, we adsorbed 0.1-µm fluorescent beads (TetraSpeck Microspheres; 0.1 µm; Thermo Fisher Scientific; T7279) on the stretching chamber that were imaged during the entirety of the SRM/SPT acquisitions.

Mechanical properties of the micromechanical device. We tested numerically and experimentally the mechanical properties of our stretching device, being aware that one intrinsic feature of uniaxial stretching is that the substrate is stretched along the deformation axis and compressed perpendicular to this, with potential constriction effects at large deformation. We tested whether our device could allow us to reach a controlled and homogeneous strain over the observation area. Using a finite element simulation software (COMSOL Multiphysics), we simulated the surface stress and displacement for a defined stretching percentage. Our simulations showed that the surface stresses in the central observation chamber are expected to be remarkably uniform and uniaxial up to 90% stretch (Extended Data Fig. 1a). The resulting displacement fields, which increased proportionally with the distance from the frame limit (holding arm side), were also homogenous.

To experimentally assess whether the strain was homogeneous, we used micro-contact printing to imprint the PDMS with 100 µm × 100 µm fluorescent squares of rhodamine-enriched fibronectin (Extended Data Fig. 1c). We applied trapeze-like patterns, composed of stretch–plateau–relax phases, and measured the resulting x and y deformations. Not only were the stretches perfectly reproducible at 30, 60 and 90%, but the estimated stretch and measured elongation of the micro-pattern were in very good agreement. Deformations in the axis perpendicular to the stretch were minimal both theoretically and experimentally (Extended Data Fig. 1b,d).

STED. Cells were imaged at 25 °C for the fixed experiments (Fig. 1f,g and Extended Data Fig. 2) and at 37 °C for the live experiments (Extended Data Fig. 2) in the micromechanical device with an inverted confocal microscope (Leica SP8 WLL2) equipped with a HC PL APO CS2 motCORR 93× Glycerol, NA 1.3 objective. The confocal microscope was equipped of a white light laser 2 (WLL2) with freely tuneable excitation from 470–670 nm (1-nm steps). Scanning was done using a conventional scanner (10–1,800 Hz). The confocal microscope was equipped with the STED module tunable to STED microscopy. A two-dimensional STED donut was generated using a vortex phase plate. This STED microscope was equipped with three depletion lasers: 592, 660 and 775 nm. For STED microscopy, cells were imaged with a combination of a WLL2 laser and a 775-nm depletion laser. Fluorescence was collected with an internal hybrid detector. The acquisition was steered by LAS X software (Leica). For the fixed STED experiments (Fig. 1), cells were labelled with ATTO 647N-conjugated secondary antibodies. For the live STED experiments (Extended Data Fig. 2), cells were stained live for 1 h with 2 µM SiR-actin (Spirochrome) or 2 µM SiR-tubulin (Spirochrome) at 37 °C in Ringer imaging medium. The medium was rinsed once and cells were imaged afterwards.

DNA-PAINT acquisition and analysis. Cells were imaged at 25 °C in the micromechanical device with an inverted motorized microscope (Nikon Ti) equipped with a CFI Apochromat TIRF 100× oil, NA 1.49 objective and a perfect focus system (PFS-2), allowing long acquisition in TIRF illumination mode. For DNA-PAINT microscopy, cells expressing vimentin–halo were first incubated with 90 nm gold nanoparticles (Cytodiagnostics) to serve as fiducial markers. Vimentin–halo was then visualized with Cy3B-labelled DNA imager strands added to the stretching chamber at variable concentrations (2–5 nM), as previously described[34]. Cy3B-labelled strands were visualized with a 561-nm laser (Cobolt Jive). Fluorescence was collected by the combination of a dichroic filter and emission filters (dichroic: Di01-R561; emission: FF01-617/73; Semrock) and a

sensitive scientific complementary metal–oxide–semiconductor (ORCA-Flash4.0; Hammatasu). The acquisition was steered by MetaMorph software (Molecular Devices) in streaming mode at 6.7 Hz. Vimentin–GFP was imaged using a conventional GFP filter cube (excitation: FF01-472/30; dichroic: FF-495Di02; emission: FF02-520/28; Semrock). Super-resolution DNA-PAINT reconstruction and drift correction were carried out as described before, using the software package Picasso[34].

SRM in fixed cells with large stretches. The design of the micromechanical device was first modified to enable sustained stretching: (1) through a groove and threaded hole system to clamp the stretching arm; or (2) using a central bar to block the recoil of the arm. To enable low-resolution imaging of target structures before and after stretching, vimentin knockout MEFs were transfected with vimentin–GFP (for DNA-PAINT), while wild-type MEFs were transfected with tubulin–GFP (for STED). For DNA-PAINT imaging, MEFs were also transfected with vimentin–halo for posterior labelling. Before stretching, cells were imaged by low-resolution epifluorescence microscopy to capture the pre-stretching morphology through visualization of GFP-tagged proteins. Stretching was then performed outside the microscope at large percentages (30–50%), followed by rapid cell fixation (as described before) and clamping or holding of the arm with the previously mentioned systems. This allowed maintenance of the stretching throughout all of the subsequent staining steps and super-resolved imaging with STED or DNA-PAINT. Before performing super-resolution imaging, cells were again imaged with GFP markers through low-resolution epifluorescence microscopy. Fluorescent beads (TetraSpeck Microspheres; 0.1 µm; Thermo Fisher Scientific; T7279) were adsorbed on the stretching chamber and were imaged before and after the stretch to measure the stretching percentage. Vimentin–GFP or tubulin–GFP were imaged using a conventional GFP filter cube (excitation: FF01-472/30; dichroic: FF-495Di02; emission: FF02-520/28; Semrock).

PALM. Cells were imaged at 37 °C, in the micromechanical device or on glass coverslips, with an inverted motorized microscope (Nikon Ti) equipped with a CFI Apochromat TIRF 100× oil, NA 1.49 objective and a perfect focus system (PFS-2), allowing long acquisition in TIRF illumination mode. For photoactivation localization microscopy, cells expressing mEos2-/tdEos-tagged constructs were photoactivated using a 405-nm laser (Omicron) and the resulting photoconverted single-molecule fluorescence was excited with a 561-nm laser (Cobolt Jive). Both lasers illuminated the sample simultaneously. Their respective power was adjusted to keep the number of the stochastically activated molecules constant and well separated during the acquisition. Fluorescence was collected by the combination of a dichroic filter and emission filters (dichroic: Di01-R561; emission: FF01-617/73; Semrock) and a sensitive electron-multiplying charge-coupled device (Evolve; Photometric). The acquisition was steered by MetaMorph software (Molecular Devices) in streaming mode at 50 Hz. Paxillin–GFP was imaged using a conventional GFP filter cube (excitation: FF01-472/30; dichroic: FF-495Di02; emission: FF02-520/28; Semrock).

Single-molecule segmentation and tracking. Single-molecule fluorescent spots were localized and tracked over time using a combination of wavelet segmentation and simulated annealing algorithms (Izeddin et al.[78] and Racine et al.[79,80]). The spatial resolution depends on the image signal-to-noise ratio and the segmentation algorithm (Cheezum et al.[81]) and was determined using purified mEos2 adsorbed on plasma-cleaned glass coverslips or glass–PDMS assembly (10 or 50 µm) (Extended Data Fig. 3). We analysed two-dimensional distributions of single-molecule positions by bi-dimensional Gaussian fitting, the resolution being determined as $2.3\times s_{xy}$, where s_{xy} is the pointing accuracy. The pointing accuracy was ~23 nm (resolution FWHM = 23 × 2.3 = 52.9 nm) for glass, ~32 nm (resolution FWHM = 32 × 2.3 = 73.6 nm) for 10-µm glass–PDMS assembly and ~50 nm (resolution FWHM = 50 × 2.3 = 115 nm) for 50-µm glass–PDMS assembly (Extended Data Fig. 3).

SPT analysis. A typical sptPALM experiment leads to a set of at least 16,000 frames (50 Hz), analysed to extract molecule localization and dynamics. For the trajectory analysis, FAs were identified by wavelet image segmentation of the paxillin–GFP signal. The corresponding binary masks were used to sort single-particle data analyses to specific regions, outside and inside FAs. We analysed trajectories lasting at least 13 points (≥260 ms) with a custom routine written for MATLAB using the mean squared displacement (MSD) computed as equation (1):

$$\mathrm{MSD}(t = n\times\Delta t) = \frac{\sum_{i=1}^{N-n}(x_{i+n}-x_i)^2+(y_{i+n}-y_i)^2}{N-n} \quad (1)$$

where x_i and y_i are the coordinates of the label position at time $i\times\Delta t$. We defined the measured diffusion coefficient D as the slope of the affine regression line fitted to the $n = 1$–4 values of the MSD($n\times\Delta t$). The MSD was computed then fitted on a duration equal to 80% (minimum of ten points; 200 ms) of the whole stretch by equation (2):

$$\mathrm{MSD}(t) = \frac{4r_{\mathrm{conf}}^2}{3}\left(1-e^{-t/\tau}\right) \quad (2)$$

where r_{conf} is the measured confinement radius and τ is the time constant ($\tau = r_{\mathrm{conf}}^2/3D_{\mathrm{conf}}$). Trajectories were sorted in three groups: immobile; confined diffusion; and free diffusion. Immobile trajectories were defined as trajectories with $D < 0.0011\,\mu\mathrm{m}^2\,\mathrm{s}^{-1}$, corresponding to molecules that explored an area inferior to the one defined by the image spatial resolution during the time used to fit the initial slope of the MSD[24,27] (four points; 80 ms):

$$\text{glass } D_{\text{threshold}} = (0.0529\,\mu\mathrm{m})^2/(4\times4\times0.02\,\mathrm{s}) \sim 0.008\,\mu\mathrm{m}^2\,\mathrm{s}^{-1}$$

$$10\,\mu\mathrm{m}\ \text{glass}-\text{PDMS}\ D_{\text{threshold}} = (0.0736\,\mu\mathrm{m})^2/(4\times4\times0.02\,\mathrm{s}) \sim 0.017\,\mu\mathrm{m}^2\,\mathrm{s}^{-1}$$

$$50\,\mu\mathrm{m}\ \text{glass}-\text{PDMS}\ D_{\text{threshold}} = (0.115\,\mu\mathrm{m})^2/(4\times4\times0.02\,\mathrm{s}) \sim 0.041\,\mu\mathrm{m}^2\,\mathrm{s}^{-1}$$

To separate trajectories displaying free diffusion from those displaying confined diffusion, we used the time constant τ calculated for each trajectory. Confined and free-diffusing trajectories were defined as trajectories with a time constant τ inferior and superior, respectively, to half the time interval used to compute the MSD (100 ms).

SRM/SPT while stretching. We performed sptPALM on cells at 37 °C spread on the micromechanical device, using a fast acquisition frequency (50 Hz; 2,000 frames) during trapeze-like patterns composed of stretch–plateau–relax phases (Fig. 3a). We selected cells with most of their FAs aligned almost parallel to the stretching axis in the field of observation. Fluorescent single molecules were localized as described above. We generated super-resolution time-lapse sequences (frame rate: 0.5 s; 25 images) from which high-density zones of detections corresponded to immobile and slowly mobile mEos2 (refs. [24,27]). Fluorescent beads (TetraSpeck Microspheres; 0.1 µm; Thermo Fisher Scientific; T7279) were adsorbed on the stretching chamber and were imaged during the entire sptPALM acquisition to register super-resolution intensity images. All of the images were registered on a chosen origin bead (white bead in Fig. 3a,b) located as far as possible from the cell but within the stretching axis of the cell. The reference beads (magenta bead in Figs. 3–5 and Extended Data Figs. 4–6 and 8) were selected as close as possible to the cell. We tested the strain homogeneity in all experiments by tracking at least three fluorescent beads (one origin bead, one reference bead and at least one additional bead) adsorbed on the PDMS and visible during the entire acquisition. The origin bead is seen as immobile in super-resolved time lapse(s) after registration. Bead displacements, measured using kymographs, increased proportionally with the distance to the origin bead (Fig. 3a–c), attesting for the elastic response of our device. To maintain the cell in the field of observation during stretching, we compensated for *XY* displacements using manual repositioning (Nikon stage steered by a joystick) or automated stage repositioning (custom plugin developed in MetaMorph). Practically, we directly exploited the property that the displacement field increases away from the holding arm by imaging particles or cells closer to the holding arm, which required smaller *XY* repositioning while allowing 6% stretching to be reached. By convention, all stretching events were represented from the left to the right.

Kymograph generation and analysis. Kymographs were generated and analysed using an ImageJ plugin, Kymo ToolBox (F. Cordelières; Bordeaux Imaging Center). Kymographs were generated from lines of interest parallel to the stretching axis. Kymographs were analysed after manual annotation, enabling Kymo ToolBox to extract the speed, direction and duration of displacements. A custom routine written for Excel was used to extract, compile and normalize all of the measured parameters: percentage of stretch; displacements (for example, Fig. 3c, left); normalized displacements (mEos2-fused proteins normalized on the initial position of a reference bead; for example, Fig. 3c (middle) and Fig. 3e); extrapolated displacements (reference bead extrapolated on the initial position of an mEos2-fused protein; for example, Fig. 3c right); and amplitude displacements compared with the underlying PDMS (for example, Fig. 3f). For kymograph analysis, localizations of FAs were determined using paxillin–GFP acquisitions before and after trapeze-like patterns. The paxillin–GFP image was superimposed on the corresponding super-resolution time-lapse sequence of mEos2-fused proteins using the signal of fluorescent beads (TetraSpeck Microspheres; 0.1 µm; Thermo Fisher Scientific; T7279), enabling the sorting of single-particle data analyses to specific regions both outside and inside FAs (Figs. 3e, 4b–d and 5b–d and Extended Data Figs. 4b,c and 6b,c,e,f) or nascent adhesions (Extended Data Fig. 8).

Protein recruitment analysis. To study protein recruitment within integrin-based adhesions (FAs and nascent adhesions) during external stress, we performed sptPALM on cells at 37 °C on the micromechanical device, using a fast acquisition frequency (50 Hz; 4,000 frames) during trapeze-like patterns (4 or 10%) composed of stretch–plateau–relax/recoil phases (Fig. 3a). Fluorescent single molecules were localized as described above in the section 'SPT analysis'. For mature FAs, cells were seeded for 2–4 h on the micromechanical device coated with fibronectin before acquisitions. Nascent adhesions form in protrusive structures of spreading and migrating cells[61,74]. We applied ~4% trapeze-like patterns to cells spreading on the micromechanical device coated with fibronectin; nascent adhesions in lamellipodia

were visualized by paxillin–GFP. To be sure that we were imaging nascent adhesions, we spread cells on our micromechanical device under the microscope, using previously described protocols[25,61,74].

To compare trajectory densities (trc µm^{-2}; Figs. 6c,h and 7c,j and Extended Data Fig. 7), we selected intervals with the same number of frames for every phase of a trapeze-like pattern (before stretch, during plateau and after relaxation). For experiments on zyxin–mEos3.2 and vinculin–mEos2 in FAs, as well as talin-C in nascent adhesions, we chose intervals of 8 s (400 frames; 50 Hz). For experiments on vinculin–mEos2 in nascent adhesions, we chose intervals of 40 s (2,000 frames; 50 Hz). Finally, for experiments on vinculin–mEos2 (10% stretch), we chose intervals of 80 s (4,000 frames; 50 Hz). Then, we quantified for each phase the number of trajectories with length ≥2 inside integrin-based adhesions (FAs and nascent adhesions). Integrin-based adhesions were outlined with manually drawn regions of interest. Trajectory densities (trc µm^{-2}) were obtained by dividing the number of trajectories by the total area of regions of interest for each cell. This value was then normalized to the density obtained before stretching to obtain variations of track density. We defined a threshold of 1.1-fold increase for responding cells under all conditions.

To display protein recruitment throughout trapeze-like stretch–plateau–relax patterns (Figs. 6b,g and 7b,i and Extended Data Fig. 7), we generated super-resolution time-lapse sequences (frame rate: 0.5 s; 25 images) as described above in the section 'SRM/SPT while stretching'. Then, for each time interval, we summed the corresponding super-resolved images.

To study the temporal molecular recruitment of vinculin–mEos2 in nascent adhesions during the plateau phase (Fig. 7f), we first computed the number of single-molecule detections per frame throughout two phases: before stretch and during plateau, immediately after the stretching phase. Only cells kept in focus from the beginning to the end of the plateau were selected to ensure a complete characterization of molecular recruitment. For each cell, the number of detections per frame at the plateau phase was divided by the average of detections obtained before stretch. This enabled detection of the fold increase in mEos2 detections throughout the entire plateau. No quantification was performed during the stretching due to constant jittering of the cell, which prevented consistent detection of single molecules.

To visualize the spatial molecular recruitment of vinculin–mEos2 and zyxin–mEos3.2 during the plateau phase (Figs. 6d,e,j and 7d,e,k), we employed two different strategies: generation of kymographs (see the section 'Kymograph generation and analysis') and colour coding of super-resolved time lapses (2 Hz). For colour coding of super-resolved time lapses, we only selected cells kept in focus from the beginning to the end of the plateau. Super-resolved time lapses were then divided into four intervals, coloured in red, green, blue and yellow (in crescent time order).

Statistics and reproducibility. Averages, s.e.m. values and s.d. values were calculated and are shown in the graphs. Respective *n* values are shown in the figure captions and in the source data files. The indicated *P* values were obtained using two-tailed unpaired/paired Student's *t*-tests, Mann–Whitney-*U* rank-sum tests or two-tailed Wilcoxon matched-pairs signed-rank tests. Experiments on 30% stretching and diffusion coefficients were performed five times independently with identical results (Fig. 2). Experiments on the acute mechanical response of proteins (Figs. 3–5 and Extended Data Figs. 4–6 and 8) were performed three or four times independently (depending on the condition, and except for experiments on actin–mEos2 in blebbistatin-treated MEFs, which were only performed twice independently) with identical results. Experiments on protein recruitment and reorganization (Figs. 6 and 7 and Extended Data Fig. 7) were performed three or four times (depending on the condition) independently with identical results. Some experiments were performed only twice independently; they are specified in this section, as well as the respective figure captions. Experiments on the acute mechanical response of actin–mEos2 in blebbistatin-treated MEFs were performed twice independently (Fig. 5d,e and Extended Data Fig. 6d–f). Experiments on live STED imaging of SiR-tubulin after 30% stretching were performed twice independently (Extended Data Fig. 2e,f). Experiments on diffusion coefficients, lengths and densities of trajectories of β3-integrin–mEos2 in 10 and 50 µm PDMS elastomers were performed twice independently (Extended Data Fig. 3c–h). Experiments on the stretching and rupture of stress fibres labelled with SiR-actin were performed twice independently (Extended Data Fig. 10a,b). Experiments on the stretching and recruitment of α-actinin–GFP to stress fibres were performed twice independently (Extended Data Fig. 10e,f)

Reporting Summary. Further information on research design is available in the Nature Research Reporting Summary linked to this article.

Data availability

All data that support the findings of this study are available from the corresponding author upon reasonable request. Source data are provided with this paper.

Code availability

MATLAB codes for analysis of sptPALM trajectories and MSD computing are available from the corresponding author on reasonable request.

References

71. Gregor, M. et al. Mechanosensing through focal adhesion-anchored intermediate filaments. *FASEB J.* **28**, 715–729 (2014).
72. Meier, M. et al. Vimentin coil 1A—a molecular switch involved in the initiation of filament elongation. *J. Mol. Biol.* **390**, 245–261 (2009).
73. Mignot, C. et al. Dynamics of mutated GFAP aggregates revealed by real-time imaging of an astrocyte model of Alexander disease. *Exp. Cell Res.* **313**, 2766–2779 (2007).
74. Giannone, G. et al. Periodic lamellipodial contractions correlate with rearward actin waves. *Cell* **116**, 431–443 (2004).
75. Vicente, F. N. et al. A micromechanical stretching device compatible with super-resolution microscopy. *Protoc. Exch.* https://doi.org/10.21203/rs.3.pex-961/v1 (2020).
76. Lee, J. N., Park, C. & Whitesides, G. M. Solvent compatibility of poly(dimethylsiloxane)-based microfluidic devices. *Anal. Chem.* **75**, 6544–6554 (2003).
77. Descloux, A., Grußmayer, K. S. & Radenovic, A. Parameter-free image resolution estimation based on decorrelation analysis. *Nat. Methods* **16**, 918–924 (2019).
78. Izeddin, I. et al. Wavelet analysis for single molecule localization microscopy. *Opt. Exp.* **20**, 2081–2095 (2012).
79. Racine, V. et al. Multiple-target tracking of 3D fluorescent objects based on simulated annealing. *IEEE Int. Symp. Biomed. Imag.* **2006**, 1020–1023 (2006).
80. Racine, V. et al. Visualization and quantification of vesicle trafficking on a three-dimensional cytoskeleton network in living cells. *J. Microsc.* **225**, 214–228 (2007).
81. Cheezum, M. K., Walker, W. F. & Guilford, W. H. Quantitative comparison of algorithms for tracking single fluorescent particles. *Biophys. J.* **81**, 2378–2388 (2001).

Acknowledgements

We thank Z. Karatas, M. Fabre, R. Sterling and J. Carrere for technical assistance, T. Orré for helpful discussions, C. Poujol and S. Marais (Bordeaux Imaging Center) for technical help and F. Cordelières (Bordeaux Imaging Center) for support with the kymograph analysis (Kymo ToolBox). We thank J. B. Sibarita (IINS, Bordeaux, France) for support with the sptPALM analysis, V. Studer (IINS, Bordeaux, France) and P. O. Strale (Alvéole) for important discussions on microfabrication, M. Cabilic (IINS, Bordeaux, France) for the repositioning plugin developed in MetaMorph, T. Schlichthärle, L. Fischer and R. Jungmann (Max Planck Institute of Biochemistry, Munich, Germany) and C. Grashoff (Institute for Molecular Cell Biology, Münster, Germany) for providing materials, support and important discussions on DNA-PAINT, P. Kanchanawong (MBI, NUS, Singapore) for providing the talin1-22–tdEOS (talin-C), tdEOS-18–talin1 (talin-N) and mEos2-7–talinABS (THATCH) constructs. We acknowledge financial support from the French Ministry of Research and CNRS, ANR grant Integractome (to G.G.), ANR grant FastNano (to G.G.), ANR grant IntegrinNanoPlan (to G.G.), ANR Decav-Recav (to P.N.), ANR MecanoCav (to P.N.), Fondation pour la Recherche Médicale (to G.G.) and the Institut National du Cancer (to P.N.).

Author contributions

G.G. conceived of and coordinated the project. G.G., P.N. and O.R. conceptualized the experiments and the stretching device. F.W., S.M., D.S. and F.N.V. developed and characterized the optical and mechanical properties of the stretching device. F.N.V. performed and analysed the experiments combining cell stretching and STED on microtubules and the actin cytoskeleton. F.N.V. and C.L. performed and analysed the experiments combining cell stretching and DNA-PAINT on vimentin intermediate filaments. F.N.V., S.M. and F.W. performed the experiments combining cell stretching and SRM/SPT on mature FAs. F.N.V. and G.G. analysed the experiments combining cell stretching and SRM/SPT on mature FAs. F.N.V. performed and analysed the experiments combining cell stretching and SRM/SPT on early nascent adhesions. A.M. developed analysis routines for kymographs. R.V. conceptualized the physical model. G.G. and P.N. wrote the manuscript with input from all authors.

Competing interests

The authors declare no competing interests.

Additional information

Extended data is available for this paper at https://doi.org/10.1038/s41556-020-0548-2.

Supplementary information is available for this paper at https://doi.org/10.1038/s41556-020-0548-2.

Correspondence and requests for materials should be addressed to G.G.

Reprints and permissions information is available at www.nature.com/reprints.

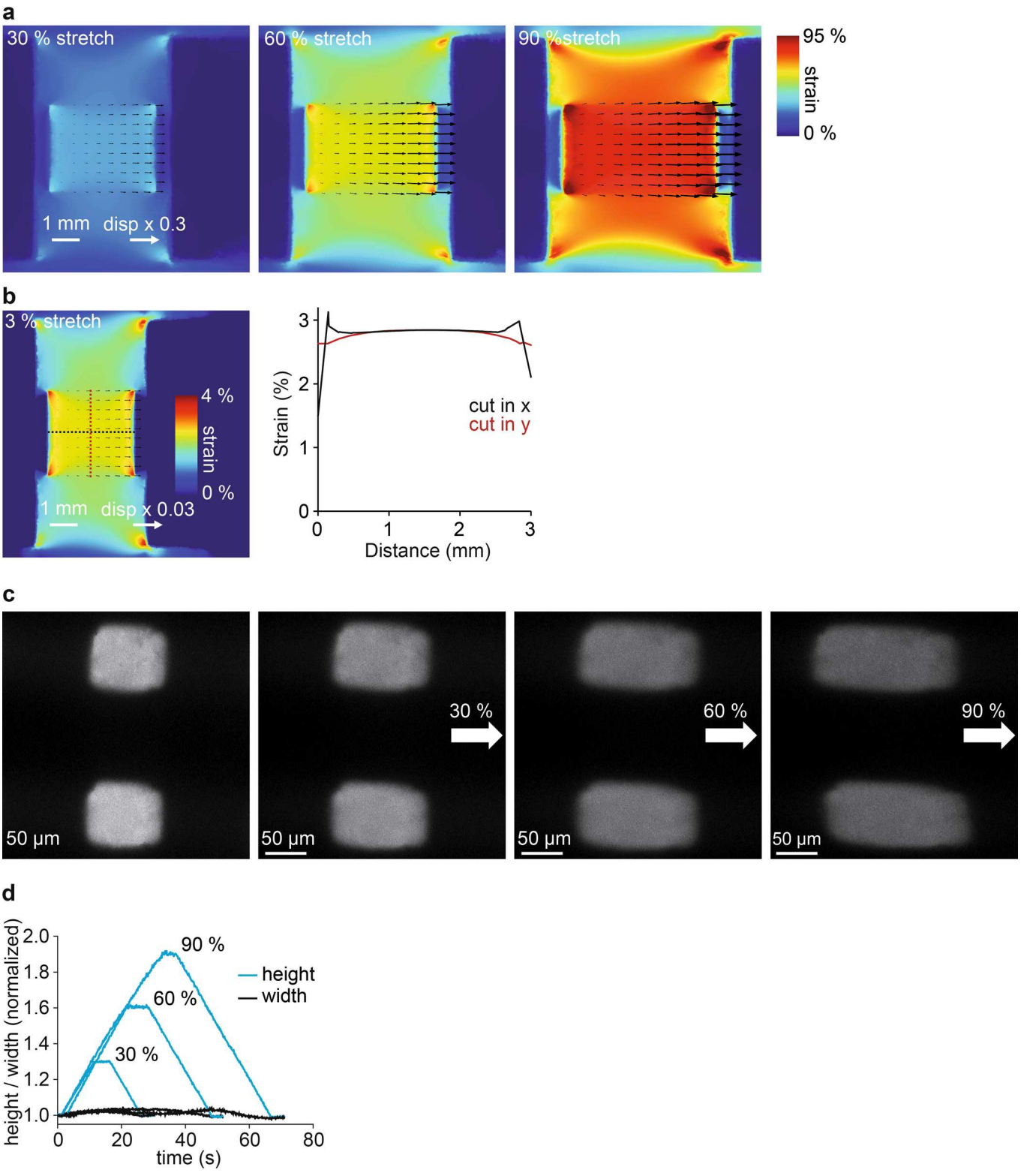

Extended Data Fig. 1 | Mechanical properties of the stretchable substrate compatible with SRM and SPT. a, Numerical simulation using COMSOL Multiphysics of 30 % (left), 60 % (middle) and 90 % (left) stretches for a 10 µm PDMS assembly. The first principal strain is color coded from 0 to 95 %, arrows display displacement fields (XY plane), scale factor 0.3. Scale bar, 1 mm. **b**, Numerical simulation of a 3 % stretch (left). The first principal strain is color coded from 0 to 4 %, arrows display displacement fields (XY plane), scale factor 0.03. Scale bar, 1 mm. Right, line plots of the first principle strain along the main axes of the stretching chamber. In both axes, the strain was in large parts nearly constant (for 0.5 mm < x,y < 2.5 mm). **c**, Images of fluorescent micropatterns (100 ×100 µm) on 10 µm PDMS assembly before (left) and after 30 % (middle left), 60 % (middle right) and 90 % (right) stretches. Scale bar, 50 µm. See Supplementary Video 2. **d**, Variation of micropatterns height (blue) and width (black) as function of time during successive trapeze-like patterns (30 %, 60 %, 90 %). Data are representative of 4 independent experiments (30 %) or 2 independent experiments (60 %, 90 %).

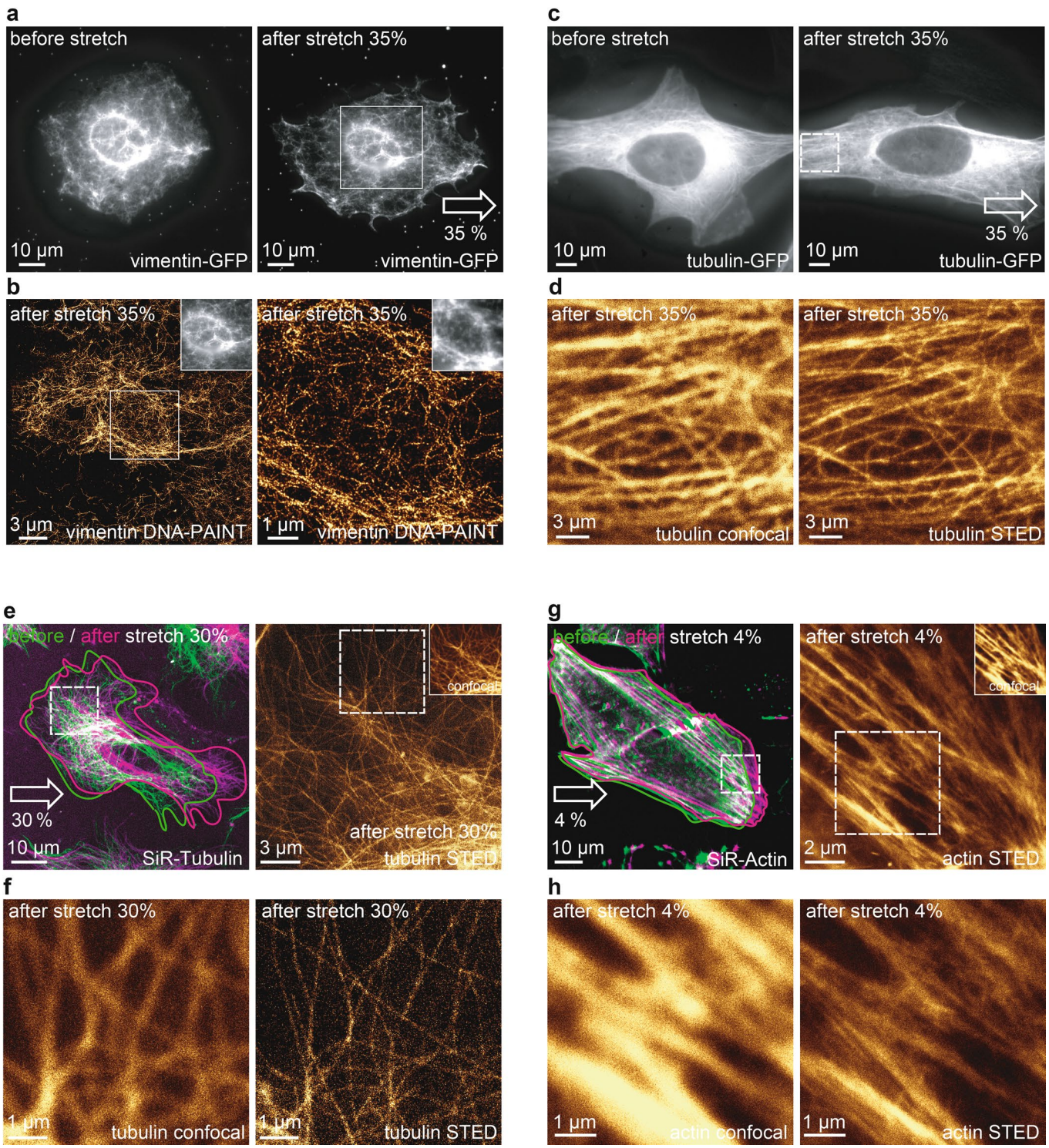

Extended Data Fig. 2 | See next page for caption.

Extended Data Fig. 2 | The stretchable elastic substrate enables to acquire SRM images of cellular structures deeper into the cells and live SRM images on cells that experience stretching. a, Fluorescence image of vimentin-GFP in a vimentin Knock Out MEF on the 10 µm PDMS stretching device before (left) and after (right) 35% stretching (right direction) followed by rapid cell fixation. **b**, DNA-PAINT super-resolution images of vimentin after 35% stretching. Corresponding image of outlined area in right panel of a, highlighting the nucleus (left). Magnified section from outlined area in the left (right). Inset: Vimentin-GFP epifluorescence images. **c**, Fluorescence image of tubulin-GFP in a MEF on the 10 µm PDMS stretching device before (left) and after (right) 35% stretching (right direction) followed by rapid cell fixation. **d**, Confocal (left) and STED super-resolution images (right) of endogenous tubulin labeled with ATTO-647N after 35% stretching for the outlined area in the right panel of c displayed at a higher magnification. **e**, Low resolution confocal image of SiR-Tubulin in a MEF on the PDMS stretching device before (green) and after (magenta) 30 % stretching (left). Outlines represent cell contour. Live cell STED image of SiR-Tubulin after 30% stretching (right), corresponding to the outlined area in the left. Inset: SiR-Tubulin confocal image. **f**, Low resolution confocal image (left) and STED image (right) of SiR-Tubulin for the outlined area in the right panel of e displayed at a higher magnification. **g**, Low resolution confocal image of SiR-Actin in a MEF on the PDMS stretching device before (green) and after (magenta) 4 % stretching (left). Outlines represent cell contour. Live cell STED image of SiR-Actin after 4 % stretching, corresponding to the outlined area in the left panel (right). Inset: SiR-Actin confocal image. **h**, Low resolution confocal image (left) and STED image (right) of SiR-Actin for the outlined area in the right panel of g displayed at a higher magnification. Data are representative of 3 independent experiments (**a-d**, **g**, **h**) or 2 independent experiments (**e**, **f**).

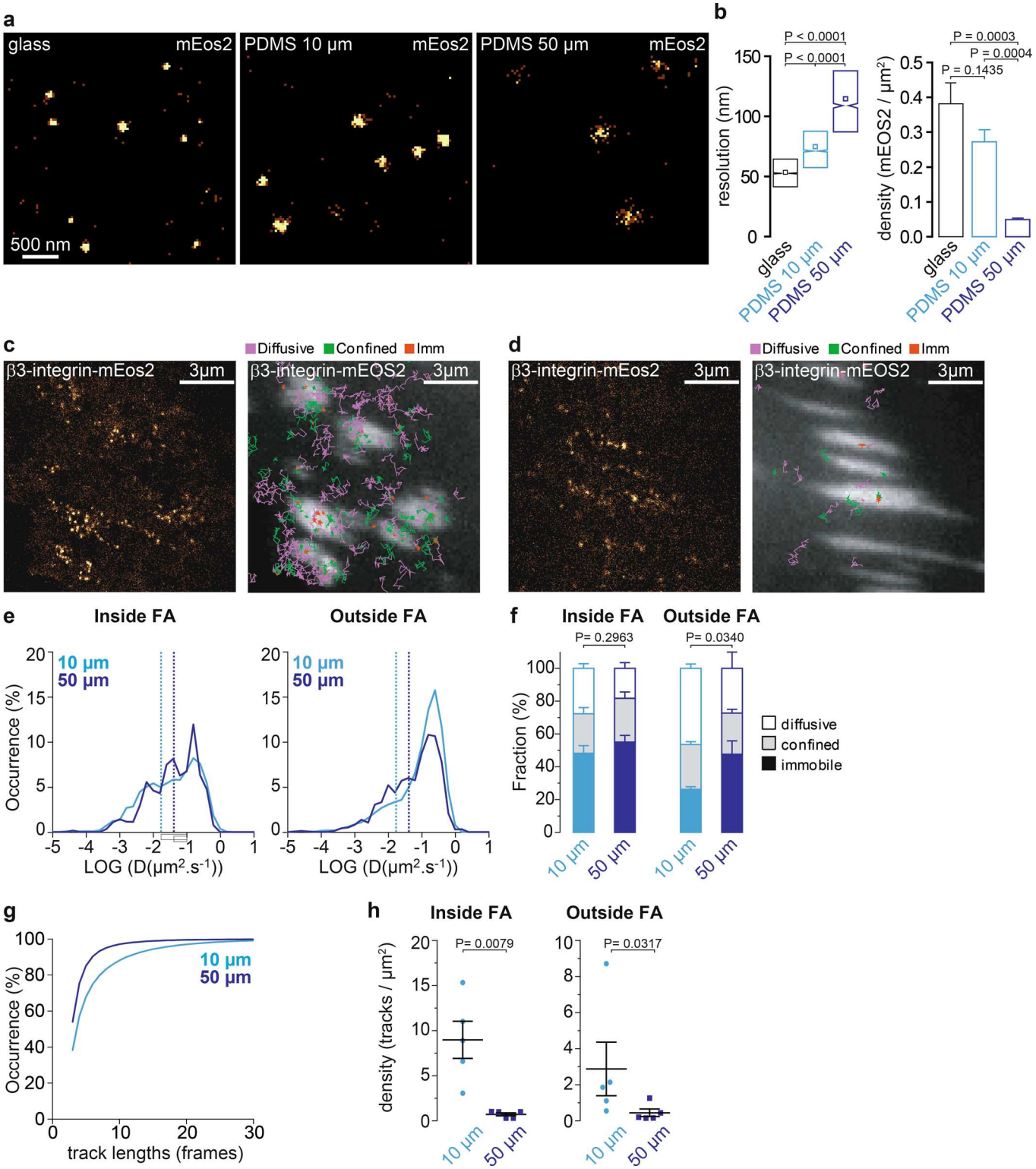

Extended Data Fig. 3 | See next page for caption.

Extended Data Fig. 3 | The stretchable elastic substrate is compatible with single molecule localization microscopy. a, Super-resolution intensity images of purified mEos2 adsorbed on glass (left), 10 μm (middle) and 50 μm (right) PDMS assemblies. Scale bars, 500 nm. **b**, Spatial resolution (left) and density of mEos2 detection (right) for glass, 10 μm and 50 μm PDMS. Box plots: median (line) and mean (square) ± percentile (25%–75%). Density: mean ± s.e.m. Glass: n = 4472 point spread functions (PSFs). 10 μm: n = 3065 PSFs. 50 μm: n = 1864 PSFs. **c**, **d**, Super-resolution intensity images of β3-integrin-mEos2 in a MEF obtained from a sptPALM sequence (50 Hz, 80 s) on 10 μm (**c**) or 50 μm (**d**) PDMS. Color-coded trajectories overlaid on GFP-Paxillin-labelled adhesion sites (greyscale) displaying free diffusion (magenta), confined diffusion (green) and immobilization (red) (right). Scale bars, 3 μm. **e**, Distributions of diffusion coefficient D of mEos2-β3-integrin trajectories inside (left) and outside (right) FAs on 10 μm (light blue) or 50 μm (dark blue) PDMS. Immobilized proteins correspond to $D < 0.017\ \mu m^2.s^{-1}$ (light blue line) for 10 μm PDMS and $D < 0.041\ \mu m^2.s^{-1}$ (dark blue line) for 50 μm PDMS. **f**, Fraction of proteins undergoing free diffusion, confined diffusion or immobilization inside (left) and outside (right) FAs (mean ± s.e.m.). **g**, Cumulative distributions of trajectory lengths for 10 μm (light blue) and 50 μm (dark blue) PDMS. **h**, Densities of mEos2 trajectories inside (left) and outside (right) FAs for 10 μm (light blue) and 50 μm (dark blue) PDMS (mean ± s.e.m.). **c**, **d**, Data are representative of 2 independent experiments. **e-h**. Data pooled from 2 independent experiments: 10 μm, n = 5 cells (14720 trajectories); 50 μm, n = 5 cells (2028 trajectories). Where indicated, statistical significances were obtained using two-tailed Student's t-tests or two-tailed Mann–Whitney rank sum tests. Statistical source data can be found at ED Source Data Fig. 3.

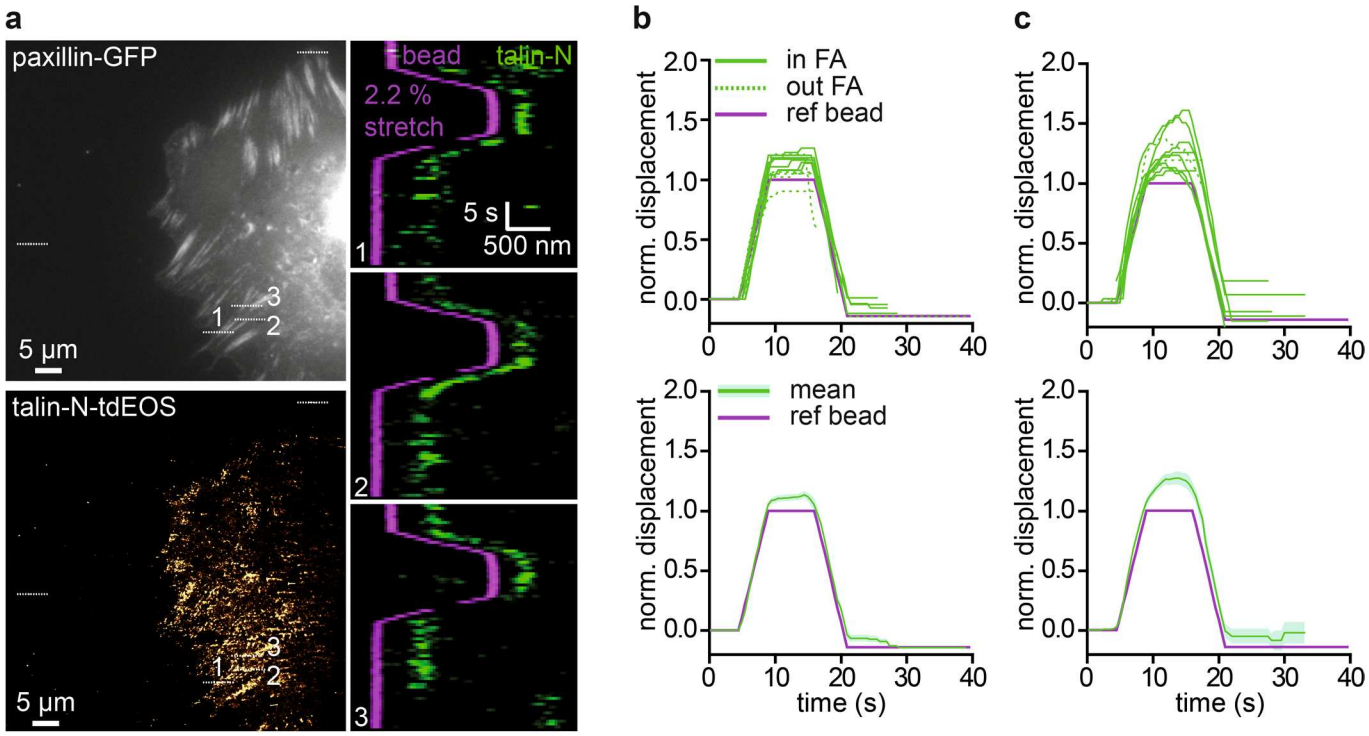

Extended Data Fig. 4 | Elastic and inelastic mechanical response of talin-N to trapeze-like patterns. a, Fluorescence image of paxillin-GFP in a MEF on the 10 µm PDMS stretching device before stretching (right direction) (top left). Projection of all tdEos-talin-N super-resolution intensity images of a trapeze-like pattern time-lapse (stretching 2.2 %, 2 Hz, 40 s) (bottom left). Scale bar, 5 µm. Right, tdEos-talin-N kymographs generated from the trapeze-like pattern time-lapse (as shown in the left, dashed lines). Horizontal axis, space (500 nm); vertical axis, time (5 s). The magenta kymograph corresponds to the reference bead, and the green kymographs correspond to tdEos-talin-N. **b**, Displacement versus time plot for elastic responses of tdEos-talin-N (green lines) after normalization to the initial position of the reference bead (magenta line) (top). Corresponding mean displacement ± s.e.m. (bottom). **c**, Same as b for inelastic responses of tdEos-talin-N. **b-c**, Data pooled from 3 or 4 independent experiments. beads (n = 52 kymographs from 3 independent experiments); tdEos-talin-N (n = 98 kymographs pooled from 4 independent experiments). Source data can be found at ED Source Data Fig. 4.

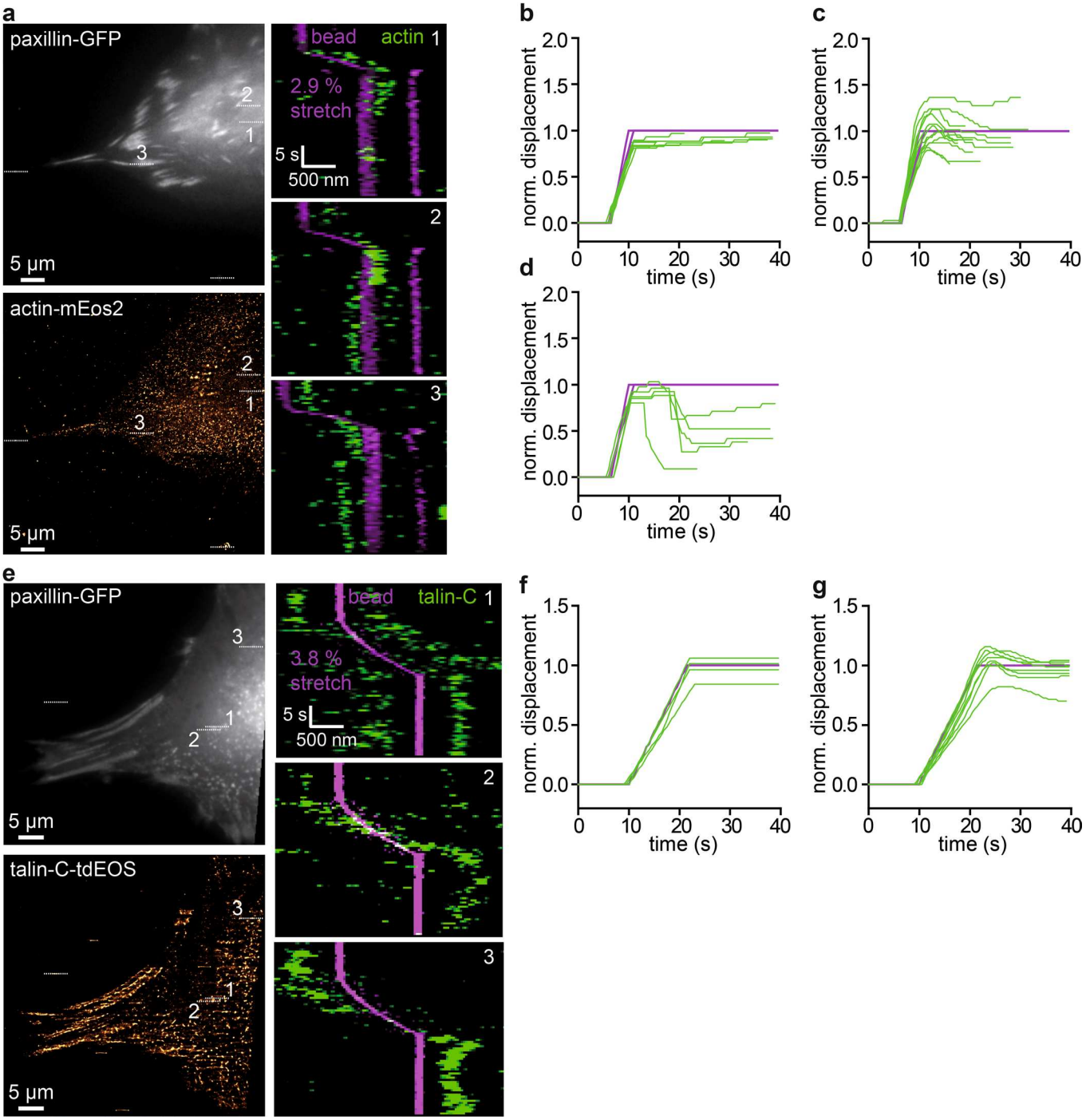

Extended Data Fig. 5 | Elastic and inelastic mechanical responses of actin and talin-C to single stretch-plateau patterns. a, Fluorescence image of paxillin-GFP in a MEF on the 10 µm PDMS stretching device before stretching (right direction) (top left). Projection of all actin-mEos2 super-resolution intensity images of a single stretch-plateau pattern time-lapse (stretching 2.9 %, 2 Hz, 40 s) (bottom left). Scale bar, 5 µm. Right, actin-mEos2 kymographs generated from the single stretch-plateau pattern time-lapse (as shown in the left, dashed lines). Horizontal axis, space (500 nm); vertical axis, time (5 s). The magenta kymograph corresponds to the reference bead, and the green kymographs correspond to actin-mEos2. **b**, Displacement versus time plot for elastic responses of actin-mEos2 (green lines) after normalization to the initial position of the magenta reference bead (magenta line). **c**, Same as b for inelastic responses of actin-mEos2. **d**, same as b for plastic deformation responses of actin-mEos2. **e**, Fluorescence image of paxillin-GFP in a MEF on the 10 µm PDMS stretching device before stretching (right direction) (top left). Projection of all talin-C-tdEos super-resolution intensity images of a single stretch-plateau pattern time-lapse (stretching 3.8 %, 2 Hz, 40 s) (bottom left). Right, talin-C-tdEos kymographs generated from the single stretch-plateau pattern time-lapse (as shown in the left, dashed lines). Horizontal axis, space (500 nm); vertical axis, time (5 s). The magenta kymograph corresponds to the reference bead, and the green kymographs correspond to talin-C-tdEos. **f**, Displacement versus time plot for elastic responses of talin-C-tdEos (green lines) after normalization to the initial position of the reference bead (magenta line). **g**, Same as b for inelastic responses of talin-C-tdEos. **b-g**, Data pooled from independent experiments: beads (n = 52 kymographs pooled from 3 independent experiments); talin-C-tdEos (n = 117 kymographs pooled from 3 independent experiments); actin-mEos2 (n = 65 kymographs pooled from 3 independent experiments).

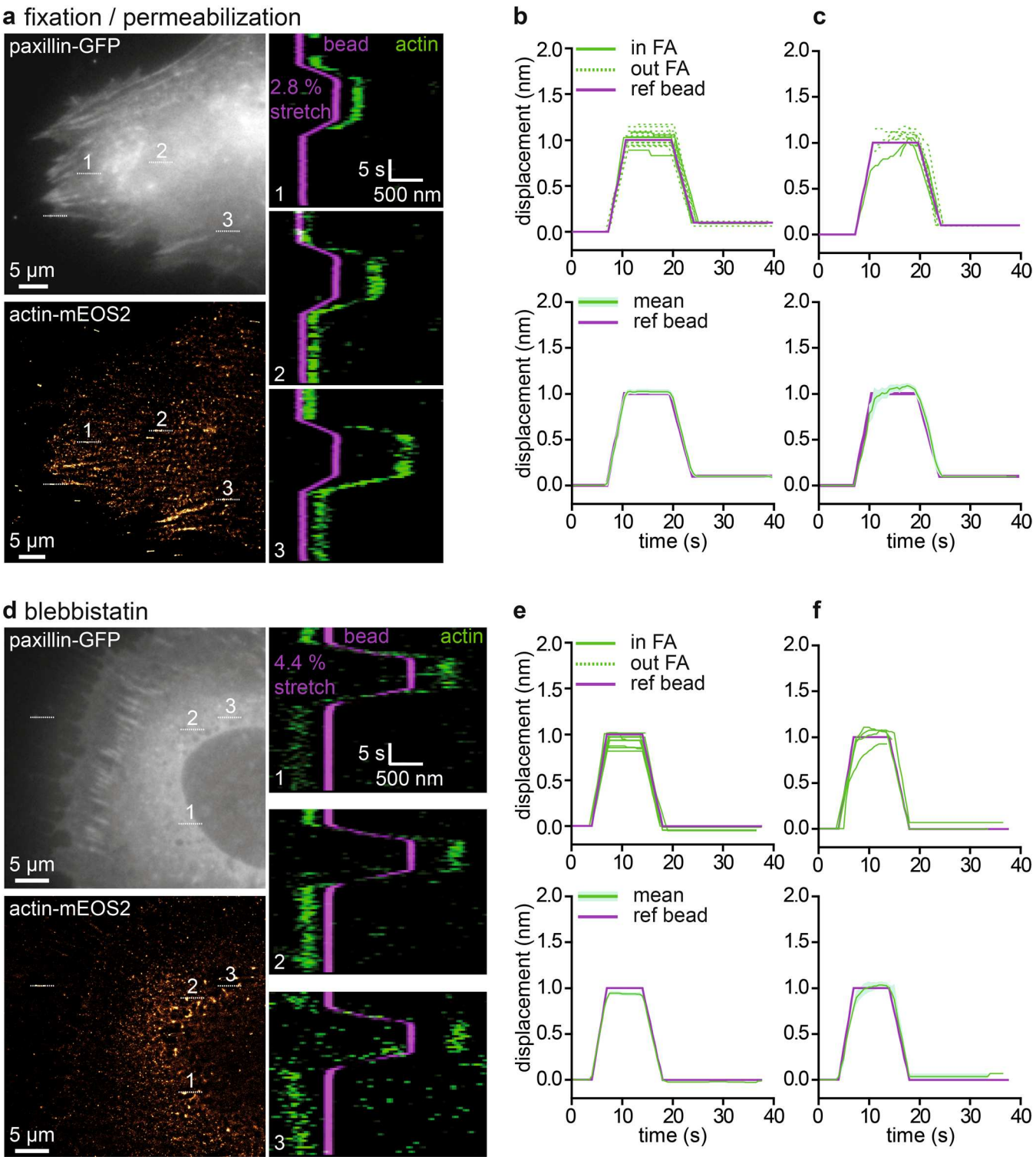

Extended Data Fig. 6 | Elastic and inelastic mechanical response of actin to trapeze-like patterns after fixation and blebbistatin treatment. a, Fluorescence image of paxillin-GFP in a fixed and permeabilized MEF on the 10 µm PDMS stretching device before stretching (right direction) (top left). Projection of all actin-mEos2 super-resolution intensity images of a trapeze-like pattern time-lapse (stretching 2.8 %, 2 Hz, 40 s) (bottom left). Right, actin-mEos2 kymographs generated from the trapeze-like pattern time-lapse (as shown in the left, dashed lines). Horizontal axis, space (500 nm); vertical axis, time (5 s). The magenta kymograph corresponds to the reference bead, and the green kymographs correspond to actin-mEos2. **b**, Displacement versus time plot for elastic responses of actin-mEos2 in fixed/permeabilized cells (green lines) after normalization to the initial position of the reference bead (magenta line) (top). Corresponding mean displacement ± s.e.m. (bottom). **c**, Same as b for inelastic responses of actin-mEos2 in fixed/permeabilized cells. **d**, same as a for a MEF treated with blebbistatin. **e**, same as b for a MEF treated with blebbistatin. **f**, same as c for a MEF treated with blebbistatin. **b-f**, Data pooled from 2 or 3 independent experiments: beads (n = 52 kymographs pooled from 3 independent experiments; actin-mEos2 (n = 65 kymographs from 3 independent experiments); actin-mEos2 blebbistatin (n = 83 kymographs from 2 independent experiments). Source data can be found at ED Source Data Fig. 6.

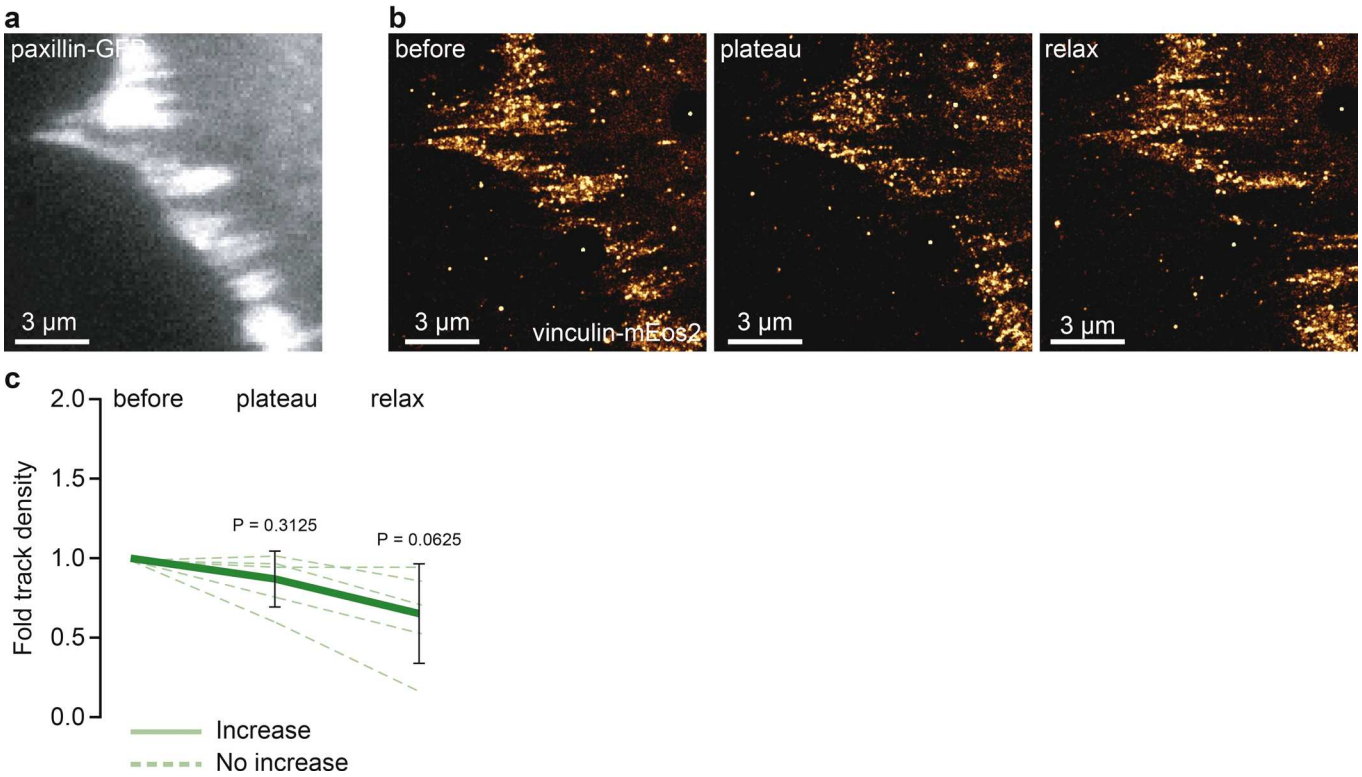

Extended Data Fig. 7 | Vinculin is not recruited to mature integrin-based adhesions by large scale (10 %) stretching. a, Fluorescence image of paxillin-GFP in a MEF on the 10 µm PDMS stretching device before stretching (right direction). **b**, Projection of vinculin-mEos2 super-resolution intensity images for the three phases of a trapeze-like pattern (stretching 12.6 %, 2 Hz, 80 s per phase): before (left), plateau (middle) and relax (right). **c**, Variation of trajectory density (trc/µm^2) for vinculin-mEos2 (n = 5 cells pooled from 3 independent experiments) throughout trapeze-like patterns (mean ± s.d.). The density of trajectories was normalized to the value obtained before stretching. Individual cells (green), mean trajectory ratio ± s.d. (bold green), increase > 1.1 (plain), < 1.1 (dotted). **a,b**, Data are representative of 3 independent experiments. Statistical significance was calculated using two-tailed Wilcoxon matched-pairs signed rank tests. Statistical source data can be found at ED Source Data Fig. 7.

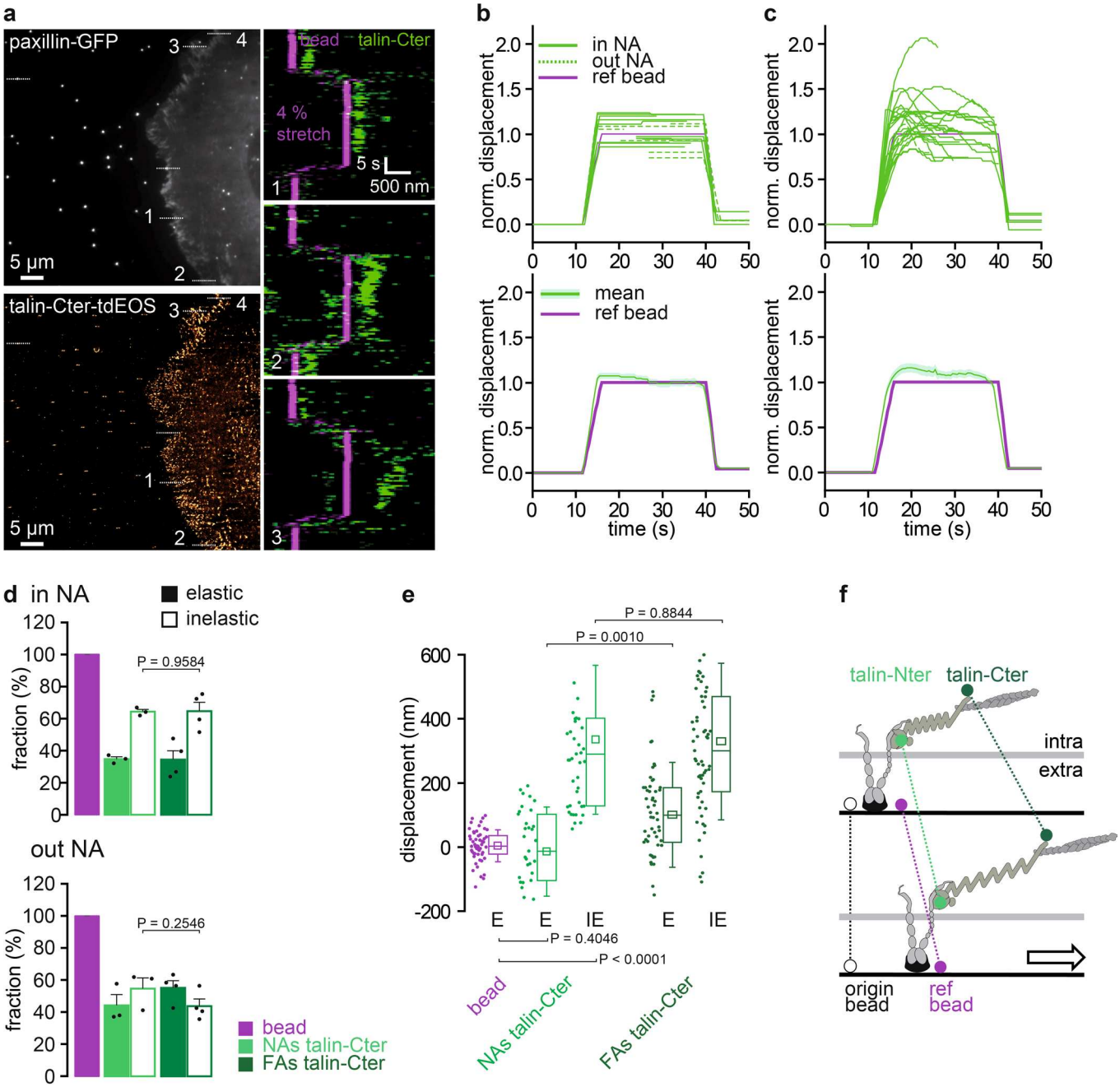

Extended Data Fig. 8 | Elastic and inelastic mechanical response of talin-C to trapeze-like patterns in nascent integrin-based adhesions. a, Fluorescence image of paxillin-GFP in a spreading MEF on the 10 µm PDMS stretching device before stretching (right direction) (top left). Projection of all talin-C-tdEos super-resolution intensity images of a trapeze-like pattern time-lapse (stretching 3.7 %, 2 Hz, 40 s) (bottom left). Scale bar = 5 µm. Right, talin-C-tdEos kymographs generated from the trapeze-like pattern time-lapse (as shown in the left, dashed lines). Horizontal axis, space (500 nm); vertical axis, time (5 s). The magenta kymograph corresponds to the reference bead, and the green kymographs correspond to talin-C-tdEos. Scale bar = 5 µm. **b**, Displacement versus time plot for elastic responses of talin-C-tdEos (green lines) after normalization to the initial position of the reference bead (magenta line) (top). Corresponding mean displacement ± s.e.m. (bottom). **c**, Same as b for inelastic responses of talin-C-tdEos. **d**, Fractions of elastic and inelastic responses inside and outside FAs for talin-C-tdEos. Values represent the average of fractions obtained from three independent experiments (mean ± s.e.m.). **e**, Box plots displaying the median (line), mean (square) ± percentile (25%–75%) and s.d. (whiskers) of local displacements for talin-C-tdEos for elastic (E) and inelastic (IE) responses after subtraction of the extrapolated PDMS displacements.**b-e**, Data pooled from independent experiments: beads (for **e**, n = 52 kymographs from 3 independent experiments); talin-C-tdEos NAs (for **d**, n = 3 stretches and for **e**, n = 111 kymographs, both pooled from 3 independent experiments).; talin-C-tdEos FAs (for **d**, n = 4 stretches and for **e**, n = 117 kymographs, both pooled from 3 independent experiments). **f**, Schematic representation of the acute mechanical response of talin-N and talin-C compared to β3-integrin Statistical significances were obtained using two-tailed unpaired Student's t-tests. Statistical source data can be found at ED Source Data Fig. 8.

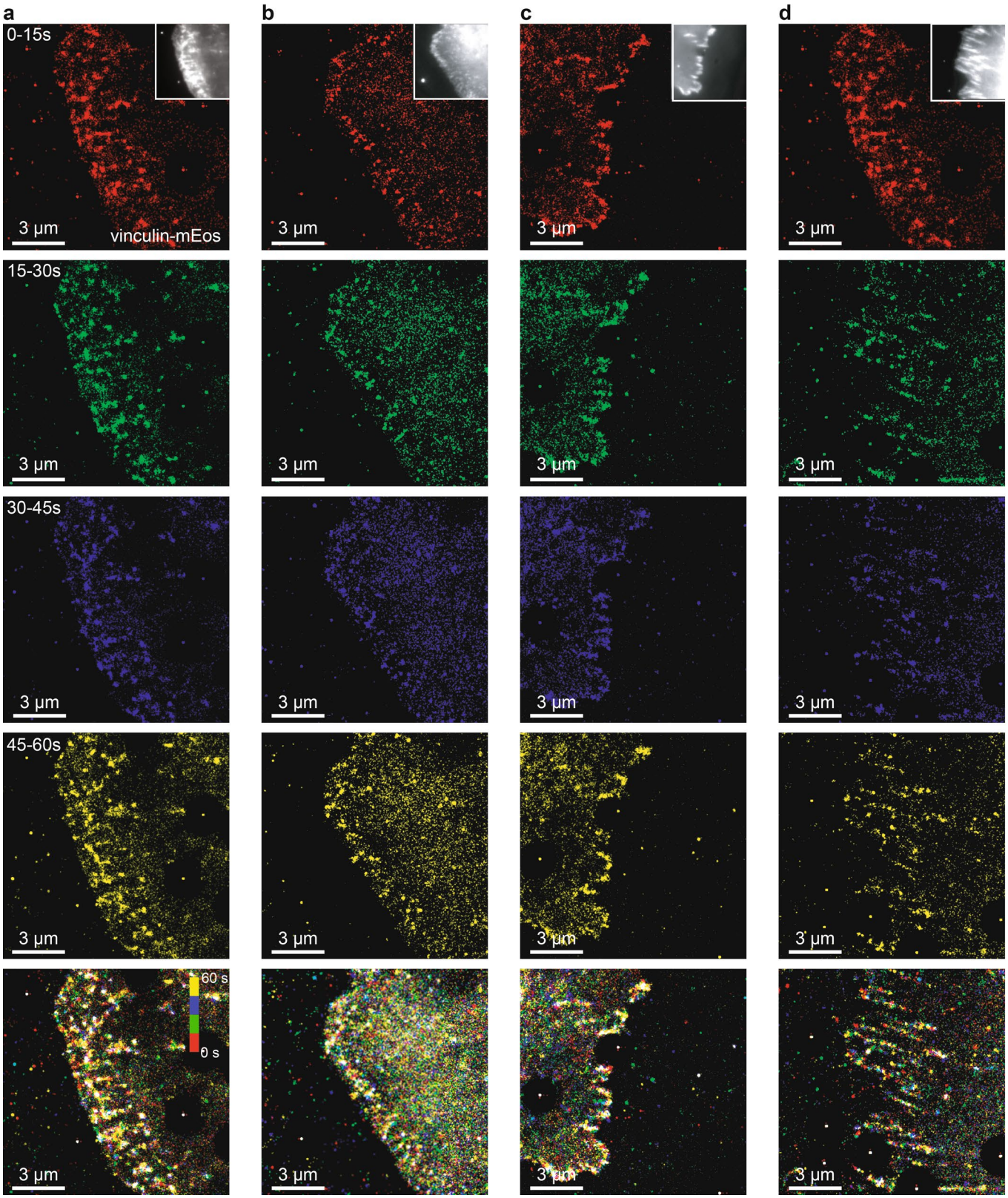

Extended Data Fig. 9 | Vinculin does not exhibit region-selective recruitment in nascent adhesions after small-scale (4 %) stretching. a, Separated color-coded projection of vinculin-mEos2 intensity images during the plateau phase of stretching (inset, paxillin-GFP) (red 0–15 s, green 15-30 s, blue 30-45 s, yellow 45-60 s). This cell corresponds to the cell displayed in Fig. 7a–f. **b–d**, same as **a** for other cells displaying increased detections of vinculin-mEos2 during the plateau phase. Scale bar = 3 µm. **a**–**d**, Data are representative of 3 independent experiments.

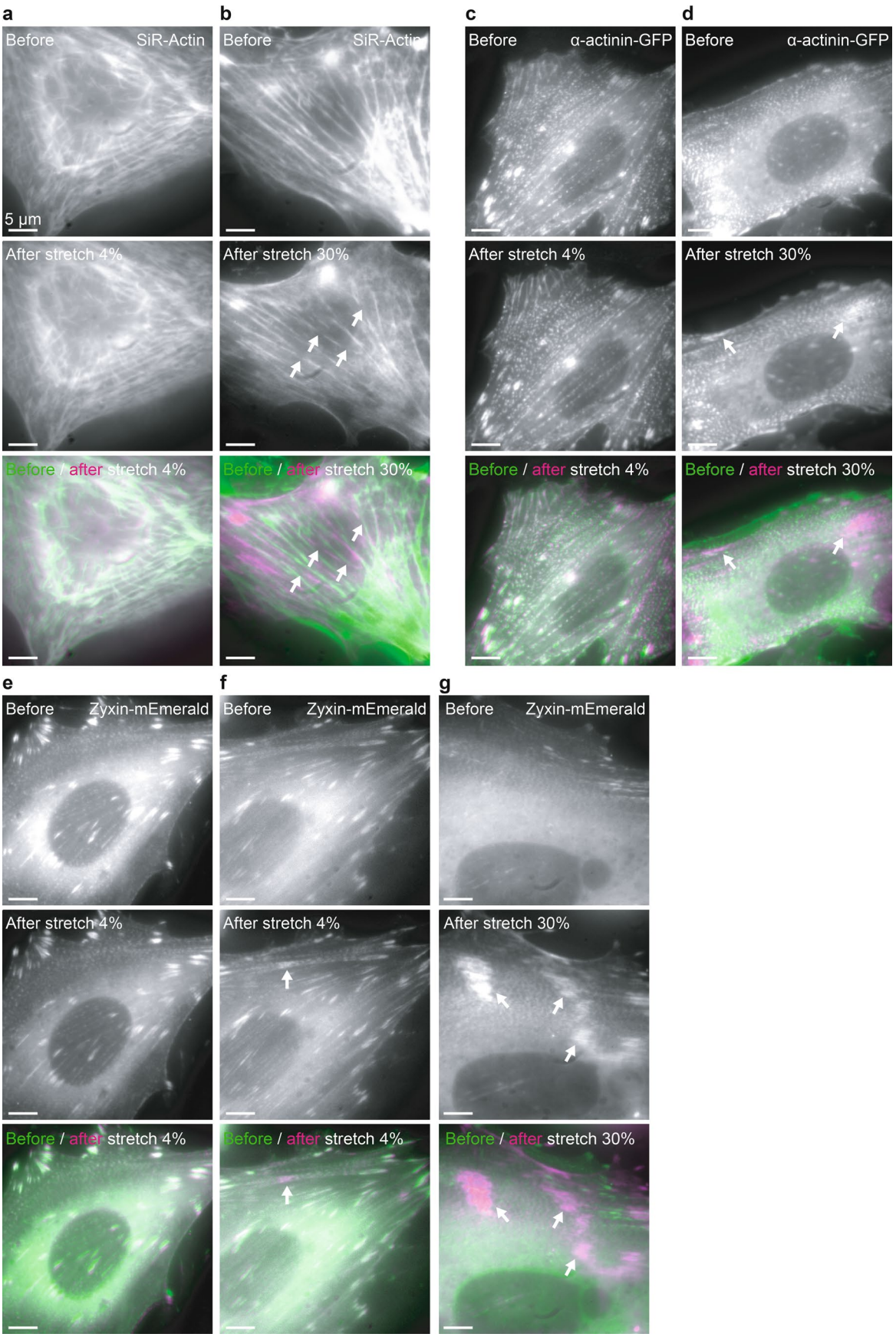

Extended Data Fig. 10 | See next page for caption.

Extended Data Fig. 10 | Trapeze-like patterns (~ 4 %) are not triggering stress fiber ruptures and repair. a, Low resolution fluorescence image of SiR-Actin in a MEF on the PDMS stretching device before stretching (top), after a ~ 4% small stretch (middle), merge image (bottom) (0 out of 8 cells exhibited ruptures). **b**, Low resolution epifluorescence image of SiR-Actin in a MEF on the PDMS before stretching (top), after a ~ 30% large stretch (middle), merge image (bottom). Arrows display stress fibers (SFs) ruptures (3 out of 3 cells exhibited ruptures). **c**, same as **a** (~ 4% stretch) for a MEF expressing α-actinin-GFP (0 out of 6 cells exhibited recruitment). **d**, same as **b** (~ 30 % stretch) for a MEF expressing α-actinin-GFP. Arrows display major recruitment of α-actinin-GFP to SFs (2 out of 2 cells exhibited recruitment). **e**, same as **a** (~ 4% stretch) for a MEF expressing zyxin-mEmerald. **f**, same as **a** (~ 4% stretch) for a MEF expressing zyxin-mEmerald and displaying a local recruitment of zyxin-mEmerald on SFs (arrow) (3 out of 12 cells exhibited recruitment). **g**, same as **b** (~ 30 % stretch) for a MEF expressing zyxin-mEmerald. Arrows display major recruitment of zyxin-mEmerald to SFs (2 out of 2 cells exhibited recruitment). Scale bar = 5 µm. **a-d**, **g**, Data are representative of 2 independent experiments. **e**, **f**, Data are representative of 4 independent experiments.

nature research

Corresponding author(s): Gregory Giannone

Last updated by author(s): Mar 22, 2020

Reporting Summary

Nature Research wishes to improve the reproducibility of the work that we publish. This form provides structure for consistency and transparency in reporting. For further information on Nature Research policies, see Authors & Referees and the Editorial Policy Checklist.

Statistics

For all statistical analyses, confirm that the following items are present in the figure legend, table legend, main text, or Methods section.

n/a	Confirmed
☐	☒ The exact sample size (*n*) for each experimental group/condition, given as a discrete number and unit of measurement
☐	☒ A statement on whether measurements were taken from distinct samples or whether the same sample was measured repeatedly
☐	☒ The statistical test(s) used AND whether they are one- or two-sided *Only common tests should be described solely by name; describe more complex techniques in the Methods section.*
☒	☐ A description of all covariates tested
☐	☒ A description of any assumptions or corrections, such as tests of normality and adjustment for multiple comparisons
☐	☒ A full description of the statistical parameters including central tendency (e.g. means) or other basic estimates (e.g. regression coefficient) AND variation (e.g. standard deviation) or associated estimates of uncertainty (e.g. confidence intervals)
☐	☒ For null hypothesis testing, the test statistic (e.g. *F*, *t*, *r*) with confidence intervals, effect sizes, degrees of freedom and *P* value noted *Give P values as exact values whenever suitable.*
☒	☐ For Bayesian analysis, information on the choice of priors and Markov chain Monte Carlo settings
☒	☐ For hierarchical and complex designs, identification of the appropriate level for tests and full reporting of outcomes
☒	☐ Estimates of effect sizes (e.g. Cohen's *d*, Pearson's *r*), indicating how they were calculated

Our web collection on statistics for biologists contains articles on many of the points above.

Software and code

Policy information about availability of computer code

Data collection	Simulations of surface stress and displacement for a defined stretching percentage were performed with a finite element simulation software (COMSOL Multiphysics). sptPALM and DNA-PAINT acquisitions were steered by the Metamorph software (Molecular Devices, version 7.10.2) as detailed in the methods section. Automated stage repositioning during stretching acquisitions were performed using a custom plugin developed in Metamorph (M. Cabilic, J.B. Sibarita, IINS, Bordeaux, France). The STED acquisitions were steered by LASX Software (Leica).
Data analysis	Single molecule localization microscopy (SMLM) and single protein tracking (SPT) acquisitions were analyzed using the Metamorph software (Molecular Devices) using a custom computer code written for Metamorph (J.B. Sibarita, IINS, Bordeaux, France). Full analysis of trajectories (diffusion coefficient D; distributions of D; diffusion modes (immobile, confined, free-diffusive); confinement radius) were performed with a custom routine written for Matlab using computation of the mean squared displacement as desribed previously (Rossier et al., Nature Cell Biology 2012; Chazeau et al., EMBO J 2014). Kymographs were generated and analyzed using a custom ImageJ plugin (Kymo ToolBox, F. Cordelières, Bordeaux Imaging Center, BIC). Super-resolution DNA-PAINT reconstruction and drift correction were carried out as described in the following reference, using the software package Picasso. Schnitzbauer, J., Strauss, M. T., Schlichthaerle, T., Schueder, F. & Jungmann, R. Super-resolution microscopy with DNA-PAINT. Nat. Protoc. 12, 1198–1228 (2017). Spatial resolution of DNA-PAINT acquisitions was measured using ImageJ and MATLAB. The spatial resolution of STED acquisitions was measured with a recently described ImageJ decorrelation plugin (single version, downloaded from GitHub). Descloux, A., Grußmayer, K. S. & Radenovic, A. Parameter-free image resolution estimation based on decorrelation analysis. Nat. Methods 16, 918–924 (2019).

For manuscripts utilizing custom algorithms or software that are central to the research but not yet described in published literature, software must be made available to editors/reviewers. We strongly encourage code deposition in a community repository (e.g. GitHub). See the Nature Research guidelines for submitting code & software for further information.

Data

Policy information about availability of data

All manuscripts must include a data availability statement. This statement should provide the following information, where applicable:

- Accession codes, unique identifiers, or web links for publicly available datasets
- A list of figures that have associated raw data
- A description of any restrictions on data availability

The datasets generated during and/or analyzed during the current study are not publicly available due to their large size but are available from the corresponding author on reasonable request.

Field-specific reporting

Please select the one below that is the best fit for your research. If you are not sure, read the appropriate sections before making your selection.

☒ Life sciences ☐ Behavioural & social sciences ☐ Ecological, evolutionary & environmental sciences

For a reference copy of the document with all sections, see nature.com/documents/nr-reporting-summary-flat.pdf

Life sciences study design

All studies must disclose on these points even when the disclosure is negative.

Sample size	No statistical calculations were used to predict the sample size. All results for each condition correspond to datasets from at least 3 independent experiments. Arithmetic means and s.e.m. were calculated and are shown in graphs. Respective n values are shown in figure captions and Supplementary Tables 1-5. For experiments combining sequentially sptPALM (50 Hz) and cell stretching, the sample size was not pre-chosen, but was kept similar between experimental conditions to account for the differences of diffusive behavior and differences of density of detection and trajectories. We imaged 5 cells per condition to account for cell to cell variability. Each cell was analyzed independently and the distribution of the diffusion coefficients computed from 2000-15,000 trajectories. The statistical n for the fractions of trajectories in the different diffusion modes (immobile, confined and free-diffusive) corresponds to the number of cells analyzed (Fig. 2, Extended Data Fig. 3, Supplementary Table 2). Statistical n for diffusion coefficient and densities of trajectories correspond to the number of trajectories (Fig. 2, Extended Data Fig. 3, Supplementary Tables 1,2). For experiments combining simultaneously SMLM super-resolved timelapses (2 Hz) and cell stretching, the sample size was not pre-chosen, but was kept similar between experimental conditions to account for the differences of diffusive behavior and differences of density of detection and trajectories. We imaged ≥3 cells and performed ≥3 stretches (Fig. 3,4,5,6,7 Extended Data Fig. 7,8). For experiments on mechanical responses, the sample size was not pre-chosen, but was kept similar between experimental conditions to account for the differences of mechanical responses, while being based on the maximum number of cells that could be reliably analyzed within a reasonable time frame. We generated between 55 to 117 kymographs per condition to account for cell to cell variability (Fig 3,4,5, Extended Data Fig. 8). Statistical n for fractions of elastic and inelastic mechanical responses corresponds to the number of stretches analyzed (Fig. 4,5, Extended Data Fig. 8, Supplementary Table 3). Statistical n for displacements of elastic and inelastic mechanical responses corresponds to the number of kymographs analyzed (Fig. 3,4,5, Extended Data Fig. 8, Supplementary Table 3). For experiments on stretching and protein recruitment, the sample size was not pre-chosen, but was kept similar between experimental conditions to account for the differences of mechanical responses, while being based on the maximum number of cells that could be reliably analysed within a reasonable time frame. Statistical n for track density variations corresponds to the number of cells analyzed (Fig.6, 7 Extended Data Figure 7, Supplementary Table 5). For experiments using purified mEos2 to determine pointing accuracies and densities of mEos2 detection, the sample size was not pre-chosen, but was kept similar between experimental conditions to account for the differences of pointing accuracies and densities of mEos2 detections. We imaged >7 fields of view generating between 1863 to 4472 point spread functions (PSF). Statistical n for pointing accuracies and densities of mEos2 detection correspond to the number of PSF analyzed (Extended Data Fig. 3, Supplementary Table 1). Statistical significances were obtained using two-tailed Student's t-tests for fractions of immobilization (Fig. 2 and Extended Data Fig. 3), pointing accuracies (Extended Data Fig. 3), densities of mEos2 detection (Extended Data Fig. 3), fractions of elastic and inelastic mechanical responses (Fig. 4,5, Extended Data Fig. 8) and displacements of elastic and inelastic mechanical responses (Fig. 3,4,5, Extended Data Fig. 8). Statistical significances were obtained using two-tailed Wilcoxon matched-pairs signed rank tests for variations in track densities (Fig. 6,7 Extended Data Fig. 7). Statistical significances were obtained using a non-parametric, two-tailed Mann–Whitney rank sum test for diffusion coefficient (Supplementary Table 2) and densities of trajectories (Extended Data Fig.3). We will include this statement in the methods section. P values are indicated on all the main and extended data figures.
Data exclusions	In all experiments combining simultaneously SMLM and cell stretching we tested the strain homogeneity, by tracking at least 3 fluorescent beads (1 origin bead, 1 reference bead and at least 1 additional bead) adsorbed on the PDMS and visible during the entire acquisition. If the strain was not homogeneous during stretching experiments, displaying nonlinear displacements, the experiments were not analyzed. Exclusion criteria were defined after development and validation of the stretching device.
Replication	All results for each condition correspond to data from either 2 or 3 independent experiments. This is detailed in the 'Sample Size' section, along with description of statistical n for each datasets. All experimental conditions were carefully normalized to minimize variability. This includes, cell transfection, delay between transfection and imaging, cell density. We tested the strain homogeneity in all experiments combining SRM/SPT and cell stretching. All attempts at replication were successful.
Randomization	All analyzed cells were selected from homogeneous and linear strains, hence there was no randomization.
Blinding	Our experiments were not done blind. However, we used computer-based single molecule detection and tracking and analysis with as many cells as was practical to analyse to minimise bias.

Reporting for specific materials, systems and methods

We require information from authors about some types of materials, experimental systems and methods used in many studies. Here, indicate whether each material, system or method listed is relevant to your study. If you are not sure if a list item applies to your research, read the appropriate section before selecting a response.

Materials & experimental systems

n/a	Involved in the study
☐	☒ Antibodies
☐	☒ Eukaryotic cell lines
☒	☐ Palaeontology
☒	☐ Animals and other organisms
☒	☐ Human research participants
☒	☐ Clinical data

Methods

n/a	Involved in the study
☒	☐ ChIP-seq
☒	☐ Flow cytometry
☒	☐ MRI-based neuroimaging

Antibodies

Antibodies used

The following antibodies were used.
1. mouse monoclonal antibody against α-tubulin (1:750, 236-10501, A11126, Thermo Fisher Scientific), 2. ATTO647N-dye-conjugated antibody against mouse IgG (1:1000, Sigma-Aldrich, 50185-1ML-F).

Validation

The mouse monoclonal antibody against mouse α-tubulin was validated in this manuscript: Jenks, A. D. et al. Primary Cilia Mediate Diverse Kinase Inhibitor Resistance Mechanisms in Cancer. Cell Rep. 23, 3042–3055 (2018).

Eukaryotic cell lines

Policy information about cell lines

Cell line source(s)

The mouse embryonic fibroblast cell line used in this study was previously described in: Su J, Muranjan M, Sap J. (1999). Receptor protein tyrosine phosphatase alpha activates Src-family kinases and controls integrin-mediated responses in fibroblasts. Curr Biol. 9(10):505-11. Primary embryonic fibroblasts were isolated from E13–E15 day old RPTPα+/+ embryos. A retroviral vector expressing polyoma large T antigen from the SV40 virus was used to immortalize the cultures.

Vimentin Knock Out mouse embryonic fibroblast cell line were kindly provided by Harald Herrmann and Gerhard Wiche/ Cécile Leduc, and were previously described.
Gregor, M. et al. Mechanosensing through focal adhesion-anchored intermediate filaments. FASEB J. 28, 715–29 (2014).
Meier, M. et al. Vimentin Coil 1A—A Molecular Switch Involved in the Initiation of Filament Elongation. J. Mol. Biol. 390, 245–261 (2009).

Authentication

The authentication for mouse embryonic fibroblasts (MEFs) and vimentin knock out mouse embryonic fibroblast (MEF KO Vimentin) cell lines was performed by the laboratory responsible for the cell line generation.

Mycoplasma contamination

The cell line used in this study is regularly tested for Mycoplasma, all cells lines have been verified as Mycoplasma free.

Commonly misidentified lines
(See ICLAC register)

The cell line used in this study is not a misidentified line.

nature cell biology

SUPPLEMENTARY INFORMATION

https://doi.org/10.1038/s41556-020-0548-2

In the format provided by the authors and unedited.

Cell stretching is amplified by active actin remodelling to deform and recruit proteins in mechanosensitive structures

Sophie Massou[1,2,7], Filipe Nunes Vicente[1,2,7], Franziska Wetzel[3,4,7], Amine Mehidi[1,2], Dan Strehle[3,4], Cecile Leduc[5], Raphaël Voituriez[6], Olivier Rossier[1,2], Pierre Nassoy[3,4] and Grégory Giannone[1,2] ✉

[1]Interdisciplinary Institute for Neuroscience, UMR 5297, Université de Bordeaux, Bordeaux, France. [2]Interdisciplinary Institute for Neuroscience, UMR 5297, CNRS, Bordeaux, France. [3]Laboratoire Photonique Numérique et Nanosciences, UMR 5298, Université de Bordeaux, Talence, France. [4]Laboratoire Photonique Numérique et Nanosciences, UMR 5298, Institut d'Optique and CNRS, Talence, France. [5]Cell Polarity, Migration and Cancer Unit, UMR 3691, Institut Pasteur Paris and CNRS, Paris, France. [6]Laboratoire Jean Perrin and Laboratoire de Physique Théorique de la Matière Condensée, CNRS - Sorbonne Université, Paris, France. [7]These authors contributed equally: Sophie Massou, Filipe Nunes Vicente, Franziska Wetzel.
✉e-mail: gregory.giannone@u-bordeaux.fr

Supplementary Notes 1-2

Supplementary Note 1

Design of the micromechanical device compatible with super-resolution microscopy

The simultaneous combination of super-resolution microscopy (SRM) or single protein tracking (SPT) with cell stretching is extremely challenging, since it requires to combine glass-like optical properties with mechanical stability of the imaged plane during substrate deformation. The micromechanical device we designed is compatible with the two major classes of SRM: stochastic approaches based on Single Molecule Localization Microscopy (SMLM: PALM, STORM, PAINT) that use time and space decorrelation of single molecules emission[17–19]; and targeted light-structuring techniques that control the emission states at precisely defined positions in the sample (STED (Stimulated Emission Depletion), RESOLFT (REversible Saturable OpticaL Fluorescence Transitions))[17–19]. SMLM/SPT require the optimal signal to noise ratio of single molecules emission to attain the best spatial resolution (typically 10-50 nm)[17–19]. SMLM/SPT techniques are thus ideally performed in the total internal reflection fluorescence (TIRF) or oblique illumination modes using high numerical aperture (NA) short working distance oil immersion objectives matching the index of refraction of glass slides[18,19,27,78]. In addition, SMLM/SPT techniques rely on object reconstruction or tracking from thousands of imaging planes, which implies perfect mechanical stability of the sample while imaging. This is incompatible with large deformations and displacements of the substrate in the axis (Z) and plane (XY) of observation during stretching. However, in most commercial configurations, cell stretching is performed using macroscopic devices and imaged after fixation, or thick elastomeric substrates are stretched in combination with low NA objectives and upright microscopes[42,53]. Various custom-made devices could potentially enable simultaneous stretching and live cell imaging, although they are either limited to low-magnification imaging or incompatible with continuous automatic focusing during stretching, preventing to capture the immediate response of cells to stretch[2,9,79–82]. The fabrication of thin (150 µm) polydimethylsiloxane (PDMS) substrates mounted on a small actuator enabled the sequential combination of cell stretching and TIRF[2]. However, using this strategy, faint detection of individual purified photo-activatable fluorescent proteins (e.g. mEos2) required several hundred milliseconds of exposure which is incompatible with efficient SPT or SMLM. We hypothesized that this decrease in signal to noise ratio was due to the significant index mismatch between PDMS and glass ($n_{PDMS=}$1.41, n_{Glass}=1.52). While one solution could be to use higher refractive index PDMS derivative[83], our strategy was to reduce the optical path through PDMS and thus to reduce the PDMS thickness to recover glass-like optical properties.

Our micromechanical device could be used to acquire SRM images both in the TIRF and oblique illumination modes. The TIRF mode will only allow to obtain super-resolved images of structures

within 200 nm of the PDMS-water interface at the ventral plasma membrane (e.g. integrin-based adhesions (Fig. 2), actin-based lamellipodium, caveolae…). However, the oblique illumination mode enables to image cellular structures few microns deeper into the cells[78]. To demonstrate that we could use different techniques of SRM, we performed DNA-PAINT acquisitions on intermediate filaments. Our strategy allowed to acquire long lasting DNA-PAINT acquisitions (2-3 h) required to obtain super-resolution images, such as vimentin intermediate filaments in MEFs after live stretching (30-50 %) followed by rapid cell fixation (Fig. 1d,e). Using the oblique illumination we could obtain SR images deeper in the cell, for example vimentin filaments swirling around the nucleus (Extended Data Fig. 2b).

In addition, we demonstrated that our micromechanical device is also compatible with STED nanoscopy. STED is performed in the confocal (point scanning) mode also enabling to acquire super-resolved images several microns deeper within the cell. In that case we obtained SR images of microtubules in MEFs after live stretching (30-50 %) followed by rapid cell fixation (Fig. 1f,g, Extended Data Fig. 2c). We also acquired STED images of microtubules and the actin cytoskeleton using SiR-tubulin and SiR-actin labeling in live MEFs that experience stretching (Extended Data Fig. 2e-h). Freed from the constraint of sequential acquisitions of single molecule emission, STED nanoscopy offers better temporal resolution.

Supplementary Note 2

Rise time and recoil time of the arched-shaped inelastic responses are triggered by distinct mechanisms

We characterized the rising part of the inelastic molecular responses by assuming a viscoelastic behavior with a characteristic time constant τ_1. Using an exponential fit $\Delta x\left(1-e^{-t/\tau_1}\right)$ with Δx the magnitude of the overshoot, we found that the characteristic rise time τ_1 for the arched-shaped inelastic responses of talin-C and actin-mEos2 were similar, respectively 1.7 ± 0.1 s and 1.6 ± 0.1 s (see Source Data for Fig. 4c). The maximal instantaneous displacement rates for talin-C (~ 120 $nm.s^{-1}$) and actin-mEos2 (~ 106 $nm.s^{-1}$) were faster than the flow of talin or actin measured in adhesive structures or the lamella (~ 5-10 $nm.s^{-1}$)[27,40], suggesting that the actin flow is not driving the inelastic responses. Furthermore, a unidirectional actin flow could not explain changes in directions occurring during the overshoot and recoil phases. In order to compare the rise time from the recoil time τ_2 for individual actin-mEos2, we applied single stretch-plateau patterns that allowed us to examine the recoil phase independently from the relax phase (Extended Data Fig. 5). Fitting with an exponential decay $\Delta x \cdot e^{-t/\tau_2} + x_s$ with Δx the magnitude of the decay and x_s the stationary location of the tracked molecules, we found that the characteristic recoil time of actin-mEos2 τ_2 was longer (4.6 ± 0.6 s) than the rise time (see Source Data for Fig. 4c), suggesting that they are triggered by distinct mechanisms.

Elastic heterogeneous passive model implies a rigid cell.

For the heterogeneously elastic model (Fig. 5g), the cell is composed of softer elements (e.g. talin) in series with stiffer elements (e.g. integrin and actin). Under an imposed strain, the softer elements will undergo larger displacements than their corresponding reference point in the underlying homogeneous substrate. By considering a cell of length L, composed of a rigid fraction z, the imposed strain (e.g. 3%) on the PDMS induces a total displacement of:

$$\Delta X = 0.03 \cdot L$$

Exerted only on the soft fraction of length:

$$(1 - z) \cdot L$$

The effective strain for the soft fraction is then:

$$\Delta X/((1 - z) \cdot L) = 0.03/(1 - z).$$

Thus, deforming talin from 50 nm to the measured ~ 300 nm, corresponds to an effective strain of ~ 600 %, which would imply a rigid fraction of ~ 99.5 %.

References

78. Giannone, G. *et al.* Dynamic superresolution imaging of endogenous proteins on living cells at ultra-high density. *Biophys J* **99**, 1303–1310 (2010).

79. Jungbauer, S., Gao, H., Spatz, J. P. & Kemkemer, R. Two characteristic regimes in frequency-dependent dynamic reorientation of fibroblasts on cyclically stretched substrates. *Biophys J* **95**, 3470–3478 (2008).

80. Kosmalska, A. J. *et al.* Physical principles of membrane remodelling during cell mechanoadaptation. *Nat. Commun.* **6**, 7292 (2015).

81. Wang, D. *et al.* Tissue-specific mechanical and geometrical control of cell viability and actin cytoskeleton alignment. *Sci. Rep.* **4**, 6160 (2014).

82. Camelliti, P., Gallagher, J. O., Kohl, P. & McCulloch, A. D. Micropatterned cell cultures on elastic membranes as an in vitro model of myocardium. *Nat. Protoc.* **1**, 1379–1391 (2006).

83. Gutierrez, E. *et al.* High refractive index silicone gels for simultaneous total internal reflection fluorescence and traction force microscopy of adherent cells. *PLoS One* **6**, e23807 (2011).

2. Assess the impact of mechanical stretch in the nano-organization and dynamics of mechanosensitive protein assemblies in neurons

In this chapter of the results, I present our efforts to study the mechanosensitive response of the membrane periodic skeleton (MPS) in axons. This constitutes my second PhD project, which is currently underway. As of now, we have two main goals: 1) assess the impact of large and sustained stretching on nanoscale MPS reorganization and 2) capture the acute mechanical response of MPS proteins to small scale stretching. With these aims in mind, I will describe how we 1) modified the design and composition of the stretching device to enable the culture of dissociated hippocampal neurons; 2) implemented DNA-PAINT and STED imaging assess changes in nanoscale organization of the MPS and 3) combined *in ovo* electroporation of chick spinal cord and explant culture to capture the acute mechanical response of MPS proteins such as actin. Finally, I will present new developments on micropatterning of the stretching device to control cell geometry, orientation and adhesion during stretching.

1. Introduction

In the first section of the results, by combining cell stretching and SRM, we could reveal at the nanoscale the mechanical response of mechano-sensitive structures(Massou, Nunes Vicente, Wetzel et al. 2020). This methodology enables to capture the acute mechanical response of individual proteins inside mechanosensitive structures. Overall, our device provides the novelty of assessing individual protein deformations as well as their spatiotemporal recruitment/reorganization upon stretching.

We now want to apply our micromechanical stretching device to understand whether certain macromolecular assemblies are mechano-sensitive in response to external forces. The actin-spectrin MPS of neurons (Vassilopoulos et al., 2019; Xu et al., 2013) falls into the latter category; a highly specialized macromolecular complex with a potential mechanosensitive role.

Recent evidence points to emerging functions of the MPS as a signaling platform and as a mechanoprotective element in the axon (Dubey et al., 2020; Zhou et al., 2019). However, the mechanosensitive role of the MPS is still unclear. Spectrin, one of the main organizers of the MPS (Zhong et al., 2014), is essential for maintaining tension in C.elegans touch receptor neurons (Krieg et al., 2014) and to protect neurons from mechanical stress (Krieg et al. 2017). Moreover, it also displays mechanosensitive behaviors in different cell types (Duan et al., 2018; Wu et al., 2017). Many of these roles could be related to unfolding and refolding of spectrin helix bundle domains (Brown et al., 2015). In this regard, the MPS has been shown to act as a shock buffer during neuronal strains by unfolding repeat domains in tetramers of βII-spectrin (Dubey et al., 2020). Recent observations also characterized the MPS as an actomyosion network regulating axonal diameter, conduction and structural plasticity(Berger et al., 2018; Costa et al., 2020). Therefore, MPS could act as a mechanosensitive structure through actomyosin contractility and force-dependent unfolding/refolding of spectrin helix bundle domains. Unfolding of spectrin in response to force could expose binding domains and induce recruitment of specific transmembrane proteins, similar to what is seen for talin (Ciobanasu et al., 2014; Del Rio et al., 2009; Yao et al., 2016). Other MPS proteins could also contribute for mechanosensing, such as adducin (Leite et al., 2016). Overall, our hypothesis is that protein deformation and reorganization within the MPS constitute a molecular mechanism for axonal mechano-sensitivity. This could impact in the organization of sodium channels at the AIS (Leterrier et al., 2015), generation/transmission of action potentials(Costa et al., 2020) or ERK signaling (Zhou et al., 2019).

To approach this question, we initially chose to divide experiments into two main goals: 1) Assess the acute mechanical response and reorganization of βII-spectrin, actin and other MPS-associated proteins in response to stretching and 2) Evaluate the impact of large scale stretching in the nanoscale organization of the MPS.

2. Results

2.1. Adapting the micromechanical stretching device to neuronal culture

In order to assess the mechanosensitive response of the MPS, we decided to use primary rat hippocampal neurons at embryonic day 17 (E17), which are often used to image the MPS (Xu et al., 2013; Zhong et al., 2014). Previous studies indicate that the periodic distribution of β-spectrin in primary rat hippocampal neurons is visible in the proximal axon at DIV2, reaching the middle of the axon at DIV 4 and gradually extending towards the distal end at DIV6 (Wang eLife 2014). Actin is slightly delayed, appearing around DIV 5 and acquiring a robust periodic pattern

at DIV 7. With this in mind, to allow for robust MPS development, primary rat hippocampal neurons will have to be cultured in the device at least until DIV4, ideally DIV6-7, depending on the protein to image. This would require long-term culture in our micromechanical stretching device, something that was not assessed until here. Indeed, in our previous work (Massou, Nunes Vicente, Wetzel et al. 2020), all stretching experiments were performed in cell lines (MEFs), usually in the same day of cell seeding.

Throughout this initial process, we found several technical issues. First of all, the resins used to 3D-print the device were toxic for rat hippocampal neuronal cultures after 3-4 days in culture. Moreover, we experienced severe bacterial contaminations due to the absence of a suitable sterilization method for the 3D-printed devices. We found these were indeed originating from the device because neurons grew normally in PDMS elastomers without the 3D-printed device. To tackle these issues, we first sought to change the material composition of the device. Initially, we 3D-printed the device in polylactic acid (PLA) through fused deposition modelling (FDM). However, PLA was also toxic after 3-4 days in culture and it released autofluorescence particles in solution. We decided thus to employ a different strategy, by changing the material of the device to Polymethyl Methacrylate (PMMA) (Evonik, Germany), also known as Plexiglas. The new PMMA device was 3D-milled using a Computer Numerical Control (CNC) system (CharlyRobo). Besides changing the material, we also changed the design of the micromechanical stretching device, which could not be filled with enough medium for long culture periods (Fig. 41). More precisely, we modified the shape of the stretching arm and we increased the height of the holding arm in order to expand the volume of culture medium we can add to the device (Fig. 41a). To enable sustained stretching after fixation, we added a groove and thread system allowing to clamp the device after stretching (Fig. 41b). Before culturing neurons in the new device, we had to find a strategy to sterilize them, in order to avoid bacterial contaminations. Previous methods had shown that PMMA chemical sterilization might be a good alternative to processes such as autoclaving or UV, which can alter the structure and surface morphology of PMMA parts (Münker et al., 2018). Peracetic acid, which is often used for disinfection in the medical field, has been successfully used to sterilize heat-labile scaffolds (Yoganarasimha et al., 2014). Thus, we sterilized the 3D-milled PMMA device with a peracetic acid-based detergent (Peralex 9 Hecto) before attaching it to the PDMS elastomer. We then cultured rat hippocampal neurons in the sterilized devices in Neurobasal/B27 supplemented with Penicillin/Stretopmycin. By combining new PMMA-based devices and chemical sterilization, we were able to culture viable rat hippocampal neurons on a functional micromechanical stretching device up to DIV8 without contaminations (Fig. 41c). However, we are limited to DIV5 for cell stretching experiments due to technical constraints, since the PDMS elastomer stops gliding on the glass slide after DIV5. Moreover, the same device could be used several times for culturing neurons after repeated sterilization. Thus, PMMA-based devices can be sterilized with peracetic acid and used for culturing hippocampal neurons.

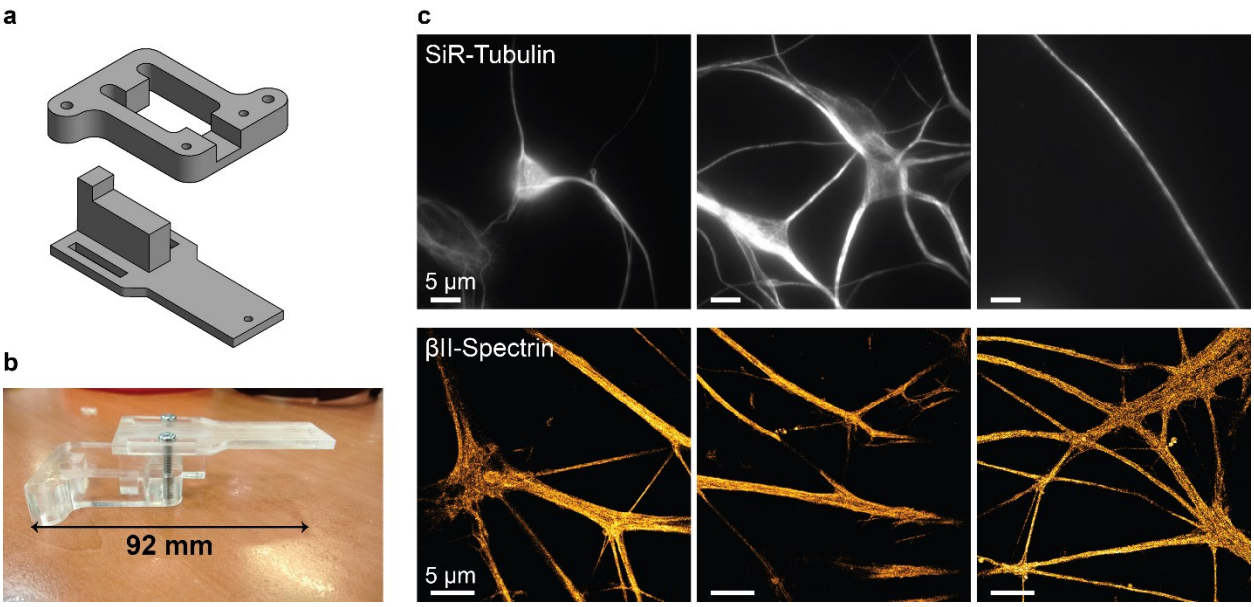

Figure 41: New PMMA-based stretching device enables long-term culture of primary hippocampal neurons until DIV 8

a, Computer assisted design (CAD) plans of the new PMMA-based micromechanical stretching device, with a modified fixed arm (top) and stretching arm (bottom). Besides the change of material, the height of the fixed arm was increased and two threaded holes were added for clamping the stretching arm (top). The width of the stretching arm was increased in order to introduce two long grooves, which allow to clamp the stretching arm to the threaded holes in the fixed arm by using two metallic screws (bottom). **b,** New, 3D-milled PMMA-based micromechanical stretching device, with the stretching arm clamped to the fixed arm through the screw groove system. **c,** Epifluorescence live images of SiR-Tubulin in DIV 3 rat hippocampal neurons (top) and confocal images of immunolabelled βII-Spectrin in DIV 8 rat hippocampal neurons (bottom), both cultured on the stretching device.

2.2. Assessing the impact of stretching in the nanoscale organization and dynamics of the MPS

Successful implementation of neuronal culture on our micromechanical device opened the door for MPS stretching in neurons combined with SRM and SPT. Two main axis can be explored: 1) assess the impact of large and sustained stretching on the nanoscale reorganization of the MPS; and 2) study the acute mechanical response of MPS proteins to stretch in live neurons. As of now, we have mostly developed the new version of the micromechanical device for the two types of experiments: this has involved new culture systems, protein transfection methods and imaging techniques. However, due to time constraints linked to the work on NCB, we could not perform systematic observations, which we hope to resume briefly.

2.2.1. Impact of large and sustained stretching on nanoscale MPS reorganization

For this particular set of experiments, we opted for performing large stretching followed by fixation and labelling for SRM, (Massou, Nunes Vicente, Wetzel et al. 2020). Here, we successfully combined this protocol with both STED and DNA-PAINT imaging of cytoskeletal proteins post-live stretch and fixation. Therefore, we chose both STED and DNA-PAINT as possible imaging techniques for assessing the effect of large stretching in MPS nanoscale organization. STED imaging of the MPS is widely described in literature for different neuronal types and subcellular compartments (Bär et al., 2016; D'Este et al., 2015, 2016, 2017). For STED, we labelled neurons with a primary antibody against βII-Spectrin (BD Bioscences), followed by a secondary antibody coupled to ATTO647N (Fig. 42a). On the other hand, although DNA-PAINT has not been used to image the MPS, the resolution and the diversity of structures imaged by this technique make it a highly suitable method, especially in stretching and fixation experiments. For DNA-PAINT imaging, we opted by labelling DIV 4 neurons for βII-Spectrin followed by a secondary antibody anti-mouse coupled to a P12 DNA docking strand. We then imaged βII-Spectrin with a P12 imager strand (Fig. 42b). In both cases, we were missing an axonal marker, which in the future will be required in order to ascertain that the imaged structures are axons. Nonetheless, some periodic structures appear to be visible in axonal-like structures for both conditions. Further imaging will be required.

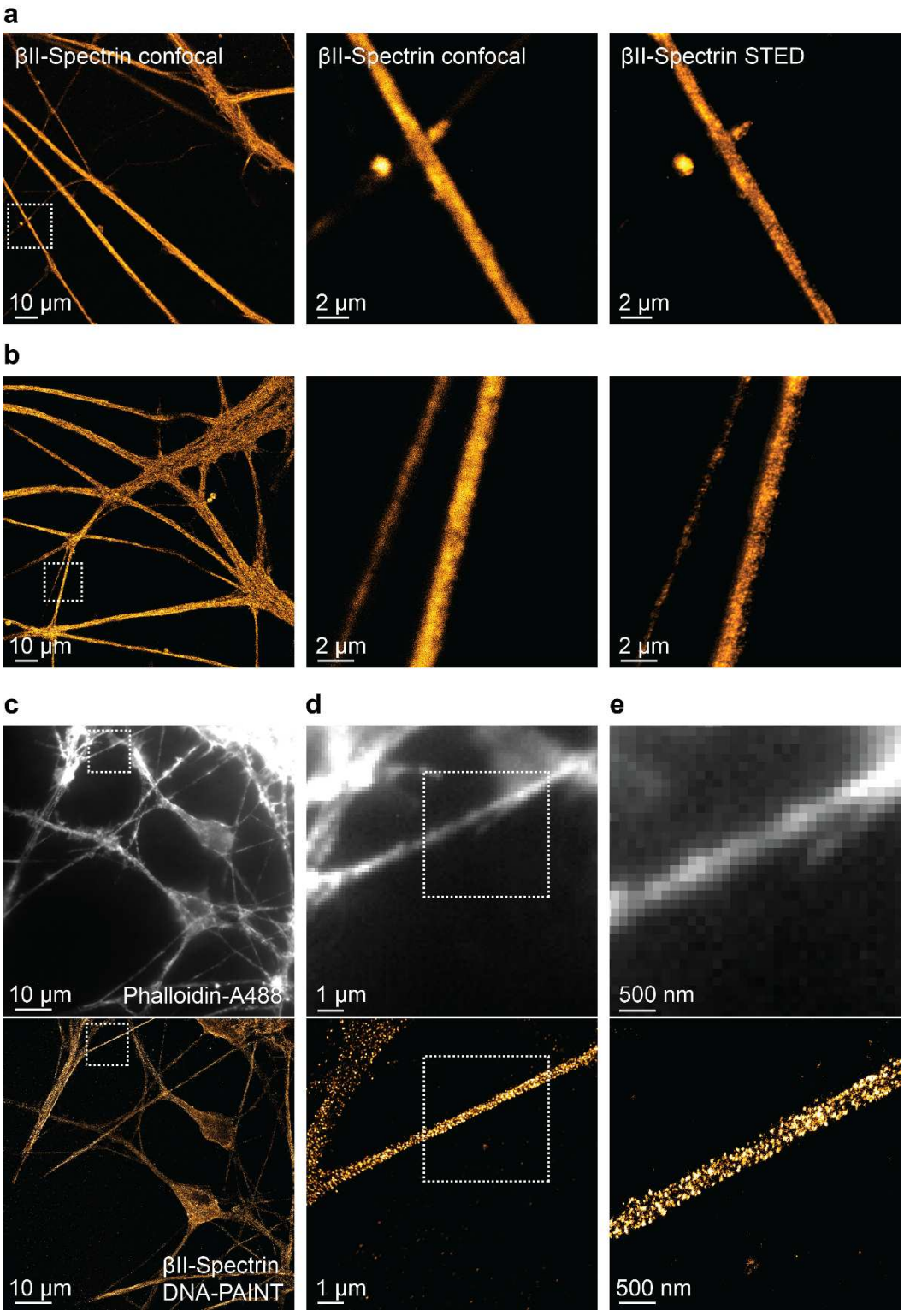

Figure 42: Imaging the MPS with STED and DNA-PAINT in hippocampal neurons cultured on the stretching device

a,b, Low resolution confocal image (left) of immunolabelled βII-Spectrin in DIV8 hippocampal neurons in the stretching device. Low resolution confocal image (left) and STED super-resolved image (right) of

immunolabelled βII-Spectrin in an axon of DIV8 hippocampal neurons for the outlined area in the left panel displayed at a higher magnification. **c,** Low resolution epifluorescence image (top) and DNA-PAINT super-resolved image (bottom) of immunolabelled βII-Spectrin in hippocampal DIV4 neurons on the PDMS stretching device. Scale bars: 10 µm. **d,** Low resolution epifluorescence image (top) and DNA-PAINT super-resolved image (bottom) of immunolabelled βII-Spectrin in an axon of hippocampal DIV4 neurons on the PDMS stretching device for the outlined area in the two panels of c displayed at a higher magnification. Scale bars: 1 µm. **e,** Low resolution epifluorescence image (top) and DNA-PAINT super-resolved image (bottom) of immunolabelled βII-Spectrin in an axon of hippocampal DIV4 neurons on the PDMS stretching device for the outlined area in the two panels of d displayed at a higher magnification. Scale bars: 500 nm.

2.2.2. Capturing the acute mechanical response of MPS proteins to small scale stretching

Concerning the second aim, studying the acute mechanical response of MPS proteins to stretch requires a different set of conditions. More precisely, it is essential to achieve simultaneous SPT/SRM imaging while stretching, in order to capture the acute mechanical response of individual proteins to external stresses (Massou, Nunes Vicente, Wetzel et al. 2020). Moreover, these experiments will be performed with small-scale (up to 6%) stretches, since this is the limit for live XYZ repositioning while stretching. Therefore, neurons have to express photoactivatable proteins in order to perform sptPALM acquisitions while stretching them simultaneously. Although we have previously performed STED in live cells that experience stretching (Massou, Nunes Vicente, Wetzel et al. 2020), STED is not compatible with capturing the acute mechanical response of individual proteins due to the constraints of the technique itself. Conversely, the effect of large stretching in nanoscale organization can be assessed after stretching and hence through labelling of endogenous proteins with STED or DNA-PAINT (Massou, Nunes Vicente, Wetzel et al. 2020).

While trying to perform simultaneous SPT/SRM and small-scale stretching on neurons, we realized that experimental conditions pose again as a major obstacle for the available transfection methods. The main one is the size of the observation window for stretching, which is more than a hundred times smaller compared to the size of the PDMS assembly. Thus, it is crucial to achieve both high cell viability and high transfection rates to have transfected healthy cells in the observation window. Electrical transfection methods such as conventional electroporation deliver moderate transfection rates but low cell viability, which is far from ideal in our experimental conditions. Nucleofection, a pulse-based modified form of electroporation, has been shown to improve both transfection rates and cell viability (Karra and Dahm, 2010). However, nucleofection still led to considerable neuronal death in our micromechanical device for both Actin-mEos2 and βII-Spectrin-mEos3.2. For this, we are currently collaborating with Mireille Montcouquiol at Neurocentre Magendie (INSERM, Bordeaux) to electroporate primary neurons for live acute stretching experiments with improved survival and transfection rate.

Alternatively, chemical transfection methods are usually simple and present low toxicity for primary cell lines. Ca2+ phosphate transfection is one of the most established methods and is very commonly used to transfect different types of primary neuronal cells. It is both cost effective and displays high cell viability; in addition, it can be used to transfect neurons at different stages of differentiation (Dahm et al., 2008; Karra and Dahm, 2010). However, the transfection rate is often around ~5%, which makes highly difficult to find transfected cells in the observation window. The limited time in culture (up to DIV5) of the device also poses as an issue for other methods. Viral transduction, which has both high efficiency and viability, has a late onset of transgene expression (5-14 days for adeno-associated viruses, for instance) (Karra and Dahm, 2010), which is not compatible with the micromechanical device. Moreover, viral transduction methods are often limited in terms of insert size (up to 5 kb for the most common viruses), which prevents the expression of proteins such as spectrin (> 10 kb for commercially available plasmids).

To tackle these issues, we opted for a new cell culture and protein expression system for studying the acute response of MPS proteins: the developing chick spinal cord coupled to *in ovo* electroporation (Delloye-Bourgeois et al., 2014; Pignata et al., 2019). This system has been extensively used to study axonal guidance mechanisms, in particular the midline crossing of commissural axons at the floor plate (FP) (Delloye-Bourgeois et al., 2014; Pignata et al., 2019). In most studies, chick spinal cord embryos are first electroporated *in ovo* with proteins of interest, which are injected into the neural tube. 48h later, proteins are ubiquitously expressed across the spinal cord; this allows to perform live imaging or functional studies with mutants (Delloye-Bourgeois et al., 2014; Pignata et al., 2019). Therefore, we thought that this system could solve protein expression issues in our device, by ensuring both high transfection rates and cell viability.

From an electroporated spinal cord, several preparations can be obtained after dissection: an 'open book' intact spinal cord, primary dissociated commissural neurons or spinal cord explants, which can be then kept in culture. We opted by choosing the spinal cord explants for acute stretching experiments on MPS. Based on previous experiments, we expected that spinal cord explants will display a quick growth after 24-48h (Fantetti and Fekete, 2011), fitting with the DIV0-5 time window to which the device is limited. One possible limitation could be whether the MPS is present or not in chicken spinal cord neurons, since this is not yet described. However, the MPS is ubiquitous for multiple neuron types in various species, including chicken, where it has been described in Dorsal Root Ganglia (DRG) neurons (Fig.34b) (Dubey et al., 2020; He et al., 2016).

In order to electroporate and dissect chick spinal cord embryos, we followed a step-by-step protocol (Delloye-Bourgeois et al., 2014) suited for expression of fluorescent proteins. After 52h of incubation at 38.5°C, chick embryos around stage HH14 (Delloye-Bourgeois et al., 2014) were electroporated *in ovo* with the protein of interest fused to a mEos tag and a GFP/tdTomato

reporter (Fig. 43a). 48h after electroporation, the spinal cord was dissected and sectioned into different explants, which were mounted on micromechanical devices pre-coated with laminin. Explants were stretched and imaged at DIV2. Spinal cord explants displayed axonal prolongations and growth cones at DIV2 (Fig. 43b). Moreover, explants showed both EGFP and Actin-mEos2 expression at DIV2 (Fig. 43b,c). This constitutes a substantial improvement in comparison to primary rat hippocampal neurons. We were also able to stretch the explant at DIV2; however, due to time constraints we are yet to obtain the acute mechanical response of actin to live small-scale stretching. We are simultaneously aiming to characterize the presence of the MPS in the explant at DIV2; for that, we employed the same protocol applied to primary neurons, labelling βII-Spectrin. So far, it is unclear whether the explants display or not the MPS at this developmental stage.

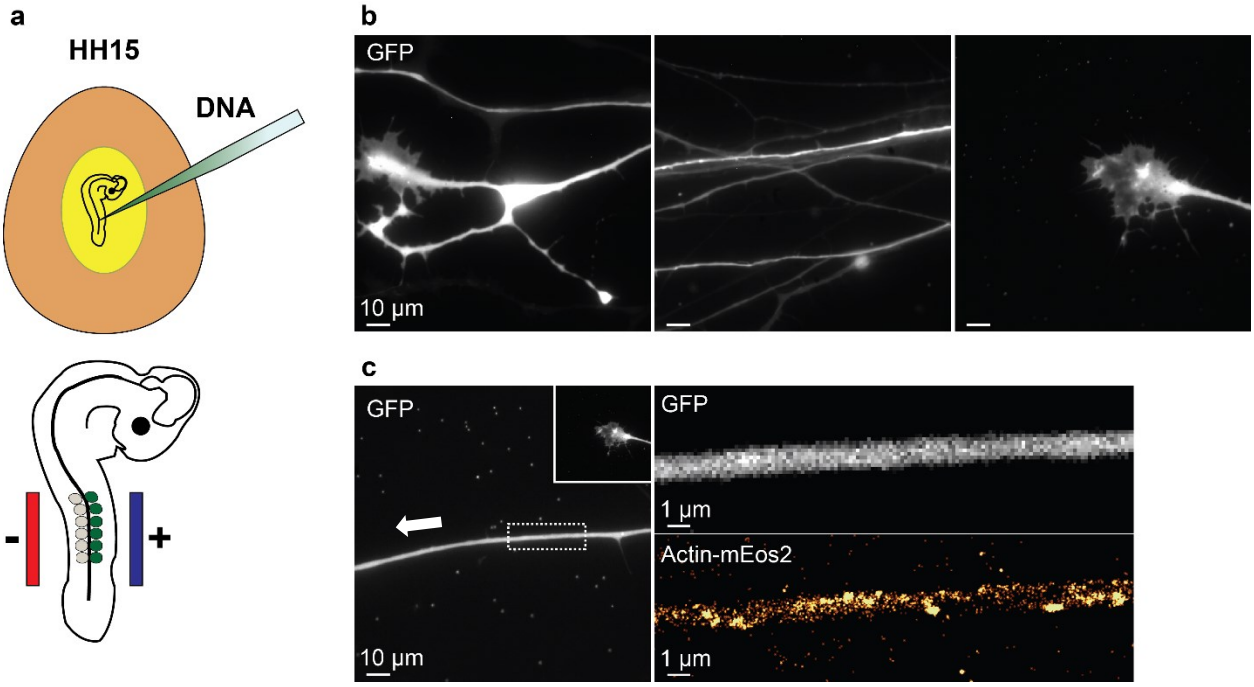

Figure 43: Chick spinal cord explants as a system to study acute mechanical response of MPS proteins

a, Schematic representation of *in ovo* electroporation of HH15 chick embryos. After cutting the top of the egg shell, exposing the embryo, DNA is injected in the neural tube with a glass capillary (top). A negative and positive electrode are then placed in the caudal region of the embryo, electroporating the neural tube (bottom), which later develops into the spinal cord. Only one side of the epithelial somites (green) is electroporated; this is visible by epifluorescence throughout dissection and sample preparation. **b,** Epifluorescence images of GFP in a DIV2 chicken spinal cord explant cultured on the PDMS stretching device at DIV2. Protein expression is visible across various neuronal compartments: cell bodies (left), axons (middle) and growth cone (right). **c,** Epifluorescence image of GFP in an axon of a chick spinal cord explant cultured on the PDMS stretching device (left). Arrow represents the direction of the growth cone. Inset: Corresponding growth cone. Scale bar: 10 µm. Low resolution epifluorescence GFP image (top right)

and projection of actin-mEos2 super-resolution intensity images (bottom right) (50 Hz, 40s) for the outlined area in the left panel displayed at a higher magnification. Scale bars: 10 µm.

2.3. Micropatterning the stretching device

Cells *in situ* are highly influenced by their microenvironment, composed by the ECM and neighboring cells. Properties of the microenvironment, such as size or rigidity, will impose specific geometries, orientations and adhesion conditions to the cells, regulating their response to force. For instance, FAs undergo disassembly when cells are perpendicular, but not parallel to stretch direction (Chen et al., 2013). Thus, the effects of uniaxial stretching in MPS dynamics and reorganization could also be different if the axon is parallel or perpendicular to stretching. Micropatterning techniques are ideal to answer these questions, since they allow a precise control of the cellular attachment, shape and spreading by engineering of the cell culture substrate. Through different micropatterning techniques, specific regions for cell spreading and adhesion are generated in the substrate, called micropatterns. Here, we decided to implement light-based micropatterning on the PDMS stretching device. The main aim is to control neuronal orientation during stretching, but micropatterning of the device can also allow to study the impact of geometry or adhesion in the acute mechanical response of proteins inside FAs. For this we used the maskless photopatterning PRIMO system (Álveole), based on the technology of Light Induced Molecular Absorption of Proteins (LIMAP) (Strale et al., 2016). This technique allows to project multiple patterns onto a single sample in a scale of minutes. First, the substrate of interest is coated with an anti-fouling molecule, in this case composed of poly (L—Lysine) backbone and poly(ethylene glycol) (PLL-PEG) side-chains. PLL-PEG coating prevents the adsorption of biomolecules (e.g. proteins) on the substrate. A digital micromirror device (DMD) will then project UV-structured light onto the substrate of interest, activating a photoactivatable reagent (PLPP). The light-activated PLPP will degrade the anti-fouling coating, allowing for the specific adsorption of proteins on the UV-projected micropatterns and, consequently, specific cell adhesion (Fig. 44).

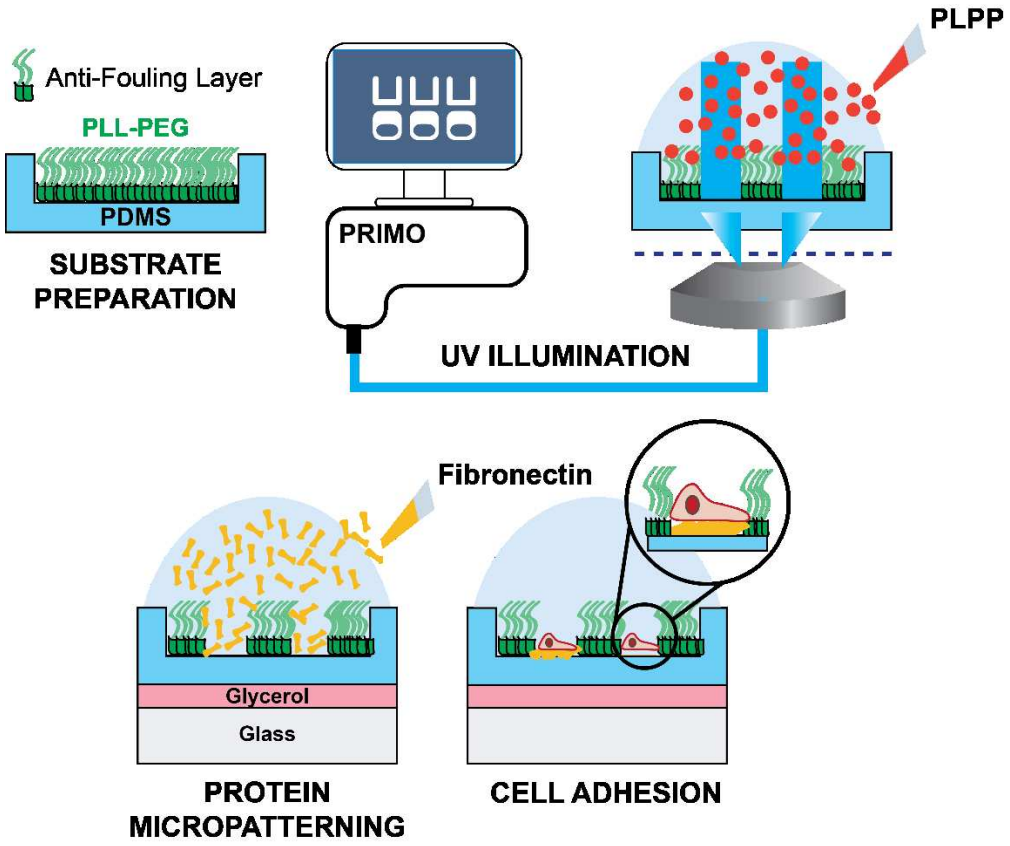

Figure 44: Schematic of LIMAP micro-patterning protocol applied to the stretching device

First, PDMS is coated with an anti-fouling layer composed by PLL-PEG. Patterns are projected with a DMD using the PRIMO (Alvéole) system, degrading the anti-fouling layer through PLPP photo-activation. Fibronectin is added to the micropatterns and cells are then spread on the micropatterned PDMS substrate.

We first started by optimizing the LIMAP/PRIMO method for PDMS substrates and MEFs. We first coated the PDMS elastomer with Poly-L-Lysine and PEG-SVA, as described by the manufacturer (PRIMO). We then projected different patterns (squares, arrows, circles) (Fig.45). LIMAP micropatterning of PDMS was then performed on the 3 x 3 mm observation chamber, with at least 100 micropatterns generated for each shape. After micropatterning, the device was fully assembled and coated with fibronectin. Successful micropatterning of the device could be observed with Protein A-Alexa Fluor 647 for the pattern, meaning we can perform LIMAP micropatterning on the stretching device (Fig. 45).

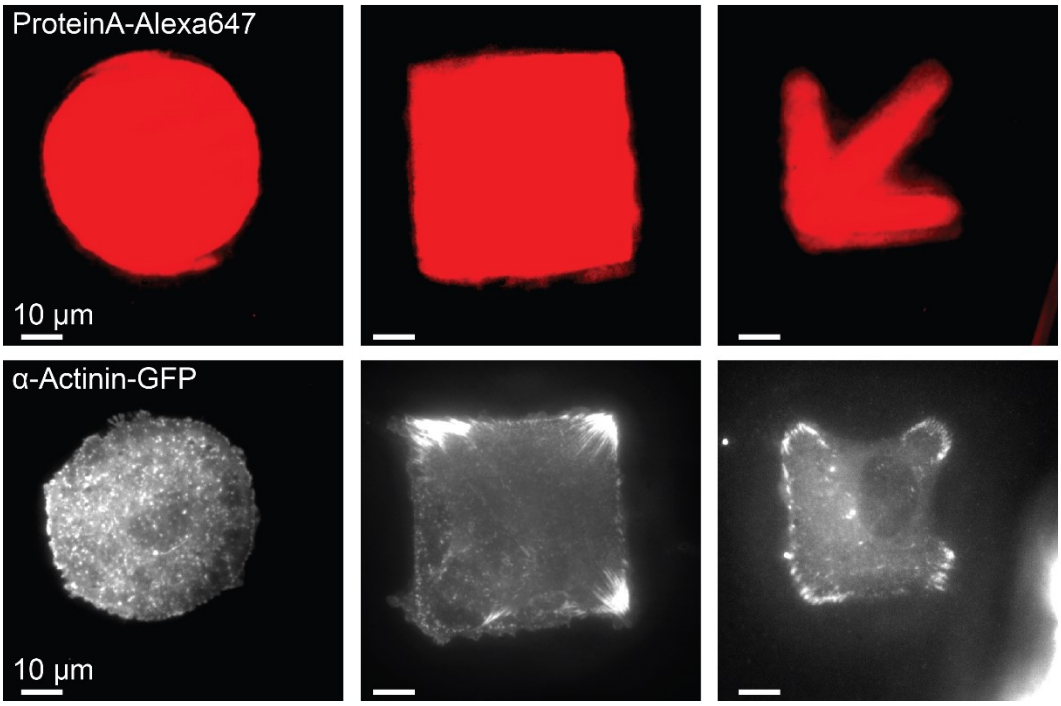

Figure 45: Micro-patterning of the stretching device

Different micropatterns imprinted on the PDMS stretching device, labelled with proteinA-Alexa647 (top), and respective epifluorescence images of MEFs transfected with α-actinin-GFP and seeded on the micropatterns. Patterns correspond to a projected area of 1400 µm^2. Scale bars: 10 µm.

We then tried to combine stretching of MEFs on micropatterned substrates with live SPT/SRM. For this, we defined a micropattern for proof-of-concept experiments, composed of one adhesive area and a non-adhesive area inside a square (WINDOW) (Fig. 46a). We chose this pattern because it allows to capture the acute mechanical response of proteins in two different conditions in the same cell: adhesion to the substrate and 'suspension'. This could give rise to multiple differences; for instance, it is more likely that IAS proteins will not be engaged with either the ECM or the actomyosin machinery in the non-adhesive region. Thus, adhesion to the substrate could modulate the inelastic and elastic responses we observed for proteins such as talin. In a region where adhesion is not favored, talin engagement with integrins and the actomyosin machinery will likely be lower than in adhesive regions. This could decrease talin unfolding through actomyosin contractility and thus decrease the inelastic fraction. Alternatively, it also poses as a valuable system to study cytoskeletal proteins such as spectrin. Although we are more focused on the role of spectrin in MPS mechanosensing, spectrin is a ubiquitous protein with structural and scaffolding functions (Bennett and Lorenzo, 2013; Machnicka et al., 2014). Interestingly, it associates with other proteins to establish plasma membrane domains and

anchor membrane proteins such as cell adhesion molecules (Bennett and Lorenzo, 2013; Machnicka et al., 2014). Thus, the mechanical response of spectrin could also be influenced by the adhesion to the substrate.

For the experimental procedure, we adapted the dimension of each projected pattern to correspond to a projected area of ~1400 µm^2 which ensured optimal cell spreading. After PLL-PEG coating and projecting the micropattern on the device, we spread cells expressing βII-Spectrin-mEos3.2 on the device to perform simultaneous live cell stretching (~2-5%) combined with SPT. We successfully stretched cells on micropatterns with 3% trapeze-like patterns and captured the acute mechanical responses of individual BII-Spectrin using sptPALM (Fig. 46a). Kymographs were extracted for regions of contact or no contact with the substrate (Fig. 46b). In conclusion, we demonstrated that we are able to combine micropatterning with live cell stretching and SPT. This paves the way for future studies on the effect of cell geometry and adhesion in the deformations and reorganizations of proteins inside mechanosensitive structures.

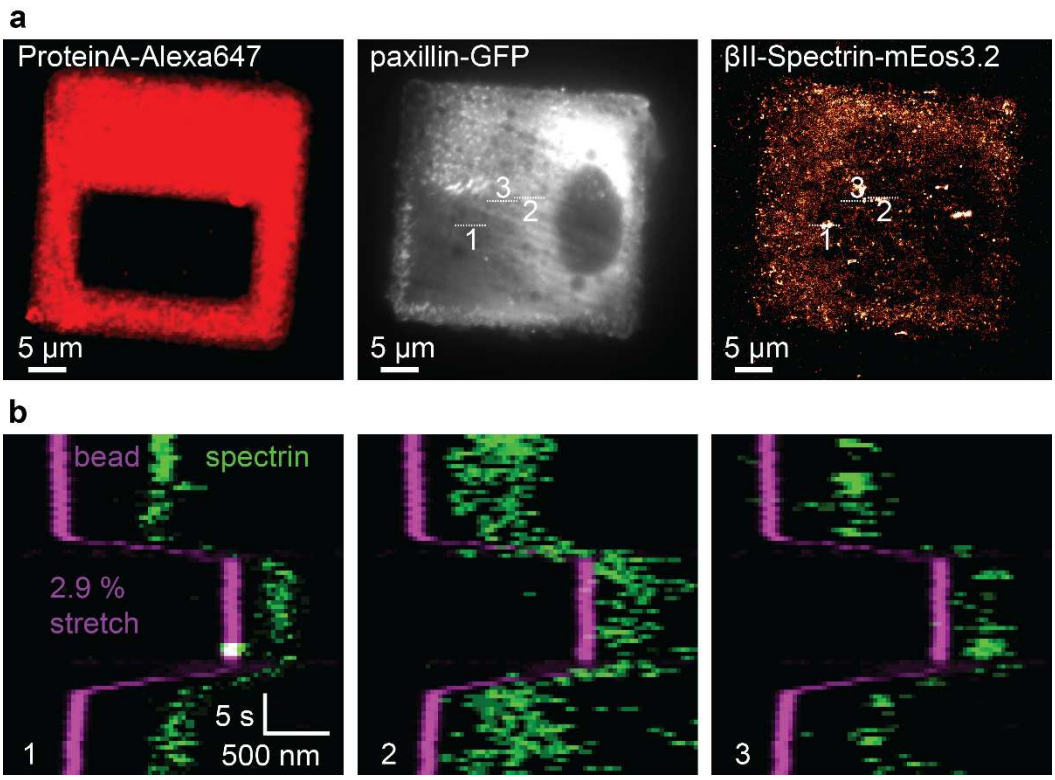

Figure 46: Capturing the acute mechanical response of βII-Spectrin in micro-patterned cells

a, Epifluorescence image of a WINDOW micropattern on the PDMS stretching device, labelled with ProteinA-Alexa 647 (left), corresponding to a projected area of 1400 µm^2. Epifluorescence image of paxillin-GFP in a MEF seeded on a micropattern on the PDMS stretching device (middle). Projection of all βII-Spectrin-mEos3.2 super-resolution intensity images of a trapeze-like pattern time-lapse (stretching 2.9 %, 2 Hz, 40 s) (right). Scale bar, 5 µm. **b,** Right, βII-Spectrin-mEos3.2 kymographs generated from the

trapeze-like pattern time-lapse (as shown in the left and middle panels in a, dashed lines). x-axis, space (500 nm); y-axis, time (5 s). The magenta kymograph corresponds to the reference bead, and the green kymographs correspond to βII-Spectrin-mEos3.2.

3. Unveiling the nano-scale dynamics and organization of β3-integrin at dendritic spines

As previously mentioned in the chapter 5 of the Introduction, β1 and β3-integrins regulate synaptic transmission and plasticity in mature neurons. β3-integrin, in particular, can regulate homeosynaptic plasticity and AMPA receptor (AMPAR) endocytosis. However, it is still unclear how β3-integrin is recruited and activated at spines. Over the course of my thesis, I developed a third project focused on the nanoscale dynamics and organization and of β3-integrin in dendritic spines. Here I present preliminary results of the project, some of which will be included in a publication from the group of Matthieu Sainlos (IINS, University of Bordeaux). This project is still in development at the lab, due to time constraints from the two main projects on cell stretching and molecular mechanosensing.

1. Introduction

In the developing brain, integrins control stem cell differentiation, neuronal migration, neurite outgrowth and synapse development. The crosstalk between integrin-ECM interactions, growth factors and other adhesive proteins such as nectin or L1CAM is critical to drive neuronal migration along radial glia (Förster et al., 2002; Needham et al., 2001), as well as axonal outgrowth (Pasterkamp Nature 2003). Their role in early development could influence neuronal function in the mature brain, as seen for developmental β1-integrin in the orbitofrontal cortex (DePoy et al., 2019).

In mature synapses, integrins appear to regulate synaptic transmission and plasticity, as well as to shape neural circuit properties. The main variants involved in these processes are β1 and β3-integrins, which are thought to modulate trafficking and dynamics of neurotransmitter receptors (Charrier et al., 2010; Cingolani et al., 2008; Pozo et al., 2012). Together, they have been shown for instance to control the dwelling time of glycine receptors at inhibitory synapses, influencing neuronal excitability (Charrier et al., 2010).

β3-integrin, in particular, appears to play an essential role in maintaining the number and composition of synaptic AMPA receptors (AMPARs), which could be independent on integrin activation state. This, in turn, is required for homeostatic synaptic scaling of AMPARs (Cingolani et al., 2008). This, in turn, might be dependent on interactions between β3-integrins and the GluA2 subunit, regulating AMPAR endocytosis (Pozo et al., 2012). However, little is known about the nano-organization of postsynaptic β3-integrin or how it is recruited to dendritic spines. In parallel, the modulation of postsynaptic β3-integrins via ECM ligands under physiological conditions needs further clarification.

Here, we tried to address some these questions by studying β3-integrin nanoscale dynamics and organization in mature rat hippocampal neurons (DIV 14-16). For this, we have used a combination of sptPALM, DNA-PAINT and strategies to regulate integrin activation (Mn2+, mutants).

2. Methods

We performed all our experiments in mature rat hippocampal neurons. Preparation of cultured neurons was performed as previously described (Giannone et al., 2013). Dissociated hippocampal neurons from 18-day-old rat (Sprague Dawley) embryos were cultured on glass coverslips following the Banker protocol. Around DIV7-8, neurons were transfected with the protein of interest and a GFP reporter, using the calcium phosphate method (ref). Neurons were imaged at DIV 14-16. Live imaging with sptPALM was performed as described in the Methods Chapter in annex. For DNA-PAINT, cells were first fixed in 4% PFA labelled and imaged as previously described (Massou, Nunes Vicente, Wetzel et al. 2020). Analysis of sptPALM was carried as described in the Methods chapter on Annex 1. Spines and shafts were manually traced in Metamorph Software. Analysis of DNA-PAINT was carried as previously described (Massou, Nunes Vicente, Wetzel et al. 2020).

3. Results and discussion

We first observed the nanoscale dynamics of β3-integrin-wt-mEos2 in dendritic spines either in control conditions or after incubation with Mn^{2+}, which is an integrin activator (Fig. 47) (Rossier et al., 2012). In control conditions, β3-integrin-wt immobilization fraction was slightly higher for spines compared to shafts (Fig. 47a,e,f)(non-significant). Mn^{2+} was incubated at 5 mM for 30 minutes and washed before the sptPALM acquisitions. We found that treatment of neurons with Mn^{2+} lead to a significant increase of β3-integrin immobilizations in both the spines and shafts (Fig. 47b,e,f). This indicates that, similar to fibroblasts, activation of β3-integrin in dendritic spines is correlated with its immobilization. To further dissect the mechanism behind

this immobilization, we employed a mutant version of β3-integrin, β3-119Y, which prevents binding to the RGD sequence of fibronectin (Rossier et al., 2012). In contrast to β3-WT, Mn^{2+} stimulation did not increase β3-D119Y immobilization in both spines and shafts (Fig. 47c,de,f), demonstrating that β3-integrin immobilization is dependent on fibronectin binding. This is consistent with previous results on mature FAs in MEFs (Rossier et al., 2012).

To further dissect the synaptic roles of β3-integrin, we are characterizing the nanoscale organization of β3-integrin in regards to the postsynaptic density (PSD) protein 95 (PSD-95)(Feng and Zhang, 2009). This scaffolding protein is instrumental for the molecular organization of the post-synapse, regulating trafficking of glutamate receptors such as AMPARs or N-methyl-D-aspartate (NMDA) type-receptors (Huganir and Nicoll, 2013). PSD-95 is crucial for synaptic development and plasticity, and has been involved in various disorders (Grant, 2012; Zheng et al., 2011a). Thus, β3-integrin could associate to PSD-95 to regulate trafficking of AMPARs, among other roles. To assess this, we are first implementing dual-color DNA-PAINT for β3-integrin and PSD-95 in dendritic spines of mature DIV 14-16 neurons. We started by imaging endogenous PSD-95 with DNA-PAINT. For this, we used a PDZ-based fragment that binds endogenous PSD-95, named Xph20. This tool was developed by the group of Matthieu Sainlos at IINS (CNRS, University of Bordeaux) and optimized by us for DNA-PAINT imaging. We found that Xph20-SNAP delivers a precise labelling of PSD-95 in dendritic spines with DNA-PAINT (Fig. 48a,b), allowing to visualize the different organizations of PSD-95 (Fig. 48b). As of now, we are trying to implement dual-color DNA-PAINT with β3-integrin.

In conclusion, our data suggests that a fraction of β3-integrin is immobilized in dendritic spines at the basal state, which in turn can be significantly enhanced by acute activation. This appears to be dependent on extracellular signaling, although the involved ligands are yet to be found. Moreover, the nature of this immobilizations needs to be clarified, since they could stem from endocytosis or arise from β3-integrin recruitment and immobilization. In parallel, dual-color DNA-PAINT will provide us a better picture of β3-integrin nanoscale organization in spines.

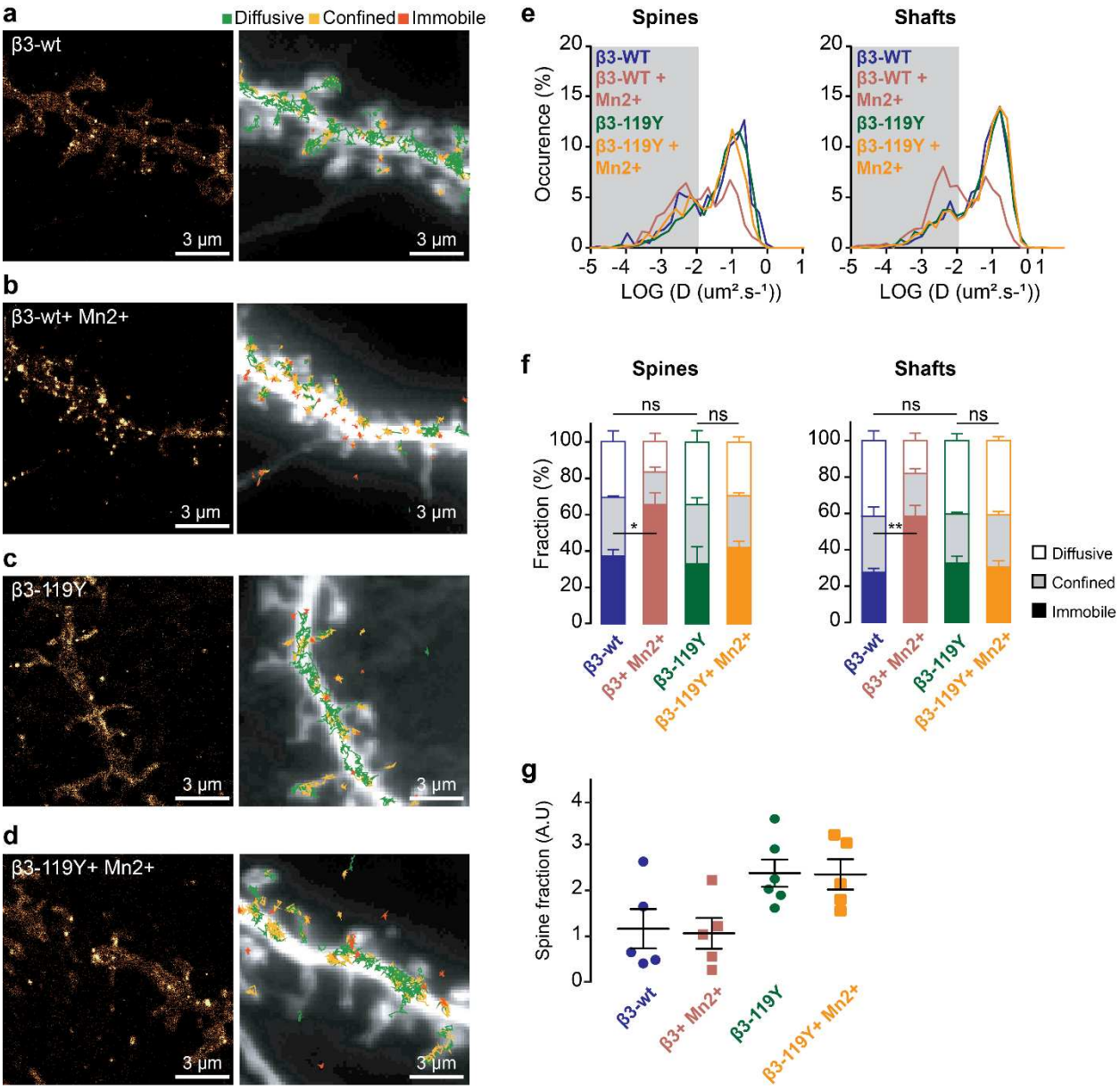

Figure 47: β3-Integrin activation leads to immobilization and is dependent on extracellular signaling

a-b, Super–resolution intensity images of β3-integrin-mEos2 at basal state (a) or after Mn^{2+} stimulation (b) in the dendrites of a hippocampal neuron at DIV 16 obtained from a sptPALM sequence (left) (50 Hz, 80 s). Right: color-coded trajectories overlaid on dendrites labelled by GFP (greyscale) show the diffusion modes: free diffusion (green), confined diffusion (yellow) and immobilization (red) **c,d,** same as a,b, but for β3-integrin-119Y-mEos in untreated neurons (c) or after Mn^{2+} stimulation (d). Scale bars: 3µm. **e,** Average distribution of the diffusion coefficient D at dendritic spines vs shafts for all conditions. Grey area - D < 0.011 µm².s-1 - immobilized proteins. **f,** Fraction of proteins undergoing free diffusion, confined diffusion or immobilization in spines and shafts (mean ± S.E.M). (E) Distribution of spine enrichment: black line represents the average of the ratio between spine and shaft detections. ns, *P > 0.05;**P < 0.01; ***P < 0.001.

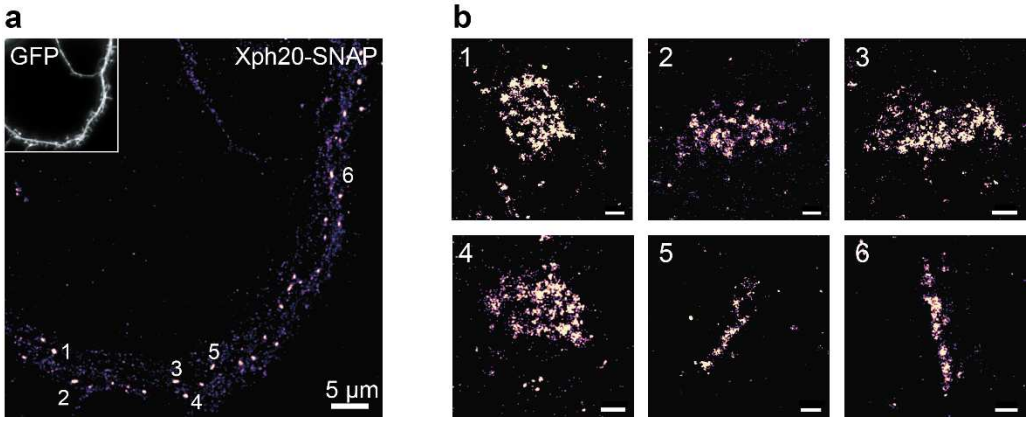

Figure 48: Implementing DNA-PAINT to study post-synaptic nano-scale organization of receptors and PSD-95

a, DNA-PAINT image of Xph20-SNAP in a dendrite of a DIV 14 hippocampal neuron (10 Hz, 32000 frames). Inset: GFP image of the dendrite. Scale bar: 5 µm. b) DNA-PAINT images of Xph20-SNAP in individual dendritic spines for the regions, corresponding to the numbered regions in a and displayed at a higher magnification. Different spine orientations can be observed. Scale bar: 100 nm (for all six regions).

DISCUSSION AND PERSPECTIVES

1. Molecular mechanosensing: stretching to a new border

Mechanotransduction and mechanobiology have evolved a long way from the groundbreaking work of D'Arcy Thompson more than a hundred years ago(Thompson and Bonner, 2014). Propelled by new imaging methods, force sensors, laser/magnetic tweezers and proteomics, we now acknowledge how important mechanical forces are in controlling cell behavior at multiple levels. We now find ourselves at a crossroads between two paths; going 'big', by studying the influence of mechanical forces in tissue physiology and collective cell behavior, or going 'small', by identifying and dissecting the molecular mechanisms behind mechanotransduction. In this thesis, I chose the 'small' path but keeping in mind the context of live cells, where molecular mechanosensing results from the the interplay of various proteins, pathways and subcellular structures.

Mechanosensing, a key event in mechanotransduction, is based on the deformation and reorganization of proteins in response to mechanical forces. It is undeniable that a molecular understanding of mechanosensing emerged from *in vitro* single molecule force spectroscopy studies (Huang et al., 2017b; Kong et al., 2009; Del Rio et al., 2009; Sawada et al., 2006). Through techniques such as optical and magnetic tweezers or AFM, it was shown how proteins are unfolded by mechanical stretch, triggering their phosphorylation (Sawada et al., 2006), cleavage ((Stephenson and Avis, 2012)) or the recruitment of partners (Del Rio et al., 2009). Similar approaches allowed to characterize the destabilization or reinforcement of interactions by mechanical forces, revolutionizing the way we look at adhesions (Buckley et al., 2014; Huang et al., 2017b). However, it is unclear whether some of these principles will be maintained in live cells. Will vinculin form a catch bond with actin with the exact same directionality towards the pointed (-) end of actin filaments? Or will talin unfolding induced by actomyosin tension indeed recruit vinculin? Nonetheless, force spectroscopy studies in living cells allowed to characterize mechanosensing in a cellular context, hence further revealing its dependence on single protein interactions (Choquet et al., 1997; Chronopoulos et al., 2020; Feng et al., 2017; Giannone et al., 2003; Jiang et al., 2003). Still, these studies have relied on the manipulation of individual proteins on dorsal surfaces of cells. Thus, no experimental strategies were able to apply external forces to cells while simultaneously capturing the mechanical response of individual proteins in crowded macromolecular structures such as IAS. This is even more relevant since we now see IAS as nano-partitioned structures where dynamics of individual proteins reflect their function and mechanical engagement. Accessing these dynamics and force patterns is crucial to fully understand mechanosensing at IASs.

Here, by combining cell stretching with SRM and SPT, we could reveal at the nanoscale the mechanical response of mechano-sensitive structures. This enables to study how polarized

macromolecular complexes, composed of distinct functional nano-domains, reorganize upon external stretch. In this work, we have focused mostly on IASs, but our approach is also suitable for microtubules, intermediate filaments and stress fibers. In the context of live stretching, we could capture 1) force-dependent protein unfolding or deformations or 2) force-dependent protein recruitments and reorganizations of individual proteins in mechanosensitive structures.

2. Acute mechanical response of proteins

To study the acute mechanical response of proteins, we compared the kymographs from both beads and single molecules inside and outside mature FAs during small scale (2-5%) stretching combined with SPT. Initially, we found that β_3-integrin displayed elastic responses, suggesting that stationary β_3-integrin molecules remained anchored to fibronectin during PDMS stretching. The response of integrins can thus be used as a 'benchmark' for other IAS proteins, suggesting their behavior will reflect their connection to different binding partners such as the ECM or actin filaments. We then found that actin filaments and talin displayed both elastic but and inelastic responses. The latter were characterized by lagged and transient (~5 s) local displacements (~250 nm) associated with talin deformations, as seen by the larger fraction of inelastic responses for talin-C compared to talin-N. The lower fraction of inelastic responses for Talin-N reflects binding to integrins, again showing how the acute mechanical response reflects the various linkages to IAS components. The amplitude of local talin displacements for talin-C (~330 nm) was in agreement with the values previously observed for talin unfolding *in vitro* (Yao et al., 2016). One interesting question is if these displacements represent unfolding of VBS-containing rod domains or simply the extension of talin without exposing VBS. Moreover, we only assessed the acute mechanical response of talin-1 in our observations. However, talin-1 and talin-2 are differentially engaged with the force transduction machinery in fibroblasts (Austen et al., 2015), which could give rise to different mechanical responses. Talin-2 is more exposed to tension in fibroblasts and, in the absence of F-actin binding to the C-terminal, talin-2 can still retain its tension and recruit vinculin. Thus, talin-2 could have a lower fraction of inelastic responses by engaging actomyosin-independent mechanisms, which would not lead to talin deformation in response to amplification of external forces. The inelastic responses of actin were decreased by cell fixation and myosin II inhibition with blebbistatin, indicating a mechanism driven by active remodelling of the actin cytoskeleton. Thus, protein deformations inside IASs are not triggered by direct transmission of the external stretch. Interestingly, the inelastic responses of actin are not completely abolished by cell fixation or myosin II inhibition blebbistatin; this could arise from passive viscoelastic mechanisms that still occur in these conditions.

The inelastic responses of actin and talin could also involve stress fiber ruptures and strains. These can be induced by external stresses (Hoffman et al., 2012) or by increased

contractility (Oakes et al., 2017; Smith et al., 2010), and are repaired by recruiting zyxin , α-actinin and VASP, regulating SF homeostasis (Hoffman et al., 2012; Oakes et al., 2017). These mechanisms could lead to inelastic responses of talin and actin. For instance, if a SF is partially ruptured, some population of talin-C could be essentially disconnected, giving rise to the elastic behavior. Conversely, the talin-C that remains connected to the stress fibers may experience the delayed stretching in a myosin-II dependent fashion, through stress fiber homeostasis mechanisms (Oakes Nat Comm 2017). However, in the discussion of our publication, we showed that small scale stretching does not cause any major SF ruptures/strains, as well as recruitment of zyxin or α-actinin. We also discuss how the few plastic ruptures we observed in single stretch-plateau patterns do not correspond to inelastic responses. These results support our model where inelastic responses are triggered by by active, transient and reversible reorganizations of the actin cytoskeleton. Further details can be found in the discussion of our publication.

In this section, we used blebbistatin a chemical inhibitor of all the 3 myosin II isoforms MIIA, MIIB and MIIC (Rauscher et al., 2018), which have distinct kinetic properties (Vicente-Manzanares et al., 2009) and roles in cell and tissue function (Heuzé et al., 2019; Wang et al., 2010). Hence, it would be of interest to inhibit/knockout specific isoforms of myosin II to fully dissect the role of myosin II in actin remodelling and inelastic responses. For instance, myosin IIA has the highest ATP hydrolysis rate and propels actin filaments more rapidly. On the other hand, myosin IIB has the highest duty rate, which is the time bound to actin in a force-generating state, as well as a higher affinity for ADP (Vicente-Manzanares et al., 2009). Thus, myosin IIB is particularly adapted to exert tension on actin filaments for longer periods and with less energy expenditure compared to myosin IIA. In adhesive structures, myosin IIA generates mechanical tugging forces for high junctional stress, while myosin IIB maintains a branched actin network to sustain high tension along cell-cell interface (Heuzé et al., 2019). Moreover, disrupting myosin IIA structure reduces FA size and number and leads to abnormal stress fibers (Wang et al., 2010). Therefore, in the context of our experiments, myosin IIA could be specifically required to mediate transient remodelling mechanisms through mechanical tugging forces acting on IAS. This would depend on a faster propelling of actin filaments and high ATP hydrolysis rate. Conversely, myosin IIB could be more important to maintain the tension on actin filaments through its specialized kinetic properties, hence being more important for adaptive mechanisms during sustained stretching. In addition, we could check whether ROCK inhibition with Y-27632 would have a similar effect in decreasing inelastic responses. Finally, it would also be of interest to explore the acute mechanical response of the different myosin II isoforms.

3. Force-dependent protein recruitment and reorganizations

At the molecular level, mechanical forces reinforce or destabilize interactions and expose hidden binding sites fostering protein recruitment, as demonstrated for IAS or adherens junctions. Combining cell stretching with SRM or SPT yields molecular resolution on protein reorganizations which can be spatially and temporally heterogeneous within mechano-sensitive structures. Previously conceived stretching devices were used for studying protein recruitment and reorganization at structures such as IAS (Chen et al., 2013), nucleus (Nava et al., 2020), SFs (Hoffman et al., 2012) or cell-cell contacts (Gao et al., 2018). However, in many of these cases, protein recruitment was measured before/after stretch with epifluorescence or confocal microscopy. Thus, there was no real-time nanoscale measuremnent of protein reorganizations in mechano-sensitive structures as the cell is stretched/relaxed.

Here, we found that neither small (4%) nor large (10%) stretching induce vinculin recruitment at mature FAs. Conversely, small-scale 4% stretching induced a delayed vinculin recruitment to NAs, which is reduced but not completely reverted after relaxation. This supports the hypothesis that substrate stretching is not directly driving talin unfolding. Instead, our results are consistent with a model where external stresses applied to cells trigger subsequent cellular active responses, e.g. active actin reorganization, leading to protein unfolding and recruitment. The fraction of talin-C displaying inelastic responses was similar for NAs and mature FAs, which suggests talin unfolding in NAs in response to external stresses. Moreover, this vinculin recruitment occurs mainly on talin residing in NAs, since 4% stretching did not led to a significant recruitment of talin. Finally, by establishing how vinculin recruitment is delayed, we have also shown how our device can deliver both spatial and temporal measurements of nanoscale protein reorganization.

We observed talin unfolding in both mature FAs and NAs. Thus, we could expect vinculin recruitment in both cases, in light of *in vitro* studies with purified talin rod domains and vinculin (Del Rio et al., 2009; Yao et al., 2016). However, our results are unexpected but not completely surprising, since the tensional states and force history of talin can influence the ability to recruit vinculin. Vinculin-unloaded talin recruits vinculin upon an initial stretch, while vinculin-loaded talin can be stretched over 500 nm *in vitro* without unfolding of VBS-containing domains or recruitment of additional vinculin. Thus, talin stretching and vinculin recruitment can occur independently, and some of inelastic responses might precisely reflect this. Moreover, vinculin has to work mechanically against the pulling force on talin to stabilize binding to VBS in rod domains (Tapia-Rojo et al., 2020). When the force on the integrin-talin-F-actin linkage becomes too high, vinculin binding would be more unfavorable, leading to dissociation of talin-vinculin complex. When subjected to very high forces (> 25 pN), vinculin dissociates from talin rod

domains due to helix-to-coil transitions (Yao et al., 2014). Therefore the undetectable molecular recruitment of vinculin in mature FAs might be explained by simultaneous recruitment and dissociation upon cell stretching. To dissect this, we could employ talin FRET sensors, which would provide us with a correlation between talin tensional states and vinculin recruitment/dissociation at mature FAs.

By contrast to mature FAs, newly recruited talin into NAs might have lower tensional sates, free from any previous stretching, with all vinculin binding sites available for recruitment to trigger maturation to FAs. The force on integrin-talin-F-actin linkages is lower at NAs, hence vinculin binding and consequent domain coil-to-helix contraction is favorable under this force regime (Tapia-Rojo et al., 2020). Previous studies have shown that external forces applied with optically trap beads induce focal complex formation, characterized by progressive vinculin recruitment. Given that focal complexes are closer to NAs in terms of IAS maturation stage, this study supports how vinculin can be recruited to maturing IAS, in order to strengthen the integrin-fibronectin-cytoskeleton linkage (Galbraith et al., 2002). This idea is consistent with the axial redistribution of vinculin observed in NAs using tridimensional SRM iPALM in fixed cells. Finally, the presence of talin isoforms could again give rise to different responses. Talin-2, by opposition to talin-1, does not rely on actomyosin tension to promote vinculin recruitment to the N-terminal rod domains (Austen et al., 2015). Therefore, it is possible that in both FAs and NAs talin-2 stretching will not trigger vinculin recruitment.

Recently, *in vitro* studies have demonstrated how actomyosin tension can trigger RIAM dissociation after talin unfolding, followed by vinculin recruitment. Thus, it would be of interest to assess the reorganization of RIAM at NAs and FAs during trapeze-like patterns, which trigger talin unfolding. Based on our results, it is possible that vinculin recruitment to NAs during 4% stretching could be preceded by RIAM dissociation, which would decrease RIAM levels at NAs. Moreover, the R3 talin rod domain contains a RIAM binding site and it unfolds *in vitro* in response to actomyosin tension, releasing RIAM and binding vinculin (Vigouroux et al., 2020). Since R3 is considered the initial mechanosensitive switch of talin for vinculin recruitment (Yao et al., 2016), it is likely that RIAM bound to R3 will dissociate when talin is unfolded in NAs. Moreover, RIAM dissociation would further contribute for the delayed recruitment of vinculin, as previously shown *in vitro* (Vigouroux et al., 2020). RIAM nanoscale dynamics in IASs are; characterizing them would be of great assistance for this hypothesis.

Zyxin is a highly dynamic protein within IAS (Legerstee et al., 2019; Stutchbury et al., 2017) whose localization can change according to mechanical stress. Zyxin can accumulate in FAs in response to uniaxial sustained cell stretching and local deformation (Hirata et al., 2008). Conversely, in response to uniaxial cyclic stretching, zyxin dissociates from mature FAs and accumulates in SFs (Hoffman et al., 2012; Yoshigi et al., 2005) or in the nucleus (Cattaruzza et al., 2004). Here, we observed zyxin recruitment – albeit not in all cases – to mature FAs in response

to a small-scale, ~4% trapeze-like stretching, consistent with previous observations (Hirata et al., 2008). This response also reveals the versatile force-sensing nature of zyxin according to the stretching protocol. Previous reports of zyxin dissociation from mature FAs and accumulation in SFs were observed for cyclic stretching (Hoffman et al., 2012; Yoshigi et al., 2005), which induces SF thickening and reorientation to ensure cytoskeletal stability and adaptation, dependent on the recruitment of zyxin and downstream partners VASP and α-actinin (Hoffman et al., 2012; Smith et al., 2010). Instead, here we applied a small-scale ~4% single stretch, which will likely induce an effect more similar to previously applied sustained (3 min) stretching (Hirata et al., 2008). A previous study has also reported zyxin accumulation in force-bearing sites on migrating cells (Uemura et al., 2011), implying that zyxin could also be recruited to IAS in response to force. Zyxin recruitment to mature FAs upon mechanical stretching is likely mediated by LIM domains, since these are required for targeting the protein to IASs and force-bearing sites (Hoffman et al., 2012; Uemura et al., 2011). Finally, in our protocol, we observed no major SF ruptures/strains or zyxin recruitment to SFs upon 4% stretching, confirming that zyxin is not substantially translocated from FAs to SFs.

Zyxin recruitment was only observed for 50% of the cases; this could arise from a combination of factors. First, compared to a previous study on zyxin recruitment after stretching, we used a smaller scale (4%) trapeze-like stretch instead of a 50%, 3-min sustained stretch. Second, the fast turnover rate and high mobile fractions of zyxin in IAS (Legerstee et al., 2019; Stutchbury et al., 2017) could lead to quick association/dissociation during stretching. Finally, mobile zyxin pools could be further influenced by IAS orientation and positioning (Legerstee et al., 2019), further dictating the force-sensing response. IAS orientation appears to be important in the force-sensing response, since zyxin recruitment to F-actin-IAS complexes has shown to decrease when their orientation angle in regards to stretch is larger (Hirata et al., 2008).

To further characterize zyxin nanoscale reorganization/recruitment in response to stretching, we are currently combining live cell stretching and RESOLFT nanoscopy, with the help of Ani Jose, a postdoc at the lab. RESOLFT nanoscopy requires less intensity to obtain a super-resolved image, thereby reducing the effect of photobleaching and enabling long term live cell imaging(Staudt et al., 2011). With RESOLFT nanoscopy, we can study the dynamic reorganizations of IAS proteins at the nanoscale over a longer period of time. Previous observations from Ani Jose have revealed fluctuations of zyxin levels in IAS, which can be modulated by substrate stiffness and intracellular contractility. Combination of RESOLFT with cell stretching would reveal how zyxin fluctuations are modulated by external forces transmitted to IAS.

Besides zyxin, the IAS protein paxillin also possesses LIM domains, and previous studies have shown that paxillin is recruited to FAs in response to biaxial 10% stretching (Sawada and Sheetz, 2002b) and shortly after (~ 3min) 5 and 10% uniaxial sustained stretch (Chen PNAS 2013). Moreover, local application of force with beads can also trigger the formation of IAS and

consequent paxillin recruitment (Von Wichert JCB 2003). Therefore, paxillin could be recruited both to mature FAs and NAs upon 4% stretching. However, paxillin recruitment to IAS has also been shown to be independent of actomyosin contractility (Zhou et al., 2017), which is required for the active actin remodeling driving inelastic responses to 4% stretching. Hence, paxillin could indeed be recruited to mature FAs in situations of sustained or large stretching, but it is still unclear whether transient amplifications of external stresses could have a similar effect. In addition, paxillin phosphorylation mediates vinculin axial localization in IAS throughout their maturation (Case et al., 2015), as well as a specific, labile paxillin-vinculin interaction at NAs (Pasapera et al., 2010). Therefore, recruitment of vinculin to NAs upon 4% stretching could be associated with increased paxillin phosphorylation. Moreover, paxillin phosphorylation is dependent on myosin II activity, which recruits and phosphorylates FAK. Since external stresses trigger an actomyosin-dependent response, it is likely that myosinII activity in response to stretch will increase FAK and paxillin phosphorylation. This could facilitate targeting or association of vinculin to maturing IAS. FAK is also phosphorylated by mechanical stretching (Chen et al., 2013) further strengthening this hypothesis. Phosphorylation of other proteins such as Src-family kinases (SFKs) have also shown to be enhanced by force and cytoskeleton stretching (Giannone and Sheetz, 2006; Tamada et al., 2004). Increased SFK activity can induce or decrease association of paxillin to IAS, hence posing as another possible mechanism of regulation of paxillin recruitment to IAS by mechanical stretching.

Here, we studied the recruitment and reorganization of vinculin and zyxin in IAS in response to mechanical stretching. Nonetheless, these components could also present inelastic/elastic responses as a function of this active response. However, the turnover of zyxin and vinculin in IAS are faster than integrin or talin:

- zyxin-GFP [t1/2 ~ 7 s (Lele et al., 2006); ~ 9.4 s (Stutchbury et al., 2017)];
- vinculin-GFP [t1/2 ~ 9 s (Von Wichert et al., 2003b), t1/2 ~ 11 s (Lele et al., 2006), t1/2 ~ 20 s (Humphries et al., 2007), t1/2 ~ 39.8 s (Stutchbury et al., 2017)];
- talin-GFP [t1/2 ~ 49.4 s (Stutchbury et al., 2017), t1/2 ~ 62 s (Himmel et al., 2009)];
- beta3-integrin [t1/2 ~ 300-600 s (Ballestrem et al., 2001), t1/2 ~ 225 s (Cluzel et al., 2005)].

As a consequence, the analysis of the elastic and inelastic responses of these proteins will be more challenging, since the number of kymographs spanning the whole duration or, at least half the duration, of the trapeze-like patterns will be low. This is especially true for zyxin which possesses one of the fastest turnovers among IAS proteins; it was highly difficult to obtain kymographs for our trapeze-like stretching experiments with zyxin, even at half of the duration.

4. What drives active remodelling?

It is still unclear how external forces can trigger an active remodeling of the actin cytoskeleton. Recent observations have identified an isotropic actin network in cells (Eghiaian et al., 2015; Svitkina, 2018) which can integrate SFs and display contractile activity (Vignaud et al., 2020). The ABP Filamin A, which is mechanosensitive (Ehrlicher et al., 2011), is important to connect the isotropic actin network to SFs. In response to cyclic stretching, FilaminA is necessary for the isotropic increase of talin tension, probably by distributing the isotropic network tension through mature FAs (Kumar et al., 2019). Therefore, external forces could alter the contractile activity of the isotropic actin network, then distributed throughout IASs via filamin, changing talin tension and leading to talin unfolding. Assessing changes in talin tension with FRET sensors (Austen et al., 2015; Ringer et al., 2017) could provide further insight, as well as performing such experiments in FilaminA knock-out cells, which have impaired tension distribution (Kumar et al., 2019). In addition, filamin, myosin II and α-actinin were shown to display mechanosensitive accumulation in response to external stresses (Schiffauer CB 2016), which could contribute for the active remodelling of the actin cytoskeleton. This accumulation started at 30s after deformation, which surpasses the plateau duration for our trapeze-like stretches. However, in the aforementioned study, mechanoaccumulation was induced with micropipette aspiration of individual cells, and no nanoscale observations were performed. In our conditions, 4% mechanical stretching could trigger faster nanoscale reorganizations of these proteins, as we also observed for zyxin and vinculin. Moreover, the mechanoaccumulative behavior of myosin II is cell type and cell cycle-specific for myosin IIB isoform but not for the others (Schiffauer CB 2016), again showing how myosin isoforms contribute differently to the mechanical response of the cell.

5. Stretching protocol and mechanosensitive response

As we previously discussed in this work, the type of stretching strongly influences its effects; this includes parameters such as the magnitude, strain rate, duration and (Cui et al., 2015; Hsu et al., 2010). Here, we mostly used a physiological, 4% uniaxial stretch with a plateau pattern to study protein deformation and reorganization, in cells not subjected to any previous strain. Thus, it is possible that some of the responses we observed could change in the presence of different stretching protocols, such as cyclic stretching, pre-strain or sustained stretching.

In response to cyclic stretching, cells reorient their long axis and their stress fibers perpendicular to the direction of stretch (Cui et al., 2015; Hoffman et al., 2012; Hsu et al., 2010; Nava et al., 2020). Persistent increases (Cui et al., 2015) or decreases (Faust Plos One 2011) in spreading can also be observed, depending on the stiffness of the substrate. Thus, reorganization of the cytoskeleton upon cyclic stretching could further modulate the active actin remodeling

leading to protein deformation during 4% trapeze-like patterns. Moreover, zyxin is known to be mobilized to SFs in response to uniaxial cyclic stretch (Hoffmann MBoC 2012); this, in turn, could reduce zyxin recruitment to mature FAs upon 4% stretching.

Many of the studied effects of cyclic stretch are often focused on long term processes (spreading, growth) which persist long after the stimulation (Cui et al., 2015; Faust et al., 2011; Hsu et al., 2010); studying acute mechanical responses or protein reorganizations would provide a more immediate assessment of the impacts of cyclic stretch. Still, it is feasible that protein deformation or recruitment could change throughout time after cyclic stretch, as the cell further adapts to its new condition. However, cyclic stretch also produces transient increases in mitogen-activated protein kinases such as c-Jun NH2- terminal kinase (JNK), extracellular signal-regulated kinase (ERK) and p38 (Hsu et al., 2010). These mechanisms could further influence nanoscale protein deformations and reorganizations in cells pre-subjected to cyclic stretch. Many of these alterations can be further influenced by changing the frequency or the duration of cyclic stretch itself (Cui et al., 2015; Hsu et al., 2010).

The mechanical 'memory' of the cell can also influence the response to mechanical stretch. Cells can sense the energy of a pre-stretched substrate (prior to their seeding) which will already modify their stiffness even without further deformation (Panzetta et al., 2019). If the 'sensing' mechanism already involves an active remodeling of actin cytoskeleton, then the acute mechanical response of proteins upon further stretching – such as talin unfolding - could be influenced by pre-strain substrate energy. Additionally, pre-straining the substrate could allow for cell compression, something we did not explore in our experiments. Cell compression, although less studied than stretching, is a common stimuli which drives tumor invasion (Tse et al., 2012) and morphogenesis (Zhang et al., 2011).

Sustained stretching is also common in different physiological and pathological contexts, and also has specific effects in cell function and IAS morphology (Chen et al., 2013). Sustained stretch of 5 and 10% lead to rapid growth of mature FAs followed by a slow disassembly of FAs perpendicular to stretch, dependent on calpain-2 and FAK activation (Chen et al., 2013). In our work, we performed some the experiments before and after large stretching; these can be considered a form of sustained stretching, since live SRM/SPT acquisitions were obtained when the cell is still stretched. However, sustained stretching was only maintained for 5 minutes before relaxing the cell. This is enough to trigger FA rapid growth, occurring within the first 5 minutes of sustained stretching. Accordingly, we observed FA expansion at 30% sustained stretching. However, processes such as mature FA orientation-specific disassembly are slower, starting around 5 minutes of sustained stretching and persisting throughout 20-30 min (Chen et al., 2013). Here, orthogonal strain in perpendicular FAs increases net force on misaligned molecules, triggering activation of downstream events such as FAK and calpain-2 activation, leading to FA disassembly. Rapid FA growth, conversely, is triggered by baseline FAK activity in all FAs, but only

perpendicular FAs reach a threshold of FAK activity due to their orientation (Chen et al., 2013). Interestingly, the long-term effects of sustained stretching could affect protein reorganization or dynamics due to FA disassembly. In our work, we observed no effects of sustained stretching in vinculin recruitment (10% stretch) or nanoscale β3-integrin dynamics (30% stretch). However, it is likely that slower, FAK/calpain-2-mediated disassembly of FAs could also trigger vinculin dissociation via talin cleavage by calpain-2 or increase β3-integrin diffusion. To assess this, acquisitions after stretching could be performed over longer timescales.

6. Possible limitations and drawbacks of the micromechanical device

Despite its power and applications, our approach does not come without its drawbacks or limitations. One of them, common to various systems of stretching, is that the force applied to cells/proteins cannot be measured; although we capture the mechanical response of individual proteins, we do not know how much force we apply to them. This could be assessed with different molecular force sensors, either FRET-based (Austen et al., 2015; Grashoff et al., 2010; Ringer et al., 2017) or DNA hairpin-based (Stabley et al., 2012; Zhang et al., 2014). By measuring, for instance, forces applied on integrins with DNA hairpin sensors (Zhang et al., 2014), it would be possible to understand how the external stresses are sensed at IAS. Simultaneously, using intracellular FRET sensors for talin or vinculin could provide inputs on how active contractile mechanisms distribute force during external stresses. The recent tPAINT implementation (Brockman et al., 2020) is also a suitable method to further dissect mechanical forces at the nanoscale in our device, which is compatible with DNA-PAINT-like approaches.

We have previously discussed about different stretching protocols enabled by the micromechanical device. However, these are all limited to uniaxial stretching. Indeed, the design of the device, as of now, does not enable isotropic stretching as PDMS circular membranes (Schürmann et al., 2016) or equibiaxial stretching as pillar-based systems (Tijore et al., 2018). Thus, we cannot exclude that certain mechanosensitive mechanisms could only be activated during isotropic or equibiaxial stretching. Alternatively, some of the mechanisms that we observed could also be modulated by isotropic or equibiaxial stretching. In order to achieve this unique combination between SRM, SPT and live cell stretching, we have for now aimed only at studying uniaxial stretch. Further developments are required to expand the modes of stretching, thus bringing our system closer to stretching events *in vivo*.

7. Future applications for cell stretching and SRM/SPT

By combining SRM and SPT with live cell stretching, our approach can be used to decipher at the molecular level other mechano-sensitive structures such as the caveolae(Sinha et al., 2011), kineotchores (Dumont et al., 2012b), hemidesmosomes (Zhang et al., 2011) or the nucleus (Nava et al., 2020). In parallel, our micromechanical stretching device can also be used to explore potential mechanosensitive structures such as the Membrane Periodic Skeleton (MPS) in neurons(Xu et al., 2013).

7.1. MPS

The MPS is emerging as an important component of axon physiology and neuronal function. Recent evidence points to the MPS as a shock buffer against mechanical loads (Dubey et al., 2020), an actomyosin network regulating axonal expansion/contraction (Costa et al., 2020) and a signaling platform regulating RTK transactivation (Zhou et al., 2019) or axonal degeneration (Unsain et al., 2018). Here, we aimed to explore mechanosensing of the MPS by using our micromechanical stretching device compatible with SRM and SPT. Although we have no concrete results yet, due to time constraints, we have adapted our device for neuronal cultures, SRM/SPT imaging of MPS proteins and micropatterning. These modifications enable us to perform two major types of experiments, similar to what we achieved for IAS: 1) assess the impact of stretching in the nanoscale reorganization of the MPS and 2) study the acute mechanical response of MPS proteins.

By modifying the material and the design of the stretching device, we enabled long-term culturing rat hippocampal neurons until DIV 8 or chick spinal cord explants until DIV 3. However, after DIV5, it is no longer possible to stretch the PDMS membrane. This is probably caused by the adsorption of the glycerol layer onto the PDMS, which can no longer glide on the glass slide. For now, this is not a major issue, as the MPS – and in particular βII-spectrin periodicity - is present in the proximal and middle regions of the axon at DIV 5 (Zhong et al., 2014). Still, if we want to conduct observations in the specialized βIV-spectrin-ankyrin G periodic lattice in the axon initial segment, we would need to achieve stretching after DIV 8 (Zhong et al., 2014). Such developments would also allow to study the effect of stretching in mature dendritic spines, which exhibit the MPS in the spine necks around DIV 16 (Bär et al., 2016). Indeed, it would be relevant to compare the mechanical response of the MPS in dendrites vs axons, and assess whether mechanical stretching could even influence synaptic transmission or AMPAR trafficking. As an alternative to primary rat hippocampal neurons, we could use primary chick neurons from dorsal root ganglia (DRG), which already exhibit a robust MPS periodicity (through βII-spectrin) at DIV 4 (Dubey et al., 2020). We have adapted the device to chick spinal cord explants, which leads us to

believe that the device is compatible with primary DRG chick neurons. All the modifications performed in the device render it suitable for a variety of cell and explant models requiring long-term culture: this includes endothelial cells, DRG explants or *Drosophila* primary neurons and embryo fillets, among others.

Mechanical stretching could lead to nanoscale alterations in MPS periodicity or in the diameter of actin rings. This could depend on the magnitude of stretching but also on the frequency, strain rate or duration. To dissect this, we needed to implement nanoscale imaging of MPS in neurons cultured on the stretching device. For this end, we have imaged MPS protein βII-spectrin in rat hippocampal neurons cultured in the device using DNA-PAINT and STED. Both techniques are ideal to characterize changes in actin ring diameter or in the periodicity of the MPS. Other SRM/SPT techniques such as sptPALM are more suited for studying the acute mechanical response of proteins. Nonetheless, there are reports of the MPS imaging with PALM (Zhong eLife 2014), although this would require transfection with photoactivatable proteins. As of now, due to time constraints and optimization of the system, we have no quantifications of MPS periodicity, and thus we have not performed any stretching experiments. However, DNA-PAINT appears to provide a more clear observation of the MPS compared to STED. DNA-PAINT delivers better spatial resolution than STED, and can be easily multiplexed, allowing to visualize multiple MPS proteins ((Schnitzbauer et al., 2017) DNA-PAINT would thus be technique of choice for imaging neurons after large and sustained stretching followed by cell fixation. Conversely, STED can be used to image the MPS in live neurons, which could allow to capture the nanoscale MPS structure before and after stretching for the same neuron, something impossible with DNA-PAINT. Due to photodamage/photobleaching caused by STED, this would be especially achievable with rescue (Staudt et al., 2011), protected (Danzl et al., 2016) or parallelized (Bergermann et al., 2015) STED modalities. Still, STED could be also used fixed cells after large and sustained stretching, since it has been previously used to study changes MPS nanoscale organization after trophic factor withdrawal (Unsain et al., 2018), among other stimuli. Finally, we are currently implementing STORM SRM imaging (Bates et al., 2007) in our device, which would further increase the array of techniques to study MPS reorganization induced by mechanical stretching.

Once we have fine-tuned MPS imaging, we intend to perform different stretching protocols to assess changes in MPS nanoscale organization. These include both large and small-scale stretching, as well as cyclic stretching. Through such experiments, we can for instance mimic a context of traumatic neuronal stretching and assess its consequences on the nanoscale reorganization of the MPS. This could be achieved by first perform large (50-100 %) and sustained stretching at the first stages of neuronal development. This will enable to characterize the stretching threshold leading to MPS degeneration, and to test if this loss leads to local axon injuries, as demonstrated for diffuse axonal injury (Vieira et al., 2016; Yap et al., 2017). Based on

these parameters, we could also perform repetitive and long-lasting sub-threshold stretching, which has been shown to trigger diffuse axonal injury (Yap et al., 2017).

To study the acute mechanical response of MPS proteins, we have implemented a new method to achieve expression of photoactivatable proteins in neurons. By using *in ovo* electroporation, we could express actin-mEos2 in chick spinal cord explants grown on the device. One aspect still to confirm is whether chick spinal cord neurons exhibit the MPS at DIV2/3. However, the presence of the MPS in culture models of chick neurons around a similar developmental stage strongly supports this (Dubey et al., 2020). Still, this needs to be assessed before performing any observations studies. Once we assess this, we intend to use this same approach to express various MPS proteins and study their acute mechanical response. Spectrin is likely to exhibit an inelastic behavior, since it acts as a shock buffer in the MPS and possesses several tandem repeats which can unfold upon mechanical stretching. Since the MPS appears to constitute an actomyosin network (Costa et al., 2020), it is likely that mechanical stretching can induce transient and active actin remodelling, leading to protein deformations and inelastic responses to mechanical stretching. These in turn could be inhibited by blebbistatin, as we previously observed. Myosin II inhibition affects axonal expansion and contraction (Costa et al., 2020), suggesting that active actomyosin remodelling processes continuously occur at the level of the MPS. Stretching experiments could be further combined with optical electrophysiological recordings, using for instance the Optopatch approach(Hochbaum et al., 2014) .

7.2. Caveolae

Caveolae are cup-shaped 60-80 nm uncoated invaginations of the plasma membrane, enriched in cholesterol and sphingolipids (Sinha et al., 2011). They are abundantly expressed on various cell types including vascular endothelial cells, epithelial cells, adipocytes, fibroblasts, and smooth muscle cells, but not on neuronal cells or lymphocytes (Parton and Del Pozo, 2013). The core component of caveolae are caveolins (Cav) (Rothberg et al., 1992), a family of membrane proteins with three mammalian isoforms: Cav1, Cav2 and Cav3. Caveolins associate to cytoplasmic proteins known as cavins to regulate caveolae structure and function (Bastiani et al., 2009). Caveolae are considered mechanosensitive structures as they respond to various different mechanical forces. Acute mechanical stress induced by osmotic swelling or by uniaxial stretching results in a rapid decrease of the number of caveolae at the cell surface in endothelial cells (Sinha et al., 2011). This occurs due to the disassembly and flattening of caveolae in response to mechanical force, a mechanism which is thought to buffer membrane tension (Sinha et al., 2011). Flattening of caveolae leads to a decrease in caveolin-cavin interactions, with caveolin release into the bulk membrane and cavin release into the cytosol (Sinha et al., 2011). Thus, both cavins and caveolins could have a role in caveolin mechanosensing; moreover, caveolae mediate various

signal transduction pathways via caveolins and cavins. For instance, phosphorylation of Cav1 can regulate IAS stability and cell migration (Grande-García et al., 2007), as well as stretch-mediated activation of protein kinase B (Zhang et al., 2007). Cavin, on the other hand, can also propagate signals to target effectors, such as transcription factors (Bai et al., 2011). Therefore, release of both components in response to mechanical stretch could activate several of these pathways. For this, we want to understand whether mechanical stretch increases diffusion of Cav1, which could indicate that the protein is 'released' to elicit other pathways. This work is being performed in collaboration with the group of Christophe Lamaze at Institut Curie (Paris, France). We are assessing the impact of mechanical stretching in caveolin nanoscale dynamics and reorganization in endothelial cells, using sptPALM and DNA-PAINT, respectively.

APPENDIX

1. Single-Protein Tracking to Study Protein Interactions during integrin-based migration

As previously mentioned in the Methods and Approaches section, I have also wrote, together with other colleagues, a Book Chapter in single protein tracking to study protein interactions during integrin-based migration. This book chapter, soon to be published in Methods in Molecular Biology, covers all the technical aspects of sptPALM acquisitions to study nanoscale protein dynamics in various subcellular structures (IAS, lamellipodium). Thus, it serves as a complement on SRM and SPT to the Methods and Approaches section

Chapter 8

Single-Protein Tracking to Study Protein Interactions during integrin-based migration

A.V. Radhakrishnan[1,2], Tianchi Chen[1,2], Filipe Nunes Vicente[1,2], Thomas Orré[1,2], Amine Mehidi[1,2,3], Olivier Rossier[1,2], Grégory Giannone[1,2,*]

[1] Univ. Bordeaux, Interdisciplinary Institute for Neuroscience, UMR 5297, F-33000 Bordeaux, France
[2] CNRS, Interdisciplinary Institute for Neuroscience, UMR 5297, F-33000 Bordeaux, France
[3] Department of Biochemistry, University of Geneva, Geneva, Switzerland.

* Correspondence: gregory.giannone@u-bordeaux.fr

Abstract

Cell migration is a complex biophysical process which involves the coordination of molecular assemblies including integrin-dependent adhesions, signaling networks, force-generating cytoskeletal structures incorporating actin polymerization and myosin activity. During the last decades, proteomic studies have generated impressive protein-protein interaction maps, although the sub-cellular location, duration, strength, sequence and nature of these interactions are still concealed. In this chapter we describe how recent developments in super resolution microscopy (SRM) and single protein tracking (SPT) start to unravel protein interactions and actions in subcellular molecular assemblies driving cell migration.

Key words: Single-protein tracking, Super-resolution microscopy, Optogenetics, Supercritical-angle fluorescence emission, Integrin-dependent adhesion, actin-based lamellipodium

Running title: Single-molecule integrin tracking

Abbreviations

SMLM	Single-Molecule Localization Microscopy

PALM	Photo-Activation Localization Microscopy
SPT	Single Particle Tracking
MSD	Mean square displacement
FWHM	Full width at half maximum
CRISPR	Clustered regularly interspaced short palindromic repeats
Cas9	CRISPR associated protein 9
FBS	Fetal bovine serum
mEos2	Monomeric Eos2
WRC	Wave Regulatory Complex
DONALD	Direct Optical Nanoscopy with Axially Localized Detection
FRAP	Fluorescence Recovery After Photobleaching
SAFe	Supercritical Angle Fluorescence emission
TIRF	Total Internal Reflection Fluorescence
dSTORM	direct Stochastic Optical Reconstruction Microscopy

1 Introduction

Cell migration is an important function involved in various biological processes such as embryo development [1], wound healing [2,3] and cancer cell metastasis [4]. The movement is usually mediated by protrusive membrane structures like lamellipodia, a flat cellular domain that is composed of a dynamic machinery of actin cytoskeleton, adhesion complexes and various regulators [5-7]. At the tip of the lamellipodium, branched actin networks are formed through the nucleator Arp2/3 and nucleation promoting factors such as the SCAR/WAVE complex [8,9] under the regulation of small GTPases Rho, Rac and Cdc42 [10,11]. Actin polymerization induces a retrograde flow of assembled actin that engages and binds to nascent adhesions, while exerting force on the substrate through cell-matrix adhesions to facilitate cell migration [12,13]. The periodic protrusion and contraction of the lamellipodium associated with non-muscle myosin II can also exert forces on the adhesions to help their formation and growth [14,15]. At the rear of the lamellipodium, myosin II pulls on actin filaments and remodels them to form stress fibers that connect to and exert force on the substrate through mature focal adhesions [16-18]. Thus, many important macromolecules undergo motions and transient interactions that are essential to their function. These molecules form nano-machine-like protein complexes that control actin assembly and adhesion formation, thus they must be tightly regulated at specific locations at precise times.

Cell adhesion to the extracellular matrix (ECM) is one of the fundamental processes that are central in many developmental as well as pathophysiological contexts [19-21]. Cell-matrix adhesion is mainly mediated by ubiquitously expressed transmembrane receptors called integrins, which bind to ECM ligands like collagens, laminins or fibronectin (FN). At the same time, they connect to the filamentous F-actin cytoskeleton [19-21]. Integrins function as heterodimers. In mammals, 18 α and 8 β subunits combine in a restricted manner to form 24 specific receptors, most of which exhibit specific ligand binding and display unique mechanical biochemical signaling properties [19]. Each integrin subunit has a large extracellular domain that constitutes the ligand binding domain, a single transmembrane domain and a cytoplasmic tail of variable length. Since the short cytoplasmic tails of integrins lack enzymatic and F-actin-binding activity, they depend on the assembly of adaptor and signaling proteins onto their cytoplasmic tails for signal propagation [22]. The resulting integrin adhesion sites (IAS) can consist of hundreds of different proteins, and each integrin receptor assembles a specialized adhesion complex with distinct molecular organization, life span and mechano-chemical signaling potential [23,24]. Moreover, within the same IAS, distinct integrin-class receptors having proper biochemical and mechanical signaling, coexist and cooperate to determine the function of the IAS as a whole [25,26]. A remarkable property of integrins is their tunable affinity, which enables them to reversibly switch from an inactive to an active state after binding of intracellular activators [27,28]. Interestingly, many proteins compete for a few binding sites on the short cytoplasmic tails of β integrins, implying that regulatory processes control the spatiotemporal reversible binding of β-integrins [22]. For instance, the small intracellular tail of integrins harbors

close-by binding sites for regulators controlling integrin activation state. Talin and kindlin may cooperate to activate integrins by binding to different regions of the β integrin tail, while ICAP-1 competes with kindlin to prevent integrin activation [22,29]. The protein networks in the IAS have been named integrin 'adhesomes' and were determined by both mass spectrometry approaches [30-32] and data mining [33,34]. The components of integrin-based adhesive structures are regrouped in functional families including adhesion receptors, adaptor proteins, actin regulators, kinases/phosphatases, Rho GTPases, lipids and enzymes of proteolytic activities. A meta-analysis collecting data from several proteomic studies [34] reported that thousands of proteins are enriched in the IAS. Cross-analysis of the different datasets identified a subset of 60 proteins, comprising the "consensus adhesome", systematically detected in IAS. These proteins could be grouped in four sub-networks of protein interactions: (i) α-actinin-zyxin-VASP, (ii) FAK-paxillin, (iii) kindlin-ILK-PINCH, and (iv) talin-vinculin [34]. These IAS components can attain different phosphorylation states, and some are specifically recruited by given integrin subtypes [26,30,35,36]. Proteomic studies have also demonstrated that IAS maturation associated with mechanical tension affect their composition. Myosin-II inhibition decreases the recruitment of most consensus adhesome proteins in the IAS, in particular actin-binding proteins including α-actinin and VASP [34], and LIM-domain proteins such as zyxin and paxillin [26]. Nevertheless, the recruitment of a subset of IAS components could also be increased after myosin-II inhibition, including β-Pix, a Rac1 activator promoting the formation of actin-based lamellipodial protrusions but inhibiting adhesion maturation [32].

However, such interaction maps are not taking into account the sub-cellular location, duration, strength, order of recruitment, and nature (competitive or cooperative) of these interactions. Furthermore, forces exerted on critical IAS proteins control their binding and enzymatic activities, stabilize and destabilize interactions, reveal domains of interactions and induce post-translational modifications [37-40]. Therefore, it is of great interest to develop new advanced imaging methods to detect and measure not only the position and dynamics of cellular components at the nanometer level but also their interactions and how mechanical forces control those interactions.

Surrounded by a complex and dynamic macromolecular environment, the IAS is the nexus of a subcellular system comprising multiple organelles: the plasma membrane, actin and microtubule cytoskeletons, lipid vesicles, and the cytosol composed of soluble proteins. Thus, proteins entering or leaving a specific location within the IAS may use a path involving any of these components, and the available paths may change during IAS maturation. IAS building blocks may be individual proteins or pre-assembled complexes [41,42], which reorganize their interactions as the IAS matures. Thus, once inside the IAS, the multivalence and combinatorial diversity of interactions between the constituents enables internal reorganization of the building blocks to support IAS functions. The majority of knowledge about protein interactions during integrin activation is paradoxically derived from studies in which the complexity of the adhesive structures found in adherent cells was reduced or even absent, such as by flow cytometry with suspended cells [43]

and by *in vitro* biochemistry [44], in which cases the intricate and dynamic interactions between binding partners in the IAS are ignored, let alone the complex and diverse *in vivo* cellular environment that may functionally modify and control these interactions. In order to understand the spatial temporal assembly of IAS, especially at the scale of nanometers and microseconds, where proteins interact and cluster, there is a clear need for techniques that can reveal the fast dynamics and transient interactions of IAS components, illuminate the nanoscale organization, and detect the subcellular location and duration of molecular events. The recent development of single protein tracking (SPT) and super-resolution microscopy (SRM) techniques has provided the possibility to quantitatively study protein motion and location within subcellular macromolecular complexes in their native environment, revealing of their interactions with other proteins and clustering behavior, amid various mechanisms of regulation [25,45-48]. What information about protein interactions in the IAS can we glean from the SPT trajectories and SRM? (**Figure 1**)

First, SPT trajectories reveal the diffusion and immobilization events of proteins (**Figure 1B-C**). The frequency of integrin immobilization within the IAS is higher than outside, indicating integrin-binding to extracellular ligand or intracellular IAS components, while integrin immobilization also correlates with its activation, as shown by treatment with Mn^{2+} or mutation [25]. Increase in immobilization has also been observed for small GTPases such as Rac1 in integrin-dependent focal adhesions [49], in neuronal dendritic spines [46] and in lamellipodia of motile cells [48].

Second, SPT shows the location and dynamic nature of protein interactions within the IAS (**Figure 1A**), as a substantial fraction of integrins inside IAS can engage in free diffusion, and individual integrin molecules cycle from diffusion to immobilization states which can last for seconds to tens of seconds [25,50,51]. This dynamic interaction, characterized by increased fraction and duration of immobilization, is associated with integrin activation and is controlled by the interaction of integrins with specific activators and inhibitors. These interactions are also compartmentalized in a given area that is regulated by membrane nano-topology, as demonstrated for cancer cells [52]. The apparent diffusion coefficient of integrin is also lower inside the IAS compared to outside [25], potentially due to confinement, but also suggesting transient interactions with IAS components and other effects of local protein crowding.

Third, SPT and SRM revealed the 3D nanoscale organization and segregation of proteins into functional nanodomains as well as the path used by crucial integrin activators to reach these domains and activate integrins (**Figure 1E**). 3D super-resolution microscopy with iPALM has shown the distinct layers of IAS protein axial organization, where an integrin signaling layer near the membrane contains the cytoplasmic tail of integrin, paxillin and FAK, a force transduction layer in between contains talin and vinculin and an actin regulatory layer deeper inside the cytosol containing actin, zyxin, VASP and alpha-actinin [53]. Individual proteins such as talin can span different layers

and proteins such as vinculin also shows specific orientation and can shuttle between different layers depending on its activation state [13]. Whereas talin exhibits no membrane free-diffusion and is thus directly recruited to IAS directly from the cytosol [25], kindlin can diffuse on the membrane due to its PH domain [54]. With SPT, we are beginning to understand how proteins travel in different routes to reach designated functional layers. Indeed, deletion of the PH domain of kindlin resulted in its upward shift from the integrin layer localization [54]. In the integrin signaling layer, β3 and β1 integrins which show different force sensitivity and association with downstream signaling partners, suggesting different roles in force generation, sensing and maintenance [26], are also spatially segregated in 2D into distinct nanodomains within the IAS and exhibit different diffusion and flow dynamics [25]. Such segregation and distinct molecular dynamics have also been shown with SRM for active and inactive β1 integrins [55], and with SPT for different TGFβ receptors in the IAS [56].

Finally, the functional activity and regional specificity of non-structural signaling proteins that undergo fast cycles of activation and inactivation as well as engage in transient interactions with their substrates can be studied by SPT. Rho GTPases, a family of signaling proteins that can switch between active and inactive states by exchanging GDP to GTP and hydrolyzing GTP to GDP, including RhoA and Rac1, are important regulators of cell migration and IAS formation during lamellipodial protrusion [11,57-59]. The constitutive mutant Rac1-Q61L, potentially binding more strongly to downstream effectors, exhibits more immobilizations at the lamellipodium tip compared to wild-type Rac1 (Rac1-WT) [48], showing SPT's ability to detect transient binding events whereas classical fluorescence microscopy could not reveal enrichment of active Rac1 at the lamellipodium tip [58]. SPT can also be combined with newly developed optogenetic techniques that can photo-activate proteins, making it possible to study their functions in live cells such as Rac1 [60,61]. By recruiting a Rac1 GEF Tiam1 to the plasma membrane through light-induced binding between Tiam1-CRY2 to membrane-anchored CIBN [62], it was shown that Rac1 photo-activation driving protrusion needs to happen close to the tip of the lamellipodium but not a few microns behind, however, the activation of Rac1 did not significantly increase its immobilization, pointing to a model of short-ranged and short-lived Rac1 activation and downstream signaling that depend on transient interactions and rapid inactivation [48].

Therefore SPT/SRM techniques are complementary to biochemical approaches and have become crucial to establish protein dynamics as readout of protein functions and interactions in complex macromolecular assemblies, having seen applications in diverse fields such as EGFR dimerization [63], TCR signaling [64] and AMPR receptor clustering [65] in addition to integrin adhesions. Here we describe how the combination of SRM/SPT with recent technological advances in genome editing, optogenetic control of signaling pathways and three dimensional imaging can help us unravel the intricate protein interaction dynamics within the IAS.

2 Materials

2.1 Solutions and reagents

1. Cell culture tested products to be used for all the preparations
2. Commercial 0.05% trypsin, 0.02% EDTA solution
3. Cell culture medium: Dulbecco's modified Eagle medium, high glucose (DMEM), 10% fetal bovine serum (FBS), GlutaMAX supplement, 100 U/ml penicillin–streptomycin, 1 mM sodium pyruvate, 15 mM HEPES.
4. Purified human fibronectin solution (10 µg/ml) in Phosphate buffered saline (PBS)
5. Nitric acid solution (65% wt/wt in water).
6. Trypsin inactivation medium: DMEM, 1 mg/ml soybean trypsin inhibitor, GlutaMAX supplement, 100 U/ml penicillin–streptomycin, 1 mM sodium pyruvate, 15 mM HEPES.
7. Ringer solution: 150 mM NaCl, 5 mM KCl, 2 mM CaCl2, 2 mM MgCl2, 10 mM HEPES 11 mM glucose at pH 7.4.
8. 4% PFA – 0.2% Glutaraldehyde solution in PBS.
9. 150 mM Glycine in PBS.
10. 0.2% Triton X-100 in PBS.
11. 3% BSA in PBS.
12. Anti-GFP nanobodies coupled to AlexaFluor-647.
13. STORM-adapted buffers (Abbelight).

2.2 Other consumables and equipment

1. Nucleofector™ transfection kit for MEF-1 and Nucleofector™ 2b device (Amaxa™) (see **Note 1**)
2. Marienfield #1.5H coverslips matching to imaging chamber dimensions.
3. 75 cm^2 flasks for cell culture.
4. Fiducial markers (for example, Multi-color fluorescent microbeads Tetraspeck, Invitrogen)

5. Incubator at 37 °C supplied with humidified air containing 5% CO2.

2.3 Image acquisition

In general, this is a close to the state of the art protocol that requires the acquisition of superresolution images. We describe the procedure we use, based on a Nikon inverted microscopy with a TIRF/superresolution module from Abbelight. Other techniques may be available, but the requirement is that the technique of choice is SMLM.

1. Nikon inverted motorised microscope (Nikon Ti)

2. Super-resolution optimized ×100 1.49 NA PL-APO Nikon objective

3. Perfect Focus System, Nikon

4. Lasers (continuous wave) depending on the fluorophore to be imaged, e.g., 405nm, 488 nm, 561 nm and 643 nm lasers. Those lasers are dedicated for, photo-excitation photo-switching and photo-activation of the fluorescent proteins and organic fluorophores. For instance, 405 nm laser is used for photo-switching of mEos-tagged proteins and then mEos is imaged upon illumination with 561 nm laser. The latter should be kept at the same intensity throughout all the experimental conditions to conserve the same pointing accuracy. On the other hand, 643 nm laser is used for imaging organic fluorophores for SAFe.

5. iLas2 illumination control system or equivalent design for TIRF illumination.

6. Optical and opto-mechanical components including mirrors, dichroic filters, and lenses the corresponding wavelengths used.

7. Scientific complementary metal-oxide semiconductor (sCMOS) camera (e.g., Orca Flash4 by Hamamatsu) or low noise highly sensitive electron-multiplying charge-coupled device (EMCCD) camera (e.g., Evolve, Photometrics).

8. Computer with relevant software for image acquisition, image processing, and visualization (see **Note 2**).

9. Fast shutter (Uniblitz) or AOTF (AA optoelectronic).

10. Ludin sample holder (Life Imaging Services) or equivalent designs.

11. Supercritical-angle fluorescence emission (SAFe) module (Abbelight) (see **Note 3).**

12. Buffers for d-STORM acquisition (Abbelight).

3 Methods

The following procedures describe sample preparation, image acquisition and data analysis for different single molecule imaging techniques; sptPALM, fast sptPALM, sptPALM coupled to optogenetics and 3D supercritical-angle fluorescence emission (SAFe). In all cases, the protein of interest is coupled to a photoactivatable/convertible fluorophore or to GFP and is often referred as "protein of interest".

3.1 Cell preparation

We describe here a procedure for Mouse Embryonic Fibroblasts (MEF). Actively dividing immortalized MEFs, cultured in DMEM with 10% FBS in 75 cm^2 flasks are detached with trypsin/EDTA solution (1.5 mL). Trypsin is inactivated immediately after detachment by adding serum containing DMEM (5 ml). Cells are then counted and cell suspension volume is adjusted to keep 1–2 million cells per tube per experimental condition.

1. Centrifuge cells at 300 × *g* for 5 min
2. Resuspended the cell pellet in transfection reagent and mix with the DNA plasmids.
3. For PALM experiments, Cells are usually co-transfected with DNAs encoding for the protein of interest, (3–5 µg per condition, e.g., mEos2-β1-integrin, see **Note 4**), and for a GFP-coupled reporter of the structure of interest (1–2 µg per condition, e.g., GFP-paxillin for adhesive structures, GFP-α-actinin for lamellipodia).
4. For 3D SAFe microscopy, cells are transfected with DNA encoding for the fusion protein (2-3 µg per condition, e.g., Kindlin-GFP, see **Note 4**).
5. For experiments combining sptPALM and optogenetic activation or inhibition of proteins, cells are co-transfected with DNAs encoding for the protein of interest and for the set of proteins enabling optogenetic control of the target protein. In the example we give here, we track mEos2-Rac1 while triggering its activation with light-induced recruitment to the plasma membrane of a cytosolic guanine nucleotide exchange factor (GEF) of Rac1. Membrane recruitment of a Rac1-GEF (e.g. Tiam1) is triggered by interaction of the cryptochrome CRY2 to its membrane-anchored CIBN partner (**Figure 1D**). Cells are co-transfected with DNAs encoding for the protein of interest (~6 µg per condition; e.g., mEos2-Rac1), with the Rac1-GEF fused to the CRY2 cryptochrome (~3 µg per condition; e.g., Tiam1-CRY2-IRFP) and for

the GFP-coupled CIBN partner of CRY2 fused with a membrane-anchoring domain CAAX (~3 µg per condition; e.g., CIBN-GFP-CAAX).

6. For all cases, cells are then electroporated with the Nucleofector™ 2b Device using the MEF T-020 program (Lonza Nucleofactor protocol) (see **Note 1**).

7. After electroporation, cells are replated in a 6-well plate (about 0.3 million cells/well) in preheated culture medium and placed in a 37 °C incubator with humidified air containing 5% CO2

3.2 Cleaning of glass substrates

Before matrix coating, coverslips need to be cleaned to ensure absence of non-specific adsorption of fluorescent materials.

1. Coverslips are aligned in ceramic racks and placed in concentrated nitric acid (65% wt/wt) bath in staining glass boxes overnight.

2. The racks are moved in ultrapure water bath in other staining glass boxes to rinse the coverslips. Six changes of ultrapure water bath every 30 min (or more) are required.

3. Coverslips are quickly rinsed in absolute ethanol.

4. Ceramic racks are placed in a glass beaker, covered with aluminum foil and sterilized in an oven at 240 °C for 8 h.

3.3 Matrix protein coatings on coverslips

This procedure is usually done a day before, or the same day of the imaging experiment.

1. Cleaned coverslips are covered with a 10 µg/ml fibronectin solution (1 ml per coverslip) and incubated at 37 °C for 1 to 1.5 hours.

2. After incubation, fibronectin solution is aspirated and coverslips are washed three times in PBS, and can be stored in PBS medium at 4 °C for further use.

3.4 Sample preparation

1. Cells are washed twice with PBS after culture medium is removal.

2. Incubate with trypsin–EDTA solution (0.3 ml per well) for 1–3 min at 37 °C for detaching cells.

3. Trypsin is inactivated with trypsin inactivation medium (1 ml per well) and cells are counted (use any conventional cell counting method).

4. After centrifugation at 300 ×g for 5 min, cells are resuspended in Ringer medium (1–2 ml).

5. Plate cells according to specific types of experiment: processes given below pertain to specific experiments involving studies on adhesive structures or lamellipodia.

3.5 sptPALM experiments

3.5.1 Single protein tracking inside and outside IAS

1. Plate 50,000 cells per coverslip are plated on the fibronectin coated coverslips in Ringer medium.

2. After 3 hours, coverslips can be mounted on an open chamber with approximately 1 ml of Ringer medium for imaging.

3.5.2 Single protein tracking inside and outside lamellipodia (see **Note 5**)

1. After resuspension, cells are incubated at 37 °C and 5% CO2 for 30 min, to allow integrin turnover after trypsin degradation before plating.

2. 10,000– 20,000 cells are loaded directly on fibronectin coated cover- slips mounted on an open chamber containing ~800 µl of Ringer medium.

3. Imaging is started when cells start spreading and forming lamellipodia, typically 5–10 min after loading.

3.5.3 Supercritical Angle Fluorescence and Localization Microscopy.

This step is to be followed after 3.5.1 or 3.5.2, depending on the structures of interest to be studied.

1. Fix cells using 4% PFA – 0.2% Glutaraldehyde in PBS for 15-20 minutes at RT.
2. Quench fix buffer with 150 mM Glycine in PBS for 20 minutes.
3. Permeabilize with 0.2% Triton X-100 in PBS for 8 minutes.
4. Block in 3% BSA in PBS for 1h.
5. Label cells with anti-GFP nanobodies tagged with AlexaFluor-647 overnight at 4ºC.
6. Mount on a microscope-adapted device using STORM-adapted buffers.

3.5.4 Image acquisition

1. Using a power meter, the intensities of the appropriate lasers are verified at the objective plane and a calibration chart is obtained to adjust to the desired levels. In the case of mEos2 imaging, we typically use a 561 nm beam power ranging from 4 to 8 mW at objective output to allow single fluorophores to emit on several consecutive recorded planes before photobleaching.

2. Acquisitions are to be made in the Total Internal Reflection Fluorescence (TIRF) mode, using an inverted motorized microscope (Nikon Ti) equipped with a 1.49 NA 100× oil immersion objective and a Perfect Focus System, placed in a thermostatic enclosure at 37 °C.

3. Different acquisition modes can be adopted based on types of experiment:

    1. Classical sptPALM acquisition: upon observation of the GFP-fused reporter of the structure of interest, cells are selected for single-molecule imaging. A subregion of the camera field of view is selected for recording at high frequency (typically 20–50 Hz, *see* **Note 6**), in order to study the diffusive behavior of a protein of interest within a given region of the cell. Several sequences of single-molecule imaging are then continuously recorded (for a total of 5000–20,000 images, *see* **Note 7**), interlaced with images of the fluorescent reporter to monitor possible displacement of the structures of interest such as the IAS and the lamellipodium.

    2. Fast sptPALM acquisition: fast sptPALM acquisitions are similar to conventional sptPALM except that they are only possible with a sCMOS camera (**Figure 1C**). To reach acquisition frequencies of 333 Hz it is nevertheless necessary to adjust certain acquisition parameters. The sub-region must necessarily be positioned in the center of the chip with

a size of 500x100 pixels (horizontal x vertical). For the acquisitions, 561 nm laser power is kept at 10mW.

3. sptPALM acquisition coupled with Optogenetics: optogenetic activation of Rac1 results from the light-induced recruitment to the plasma membrane of a Rac1-GEF, Tiam1 (**Figure 1D**). This recruitment is visualized by the acquisition of Tiam1-CRY2-IRFP images every 20s. The photoactivation (~500 ms) is done only after a base line of 4 Tiam1-CRY2-IRFP images. Observation of the Rac1 behavior during the perturbation is recorded by sptPALM sequences of mEos2-Rac1-WT (10 s, 500 images, 50 Hz) acquired in between each Tiam1-CRY2-IRFP images. The Tiam1-CRY2-IRFP and mEos2-Rac1-WT acquisitions are recorded respectively with 643 nm and 561 nm lasers with TIRF illumination. Photoactivation of CRY2 is done by a FRAP head, (Roper Scientific) to illuminate with the 488 nm laser in defined regions of interest (ROI). During the photoactivation the ROI is also illuminated with 405 laser to photoconvert mEos2-Rac1-WT that may have been activated by Tiam1 (see **Note 8**). Rac1 activation triggers lamellipodium protrusion when the ROI of optogenetic activation encompasses the lamellipodial tip, but not if the ROI is located 3 µm behind the lamellipodial tip [48] (**Figure 2A,B**).

4. Supercritical Angle Fluorescence and Localization Microscopy studies: for the STORM imaging, we use GFP-tagged proteins recognized by anti-GFP nanobodies labelled with AlexaFluor-647 [66,54]. To achieve single molecule regime in dSTORM acquisitions, a dedicated buffer (Smart kit, Abbelight) is used (See Materials, 2.2). The diffraction limited epifluorescence images are acquired at low illumination irradiance (0.15 $kW.cm^{-2}$), while dSTORM images are obtained using a high illumination irradiance (4 $kW.cm^{-2}$) until a sufficient molecule density is obtained (around 1 molecule per μm^2), after which the acquisition can be started. The exposure time is set at 50 ms, the optimal timing with the buffer to capture all emitted photons in a single frame. All the acquisitions are performed using the Nemo software (Abbelight).

3.6 Data treatment and analysis

3.6.1 Single molecule localization and generation of super-resolved Image

This step is performed after the experiment, as treatment and analysis of single-molecule images are very demanding in terms of computing power. In the single-molecule images, single molecule emissions appear as diffracted bright spots. The original images are subjected to decomposition into wavelet maps using custom algorithms. Further each fluorophore is localized on segmented images by centroid computation. Custom-watershed algorithm are used to separate close molecules [67].

This procedure provides similar localization precision as more conventional Gaussian fitting, but with a tenfold decreased computation time. The single-molecule detections can then be plotted on a single image, forming a super resolved reconstruction (SRR) image (**Figure 1A**).

The pointing accuracy for the setup can be obtained by repetitively imaging purified mEos2 proteins adsorbed on a glass coverslip. As measured with the Full Width at Half Maximum (FWHM) of the obtained distribution of localizations, the typical resolution of our system is around 20-50 nm.

3.6.2 Analysis of single protein tracking experiments

Single particle detection procedure generates multiple localizations that store the center x and y positions of each molecule. A fluorescent molecule emits fluorescence for a short time in consecutive frames before being bleached, enters a dark state or diffuse out of focus. If an optimal density of fluorophores are activated simultaneously and diffusion does not result in path crossing between neighboring frames for nearby fluorophores, the trajectory of a molecule can be confidently tracked by linking detected localizations for neighboring frames with a simulated annealing algorithm [68,69]. While different methods have been used to analyze the diffusive behaviors of molecules [70,71], we present here a simple but powerful way of analysis based on Mean Square Displacement (MSD) computation [25,46,49]. Note should be taken when using this analysis, since it assumes that the molecules in question undergoes 2D membrane diffusion or immobilization on a fixed point in space. Other types of movement such as fast and slow directed motion will need to be treated differently. First, the MSD at each time interval n*Δ t is calculated for each trajectory based on the following formula:

$$\mathrm{MSD}\left(t = n \cdot \Delta t\right) = \frac{\sum_{i=1}^{N-n} \left(x_{i+n} - x_i\right)^2 + \left(y_{i+n} - y_i\right)^2}{N-n}. \qquad (1)$$

where N is the number of data points (frames), x(t) and y(t) are x and y coordinates at timepoint t. Plots of the MSD curves against time interval (**Figure 1B**) provide information to distinguish between different modes of motion: for freely diffusing molecules MSD increases linearly with time; molecules in confinement shows linear increase of MSD at short time scales and decreasing slopes of MSD at longer time scales; immobile molecules show a flat MSD close to zero with deviation depending on localization precision (see **Note 9**). For molecules undergoing fast directed movement, the MSD increases with time squared, but for molecules undergoing slow diffusion, the shape of the curve is close to zero at the short time scale plotted here and cannot be distinguished from immobile ones (see **Note 10).** Therefore, the diffusive behavior of each molecular trajectory can be characterized by fitting the MSD curve to different diffusion models. Because the later time points of the MSD

comes from the average of fewer data points and are less accurate, we routinely discard the latter 20%-40% of the MSD for the fitting. For short trajectories (10–20 time points), as obtained with fluorescent proteins, 60–80% of the first MSD points are included for fitting. In the following formula:

$$\mathrm{MSD}(t) = \frac{4r_{\mathrm{conf}}^2}{3}(1 - \mathrm{e}^{-t/\tau}) \qquad (2)$$

r_{conf} is the measured confinement radius, and the time constant $\tau = (r^2_{conf}/3D_{conf})$. We consider the molecules as immobile if the calculated D< Dthreshold. The value of Dthreshold is obtained by considering the confinement area is defined by the image spatial resolution. We can distinguish between confined and free diffusion by comparing the time constant τ obtained for each trajectory with half the minimum time interval used to compute the MSD. Confined and free-diffusing trajectories were defined as trajectories with a time constant τ respectively inferior and superior to half the time interval used to compute the MSD. The apparent Diffusion coefficient (D) can be calculated by taking of the slope of a linear fit for the first few points (we usually take the first 4 points) of the MSD, for free and confined diffusion (see **Note 11**). Analysis can then be filtered by computing MSD for particular subregions of interest of the raw images. This allows to compare the diffusive behavior of the target protein inside and outside a structure of interest, such as the IAS or the lamellipodium. Based on this approach, we could reveal that integrins are freely diffusing outside IASs, but they undergo immobilization inside IASs due to activation via a FN-integrin-talin tripartite interaction [25]. Moreover, we could also show that Rac1 GTPase is transiently immobilized at the lamellipodium tip, which is correlated with protein activation [48].

3.6.3 Fast sptPALM measurements

Transient protein-protein interactions are key components in signaling and regulatory networks [72]. These include signaling cascades such as the Epidermal Growth Factor (EGF) pathway or RhoA/Rac1 GTPase-effector interactions at the lamellipodium. For instance, we found that Rac1-WT is less immobilized at the lamellipodium tip compared to constitutively active Rac1-Q61L (see **Note 12**). This suggests that dwell times of interaction between activated Rac1-WT and effectors are shorter than our acquisition frequency. To bypass this type of limitations, we can increase the acquisition frequency by changing the acquisition device from an EMCCD to sCMOS camera (**Figure 1C)**. Conventional sptPALM acquisitions with EMCCD cameras are limited by the readout speed of the camera to about 70 full frames per second [73]. Conversely, sCMOS cameras possess a higher quantum efficiency, a larger field-of-view (FOV) and much faster readout speeds compared to EMCCD cameras. For instance, sCMOS cameras are capable of imaging a 2048 ×

2048 pixel FOV at 100 frames per second; EMCCD cameras are limited to a 512 × 512 FOV at a maximum speed of 56 FPS [74]. With this, we can increase the acquisition frequency of sptPALM experiments from 50 Hz to 333 Hz to more efficiently capture transient interactions between proteins (**Figure 1C**). For a fast PALM experiment, changes in frequency will change the total time of each acquisition (from 30 s (1500 frames) to 12 s (4000 frames)), as well as the resolution of the system (49 nm at 333 Hz for sCMOS vs 59 nm at 50 Hz for EMCCD) and the parameters for MSD computing (duration of the minimum trajectory length for analysis) [48].

3.6.4 sptPALM acquisition coupled with optogenetics

One of the main benefits of optogenetic methods consists in achieving spatiotemporal control of protein activation and interaction with high precision. For instance, using the CRY2-CIBN system coupled to Rac1, we can explore the effects of subcellular Rac1 activation on lamellipodium formation [47,48]. Two sets of data can be extracted from this particular type of experiments. First, by changing the region of illumination between two subcellular areas, e.g. the lamellipodium tip and the back of the lamellipodium, we can study the effect of protein activation in specific endogenous pathways/processes, i.e. cell migration. We found indeed that Rac1 activation leads to cell protrusion and that Rac1 is specifically activated at the lamellipodium tip and rapidly inactivated beyond the illuminated region. Second, by computing again the MSD for particular subcellular regions, we can extract the diffusive behavior of the protein outside and inside the illuminated region. In the case of Rac1, we found no differences of diffusion/immobilization outside and inside the illuminated region.

3.6.5 Analysis of SAFe measurements

The nanoscale architecture of adhesive structures [53] has previously been elucidated by an implementation combining photo-activated localization microscopy with single-photon, simultaneous multiphase interferometry (known as iPALM, interferometric photoactivated localization microscopy), which provides sub-20-nm 3D protein localization [75]. With comparatively simpler instrumentation, a combination of another two techniques, direct stochastic optical reconstruction microscopy (dSTORM) [76-78] and supercritical-angle fluorescence emission (SAFe) detection, known as direct optical nanoscopy with axially localized detection (DONALD), could be used to study single molecule distribution with an isotropic 3-D localisation precision of 15 nm within specimens ~200 nm above the coverslip [79]. After describing the working principle of this method, we outline how we can use a commercial implementation of SAFe (Abbelight) to elucidate the 3D organization of proteins in IAS, more specifically, to study the localization of kindlin, a crucial integrin activator [54].

When light enters from a medium of higher refractive index to a lower one at higher angles of incidence than a critical angle θ_c, Total Internal Reflection (TIR) happens and if the fluorophore is

located in the medium at a distance d comparable to its emission wavelength (0 < d < λem), its near field component is converted into light that propagates beyond the critical angle which is known as supercritical-angle fluorescence emission (SAFe). When the fluorophore is in direct contact with the interface (d = 0), the SAFe intensity is potentially equal to as much as half the amount of all fluorescence intensity emitted into the coverslip, **(Figure 3A).** The SAFe intensity decreases with increase in separation (d > 0) [80]. This dependence of the near field SAFe intensity on the distance of fluorophores from the coverslip, can used to estimate their axial positions. The number of photons from under-critical angle fluorescence (UAF) (emitted within a cone that is limited by angle θc), N_{UAF} remains nearly constant as a function of the interface fluorophore distance d. But the number of SAF photons (N_{SAF}) decreases approximately exponentially with d [81]. Hence, the simultaneous measurement of these photon numbers and computation of the fluorophore SAF ratio, N_{SAF}/N_{UAF} for each detected fluorophore can be used to determine the absolute axial position of the fluorophore [79,82]. Validation of this imaging principle has been also carried out using Origami tetrahedral [82].

With the SAFe module, d-STORM data is acquired and processed with NEMO software (Abbelight). After removing the background signal, molecules were detected and the numbers of SAF and UAF photons were measured to extract the corresponding axial positions as described [54,79] **(Figure 3A**). Lateral drifts are corrected from the localized data using a cross-correlation based algorithm. DONALD is free of any axial drift, as the supercritical emission allows one to extract the absolute axial position of the fluorophore with reference to the coverslip/sample interface [54].

For image display, molecules detected 200 nm above the surface are discarded to improve the contrast in the IAS/plasma membrane layer (**Figure 3C**). On the super-resolution reconstructed image, each pixel value corresponds to the average axial localization of single molecules detected in this pixel (size: 15 nm) (**Figure 3C**). For ease of observation, the obtained images are smoothed using a xy mean filter with a 5x5 kernel. For the curve of occurrence, all detections are included and Z distributions are plotted **(Figure 3B)** [54]. Kindlin-2 potentially binds proteins on multiple IAS nano-layers (i.e. integrin, ILK, actin, paxillin) [83-85]. To test whether kindlin-2 function could rely on its shifting from one layer to another in IAS, we used a commercial SAFe module (Abbelight) and the ratiometric approach, for investigating its 3D localization within the nano-layers of IAS (See **Note 13**). With GFP-paxillin defining the upper bound of the integrin layer (zpeak: 58 nm), GFP-kindlin-2-WT was found concentrated in the integrin layer at the vicinity of the plasma membrane (z-peak: 48.5nm) (**Figure 3C**). Thus, high kindlin-2 membrane recruitment and free-diffusion mediated by its PH domain occur in close proximity to integrins. Inhibition of kindlin binding to integrins (kindlin-2-QW) had a small-scale impact on kindlin localization (zpeak: 53 nm), whereas deletion of the PH domain resulted in its upward shift from the integrin layer localization (zpeak: 66 nm) (**Figure 3C-D**). Therefore, the PH domain of kindlin is also required to target kindlin to the proper functional nano-layer where it will act, namely the integrin layer.

3.6.6 Using mutants of integrin/regulators

In the highly complex and crowed environment of IAS, integrin regulation and activation (see **Note 14**) are highly dependent on interactions with multiple binding partners, which can be revealed by sptPALM and SRM [23,86]. To further probe these chains of interactions, we can employ a series of known integrins and regulators mutations which prevent or stabilize interactions with their binding partners. These strategies can be combined with genetic knock-out cell models for the protein of interest (see **Note 4**). Below we give several examples illustrating how this strategy could be used to decipher the sequence of molecular events/interactions leading to integrin activations in mature IAS.

1. Protein mutants can provide additional information on the immobilization and diffusion of proteins linked to different interactions. According to our previous findings, integrin activation is correlated with immobilization of integrin and associated activators, while inhibition is characterized by free-diffusion. Therefore, diffusive properties are one of the readouts to probe FN/integrins/regulators/F-actin connections. We showed that a constitutively active mutant of β3-integrin (β3-N305T) increased integrin immobilization outside IASs linked to extracellular matrix binding [25]. Moreover, mutants of β3-integrin that prevent either binding to fibronectin (β3-D119Y) or talin (β3-Y747A) lead to decreased fractions of immobilization of β3-integrin inside IAS, as well as shorter immobilization times within IASs [25](see **Note 15**). Hence, we demonstrated that a FN-integrin-talin tripartite interaction is crucial for a full long-lived integrin immobilization. To further characterize integrin activation, we also studied the dynamics of integrin mutants which decrease β1 and β3-integrin interactions with kindlin- (β1-Y795A and β3-Y759A). We found that both mutations decreased the fractions of immobilized integrins, although the effect was stronger for β1-integrin [54].

2. Protein mutants can help tracing the path used by crucial integrin regulators to reach functional nanodomains and activate integrins. We showed that Talin, for instance, displays almost no membrane free-diffusion inside and outside IASs. Due to the acquisition frequency and TIRF illumination of a sptPALM experiment, it is impossible to detect cytosolic free diffusion of a protein. Therefore, Talin is mostly cytosolic and it is not co-diffusing with integrins outside or inside IAS. To further dissect the mechanism, we employed two short forms of Talin; the C-terminal THATCH mutant, comprising an actin and vinculin-binding site, did not display membrane free-diffusion and has an immobile fraction similar to full-length talin [25].On the other hand, talin head alone exhibited prominent membrane diffusion outside and inside IAS, but no immobilization inside IAS. These differences reflect the auto-inhibition of talin in the cytosol, which will likely be relieved inside the IAS. Therefore, the results suggest that talin is recruited to IASs directly from a cytosolic pool, a process mediated by actin or vinculin. A similar rationale was applied to kindlin-2, which can associate to the plasma membrane through multiple phospholipid motifs found on its FO, F1 and PH domain

[87].We found that kindlin, similar to talin, is immobile and enriched in IAS; however, unlike talin, kindlin displays membrane free diffusion outside and inside the IAS. Thus, we decided to either mutate the PH domain in order to prevent interaction with phosphoinositides (K390A) or to delete it entirely (kindlin-2-ΔPH). While the point mutation only slightly reduced membrane free-diffusion of kindlin-2 outside IAS, deletion of PH domain had a much noticeable impact in decreasing membrane free-diffusion both inside and outside IAS[66]. We thus showed that kindlin-2 PH domain is required for its membrane free-diffusion. Further studies with SAF 3D nanoscopy and kindlin-2 mutants demonstrated that the PH domain of kindlin is also required to target kindlin to the functional nano-layer where it will act, the integrin layer.

3. Protein mutants are useful tools to study signaling proteins that undergo transient interactions with modulators and effectors. For instance, Rho GTPases are crucial for cytoskeleton reorganization in the context of cell migration [88]. Using gain- or loss-of-function mutants, we demonstrated that there is a strong correlation between protein dynamics and protein activation and/or binding states [25,48]. For example, using sptPALM with loss- or gain-of-function mutants of Rac1, we revealed that Rac1 activation is correlated with its interaction with effectors at the tip of protrusive structures, at remote locations from sites of Rac1 activation (e.g. IAS) [48]. We showed that a constitutively active Rac1-Q61L mutant exhibits more immobilizations and slower free diffusions at the lamellipodium tip compared to Rac1-WT, while a fast cycling Rac1-F28L mutant has a more similar behavior to Rac1-WT. Conversely, an inactive Rac1-T17N mutant displays predominantly free diffusions and no selective immobilizations. We then sought to capture more efficiently these transient immobilizations by performing fastPALM acquisitions at 333 Hz. This resulted in an enhanced difference of diffusive behavior between WT and active Rac1 mutants (Q61L and F28L). Indeed, fast PALM revealed larger fractions of immobilization for the fast cycling F28L mutant, which were not captured at 50 Hz acquisition frequencies. Nonetheless, even a frequency of 333 Hz was too slow to detect the bulk of Rac1-WT immobilizations, suggesting that most Rac1-effector interactions at the lamellipodium tip are transient and less than a few dozen milliseconds long. This correlation between Rac1 activation and immobilization was also shown to occur in IAS, with constitutively active Rac1 mutant G12V displaying increased immobilization in IAS, while inactive mutant T17N was mostly mobile [49].

4 Notes

1. Select the appropriate program in the Amaxa equipment suitable to the cell lines indicated. Also use transfection reagents suitable to the cell lines used.

2. We used Metamorph (Molecular Devices) for 2-D acquisition, image processing and visualization. Wavetracer commercial software [89] or free alternatives are available as well. ThunderSTORM [90] for superresolution reconstruction, ICY [91] with spot detector and spot tracker plugins for single particle detection and tracking [92] are also frequently used. Kymotoolbox ImageJ plug-in is available from Fabrice Cordelières [93]. Nemo software (Abbelight) is used for 3D-SAF acquisition and processing.

3. Alternatively, for the optical setup for 3D imaging using DONALD, we used an Olympus IX83 inverted microscope with an autofocus system. The excitation path was composed of three laser lines: 637 nm, 532 nm and 405 nm (Errol lasers) and a TIRF module (Errol lasers) used in combination with a matched 390/482/532/640 multiband filter (LF405/488/532/635-A-000, Semrock). The fluorescence was collected through an Olympus x100 1.49 NA oil immersion objective lens. The detection path was composed of a SAF module (Abbelight) and a Flash 4 v3 (Hamamatsu).

4. The majority of SPT experiments presented here were performed in cellular systems in which the wild-type form of the studied protein is already expressed at the endogenous level. In that case, transfection with the WT tagged protein (e.g. mEos2, mEos3.2) will lead to over-expression of the target protein. Although this ensures the labelling density necessary for high effective resolution, it can induce functional consequences, besides the inherent experimental variations associated to protein transfection. With the development of genomic editing, it is now possible to engineer cellular systems with CRISPR-Cas9 to endogenously express a specific protein labelled with a tag compatible with single protein tracking and super-resolution microscopy [94]. This produces systems with stable expression patterns of tagged protein expression and removes the variability associated to plasmid transfection. In the context of genetic modifications, studies on protein function can also be performed on a background where the endogenous protein has been deleted. This is of particular interest when employing different mutants to further characterize protein function and organization. Knock-out cell models, either from animal cell lines or obtained using CRISPR/Cas-9, allow link diffusive behavior and protein function. The ability to rescue or not a particular phenotype caused by endogenous protein deletion can reveal the importance of specific dynamics and domains present in IAS proteins. For instance, fibroblasts double KO for kindlin-1 and kindlin-2 are unable to spread and to form IAS. By studying the diffusive behavior of kindlin-2 mutants and their ability to trigger cell spreading or the formation of IAS in kindlin-1,2 double KO, we demonstrated that kindlin membrane free-diffusion is key to trigger integrin activation

[54]. KO cell models can be applied for other dynamic structures in cell migration, such as the lamellipodium. Indeed, we have also characterized the interaction between Rac1 and the WAVE complex in cells where Sra1 and PIR121 had been genetically disrupted by CRISPR/Cas9 (Sra1/PIR121-KO) [95]; Sra1 is an element of WAVE protein complex. By rescuing these cell lines with constitutively activated Sra1 mutants, we could modulate WAVE complex activation and interactions with Rac1 [48]. Consistent with other results, we showed that immobilizations of activated Rac1 depend on interactions with WAVE complex at the lamellipodium tip.

5. To test that we were not performing experiments on cells having aberrant protrusive behaviors, we also measured rates of lamellipodium protrusion for the cells used for sptPALM analysis. The rates of protrusion for the cells analyzed in different conditions were not dramatically different among another. This suggests that, in our acquisition conditions, levels of expression of distinct mEos2-fused proteins were not triggering dramatic effects on lamellipodium protrusion.

6. Fast diffusion of proteins requires tracking with a high temporal resolution. We routinely use 50Hz imaging frequency on a center quadrant of 512-by-512 pixel EMCCD camera. While EMCCD provides high signal to noise ratio with weak single fluorophores, faster imaging speed can be achieved by reducing the area of imaging on the camera chip, which is a limiting factor for the speed of data transfer. Alternatively, sCMOS cameras can be used, as further elaborated in the section 3.6.3.

7. For a typical PALM acquisition, twenty thousand or more tracks can be collected from a cell, in batches of 4000 frames of recording. While longer acquisition time can generate more trajectories, photo-toxicity may change the behavior of cells and protein dynamics, the experimenter should control the laser intensity and imaging time to optimize according to cell type and protein studied.

8. Using the 405 laser only in the ROI prevents unwanted Tiam1 photoactivation outside the ROI, since CRY2 is sensitive to blue light (405–488 nm).

9. Molecules may transition between different states of diffusion and immobilization. Longer trajectories may include mixed diffusion states in the same trajectory, thus underestimate the diffusion coefficient when calculating it from the MSD curve. The experimenter should examine the individual trajectories and determine whether the protein of interest undergoes frequent transitions between states. If this is the case, acquiring shorter tracks or breaking the trajectories into short pieces can help mitigate the issue, albeit increasing the variation of

MSD curve. Alternatively, a rolling MSD analysis can help identify different diffusion states and segment accordingly

10. A single fluorophore can undergo “blinking” for tens of seconds. Therefore, it is possible to track a slowly moving fluorophore for a prolonged duration by reconnecting emissions from different time points. Directed movements of proteins can thereby be analyzed by tracking the position of individual proteins over time. In addition, to understand slow dynamics, kymographs (position over time) can be created in a region of interest by a straight line or a segmented line is typically drawn directly on the superresolution time-lapse movie. By merging several superresolved reconstruction images (e.g., 25 images) obtained from 50 Hz single-molecule imaging, a SR time lapse movie (e.g., 2 Hz) is generated. From this, different parameters such as the speed, direction and dwell time of proteins are extracted.

11. To make sure that the observed dynamics are specific to the protein of interest and not arising from any protein density distributions, we also analyse trajectories of mEOS2 fused to the trans-membrane domain of the PDGF receptor (mEOS2–TM) or anchored to inner leaflet lipids (CAAX–mEOS2; (C; cysteine; A, aliphatic residue; X, any amino acid).

12. Since high levels of expression of Rho GTPase mutants might affect lamellipodia formation, dynamics and morphologies [96,97], acquisitions are to be performed only on cells able to spread and polarize, and in the absence of dramatic phenotypes such as (i) being unable to spread but forming membrane tubules (high levels of RhoA-Q63L expression), (ii) bearing numerous lamellipodia (high levels of Rac1-Q61L). Analyze cells displaying an active, protrusive lamellipodium, in phase 2 of spreading (according to [14,15]).

13. Kindlin-1, Kindlin-2 double knock-out cells ($Kind^{Ko}$) cell line was provided by Reinhard Fässler (Max Planck Institute of Biochemistry, Martinsried) and are described elsewhere [83]. Absence of mycoplasma contamination was assessed using the MycoAlert detection kit (Lonza).

14. Integrin activation can be induced by replacing the cell media (Ringer+glucose) with a Ringer+glucose solution with $MnCl_2$ at 5 mM, at least 5 minutes before acquisition.

15. Differences in the dynamic behavior of WT and mutant β_3-integrins were not correlated with their surface expression levels measured by fluorescence-activated cell sorting (FACS) or using the density of mEOS2 detections. Dynamics of WT and mutant β3-integrins were not

affected by the probes used to localize IAS (GFP–paxillin or GFP–VASP), or by the presence of endogenous β3-integrins, as indicated by experiments performed in β_3 -integrin $^{-/-}$ MEFs.

References

1. Montell DJ, Rorth P, Spradling AC (1992) slow border cells, a locus required for a developmentally regulated cell migration during oogenesis, encodes Drosophila C/EBP. Cell 71 (1):51-62. doi:10.1016/0092-8674(92)90265-e

2. Grinnell F (1992) Wound repair, keratinocyte activation and integrin modulation. Journal of cell science 101 (Pt 1):1-5

3. Abreu-Blanco MT, Verboon JM, Liu R, Watts JJ, Parkhurst SM (2012) Drosophila embryos close epithelial wounds using a combination of cellular protrusions and an actomyosin purse string. Journal of cell science 125 (Pt 24):5984-5997. doi:10.1242/jcs.109066

4. Friedl P, Locker J, Sahai E, Segall JE (2012) Classifying collective cancer cell invasion. Nature cell biology 14 (8):777-783. doi:10.1038/ncb2548

5. Pollard TD, Borisy GG (2003) Cellular motility driven by assembly and disassembly of actin filaments. Cell 112 (4):453-465. doi:10.1016/s0092-8674(03)00120-x

6. Ridley AJ, Schwartz MA, Burridge K, Firtel RA, Ginsberg MH, Borisy G, Parsons JT, Horwitz AR (2003) Cell migration: integrating signals from front to back. Science 302 (5651):1704-1709. doi:10.1126/science.1092053

7. Ridley AJ (2011) Life at the leading edge. Cell 145 (7):1012-1022. doi:10.1016/j.cell.2011.06.010

8. Svitkina TM, Borisy GG (1999) Arp2/3 complex and actin depolymerizing factor/cofilin in dendritic organization and treadmilling of actin filament array in lamellipodia. The Journal of cell biology 145 (5):1009-1026. doi:10.1083/jcb.145.5.1009

9. Chen Z, Borek D, Padrick SB, Gomez TS, Metlagel Z, Ismail AM, Umetani J, Billadeau DD, Otwinowski Z, Rosen MK (2010) Structure and control of the actin regulatory WAVE complex. Nature 468 (7323):533-538. doi:10.1038/nature09623

10. Ridley AJ, Paterson HF, Johnston CL, Diekmann D, Hall A (1992) The small GTP-binding protein rac regulates growth factor-induced membrane ruffling. Cell 70 (3):401-410. doi:10.1016/0092-8674(92)90164-8

11. Machacek M, Hodgson L, Welch C, Elliott H, Pertz O, Nalbant P, Abell A, Johnson GL, Hahn KM, Danuser G (2009) Coordination of Rho GTPase activities during cell protrusion. Nature 461 (7260):99-103. doi:10.1038/nature08242

12. Ponti A, Machacek M, Gupton SL, Waterman-Storer CM, Danuser G (2004) Two distinct actin networks drive the protrusion of migrating cells. Science 305 (5691):1782-1786. doi:10.1126/science.1100533

13. Case LB, Baird MA, Shtengel G, Campbell SL, Hess HF, Davidson MW, Waterman CM (2015) Molecular mechanism of vinculin activation and nanoscale spatial organization in focal adhesions. Nature cell biology 17 (7):880-892. doi:10.1038/ncb3180

14. Giannone G, Dubin-Thaler BJ, Dobereiner HG, Kieffer N, Bresnick AR, Sheetz MP (2004) Periodic lamellipodial contractions correlate with rearward actin waves. Cell 116 (3):431-443. doi:10.1016/s0092-8674(04)00058-3

15. Giannone G, Dubin-Thaler BJ, Rossier O, Cai Y, Chaga O, Jiang G, Beaver W, Dobereiner HG, Freund Y, Borisy G, Sheetz MP (2007) Lamellipodial actin mechanically links myosin activity with adhesion-site formation. Cell 128 (3):561-575. doi:10.1016/j.cell.2006.12.039

16. Hotulainen P, Lappalainen P (2006) Stress fibers are generated by two distinct actin assembly mechanisms in motile cells. The Journal of cell biology 173 (3):383-394. doi:10.1083/jcb.200511093

17. Koestler SA, Auinger S, Vinzenz M, Rottner K, Small JV (2008) Differentially oriented populations of actin filaments generated in lamellipodia collaborate in pushing and pausing at the cell front. Nature cell biology 10 (3):306-313. doi:10.1038/ncb1692

18. Vicente-Manzanares M, Ma X, Adelstein RS, Horwitz AR (2009) Non-muscle myosin II takes centre stage in cell adhesion and migration. Nature reviews Molecular cell biology 10 (11):778-790. doi:10.1038/nrm2786

19. Hynes RO (2002) Integrins: bidirectional, allosteric signaling machines. Cell 110 (6):673-687. doi:10.1016/s0092-8674(02)00971-6

20. Geiger B, Spatz JP, Bershadsky AD (2009) Environmental sensing through focal adhesions. Nature reviews Molecular cell biology 10 (1):21-33. doi:10.1038/nrm2593

21. Humphrey JD, Dufresne ER, Schwartz MA (2014) Mechanotransduction and extracellular matrix homeostasis. Nature reviews Molecular cell biology 15 (12):802-812. doi:10.1038/nrm3896

22. Legate KR, Fassler R (2009) Mechanisms that regulate adaptor binding to beta-integrin cytoplasmic tails. Journal of cell science 122 (Pt 2):187-198. doi:10.1242/jcs.041624

23. Orre T, Rossier O, Giannone G (2019) The inner life of integrin adhesion sites: From single molecules to functional macromolecular complexes. Experimental cell research 379 (2):235-244. doi:10.1016/j.yexcr.2019.03.036

24. Sun Z, Guo SS, Fassler R (2016) Integrin-mediated mechanotransduction. The Journal of cell biology 215 (4):445-456. doi:10.1083/jcb.201609037

25. Rossier O, Octeau V, Sibarita JB, Leduc C, Tessier B, Nair D, Gatterdam V, Destaing O, Albiges-Rizo C, Tampe R, Cognet L, Choquet D, Lounis B, Giannone G (2012) Integrins beta1 and beta3 exhibit distinct dynamic nanoscale organizations inside focal adhesions. Nature cell biology 14 (10):1057-1067. doi:10.1038/ncb2588

26. Schiller HB, Hermann MR, Polleux J, Vignaud T, Zanivan S, Friedel CC, Sun Z, Raducanu A, Gottschalk KE, Thery M, Mann M, Fassler R (2013) beta1- and alphav-class integrins cooperate to regulate myosin II during rigidity sensing of fibronectin-based microenvironments. Nature cell biology 15 (6):625-636. doi:10.1038/ncb2747

27. Moser M, Legate KR, Zent R, Fassler R (2009) The tail of integrins, talin, and kindlins. Science 324 (5929):895-899. doi:10.1126/science.1163865

28. Shattil SJ, Kim C, Ginsberg MH (2010) The final steps of integrin activation: the end game. Nature reviews Molecular cell biology 11 (4):288-300. doi:10.1038/nrm2871

29. Bouvard D, Pouwels J, De Franceschi N, Ivaska J (2013) Integrin inactivators: balancing cellular functions in vitro and in vivo. Nature reviews Molecular cell biology 14 (7):430-442. doi:10.1038/nrm3599

30. Humphries JD, Byron A, Bass MD, Craig SE, Pinney JW, Knight D, Humphries MJ (2009) Proteomic analysis of integrin-associated complexes identifies RCC2 as a dual regulator of Rac1 and Arf6. Science signaling 2 (87):ra51. doi:10.1126/scisignal.2000396

31. Schiller HB, Friedel CC, Boulegue C, Fassler R (2011) Quantitative proteomics of the integrin adhesome show a myosin II-dependent recruitment of LIM domain proteins. EMBO reports 12 (3):259-266. doi:10.1038/embor.2011.5

32. Kuo JC, Han X, Hsiao CT, Yates JR, 3rd, Waterman CM (2011) Analysis of the myosin-II-responsive focal adhesion proteome reveals a role for beta-Pix in negative regulation of focal adhesion maturation. Nature cell biology 13 (4):383-393. doi:10.1038/ncb2216

33. Zaidel-Bar R, Itzkovitz S, Ma'ayan A, Iyengar R, Geiger B (2007) Functional atlas of the integrin adhesome. Nature cell biology 9 (8):858-867. doi:10.1038/ncb0807-858

34. Horton ER, Byron A, Askari JA, Ng DHJ, Millon-Fremillon A, Robertson J, Koper EJ, Paul NR, Warwood S, Knight D, Humphries JD, Humphries MJ (2015) Definition of a consensus integrin adhesome and its dynamics during adhesion complex assembly and disassembly. Nature cell biology 17 (12):1577-1587. doi:10.1038/ncb3257

35. Byron A, Humphries JD, Craig SE, Knight D, Humphries MJ (2012) Proteomic analysis of alpha4beta1 integrin adhesion complexes reveals alpha-subunit-dependent protein recruitment. Proteomics 12 (13):2107-2114. doi:10.1002/pmic.201100487

36. Robertson J, Jacquemet G, Byron A, Jones MC, Warwood S, Selley JN, Knight D, Humphries JD, Humphries MJ (2015) Defining the phospho-adhesome through the phosphoproteomic analysis of integrin signalling. Nature communications 6:6265. doi:10.1038/ncomms7265

37. Kechagia JZ, Ivaska J, Roca-Cusachs P (2019) Integrins as biomechanical sensors of the microenvironment. Nature reviews Molecular cell biology 20 (8):457-473. doi:10.1038/s41580-019-0134-2

38. Evans EA, Calderwood DA (2007) Forces and bond dynamics in cell adhesion. Science 316 (5828):1148-1153. doi:10.1126/science.1137592

39. Moore SW, Roca-Cusachs P, Sheetz MP (2010) Stretchy proteins on stretchy substrates: the important elements of integrin-mediated rigidity sensing. Developmental cell 19 (2):194-206. doi:10.1016/j.devcel.2010.07.018

40. Sun Z, Costell M, Fassler R (2019) Integrin activation by talin, kindlin and mechanical forces. Nature cell biology 21 (1):25-31. doi:10.1038/s41556-018-0234-9

41. Hoffmann JE, Fermin Y, Stricker RL, Ickstadt K, Zamir E (2014) Symmetric exchange of multi-protein building blocks between stationary focal adhesions and the cytosol. eLife 3:e02257. doi:10.7554/eLife.02257

42. Han SJ, Dean KM, Whitewood J, Bachir A, Guttierrez E, Groisman A, Horwitz AR, Goult BT, Danuser G (2019) Formation of talin-vinculin pre-complexes dictates maturation of nascent adhesions by accelerated force transmission and vinculin recruitment. bioRxiv:735183. doi:10.1101/735183

43. Tadokoro S, Shattil SJ, Eto K, Tai V, Liddington RC, de Pereda JM, Ginsberg MH, Calderwood DA (2003) Talin binding to integrin beta tails: a final common step in integrin activation. Science 302 (5642):103-106. doi:10.1126/science.1086652

44. Woodside DG, Obergfell A, Talapatra A, Calderwood DA, Shattil SJ, Ginsberg MH (2002) The N-terminal SH2 domains of Syk and ZAP-70 mediate phosphotyrosine-independent binding to integrin beta cytoplasmic domains. The Journal of biological chemistry 277 (42):39401-39408. doi:10.1074/jbc.M207657200

45. Sungkaworn T, Jobin ML, Burnecki K, Weron A, Lohse MJ, Calebiro D (2017) Single-molecule imaging reveals receptor-G protein interactions at cell surface hot spots. Nature 550 (7677):543-547. doi:10.1038/nature24264

46. Chazeau A, Mehidi A, Nair D, Gautier JJ, Leduc C, Chamma I, Kage F, Kechkar A, Thoumine O, Rottner K, Choquet D, Gautreau A, Sibarita JB, Giannone G (2014) Nanoscale segregation of actin nucleation and elongation factors determines dendritic spine protrusion. The EMBO journal 33 (23):2745-2764. doi:10.15252/embj.201488837

47. Remorino A, De Beco S, Cayrac F, Di Federico F, Cornilleau G, Gautreau A, Parrini MC, Masson JB, Dahan M, Coppey M (2017) Gradients of Rac1 Nanoclusters Support Spatial Patterns of Rac1 Signaling. Cell reports 21 (7):1922-1935. doi:10.1016/j.celrep.2017.10.069

48. Mehidi A, Rossier O, Schaks M, Chazeau A, Biname F, Remorino A, Coppey M, Karatas Z, Sibarita JB, Rottner K, Moreau V, Giannone G (2019) Transient Activations of Rac1 at the Lamellipodium Tip Trigger Membrane Protrusion. Current biology : CB 29 (17):2852-2866 e2855. doi:10.1016/j.cub.2019.07.035

49. Shibata AC, Chen LH, Nagai R, Ishidate F, Chadda R, Miwa Y, Naruse K, Shirai YM, Fujiwara TK, Kusumi A (2013) Rac1 recruitment to the archipelago structure of the focal adhesion through the fluid membrane as revealed by single-molecule analysis. Cytoskeleton 70 (3):161-177. doi:10.1002/cm.21097

50. Tsunoyama TA, Watanabe Y, Goto J, Naito K, Kasai RS, Suzuki KGN, Fujiwara TK, Kusumi A (2018) Super-long single-molecule tracking reveals dynamic-anchorage-induced integrin function. Nature chemical biology 14 (5):497-506. doi:10.1038/s41589-018-0032-5

51. Leduc C, Si S, Gautier J, Soto-Ribeiro M, Wehrle-Haller B, Gautreau A, Giannone G, Cognet L, Lounis B (2013) A highly specific gold nanoprobe for live-cell single-molecule imaging. Nano letters 13 (4):1489-1494. doi:10.1021/nl304561g

52. Paszek MJ, DuFort CC, Rossier O, Bainer R, Mouw JK, Godula K, Hudak JE, Lakins JN, Wijekoon AC, Cassereau L, Rubashkin MG, Magbanua MJ, Thorn KS, Davidson MW, Rugo HS, Park JW, Hammer DA, Giannone G, Bertozzi CR, Weaver VM (2014) The cancer glycocalyx mechanically primes integrin-mediated growth and survival. Nature 511 (7509):319-325. doi:10.1038/nature13535

53. Kanchanawong P, Shtengel G, Pasapera AM, Ramko EB, Davidson MW, Hess HF, Waterman CM (2010) Nanoscale architecture of integrin-based cell adhesions. Nature 468 (7323):580-584. doi:10.1038/nature09621

54. Orré T, Karatas Z, Kastberger B, Cabriel C, Böttcher RT, Lévêque-Fort S, Sibarita JB, Fässler R, Wehrle-Haller B, Rossier O, Giannone G (202) Molecular motion and tridimensional nanoscale localization of kindlin control integrin activation in focal adhesions. bioRxiv

55. Spiess M, Hernandez-Varas P, Oddone A, Olofsson H, Blom H, Waithe D, Lock JG, Lakadamyali M, Stromblad S (2018) Active and inactive beta1 integrins segregate into distinct nanoclusters in focal adhesions. The Journal of cell biology 217 (6):1929-1940. doi:10.1083/jcb.201707075

56. Rys JP, DuFort CC, Monteiro DA, Baird MA, Oses-Prieto JA, Chand S, Burlingame AL, Davidson MW, Alliston TN (2015) Discrete spatial organization of TGFbeta receptors couples receptor multimerization and signaling to cellular tension. eLife 4:e09300. doi:10.7554/eLife.09300

57. Kiosses WB, Shattil SJ, Pampori N, Schwartz MA (2001) Rac recruits high-affinity integrin alphavbeta3 to lamellipodia in endothelial cell migration. Nature cell biology 3 (3):316-320. doi:10.1038/35060120

58. Del Pozo MA, Kiosses WB, Alderson NB, Meller N, Hahn KM, Schwartz MA (2002) Integrins regulate GTP-Rac localized effector interactions through dissociation of Rho-GDI. Nature cell biology 4 (3):232-239. doi:10.1038/ncb759

59. Pertz O, Hodgson L, Klemke RL, Hahn KM (2006) Spatiotemporal dynamics of RhoA activity in migrating cells. Nature 440 (7087):1069-1072. doi:10.1038/nature04665

60. Wu YI, Frey D, Lungu OI, Jaehrig A, Schlichting I, Kuhlman B, Hahn KM (2009) A genetically encoded photoactivatable Rac controls the motility of living cells. Nature 461 (7260):104-108. doi:10.1038/nature08241

61. Yazawa M, Sadaghiani AM, Hsueh B, Dolmetsch RE (2009) Induction of protein-protein interactions in live cells using light. Nature biotechnology 27 (10):941-945. doi:10.1038/nbt.1569

62. Valon L, Etoc F, Remorino A, di Pietro F, Morin X, Dahan M, Coppey M (2015) Predictive Spatiotemporal Manipulation of Signaling Perturbations Using Optogenetics. Biophysical journal 109 (9):1785-1797. doi:10.1016/j.bpj.2015.08.042

63. Kasai RS, Suzuki KG, Prossnitz ER, Koyama-Honda I, Nakada C, Fujiwara TK, Kusumi A (2011) Full characterization of GPCR monomer-dimer dynamic equilibrium by single molecule imaging. The Journal of cell biology 192 (3):463-480. doi:10.1083/jcb.201009128

64. Dustin ML, Depoil D (2011) New insights into the T cell synapse from single molecule techniques. Nature reviews Immunology 11 (10):672-684. doi:10.1038/nri3066

65. Opazo P, Sainlos M, Choquet D (2012) Regulation of AMPA receptor surface diffusion by PSD-95 slots. Current opinion in neurobiology 22 (3):453-460. doi:10.1016/j.conb.2011.10.010

66. Chamma I, Rossier O, Giannone G, Thoumine O, Sainlos M (2017) Optimized labeling of membrane proteins for applications to super-resolution imaging in confined cellular environments using monomeric streptavidin. Nature protocols 12 (4):748-763. doi:10.1038/nprot.2017.010

67. Izeddin I, Boulanger J, Racine V, Specht CG, Kechkar A, Nair D, Triller A, Choquet D, Dahan M, Sibarita JB (2012) Wavelet analysis for single molecule localization microscopy. Optics express 20 (3):2081-2095. doi:10.1364/OE.20.002081

68. Racine V, Hertzog A, Jouanneau J, Salamero J, Kervrann C, Sibarita J Multiple-target tracking of 3D fluorescent objects based on simulated annealing. In: 3rd IEEE International Symposium on Biomedical Imaging: Nano to Macro, 2006., 6-9 April 2006 2006. pp 1020-1023. doi:10.1109/ISBI.2006.1625094

69. Racine V, Sachse M, Salamero J, Fraisier V, Trubuil A, Sibarita JB (2007) Visualization and quantification of vesicle trafficking on a three-dimensional cytoskeleton network in living cells. Journal of microscopy 225 (Pt 3):214-228. doi:10.1111/j.1365-2818.2007.01723.x

70. Das S, Yin T, Yang Q, Zhang J, Wu YI, Yu J (2015) Single-molecule tracking of small GTPase Rac1 uncovers spatial regulation of membrane translocation and mechanism for polarized signaling. Proceedings of the National Academy of Sciences of the United States of America 112 (3):E267-276. doi:10.1073/pnas.1409667112

71. El Beheiry M, Dahan M, Masson JB (2015) InferenceMAP: mapping of single-molecule dynamics with Bayesian inference. Nature methods 12 (7):594-595. doi:10.1038/nmeth.3441

72. De Keersmaecker H, Camacho R, Rantasa DM, Fron E, Uji IH, Mizuno H, Rocha S (2018) Mapping Transient Protein Interactions at the Nanoscale in Living Mammalian Cells. ACS nano 12 (10):9842-9854. doi:10.1021/acsnano.8b01227

73. Huang F, Hartwich TM, Rivera-Molina FE, Lin Y, Duim WC, Long JJ, Uchil PD, Myers JR, Baird MA, Mothes W, Davidson MW, Toomre D, Bewersdorf J (2013) Video-rate nanoscopy using sCMOS camera-specific single-molecule localization algorithms. Nature methods 10 (7):653-658. doi:10.1038/nmeth.2488

74. Almada P, Culley S, Henriques R (2015) PALM and STORM: Into large fields and high-throughput microscopy with sCMOS detectors. Methods 88:109-121. doi:10.1016/j.ymeth.2015.06.004

75. Shtengel G, Galbraith JA, Galbraith CG, Lippincott-Schwartz J, Gillette JM, Manley S, Sougrat R, Waterman CM, Kanchanawong P, Davidson MW, Fetter RD, Hess HF (2009) Interferometric fluorescent super-resolution microscopy resolves 3D cellular ultrastructure. Proceedings of the National Academy of Sciences of the United States of America 106 (9):3125-3130. doi:10.1073/pnas.0813131106

76. Rust MJ, Bates M, Zhuang X (2006) Sub-diffraction-limit imaging by stochastic optical reconstruction microscopy (STORM). Nature methods 3 (10):793-795. doi:10.1038/nmeth929

77. van de Linde S, Loschberger A, Klein T, Heidbreder M, Wolter S, Heilemann M, Sauer M (2011) Direct stochastic optical reconstruction microscopy with standard fluorescent probes. Nature protocols 6 (7):991-1009. doi:10.1038/nprot.2011.336

78. Huang B, Wang W, Bates M, Zhuang X (2008) Three-dimensional super-resolution imaging by stochastic optical reconstruction microscopy. Science 319 (5864):810-813. doi:10.1126/science.1153529

79. Bourg N, Mayet C, Dupuis G, Barroca T, Bon P, Lécart S, Fort E, Lévêque-Fort S (2015) Direct optical nanoscopy with axially localized detection. Nature Photonics 9 (9):587-593. doi:10.1038/nphoton.2015.132

80. Fort E, Grésillon S (2007) Surface enhanced fluorescence. Journal of Physics D: Applied Physics 41 (1):013001. doi:10.1088/0022-3727/41/1/013001

81. Ruckstuhl T, Rankl M, Seeger S (2003) Highly sensitive biosensing using a supercritical angle fluorescence (SAF) instrument. Biosensors & bioelectronics 18 (9):1193-1199. doi:10.1016/s0956-5663(02)00239-7

82. Deschamps J, Mund M, Ries J (2014) 3D superresolution microscopy by supercritical angle detection. Optics express 22 (23):29081-29091. doi:10.1364/OE.22.029081

83. Theodosiou M, Widmaier M, Bottcher RT, Rognoni E, Veelders M, Bharadwaj M, Lambacher A, Austen K, Muller DJ, Zent R, Fassler R (2016) Kindlin-2 cooperates with talin to activate integrins and induces cell spreading by directly binding paxillin. eLife 5:e10130. doi:10.7554/eLife.10130

84. Hirbawi J, Bialkowska K, Bledzka KM, Liu J, Fukuda K, Qin J, Plow EF (2017) The extreme C-terminal region of kindlin-2 is critical to its regulation of integrin activation. The Journal of biological chemistry 292 (34):14258-14269. doi:10.1074/jbc.M117.776195

85. Shi X, Ma YQ, Tu Y, Chen K, Wu S, Fukuda K, Qin J, Plow EF, Wu C (2007) The MIG-2/integrin interaction strengthens cell-matrix adhesion and modulates cell motility. The Journal of biological chemistry 282 (28):20455-20466. doi:10.1074/jbc.M611680200

86. Rossier O, Giannone G (2016) The journey of integrins and partners in a complex interactions landscape studied by super-resolution microscopy and single protein tracking. Experimental cell research 343 (1):28-34. doi:10.1016/j.yexcr.2015.11.004

87. Calderwood DA, Campbell ID, Critchley DR (2013) Talins and kindlins: partners in integrin-mediated adhesion. Nature reviews Molecular cell biology 14 (8):503-517. doi:10.1038/nrm3624

88. Heasman SJ, Ridley AJ (2008) Mammalian Rho GTPases: new insights into their functions from in vivo studies. Nature reviews Molecular cell biology 9 (9):690-701. doi:10.1038/nrm2476

89. Kechkar A, Nair D, Heilemann M, Choquet D, Sibarita JB (2013) Real-time analysis and visualization for single-molecule based super-resolution microscopy. PloS one 8 (4):e62918. doi:10.1371/journal.pone.0062918

90. Ovesny M, Krizek P, Borkovec J, Svindrych Z, Hagen GM (2014) ThunderSTORM: a comprehensive ImageJ plug-in for PALM and STORM data analysis and super-resolution imaging. Bioinformatics 30 (16):2389-2390. doi:10.1093/bioinformatics/btu202

91. de Chaumont F, Dallongeville S, Chenouard N, Herve N, Pop S, Provoost T, Meas-Yedid V, Pankajakshan P, Lecomte T, Le Montagner Y, Lagache T, Dufour A, Olivo-Marin JC (2012) Icy: an open bioimage informatics platform for extended reproducible research. Nature methods 9 (7):690-696. doi:10.1038/nmeth.2075

92. Chenouard N, Bloch I, Olivo-Marin JC (2013) Multiple hypothesis tracking for cluttered biological image sequences. IEEE transactions on pattern analysis and machine intelligence 35 (11):2736-3750. doi:10.1109/TPAMI.2013.97

93. Zala D, Hinckelmann MV, Yu H, Lyra da Cunha MM, Liot G, Cordelieres FP, Marco S, Saudou F (2013) Vesicular glycolysis provides on-board energy for fast axonal transport. Cell 152 (3):479-491. doi:10.1016/j.cell.2012.12.029

94. Khan AO, Simms VA, Pike JA, Thomas SG, Morgan NV (2017) CRISPR-Cas9 Mediated Labelling Allows for Single Molecule Imaging and Resolution. Scientific reports 7 (1):8450. doi:10.1038/s41598-017-08493-x

95. Schaks M, Singh SP, Kage F, Thomason P, Klunemann T, Steffen A, Blankenfeldt W, Stradal TE, Insall RH, Rottner K (2018) Distinct Interaction Sites of Rac GTPase with WAVE Regulatory Complex Have Non-redundant Functions in Vivo. Current biology : CB 28 (22):3674-3684 e3676. doi:10.1016/j.cub.2018.10.002

96. Pertz O (2010) Spatio-temporal Rho GTPase signaling - where are we now? Journal of cell science 123 (Pt 11):1841-1850. doi:10.1242/jcs.064345

97. Cherfils J, Zeghouf M (2013) Regulation of small GTPases by GEFs, GAPs, and GDIs. Physiological reviews 93 (1):269-309. doi:10.1152/physrev.00003.2012

Figures and captions

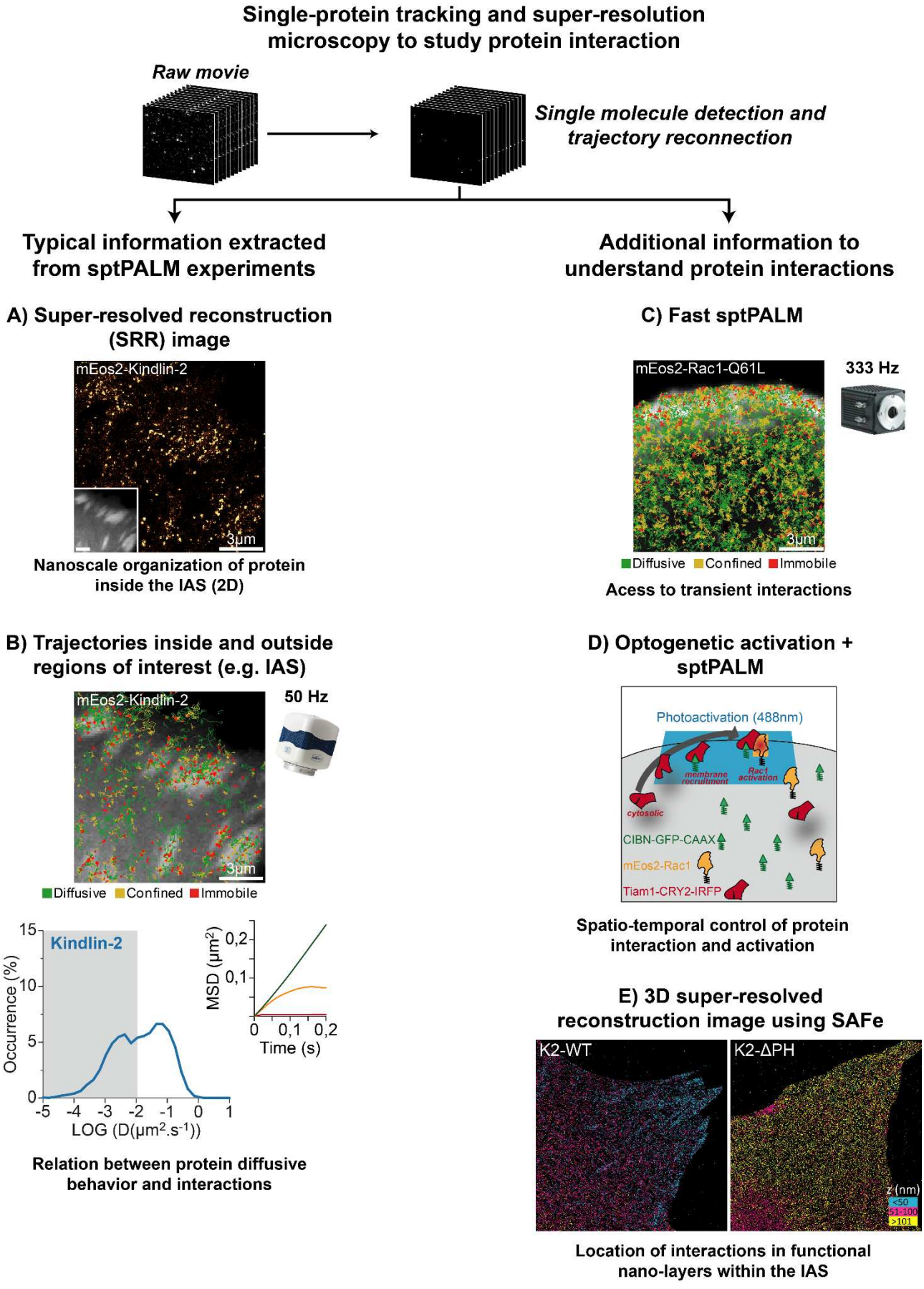

Figure 1: Schematic for spt-PALM and super-resolution microscopy techniques to study protein interaction.

(A-B) Typical information extracted from sptPALM experiments **A)** Super-resolved reconstructed image from the single molecule detection and localization data for mEos2-Kindlin-2-WT in a MEF, obtained from a sptPALM acquisition at 50 Hz (duration: 80s) using an EMCCD camera. (scale bar 3 micrometer). Inset: low-resolution image of Paxillin-GFP, co-expressed for IAS labelling. **B)** Super-resolved trajectories obtained by reconnecting the detections of mEos2-Kindlin-2-WT, overlaid on IAS. Trajectories are color-coded to show the different diffusion modes: free diffusion (green), confined (yellow) and immobile (red) (top). Distribution of the diffusion coefficient D computed from the trajectories of mEos2-Kindlin-2-WT obtained inside IAS (bottom, left). The grey area including D values inferior to 0.011 $\mu m^2.s^{-1}$ corresponds to immobilized proteins. Values represent the average of the distributions obtained from different cells. Inset, MSD for trajectories corresponding to freely diffusive, confined and immobile motion (green, yellow and red respectively) (bottom, right). **(C-E)** Additional information extracted from sptPALM and SAFe experiments. **C)** Super-resolved trajectories of mEos-Rac1-Q61L in the lamellipodium of a spreading MEF, obtained from a fast sptPALM acquisition with a sCMOS Camera at 333Hz (duration: 12s). Trajectories are overlaid on a lamellipodium expressing α-actinin-GFP and color-coded to show the different diffusion modes. **D)** Schematic of Rac1 optogenetic activation at the lamellipodium tip with CRY2-CIBN system. **E)** 3D super-resolution images obtained by SAFe in combination with dSTORM imaging using anti-GFP nanobodies for Kindlin2-WT and Kindlin2-ΔPH. For each pixel, the average axial localization of detected single molecules is color-coded.

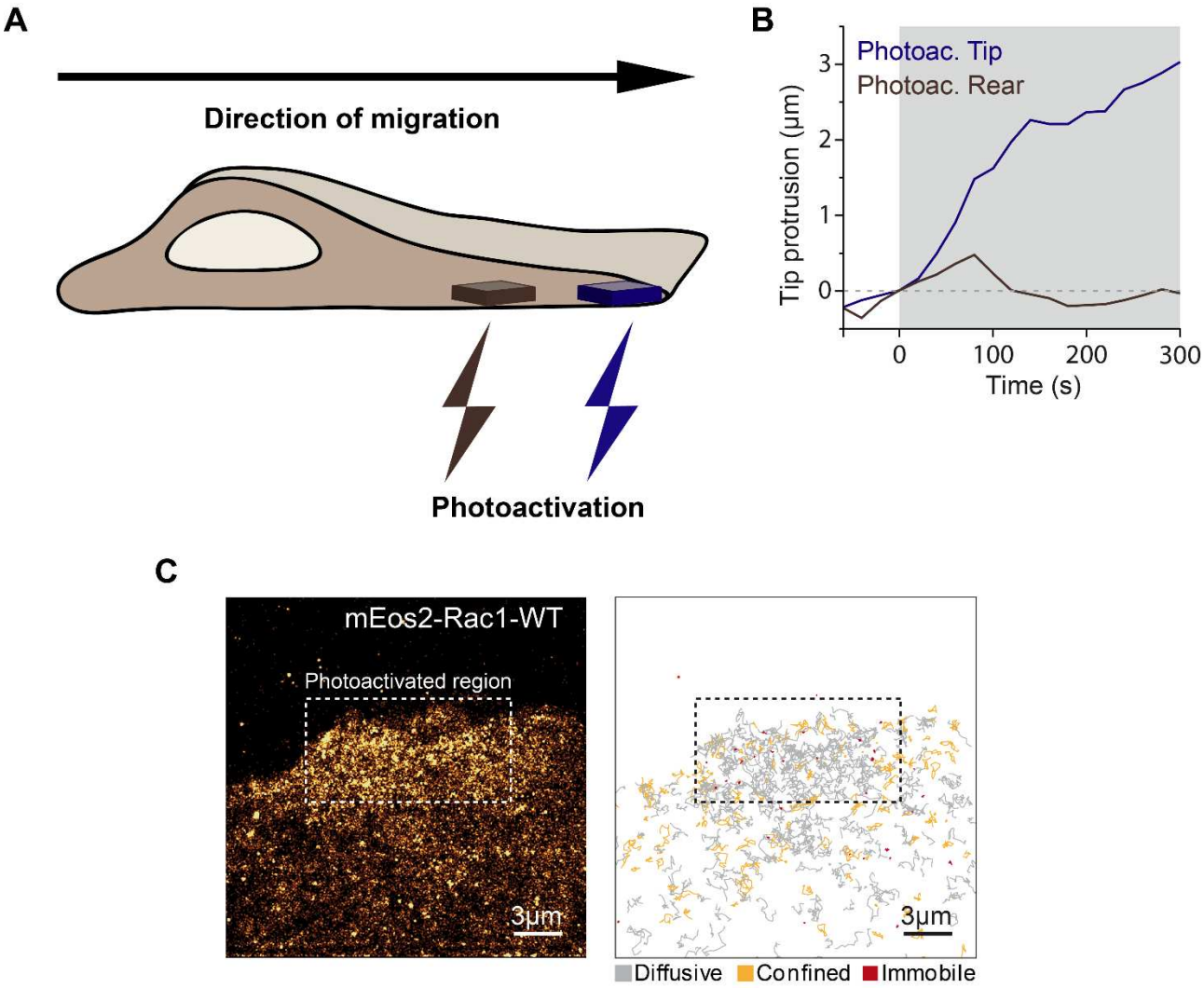

Figure 2: sptPALM coupled with optogenetic activation used to study molecular origins of lamellipodial protrusions in the context of integrin based migrations. A) Schematic representation of optogenetic Rac1 activation within the lamellipodial tip (blue) or the region at the rear of the lamellipodium (brown) of a migrating cell**. B)** Lamellipodium protrusion after photoactivation at the tip (blue or the rear (brown) as a function of time before and during photoactivation (gray area). **C)** Super-resolution intensity image obtained from a sptPALM acquisition of mEos2-Rac1-WT in the lamellipodium of a spreading MEF after optogenetic membrane recruitment of Tiam1-CRY2-IRFP (left; same cell as B). Corresponding trajectories are shown (right). Adapted from Mehidi, 2019 [48].

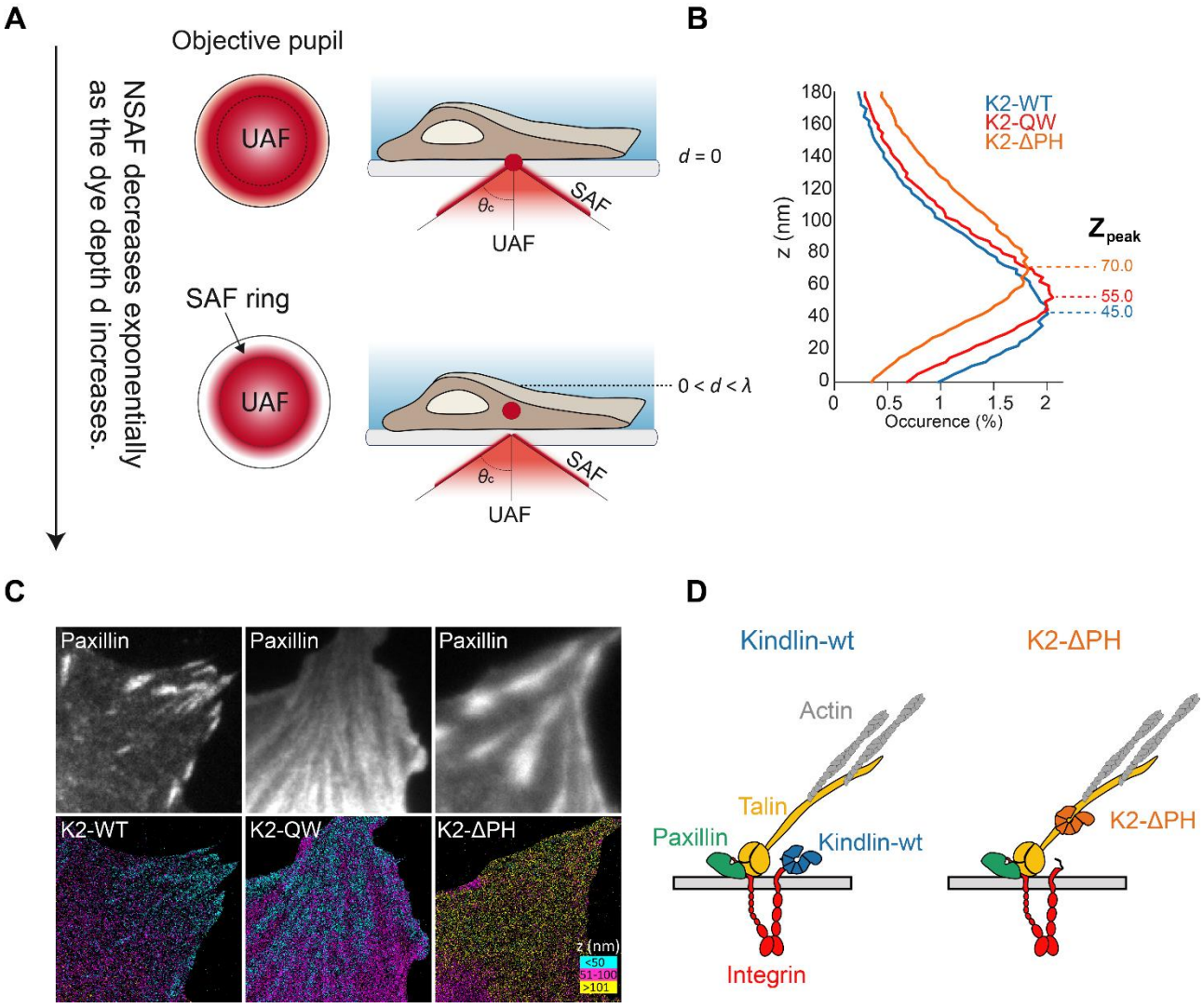

Figure 3. Illustration of SAF measurements in IAS revealing the 3-D organization of proteins. **A)** Principle of separation of Super-critical (SAF) and Under-critical angle fluorescence (UAF) using SAF ring, UAF intensity is nearly constant both for d=0 and for 0 < d < λemission, where as the near field SAF intensity in the annular region decreases with depth almost exponentially; Adapted from Bourg et al, Nat. Photonics, 2015 [79]. **B)** Changes in peak values of the height distributions of K2-WT and K2-QW are comparable (~50nm) whereas the peak value for K2-ΔPH showed significant changes **C)** Images with z(height) distribution of K2-WT, K2-QW and K2-ΔPH reconstructed from the DONALD measurements, detections for z <50nm represented in cyan, 50nm < z < 100nm in magenta and for z >100nm in yellow respectively, notice that K2-ΔPH detections are not enriched into IAS defined by paxillin fluorescence D) Schematic to illustrate the result that Kindlin-WT is at the membrane proximal integrin layer, whereas deletion of PH domain causes alteration in the axial distribution peaking at higher z-values, indicating that the PH domain is necessary for Kindlin localization to integrin nano-layer and enrichment in IAS.

REFERENCES

Abbe, E. (1873). Beiträge zur Theorie des Mikroskops und der mikroskopischen Wahrnehmung. Arch. Für Mikroskopische Anat.

Abbondanzieri, E.A., Greenleaf, W.J., Shaevitz, J.W., Landick, R., and Block, S.M. (2005). Direct observation of base-pair stepping by RNA polymerase. Nature.

Aermes, C., Hayn, A., Fischer, T., and Mierke, C.T. (2020). Environmentally controlled magnetic nano-tweezer for living cells and extracellular matrices. Sci. Rep.

Airy, G.B. (1835). On the Diffraction of an Object-glass with Circular Aperture. Trans. Cambridge Philos. Soc. *Vol. 5*, p.283.

Alcaino, C., Knutson, K.R., Treichel, A.J., Yildiz, G., Strege, P.R., Linden, D.R., Li, J.H., Leiter, A.B., Szurszewski, J.H., Farrugia, G., et al. (2018). A population of gut epithelial enterochromaffin cells is mechanosensitive and requires Piezo2 to convert force into serotonin release. Proc. Natl. Acad. Sci. U. S. A.

Alenghat, F.J., Fabry, B., Tsai, K.Y., Goldmann, W.H., and Ingber, D.E. (2000). Analysis of cell mechanics in single vinculin-deficient cells using a magnetic tweezer. Biochem. Biophys. Res. Commun.

Alexandrova, A.Y., Arnold, K., Schaub, S., Vasiliev, J.M., Meister, J.J., Bershadsky, A.D., and Verkhovsky, A.B. (2008). Comparative dynamics of retrograde actin flow and focal adhesions: Formation of nascent adhesions triggers transition from fast to slow flow. PLoS One.

Anishkin, A., Loukin, S.H., Teng, J., and Kung, C. (2014). Feeling the hidden mechanical forces in lipid bilayer is an original sense. Proc. Natl. Acad. Sci. U. S. A.

Anwar, M.A., Shalhoub, J., Lim, C.S., Gohel, M.S., and Davies, A.H. (2012). The effect of pressure-induced mechanical stretch on vascular wall differential gene expression. J. Vasc. Res.

Araki, I., Du, S., Kobayashi, H., Sawada, N., Mochizuki, T., Zakoji, H., and Takeda, M. (2008). Roles of mechanosensitive ion channels in bladder sensory transduction and overactive bladder. Int. J. Urol.

Arbore, C., Perego, L., Sergides, M., and Capitanio, M. (2019). Probing force in living cells with optical tweezers: from single-molecule mechanics to cell mechanotransduction. Biophys. Rev.

Ash, E.A., and Nicholls, G. (1972). Super-resolution aperture scanning microscope. Nature.

Ashkin, A. (1997). Optical trapping and manipulation of neutral particles using lasers. Proc. Natl. Acad. Sci. U. S. A.

Ashkin, A., Dziedzic, J.M., and Chu, S. (1986). Observation of a single-beam gradient-force optical trap for dielectric particles in air. Opt. Lett.

Atherton, P., Stutchbury, B., Wang, D.Y., Jethwa, D., Tsang, R., Meiler-Rodriguez, E., Wang, P., Bate, N., Zent, R., Barsukov, I.L., et al. (2015). Vinculin controls talin engagement with the actomyosin machinery. Nat. Commun. *6*.

Atherton, P., Stutchbury, B., Jethwa, D., and Ballestrem, C. (2016). Mechanosensitive

components of integrin adhesions: Role of vinculin. Exp. Cell Res. *343*, 21–27.

Atherton, P., Lausecker, F., Carisey, A., Gilmore, A., Critchley, D., Barsukov, I., and Ballestrem, C. (2020). Relief of talin autoinhibition triggers a force-independent association with vinculin. J. Cell Biol. *219*, 1–16.

Aumeier, C., Schaedel, L., Gaillard, J., John, K., Blanchoin, L., and Théry, M. (2016). Self-repair promotes microtubule rescue. Nat. Cell Biol. *18*, 1054–1064.

Austen, K., Ringer, P., Mehlich, A., Chrostek-Grashoff, A., Kluger, C., Klingner, C., Sabass, B., Zent, R., Rief, M., and Grashoff, C. (2015). Extracellular rigidity sensing by talin isoform-specific mechanical linkages. Nat. Cell Biol. *17*, 1597–1606.

Avery, A.W., Thomas, D.D., and Hays, T.S. (2017). β-III-spectrin spinocerebellar ataxia type 5 mutation reveals a dominant cytoskeletal mechanism that underlies dendritic arborization. Proc. Natl. Acad. Sci.

Bachir, A.I., Zareno, J., Moissoglu, K., Plow, E.F., Gratton, E., and Horwitz, A.R. (2014). Integrin-associated complexes form hierarchically with variable stoichiometry in nascent adhesions. Curr. Biol. *24*, 1845–1853.

Bai, L., Deng, X., Li, J., Wang, M., Li, Q., An, W., A, D., and Cong, Y.S. (2011). Regulation of cellular senescence by the essential caveolar component PTRF/Cavin-1. Cell Res.

Bakolitsa, C., Cohen, D.M., Bankston, L.A., Bobkov, A.A., Dadwell, G.W., Jennings, L., Crithcley, D.R., Craig, S.W., and Liddington, R.C. (2004). Structural basis for vinculin activation at sites of cell adhesion. Nature *430*, 583–586.

Balaban, N.Q., Schwarz, U.S., Riveline, D., Goichberg, P., Tzur, G., Sabanay, I., Mahalu, D., Safran, S., Bershadsky, A., Addadi, L., et al. (2001). Force and focal adhesion assembly: A close relationship studied using elastic micropatterned substrates. Nat. Cell Biol.

Ballestrem, C., Hinz, B., Imhof, B.A., and Wehrle-Haller, B. (2001). Marching at the front and dragging behind: Differential αVβ3-integrin turnover regulates focal adhesion behavior. J. Cell Biol.

Balzarotti, F., Eilers, Y., Gwosch, K.C., Gynnå, A.H., Westphal, V., Stefani, F.D., Elf, J., and Hell, S.W. (2017). Nanometer resolution imaging and tracking of fluorescent molecules with minimal photon fluxes. Science (80-.).

Banes, A.J. (2013). Out of academics: Education, entrepreneurship and enterprise. Ann. Biomed. Eng.

Bar-Kochba, E., Scimone, M.T., Estrada, J.B., and Franck, C. (2016). Strain and rate-dependent neuronal injury in a 3D in vitro compression model of traumatic brain injury. Sci. Rep.

Bär, J., Kobler, O., Van Bommel, B., and Mikhaylova, M. (2016). Periodic F-actin structures shape the neck of dendritic spines. Sci. Rep. *6*, 1–9.

Bard, L., Boscher, C., Lambert, M., Mège, R.M., Choquet, D., and Thoumine, O. (2008). A molecular clutch between the actin flow and N-cadherin adhesions drives growth cone migration. J. Neurosci.

Barnes, J.M., Przybyla, L., and Weaver, V.M. (2017). Tissue mechanics regulate brain development, homeostasis and disease. J. Cell Sci.

Bastiani, M., Liu, L., Hill, M.M., Jedrychowski, M.P., Nixon, S.J., Lo, H.P., Abankwa, D., Luetterforst, R., Fernandez-Rojo, M., Breen, M.R., et al. (2009). MURC/Cavin-4 and cavin family members form tissue-specific caveolar complexes. J. Cell Biol.

Bates, M., Huang, B., Dempsey, G.T., and Zhuang, X. (2007). Multicolor super-resolution imaging with photo-switchable fluorescent probes. Science (80-.). *317*, 1749–1753.

Bayly, P. V., Cohen, T.S., Leister, E.P., Ajo, D., Leuthardt, E.C., and Genin, G.M. (2005). Deformation of the human brain induced by mild acceleration. J. Neurotrauma.

Bays, J.L., and DeMali, K.A. (2017). Vinculin in cell–cell and cell–matrix adhesions. Cell. Mol. Life Sci. *74*, 2999–3009.

Beaulieu-Laroche, L., Christin, M., Donoghue, A., Agosti, F., Yousefpour, N., Petitjean, H., Davidova, A., Stanton, C., Khan, U., Dietz, C., et al. (2020). TACAN Is an Ion Channel Involved in Sensing Mechanical Pain. Cell *180*, 956-967.e17.

Behm, D.G., Blazevich, A.J., Kay, A.D., and McHugh, M. (2015). Acute effects of muscle stretching on physical performance, range of motion, and injury incidence in healthy active individuals: A systematic review. Appl. Physiol. Nutr. Metab.

Bennett, V., and Lorenzo, D.N. (2013). Spectrin- and Ankyrin-Based Membrane Domains and the Evolution of Vertebrates (Elsevier Inc.).

Berger, S.L., Leo-Macias, A., Yuen, S., Khatri, L., Pfennig, S., Zhang, Y., Agullo-Pascual, E., Caillol, G., Zhu, M.S., Rothenberg, E., et al. (2018). Localized Myosin II Activity Regulates Assembly and Plasticity of the Axon Initial Segment. Neuron.

Bergermann, F., Alber, L., Sahl, S.J., Engelhardt, J., and Hell, S.W. (2015). 2000-fold parallelized dual-color STED fluorescence nanoscopy. Opt. Express.

Bershadsky, A., Chausovsky, A., Becker, E., Lyubimova, A., and Geiger, B. (1996). Involvement of microtubules in the control of adhesion-dependent signal transduction. Curr. Biol.

Betzig, E., Patterson, G.H., Sougrat, R., Lindwasser, O.W., Olenych, S., Bonifacino, J.S., Davidson, M.W., Lippincott-Schwartz, J., and Hess, H.F. (2006). Imaging intracellular fluorescent proteins at nanometer resolution. Science (80-.).

Beugnon, J., Tuchendler, C., Marion, H., Gaëtan, A., Miroshnychenko, Y., Sortais, Y.R.P., Lance, A.M., Jones, M.P.A., Messin, G., Browaeys, A., et al. (2007). Two-dimensional transport and transfer of a single atomic qubit in optical tweezers. Nat. Phys.

Bianchi, F., Pereno, V., George, J.H., Thompson, M.S., and Ye, H. (2019). Membrane Mechanical Properties Regulate the Effect of Strain on Spontaneous Electrophysiology in Human iPSC-Derived Neurons. Neuroscience *404*, 165–174.

Bieling, P., Li, T. De, Weichsel, J., McGorty, R., Jreij, P., Huang, B., Fletcher, D.A., and Mullins, R.D. (2016). Force Feedback Controls Motor Activity and Mechanical Properties of Self-Assembling Branched Actin Networks. Cell *164*, 115–127.

Bisi, S., Disanza, A., Malinverno, C., Frittoli, E., Palamidessi, A., and Scita, G. (2013). Membrane and actin dynamics interplay at lamellipodia leading edge. Curr. Opin. Cell Biol.

Biyasheva, A., Svitkina, T., Kunda, P., Baum, B., and Borisy, G. (2004). Cascade pathway of filopodia formation downstream of SCAR. J. Cell Sci.

Blanchard, A.T., and Salaita, K. (2019). Emerging uses of DNA mechanical devices. Science (80-.). *365*, 1080–1081.

Blanchoin, L., Boujemaa-Paterski, R., Sykes, C., and Plastino, J. (2014). Actin dynamics, architecture, and mechanics in cell motility. Physiol. Rev. *94*, 235–263.

Block, J., Witt, H., Candelli, A., Danes, J.C., Peterman, E.J.G., Wuite, G.J.L., Janshoff, A., and Köster, S. (2018). Viscoelastic properties of vimentin originate from nonequilibrium conformational changes. Sci. Adv. *4*.

Block, S.M., Goldstein, L.S.B., and Schnapp, B.J. (1990). Bead movement by single kinesin molecules studied with optical tweezers. Nature.

Bonakdar, N., Luczak, J., Lautscham, L., Czonstke, M., Koch, T.M., Mainka, A., Jungbauer, T., Goldmann, W.H., Schröder, R., and Fabry, B. (2012). Biomechanical characterization of a desminopathy in primary human myoblasts. Biochem. Biophys. Res. Commun.

Bouchet, B.P., Gough, R.E., Ammon, Y.C., van de Willige, D., Post, H., Jacquemet, G., Maarten Altelaar, A.F., Heck, A.J.R., Goult, B.T., and Akhmanova, A. (2016). Talin-KANK1 interaction controls the recruitment of cortical microtubule stabilizing complexes to focal adhesions. Elife.

Bouissou, A., Proag, A., Bourg, N., Pingris, K., Cabriel, C., Balor, S., Mangeat, T., Thibault, C., Vieu, C., Dupuis, G., et al. (2017). Podosome Force Generation Machinery: A Local Balance between Protrusion at the Core and Traction at the Ring. ACS Nano.

Bourg, N., Mayet, C., Dupuis, G., Barroca, T., Bon, P., Lécart, S., Fort, E., and Lévêque-Fort, S. (2015). Direct optical nanoscopy with axially localized detection. Nat. Photonics *9*, 587–593.

Bouvard, D., Pouwels, J., De Franceschi, N., and Ivaska, J. (2013). Integrin inactivators: balancing cellular functions in vitro and in vivo. Nat. Rev. Mol. Cell Biol. *14*, 430–442.

Brangwynne, C.P., MacKintosh, F.C., and Weitz, D.A. (2007). Force fluctuations and polymerization dynamics of intracellular microtubules. Proc. Natl. Acad. Sci. U. S. A.

Brockman, J.M., Blanchard, A.T., Pui-Yan, V., Derricotte, W.D., Zhang, Y., Fay, M.E., Lam, W.A., Evangelista, F.A., Mattheyses, A.L., and Salaita, K. (2018). Mapping the 3D orientation of piconewton integrin traction forces. Nat. Methods *15*, 115–118.

Brockman, J.M., Su, H., Blanchard, A.T., Duan, Y., Meyer, T., Quach, M.E., Glazier, R., Bazrafshan, A., Bender, R.L., Kellner, A. V., et al. (2020). Live-cell super-resolved PAINT imaging of piconewton cellular traction forces. Nat. Methods.

Brohawn, S.G., Su, Z., and MacKinnon, R. (2014). Mechanosensitivity is mediated directly by the lipid membrane in TRAAK and TREK1 K+ channels. Proc. Natl. Acad. Sci. U. S. A.

Brouhard, G.J., and Rice, L.M. (2018). Microtubule dynamics: An interplay of biochemistry and mechanics. Nat. Rev. Mol. Cell Biol. *19*, 451–463.

Brown, J.W., Bullitt, E., Sriswasdi, S., Harper, S., Speicher, D.W., and McKnight, C.J. (2015). The Physiological Molecular Shape of Spectrin: A Compact Supercoil Resembling a Chinese Finger Trap. PLoS Comput. Biol. *11*, 1–20.

Buckley, C.D., Tan, J., Anderson, K.L., Hanein, D., Volkmann, N., Weis, W.I., Nelson, W.J., and Dunn, A.R. (2014). The minimal cadherin-catenin complex binds to actin filaments under force. Science (80-.). *346*.

Bukalo, O., Schachner, M., and Dityatev, A. (2007). Hippocampal metaplasticity induced by deficiency in the extracellular matrix glycoprotein tenascin-R. J. Neurosci.

Burnette, D.T., Manley, S., Sengupta, P., Sougrat, R., Davidson, M.W., Kachar, B., and Lippincott-Schwartz, J. (2011). A role for actin arcs in the leading-edge advance of migrating cells. Nat. Cell Biol.

Burridge, K., and Guilluy, C. (2016). Focal adhesions, stress fibers and mechanical tension. Exp. Cell Res. *343*, 14–20.

Buxboim, A., Swift, J., Irianto, J., Spinler, K.R., Dingal, P.C.D.P., Athirasala, A., Kao, Y.R.C., Cho, S., Harada, T., Shin, J.W., et al. (2014). Matrix elasticity regulates lamin-A,C phosphorylation and turnover with feedback to actomyosin. Curr. Biol.

Byron, A., Humphries, J.D., Craig, S.E., Knight, D., and Humphries, M.J. (2012). Proteomic analysis of α4β1 integrin adhesion complexes reveals α-subunit-dependent protein recruitment. Proteomics.

Cabriel, C., Bourg, N., Jouchet, P., Dupuis, G., Leterrier, C., Baron, A., Badet-Denisot, M.A., Vauzeilles, B., Fort, E., and Lévêque-Fort, S. (2019). Combining 3D single molecule localization strategies for reproducible bioimaging. Nat. Commun. *10*, 1–10.

Calderwood, D.A., Campbell, I.D., and Critchley, D.R. (2013). Talins and kindlins: Partners in integrin-mediated adhesion. Nat. Rev. Mol. Cell Biol.

Call, G.S., Chung, J.Y., Davis, J.A., Price, B.D., Primavera, T.S., Thomson, N.C., Wagner, M. V., and Hansen, M.D.H. (2011). Zyxin phosphorylation at serine 142 modulates the zyxin head-tail interaction to alter cell-cell adhesion. Biochem. Biophys. Res. Commun.

Carisey, A., Tsang, R., Greiner, A.M., Nijenhuis, N., Heath, N., Nazgiewicz, A., Kemkemer, R., Derby, B., Spatz, J., and Ballestrem, C. (2013). Vinculin regulates the recruitment and release of core focal adhesion proteins in a force-dependent manner. Curr. Biol. *23*, 271–281.

Carlsson, L., Nyström, L.E., Sundkvist, I., Markey, F., and Lindberg, U. (1977). Actin polymerizability is influenced by profilin, a low molecular weight protein in non-muscle cells. J. Mol. Biol.

Carrion-Vazquez, M., Li, H., Lu, H., Marszalek, P.E., Oberhauser, A.F., and Fernandez, J.M. (2003). The mechanical stability of ubiquitin is linkage dependent. Nat. Struct. Biol.

Carstens, K.E., Phillips, M.L., Pozzo-Miller, L., Weinberg, R.J., and Dudek, S.M. (2016). Perineuronal nets suppress plasticity of excitatory synapses on CA2 pyramidal neurons. J. Neurosci.

Case, L.B., and Waterman, C.M. (2015). Integration of actin dynamics and cell adhesion by a three-dimensional, mechanosensitive molecular clutch. Nat. Cell Biol.

Case, L.B., Baird, M.A., Shtengel, G., Campbell, S.L., Hess, H.F., Davidson, M.W., and Waterman, C.M. (2015). Molecular mechanism of vinculin activation and nanoscale spatial organization in focal adhesions. Nat. Cell Biol. *17*, 880–892.

Cattaruzza, M., Lattrich, C., and Hecker, M. (2004). Focal Adhesion Protein Zyxin is a Mechanosensitive Modulator of Gene Expression in Vascular Smooth Muscle Cells. Hypertension.

Celli, L., Ryckewaert, J.-J., Delachanal, E., and Duperray, A. (2006). Evidence of a Functional Role for Interaction between ICAM-1 and Nonmuscle α-Actinins in Leukocyte Diapedesis. J. Immunol.

Chamma, I., and Thoumine, O. (2018). Dynamics, nanoscale organization, and function of synaptic adhesion molecules. Mol. Cell. Neurosci.

Charrier, C., Machado, P., Tweedie-Cullen, R.Y., Rutishauser, D., Mansuy, I.M., and Triller, A. (2010). A crosstalk between β1 and β3 integrins controls glycine receptor and gephyrin trafficking at synapses. Nat. Neurosci. *13*, 1388–1395.

Chazeau, A., Mehidi, A., Nair, D., Gautier, J.J., Leduc, C., Chamma, I., Kage, F., Kechkar, A., Thoumine, O., Rottner, K., et al. (2014). Nanoscale segregation of actin nucleation and elongation factors determines dendritic spine protrusion. EMBO J. *33*, 2745–2764.

Chazeau, A., Garcia, M., Czöndör, K., Perrais, D., Tessier, B., Giannone, G., and Thoumine, O. (2015). Mechanical coupling between transsynaptic N-cadherin adhesions and actin flow stabilizes dendritic spines. Mol. Biol. Cell.

Cheah, J.S., Jacobs, K.A., Heinrich, V., Lo, S.H., and Yamada, S. (2019). Force-induced recruitment of cten along keratin network in epithelial cells. Proc. Natl. Acad. Sci. U. S. A.

Chen, H., Choudhury, D.M., and Craig, S.W. (2006). Coincidence of actin filaments and talin is required to activate vinculin. J. Biol. Chem.

Chen, Y., Pasapera, A.M., Koretsky, A.P., and Waterman, C.M. (2013). Orientation-specific responses to sustained uniaxial stretching in focal adhesion growth and turnover. Proc. Natl. Acad. Sci. U. S. A. *110*, E2352-61.

Chen, Y., Lee, H., Tong, H., Schwartz, M., and Zhu, C. (2017). Force regulated conformational change of integrin αVβ3. Matrix Biol.

Chen, Z., Borek, D., Padrick, S.B., Gomez, T.S., Metlagel, Z., Ismail, A.M., Umetani, J., Billadeau, D.D., Otwinowski, Z., and Rosen, M.K. (2010). Structure and control of the actin regulatory WAVE complex. Nature *468*, 533–538.

Chinthalapudi, K., Rangarajan, E.S., Patil, D.N., George, E.M., Brown, D.T., and Izard, T. (2014). Lipid binding promotes oligomerization and focal adhesion activity of vinculin. J. Cell Biol.

Chmyrov, A., Keller, J., Grotjohann, T., Ratz, M., D'Este, E., Jakobs, S., Eggeling, C., and Hell, S.W. (2013). Nanoscopy with more than 100,000 "doughnuts." Nat. Methods.

Choi, C.K., Vicente-Manzanares, M., Zareno, J., Whitmore, L.A., Mogilner, A., and Horwitz, A.R. (2008). Actin and α-actinin orchestrate the assembly and maturation of nascent adhesions in a myosin II motor-independent manner. Nat. Cell Biol. *10*, 1039–1050.

Choquet, D., Felsenfeld, D.P., and Sheetz, M.P. (1997). Extracellular matrix rigidity causes strengthening of integrin- cytoskeleton linkages. Cell.

Chronopoulos, A., Thorpe, S.D., Cortes, E., Lachowski, D., Rice, A.J., Mykuliak, V. V., Róg, T., Lee, D.A., Hytönen, V.P., and del Río Hernández, A.E. (2020). Syndecan-4 tunes cell mechanics by activating the kindlin-integrin-RhoA pathway. Nat. Mater.

Cingolani, L.A., Thalhammer, A., Yu, L.M.Y., Catalano, M., Ramos, T., Colicos, M.A., and Goda, Y. (2008). Activity-Dependent Regulation of Synaptic AMPA Receptor Composition and Abundance by β3 Integrins. Neuron *58*, 749–762.

Ciobanasu, C., Faivre, B., and Le Clainche, C. (2014). Actomyosin-dependent formation of the mechanosensitive talin-vinculin complex reinforces actin anchoring. Nat. Commun. *5*, 3095.

Cirka, H., Monterosso, M., Diamantides, N., Favreau, J., Wen, Q., and Billiar, K. (2016). Active Traction Force Response to Long-Term Cyclic Stretch Is Dependent on Cell Pre-stress. Biophys. J. *110*, 1845–1857.

Cluzel, C., Saltel, F., Lussi, J., Paulhe, F., Imhof, B.A., and Wehrle-Haller, B. (2005). The mechanisms and dynamics of αvβ3 integrin clustering in living cells. J. Cell Biol.

Cohen, D.M., Chen, H., Johnson, R.P., Choudhury, B., and Craig, S.W. (2005). Two distinct head-tail interfaces cooperate to suppress activation of vinculin by talin. J. Biol. Chem.

Costa, A.R., Pinto-Costa, R., Sousa, S.C., and Sousa, M.M. (2018). The Regulation of Axon Diameter: From Axonal Circumferential Contractility to Activity-Dependent Axon Swelling. Front. Mol. Neurosci.

Costa, A.R., Sousa, S.C., Pinto-Costa, R., Mateus, J.C., Lopes, C.D.F., Costa, A.C., Rosa, D., Machado, D., Pajuelo, L., Wang, X., et al. (2020). The membrane periodic skeleton is an actomyosin network that regulates axonal diameter and conduction. Elife.

Coste, B., Mathur, J., Schmidt, M., Earley, T.J., Ranade, S., Petrus, M.J., Dubin, A.E., and Patapoutian, A. (2010). Piezo1 and Piezo2 are essential components of distinct mechanically activated cation channels. Science (80-.).

Courtemanche, N., Lee, J.Y., Pollard, T.D., and Greene, E.C. (2013). Tension modulates actin filament polymerization mediated by formin and profilin. Proc. Natl. Acad. Sci. U. S. A.

Cui, Y., Hameed, F.M., Yang, B., Lee, K., Pan, C.Q., Park, S., and Sheetz, M. (2015). Cyclic stretching of soft substrates induces spreading and growth. Nat. Commun. *6*, 1–8.

Cukierman, E., Pankov, R., Stevens, D.R., and Yamada, K.M. (2001). Taking cell-matrix adhesions to the third dimension. Science (80-.).

D'Este, E., Kamin, D., Göttfert, F., El-Hady, A., and Hell, S.W. (2015). STED Nanoscopy Reveals the Ubiquity of Subcortical Cytoskeleton Periodicity in Living Neurons. Cell Rep.

D'Este, E., Kamin, D., Velte, C., Göttfert, F., Simons, M., and Hell, S.W. (2016). Subcortical cytoskeleton periodicity throughout the nervous system. Sci. Rep.

D'Este, E., Kamin, D., Balzarotti, F., and Hell, S.W. (2017). Ultrastructural anatomy of nodes of Ranvier in the peripheral nervous system as revealed by STED microscopy. Proc. Natl. Acad. Sci.

Dahm, R., Zeitelhofer, M., Götze, B., Kiebler, M.A., and Macchi, P. (2008). Visualizing mRNA Localization and Local Protein Translation in Neurons. Methods Cell Biol.

Danzl, J.G., Sidenstein, S.C., Gregor, C., Urban, N.T., Ilgen, P., Jakobs, S., and Hell, S.W. (2016). Coordinate-targeted fluorescence nanoscopy with multiple off states. Nat. Photonics.

Das, R., Wieser, S., and Krieg, M. (2019). Neuronal stretch reception – Making sense of the mechanosense. Exp. Cell Res. *378*, 104–112.

Dedden, D., Schumacher, S., Kelley, C.F., Zacharias, M., Biertümpfel, C., Fässler, R., and Mizuno, N. (2019). The Architecture of Talin1 Reveals an Autoinhibition Mechanism. Cell.

Delloye-Bourgeois, C., Jacquier, A., Falk, J., and Castellani, V. (2014). Use of pHluorin to assess

the dynamics of axon guidance receptors in cell culture and in the chick embryo. J. Vis. Exp. 1–8.

DeMali, K.A., Barlow, C.A., and Burridge, K. (2002). Recruitment of the Arp2/3 complex to vinculin: Coupling membrane protrusion to matrix adhesion. J. Cell Biol.

DePoy, L.M., Shapiro, L.P., Kietzman, H.W., Roman, K.M., and Gourley, S.L. (2019). β1-Integrins in the Developing Orbitofrontal Cortex Are Necessary for Expectancy Updating in Mice. J. Neurosci.

Derényi, I., Jülicher, F., and Prost, J. (2002). Formation and Interaction of Membrane Tubes. Phys. Rev. Lett.

Despotović, S.Z., Milićević, Đ.N., Krmpot, A.J., Pavlović, A.M., Živanović, V.D., Krivokapić, Z., Pavlović, V.B., Lević, S., Nikolić, G., and Rabasović, M.D. (2020). Altered organization of collagen fibers in the uninvolved human colon mucosa 10 cm and 20 cm away from the malignant tumor. Sci. Rep.

Dickson, R.M., Cubittt, A.B., Tsient, R.Y., and Moerner, W.E. (1997). On/off blinking and switching behaviour of single molecules of green fluorescent protein. Nature.

Dietz, H., Berkemeier, F., Bertz, M., and Rief, M. (2006). Anisotropic deformation response of single protein molecules. Proc. Natl. Acad. Sci. U. S. A.

Dmitrieff, S., and Nédélec, F. (2016). Amplification of actin polymerization forces. J. Cell Biol.

van den Dries, K., Nahidiazar, L., Slotman, J.A., Meddens, M.B.M., Pandzic, E., Joosten, B., Ansems, M., Schouwstra, J., Meijer, A., Steen, R., et al. (2019a). Modular actin nano-architecture enables podosome protrusion and mechanosensing. Nat. Commun.

van den Dries, K., Linder, S., Maridonneau-Parini, I., and Poincloux, R. (2019b). Probing the mechanical landscape – new insights into podosome architecture and mechanics. J. Cell Sci.

Van Den Dries, K., Meddens, M.B.M., De Keijzer, S., Shekhar, S., Subramaniam, V., Figdor, C.G., and Cambi, A. (2013). Interplay between myosin IIA-mediated contractility and actin network integrity orchestrates podosome composition and oscillations. Nat. Commun.

Duan, R., Kim, J.H., Shilagardi, K., Schiffhauer, E.S., Lee, D.M., Son, S., Li, S., Thomas, C., Luo, T., Fletcher, D.A., et al. (2018). Spectrin is a mechanoresponsive protein shaping fusogenic synapse architecture during myoblast fusion. Nat. Cell Biol. *20*, 688–698.

Duarte, S., Viedma-Poyatos, Á., Navarro-Carrasco, E., Martínez, A.E., Pajares, M.A., and Pérez-Sala, D. (2019). Vimentin filaments interact with the actin cortex in mitosis allowing normal cell division. Nat. Commun.

Dubey, S., Bhembre, N., Bodas, S., Ghose, A., Callan-Jones, A., and Pullarkat, P. (2019). The axonal actin-spectrin lattice acts as a tension buffering shock absorber. BioRxiv 510560.

Dubey, S., Bhembre, N., Bodas, S., Veer, S., Ghose, A., Callan-Jones, A., Pullarkat, P., and Sens, P. (2020). The axonal actin-spectrin lattice acts as a tension buffering shock absorber. Elife.

DuChez, B.J., Doyle, A.D., Dimitriadis, E.K., and Yamada, K.M. (2019). Durotaxis by Human Cancer Cells. Biophys. J.

Dufrêne, Y.F., Ando, T., Garcia, R., Alsteens, D., Martinez-Martin, D., Engel, A., Gerber, C., and Müller, D.J. (2017). Imaging modes of atomic force microscopy for application in molecular and

cell biology. Nat. Nanotechnol. *12*, 295–307.

Dumont, S., Salmon, E.D., and Mitchison, T.J. (2012a). Deformations within moving kinetochores reveal different sites of active and passive force generation. Science *337*, 355–358.

Dumont, S., Salmon, E.D., and Mitchison, T.J. (2012b). Deformations within moving kinetochores reveal different sites of active and passive force generation. Science (80-.).

Dupont, S., Morsut, L., Aragona, M., Enzo, E., Giulitti, S., Cordenonsi, M., Zanconato, F., Le Digabel, J., Forcato, M., Bicciato, S., et al. (2011). Role of YAP/TAZ in mechanotransduction. Nature.

Dutta, P.K., Zhang, Y., Blanchard, A.T., Ge, C., Rushdi, M., Weiss, K., Zhu, C., Ke, Y., and Salaita, K. (2018). Programmable Multivalent DNA-Origami Tension Probes for Reporting Cellular Traction Forces. Nano Lett.

Dzhashiashvili, Y., Zhang, Y., Galinska, J., Lam, I., Grumet, M., and Salzer, J.L. (2007). Nodes of Ranvier and axon initial segments are ankyrin G-dependent domains that assemble by distinct mechanisms. J. Cell Biol.

Efimova, N., and Svitkina, T.M. (2018). Branched actin networks push against each other at adherens junctions to maintain cell-cell adhesion. J. Cell Biol.

Eghiaian, F., Rigato, A., and Scheuring, S. (2015). Structural, mechanical, and dynamical variability of the actin cortex in living cells. Biophys. J.

Ehrlicher, A.J., Nakamura, F., Hartwig, J.H., Weitz, D.A., and Stossel, T.P. (2011). Mechanical strain in actin networks regulates FilGAP and integrin binding to filamin A. Nature *478*, 260–263.

Elosegui-Artola, A., Oria, R., Chen, Y., Kosmalska, A., Pérez-González, C., Castro, N., Zhu, C., Trepat, X., and Roca-Cusachs, P. (2016). Mechanical regulation of a molecular clutch defines force transmission and transduction in response to matrix rigidity. Nat. Cell Biol. *18*, 540–548.

Etienne-Manneville, S. (2013). Microtubules in cell migration. Annu. Rev. Cell Dev. Biol.

Evans, E., and Kinoshita, K. (2007). Using Force to Probe Single-Molecule Receptor-Cytoskeletal Anchoring Beneath the Surface of a Living Cell. Methods Cell Biol.

Evans, E.A., and Calderwood, D.A. (2007). Forces and bond dynamics in cell adhesion.

Evans, E., Leung, A., Heinrich, V., and Zhu, C. (2004). Mechanical switching and coupling between two dissociation pathways in a P-selectin adhesion bond. Proc. Natl. Acad. Sci. U. S. A.

Ezratty, E.J., Partridge, M.A., and Gundersen, G.G. (2005). Microtubule-induced focal adhesion disassembly is mediated by dynamin and focal adhesion kinase. Nat. Cell Biol.

Fantetti, K.N., and Fekete, D.M. (2011). Dissection and culture of chick statoacoustic ganglion and spinal cord explants in collagen gels for neurite outgrowth assays. J. Vis. Exp.

Faust, U., Hampe, N., Rubner, W., Kirchgeßner, N., Safran, S., Hoffmann, B., and Merkel, R. (2011). Cyclic stress at mHz frequencies aligns fibroblasts in direction of zero strain. PLoS One.

Fazal, F.M., Koslover, D.J., Luisi, B.F., and Block, S.M. (2015). Direct observation of processive exoribonuclease motion using optical tweezers. Proc. Natl. Acad. Sci. U. S. A.

Feng, W., and Zhang, M. (2009). Organization and dynamics of PDZ-domain-related supramodules in the postsynaptic density. Nat. Rev. Neurosci.

Feng, Y., Abney, T.M., Okamoto, R.J., Pless, R.B., Genin, G.M., and Bayly, P. V. (2010). Relative brain displacement and deformation during constrained mild frontal head impact. J. R. Soc. Interface.

Feng, Y., Brazin, K.N., Kobayashi, E., Mallis, R.J., Reinherz, E.L., and Lang, M.J. (2017). Mechanosensing drives acuity of αβ T-cell recognition. Proc. Natl. Acad. Sci. U. S. A.

Fife, C.M., McCarroll, J.A., and Kavallaris, M. (2014). Movers and shakers: Cell cytoskeleton in cancer metastasis. Br. J. Pharmacol.

Foley, E.A., and Kapoor, T.M. (2013). Microtubule attachment and spindle assembly checkpoint signalling at the kinetochore. Nat. Rev. Mol. Cell Biol.

Footer, M.J., Kerssemakers, J.W.J., Theriot, J.A., and Dogterom, M. (2007). Direct measurement of force generation by actin filament polymerization using an optical trap. Proc. Natl. Acad. Sci. U. S. A.

Förster, E., Tielsch, A., Saum, B., Weiss, K.H., Johanssen, C., Graus-Porta, D., Müller, U., and Frotscher, M. (2002). Reelin, disabled 1, and β1 integrins are required for the formation of the radial glial scaffold in the hippocampus. Proc. Natl. Acad. Sci. U. S. A.

Franker, M.A.M., and Hoogenraad, C.C. (2013). Microtubule-based transport -basic mechanisms, traffic rules and role in neurological pathogenesis. J. Cell Sci.

Friedland, J.C., Lee, M.H., and Boettiger, D. (2009). Mechanically activated integrin switch controls alpha5beta1 function. Science (80-.). *323*, 642–644.

Frischknecht, R., Heine, M., Perrais, D., Seidenbecher, C.I., Choquet, D., and Gundelfinger, E.D. (2009). Brain extracellular matrix affects AMPA receptor lateral mobility and short-term synaptic plasticity. Nat. Neurosci. *12*, 897–904.

Fritz, J., Katopodis, A.G., Kolbinger, F., and Anselmetti, D. (1998). Force-mediated kinetics of single P-selectin/ligand complexes observed by atomic force microscopy. Proc. Natl. Acad. Sci. U. S. A.

Fujiwara, S., Ohashi, K., Mashiko, T., Kondo, H., and Mizuno, K. (2016). Interplay between Solo and keratin filaments is crucial for mechanical forceinduced stress fiber reinforcement. Mol. Biol. Cell.

Galbraith, C.G., Yamada, K.M., and Sheetz, M.P. (2002). The relationship between force and focal complex development. J. Cell Biol. *159*, 695–705.

Galiano, M.R., Jha, S., Ho, T.S.Y., Zhang, C., Ogawa, Y., Chang, K.J., Stankewich, M.C., Mohler, P.J., and Rasband, M.N. (2012). A distal axonal cytoskeleton forms an intra-axonal boundary that controls axon initial segment assembly. Cell.

Galkin, V.E., Orlova, A., Kudryashov, D.S., Solodukhin, A., Reisler, E., Schröder, G.F., and Egelman, E.H. (2011). Remodeling of actin filaments by ADF/cofilin proteins. Proc. Natl. Acad. Sci. U. S. A.

Gao, H., Metz, J., Teanby, N.A., Ward, A.D., Botchway, S.W., Coles, B., Pollard, M.R., and Sparkes, I. (2016). In vivo quantification of peroxisome tethering to chloroplasts in tobacco

epidermal cells using optical tweezers1[OPEN]. Plant Physiol.

Gao, R., Asano, S.M., Upadhyayula, S., Pisarev, I., Milkie, D.E., Liu, T.L., Singh, V., Graves, A., Huynh, G.H., Zhao, Y., et al. (2019). Cortical column and whole-brain imaging with molecular contrast and nanoscale resolution. Science (80-.). *363*.

Gao, X., Acharya, B.R., Engl, W.C.O., De Mets, R., Thiery, J.P., Yap, A.S., and Viasnoff, V. (2018). Probing compression versus stretch activated recruitment of cortical actin and apical junction proteins using mechanical stimulations of suspended doublets. APL Bioeng.

Gardel, M.L., Sabass, B., Ji, L., Danuser, G., Schwarz, U.S., and Waterman, C.M. (2008). Traction stress in focal adhesions correlates biphasically with actin retrograde fl ow speed. J. Cell Biol.

Geiger, B., and Yamada, K.M. (2011). Molecular architecture and function of matrix adhesions. Cold Spring Harb. Perspect. Biol.

Giannone, G., and Sheetz, M.P. (2006). Substrate rigidity and force define form through tyrosine phosphatase and kinase pathways. Trends Cell Biol.

Giannone, G., Jiang, G., Sutton, D.H., Critchley, D.R., and Sheetz, M.P. (2003). Talin1 is critical for force-dependent reinforcement of initial integrin-cytoskeleton bonds but not tyrosine kinase activation. J. Cell Biol. *163*, 409–419.

Giannone, G., Dubin-Thaler, B.J., Döbereiner, H.G., Kieffer, N., Bresnick, A.R., and Sheetz, M.P. (2004). Periodic lamellipodial contractions correlate with rearward actin waves. Cell *116*, 431–443.

Giannone, G., Dubin-Thaler, B.J., Rossier, O., Cai, Y., Chaga, O., Jiang, G., Beaver, W., Döbereiner, H.G., Freund, Y., Borisy, G., et al. (2007). Lamellipodial Actin Mechanically Links Myosin Activity with Adhesion-Site Formation. Cell *128*, 561–575.

Giannone, G., Mège, R.M., and Thoumine, O. (2009). Multi-level molecular clutches in motile cell processes. Trends Cell Biol. *19*, 475–486.

Giannone, G., Hosy, E., Levet, F., Constals, A., Schulze, K., Sobolevsky, A.I.I., Rosconi, M.P., Gouaux, E., Tampe, R., Choquet, D., et al. (2010). Dynamic superresolution imaging of endogenous proteins on living cells at ultra-high density. Biophys J *99*, 1303–1310.

Giannone, G., Mondin, M., Grillo-Bosch, D., Tessier, B., Saint-Michel, E., Czöndör, K., Sainlos, M., Choquet, D., and Thoumine, O. (2013). Neurexin-1β Binding to Neuroligin-1 Triggers the Preferential Recruitment of PSD-95 versus Gephyrin through Tyrosine Phosphorylation of Neuroligin-1. Cell Rep.

Gittes, F., Mickey, B., Nettleton, J., and Howard, J. (1993). Flexural rigidity of microtubules and actin filaments measured from thermal fluctuations in shape. J. Cell Biol.

Goetz, J.G., Minguet, S., Navarro-Lérida, I., Lazcano, J.J., Samaniego, R., Calvo, E., Tello, M., Osteso-Ibáñez, T., Pellinen, T., Echarri, A., et al. (2011). Biomechanical remodeling of the microenvironment by stromal caveolin-1 favors tumor invasion and metastasis. Cell.

Goetz, J.G., Steed, E., Ferreira, R.R., Roth, S., Ramspacher, C., Boselli, F., Charvin, G., Liebling, M., Wyart, C., Schwab, Y., et al. (2014). Endothelial cilia mediate low flow sensing during zebrafish vascular development. Cell Rep.

Goforth, P.B., Ren, J., Schwartz, B.S., and Satin, L.S. (2011). Excitatory synaptic transmission and

network activity are depressed following mechanical injury in cortical neurons. J. Neurophysiol.

Gosse, C., and Croquette, V. (2002). Magnetic tweezers: Micromanipulation and force measurement at the molecular level. Biophys. J.

Gough, R.E., and Goult, B.T. (2018). The tale of two talins – two isoforms to fine-tune integrin signalling. FEBS Lett.

Goult, B.T., Bate, N., Anthis, N.J., Wegener, K.L., Gingras, A.R., Patel, B., Barsukov, I.L., Campbell, I.D., Roberts, G.C.K., and Critchley, D.R. (2009). The structure of an interdomain complex that regulates Talin activity. J. Biol. Chem.

Goult, B.T., Yan, J., and Schwartz, M.A. (2018). Talin as a mechanosensitive signaling hub. J. Cell Biol. *217*, 3776–3784.

Grande-García, A., Echarri, A., De Rooij, J., Alderson, N.B., Waterman-Storer, C.M., Valdivielso, J.M., and Del Pozo, M.A. (2007). Caveolin-1 regulates cell polarization and directional migration through Src kinase and Rho GTPases. J. Cell Biol.

Grant, S.G.N. (2012). Synaptopathies: Diseases of the synaptome. Curr. Opin. Neurobiol.

Grashoff, C., Hoffman, B.D., Brenner, M.D., Zhou, R., Parsons, M., Yang, M.T., McLean, M.A., Sligar, S.G., Chen, C.S., Ha, T., et al. (2010). Measuring mechanical tension across vinculin reveals regulation of focal adhesion dynamics. Nature *466*, 263–266.

Grotjohann, T., Testa, I., Leutenegger, M., Bock, H., Urban, N.T., Lavoie-Cardinal, F., Willig, K.I., Eggeling, C., Jakobs, S., and Hell, S.W. (2011). Diffraction-unlimited all-optical imaging and writing with a photochromic GFP. Nature.

Gwosch, K.C., Pape, J.K., Balzarotti, F., Hoess, P., Ellenberg, J., Ries, J., and Hell, S.W. (2020). MINFLUX nanoscopy delivers 3D multicolor nanometer resolution in cells. Nat. Methods.

Hall, M.S., Alisafaei, F., Ban, E., Feng, X., Hui, C.Y., Shenoy, V.B., and Wu, M. (2016). Fibrous nonlinear elasticity enables positive Mechanical feedback between cells and ECMs. Proc. Natl. Acad. Sci. U. S. A.

Han, M.K.L., and de Rooij, J. (2016). Converging and Unique Mechanisms of Mechanotransduction at Adhesion Sites. Trends Cell Biol. *26*, 612–623.

Han, B., Zhou, R., Xia, C., and Zhuang, X. (2017). Structural organization of the actin-spectrin–based membrane skeleton in dendrites and soma of neurons. Proc. Natl. Acad. Sci. *114*, E6678–E6685.

Harasim, M., Wunderlich, B., Peleg, O., Kröger, M., and Bausch, A.R. (2013). Direct observation of the dynamics of semiflexible polymers in shear flow. Phys. Rev. Lett.

Harris, A.R., Jreij, P., and Fletcher, D.A. (2018). Mechanotransduction by the Actin Cytoskeleton: Converting Mechanical Stimuli into Biochemical Signals. Annu. Rev. Biophys. *47*, 617–631.

Havel, L.S., Kline, E.R., Salgueiro, A.M., and Marcus, A.I. (2014). Vimentin regulates lung cancer cell adhesion through a VAV2-Rac1 pathway to control focal adhesion kinase activity. Oncogene.

Hawkins, T., Mirigian, M., Selcuk Yasar, M., and Ross, J.L. (2010). Mechanics of microtubules. J. Biomech.

Hayakawa, K., Sakakibara, S., Sokabe, M., and Tatsumi, H. (2014). Single-molecule imaging and kinetic analysis of cooperative cofilin-actin filament interactions. Proc. Natl. Acad. Sci. U. S. A.

He, J., Zhou, R., Wu, Z., Carrasco, M.A., Kurshan, P.T., Farley, J.E., Simon, D.J., Wang, G., Han, B., Hao, J., et al. (2016). Prevalent presence of periodic actin–spectrin-based membrane skeleton in a broad range of neuronal cell types and animal species. Proc. Natl. Acad. Sci. *113*, 6029–6034.

Helfand, B.T., Mendez, M.G., Murthy, S.N.P., Shumaker, D.K., Grin, B., Mahammad, S., Aebi, U., Wedig, T., Wu, Y.I., Hahn, K.M., et al. (2011). Vimentin organization modulates the formation of lamellipodia. Mol. Biol. Cell.

Hell, S.W., and Wichmann, J. (1994). Breaking the diffraction resolution limit by stimulated emission: stimulated-emission-depletion fluorescence microscopy. Opt. Lett. *19*, 780.

Helms, G., Dasanna, A.K., Schwarz, U.S., and Lanzer, M. (2016). Modeling cytoadhesion of Plasmodium falciparum-infected erythrocytes and leukocytes—common principles and distinctive features. FEBS Lett.

Van Helvert, S., Storm, C., and Friedl, P. (2018). Mechanoreciprocity in cell migration. Nat. Cell Biol. *20*, 8–20.

Herrmann, H., and Aebi, U. (2016). Intermediate filaments: Structure and assembly. Cold Spring Harb. Perspect. Biol.

Heuzé, M.L., Sankara Narayana, G.H.N., D'Alessandro, J., Cellerin, V., Dang, T., Williams, D.S., Van Hest, J.C.M., Marcq, P., Mège, R.M., and Ladoux, B. (2019). Myosin II isoforms play distinct roles in adherens junction biogenesis. Elife *8*, 1–30.

Himmel, M., Ritter, A., Rothemund, S., Pauling, B. V., Rottner, K., Gingras, A.R., and Ziegler, W.H. (2009). Control of high affinity interactions in the Talin C terminus: How Talin domains coordinate protein dynamics in cell adhesions. J. Biol. Chem.

Hirata, H., Tatsumi, H., and Sokabe, M. (2008). Mechanical forces facilitate actin polymerization at focal adhesions in a zyxin-dependent manner. J. Cell Sci. *121*, 2795–2804.

Hochbaum, D.R., Zhao, Y., Farhi, S.L., Klapoetke, N., Werley, C.A., Kapoor, V., Zou, P., Kralj, J.M., MacLaurin, D., Smedemark-Margulies, N., et al. (2014). All-optical electrophysiology in mammalian neurons using engineered microbial rhodopsins. Nat. Methods.

Hoffman, B.D., Grashoff, C., and Schwartz, M.A. (2011). Dynamic molecular processes mediate cellular mechanotransduction. Nature.

Hoffman, L.M., Jensen, C.C., Chaturvedi, A., Yoshigi, M., and Beckerle, M.C. (2012). Stretch-induced actin remodeling requires targeting of zyxin to stress fibers and recruitment of actin regulators. Mol. Biol. Cell *23*, 1846–1859.

Hoffmann, J., Fermin, Y., Stricker, R. LO, Ickstadt, K., and Zamir, E. (2014). Symmetric exchange of multi-protein building blocks between stationary focal adhesions and the cytosol. Elife *3*, 1–18.

Holmes, K.C., Popp, D., Gebhard, W., and Kabsch, W. (1990). Atomic model of the actin filament. Nature.

Horton, E.R., Byron, A., Askari, J.A., Ng, D.H.J., Millon-Frémillon, A., Robertson, J., Koper, E.J., Paul, N.R., Warwood, S., Knight, D., et al. (2015). Definition of a consensus integrin adhesome

and its dynamics during adhesion complex assembly and disassembly. Nat. Cell Biol. *17*, 1577–1587.

Hotulainen, P., and Hoogenraad, C.C. (2010). Actin in dendritic spines: Connecting dynamics to function. J. Cell Biol.

Hotulainen, P., and Lappalainen, P. (2006). Stress fibers are generated by two distinct actin assembly mechanisms in motile cells. J. Cell Biol. *173*, 383–394.

Howard, J., and Garzon-Coral, C. (2017). Physical Limits on the Precision of Mitotic Spindle Positioning by Microtubule Pushing forces: Mechanics of mitotic spindle positioning. BioEssays.

Hsu, H.J., Lee, C.F., Locke, A., Vanderzyl, S.Q., and Kaunas, R. (2010). Stretch-induced stress fiber remodeling and the activations of JNK and ERK depend on mechanical strain rate, but not FAK. PLoS One *5*.

Hu, J., Li, Y., Hao, Y., Zheng, T., Gupta, S.K., Parada, G.A., Wu, H., Lin, S., Wang, S., Zhao, X., et al. (2019). High stretchability, strength, and toughness of living cells enabled by hyperelastic vimentin intermediate filaments. Proc. Natl. Acad. Sci. U. S. A. *116*, 17175–17180.

Hu, K., Ji, L., Applegate, K.T., Danuser, G., and Waterman-Storer, C.M. (2007). Differential transmission of actin motion within focal adhesions. Science (80-.). *315*, 111–115.

Huang, B., Jones, S.A., Brandenburg, B., and Zhuang, X. (2008). Whole-cell 3D STORM reveals interactions between cellular structures with nanometer-scale resolution. Nat. Methods *5*, 1047–1052.

Huang, C.Y.M., Zhang, C., Ho, T.S.Y., Oses-Prieto, J., Burlingame, A.L., Lalonde, J., Noebels, J.L., Leterrier, C., and Rasband, M.N. (2017a). αII spectrin forms a periodic cytoskeleton at the axon initial segment and is required for nervous system function. J. Neurosci.

Huang, D.L., Bax, N.A., Buckley, C.D., Weis, W.I., and Dunn, A.R. (2017b). Vinculin forms a directionally asymmetric catch bond with F-actin. Science (80-.). *357*, 703–706.

Huang, Z., Shimazu, K., Woo, N.H., Zang, K., Müller, U., Lu, B., and Reichardt, L.F. (2006). Distinct roles of the β1-class integrins at the developing and the mature hippocampal excitatory synapse. J. Neurosci.

Huganir, R.L., and Nicoll, R.A. (2013). AMPARs and synaptic plasticity: The last 25 years. Neuron.

Hughes, M.L., and Dougan, L. (2016). The physics of pulling polyproteins: A review of single molecule force spectroscopy using the AFM to study protein unfolding. Reports Prog. Phys. *79*, 76601.

Humphrey, J.D., Dufresne, E.R., and Schwartz, M.A. (2014). Mechanotransduction and extracellular matrix homeostasis. Nat. Rev. Mol. Cell Biol. *15*, 802–812.

Humphries, J.D., Wang, P., Streuli, C., Geiger, B., Humphries, M.J., and Ballestrem, C. (2007). Vinculin controls focal adhesion formation by direct interactions with talin and actin. J. Cell Biol. *179*, 1043–1057.

Humphries, J.D., Byron, A., Bass, M.D., Craig, S.E., Pinney, J.W., Knight, D., and Humphries, M.J. (2009). Proteomic analysis of integrin-associated complexes identifies RCC2 as a dual regulator of Rac1 and Arf6. Sci. Signal.

Inavalli, V.V.G.K., Lenz, M.O., Butler, C., Angibaud, J., Compans, B., Levet, F., Tønnesen, J., Rossier, O., Giannone, G., Thoumine, O., et al. (2019). A super-resolution platform for correlative live single-molecule imaging and STED microscopy. Nat. Methods.

Ivaska, J., Vuoriluoto, K., Huovinen, T., Izawa, I., Inagaki, M., and Parker, P.J. (2005). PKCε-mediated phosphorylation of vimentin controls integrin recycling and motility. EMBO J.

Iwashita, M., Kataoka, N., Toida, K., and Kosodo, Y. (2014). Systematic profiling of spatiotemporal tissue and cellular stiffness in the developing brain. Dev. *141*, 3793–3798.

Jagannathan Rajagopalan, Alireza Tofangchi, and Saif, M.T.A. (2010). Drosophila neurons actively regulate axonal tension in vivo. Biophys. J. *99*, 3208–3215.

Jansen, K.A., Atherton, P., and Ballestrem, C. (2017). Seminars in Cell & Developmental Biology Mechanotransduction at the cell-matrix interface. Semin. Cell Dev. Biol. *71*, 75–83.

Janson, M.E., and Dogterom, M. (2004). A bending mode analysis for growing microtubules: evidence for a velocity-dependent rigidity. Biophys. J.

Jégou, A., Carlier, M.F., and Romet-Lemonne, G. (2013). Formin mDia1 senses and generates mechanical forces on actin filaments. Nat. Commun. *4*, 1–7.

Jiang, G., Giannone, G., Critchley, D.R., Fukumoto, E., and Sheetz, M.P. (2003). Two-piconewton slip bond between fibronectin and the cytoskeleton depends on talin. Nature *424*, 334–337.

Jiang, G., Huang, A.H., Cai, Y., Tanase, M., and Sheetz, M.P. (2006). Rigidity sensing at the leading edge through alphavbeta3 integrins and RPTPalpha. Biophys. J.

Jimenez, A., Friedl, K., and Leterrier, C. (2020). About samples, giving examples: Optimized Single Molecule Localization Microscopy. Methods *174*, 100–114.

Jiu, Y., Peränen, J., Schaible, N., Cheng, F., Eriksson, J.E., Krishnan, R., and Lappalainen, P. (2017). Vimentin intermediate filaments control actin stress fiber assembly through GEF-H1 and RhoA. J. Cell Sci.

Johnson, C.P., Tang, H.Y., Carag, C., Speicher, D.W., and Discher, D.E. (2007). Forced unfolding of proteins within cells. Science (80-.). *317*, 663–666.

Jungbauer, S., Gao, H., Spatz, J.P., and Kemkemer, R. (2008). Two characteristic regimes in frequency-dependent dynamic reorientation of fibroblasts on cyclically stretched substrates. Biophys. J. *95*, 3470–3478.

Jungmann, R., Steinhauer, C., Scheible, M., Kuzyk, A., Tinnefeld, P., and Simmel, F.C. (2010). Single-molecule kinetics and super-resolution microscopy by fluorescence imaging of transient binding on DNA origami. Nano Lett.

Jungmann, R., Avendaño, M.S., Woehrstein, J.B., Dai, M., Shih, W.M., Yin, P., Avenda??o, M.S., Woehrstein, J.B., Dai, M., Shih, W.M., et al. (2014). Multiplexed 3D cellular super-resolution imaging with DNA-PAINT and Exchange-PAINT. Nat. Methods *11*, 313–318.

Jungmann, R., Avendaño, M.S., Dai, M., Woehrstein, J.B., Agasti, S.S., Feiger, Z., Rodal, A., and Yin, P. (2016). Quantitative super-resolution imaging with qPAINT. Nat. Methods *13*, 439–442.

Jurado, C., Haserick, J.R., and Lee, J. (2005). Slipping or gripping? Fluorescent speckle microscopy in fish keratocytes reveals two different mechanisms for generating a retrograde

flow of actin. Mol. Biol. Cell.

Kanchanawong, P., Shtengel, G., Pasapera, A.M., Ramko, E.B., Davidson, M.W., Hess, H.F., and Waterman, C.M. (2010). Nanoscale architecture of integrin-based cell adhesions. Nature *468*, 580–584.

Karra, D., and Dahm, R. (2010). Transfection techniques for neuronal cells. J. Neurosci.

Kassianidou, E., Kalita, J., and Lim, R.Y.H. (2019). The role of nucleocytoplasmic transport in mechanotransduction. Exp. Cell Res.

Katsuno, H., Toriyama, M., Hosokawa, Y., Mizuno, K., Ikeda, K., Sakumura, Y., and Inagaki, N. (2015). Actin migration driven by directional assembly and disassembly of membrane-anchored actin filaments. Cell Rep. *12*, 648–660.

Kechagia, J.Z., Ivaska, J., and Roca-Cusachs, P. (2019). Integrins as biomechanical sensors of the microenvironment. Nat. Rev. Mol. Cell Biol.

Keeling, M.C., Flores, L.R., Dodhy, A.H., Murray, E.R., and Gavara, N. (2017). Actomyosin and vimentin cytoskeletal networks regulate nuclear shape, mechanics and chromatin organization. Sci. Rep. *7*, 1–14.

Kellermayer, M.S.Z., Smith, S.B., Granzier, H.L., and Bustamante, C. (1997). Folding-unfolding transitions in single titin molecules characterized with laser tweezers. Science (80-.).

Kerstein, P.C., Nichol, R.H., and Gomez, T.M. (2015). Mechanochemical regulation of growth cone motility. Front. Cell. Neurosci. *9*, 1–16.

Khatau, S.B., Hale, C.M., Stewart-Hutchinson, P.J., Patel, M.S., Stewart, C.L., Searson, P.C., Hodzic, D., and Wirtz, D. (2009). A perinuclear actin cap regulates nuclear shape. Proc. Natl. Acad. Sci. U. S. A.

Kilian, N., Goryaynov, A., Lessard, M.D., Hooker, G., Toomre, D., Rothman, J.E., and Bewersdorf, J. (2018). Assessing photodamage in live-cell STED microscopy. Nat. Methods.

Kim, I.H., Racz, B., Wang, H., Burianek, L., Weinberg, R., Yasuda, R., Wetsel, W.C., and Soderling, S.H. (2013). Disruption of Arp2/3 results in asymmetric structural plasticity of dendritic spines and progressive synaptic and behavioral abnormalities. J. Neurosci.

Kim, J., Feng, J., Jones, C.A.R., Mao, X., Sander, L.M., Levine, H., and Sun, B. (2017). Stress-induced plasticity of dynamic collagen networks. Nat. Commun.

Klapholz, B., and Brown, N.H. (2017). Talin - The master of integrin adhesions. J. Cell Sci. *130*, 2435–2446.

Klapholz, B., Herbert, S.L., Wellmann, J., Johnson, R., Parsons, M., and Brown, N.H. (2015). Alternative mechanisms for talin to mediate integrin function. Curr. Biol. *25*, 847–857.

Klar, T.A., Jakobs, S., Dyba, M., Egner, A., and Hell, S.W. (2000). Fluorescence microscopy with diffraction resolution barrier broken by stimulated emission. Proc. Natl. Acad. Sci. U. S. A.

Klotzsch, E., Smith, M.L., Kubow, K.E., Muntwyler, S., Little, W.C., Beyeler, F., Gourdon, D., Nelson, B.J., and Vogel, V. (2009). Fibronectin forms the most extensible biological fibers displaying switchable force-exposed cryptic binding sites. Proc. Natl. Acad. Sci. U. S. A.

Kluger, C., Braun, L., Sedlak, S.M., Pippig, D.A., Bauer, M.S., Miller, K., Milles, L.F., Gaub, H.E.,

and Vogel, V. (2020). Different Vinculin Binding Sites Use the Same Mechanism to Regulate Directional Force Transduction. Biophys. J. *118*, 1344–1356.

Kommaddi, R.P., Das, D., Karunakaran, S., Nanguneri, S., Bapat, D., Ray, A., Shaw, E., Bennett, D.A., Nair, D., and Ravindranath, V. (2018). Aβ mediates F-actin disassembly in dendritic spines leading to cognitive deficits in alzheimer's disease. J. Neurosci.

Kong, F., García, A.J., Mould, A.P., Humphries, M.J., Zhu, C., Garcia, A.J., Mould, A.P., Humphries, M.J., Zhu, C., and García, A.J. (2009). Demonstration of catch bonds between an integrin and its ligand. J. Cell Biol. *185*, 1275–1284.

Kong, F., Li, Z., Parks, W.M., Dumbauld, D.W., García, A.J., Mould, A.P., Humphries, M.J., and Zhu, C. (2013). Cyclic mechanical reinforcement of integrin-ligand interactions. Mol. Cell.

Korobova, F., and Svitkina, T.M. (2010). Molecular architecture of synaptic actin cytoskeleton in hippocampal neurons reveals a mechanism of dendritic spine morphogenesis. Mol. Biol. Cell.

Koser, D.E., Thompson, A.J., Foster, S.K., Dwivedy, A., Pillai, E.K., Sheridan, G.K., Svoboda, H., Viana, M., Costa, L.D.F., Guck, J., et al. (2016). Mechanosensing is critical for axon growth in the developing brain. Nat. Neurosci.

Kovar, D.R., and Pollard, T.D. (2004). Insertional assembly of actin filament barbed ends in association with formins produces piconewton forces. Proc. Natl. Acad. Sci. U. S. A.

Kovar, D.R., Harris, E.S., Mahaffy, R., Higgs, H.N., and Pollard, T.D. (2006). Control of the assembly of ATP- and ADP-actin by formins and profilin. Cell.

Kress, H., Stelzer, E.H.K., Holzer, D., Buss, F., Griffiths, G., and Rohrbach, A. (2007). Filopodia act as phagocytic tentacles and pull with discrete steps and a load-dependent velocity. Proc. Natl. Acad. Sci. U. S. A.

Krieg, M., Dunn, A.R., and Goodman, M.B. (2014). Mechanical control of the sense of touch by β-spectrin. Nat. Cell Biol. *16*, 224–233.

Krieg, M., Stühmer, J., Cueva, J.G., Fetter, R., Spilker, K., Cremers, D., Shen, K., Dunn, A.R., and Goodman, M.B. (2017a). Genetic defects in β-spectrin and tau sensitize C. Elegans axons to movement-induced damage via torque-tension coupling. Elife.

Krieg, M., Stühmer, J., Cueva, J.G., Fetter, R., Spilker, K., Cremers, D., Shen, K., Dunn, A.R., and Goodman, M.B. (2017b). Genetic defects in β-spectrin and tau sensitize C. Elegans axons to movement-induced damage via torque-tension coupling. Elife *6*, 1–35.

Krieg, M., Fläschner, G., Alsteens, D., Gaub, B.M., Roos, W.H., Wuite, G.J.L., Gaub, H.E., Gerber, C., Dufrêne, Y.F., and Müller, D.J. (2019). Atomic force microscopy-based mechanobiology. Nat. Rev. Phys. *1*, 41–57.

Kuhlman, P.A., Hughes, C.A., Bennett, V., and Fowler, V.M. (1996). A New Function for Adducin. J. Biol. Chem.

Kumar, A., Anderson, K.L., Swift, M.F., Hanein, D., Volkmann, N., and Schwartz, M.A. (2018). Local Tension on Talin in Focal Adhesions Correlates with F-Actin Alignment at the Nanometer Scale. Biophys. J.

Kumar, A., Shutova, M.S., Tanaka, K., Iwamoto, D. V., Calderwood, D.A., Svitkina, T.M., and Schwartz, M.A. (2019). Filamin A mediates isotropic distribution of applied force across the

actin network. J. Cell Biol. *218*, 2481–2491.

Labernadie, A., Bouissou, A., Delobelle, P., Balor, S., Voituriez, R., Proag, A., Fourquaux, I., Thibault, C., Vieu, C., Poincloux, R., et al. (2014). Protrusion force microscopy reveals oscillatory force generation and mechanosensing activity of human macrophage podosomes. Nat. Commun.

Ladoux, B., and Mège, R.M. (2017). Mechanobiology of collective cell behaviours. Nat. Rev. Mol. Cell Biol. *18*, 743–757.

Lam, D., Enright, H.A., Cadena, J., Peters, S.K.G., Sales, A.P., Osburn, J.J., Soscia, D.A., Kulp, K.S., Wheeler, E.K., and Fischer, N.O. (2019). Tissue-specific extracellular matrix accelerates the formation of neural networks and communities in a neuron-glia co-culture on a multi-electrode array. Sci. Rep.

Lamar, J.M., Stern, P., Liu, H., Schindler, J.W., Jiang, Z.G., and Hynes, R.O. (2012). The Hippo pathway target, YAP, promotes metastasis through its TEAD-interaction domain. Proc. Natl. Acad. Sci. U. S. A.

Lamoureux, P., Ruthel, G., Buxbaum, R.E., and Heidemann, S.R. (2002). Mechanical tension can specify axonal fate in hippocampal neurons. J. Cell Biol. *159*, 499–508.

Lan, T.H., Huang, X.Q., and Tan, H.M. (2013). Vascular fibrosis in atherosclerosis. Cardiovasc. Pathol.

Lantoine, J., Grevesse, T., Villers, A., Delhaye, G., Mestdagh, C., Versaevel, M., Mohammed, D., Bruyère, C., Alaimo, L., Lacour, S.P., et al. (2016). Matrix stiffness modulates formation and activity of neuronal networks of controlled architectures. Biomaterials *89*, 14–24.

Latorre, E., Kale, S., Casares, L., Gómez-González, M., Uroz, M., Valon, L., Nair, R. V., Garreta, E., Montserrat, N., del Campo, A., et al. (2018). Active superelasticity in three-dimensional epithelia of controlled shape. Nature *563*, 203–208.

Lavelin, I., Wolfenson, H., Patla, I., Henis, Y.I., Medalia, O., Volberg, T., Livne, A., Kam, Z., and Geiger, B. (2013). Differential Effect of Actomyosin Relaxation on the Dynamic Properties of Focal Adhesion Proteins. PLoS One.

Lawson, C., Lim, S.T., Uryu, S., Chen, X.L., Calderwood, D.A., and Schlaepfer, D.D. (2012). FAK promotes recruitment of talin to nascent adhesions to control cell motility. J. Cell Biol.

Lazarus, C., Soheilypour, M., and Mofrad, M.R.K. (2015). Torsional Behavior of Axonal Microtubule Bundles. Biophys. J.

Leduc, C., Si, S., Gautier, J., Soto-Ribeiro, M., Wehrle-Haller, B., Gautreau, A., Giannone, G., Cognet, L., and Lounis, B. (2013). A highly specific gold nanoprobe for live-cell single-molecule imaging. Nano Lett.

Lee, H.S., Lim, C.J., Puzon-McLaughlin, W., Shattil, S.J., and Ginsberg, M.H. (2009). RIAM activates integrins by linking talin to Ras GTPase membrane-targeting sequences. J. Biol. Chem.

Legerstee, K., Geverts, B., Slotman, J.A., and Houtsmuller, A.B. (2019). Dynamics and distribution of paxillin, vinculin, zyxin and VASP depend on focal adhesion location and orientation. Sci. Rep. *9*, 1–18.

Leite, S.C., Sampaio, P., Sousa, V.F., Nogueira-Rodrigues, J., Pinto-Costa, R., Peters, L.L., Brites,

P., and Sousa, M.M. (2016). The Actin-Binding Protein α-Adducin Is Required for Maintaining Axon Diameter. Cell Rep. *15*, 490–498.

Lele, T.P., Pendse, J., Kumar, S., Salanga, M., Karavitis, J., and Ingber, D.E. (2006). Mechanical forces alter zyxin unbinding kinetics within focal adhesions of living cells. J. Cell. Physiol.

Leterrier, C., Vacher, H., Fache, M.P., D'Ortoli, S.A., Castets, F., Autillo-Touat, A., and Dargent, B. (2011). End-binding proteins EB3 and EB1 link microtubules to ankyrin G in the axon initial segment. Proc. Natl. Acad. Sci. U. S. A.

Leterrier, C., Potier, J., Caillol, G., Debarnot, C., Rueda Boroni, F., and Dargent, B. (2015). Nanoscale Architecture of the Axon Initial Segment Reveals an Organized and Robust Scaffold. Cell Rep. *13*, 2781–2793.

Levental, K.R., Yu, H., Kass, L., Lakins, J.N., Egeblad, M., Erler, J.T., Fong, S.F.T., Csiszar, K., Giaccia, A., Weninger, W., et al. (2009). Matrix Crosslinking Forces Tumor Progression by Enhancing Integrin Signaling. Cell.

Li, D., Shao, L., Chen, B.C., Zhang, X., Zhang, M., Moses, B., Milkie, D.E., Beach, J.R., Hammer, J.A., Pasham, M., et al. (2015a). Extended-resolution structured illumination imaging of endocytic and cytoskeletal dynamics. Science (80-.).

Li, T., Zheng, F., Cheung, M., Wang, F., and Fu, C. (2015b). Fission yeast mitochondria are distributed by dynamic microtubules in a motor-independent manner. Sci. Rep.

Li, W., Feng, Z., Sternberg, P.W., and Xu, X.Z.S. (2006). A C. elegans stretch receptor neuron revealed by a mechanosensitive TRP channel homologue. Nature.

Liang, X., and Howard, J. (2018). Structural Biology: Piezo Senses Tension through Curvature. Curr. Biol.

Liu, C.Y., Lin, H.H., Tang, M.J., and Wang, Y.K. (2015a). Vimentin contributes to epithelial-mesenchymal transition ancer cell mechanics by mediating cytoskeletal organization and focal adhesion maturation. Oncotarget.

Liu, J., Wang, Y., Goh, W.I., Goh, H., Baird, M.A., Ruehland, S., Teo, S., Bate, N., Critchley, D.R., Davidson, M.W., et al. (2015b). Talin determines the nanoscale architecture of focal adhesions. Proc. Natl. Acad. Sci. U. S. A. *112*, E4864–E4873.

Liu, Y., Medda, R., Liu, Z., Galior, K., Yehl, K., Spatz, J.P., Cavalcanti-Adam, E.A., and Salaita, K. (2014). Nanoparticle tension probes patterned at the nanoscale: Impact of integrin clustering on force transmission. Nano Lett.

Liu, Y., Yehl, K., Narui, Y., Salaita, K.S., Dutta, P.K., Zhang, Y., Blanchard, A.T., Ge, C., Rushdi, M., Weiss, K., et al. (2016). DNA-based nanoparticle tension sensors reveal that T-cell receptors transmit defined pN forces to their antigens for enhanced fidelity. Nat. Methods *13*, 1–10.

Lo, C.M., Wang, H.B., Dembo, M., and Wang, Y.L. (2000). Cell movement is guided by the rigidity of the substrate. Biophys. J. *79*, 144–152.

Loh, P.Y., Yeoh, W.L., Nakashima, H., and Muraki, S. (2018). Deformation of the median nerve at different finger postures and wrist angles. PeerJ.

Long, K.R., and Huttner, W.B. (2019). How the extracellular matrix shapes neural development. Open Biol.

López-Colomé, A.M., Lee-Rivera, I., Benavides-Hidalgo, R., and López, E. (2017). Paxillin: A crossroad in pathological cell migration. J. Hematol. Oncol.

Lorenzo, D.N., Badea, A., Zhou, R., Mohler, P.J., Zhuang, X., and Bennett, V. (2019). βII-spectrin promotes mouse brain connectivity through stabilizing axonal plasma membranes and enabling axonal organelle transport. Proc. Natl. Acad. Sci. *116*, 15686–15695.

Lukinavičius, G., Reymond, L., D'Este, E., Masharina, A., Göttfert, F., Ta, H., Güther, A., Fournier, M., Rizzo, S., Waldmann, H., et al. (2014). Fluorogenic probes for live-cell imaging of the cytoskeleton. Nat. Methods.

Machesky, L.M., Mullins, R.D., Higgs, H.N., Kaiser, D.A., Blanchoin, L., May, R.C., Hall, M.E., and Pollard, T.D. (1999). Scar, a WASp-related protein, activates nucleation of actin filaments by the Arp2/3 complex. Proc. Natl. Acad. Sci. U. S. A.

Machnicka, B., Czogalla, A., Hryniewicz-Jankowska, A., Bogusławska, D.M., Grochowalska, R., Heger, E., and Sikorski, A.F. (2014). Spectrins: A structural platform for stabilization and activation of membrane channels, receptors and transporters. Biochim. Biophys. Acta - Biomembr. *1838*, 620–634.

Maglione, M., and Sigrist, S.J. (2013). Seeing the forest tree by tree: Super-resolution light microscopy meets the neurosciences. Nat. Neurosci.

Magou, G.C., Pfister, B.J., and Berlin, J.R. (2015). Effect of acute stretch injury on action potential and network activity of rat neocortical neurons in culture. Brain Res.

Margadant, F., Chew, L.L., Hu, X., Yu, H., Bate, N., Zhang, X., and Sheetz, M. (2011). Mechanotransduction in vivo by repeated talin stretch-relaxation events depends upon vinculin. PLoS Biol *9*, e1001223.

Marshall, B.T., Long, M., Piper, J.W., Yago, T., McEver, R.P., and Zhu, C. (2003). Direct observation of catch bonds involving cell-adhesion molecules. Nature.

Martinac, B. (2014). The ion channels to cytoskeleton connection as potential mechanism of mechanosensitivity. Biochim. Biophys. Acta - Biomembr.

Martino, F., Perestrelo, A.R., Vinarský, V., Pagliari, S., and Forte, G. (2018). Cellular mechanotransduction: From tension to function. Front. Physiol. *9*, 1–21.

Martynova, N.Y., Eroshkin, F.M., Ermolina, L. V., Ermakova, G. V., Korotaeva, A.L., Smurova, K.M., Gyoeva, F.K., and Zaraisky, A.G. (2008). The LIM-domain protein zyxin binds the homeodomain factor Xanf1/Hesx1 and modulates its activity in the anterior neural plate of Xenopus laevis embryo. Dev. Dyn.

Massou, S., Vicente, F.N., Wetzel, F., Mehidi, A., Strehle, D., Leduc, C., Voituriez, R., Rossier, O., Nassoy, P., and Giannone, G. (2020). Cell stretching is amplified by active actin remodeling to deform and recruit proteins in mechanosensitive structures. Nat. Cell Biol.

Mazzuoli, G., and Schemann, M. (2012). Mechanosensitive enteric neurons in the myenteric plexus of the mouse intestine. PLoS One.

Mehidi, A., Rossier, O., Schaks, M., Chazeau, A., Binamé, F., Remorino, A., Coppey, M., Karatas, Z., Sibarita, J.-B.B., Rottner, K., et al. (2019). Transient Activations of Rac1 at the Lamellipodium Tip Trigger Membrane Protrusion. Curr. Biol. *29*.

Mierke, C.T., Kollmannsberger, P., Zitterbart, D.P., Smith, J., Fabry, B., and Goldmann, W.H. (2008). Mechano-coupling and regulation of contractility by the vinculin tail domain. Biophys. J.

Mikhaylova, M., Bär, J., van Bommel, B., Schätzle, P., YuanXiang, P.A., Raman, R., Hradsky, J., Konietzny, A., Loktionov, E.Y., Reddy, P.P., et al. (2018). Caldendrin Directly Couples Postsynaptic Calcium Signals to Actin Remodeling in Dendritic Spines. Neuron *97*, 1110-1125.e14.

Milles, L.F., Schulten, K., Gaub, H.E., and Bernardi, R.C. (2018). Molecular mechanism of extreme mechanostability in a pathogen adhesin. Science (80-.).

Moeendarbary, E., Valon, L., Fritzsche, M., Harris, A.R., Moulding, D.A., Thrasher, A.J., Stride, E., Mahadevan, L., and Charras, G.T. (2013). The cytoplasm of living cells behaves as a poroelastic material. Nat. Mater.

Mohammadi, H., and Sahai, E. (2018). Mechanisms and impact of altered tumour mechanics. Nat. Cell Biol. *20*, 766–774.

Monkley, S.J., Zhou, X.H., Kinston, S.J., Giblett, S.M., Hemmings, L., Priddle, H., Brown, J.E., Pritchard, C.A., Critchley, D.R., and Fässler, R. (2000). Disruption of the talin gene arrests mouse development at the gastrulation stage. Dev. Dyn.

Moore, D.L., Blackmore, M.G., Hu, Y., Kaestner, K.H., Bixby, J.L., Lemmon, V.P., and Goldberg, J.L. (2009). KLF family members regulate intrinsic axon regeneration ability. Science (80-.).

Moore, S.W., Roca-Cusachs, P., and Sheetz, M.P. (2010). Stretchy proteins on stretchy substrates: The important elements of integrin-mediated rigidity sensing. Dev. Cell *19*, 194–206.

Mooren, O.L., Galletta, B.J., and Cooper, J.A. (2012). Roles for actin assembly in endocytosis. Annu. Rev. Biochem.

Morimatsu, M., Mekhdjian, A.H., Chang, A.C., Tan, S.J., and Dunn, A.R. (2015). Visualizing the Interior Architecture of Focal Adhesions with High-Resolution Traction Maps. Nano Lett. *15*, 2220–2228.

Mueller, J., Szep, G., Nemethova, M., de Vries, I., Lieber, A.D., Winkler, C., Kruse, K., Small, J.V., Schmeiser, C., Keren, K., et al. (2017). Load Adaptation of Lamellipodial Actin Networks. Cell *171*, 188-200.e16.

Münker, T.J.A.G., van de Vijfeijken, S.E.C.M., Mulder, C.S., Vespasiano, V., Becking, A.G., Kleverlaan, C.J., Becking, A.G., Dubois, L., Karssemakers, L.H.E., Milstein, D.M.J., et al. (2018). Effects of sterilization on the mechanical properties of poly(methyl methacrylate) based personalized medical devices. J. Mech. Behav. Biomed. Mater.

Murphy, D.A., and Courtneidge, S.A. (2011). The “ins” and “outs” of podosomes and invadopodia: Characteristics, formation and function. Nat. Rev. Mol. Cell Biol.

Murrell, M.P., and Gardel, M.L. (2012). F-actin buckling coordinates contractility and severing in a biomimetic actomyosin cortex. Proc. Natl. Acad. Sci. U. S. A.

Myers, J.P., and Gomez, T.M. (2011). Focal adhesion kinase promotes integrin adhesion dynamics necessary for chemotropic turning of nerve growth cones. J. Neurosci.

Nagayama, K., Kimura, Y., Makino, N., and Matsumoto, T. (2012). Strain waveform dependence

of stress fiber reorientation in cyclically stretched osteoblastic cells: Effects of viscoelastic compression of stress fibers. Am. J. Physiol. - Cell Physiol.

Nakamura, F., Song, M., Hartwig, J.H., and Stossel, T.P. (2014). Documentation and localization of force-mediated filamin A domain perturbations in moving cells. Nat. Commun.

Nava, M.M., Miroshnikova, Y.A., Biggs, L.C., Whitefield, D.B., Metge, F., Boucas, J., Vihinen, H., Jokitalo, E., Li, X., García Arcos, J.M., et al. (2020). Heterochromatin-Driven Nuclear Softening Protects the Genome against Mechanical Stress-Induced Damage. Cell *181*, 800-817.e22.

Needham, L.K., Thelen, K., and Maness, P.F. (2001). Cytoplasmic domain mutations of the L1 cell adhesion molecule reduce L1-ankyrin interactions. J. Neurosci.

Neuman, K.C., and Nagy, A. (2008). Single-molecule force spectroscopy: Optical tweezers, magnetic tweezers and atomic force microscopy. Nat. Methods.

Neuman, K.C., Chadd, E.H., Liou, G.F., Bergman, K., and Block, S.M. (1999). Characterization of photodamage to Escherichia coli in optical traps. Biophys. J.

Nicoletta I. Petridou, Zoltán Spiró, and Carl-Philipp Heisenberg (2017). Multiscale force sensing in development. Nat. Cell Biol. *19*, 581–588.

Niediek, V., Born, S., Hampe, N., Kirchgeßner, N., Merkel, R., and Hoffmann, B. (2012). Cyclic stretch induces reorientation of cells in a Src family kinase- and p130Cas-dependent manner. Eur. J. Cell Biol.

Nieswandt, B., Moser, M., Pleines, I., Varga-Szabo, D., Monkley, S., Critchley, D., and Fässler, R. (2007). Loss of talin1 in platelets abrogates integrin activation, platelet aggregation, and thrombus formation in vitro and in vivo. J. Exp. Med.

Nishizaka, T., Shi, Q., and Sheetz, M.P. (2000). Position-dependent linkages of fibronectin-integrin-cytoskeleton. Proc. Natl. Acad. Sci. U. S. A.

Nobes, C.D., and Hall, A. (1995). Rho, Rac, and Cdc42 GTPases regulate the assembly of multimolecular focal complexes associated with actin stress fibers, lamellipodia, and filopodia. Cell.

Nolting, J.F., and Köster, S. (2013). Influence of microfluidic shear on keratin networks in living cells. New J. Phys.

Nonomura, K., Woo, S.H., Chang, R.B., Gillich, A., Qiu, Z., Francisco, A.G., Ranade, S.S., Liberles, S.D., and Patapoutian, A. (2017). Piezo2 senses airway stretch and mediates lung inflation-induced apnoea. Nature.

Oakes, P.W., Wagner, E., Brand, C.A., Probst, D., Linke, M., Schwarz, U.S., Glotzer, M., and Gardel, M.L. (2017). Optogenetic control of RhoA reveals zyxin-mediated elasticity of stress fibres. Nat. Commun. *8*.

Oberhauser, A.F., Marszalek, P.E., Erickson, H.P., and Fernandez, J.M. (1998). The molecular elasticity of the extracellular matrix protein tenascin. Nature.

Oberhauser, A.F., Hansma, P.K., Carrion-Vazquez, M., and Fernandez, J.M. (2001). Stepwise unfolding of titin under force-clamp atomic force microscopy. Proc. Natl. Acad. Sci. U. S. A.

Odde, D.J., Ma, L., Briggs, A.H., DeMarco, A., and Kirschner, M.W. (1999). Microtubule bending

and breaking in living fibroblast cells. J. Cell Sci.

Opplert, J., and Babault, N. (2018). Acute Effects of Dynamic Stretching on Muscle Flexibility and Performance: An Analysis of the Current Literature. Sport. Med.

Oria, R., Wiegand, T., Escribano, J., Elosegui-Artola, A., Uriarte, J.J., Moreno-Pulido, C., Platzman, I., Delcanale, P., Albertazzi, L., Navajas, D., et al. (2017). Force loading explains spatial sensing of ligands by cells. Nature *552*, 219–224.

Orre, T., Karatas, Z., Kastberger, B., Cabriel, C., Boettcher, R.T., Leveque-Fort, S., Sibarita, J.-B., Faessler, R., Wehrle-Haller, B., Rossier, O., et al. (2020). Molecular motion and tridimensional nanoscale localization of kindlin control integrin activation in focal adhesions. BioRxiv.

Orré, T., Rossier, O., and Giannone, G. (2019). The inner life of integrin adhesion sites: From single molecules to functional macromolecular complexes. Exp. Cell Res. *379*, 235–244.

Page, P. (2012). Current concepts in muscle stretching for exercise and rehabilitation. Int. J. Sports Phys. Ther.

Pan, L., Yan, R., Li, W., and Xu, K. (2018). Super-Resolution Microscopy Reveals the Native Ultrastructure of the Erythrocyte Cytoskeleton. Cell Rep. *22*, 1151–1158.

Panzetta, V., Fusco, S., and Netti, P.A. (2019). Cell mechanosensing is regulated by substrate strain energy rather than stiffness. Proc. Natl. Acad. Sci. U. S. A. *116*, 22004–22013.

Park, Y.K., and Goda, Y. (2016). Integrins in synapse regulation. Nat. Rev. Neurosci. *17*, 745–756.

Parton, R.G., and Del Pozo, M.A. (2013). Caveolae as plasma membrane sensors, protectors and organizers. Nat. Rev. Mol. Cell Biol. *14*, 98–112.

Pasapera, A.M., Schneider, I.C., Rericha, E., Schlaepfer, D.D., and Waterman, C.M. (2010). Myosin II activity regulates vinculin recruitment to focal adhesions through FAK-mediated paxillin phosphorylation. J. Cell Biol. *188*, 877–890.

Paszek, M.J., and Weaver, V.M. (2004). The tension mounts: Mechanics meets morphogenesis and malignancy. J. Mammary Gland Biol. Neoplasia.

Paszek, M.J., DuFort, C.C., Rossier, O., Bainer, R., Mouw, J.K., Godula, K., Hudak, J.E., Lakins, J.N., Wijekoon, A.C., Cassereau, L., et al. (2014). The cancer glycocalyx mechanically primes integrin-mediated growth and survival. Nature *511*, 319–325.

Patel-Hett, S., Wang, H., Begonja, A.J., Thon, J.N., Alden, E.C., Wandersee, N.J., An, X., Mohandas, N., Hartwig, J.H., and Italiano, J.E. (2011). The spectrin-based membrane skeleton stabilizes mouse megakaryocyte membrane systems and is essential for proplatelet and platelet formation. Blood *118*, 1641–1652.

Perrier, E.T., Pavol, M.J., and Hoffman, M.A. (2011). The acute effects of a warm-up including static or dynamic stretching on countermovement jump height, reaction time, and flexibility. J. Strength Cond. Res.

Pfajfer, L., Mair, N.K., Jiménez-Heredia, R., Genel, F., Gulez, N., Ardeniz, Ö., Hoeger, B., Bal, S.K., Madritsch, C., Kalinichenko, A., et al. (2018). Mutations affecting the actin regulator WD repeat–containing protein 1 lead to aberrant lymphoid immunity. J. Allergy Clin. Immunol.

Phillips, J.B., Smit, X., De Zoysa, N., Afoke, A., and Brown, R.A. (2004). Peripheral nerves in the

rat exhibit localized heterogeneity of tensile properties during limb movement. J. Physiol.

Pignata, A., Ducuing, H., Boubakar, L., Gardette, T., Kindbeiter, K., Bozon, M., Tauszig-Delamasure, S., Falk, J., Thoumine, O., and Castellani, V. (2019). A Spatiotemporal Sequence of Sensitization to Slits and Semaphorins Orchestrates Commissural Axon Navigation. Cell Rep.

Plodinec, M., Loparic, M., Monnier, C.A., Obermann, E.C., Zanetti-Dallenbach, R., Oertle, P., Hyotyla, J.T., Aebi, U., Bentires-Alj, M., Lim, R.Y.H., et al. (2012). The nanomechanical signature of breast cancer. Nat. Nanotechnol.

Plotnikov, S. V., Pasapera, A.M., Sabass, B., and Waterman, C.M. (2012). Force fluctuations within focal adhesions mediate ECM-rigidity sensing to guide directed cell migration. Cell *151*, 1513–1527.

Polacheck, W.J., and Chen, C.S. (2016). Measuring cell-generated forces: A guide to the available tools. Nat. Methods *13*, 415–423.

Pollard, T.D. (1986). Rate constants for the reactions of ATP- and ADP-actin with the ends of actin filaments. J. Cell Biol.

Pollard, T.D., and Cooper, J.A. (2009). Actin, a central player in cell shape and movement. Science (80-.). *326*, 1208–1212.

Pollard, T.D., and Goldman, R.D. (2018). Overview of the cytoskeleton from an evolutionary perspective. Cold Spring Harb. Perspect. Biol.

Ponti, A., Machacek, M., Gupton, S.L., Waterman-Storer, C.M., and Danuser, G. (2004). Two distinct actin networks drive the protrusion of migrating cells. Science (80-.). *305*, 1782–1786.

Pozo, K., Cingolani, L.A., Bassani, S., Laurent, F., Passafaro, M., and Goda, Y. (2012). 3 integrin interacts directly with GluA2 AMPA receptor subunit and regulates AMPA receptor expression in hippocampal neurons. Proc. Natl. Acad. Sci. *109*, 1323–1328.

Praekelt, U., Kopp, P.M., Rehm, K., Linder, S., Bate, N., Patel, B., Debrand, E., Manso, A.M., Ross, R.S., Conti, F., et al. (2012). New isoform-specific monoclonal antibodies reveal different sub-cellular localisations for talin1 and talin2. Eur. J. Cell Biol.

Proske, U., and Gandevia, S.C. (2012). The proprioceptive senses: Their roles in signaling body shape, body position and movement, and muscle force. Physiol. Rev.

Qu, Y., Hahn, I., Webb, S.E.D., Pearce, S.P., and Prokop, A. (2017). Periodic actin structures in neuronal axons are required to maintain microtubules. Mol. Biol. Cell *28*, 296–308.

Rafiq, N.B.M., Nishimura, Y., Plotnikov, S. V., Thiagarajan, V., Zhang, Z., Shi, S., Natarajan, M., Viasnoff, V., Kanchanawong, P., Jones, G.E., et al. (2019). A mechano-signalling network linking microtubules, myosin IIA filaments and integrin-based adhesions. Nat. Mater. *18*, 638–649.

Rauscher, A., Gyimesi, M., Kovács, M., and Málnási-Csizmadia, A. (2018). Targeting Myosin by Blebbistatin Derivatives: Optimization and Pharmacological Potential. Trends Biochem. Sci.

Reversat, A., Gaertner, F., Merrin, J., Stopp, J., Tasciyan, S., Aguilera, J., de Vries, I., Hauschild, R., Hons, M., Piel, M., et al. (2020). Cellular locomotion using environmental topography. Nature.

Ridley, A.J., and Hall, A. (1992). The small GTP-binding protein rho regulates the assembly of

focal adhesions and actin stress fibers in response to growth factors. Cell.

Rief, M., Gautel, M., Oesterhelt, F., Fernandez, J.M., and Gaub, H.E. (1997). Reversible unfolding of individual titin immunoglobulin domains by AFM. Science (80-.).

Rief, M., Pascual, J., Saraste, M., and Gaub, H.E. (1999). Single molecule force spectroscopy of spectrin repeats: low unfolding forces in helix bundles. J. Mol. Biol. *286*, 553–561.

Ringer, P., Weißl, A., Cost, A.L., Freikamp, A., Sabass, B., Mehlich, A., Tramier, M., Rief, M., and Grashoff, C. (2017). Multiplexing molecular tension sensors reveals piconewton force gradient across talin-1. Nat. Methods *14*, 1090–1096.

Del Rio, A., Perez-Jimenez, R., Liu, R., Roca-Cusachs, P., Fernandez, J.M., and Sheetz, M.P. (2009). Stretching single talin rod molecules activates vinculin binding. Science (80-.). *323*, 638–641.

Risca, V.I., Wang, E.B., Chaudhuri, O., Chia, J.J., Geissler, P.L., and Fletcher, D.A. (2012). Actin filament curvature biases branching direction. Proc. Natl. Acad. Sci. U. S. A. *109*, 2913–2918.

Riveline, D., Zamir, E., Balaban, N.Q., Schwarz, U.S., Ishizaki, T., Narumiya, S., Kam, Z., Geiger, B., and Bershadsky, A.D. (2001). Focal contacts as mechanosensors: Externally applied local mechanical force induces growth of focal contacts by an mDia1-dependent and ROCK-independent mechanism. J. Cell Biol.

Roca-Cusachs, P., Conte, V., and Trepat, X. (2017). Quantifying forces in cell biology. Nat. Cell Biol. *19*, 742–751.

Romberg, C., Yang, S., Melani, R., Andrews, M.R., Horner, A.E., Spillantini, M.G., Bussey, T.J., Fawcett, J.W., Pizzorusso, T., and Saksida, L.M. (2013). Depletion of perineuronal nets enhances recognition memory and long-term depression in the perirhinal cortex. J. Neurosci.

Romero, S., Le Clainche, C., Didry, D., Egile, C., Pantaloni, D., and Carlier, M.F. (2004). Formin is a processive motor that requires profilin to accelerate actin assembly and associated ATP hydrolysis. Cell.

Rosowski, K.A., Boltyanskiy, R., Xiang, Y., Van den Dries, K., Schwartz, M.A., and Dufresne, E.R. (2018). Vinculin and the mechanical response of adherent fibroblasts to matrix deformation. Sci. Rep. *8*, 1–10.

Rossier, O., Octeau, V., Sibarita, J.-B.B., Leduc, C., Tessier, B., Nair, D., Gatterdam, V., Destaing, O., Albiges-Rizo, C., Tampe, R., et al. (2012). Integrins β1 and β3 exhibit distinct dynamic nanoscale organizations inside focal adhesions. Nat. Cell Biol. *14*, 1057–1067.

Rothberg, K.G., Heuser, J.E., Donzell, W.C., Ying, Y.S., Glenney, J.R., and Anderson, R.G.W. (1992). Caveolin, a protein component of caveolae membrane coats. Cell.

Rothenberg, K.E., Scott, D.W., Christoforou, N., and Hoffman, B.D. (2018). Vinculin Force-Sensitive Dynamics at Focal Adhesions Enable Effective Directed Cell Migration. Biophys. J. *114*, 1680–1694.

Ruff, C., Holt, B., and Trinkaus, E. (2006). Who's afraid of the big bad Wolff?: "Wolff's law" and bone functional adaptation. Am. J. Phys. Anthropol.

Rust, M.J., Bates, M., and Zhuang, X. (2006). Sub-diffraction-limit imaging by stochastic optical reconstruction microscopy (STORM). Nat Methods *3*, 793–795.

Rys, J.P., DuFort, C.C., Monteiro, D.A., Baird, M.A., Oses-Prieto, J.A., Chand, S., Burlingame, A.L., Davidson, M.W., and Alliston, T.N. (2015). Discrete spatial organization of TGFβ receptors couples receptor multimerization and signaling to cellular tension. Elife.

Sadler, I., Crawford, A.W., Michelsen, J.W., and Beckerle, M.C. (1992). Zyxin and cCRP: Two interactive LIM domain proteins associated with the cytoskeleton. J. Cell Biol.

Sahl, S.J., Hell, S.W., and Jakobs, S. (2017). Fluorescence nanoscopy in cell biology. Nat. Rev. Mol. Cell Biol. *18*, 685–701.

Saltel, F., Mortier, E., Hytönen, V.P., Jacquier, M.C., Zimmermann, P., Vogel, V., Liu, W., and Wehrle-Haller, B. (2009). New PI(4,5)P2- and membrane proximal integrin-binding motifs in the talin head control β3-integrin clustering. J. Cell Biol.

Sanford, K.K., Likely, G.D., and Earle, W.R. (1954). The development of variations in transplantability and morphology within a clone of mouse fibroblasts transformed to sarcoma-producing cells in vitro. J. Natl. Cancer Inst.

Sanghvi-Shah, R., and Weber, G.F. (2017). Intermediate filaments at the junction of mechanotransduction, migration, and development. Front. Cell Dev. Biol. *5*, 1–19.

Sarangapani, K.K., Qian, J., Chen, W., Zarnitsyna, V.I., Mehta, P., Yago, T., McEver, R.P., and Zhu, C. (2011). Regulation of catch bonds by rate of force application. J. Biol. Chem.

Sarkar, R., and Rybenkov, V. V. (2016). A Guide to Magnetic Tweezers and Their Applications. Front. Phys.

Sarmento, M.J., Oneto, M., Pelicci, S., Pesce, L., Scipioni, L., Faretta, M., Furia, L., Dellino, G.I., Pelicci, P.G., Bianchini, P., et al. (2018). Exploiting the tunability of stimulated emission depletion microscopy for super-resolution imaging of nuclear structures. Nat. Commun.

Sawada, Y., and Sheetz, M.P. (2002a). Force transduction by Triton cytoskeletons. J Cell Biol *156*, 609–615.

Sawada, Y., and Sheetz, M.P. (2002b). Force transduction by Triton cytoskeletons. J. Cell Biol.

Sawada, Y., Tamada, M., Dubin-Thaler, B.J., Cherniavskaya, O., Sakai, R., Tanaka, S., and Sheetz, M.P. (2006). Force Sensing by Mechanical Extension of the Src Family Kinase Substrate p130Cas. Cell *127*, 1015–1026.

Schaedel, L., John, K., Gaillard, J., Nachury, M. V., Blanchoin, L., and Thery, M. (2015). Microtubules self-repair in response to mechanical stress. Nat. Mater. *14*, 1156–1163.

Schiffhauer, E.S.S., Luo, T., Mohan, K., Srivastava, V., Qian, X., Griffis, E.R.R., Iglesias, P.A.A., and Robinson, D.N.N. (2016). Mechanoaccumulative Elements of the Mammalian Actin Cytoskeleton. Curr. Biol.

Schiller, H.B., Hermann, M.-R., Polleux, J., Vignaud, T., Zanivan, S., Friedel, C.C., Sun, Z., Raducanu, A., Gottschalk, K.-E., Théry, M., et al. (2013a). β1- and αv-class integrins cooperate to regulate myosin II during rigidity sensing of fibronectin-based microenvironments. Nat. Cell Biol. *15*, 625–636.

Schiller, H.B., Hermann, M.R., Polleux, J., Vignaud, T., Zanivan, S., Friedel, C.C., Sun, Z., Raducanu, A., Gottschalk, K.E., Théry, M., et al. (2013b). β 1 - And α v -class integrins cooperate to regulate myosin II during rigidity sensing of fibronectin-based microenvironments. Nat. Cell

Biol.

Schmidt, R., Wurm, C.A., Jakobs, S., Engelhardt, J., Egner, A., and Hell, S.W. (2008). Spherical nanosized focal spot unravels the interior of cells. Nat. Methods.

Schnitzbauer, J., Strauss, M.T., Schlichthaerle, T., Schueder, F., and Jungmann, R. (2017). Super-resolution microscopy with DNA-PAINT. Nat. Protoc. *12*, 1198–1228.

Schueder, F., Lara-Gutiérrez, J., Beliveau, B.J., Saka, S.K., Sasaki, H.M., Woehrstein, J.B., Strauss, M.T., Grabmayr, H., Yin, P., and Jungmann, R. (2017). Multiplexed 3D super-resolution imaging of whole cells using spinning disk confocal microscopy and DNA-PAINT. Nat. Commun. *8*, 1–23.

Schueder, F., Stein, J., Stehr, F., Auer, A., Sperl, B., Strauss, M.T., Schwille, P., and Jungmann, R. (2019). An order of magnitude faster DNA-PAINT imaging by optimized sequence design and buffer conditions. Nat. Methods *16*, 1101–1104.

Schulze, N., Graessl, M., Soares, A.B., Geyer, M., Dehmelt, L., and Nalbant, P. (2014). FHOD1 regulates stress fiber organization by controlling the dynamics of transverse arcs and dorsal fibers. J. Cell Sci.

Schürmann, S., Wagner, S., Herlitze, S., Fischer, C., Gumbrecht, S., Wirth-Hücking, A., Prölß, G., Lautscham, L.A., Fabry, B., Goldmann, W.H., et al. (2016). The IsoStretcher: An isotropic cell stretch device to study mechanical biosensor pathways in living cells. Biosens. Bioelectron. *81*, 363–372.

Segel, M., Neumann, B., Hill, M.F.E., Weber, I.P., Viscomi, C., Zhao, C., Young, A., Agley, C.C., Thompson, A.J., Gonzalez, G.A., et al. (2019). Niche stiffness underlies the ageing of central nervous system progenitor cells. Nature.

Serrels, B., Serrels, A., Brunton, V.G., Holt, M., McLean, G.W., Gray, C.H., Jones, G.E., and Frame, M.C. (2007). Focal adhesion kinase controls actin assembly via a FERM-mediated interaction with the Arp2/3 complex. Nat. Cell Biol.

Serres, M.P., Samwer, M., Truong Quang, B.A., Lavoie, G., Perera, U., Görlich, D., Charras, G., Petronczki, M., Roux, P.P., and Paluch, E.K. (2020). F-Actin Interactome Reveals Vimentin as a Key Regulator of Actin Organization and Cell Mechanics in Mitosis. Dev. Cell.

Shao, Y., Tan, X., Novitski, R., Muqaddam, M., List, P., Williamson, L., Fu, J., and Liu, A.P. (2013). Uniaxial cell stretching device for live-cell imaging of mechanosensitive cellular functions. Rev. Sci. Instrum.

Sharonov, A., and Hochstrasser, R.M. (2006). Wide-field subdiffraction imaging by accumulated binding of diffusing probes. Proc. Natl. Acad. Sci. U. S. A.

Shemesh, T., Bershadsky, A.D., and Kozlov, M.M. (2012). Physical model for self-organization of actin cytoskeleton and adhesion complexes at the cell front. Biophys. J.

Shergill, B., Meloty-Kapella, L., Musse, A.A., Weinmaster, G., and Botvinick, E. (2012). Optical Tweezers Studies on Notch: Single-Molecule Interaction Strength Is Independent of Ligand Endocytosis. Dev. Cell.

Shiraishi, I., Simpson, D.G., Carver, W., Price, R., Hirozane, T., Terracio, L., and Borg, T.K. (1997). Vinculin is an essential component for normal myofibrillar arrangement in fetal mouse cardiac myocytes. J. Mol. Cell. Cardiol.

Shroff, H., Galbraith, C.G., Galbraith, J.A., White, H., Gillette, J., Olenych, S., Davidson, M.W., and Betzig, E. (2007). Dual-color superresolution imaging of genetically expressed probes within individual adhesion complexes. Proc. Natl. Acad. Sci. U. S. A.

Shtengel, G., Galbraith, J.A., Galbraith, C.G., Lippincott-Schwartz, J., Gillette, J.M., Manley, S., Sougrat, R., Waterman, C.M., Kanchanawong, P., Davidson, M.W., et al. (2009). Interferometric fluorescent super-resolution microscopy resolves 3D cellular ultrastructure. Proc Natl Acad Sci U S A *106*, 3125–3130.

Siechen, S., Yang, S., Chiba, A., and Saif, T. (2009). Mechanical tension contributes to clustering of neurotransmitter vesicles at presynaptic terminals. Proc. Natl. Acad. Sci. *106*, 12611–12616.

Sigal, Y.M., Zhou, R., and Zhuang, X. (2018). Visualizing and discovering cellular structures with super-resolution microscopy. Science (80-.). *361*, 880–887.

Sigaut, L., Von Bilderling, C., Bianchi, M., Burdisso, J.E., Gastaldi, L., and Pietrasanta, L.I. (2018). Live cell imaging reveals focal adhesions mechanoresponses in mammary epithelial cells under sustained equibiaxial stress. Sci. Rep.

Sinha, B., Köster, D., Ruez, R., Gonnord, P., Bastiani, M., Abankwa, D., Stan, R. V., Butler-Browne, G., Vedie, B., Johannes, L., et al. (2011). Cells respond to mechanical stress by rapid disassembly of caveolae. Cell *144*, 402–413.

Sinkus, R., Lorenzen, J., Schrader, D., Lorenzen, M., Dargatz, M., and Holz, D. (2000). High-resolution tensor MR elastography for breast tumour detection. Phys. Med. Biol.

Sivaramakrishnan, S., Schneider, J.L., Sitikov, A., Goldman, R.D., and Ridge, K.M. (2009). Shear stress induced reorganization of the keratin intermediate filament network requires phosphorylation by protein kinase C ζ. Mol. Biol. Cell.

Slemmer, J.E., Matser, E.J.T., De Zeeuw, C.I., and Weber, J.T. (2002). Repeated mild injury causes cumulative damage to hippocampal cells. Brain.

Smith, M.A., Blankman, E., Gardel, M.L., Luettjohann, L., Waterman, C.M., and Beckerle, M.C. (2010). A Zyxin-mediated mechanism for actin stress fiber maintenance and repair. Dev. Cell *19*, 365–376.

Smith, M.A., Blankman, E., Deakin, N.O., Hoffman, L.M., Jensen, C.C., Turner, C.E., and Beckerle, M.C. (2013). LIM Domains Target Actin Regulators Paxillin and Zyxin to Sites of Stress Fiber Strain. PLoS One *8*, 1–12.

Song, X., Yang, J., Hirbawi, J., Ye, S., Perera, H.D., Goksoy, E., Dwivedi, P., Plow, E.F., Zhang, R., and Qin, J. (2012). A novel membrane-dependent on/off switch mechanism of talin FERM domain at sites of cell adhesion. Cell Res.

Spahn, C., Grimm, J.B., Lavis, L.D., Lampe, M., and Heilemann, M. (2019). Whole-Cell, 3D, and Multicolor STED Imaging with Exchangeable Fluorophores. Nano Lett.

Sparkes, I. (2016). Using optical tweezers to characterize physical tethers at membrane contact sites: Grab it, pull it, set it free? Front. Cell Dev. Biol.

Srivastava, N., Kay, R.R., and Kabla, A.J. (2017). Method to study cell migration under uniaxial compression. Mol. Biol. Cell.

Srivastava, N., Traynor, D., Piel, M., Kabla, A.J., and Kay, R.R. (2020). Pressure sensing through

Piezo channels controls whether cells migrate with blebs or pseudopods. Proc. Natl. Acad. Sci. U. S. A.

Stabley, D.R., Jurchenko, C., Marshall, S.S., and Salaita, K.S. (2012). Visualizing mechanical tension across membrane receptors with a fluorescent sensor. Nat. Methods *9*, 64–67.

Staudt, T., Engler, A., Rittweger, E., Harke, B., Engelhardt, J., and Hell, S.W. (2011). Far-field optical nanoscopy with reduced number of state transition cycles. Opt. Express.

Stephan, T., Roesch, A., Riedel, D., and Jakobs, S. (2019). Live-cell STED nanoscopy of mitochondrial cristae. Sci. Rep.

Stephenson, N.L., and Avis, J.M. (2012). Direct observation of proteolytic cleavage at the S2 site upon forced unfolding of the Notch negative regulatory region. Proc. Natl. Acad. Sci. U. S. A.

Stewart, M.P., Helenius, J., Toyoda, Y., Ramanathan, S.P., Muller, D.J., and Hyman, A.A. (2011). Hydrostatic pressure and the actomyosin cortex drive mitotic cell rounding. Nature.

Stigler, J., Ziegler, F., Gieseke, A., Gebhardt, J.C.M., and Rief, M. (2011). The complex folding network of single calmodulin molecules. Science (80-.).

Strale, P.O., Azioune, A., Bugnicourt, G., Lecomte, Y., Chahid, M., and Studer, V. (2016). Multiprotein Printing by Light-Induced Molecular Adsorption. Adv. Mater.

Strauss, S., Nickels, P.C., Strauss, M.T., Jimenez Sabinina, V., Ellenberg, J., Carter, J.D., Gupta, S., Janjic, N., and Jungmann, R. (2018). Modified aptamers enable quantitative sub-10-nm cellular DNA-PAINT imaging. Nat. Methods.

Strick, T., Allemand, J.F., Croquette, V., and Bensimon, D. (2000). Twisting and stretching single DNA molecules. Prog. Biophys. Mol. Biol.

Strick, T.R., Allemand, J.F., Bensimon, D., Bensimon, A., and Croquette, V. (1996). The elasticity of a single supercoiled DNA molecule. Science (80-.).

Stubb, A., Guzmán, C., Närvä, E., Aaron, J., Chew, T.L., Saari, M., Miihkinen, M., Jacquemet, G., and Ivaska, J. (2019). Superresolution architecture of cornerstone focal adhesions in human pluripotent stem cells. Nat. Commun. *10*.

Stutchbury, B., Atherton, P., Tsang, R., Wang, D.Y., and Ballestrem, C. (2017). Distinct focal adhesion protein modules control different aspects of mechanotransduction. J. Cell Sci. *130*, 1612–1624.

Sulchek, T.A., Friddle, R.W., Langry, K., Lau, E.Y., Albrecht, H., Ratto, T. V., DeNardo, S.J., Colvin, M.E., and Noy, A. (2005). Dynamic force spectroscopy of parallel individual Mucin1-antibody bonds. Proc. Natl. Acad. Sci. U. S. A.

Sun, Z., Guo, S.S., and Fässler, R. (2016a). Integrin-mediated mechanotransduction. J. Cell Biol.

Sun, Z., Tseng, H.Y., Tan, S., Senger, F., Kurzawa, L., Dedden, D., Mizuno, N., Wasik, A.A., Thery, M., Dunn, A.R., et al. (2016b). Kank2 activates talin, reduces force transduction across integrins and induces central adhesion formation. Nat. Cell Biol.

Sun, Z., Costell, M., and Fässler, R. (2019). Integrin activation by talin, kindlin and mechanical forces. Nat. Cell Biol.

Svitkina, T.M. (2018). Ultrastructure of the actin cytoskeleton. Curr. Opin. Cell Biol.

Svitkina, T.M., and Borisy, G.G. (1999). Arp2/3 complex and actin depolymerizing factor/cofilin in dendritic organization and treadmilling of actin filament array in lamellipodia. J Cell Biol *145*, 1009–1026.

Svoboda, K., and Block, S.M. (1994). Force and velocity measured for single kinesin molecules. Cell.

Svoboda, K., Schmidt, C.F., Schnapp, B.J., and Block, S.M. (1993). Direct observation of kinesin stepping by optical trapping interferometry. Nature.

Swaminathan, V., Kalappurakkal, J.M., Mehta, S.B., Nordenfelt, P., Moore, T.I., Koga, N., Baker, D.A., Oldenbourg, R., Tani, T., Mayor, S., et al. (2017). Actin retrograde flow actively aligns and orients ligand-engaged integrins in focal adhesions. Proc. Natl. Acad. Sci. U. S. A.

Sykes, C., and Plastino, J. (2010). Cell biology: Actin filaments up against a wall. Nature.

Symons, M.H., and Mitchison, T.J. (1991). Control of actin polymerization in live and permeabilized fibroblasts. J. Cell Biol.

Tadokoro, S., Shattil, S.J., Eto, K., Tai, V., Liddington, R.C., de Pereda, J.M., Ginsberg, M.H., and Calderwood, D.A. (2003). Talin binding to integrin beta tails: a final common step in integrin activation. Science (80-.). *302*, 103–106.

Tamada, M., Sheetz, M.P., and Sawada, Y. (2004). Activation of a signaling cascade by cytoskeleton stretch. Dev. Cell.

Tapia-Rojo, R., Alonso-Caballero, A., and Fernandez, J.M. (2020). Direct observation of a coil-to-helix contraction triggered by vinculin binding to talin. Sci. Adv.

Theodosiou, M., Widmaier, M., Böttcher, R.T., Rognoni, E., Veelders, M., Bharadwaj, M., Lambacher, A., Austen, K., Müller, D.J., Zent, R., et al. (2016). Kindlin-2 cooperates with talin to activate integrins and induces cell spreading by directly binding paxillin. Elife *5*, e10130.

Thievessen, I., Thompson, P.M., Berlemont, S., Plevock, K.M., Plotnikov, S. V., Zemljic-Harpf, A., Ross, R.S., Davidson, M.W., Danuser, G., Campbell, S.L., et al. (2013). Vinculin-actin interaction couples actin retrograde flow to focal adhesions, but is dispensable for focal adhesion growth. J. Cell Biol. *202*, 163–177.

Thompson, D.W., and Bonner, J.T. (2014). On growth and form.

Tijore, A., Yao, M., Wang, Y.-H., Nematbakhsh, Y., Hariharan, A., Teck Lim, C., and Sheetz, M. (2018). Mechanical Stretch Kills Transformed Cancer Cells. BioRxiv.

Tofangchi, A., Fan, A., and Saif, M.T.A. (2016). Mechanism of Axonal Contractility in Embryonic Drosophila Motor Neurons In Vivo. Biophys. J.

Tojkander, S., Gateva, G., and Lappalainen, P. (2012). Actin stress fibers - Assembly, dynamics and biological roles. J. Cell Sci. *125*, 1855–1864.

Tønnesen, J., Katona, G., Rózsa, B., and Nägerl, U.V. (2014). Spine neck plasticity regulates compartmentalization of synapses. Nat. Neurosci. *17*, 678–685.

Totsukawa, G., Wu, Y., Sasaki, Y., Hartshorne, D.J., Yamakita, Y., Yamashiro, S., and Matsumura, F. (2004). Distinct roles of MLCK and ROCK in the regulation of membrane protrusions and focal adhesion dynamics during cell migration of fibroblasts. J. Cell Biol.

Tse, J.M., Cheng, G., Tyrrell, J.A., Wilcox-Adelman, S.A., Boucher, Y., Jain, R.K., and Munn, L.L. (2012). Mechanical compression drives cancer cells toward invasive phenotype. Proc. Natl. Acad. Sci. U. S. A.

Tsunoyama, T.A., Watanabe, Y., Goto, J., Naito, K., Kasai, R.S., Suzuki, K.G.N., Fujiwara, T.K., and Kusumi, A. (2018). Super-long single-molecule tracking reveals dynamic-anchorage-induced integrin function. Nat. Chem. Biol. *14*, 497–506.

Tsuruta, D., and Jones, J.C.R. (2003). The vimentin cytoskeleton regulates focal contact size and adhesion of endothelial cells subjected to shear stress. J. Cell Sci.

Tyler, W.J. (2012). The mechanobiology of brain function. Nat. Rev. Neurosci.

Uemura, A., Nguyen, T.N., Steele, A.N., and Yamada, S. (2011). The LIM domain of zyxin is sufficient for force-induced accumulation of zyxin during cell migration. Biophys. J. *101*, 1069–1075.

Umans, B.D., and Liberles, S.D. (2018). Neural Sensing of Organ Volume. Trends Neurosci.

Unsain, N., Bordenave, M.D., Martinez, G.F., Jalil, S., Von Bilderling, C., Barabas, F.M., Masullo, L.A., Johnstone, A.D., Barker, P.A., Bisbal, M., et al. (2018). Remodeling of the Actin/Spectrin Membrane-associated Periodic Skeleton, Growth Cone Collapse and F-Actin Decrease during Axonal Degeneration. Sci. Rep. *8*, 3007.

Urban, N.T., Willig, K.I., Hell, S.W., and Nägerl, U.V. (2011). STED nanoscopy of actin dynamics in synapses deep inside living brain slices. Biophys. J.

Uyeda, T.Q.P., Iwadate, Y., Umeki, N., Nagasaki, A., and Yumura, S. (2011). Stretching actin filaments within cells enhances their affinity for the myosin ii motor domain. PLoS One *6*.

Vallotton, P., Ponti, A., Waterman-Storer, C.M., Salmon, E.D., and Danuser, G. (2003). Recovery, visualization, and analysis of actin and tubulin polymer flow in live cells: A fluorescent speckle microscopy study. Biophys. J.

Vangindertael, J., Camacho, R., Sempels, W., Mizuno, H., Dedecker, P., and Janssen, K.P.F. (2018). An introduction to optical super-resolution microscopy for the adventurous biologist. Methods Appl. Fluoresc.

Vassilopoulos, S., Gibaud, S., Jimenez, A., Caillol, G., and Leterrier, C. (2019). Ultrastructure of the axonal periodic scaffold reveals a braid-like organization of actin rings. Nat. Commun. *10*.

Lo Vecchio, S., Thiagarajan, R., Caballero, D., Vigon, V., Navoret, L., Voituriez, R., and Riveline, D. (2020). Collective Dynamics of Focal Adhesions Regulate Direction of Cell Motion. Cell Syst.

Vicente-Manzanares, M., Zareno, J., Whitmore, L., Choi, C.K., and Horwitz, A.F. (2007). Regulation of protrusion, adhesion dynamics, and polarity by myosins IIA and IIB in migrating cells. J. Cell Biol. *176*, 573–580.

Vicente-Manzanares, M., Ma, X., Adelstein, R.S., and Horwitz, A.R. (2009). Non-muscle myosin II takes centre stage in cell adhesion and migration. Nat. Rev. Mol. Cell Biol. *10*, 778–790.

Vieira, R. de C.A., Paiva, W.S., De Oliveira, D.V., Teixeira, M.J., De Andrade, A.F., and De Sousa, R.M.C. (2016). Diffuse axonal injury: Epidemiology, outcome and associated risk factors. Front. Neurol.

Vignaud, T., Copos, C., Leterrier, C., Tseng, Q., Blanchoin, L., Mogilner, A., Théry, M., and Kurzawa, L. (2020). Stress fibers are embedded in a contractile cortical network. 1–26.

Vigouroux, C., Henriot, V., and Le Clainche, C. (2020). Talin dissociates from RIAM and associates to vinculin sequentially in response to the actomyosin force. Nat. Commun. *11*, 1–11.

Vleugel, M., Kok, M., and Dogterom, M. (2016). Understanding force-generating microtubule systems through in vitro reconstitution. Cell Adhes. Migr. *10*, 475–494.

Walling, B.L., and Kim, M. (2018). LFA-1 in T cell migration and differentiation. Front. Immunol.

Wang, L., and Xu, X.G. (2015). Scattering-type scanning near-field optical microscopy with reconstruction of vertical interaction. Nat. Commun.

Wang, A., Ma, X., Conti, M.A., Liu, C., Kawamoto, S., and Adelstein, R.S. (2010). Nonmuscle myosin II isoform and domain specificity during early mouse development. Proc. Natl. Acad. Sci. U. S. A.

Wang, G., Simon, D.J., Wu, Z., Belsky, D.M., Heller, E., O'Rourke, M.K., Hertz, N.T., Molina, H., Zhong, G., Tessier-Lavigne, M., et al. (2019a). Structural plasticity of actin-spectrin membrane skeleton and functional role of actin and spectrin in axon degeneration. Elife *8*.

Wang, H.B., Dembo, M., Hanks, S.K., and Wang, Y.L. (2001). Focal adhesion kinase is involved in mechanosensing during fibroblast migration. Proc. Natl. Acad. Sci. U. S. A.

Wang, M.D., Yin, H., Landick, R., Gelles, J., and Block, S.M. (1997). Stretching DNA with optical tweezers. Biophys. J.

Wang, Y.X., Wang, D.Y., Guo, Y.C., and Guo, J. (2019b). Zyxin: A mechanotransductor to regulate gene expression. Eur. Rev. Med. Pharmacol. Sci. *23*, 413–425.

Waterman-Storer, C.M., and Salmon, E.D. (1997). Actomyosin-based retrograde flow of microtubules in the lamella of migrating epithelial cells influences microtubule dynamic instability and turnover and is associated with microtubule breakage and treadmilling. J. Cell Biol.

Wei, S.C., Fattet, L., Tsai, J.H., Guo, Y., Pai, V.H., Majeski, H.E., Chen, A.C., Sah, R.L., Taylor, S.S., Engler, A.J., et al. (2015). Matrix stiffness drives epithelial-mesenchymal transition and tumour metastasis through a TWIST1-G3BP2 mechanotransduction pathway. Nat. Cell Biol.

Weichsel, J., and Schwarz, U.S. (2010). Two competing orientation patterns explain experimentally observed anomalies in growing actin networks. Proc. Natl. Acad. Sci. U. S. A.

Welch, M.D., and Way, M. (2013). Arp2/3-mediated actin-based motility: A tail of pathogen abuse. Cell Host Microbe.

Wells, R.G. (2013). Tissue mechanics and fibrosis. Biochim. Biophys. Acta - Mol. Basis Dis.

Von Wichert, G., Jiang, G., Kostic, A., De Vos, K., Sap, J., and Sheetz, M.P. (2003a). RPTP-α acts as a transducer of mechanical force on αv/β3-integrin-cytoskeleton linkages. J. Cell Biol.

Von Wichert, G., Haimovich, B., Feng, G.S., and Sheetz, M.P. (2003b). Force-dependent integrin-cytoskeleton linkage formation requires downregulation of focal complex dynamics by Shp2. EMBO J.

Widdicombe, J. (2006). Reflexes from the lungs and airways: Historical perspective. J. Appl.

Physiol.

Winkelman, J.D., Anderson, C.A., Suarez, C., Kovar, D.R., and Gardel, M.L. (2020). Evolutionarily diverse LIM domain-containing proteins bind stressed actin filaments through a conserved mechanism. Proc. Natl. Acad. Sci.

Winter, F.R., Loidolt, M., Westphal, V., Butkevich, A.N., Gregor, C., Sahl, S.J., and Hell, S.W. (2017). Multicolour nanoscopy of fixed and living cells with a single STED beam and hyperspectral detection. Sci. Rep.

Wolf, K., Wu, Y.I., Liu, Y., Geiger, J., Tam, E., Overall, C., Stack, M.S., and Friedl, P. (2007). Multi-step pericellular proteolysis controls the transition from individual to collective cancer cell invasion. Nat. Cell Biol.

Wolfenson, H., Meacci, G., Liu, S., Stachowiak, M.R., Iskratsch, T., Ghassemi, S., Roca-Cusachs, P., O'Shaughnessy, B., Hone, J., and Sheetz, M.P. (2016). Tropomyosin controls sarcomere-like contractions for rigidity sensing and suppressing growth on soft matrices. Nat. Cell Biol. *18*, 33–42.

Woo, S., and Gomez, T.M. (2006). Rac1 and RhoA promote neurite outgrowth through formation and stabilization of growth cone point contacts. J. Neurosci.

Woo, S.H., Lukacs, V., De Nooij, J.C., Zaytseva, D., Criddle, C.R., Francisco, A., Jessell, T.M., Wilkinson, K.A., and Patapoutian, A. (2015). Piezo2 is the principal mechanotransduction channel for proprioception. Nat. Neurosci.

Woodside, D.G., Obergfell, A., Talapatra, A., Calderwood, D.A., Shattil, S.J., and Ginsberg, M.H. (2002). The N-terminal SH2 domains of Syk and ZAP-70 mediate phosphotyrosine-independent binding to integrin beta cytoplasmic domains. J Biol Chem *277*, 39401–39408.

Wu, P.-H.H., Aroush, D.R.-B. Ben, Asnacios, A., Chen, W.-C.C., Dokukin, M.E., Doss, B.L., Durand-Smet, P., Ekpenyong, A., Guck, J., Guz, N. V., et al. (2018). A comparison of methods to assess cell mechanical properties. Nat. Methods *15*, 491–498.

Wu, X.T., Sun, L.W., Yang, X., Ding, D., Han, D., and Fan, Y.B. (2017). The potential role of spectrin network in the mechanotransduction of MLO-Y4 osteocytes. Sci. Rep.

Wu, Y.I., Frey, D., Lungu, O.I., Jaehrig, A., Schlichting, I., Kuhlman, B., and Hahn, K.M. (2009). A genetically encoded photoactivatable Rac controls the motility of living cells. Nature *461*, 104–108.

Xu, K., Babcock, H.P., and Zhuang, X. (2012). Dual-objective STORM reveals three-dimensional filament organization in the actin cytoskeleton. Nat. Methods *9*, 185–188.

Xu, K., Zhong, G., and Zhuang, X. (2013). Actin, Spectrin, and Associated Proteins Form a Periodic Cytoskeletal Structure in Axons. Science (80-.). *339*, 452–456.

Xu, W., Baribault, H., and Adamson, E.D. (1998). Vinculin knockout results in heart and brain defects during embryonic development. Development.

Xu, Z., Schaedel, L., Portran, D., Aguilar, A., Gaillard, J., Peter Marinkovich, M., Théry, M., and Nachury, M. V. (2017). Microtubules acquire resistance from mechanical breakage through intralumenal acetylation. Science (80-.).

Yago, T., Wu, J., Wey, C.D., Klopocki, A.G., Zhu, C., and McEver, R.P. (2004). Catch bonds govern

adhesion through L-selectin at threshold shear. J. Cell Biol.

Yang, B., Przybilla, F., Mestre, M., Trebbia, J.-B., and Lounis, B. (2014a). Large parallelization of STED nanoscopy using optical lattices. Opt. Express.

Yang, B., Wolfenson, H., Chung, V.Y., Nakazawa, N., Liu, S., Hu, J., Huang, R.Y.J., and Sheetz, M.P. (2020). Stopping transformed cancer cell growth by rigidity sensing. Nat. Mater.

Yang, J., Zhu, L., Zhang, H., Hirbawi, J., Fukuda, K., Dwivedi, P., Liu, J., Byzova, T., Plow, E.F., Wu, J., et al. (2014b). Conformational activation of talin by RIAM triggers integrin-mediated cell adhesion. Nat. Commun.

Yang, Y., Nguyen, E., Mege, R.-M., Ladoux, B., and Sheetz, M.P. (2018). Local Contractions Test Rigidity of E-Cadherin Adhesions. BioRxiv.

Yao, M., Goult, B.T., Chen, H., Cong, P., Sheetz, M.P., and Yan, J. (2014). Mechanical activation of vinculin binding to talin locks talin in an unfolded conformation. Sci. Rep. *4*, 4610.

Yao, M., Goult, B.T., Klapholz, B., Hu, X., Toseland, C.P., Guo, Y., Cong, P., Sheetz, M.P., and Yan, J. (2016). The mechanical response of talin. Nat. Commun. *7*, 11966.

Yap, Y.C., King, A.E., Guijt, R.M., Jiang, T., Blizzard, C., Breadmore, M.C., and Dickson, T.C. (2017). Mild and repetitive very mild axonal stretch injury triggers cystoskeletal mislocalization and growth cone collapse. PLoS One.

Yoganarasimha, S., Trahan, W.R., Best, A.M., Bowlin, G.L., Kitten, T.O., Moon, P.C., and Madurantakam, P.A. (2014). Peracetic acid: A practical agent for sterilizing heat-labile polymeric tissue-engineering scaffolds. Tissue Eng. - Part C Methods.

Yonemura, S., Wada, Y., Watanabe, T., Nagafuchi, A., and Shibata, M. (2010). alpha-Catenin as a tension transducer that induces adherens junction development. Nat. Cell Biol. *12*, 533–542.

Yoshigi, M., Hoffman, L.M., Jensen, C.C., Yost, H.J., and Beckerle, M.C. (2005). Mechanical force mobilizes zyxin from focal adhesions to actin filaments and regulates cytoskeletal reinforcement. J. Cell Biol. *171*, 209–215.

Yu, C. han, Rafiq, N.B.M., Krishnasamy, A., Hartman, K.L., Jones, G.E., Bershadsky, A.D., and Sheetz, M.P. (2013). Integrin-matrix clusters form podosome-like adhesions in the absence of traction forces. Cell Rep.

Yvon, A.M.C., Gross, D.J., and Wadsworth, P. (2001). Antagonistic forces generated by myosin II and cytoplasmic dynein regulate microtubule turnover, movement, and organization in interphase cells. Proc. Natl. Acad. Sci. U. S. A.

Zaidel-Bar, R., Ballestrem, C., Kam, Z., and Geiger, B. (2003). Early molecular events in the assembly of matrix adhesions at the leading edge of migrating cells. J. Cell Sci. *116*, 4605–4613.

Zaidel-Bar, R., Milo, R., Kam, Z., and Geiger, B. (2007a). A paxillin tyrosine phosphorylation switch regulates the assembly and form of cell-matrix adhesions. J. Cell Sci.

Zaidel-Bar, R., Itzkovitz, S., Ma'ayan, A., Iyengar, R., and Geiger, B. (2007b). Functional atlas of the integrin adhesome. Nat. Cell Biol. *9*, 858–867.

Zhang, B., Peng, F., Wu, D., Ingram, A.J., Gao, B., and Krepinsky, J.C. (2007). Caveolin-1 phosphorylation is required for stretch-induced EGFR and Akt activation in mesangial cells. Cell.

Signal.

Zhang, H., Landmann, F., Zahreddine, H., Rodriguez, D., Koch, M., and Labouesse, M. (2011). A tension-induced mechanotransduction pathway promotes epithelial morphogenesis. Nature *471*, 99–103.

Zhang, X., Jiang, G., Cai, Y., Monkley, S.J., Critchley, D.R., and Sheetz, M.P. (2008). Talin depletion reveals independence of initial cell spreading from integrin activation and traction. Nat. Cell Biol. *10*, 1062–1068.

Zhang, Y., Ge, C., Zhu, C., and Salaita, K. (2014). DNA-based digital tension probes reveal integrin forces during early cell adhesion. Nat. Commun. *5*, 1–10.

Zhao, J., Bian, Z.C., Yee, K., Chen, B.P.C., Chien, S., and Guan, J.L. (2003). Identification of transcription factor KLF8 as a downstream target of focal adhesion kinase in its regulation of cyclin D1 and cell cycle progression. Mol. Cell.

Zhao, Q., Zhou, H., Chi, S., Wang, Y., Wang, J., Geng, J., Wu, K., Liu, W., Zhang, T., Dong, M.Q., et al. (2018). Structure and mechanogating mechanism of the Piezo1 channel. Nature.

Zheng, C.Y., Seabold, G.K., Horak, M., and Petralia, R.S. (2011a). MAGUKs, synaptic development, and synaptic plasticity. Neuroscientist.

Zheng, P., Cao, Y., and Li, H. (2011b). Facile method of constructing polyproteins for single-molecule force spectroscopy studies. Langmuir.

Zhong, G., He, J., Zhou, R., Lorenzo, D., Babcock, H.P., Bennett, V., and Zhuang, X. (2014). Developmental mechanism of the periodic membrane skeleton in axons. Elife *3*, 1–21.

Zhou, D.W., Lee, T.T., Weng, S., Fu, J., and García, A.J. (2017). Effects of substrate stiffness and actomyosin contractility on coupling between force transmission and vinculin-paxillin recruitment at single focal adhesions. Mol. Biol. Cell.

Zhou, R., Han, B., Xia, C., and Zhuang, X. (2019). Membrane-associated periodic skeleton is a signaling platform for RTK transactivation in neurons. Science (80-.). *365*, 929–934.